

Materials Horizons: From Nature to Nanomaterials

Jung Bahadur Singh

Alloy 625

Microstructure, Properties and Performance



Springer

Materials Horizons: From Nature to Nanomaterials

Series Editor

Vijay Kumar Thakur, School of Aerospace, Transport and Manufacturing,
Cranfield University, Cranfield, UK

Materials are an indispensable part of human civilization since the inception of life on earth. With the passage of time, innumerable new materials have been explored as well as developed and the search for new innovative materials continues briskly. Keeping in mind the immense perspectives of various classes of materials, this series aims at providing a comprehensive collection of works across the breadth of materials research at cutting-edge interface of materials science with physics, chemistry, biology and engineering.

This series covers a galaxy of materials ranging from natural materials to nanomaterials. Some of the topics include but not limited to: biological materials, biomimetic materials, ceramics, composites, coatings, functional materials, glasses, inorganic materials, inorganic-organic hybrids, metals, membranes, magnetic materials, manufacturing of materials, nanomaterials, organic materials and pigments to name a few. The series provides most timely and comprehensive information on advanced synthesis, processing, characterization, manufacturing and applications in a broad range of interdisciplinary fields in science, engineering and technology.

This series accepts both authored and edited works, including textbooks, monographs, reference works, and professional books. The books in this series will provide a deep insight into the state-of-art of Materials Horizons and serve students, academic, government and industrial scientists involved in all aspects of materials research.

Review Process

The proposal for each volume is reviewed by the following:

1. Responsible (in-house) editor
2. One external subject expert
3. One of the editorial board members.

The chapters in each volume are individually reviewed single blind by expert reviewers and the volume editor.

More information about this series at <https://link.springer.com/bookseries/16122>

Jung Bahadur Singh

Alloy 625

Microstructure, Properties and Performance



Springer

Jung Bahadur Singh
Mechanical Metallurgy Division
Bhabha Atomic Research Centre
Mumbai, Maharashtra, India

ISSN 2524-5384

ISSN 2524-5392 (electronic)

Materials Horizons: From Nature to Nanomaterials

ISBN 978-981-19-1561-1

ISBN 978-981-19-1562-8 (eBook)

<https://doi.org/10.1007/978-981-19-1562-8>

© The Editor(s) (if applicable) and The Author(s), under exclusive license to Springer Nature Singapore Pte Ltd. 2022

This work is subject to copyright. All rights are solely and exclusively licensed by the Publisher, whether the whole or part of the material is concerned, specifically the rights of translation, reprinting, reuse of illustrations, recitation, broadcasting, reproduction on microfilms or in any other physical way, and transmission or information storage and retrieval, electronic adaptation, computer software, or by similar or dissimilar methodology now known or hereafter developed.

The use of general descriptive names, registered names, trademarks, service marks, etc. in this publication does not imply, even in the absence of a specific statement, that such names are exempt from the relevant protective laws and regulations and therefore free for general use.

The publisher, the authors and the editors are safe to assume that the advice and information in this book are believed to be true and accurate at the date of publication. Neither the publisher nor the authors or the editors give a warranty, expressed or implied, with respect to the material contained herein or for any errors or omissions that may have been made. The publisher remains neutral with regard to jurisdictional claims in published maps and institutional affiliations.

This Springer imprint is published by the registered company Springer Nature Singapore Pte Ltd.
The registered company address is: 152 Beach Road, #21-01/04 Gateway East, Singapore 189721,
Singapore

Knowing is not understanding. There is a great difference between knowing and understanding: you can know a lot about something and not really understand it.

Charles F. Kettering

*Dedicated to
My Father Sardar Harbans Singh and
all who lost their lives during the COVID-19
Pandemic*

Foreword

The materials research at the Department of Atomic Energy (DAE) plays a vital role in providing sustaining support to the Indian nuclear program and developing advanced technologies for DAE applications. Materials Group of Bhabha Atomic Research Centre (BARC) encompasses all aspects of materials development from ore to component. It has a proactive research program for in-depth analysis of material studies using advanced characterization techniques and to establish structure–property correlations for the trouble-free operation of DAE plants. India Heavy Water Plants based on mono-thermal $\text{NH}_3\text{-H}_2$ exchange process use Alloy 625 tubes for cracking partially deuterium (D) enriched ammonia ($\text{N}(\text{H},\text{D})_3$) gas into a mixture of $(\text{H},\text{D})_2$ and N_2 gases.

Besides its use in the nuclear industry, Alloy 625 is often used in chemical processing, power, aerospace, and automobile industries owing to its unique combination of high strength, excellent fabricability and weldability, and outstanding corrosion resistance. The alloy undergoes significant microstructural modifications during long-term thermal exposure at intermediate temperatures. It develops complex microstructures by precipitating several competing intermetallic phases and carbides in the disordered nickel matrix. These microstructural changes harden the alloy and significantly reduce its ductility and toughness, often below the codal requirements. There is an extensive literature in peer-reviewed journals and conference proceedings dealing with various aspects of alloy's properties and behavior. However, a consolidation of these works is long overdue to bring all the data in an engineering perspective for the study and assessment of structural damage and properties lost. This book reflects the author's lifetime understanding of the physical metallurgy of and structure–properties correlations in Alloy 625 and other nickel-base superalloys and associated model alloys. The book provides: (i) different types of microstructural changes Alloy 625 undergoes at intermediate temperatures; (ii) properties deterioration due to such microstructural changes; (iii) corrosion behavior of the alloy in different environments; and (iv) criteria to assess the alloy damage for various destructive and non-destructive testing during in-service inspection of plants.

The book is divided into eight chapters covering almost all aspects, ranging from phase transformations, mechanical behavior, corrosion, damage mechanisms, etc.,

of Alloy 625. The author has given a detailed description of these transformations and their effects on alloy's mechanical properties to fully understand their precipitation behavior in the alloy. The author has brought the industrial data and literature together for damage assessment of service exposed Alloy 625 components. All the chapters are presented with a pedagogical introduction to metallurgical principles necessary for understanding the subject. The selection of the book's content is based on peer-reviewed literature on Alloy 625, and successful applications of concepts in resolving issues related to the failure and life-management of service exposed tubular components. A distinguishing feature of the book is a chapter exclusively for the life-management of Alloy 625 components. This monograph would prove to be of excellent value for the safe and reliable operation and maintenance of Alloy 625 components and their life extensions.

The present book will be helpful to students, researchers, and industrial professionals interested in Alloy 625.

In my judgment, the author has done a commendable job while combining various properties of Alloy 625 in this compendium. Such a compendium was missing despite a large volume of the data in the literature. I compliment the author for this achievement.



Ajit Kumar Mohanty

Dr. Ajit Kumar Mohanty
Director, Bhabha Atomic Research Centre
Member, Atomic Energy Commission
Mumbai, India
director@barc.gov.in

Preface

Ever since the introduction of Alloy 625 in the early 1960s, it continues to find several applications in aerospace, automobile, chemical processing, oil refining and production, marine, waste treatment, pulp and paper, power, and nuclear industries. The high chromium and molybdenum concentrations in Alloy 625 provide superior resistance to a wide range of corrosive environments. The alloy possesses excellent mechanical properties in the intermediate temperature range. The excellent fabricability and weldability of the alloy allow it to be easily fabricated into various products, like thin-walled tubing, reaction vessels, distillation columns, heat exchangers, valves, etc. The alloy commands nearly a 12% share of the nickel-base superalloys' world market of about 9 billion USD, growing at about 7% cumulative annual growth rate in recent years.

The alloy undergoes significant microstructural modifications during prolonged thermal exposure at intermediate temperatures. It precipitates multiple intermetallic and carbide phases in the disordered nickel matrix, including the precipitation of the $\text{Ni}_2(\text{Cr},\text{Mo})$ phase whose precipitation in Alloy 625 was first reported in the mid-1990s. The simultaneous precipitation of these phases develops a complex microstructure and hardens the alloy. Increase in the alloy's strength is accompanied by a decrease in its ductility and toughness. There are numerous reports in peer-reviewed journals and conference proceedings dealing with precipitation behavior of these phases in Alloy 625 and their effects on alloy's properties. Consolidating these works is long overdue to bring all the data together.

The microstructural changes during service exposure have a direct bearing on the mechanical properties, which often deteriorates below the components' codal requirements. Many critical components in various plants are likely to have operated for long durations and even have outlived their designed life. Such components need to be replaced regularly beyond their stipulated life. This compendium demonstrates that it is possible to reverse the damaged microstructure and rejuvenate the lost properties to codal requirements. The high cost of the alloy (about USD 26,000–35,000 per ton) makes it technically and economically justifiable to rejuvenate service spent components for utilizing them for a second service cycle.

A primary objective of the book is to bring all the results and literature together in one place, which can be used for the practice of damage assessment of the service exposed Alloy 625 components. This book is a first of its kind on Alloy 625, containing a compilation of the knowledge on the microstructural, mechanical properties and corrosion behavior of Alloy 625 since its development.

The selection of the book's content is based mainly on peer-reviewed literature on Alloy 625 and successful applications of concepts in resolving failure-analysis and rejuvenation issues of industrial processing plants. This knowledge would also be an excellent value concerning the safety, reliability, operation and maintenance of components and their life extensions in existing plants.

The book is divided into eight chapters. Chapter 1 gives a brief account of the importance of superalloys and their classifications, production, product forms and the market outlook, and the importance of Alloy 625 in a general manner. Chapter 2 briefly describes crystallographic aspects of various phases in Alloy 625 and lays a foundation for understanding their identification and evolution. The following two chapters deal with the precipitation of multiple phases and their effects on the microstructure and mechanical properties of the alloy. The precipitation of intermetallic phases significantly increases the strength of Alloy 625. Still, the alloy's sluggish aging response constrains its exploitation to age-harden it in a commercially viable manner. This led to the development of an age-hardenable variant of Alloy 625, known as Alloy 625 PLUS, by adding extra titanium to increase alloy's precipitation response without compromising the corrosion resistance and welding properties of Alloy 625. A separate chapter has been included on Alloy 625 PLUS to compare it with Alloy 625. The fabrication and corrosion behavior of Alloy 625 are discussed in individual chapters. The last chapter, on "Life Management of Alloy 625 Components", primarily addresses various types of damages the alloy undergoes at different temperatures and gives an account of properties' deterioration due to such microstructural changes.

In all the chapters, the reader is presented with a pedagogical introduction to metallurgical principles for developing an understanding of the subject covered in the chapter. An attempt is made to explain properties with illustrative examples. The alloys are usually referred to by their generic names throughout the chapters, and their compositions are mentioned in weight percent unless specified otherwise.

The book would guide engineers in the industry interested in using Alloy 625 for components' design. The book would also be helpful for students in colleges and universities pursuing advanced degrees in Materials Science and Engineering, Mechanical Engineering and Chemical Engineering, and as an international reference for lectures giving courses at both undergraduate and postgraduate levels.

Mumbai, India

Jung Bahadur Singh

Acknowledgements

It is my pleasure to acknowledge the friends and colleagues who have been helpful, directly or indirectly, in writing this book. This book is based on decades of physical metallurgy and structure–properties relation studies on Alloy 625 at Bhabha Atomic Research Centre (BARC), Mumbai. I am indebted to Late Drs. S. Banerjee and P. Mukhopadhyay for introducing me to phase transformation studies in nickel-base alloys after my joining the Materials Group of BARC. The pioneering work on the physical metallurgy of Inconel 625 and Inconel 718 alloys by Dr. M. Sundararaman laid the foundation for sustained activities on the structure–properties relationship of nickel-base superalloys at BARC. I am indebted to Dr. M. Sundararaman for his guidance on Inconel 625 and 718 alloys during the formative years of my research career at BARC.

I have been extremely fortunate to interact with many senior scientists and bright young colleagues during the course of my professional career. My sincere gratitude to my seniors and colleagues, Dr. S. Banerjee, Dr. P. Mukhopadhyay, Dr. M. Sundararaman, Dr. U. D. Kulkarni, Dr. J. K. Chakravarty, Dr. G. K. Dey, Dr. Madan-gopal Krishnan, Dr. D. Srivastava, Dr. R. Tewari, Dr. R. N. Singh, Dr. R. Kapoor, and Dr. B. C. Maji. Even informal interactions and discussions with them have enriched my understanding on physical metallurgy and structure–properties correlations. I take this opportunity to thank my younger colleagues and students, Dr. Amit Verma, Dr. K. V. Manikrishna, Dr. Shabana Khan, Smt. Malvika Karri, Shri. K. V. Ravikanth, Shri. Nachiket Keskar, Shri. Kumar Sourabh, Shri. Akash Gandhi, and Shri. T. N. Murty, who have given me many ideas and concepts that have helped this book. This list is, by no means, complete.

Interactions with scientists abroad, particularly with Late Dr. Patrick Veyssi  re and Dr. Georges Saada of ONERA, Ch  tillon, France, Drs. Alain Couret and Guy Mol  nat of CEMES Toulouse, France, and Prof. Pascal Bellon of the University of Illinois at Urbana-Champaign, USA, have been immensely helpful in nurturing understandings on many aspects of deformation behavior and phase transformations in crystalline materials.

I am grateful to the authors of various publications that have helped build my understanding and concepts on various topics covered in this book.

I acknowledge my indebtedness to Heavy Water Board (HWB) for entrusting its confidence in our group for resolving issues related to the performance, failure, and service degradation of superalloy components of its processing plants. The R&D support to HWB has given opportunities to investigate a large number of ammonia cracker tubes with different service exposures. These investigations have provided significant experience on the service degradation mechanisms and the extent of degradations during industrial exposure of the alloy.

Kind permissions by publishers Springer Nature, Elsevier, The Minerals, Metals & Materials Society, Scientific Electronic Library Online (SciELO) and by Dr. Sundararaman for allowing to use their copyright materials in the preparation of diagrams and figures are gratefully acknowledged.

I am grateful to Dr. Vivekanand Kain, Director, Materials Group, and Dr. R.N. Singh, Head, Mechanical Metallurgy Division, for their constant support and encouragement during the manuscript's preparation.

The journey of preparing the book's manuscript took about 14 months, and this would not have been possible without the generous help of many friends and students. I am grateful to Dr. Sundararaman, Dr. Madangopal Krishnan, Dr. Bikas Maji, Dr. Amit Verma, Dr. K. V. Manikrishna, Dr. Rajeev Kapoor, Smt. Malvika Karri, and Shri. Akash Gandhi for reviewing chapters critically for their technical consistency and accuracy. Their valuable comments and suggestions have helped to improve chapter's presentation. I am also grateful to Dr. S. Khan, Smt. Malvika Karri, Shri. K. V. Ravikanth, Shri. Akash Gandhi, and Shri. Kumar Sourabh for their substantial help in preparing figures and plots.

My sincere thanks to Dr. A.K. Mohanty, Director, Bhabha Atomic Research Centre, and Shri K.N. Vyas, Chairman, Atomic Energy Commission & Secretary, Department of Atomic Energy of India, for their inspiration and permission to publish this book.

I am thankful to the publisher, M/s Springer Nature, Singapore Pvt. Ltd., for publishing the book. The thorough review of the manuscript by the Editor, Ms. Priya Vyas and her team, is greatly appreciated.

The work on writing the book started during the challenging times of the COVID-19 pandemic. This pandemic has presented an unprecedented challenge to public health and led to a dramatic loss of human lives worldwide due to the virus and by denying health care to patients unrelated to COVID-19. I dedicate this book to the memory of my Father, Sardar Harbans Singh, and to all who lost their lives during the COVID-19 pandemic.

Finally, I express my indebtedness to my wife and family for their encouragement and understanding in reducing many of my responsibilities during the book's writing, which helped me focus on the writing with fewer distractions.

Jung Bahadur Singh

Contents

1	Introduction	1
1.1	High-Temperature Materials Called Superalloys	1
1.2	Journey of Superalloys	4
1.3	Alloying Additions in Superalloys	7
1.4	Types of Superalloys	11
1.4.1	Nickel-Base Superalloys	12
1.4.2	Iron-Base Superalloys	13
1.4.3	Cobalt-Base Superalloys	14
1.5	Melting and Consolidation of Superalloys	14
1.6	Product Forms	17
1.7	Market Outlook	18
1.7.1	Major Drivers	19
1.7.2	Market Size	20
1.7.3	Major Players and Tradenames	21
1.8	Alloy 625	22
1.9	Why a Book on Alloy 625?	24
	References	26
2	Phases in Alloy 625	29
2.1	Definitions of Phase, Crystal Structure and Solid-solution	29
2.2	Crystal Structures of Phases in Alloy 625	30
2.2.1	Gamma (γ) Phase	32
2.2.2	Gamma Double Prime (γ'') Phase	32
2.2.3	$\text{Ni}_2(\text{Cr}, \text{Mo})$ Phase	34
2.2.4	Delta (δ) Phase	35
2.2.5	Carbide Phases	36
2.2.6	Topologically Close-Packed Phases	38
2.3	Basic Concepts of Diffraction and Phase Identification	39
2.3.1	Diffraction Behavior of Crystalline Solids and the Bragg's Law	39
2.3.2	The Reciprocal Lattice	43

2.3.3	The Ewald Sphere	45
2.4	Lattice Correspondence Between Cubic and Non-cubic Phases	46
2.5	Identification of Phases in Alloy 625	47
2.5.1	Identification of the γ'' Phase	47
2.5.2	Identification of the $\text{Ni}_2(\text{Cr, Mo})$ Phase	50
2.5.3	Identification of the δ Phase	52
2.5.4	Identification of Carbide Phases	63
2.6	Summary	65
	References	65
3	Physical Metallurgy of Alloy 625	67
3.1	Alloying Additions in Alloy 625	67
3.1.1	Nickel	68
3.1.2	Chromium	69
3.1.3	Molybdenum	69
3.1.4	Tungsten	71
3.1.5	Niobium and Tantalum	71
3.1.6	Iron	73
3.1.7	Aluminum and Titanium	73
3.1.8	Carbon	74
3.1.9	Nitrogen	74
3.1.10	Sulfur	75
3.1.11	Phosphorus	75
3.1.12	Grain Boundary Strengthening Elements	75
3.1.13	Trace Elements	76
3.2	Characteristic Features of Phases in Alloy 625	76
3.2.1	Gamma (γ) Phase	76
3.2.2	Gamma Double Prime (γ'') Phase	78
3.2.3	Delta (δ) Phase	79
3.2.4	$\text{Ni}_2(\text{Cr, Mo})$ Phase	80
3.2.5	Carbide Phases	82
3.2.6	Topologically Close-Packed Phases	84
3.3	Solidification Behavior of Alloy 625	84
3.4	Phase Transformations in Alloy 625	88
3.5	Microstructural Evolution During Aging of Alloy 625	91
3.5.1	Precipitation of the γ'' Phase	92
3.5.2	Precipitation of the δ Phase	95
3.5.3	Precipitation of the $\text{Ni}_2(\text{Cr, Mo})$ Phase	97
3.5.4	Precipitation of the Carbide Phases	99
3.5.5	Precipitation of the TCP Phases	101
3.5.6	Precipitation-Free Zones	105
3.6	Summary	106
	References	106

4 Mechanical Behavior of Alloy 625	111
4.1 Fundamentals of Plastic Deformation of Crystalline Solids	111
4.1.1 Deformation by Slip	111
4.1.2 Deformation by Twinning	113
4.1.3 Deformation in Superlattice Compounds	115
4.2 Deformation Crystallography of Hardening Phases in Alloy 625	117
4.2.1 γ'' Phase	117
4.2.2 δ Phase	122
4.2.3 $Ni_2(Cr,Mo)$ Phase	124
4.3 Strengthening of Alloy 625	131
4.3.1 Solid-Solution Strengthening	131
4.3.2 Precipitation Strengthening	132
4.4 Deformation Micromechanisms in Alloy 625	136
4.4.1 Deformation of Particles by Shearing and Twinning	137
4.4.2 Effect of Particle Size on the Deformation Mode	138
4.5 Tensile Behavior of Alloy 625	140
4.5.1 Solution Annealed Alloy	140
4.5.2 Age-Hardened Alloy	143
4.5.3 Work-Hardening Behavior	151
4.6 Fatigue Behavior of Alloy 625	152
4.7 Creep Behavior of Alloy 625	159
4.8 Fracture Behavior of Alloy 625	165
4.9 Summary	169
References	169
5 Alloy 625 PLUS	175
5.1 Chemistry of Alloy 625 PLUS	175
5.2 Mechanical Properties of Alloy 625 PLUS	177
5.3 Microstructure of Alloy 625 PLUS	181
5.4 Summary	187
References	187
6 Fabrication	189
6.1 Hot Forming of Metals	189
6.1.1 Rate Controlling Phenomenon	190
6.1.2 Microstructural Changes during Hot Deformation	191
6.1.3 Hot Working of Alloy 625	193
6.2 Heat Treatments	196
6.2.1 Types of Heat Treatments	196
6.2.2 Prevention of Contamination	200
6.2.3 Fuels	201
6.2.4 Protective Atmosphere	201
6.3 Machining of Alloy 625	203

6.3.1	Conventional Machining	203
6.3.2	Hot Machining of Alloy 625	206
6.3.3	Non-conventional Machining	207
6.4	Welding of Alloy 625	211
6.4.1	Common Welding Practices for Alloy 625	211
6.4.2	Pre-welding Treatment of Alloy 625	214
6.4.3	Welding Metallurgy of Alloy 625	214
6.4.4	Mechanical Properties of Weldments	216
6.4.5	Weldability of Alloy 625	217
6.4.6	Post Weld Heat Treatment	221
6.4.7	Welding Behavior of Alloy 625 PLUS	224
6.5	Additive Manufacturing	225
6.5.1	Additive Manufacturing of Metals	225
6.5.2	Additive Manufacturing of Alloy 625	228
6.6	Summary	234
	References	234
7	Corrosion Behavior of Alloy 625	241
7.1	The Basic Concepts of Corrosion	242
7.1.1	The Electrochemical Principle	242
7.1.2	Polarization and Passivity	244
7.1.3	Corrosion Rate Expression	245
7.2	Role of Alloying Elements	245
7.3	General Corrosion	247
7.3.1	Hydrochloric Acid	247
7.3.2	Sulfuric Acid	248
7.3.3	Nitric Acid	249
7.3.4	Hydrofluoric Acid	251
7.3.5	Phosphoric Acid	252
7.3.6	Organic Acids	254
7.3.7	Salts	255
7.3.8	Seawater	256
7.3.9	Alkaline Solutions	257
7.4	Localized Corrosion	260
7.4.1	Pitting Corrosion	261
7.4.2	Crevice Corrosion	263
7.4.3	Intergranular Corrosion	265
7.5	Corrosion in High Temperature Pressurized Waters	267
7.5.1	Acidic High-Temperature Waters	270
7.5.2	Neutral High-Temperature Waters	272
7.5.3	Alkaline High-Temperature Waters	273
7.6	High-Temperature Corrosion	273
7.6.1	Oxidation	273
7.6.2	Carburization	275

7.6.3	Sulfidation	276
7.6.4	Halide Corrosion	277
7.6.5	Molten Salt Corrosion	279
7.7	Environmentally Assisted Cracking	280
7.7.1	Stress-Corrosion Cracking	281
7.7.2	Hydrogen Embrittlement	282
7.7.3	Sulfide Stress Cracking	283
7.8	Corrosion Behavior of Alloy 625 PLUS	285
7.9	Summary	287
	References	288
8	Life Management of Alloy 625 Components	293
8.1	Definitions of Damage, Failure, and Life	294
8.2	Basic Philosophy of Life Management	295
8.3	Damage Mechanisms in Alloy 625 During Service Exposure	296
8.3.1	Microstructural Damage	297
8.3.2	Structural Damage	299
8.4	Damage Assessment in Alloy 625	299
8.4.1	Assessment Based on Extrapolation of Statistics of Past Failures	301
8.4.2	Assessment Based on Hardness	301
8.4.3	Assessment Based on Microstructure Cataloging	302
8.4.4	Assessment of Damage by Ultrasonic Measurements	303
8.4.5	Assessment Based on Bulk Creep Damage	306
8.4.6	Assessment Based on Fracture Mechanics Analysis	307
8.4.7	Assessment Based on Microstructural Examination of Cavitation Damage	311
8.5	Life-Limiting Damage Criteria for Alloy 625 Components	311
8.5.1	Maximum Hardness of 350 BHN	313
8.5.2	Minimum 10% Elongation at the Operating Temperature	313
8.5.3	Maximum Microstructural Damage	313
8.5.4	Life Expenditure and Minimum Thickness Criteria for the Creep Dominant Damage	315
8.5.5	Class D Damage for Creep Cavitation	315
8.6	Case Studies on the Performance of Alloy 625 Ammonia Cracker Tubes	315
8.6.1	Service Degradation of Tubes and Rejuvenation of Lost Properties	317
8.6.2	Failure of Tubes at a Temperature Less Than 550 °C	320
8.6.3	Fish Mouth Opening of a Tube by Temperature Excursion	322
8.7	Summary	323
	References	324

Appendix A: Superalloy Compositions	327
Appendix B: Mechanical Properties	337
Appendix C: Physical Properties of Alloy 625	345
Appendix D: Metallography of Alloy 625	349
Appendix E: Hardness Conversion Table	355

About the Author

Dr. Jung Bahadur Singh Head, Structure of Materials Section of the Mechanical Metallurgy Division of Bhabha Atomic Research Centre (BARC), Mumbai, is a leading expert in the areas of nickel-based superalloys and structure–properties correlations. He joined BARC in 1991 after completing an advance course in nuclear engineering with metallurgy as the specialization. He did his B.Tech. in Metallurgical Engineering from Indian Institute of Technology, Kanpur, in 1990, and obtained a Ph.D. from Indian Institute of Technology, Bombay, in 2002. Dr. Singh has an accomplished career demonstrating consistent success as a researcher and a teacher and has made significant contributions in the fields of phase transformations and deformation behavior of metallic systems. He has carried out decisive experiments to advance the understanding of microstructural evolution and micro-mechanisms of plasticity in advance alloys. He is Professor of Engineering Sciences, Homi Bhabha National Institute (HBNI), Mumbai, and has taught courses related to “Physical Metallurgy,” “Plasticity and Strengthening Mechanisms in Crystalline Materials,” and “Materials characterization.” He has guided many students for their M.Tech. and Ph.D. dissertations. He has been a visiting scientist to CEMES, Toulouse, France (in 2003 and in 2004), University of Illinois at Urbana-Champaign, USA (2005–2007), Helmholtz-Zentrum Berlin, Berlin, Germany (2011), and Institut Laue Langevin (ILL), Grenoble, France (2012).

Chapter 1

Introduction



The ever-increasing requirement for high-temperature strength and better corrosion-resistant materials for increasingly higher operating temperatures and stresses in the process industry always pushes the envelope for high-performance alloys. This resulted in the development of a variety of compositionally complex alloys, often called “superalloys”, containing various alloying elements, which impart required mechanical and corrosion properties. At the same time, these alloys are very sensitive to certain impurities that need to be controlled for desired properties. These requirements entail special care during their melting and fabrication. The high-performance alloys, such as Alloy 625, have excellent combinations of mechanical strength and surface stability at high temperatures. Commercially, high-performance alloys control a sizable market size, and their economic importance is reflected in the continued research for their further development. This chapter gives an overview of the development, manufacturing, applications and market outlook of high-performance alloys.

1.1 High-Temperature Materials Called Superalloys

Superalloys are highly concentrated alloys, based on Group VIII A elements, designed to meet material challenges of high temperature and aggressive environments of gas turbine engines or industries involved in the processing of metals, chemical and nuclear waste. They exhibit excellent long-time strength and resistance against creep, corrosion, oxidation and erosion at temperatures above 650 °C, along with good surface stability. Superalloys have an austenite face-centered cubic (FCC) matrix that contains several elements in various combinations to accord desired properties. They may also contain second-phase particles to precipitate harden the austenite matrix. Superalloys can be broadly classified into three broad categories, namely, (i) iron-base superalloys; (ii) nickel-base superalloys, and; (iii) cobalt-base superalloys.

At low temperatures, under static loading conditions, properties like yield strength or ultimate tensile strength, which are measured over short-time intervals, are important for the material. Other properties, such as modulus, crack growth rates, and fracture toughness, are also important even though they are related to the strength of the material. A component designed based on these properties would continue to operate indefinitely within the designed operating conditions if no surface degradation due to environmental damage occurs. At temperatures above about $0.5T_m$ (T_m is melting temperature in Kelvin) and under dynamic loading conditions, time-dependent material behaviors like creep or fatigue also become important. Thus, creep strength or stress-rupture strength (also called rupture strength) of metal at elevated temperatures is also as important as the yield and ultimate tensile strengths. Similarly, fatigue strengths are also necessary under dynamic loading conditions, along with the yield and ultimate tensile strengths.

Superalloys are excellent materials for high-temperature applications because of their inherent strengths at elevated temperatures and phase stability [1]. All superalloys have the FCC crystal structure, even though iron and cobalt are body-centered and hexagonal, respectively, at low-temperatures. They transform to the face-centered cubic structure only at high temperatures. The addition of other elements stabilizes the face-centered structure of the two elements even at room temperature. Nickel has a face-centered cubic structure at all temperatures up to melting. Therefore, the upper limit for using superalloys is not restricted by phase transformation reactions, as observed in ferritic steels, which causes a sudden drop in their strengths. Another advantage of the austenitic matrix is its extended solubility for many alloying solutes, excellent ductility, and favorable characteristics for the precipitation strengthening phases.

The upper limit of the use of solid-solution superalloys is governed by their incipient melting temperatures. Incipient melting temperature is the temperature when the alloy melts locally and is lower than the liquidus temperature. The upper-temperature limit of precipitation-hardened alloys is governed by the solvus or stability temperature of the hardening phase. Table 1.1 gives the typical upper-temperature limit of using some wrought superalloys governed by the incipient melting or solvus/dissolution temperature of the hardening phases [2–5]. The incipient melting temperature and melting/solidification range of a superalloy is a function of its composition and prior processing. Superalloys, by their design, contain a large number of solutes, especially transition elements, in high concentrations. The transition elements often segregate during solidification to create non-equilibrium composition phases that melt at temperatures lower than the equilibrium composition. Further, as these alloys melt over a wide temperature range, superalloys do not melt at a specific temperature even in wrought conditions where the segregation effect is negligible.

The high-temperature applications of superalloys include components for aerospace and metal, chemical and nuclear processing industries that require high resistance against heat, corrosion, or both. The significance of superalloys in the modern industry can be gauged from their usage in aircraft gas turbine engines. The total contribution of superalloys in aircraft gas turbine engines in 1950s was

Table 1.1 Typical upper-temperature limit of the usage of some wrought superalloys restricted by their incipient melting temperature or solvus temperature of their hardening phases [2–5]

Alloy	Upper-temperature limit (°C)	Temperature limiting behavior
Hastelloy X	1250	Incipient melting temperature
Hastelloy 25 (L 605)	1330	Incipient melting temperature
Inconel 617	1330	Incipient melting temperature
Inconel 625	1290	Incipient melting temperature
Inconel X750	1395	Incipient melting temperature
A 286	855	Solvus of the γ' phase
Rene 95	1120	Solvus of the γ' phase
IN 100	1180–1200	Solvus of the γ' phase
U 700	1130–1150	Solvus of the γ' phase
Nimonic 80 A	960–980	Solvus of the γ' phase
Nimonic 90	1020–1060	Solvus of the γ' phase
Nimonic 105	1140–1160	Solvus of the γ' phase
Nimonic 263	910–925	Solvus of the γ' phase
Rene 41	1050–1070	Solvus of the γ' phase
Udimet 500	1050–1100	Solvus of the γ' phase
Waspaloy	1025–1040	Solvus of the γ' phase
Inconel 718	705	Stability of the γ'' phase
Custom age 625+	705	Stability of the γ'' phase
Haynes 242	705	Solvus of the $\text{Ni}_2(\text{Cr}, \text{Mo})$ phase

Table 1.2 Typical applications of superalloys in different industries and systems [6]

Industry/system	Components
Aircraft gas turbines	Disks, combustion chambers, bolts, casings, shafts, exhaust systems, cases, blades, vanes, burner cans, afterburners, thrust reversers
Steam turbine power plants	Bolts, blades, stack gas reheaters
Reciprocating engines	Turbochargers, exhaust valves, hot plugs, valve seat inserts
Metal processing	Hot-work tools and dies, casting dies
Medical applications	Dentistry uses, prosthetic devices
Space vehicles	Aerodynamically heated skins, rocket engine parts
Heat-treating equipment	Trays, fixtures, conveyor belts, baskets, fans, furnace mufflers
Nuclear power systems	Control rod drive mechanisms, valve stems, springs, ducting
Chemical and petrochemical industries	Bolts, fans, valves, reaction vessels, piping, pumps
Pollution control equipment	Scrubbers
Coal gasification and liquefaction	Heat exchangers, reheaters, piping
Metal processing mills	Ovens, afterburners, exhaust fans

about 10% by weight ¹ but had increased to 50% by 1985 [2]. Table 1.2 lists typical applications of superalloys in different industries or systems [6].

1.2 Journey of Superalloys

The insatiable thirst for high-temperature strength and better corrosion-resistant materials at increasingly higher operating temperatures and stresses has driven the development of superalloys, powered primarily by jet engine technology. The development of the stainless steel at the beginning of the twentieth century can be considered as the inception of the iron-base superalloys' journey. The British patent for Nichrome, a Ni–20Cr alloy, in 1918 served as a starting point for the development of Ni–Cr based superalloys like Nimonic and Inconel [1, 2]. Bedford, Pilling, and Merica produced a stronger Nichrome-based alloy, in 1929, by adding small amounts of titanium and aluminum, which was patented as Nimonic 80. However, in 1951, after the invention of electron microscopy, Taylor and Floyd unraveled the mystery that the precipitation of the now well-known γ' phase particles imparts Nimonic 80 a higher strength. Parallelly, a well-known cobalt-base alloy Vitallium, also known as Haynes Stellite 31, used in dentistry, was adapted for turbocharger and gas turbine

¹ The compositions of the alloys throughout the book are mentioned in weight per cent (wt%), unless specified otherwise.

applications. Besides, wrought S816 and cast X40 cobalt superalloys were introduced for gas turbine blades and vanes applications. In the late 1940s, adding molybdenum in alloy M-252 increased its solid-solution strength significantly. This started the more widespread use of refractory metals in nickel and iron-based superalloys [1]. Many of the early nickel–iron- and cobalt-base superalloys acquired additional strength by carbide phase particles' dispersion.

However, the need for high-temperature superalloys was not realized until the development of the aircraft gas turbine engines. Before gas turbine engines, the highest turbine inlet temperature of 550 °C was within the temperature capabilities of the stainless steel. The need for material with higher temperature capabilities was felt only after the successful 1937 flight of Hans von Ohain's turbine engine Heinkel in Germany and an independent 1939 flight of Whittle's engine in England. These developments had increased the turbine inlet temperature of jet engines to 780 °C, which was above the capability of conventional austenitic stainless steels. Stainless steels were then modified heavily to increase their highest operating temperatures, which led to the development of the first high-temperature superalloys, wrought Rex-78 alloy, for gas turbine engines (GTEs) [7, 8]. The advancements in the superalloy technology made rapid strides in the 1940s, driven by the developments from the World War II.

After World War II, the story of superalloys was dominated by further improvements and the invention of new alloys and new processes, driven first by the military use of jet engines and then by industries that needed industrial gas turbines. The alloy development virtually exploded in the '50s and '60s, while the process development in the '70s and '80s [7]. While the gas turbine engines prevailed upon the superalloy technology, superalloys were also developed for various other applications like high-temperature helium reactors, heat exchangers, furnaces, sour gas well equipment, etc.

The introduction of commercial vacuum melting technology in 1952 by Falih N. Darmara for better compositional control accelerated the superalloys technology. Both vacuum induction melting (VIM) and vacuum arc remelting (VAR) allowed the charge to remain molten for more extended periods, providing more time for degasification and removing volatile impurities. In addition, the two melting practices allow time for sampling and adjusting the composition of the melt. Vacuum induction melting also allows more effective use of beneficial trace elements, such as boron, manganese, and silicon, as deoxidants, which improve high-temperature properties [9]. A significant benefit of VIM was that it allowed the addition of much higher levels of aluminum and titanium to the alloy, which led to the development of widespread γ' precipitation-hardened nickel-base superalloys. Without the practice of vacuum melting and casting, these alloying elements would oxidize quickly, which renders their addition as strengthening solutes ineffective and makes the alloy unfit for most structural applications.

In 1962, H. Eiselstein patented a γ'' precipitate strengthened superalloy, Alloy 718, to cater for the needs of emerging jet engine technology. Alloy 718 replaced the highly alloyed steels and nickel-based superalloys. This alloy has been the most successful and versatile superalloy ever invented and rules the superalloy market

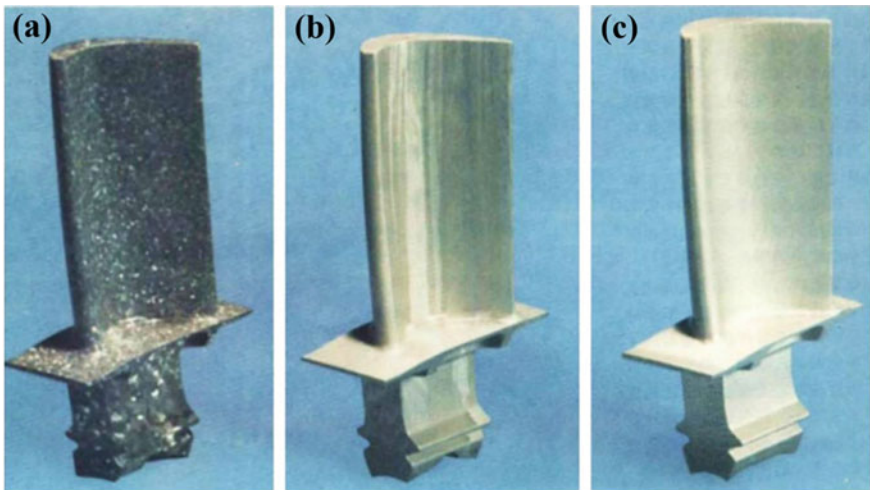


Fig. 1.1 Turbine blade castings showing conventional **a** equiaxed, **b** directionally solidified, and **c** single-crystal. Reprinted by permission from Springer Ref. [10]. Copyright (2018)

even after seven decades of its invention. The alloy is being used extensively in the aerospace, power generation, and oil and gas industries for fabricating highly engineered critical components exposed to hot corrosive environments.

By the 1970s, the superalloys had gained sufficient strength, creep resistance and adequate environmental resistance. The focus of the superalloy development had shifted to directional solidification and powder processing. One significant development was the commercialization of the directional solidification process to produce columnar and single crystal turbine blades (Fig. 1.1) [10]. The major breakthrough came around 1979 with the growth of the first commercial single crystal of PWA-1480 superalloy [11]. Single crystal blades have more creep life and permit their use at higher temperatures than their polycrystalline counterparts. Oxide dispersion strengthened (ODS) alloys were developed almost simultaneously through the powder-metallurgy route. Wrought γ' strengthened ODS alloys generate usable creep-rupture strength up to about 90% of the melting temperatures.

Later developments had seen a significant improvement in the properties of some alloys, particularly Ni–Cr–Mo alloys. A noteworthy development was the invention of a Ni–Cr–Mo precipitation-hardened alloy, Haynes 242 alloy, for gas turbine engine applications [5]. Haynes 242, and its derivative Haynes 244, are age-hardenable alloys hardened by the precipitation of $\text{Ni}_2(\text{Cr}, \text{Mo}, \text{W})$ phase [5, 12]. The $\text{Ni}_2(\text{Cr}, \text{Mo}, \text{W})$ phase differed from the usually observed γ' or γ'' hardening precipitates. In addition, the compositions of some existing alloys like Alloy 718 and Alloy 625 were modified for improvement in their properties. The modified alloys were commercialized as ATI 718 Plus [13] and Custom Age 625 Plus [4] alloys. A very recent development is the stabilization of the γ'' phase with a new composition, $(\text{Ni}, \text{Cr}, \text{W})_3(\text{Mo}, \text{Ti}, \text{Cr})$, in Ni–Cr–Mo–W–Ti alloys without the addition of niobium [14].

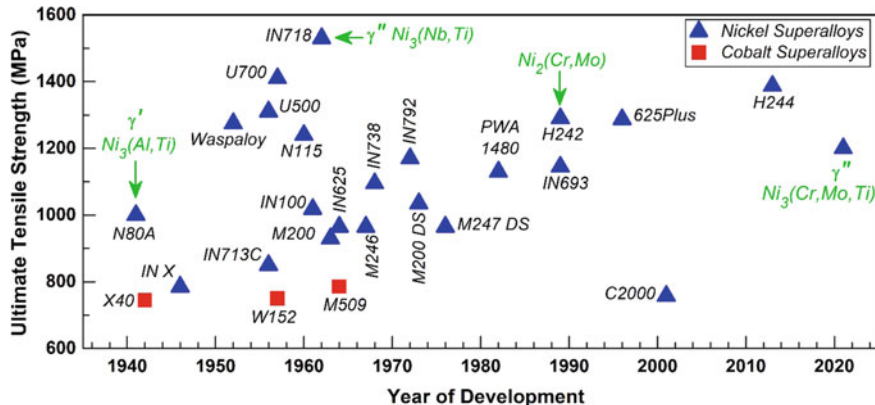


Fig. 1.2 A timeline of the developmental history of superalloys [1, 7]. Alloys arrow-marked with phases (γ' $\text{Ni}_3(\text{Al}, \text{Ti})$, γ'' $\text{Ni}_3(\text{Nb}, \text{Ti})$ or $\text{Ni}_2(\text{Cr}, \text{Mo})$) or indicate the commercial introduction of age hardenable alloys with the precipitation of respective phases. All the alloys, except for the γ'' $\text{Ni}_3(\text{Cr}, \text{Mo}, \text{Ti})$ strengthened alloys are commercial alloys. Details of commercial alloys are given in Appendix A and B. The γ'' $\text{Ni}_3(\text{Cr}, \text{Mo}, \text{Ti})$ strengthened alloy is a recently developed alloy [14].

The γ'' $(\text{Ni}, \text{Cr}, \text{W})_3(\text{Mo}, \text{Ti}, \text{Cr})$ has all the characteristic features of the γ'' Ni_3Nb phase in niobium bearing nickel alloys. The advantage of the γ'' $(\text{Ni}, \text{Cr}, \text{W})_3(\text{Mo}, \text{Ti}, \text{Cr})$ phase is that it is stable up to about 850 °C, much higher than the stability of the γ'' Ni_3Nb phase that transforms to the harmful δ phase at temperatures above 650 °C. The invention of the $(\text{Ni}, \text{Cr}, \text{W})_3(\text{Mo}, \text{Ti}, \text{Cr})$ hardened Ni–Cr–Mo alloys opens up the possibility of a new series of γ'' hardenable alloys. A timeline for the development of various types of superalloys is shown in Fig. 1.2.

1.3 Alloying Additions in Superalloys

Many elements in various combinations are added to superalloys to produce desired properties. Some elements dissolve into the solid solution, while others may induce the precipitation of second-phase particles during thermal exposure. In a solid solution, the alloying solute is distributed randomly within the host (solvent) matrix, while a precipitate may have a phase different from the matrix. The role of alloying elements and their influence on the stability of various phases depends strongly upon the position of elements in the periodic table. Based on their positions, alloying elements in superalloys can be categorized into three broad groups [1, 7, 15]: (i) Solid-solution hardener; (ii) intermetallic hardening phase former, and (iii) grain-boundary strengthener. The most common alloying additions that impart solid solution strengthening are chromium, aluminum, titanium, molybdenum, niobium, tungsten, etc. These solutes also stabilize the FCC structure of iron and cobalt solid solutions in respective superalloys. Alloying elements such as chromium, molybdenum,

niobium, tungsten, tantalum and titanium are also strong carbide formers, while chromium and molybdenum promote the formation of borides too [1]. The second group of elements are aluminum, titanium, niobium, and tantalum, which induce the formation of ordered phase particles such as $\text{Ni}_3(\text{Al}, \text{Ti})$ (γ' phase) and $\text{Ni}_3(\text{Nb}, \text{Ta}, \text{Ti})$ (γ'' phase). These solutes are characterized by atomic radii greater than nickel. The precipitation of such intermetallic phases generates a two-phase microstructure containing coherent particles of the γ' phase, γ'' phase, or both, which significantly increase the alloy's high-temperature strength and the resistance to creep deformation. Studies on the precipitation of another intermetallic phase with $\text{Ni}_2(\text{Cr}, \text{Mo}, \text{W})$ stoichiometry in nickel alloys have led to the invention of Haynes 242 and 244 alloys [4, 12]. The third group includes elements like boron, carbon, zirconium, hafnium, etc. which strengthen grain boundaries apart from forming grain-boundary precipitates. These elements have their atomic radii very different from the base element. Minor additions of carbon and boron form carbides and borides, respectively. Typical roles of major solutes in the three types of superalloys are given in Table 1.3.

Melting practices of superalloys invariably introduce some undesired tramp elements like silicon, phosphorous, sulfur, oxygen, nitrogen, etc. which need to be restricted to very low (parts-per-million) concentration levels. These elements segregate at grain boundaries and embrittle the alloy if their concentration is not restricted [7, 15]. Minor additions of some beneficial elements, like magnesium and manganese, and reactive solutes like titanium and niobium, remove detrimental effects by bonding with tramp elements. The bonding of manganese with sulfur to form MnS and titanium with nitrogen to form TiN to remove sulfur and nitrogen illustrates the beneficial roles of tramp elements.

Chromium and many other elements like aluminum, molybdenum, titanium and tungsten also resist environmental degradation. Chromium promotes the formation of the Cr_2O_3 layer on external surfaces of alloys, while the addition of aluminum enhances its oxidation resistance properties. Mo and W protect the Cr_2O_3 layer under various corrosive environments. Though Cr is the primary solute for hot corrosion resistance, the addition of titanium supplements its effect. Addition of rare earth elements lanthanum, yttrium and cerium in small quantity also promotes high temperature oxidation and corrosion resistance.

Even though elements like cobalt, chromium, molybdenum, tungsten, rhenium, etc., are added for their favorable alloying qualities, they may sometimes form undesirable topologically close-packed (TCP) phases (e.g., σ , μ , Laves, etc.) during processing and thermal aging. The precipitation of the TCP phases has little effect on yield strength of the alloy but may cause significant loss of corrosion resistance and ductility because of their hard and brittle nature.

The addition of vanadium to superalloys also contributes to their solid solution strengthening and precipitation hardening by carbide formation. However, its addition in superalloys is usually avoided because of its deleterious effects. Vanadium promotes the formation of the embrittling sigma (σ) phase. Moreover, the beneficial effects of chromium, molybdenum, and niobium at elevated temperatures outweigh the advantages of vanadium. In addition, at temperatures above 690 °C, vanadium may form V_2O_5 in oxidizing atmospheres that weaken the protective film, leading

Table 1.3 Major roles of solutes in different types of superalloys [8, 15]

Element	Iron-base	Cobalt-base	Nickel-base
Cr	<ul style="list-style-type: none"> – Improves hot corrosion and oxidation resistance – Solid-solution hardening 	<ul style="list-style-type: none"> – $M_{23}C_6$ and M_7C_3 carbide precipitation – Improves hot corrosion and oxidation resistance – Promotes TCP phases 	<ul style="list-style-type: none"> – $M_{23}C_6$ and M_7C_3 carbide precipitation – Improves hot corrosion and oxidation resistance – Moderate solid-solution hardening – Moderate increase in γ' volume fraction – Tend to stabilize Ni_2Cr phase in alloys containing more than 20% Cr – Promotes TCP phases
Al	<ul style="list-style-type: none"> – Induces γ' precipitation – Retards formation of hexagonal η Ni_3Ti phase 	<ul style="list-style-type: none"> – Improves oxidation resistance – Forms intermetallic β-CoAl 	<ul style="list-style-type: none"> – Moderate solid-solution hardening – Induces γ' precipitation – Improves oxidation resistance
Ti	<ul style="list-style-type: none"> – γ' precipitation – TiC carbide precipitation 	<ul style="list-style-type: none"> – TiC carbide precipitation – Formation of Co_3Ti intermetallic – Formation of Ni_3Ti with sufficient Ni – Reduces surface stability 	<ul style="list-style-type: none"> – Moderate solid-solution hardening – γ' precipitation – TiC carbide precipitation – Retards the precipitation of $Ni_2(Cr, Mo)$ phase particles
Mo	<ul style="list-style-type: none"> – Solid-solution hardening – Forms M_6C carbide precipitates 	<ul style="list-style-type: none"> – Solid-solution hardening – Forms Co_3Mo intermetallic precipitates – Promotes TCP phases 	<ul style="list-style-type: none"> – High solid-solution hardening – Moderate increase in γ' volume fraction – M_6C and MC carbide formation – Promotes formation of $Ni_2(Cr, Mo)$ phase particles – Promotes σ and μ TCP phases
W	<ul style="list-style-type: none"> – Solid-solution hardening – M_6C carbide precipitation 	<ul style="list-style-type: none"> – Solid-solution hardening – Formation of Co_3W intermetallic – Promotes TCP phases 	<ul style="list-style-type: none"> – High solid-solution hardening – Moderate increase in γ' volume fraction – M_6C carbide formation – Increases density – Promotes the formation of $Ni_2(Cr, Mo, W)$ particles – Promotes σ and μ TCP phases

(continued)

Table 1.3 (continued)

Element	Iron-base	Cobalt-base	Nickel-base
Ta	<ul style="list-style-type: none"> – γ'' precipitation – Forms TaC carbide precipitates 	<ul style="list-style-type: none"> – MC and M₆C carbide precipitation – Formation of Co₂Ta intermetallic – Reduces surface stability 	<ul style="list-style-type: none"> – High solid-solution hardening – TaC carbide precipitation – Large increase in γ' volume fraction – Improves oxidation resistance
Nb	<ul style="list-style-type: none"> – γ'' precipitation – NbC carbide precipitation – δ Ni₃Nb precipitation 	<ul style="list-style-type: none"> – MC and M₆C carbide precipitation – Formation of Co₂Nb intermetallic – Reduces surface stability 	<ul style="list-style-type: none"> – High solid-solution hardening – Large increase in γ' volume fraction – NbC carbide formation – γ'' precipitation – δ Ni₃Nb precipitation
Re	–	–	<ul style="list-style-type: none"> – Moderate solid-solution hardening – Increases γ/γ' lattice mismatch – Retards coarsening
Fe	– Not applicable	– Improves workability	<ul style="list-style-type: none"> – Decreases oxidation resistance – Promotes σ and Laves TCP phases – Improves workability
Co	–	– Not applicable	<ul style="list-style-type: none"> – Raises γ solidus temperature – Moderate increase in γ' volume fraction in some alloys – Raises γ' solvus temperature
Ni	<ul style="list-style-type: none"> – FCC matrix stabilizer – Inhibits TCP phase precipitation 	<ul style="list-style-type: none"> – FCC stabilizer – Decreases hot corrosion resistance 	– Not applicable
C	<ul style="list-style-type: none"> – Carbide formation – Stabilizes FCC matrix 	<ul style="list-style-type: none"> – Carbide formation – Decreases ductility 	<ul style="list-style-type: none"> – Carbide formation – Moderate solid-solution hardening
B	<ul style="list-style-type: none"> – Improves creep strength and ductility – Retards formation of grain-boundary η Ni₃Ti 	– Improves creep strength and ductility	<ul style="list-style-type: none"> – Moderate solid-solution hardening – Inhibits carbide coarsening – Improves grain-boundary strength – Improves creep strength and ductility

(continued)

Table 1.3 (continued)

Element	Iron-base	Cobalt-base	Nickel-base
Zr	<ul style="list-style-type: none"> – Improves creep strength and ductility – Retards formation of grain-boundary η Ni_3Ti 	<ul style="list-style-type: none"> – ZrC carbide formation – Improves creep strength and ductility – Reduces surface stability 	<ul style="list-style-type: none"> – Moderate solid-solution hardening – Inhibits carbide coarsening – Improves grain-boundary strength – Improves creep strength and ductility
Hf	–	–	<ul style="list-style-type: none"> – Improves creep strength and ductility – Improves grain-boundary strength – HfC formation – Promotes eutectic γ/γ' formation
V	<ul style="list-style-type: none"> – Improve notch ductility at elevated temperatures – Improves hot workability 	–	<ul style="list-style-type: none"> – Imparts extra passivation to some alloys in the certain liquid media

to catastrophic oxidation [16]. A limited number of superalloys that are known to contain small amounts of vanadium are Ni-100 alloy and alloys like Hastelloy B and Hastelloy C-276 (about 0.33% maximum) in which vanadium is added to impart extra passivation in certain liquid media [16].

1.4 Types of Superalloys

Superalloys are categorized according to the nature of the base metal. This section gives a brief overview of the three types and their classification based on the strengthening behavior. Producers of superalloys market them with tradenames. Some commonly used tradenames are Inconel, Hastelloy, Rene, Waspaloy, Incoloy, CMSX single crystal alloy, etc. Appendix A offers nominal compositions of commonly used superalloys. Further, some alloys, like Inconel 718, Incoloy 903, etc. contain nickel and iron contents in comparable amounts. Such alloys are also classified as iron-nickel alloys. However, in the present text, the classification is restricted to the already mentioned three categories (Sect. 1.1), and alloys containing comparable nickel and iron amounts are classified as nickel-based or iron-based merely on the basis of the higher of the two amount in their nominal compositions. The mechanical properties of some selected superalloys are given in Appendix B.

Table 1.4 Typical ranges of major alloying elements in different types of cast and wrought superalloys

Element	Range (%)		
	Ni-base	Fe-base	Co-base
Ni	Balance	9–33	0–35
Fe	0–38	Balance	0–21
Co	0–29	0–20	Balance
Cr	0–30	0–22	19–30
Mo	0–28	0–3	0–10
W	0–14	0–3	0–25
Al	0–7	0–1	0–1
Ti	0–5	0–3	0–4
Nb	0–6.5	0–5	0–4
Ta	0–10	0–1	0–9
Re	0–6	–	0–2

1.4.1 Nickel-Base Superalloys

High stability of the austenite nickel phase allows the addition of large amounts of various elements to tailor properties of alloys for a variety of applications. The high concentrations of solutes in nickel-base superalloys make them complex but the most exciting superalloys. They may contain up to 30% chromium, up to about 7% aluminum and titanium together, 5–15% cobalt, and many other transition elements like molybdenum, niobium, tungsten, etc. along with small amounts of boron, zirconium, magnesium, and carbon. Typical ranges of major solutes in superalloys are given in Table 1.4. The nickel-based superalloys can further be classified into two broad categories, as illustrated in Fig. 1.3. The first category contains alloys strengthened by solid-solution hardening, while the second category corresponds to alloys strengthened by the precipitation of intermetallic compounds of Ni_3X type in the nickel solid solution (γ) matrix. Alloys containing aluminum and titanium, such as Waspaloy, Astroloy, U-700, Rene 80, etc. are strengthened by the precipitation of γ' phase particles of $\text{Ni}_3(\text{Al}, \text{Ti})$ stoichiometry, while niobium bearing alloy, like Inconel 718 and Custom Age 625 Plus, are strengthened by the formation of γ'' phase precipitates of Ni_3Nb stoichiometry. Some alloys, like Alloy 718 and Alloy 706 containing niobium as well as aluminum and titanium are strengthened by both γ' and γ'' phase particles. On the other hand, solid-solution hardened alloys, such as Hastelloy N and Inconel 625, derive their strength from the side effects of major solutes. The solid solution strengthened alloys may sometimes have the precipitation of carbide particles in the austenite matrix.

A large number of nickel superalloys like C-4, C-22, C-276, Haynes 242 Alloy 625, Hastelloy S, etc. can be further classified into Ni–Cr–Mo alloys for driving their major properties, namely, strength and corrosion as well as oxidation resistance,

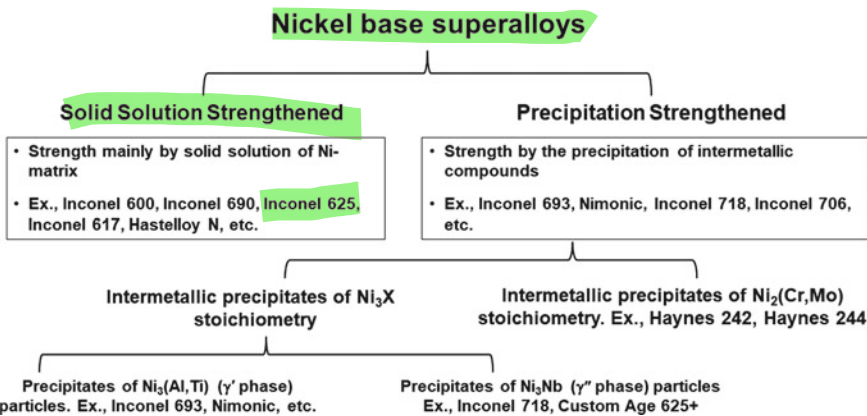


Fig. 1.3 Classification of nickel-base superalloys

from chromium and molybdenum solutes (Appendix A). Amount of chromium and molybdenum individually may vary significantly from one alloy to another but remain $5\% < Cr < 33\%$ and $5\% < Mo < 25\%$ such that they together contribute about $28\% < Cr + Mo < 40\%$. Most of these alloys are designed as solid-solution strengthened. Still, they often form Ni_2Y ($Y=Cr, Mo$) stoichiometry precipitates at temperatures ranging from about 400 to 650 °C, which increases their mechanical strengths. The formation of the $Ni_2(Cr, Mo)$ phase in Ni–Cr–Mo alloys has drawn significant attention of researchers on their hardening behavior in the last few decades. This has led to the invention of a new series of $Ni_2(Cr, Mo)$ precipitation-hardened Haynes 242 [5] and Haynes 244 [12] alloys.

The significant advantages of nickel-base superalloys are that many of them can be age-hardened by the precipitation of intermetallic γ' , γ'' and $Ni_2(Cr, Mo)$ phase particles, and have a low propensity for the formation of TCP phases compared to iron-base and cobalt-base superalloys. However, they are quite expensive. Nickel-based superalloys are most widely used for the hottest parts of gas turbine engines as blades, vanes, disks, etc. because they offer the highest strength and creep resistance at high temperatures.

1.4.2 Iron-Base Superalloys

Iron-base superalloys have evolved from austenitic stainless steel. They contain more than 20% nickel to stabilize the austenite phase and about 20% chromium to impart sufficient corrosion resistance. Iron-base superalloys are mostly solid-solution hardened, though a few of them can be precipitation-hardened that contained a high nickel content. The strengthening in precipitation-hardened alloys is primarily achieved by forming the γ' or γ'' phase, although carbides and carbonitrides may also be present. Alloys, like A286, that are strengthened by the γ' particles, typically contain about

25–35 wt% nickel, while alloys, like Incoloy 903, are strengthened by the precipitation of γ'' phase particles and includes a minimum of 40% nickel. A small amount of vanadium is sometimes added to iron-base alloys, e.g., in A286, to improve their hot workability and notch ductility at elevated temperatures.

The advantages of iron-base superalloys are their low cost and good workability. However, they have lower environmental resistance, lower strength at high temperatures and a higher propensity for forming TCP phases than nickel-base superalloys. Iron-base superalloys are suitable for applications that need high toughness at low-temperature applications like rotor fan disks, turbine casings, etc.

1.4.3 Cobalt-Base Superalloys

Cobalt crystallizes as the hexagonal close-packed phase at lower temperatures and transforms to the face-centered phase only at temperatures above 417 °C. A minimum of 10% nickel is added in cobalt-base superalloys to stabilize the FCC structure at all temperatures up to the melting point. Modern cobalt-base superalloys are characterized by solid solution strengthening. Titanium addition induces the precipitation of coherent, ordered Co_3Ti as a strengthening phase. During the late 1950s, two commercial cobalt-base alloys, Jetalloys J-1570 and J-1650, containing the coherent γ' precipitates stabilized by about 28% nickel, were briefly popular as precipitation strengthened alloys [1]. However, the rapid development of nickel-based γ' hardened alloys with superior mechanical properties and temperature stability led to their premature demise. Cobalt-base alloys also form M_{23}C_6 , M_6C , and MC carbide precipitates as in nickel-base superalloys, which are often used to impart some precipitation hardening. In addition to carbides, the cobalt-base alloys tend to form TCP phases like Co_2W and Co_7W_6 .

The significant advantages of cobalt-base superalloys are their higher incipient melting point and much superior hot corrosion resistance at high temperatures. Besides, cobalt-base alloys can be melted in air or argon, unlike the vacuum melting of nickel-base and iron-nickel-base alloys, which contain much higher amounts of reactive alloying elements like aluminum and titanium. However, cobalt-base superalloys have a higher propensity to precipitate undesirable TCP phases than nickel-base alloys. The strength of cobalt-base alloys is also limited compared to those of precipitation strengthened nickel-base or iron-base alloys. Cobalt-base alloys are suitable for applications like industrial gas turbine engines (GTEs), vanes, etc. where creep-resistant at low stresses or hot corrosion resistance is required.

1.5 Melting and Consolidation of Superalloys

Superalloys are usually produced through double melting practice, employing mainly vacuum induction melting (VIM) followed by either vacuum arc remelting (VAR) or

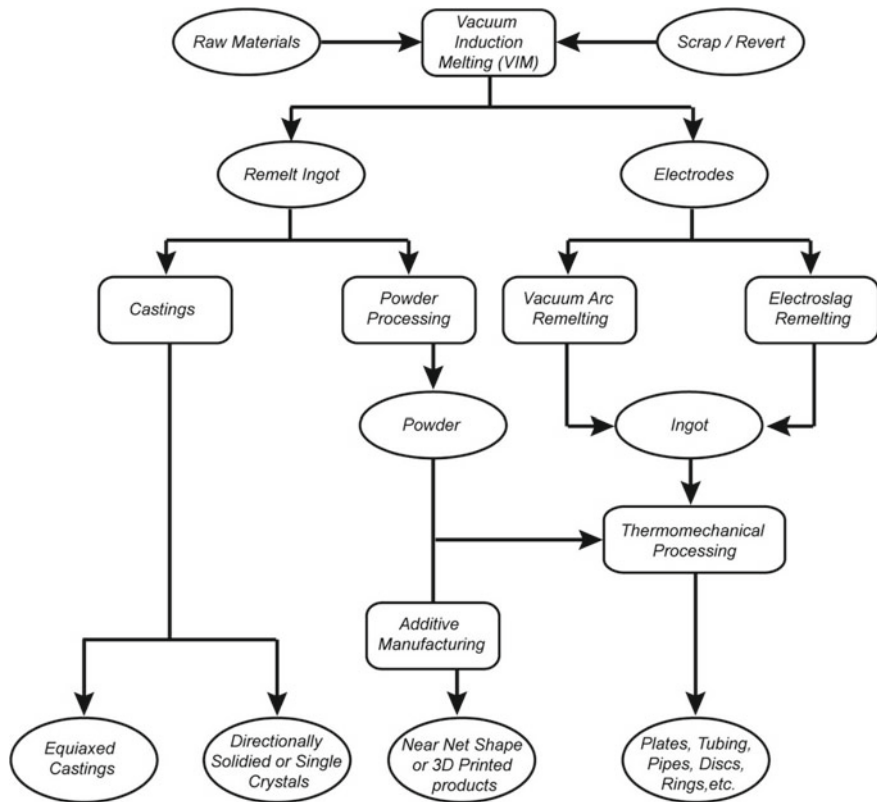


Fig. 1.4 Flow diagram of processes widely used to produce superalloy components

electro slag remelting (ESR) of the electrodes/ingots prepared by VIM. Figure 1.4 shows a flow chart of the processes used to produce superalloy products. Vacuum induction melting is the primary melting step in the process route of wrought and cast superalloys and near-net-shape products. Vacuum induction melting reduces oxygen and nitrogen contents significantly in the alloy and dramatically improves micro-cleanliness of the alloy with fewer oxides and nitrides in the final products. Additionally, it removes high-vapor-pressure impurities like lead and bismuth that may enter the alloy through the scrap circuit during the melting process. As a result, the vacuum-melted superalloys have improved fatigue and stress-rupture properties. The VIM, however, is costlier than the electric-arc furnace (EAF) or argon oxygen decarburization (AOD) processes usually employed for the production of stainless steel or other highly alloyed steels. The EAF or AOD processes are less preferred for melting superalloys as alloys pick up large amounts of impurities and undesirable elements during the melting.

The alloy ingots produced by EAF/AOD or VIM are subsequently remelted by secondary melting techniques under controlled conditions. Many inclusions are

removed by flotation or chemical and physical processes during secondary melting. The two most common secondary remelting methods are vacuum arc remelting (VAR) and electro slag remelting (ESR). The quality of ingots produced by the two remelting processes is significantly different because of the differences in the nature of impurities and defects created by the two processes and during subsequent solidification.

In VAR, an electric arc between the electrode and the bottom of the crucible (the stool) is set to melt the electrode, which drips into a water-cooled copper crucible and progressively builds the ingot. Melting is usually done in vacuum, but the partial pressure of argon or nitrogen is sometimes used to retain gas or high vapor-pressure elements in the alloy. The exposure of small volumes of molten metal to high vacuum removes harmful high-vapor-pressure elements, like lead and bismuth, that are not removed entirely during VIM. At the same time, it may also considerably reduce the concentration of the beneficial high-vapor-pressure elements such as magnesium. However, VAR does not remove sulfur, requiring appropriate raw material during the primary VIM process. The VAR significantly improves the chemical and physical homogeneity of the remelted alloy. An added advantage of the VAR process is that it inherently does not superheat the metal. This advantage of the VAR, coupled with the very high heat extraction capability of the process, makes it a better choice for economical manufacturing of the large diameter ingots of segregation-prone superalloys.

The ESR process is different from the VAR process as remelting of the electrode is done by not striking an arc under vacuum, but in the air by melting the electrode immersed in a molten slag superheated by resistance heating. It, however, appears similar to the VAR process as the ingot in both the processes is built up progressively in a water-cooled mold by melting a consumable electrode. Heat in ESR is generated by the electrical resistance of the slag that typically comprises CaF_2 along with Al_2O_3 and CaO . The molten slag provides the heat source for melting the electrode face. The metal drops pass through the molten slag, unlike the vacuum in VAR. The exposure of the molten metal to the molten slag, while it gathers into droplets on the electrode face and as it passes through the slag, reduces oxides incorporated in the alloy. The advantage of the ESR is that it dramatically reduces the sulfur content through a reaction of melt with the CaF_2 . Besides, it reduces high-vapor-pressure elements like magnesium to a lesser extent than that in VAR. An additional benefit of the ESR process is its ability to cast the alloy into rectangular cross-section slabs, which can be directly converted into plates and sheets, unlike the VAR products, which are always round/cylindrical. However, the ESR process is inherently more sensitive to the segregation of solutes than the VAR. As a result, the maximum size of segregation free ESR-ingots is smaller than that of the ingots produced by vacuum arc remelting.

Superalloys ingots are usually forged and rolled into sheets or various wrought products and shapes. However, some highly alloyed superalloys, like IN-100, Rene 95, Stellite 31, etc. or oxide dispersion strengthened alloys, which are difficult or impractical to produce by the conventional ingot metallurgy route involving melting, casting and forging, are normally processed either by casting or by adopting a

powder-metallurgy route. In addition, the powder-metallurgy route produces billets or preforms with closer control of microstructure with respect to grain size and chemical homogeneity, which cannot be achieved in highly alloyed superalloys by the ingot metallurgy route. Some powder-metallurgy processes can directly produce near-net shaped products by rapid prototyping or additive manufacturing techniques. These techniques lower the cost by reducing the weight of the expensive raw materials and minimizing the number of secondary machining operations.

1.6 Product Forms

Superalloys are available in various wrought and cast product forms depending upon their desired applications and compositions. Cast products are produced by directly solidifying the liquid metal to the final product with a net or near-net shape. In contrast, wrought products are made from the cast billets after subjecting them to extensive thermomechanical deformations by processes like forging, rolling or extrusion to achieve the desired final products or preforms.

The standard cast products are alloy ingots and billet for forgings and extrusions, and slabs for rolling into plate and sheet. For some alloys, like Alloy 625, centrifugally cast tubes are also available as per ASME Boiler and Pressure Vessel Code. Cast products like airfoils (i.e., blades and vanes) are commonly used in the hot section areas of gas turbines. Most castings are polycrystalline, but airfoils may be cast as single crystals or directionally solidified castings (Fig. 1.1). In directionally solidified castings, grains are grown parallel to each other, usually parallel to the longitudinal axis of airfoils. Single and directionally solidified crystals are commonly used as jet engine turbine blades. The limitations of cast products are their non-uniform grain size and chemical inhomogeneity. The chemical inhomogeneity arises due to solute segregation, a natural consequence of the solidification process.

Wrought alloys are more homogenous and ductile compared to cast alloys. Thermomechanical processing of alloys removes the chemical inhomogeneity of cast structures and produces uniform microstructure with optimum ductility for processing and subsequent use. Typical wrought products are:

- Forged billets and bars of cylindrical, tapered and stepped cross-sections
- Rolled coils of round and rectangular cross-sections
- Hot-rolled plates and sheets
- Hot extruded and cold pilgered tubing
- Cold drawn bar, rod, coil and wire
- Cold-rolled sheet and strip in standard and precision gauge tolerance

These products can be broadly categorized into (i) preforms and (ii) final products. Preforms, like forged round and rectangular bars or tubes, are used to produce different components, like gas turbine disks, gear components, struts, engine parts, etc. of desired specifications or specific larger shapes, like cryogenic storage tank

components, nuclear fuel element spacers, etc. for various applications. The manufacturing of these components exploits the superior ductility of the wrought material. Final products, like cold pilgered tubing or forged gas turbine disks, are directly used for desired applications. However, some highly alloyed compositions are not amenable to appreciable deformation for forming or shaping into wrought products. Such alloys are fabricated and used in the cast form.

Cast and wrought alloys may have significantly different properties, but both have advantages. The fine-grained structure and compositional homogeneity of wrought products give them uniform mechanical properties and corrosion resistance. Forged products are therefore preferred for low-cycle fatigue applications at low-to-intermediate temperatures like turbine disks. On the other hand, the coarse grain structures of casting make them intrinsically stronger and have better creep resistance than wrought structures at elevated temperatures. In addition, the composition of castings can be tailored effectively to the limits of alloy composition that are rather difficult to forge at high temperatures. That is why nickel-base superalloy castings are preferred for high-stress, high-temperature turbine blade applications because of their highest creep-rupture strength at elevated temperatures.

As noted earlier, some superalloys of highly alloyed compositions, like IN-100, Rene 95, are challenging to produce by the conventional route of melting, casting and forging, because of difficulties associated with their castings or deformation. Such alloys are usually processed by powder-metallurgy route to near-net-shape or final forging. The advent of additively manufacturing technologies over the last two decades is revolutionizing the manufacturing of complex structures, usually produced by casting or forgings. Additive manufacturing, or 3D printing, is an innovative fabricating technique in which three-dimensional structures are progressively built by depositing layers of material. It allows the creation of complex three-dimensional shapes and geometries like internal cavities and lattice structures. Traditional manufacturing techniques are more time-consuming, incapable or economically unviable to achieve such desired geometries. Additive manufacturing also allows alloy compositions that cannot be used as cast or forged products. Recently, Oak Ridge National Laboratory (ORNL) have invented a new high-strength nickel–cobalt superalloy that can be 3D-printed to crack-free and defect-resistant components, which maintain their material integrity at temperatures up to 90% of their melting point [17].

1.7 Market Outlook

The prominence of superalloys as high-performance alloys stems from their operational efficiency and reduced environmental emissions. They are used for applications in various complex processes and operations across a large spectrum of industry sectors, like aerospace and defense, oil and gas, marine, etc. These industries demand materials with extraordinary mechanical properties, corrosion resistance, or both. The global market of iron-, nickel- and cobalt-base superalloys is valued at about USD 10.6 Billion in 2020 and is expected to reach over USD 15 Billion by the end of

2026, growing at a compound annual growth rate (CAGR) of 5.6% during 2021–2026 [18]. Of this market, the most significant chunk of about 80% comprises nickel-based superalloys. The nickel superalloy market is expected to grow at a CAGR of 6.7% to acquire a market value of over USD 10 Billion by 2025 [19].

1.7.1 Major Drivers

The increasing demands for speciality materials in energy, defense, marine, and other sectors due to burgeoning population and economic developments are constantly driving the superalloys market across the globe. The Asia-Pacific region has been the largest and fastest-growing market in recent years, encompassing about 40% share of the global market. The significant contributions to the growth come from India, Japan, South Korea, and China. North America is the second-largest market due to the growing demand in aerospace, defense, and marine industries, primarily in the US. The European market is mainly driven by the rising demand in the automotive industry, particularly for passenger cars.

Based on the applications, major industry segments that drive the global superalloy markets can be classified as (i) aerospace and defense; (ii) power generation; (iii) oil and gas; (iv) refinery; (v) chemical; and (vi) others, which includes industries like marine, pulp and paper, etc. The aerospace and defense sector is among the largest superalloys market (Fig. 1.5). The surging production of commercial aircraft and the growing application of superalloys in the automotive industry is driving its market significantly. Nickel superalloys are primarily used for manufacturing gas turbine engines and rocket components like turbine blades, disks, airframes,

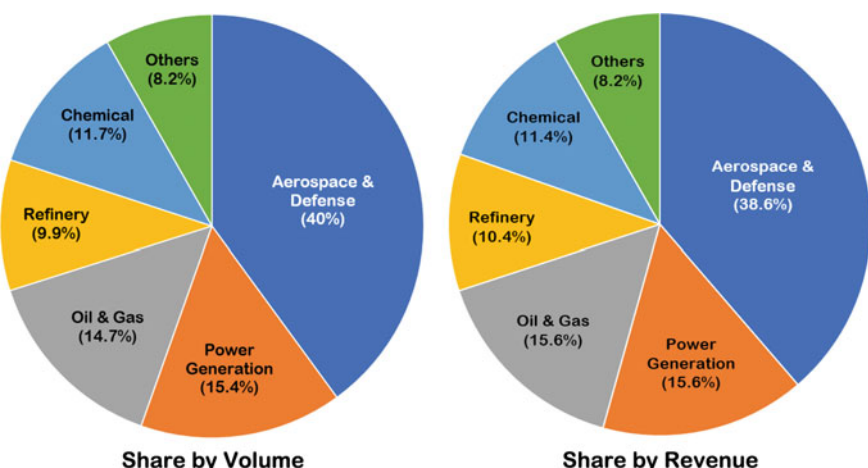


Fig. 1.5 The market share, by volume (tons) and revenue, of major industries driving the global nickel superalloy market [19]

etc. Several developed and developing countries are investing heavily in defense and space development and diversification to fulfill various national objectives of military success and defense strategy, which, in turn, are boosting the productivity of other sectors.

The energy sector is also driving the superalloys market well. The rising energy crisis across the globe is enhancing the demand for power generation using nuclear power plants. Technological advancements are pushing the limits of materials to produce steam at even higher temperatures, as in supercritical thermal plants and gas-based power plants. These plants are increasingly using nickel superalloys for various applications like gas and steam turbines, heat exchangers, scrubbers, etc. Besides, higher corrosion resistance and reduced macrofouling properties make nickel-based superalloys attractive for many applications in nuclear power plants. Other factors like gas drilling activities and rising oil prices across the globe, increasing production of premium vehicles, etc. are also boosting the sales of superalloys.

1.7.2 Market Size

Nickel-based superalloys comprise about 80% of the global superalloys market. In 2017, the global nickel-based superalloys market accounted for about 6.64 Billion USD. Segmenting the nickel superalloys market based on the type of alloys gives a good insight into the dominant alloys in the global market. Based on the type of alloys, the nickel superalloys can be divided into the following categories: (i) Alloy 600/601/602; (ii) Alloy 625; (iii) Alloy 718; (iv) Alloy 825/925; (v) Hastelloy 276/C22/X; (vi) Waspaloy; and (vii) Others. Figure 1.6 depicts the global nickel superalloys market by volume and revenue generation based on 2017 data [19]. Alloy 718 is the most widely used and takes over about 50% of the market share, both by volume and revenue. Alloy 718 takes the cake by virtue of its excellent tensile strength and creep-rupture properties in corrosive environments at high temperatures. The highest market share of Alloy 718 is on account of its maximum consumption by the aerospace and defense industry segment, which itself holds about 40% of the global superalloy market share. The market of Alloy 625 is spread across various industry segments. It controls about 12% market and is expected to grow at a CAGR of about 7% during the next five years.

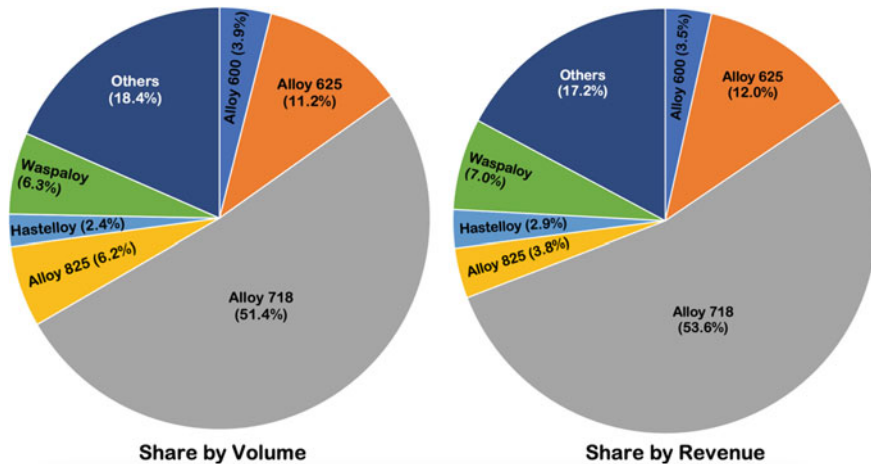


Fig. 1.6 The global market share, by volume (tons) and by revenue, of nickel-base superalloys categorized as **a** Alloy 600/601/602; **b** Alloy 625; **c** Alloy 718; **d** Alloy 825/925; **e** Hastelloy 276/C22/X; **f** Waspaloy; and **g** others [19]. Note the sectors mentioned as Alloy 600, 825, and Hastelloy represents the contributions of Alloy 600/601/602, Alloy 825/925 and Hastelloy 276/C22/X, respectively

1.7.3 Major Players and Tradenames

Over the years, many superalloy producers have come and gone. Following is the list of significant superalloy producers based in various markets across the globe:

- i. Allegheny Technologies Inc. (US)
- ii. AMG Advanced Metallurgical Group (The Netherlands)
- iii. Aperam (Luxembourg)
- iv. Beijing Cisri-Gaona Materials and Technology Co. Ltd. (China)
- v. Carpenter Technology Corporation (US)
- vi. Doncasters Group Ltd. (UK)
- vii. Hitachi Metals, Ltd. (Japan)
- viii. Mishra Dhatu Nigam Ltd. (India)
- ix. Nippon Yakin Kogyo Co., Ltd. (Japan)
- x. Sandvik (Sweden)
- xi. Shanghai Huibei Superalloy Co. Ltd. (China)
- xii. Shenyang Beiheng New Materials Co. Ltd. (China)
- xiii. Special Metals Corporation (US)
- xiv. Thyssenkrupp Aerospace Germany GmbH (Germany)
- xv. VDM Metals (Germany)

These producers market their products under various trade names. The trade name may change for a specific superalloy, but the alloy's number often remains the same. For instance, Alloy 625 is marketed as Inconel 625 and Haynes 625 by M/s Special Metals Corporation and M/s Haynes International, respectively. Table 1.5 gives a list of common tradenames for some producers.

Table 1.5 A list of some well-known tradenames

Superalloy producer	Trademark names
Special Metals Corporation	Incoloy, Inconel, Udimet, Nimonic, Monel
Haynes International	Hastelloy, Haynes, Ultimet
United Technologies	Waspaloy
Allegheny Technologies	Astroloy, René
Deloro Stellite, Inc.	Stellite
Carpenter Technology	Custom Age 625 Plus
Westinghouse Corporation	Discaloy
Martin Marietta Corporation	MAR-M
Cannon-Muskegon Corporation	CMSX

The list is not comprehensive and gives some commonly used trade names

1.8 Alloy 625

Alloy 625 is a nickel–chromium–molybdenum based alloy known for its unique combination of high strength, excellent fabricability and weldability, and outstanding corrosion resistance. It is one of the most versatile nickel-base superalloys and covers about 12% of its global market share. Invented as a solid-solution strengthened alloy by Inco Alloys International Inc. in the 1950s [20], the alloy was initially designed to replace 316-grade stainless steel in supercritical steam power plants for its metallurgical stability, i.e., no age-hardening during service. However, initial work concentrated on the strengthening effects of major individual elements, i.e., chromium, molybdenum, niobium, aluminum and titanium, was not encouraging. On the other hand, alloys containing various combinations of niobium and molybdenum in alloys containing varying amounts of nickel exhibited a significant increase in their room temperature yield strength when subjected to aging treatment at 704 °C for 16 h (Fig. 1.7) [20]. This discovery shifted the developmental activities to another alloy, Alloy 718, which later became the work-horse alloy of nickel-base superalloys.

After a hiatus, the development of Alloy 625 resumed with an alloy containing about 60% Ni, 15% Cr, 3% Nb, 2% Mo, 0.5% Al and 0.5% Ti and the rest Fe (designated as MS-2) [20]. However, by then, the intended market of Alloy 625 for supercritical steam applications had vanished. Moreover, the MS-2 alloy was only a little stronger than other existing alloys like Alloy 600. The amounts of chromium and molybdenum were then increased to 22% and 9%, respectively to improve the room temperature strength of the alloy. Fortunately, an increase in chromium and molybdenum contents also significantly increased the corrosion resistance of the alloy. Finally, a patent application was submitted in January 1962, and a US patent (Patent No. 3,160,500) was granted to its inventors H. L. Eiselstein and J. Gadbut in

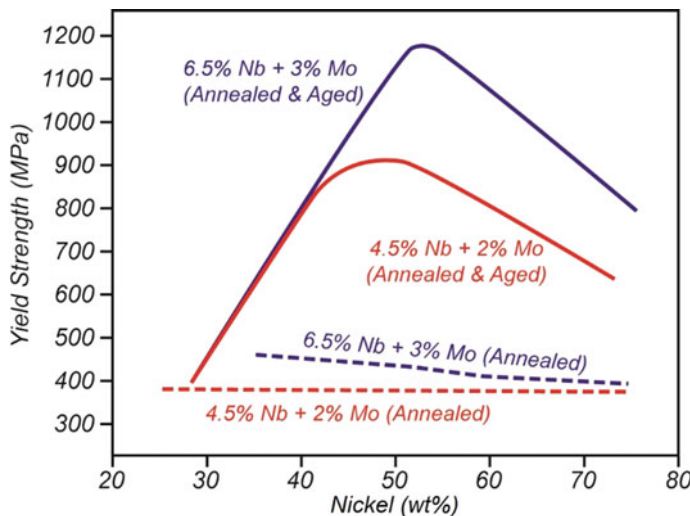


Fig. 1.7 The effect of ageing treatment on room temperature yield strength of nickel alloys containing different amounts of niobium and molybdenum and other elements like chromium, aluminium, titanium and iron, as per the design of Alloy 625. The alloys were annealed at 1038 °C for 1 h before the ageing treatment at 677–732 °C for 16 h, followed by air cooling [20]

December 1964. The composition of the alloy has changed slightly since then. The present composition is given in Table A.3 of Appendix A.

Over the years, applications of the alloy have expanded to temperatures ranging from cryogenic temperature to about 980 °C. The high concentrations of chromium and molybdenum give the alloy its high solid solution strength and resistance against uniform as well as localized corrosion (pitting and crevice) in non-oxidizing environments. About 4% niobium gives it high-temperature strength. Niobium also stabilizes against intergranular corrosion and sensitization during welding. These elements together create a high-performance alloy by imparting Alloy 625 high tensile, creep, and rupture strength; outstanding fatigue and thermal-fatigue strength; resistance against corrosion against oxidizing and reducing environments, resistance against oxidation, sulfidation and carburization; and excellent weldability and brazeability. The alloy can be readily fabricated by standard industrial processes and needs no post-weld thermal treatment to maintain its corrosion resistance.

The versatile properties of Alloy 625 under a wide range of temperatures and pressures make it a widely accepted material for applications in chemical and petrochemical industries, heavy water plants and marine engineering. The alloy is one of the most commonly used offshore materials for upstream pipework in the oil and gas industry and is compliant with NACE MR0175/ISO 15156-3 standard [21]. This standard covers the use of materials in H₂S containing environments. It allows the use of Alloy 625, in annealed or solution-annealed condition, in any combination of temperature, partial pressure of H₂S, chloride concentration and in situ pH occurring in production environments. Alloy 625 also has excellent resistance against pitting in

pressurized high-temperature water (260–316 °C), making it useful for many applications for reactor-core and control rod components in nuclear water reactors. In recent years, the alloy has been used to make exhausts for Formula 1 class racing cars [22]. The alloy is potentially useful for many more applications. It is being considered a candidate material for applications in advanced reactor concepts because of its high allowable design strength at elevated temperatures, especially between 650 and 760 °C. Table 1.6 gives a list of significant applications of Alloy 625 in different industries.

A better understanding of the alloy during service exposures and the development of new processing techniques have resulted in the introduction of new alloys, like Alloy 625 LCF and Custom Age 625 Plus alloys, based on Alloy 625 by slightly changing its composition. The LCF variant of the alloys is produced by tightly controlling the compositions of carbon, silicon, and nitrogen to very low levels employing the VIM/ESR double melting practice and controlling the grain size to ASTM #5 or smaller during thermomechanical processing. The LCF variant has an enhanced resistance to fatigue at temperatures up to about 650 °C. The Custom Age 625 Plus alloy is an age-hardenable variant of Alloy 625 in which the titanium content is increased to about 1.3% to accelerate the precipitation of the γ'' phase particles.

Alloy 625 is very close to Alloy 718 in terms of the phase transformations and the associated microstructures. Both these alloys can be precipitation strengthened primarily by the metastable γ'' phase particles. The corresponding hardening phase in both the alloys is the ordered orthorhombic δ phase based on Ni_3Nb [15]. This behavior of the two alloys is different from most precipitation-hardenable nickel-base alloys, which are strengthened by γ' phase precipitates. The Alloy 718 is a high-strength alloy intended for applications up to 700 °C with good fatigue strength and excellent stress-rupture properties. Like Alloy 625, Alloy 718 has good corrosion resistance in various aggressive environments and is resistant to oxidation up to about 1000 °C and can be used at cryogenic temperatures, down to about –250 °C. The sluggish age-hardening response of Alloy 718 enables it to be welded and annealed with no spontaneous hardening unless cooled slowly [3]. Alloy 718 contains about 17–21% chromium, 2.8–3.3% molybdenum and 4.75–5.5% niobium and much lower amounts of aluminum (0.2–0.8%) and titanium (0.65–1.15%).

1.9 Why a Book on Alloy 625?

Ever since the introduction of Alloy 625 for ultra-critical steam piping applications, it continues to find new applications in the aerospace, automobile, chemical processing, oil refining & production, marine, waste treatment, pulp & paper, power and nuclear industries. The alloy undergoes significant microstructural modifications during long term thermal exposure at intermediate temperatures. It develops complex microstructures by precipitating various intermetallic and carbide phases in the disordered nickel matrix that embrittle the alloy. However, a good understanding of their formation can help reverse the properties of the alloy to the codal values.

Table 1.6 Major applications of Alloy 625 in various industries

Industry	Properties	Applications
Fuel refining	High resistance at elevated temperatures against naphthenic acid corrosion, oxidation and sulfidation, and chloride stress-corrosion cracking	distillation tower; seamless pipes; overhead condensers; transfer lines; nozzles; return bends
Seawater applications	Excellent resistance against localized attack, high corrosion-fatigue strength, high tensile strength, and resistance to chloride stress-corrosion cracking	Mooring cables; propeller blades for boats; submarine propulsion motors; exhaust ducts of naval boats; sheathing for undersea communication cables; submarine transducer controls; steam-line bellows; electrical cable connectors, fasteners and flexure devices; oceanographic instrument components
Aerospace industry	High tensile, creep and rupture strength, outstanding fatigue strength and excellent weldability	Aircraft ducting systems, exhaust systems, thrust-reverser systems; fuel and hydraulic line tubing; heat exchanger tubing; honeycomb structures for housing engine controls; spray bars, bellows, turbine shroud rings; combustion system transition liners; turbine seals; compressor vanes; and thrust-chamber tubing for rocket
Chemical processing	Good combination of strength and corrosion resistance against oxidizing as well as reducing corrosive media at elevated temperatures	Bubble caps; tubing; reaction vessels; distillation columns; heat exchangers; transfer piping; valves, etc.
Core and control rod components of nuclear water reactors	Strength and resistance against localized corrosion in high temperature (260–316 °C) waters	Valves; stems; tubing; springs
Hydrocracking and catalytic cracking units	Good combination strength and resistance against hydrogen sulfide (high-temperature corrosion), and ammonia and ammonium sulfide (lower-temperature corrosion and erosion-corrosion)	Pressure containing cracking units; reaction vessels; tubing

The book provides content to those who desire to develop a complete understanding of Alloy 625. The book's emphasis is on the relationships between the microstructure and its mechanical properties, and their variation during prolonged service exposures. It also provides an overview of its corrosion behavior in various environments. The book would be helpful as a guide to practicing engineers in the industry interested in using Alloy 625 and in academia for students pursuing advanced courses in Materials Science.

The book is divided into eight chapters, including the "Introduction" chapter, to introduce the high-performance alloys "Superalloys". The chapter gives the reader an overview of different aspects of the superalloys in general, including their contribution to the global economy. Other chapters exclusively deal with "Phases", "Microstructure", "Mechanical Behavior", "Corrosion Behavior", "Fabrication", and "Life Management" of Alloy 625 components. A separate chapter has been included on "Alloy 625 PLUS" to give readers a brief account of the age-hardenable variant of Alloy 625. These properties of the alloy are compared with those of many other alloys. All the alloys are referred to mostly through their generic names throughout the book.

References

1. Sims CT (1987) In: Sims CT, Stoloff NS, Hagel WC (eds) Superalloys II: high temperature materials for aerospace and industrial power, Chapter 1. Wiley, New York. ISBN: 0-471-01147-9
2. Donachie MJ (2002) Superalloys: a technical guide, 2nd edn, Chapter 14. ASM International. ISBN: 0-87170-749-7
3. Inconel alloy 718, 2007. <https://www.specialmetals.com/documents/technical-bulletins/inc-one/inconel-alloy-718.pdf>
4. CarTech ® Custom Age 625 PLUS® Alloy identification type analysis, n.d. <https://www.cartechtechnology.com/hubfs/7407324/Material%20Safety%20Data%20Sheets/725.pdf>
5. HAYNES ® 242 alloy data sheet, 2020, http://haynesintl.com/docs/default-source/pdfs/new-alloy-brochures/high-temperature-alloys/brochures/242-brochure.pdf?sfvrsn=a17229d4_28
6. Donachie MJ (2002) Superalloys: a technical guide, 2nd edn., Chapter 1. ASM International. ISBN: 0-87170-749-7.
7. Geddes B, Leon H, Huang X (2010) Superalloys: alloying and performance. ASM International. ISBN-10: 0-61503-040-9
8. Energy Conversion, Encyclopedia Britannica, 15th edn., 18 (2002) 332–413
9. Holt RT, Wallace W (1976) Impurities and trace elements in nickel-base superalloys. Int Met Rev 21:1–24. <https://doi.org/10.1179/imtr.1976.21.1.1>
10. Zhang D, Cheng Y, Jiang R, Wan N (2018) Introduction. In: Turbine blade investment casting die technology. Springer, Berlin, Heidelberg. https://doi.org/10.1007/978-3-662-54188-3_1
11. Poole JM, Fischer JJ, Hack GAJ, McColvin GM (1994), advances in high temperature structural materials and protective coatings. National Research Council of Canada <http://www.empri.edu/hartford/-ernesto/F2011/EP/MaterialsforStudents/Opsahl/Hetmanczyk2007.PDF>
12. HAYNES® 244® alloy data sheet, 2020. <http://haynesintl.com/docs/default-source/pdfs/new-alloy-brochures/high-temperature-alloys/brochures/244-brochure.pdf>
13. Cao WD (2004) Nickel-base alloy, U.S. Patent 6730264 B2
14. Verma A, Singh JB (2021) Stabilization of a D022 phase in Ni–Cr–Mo–W–Ti Alloys. Metall Mater Trans A 52:4317–4323. <https://doi.org/10.1007/s11661-021-06404-4>

15. Ross EW, Sims CT (1987) In: Sims CT, Stoloff NS, Hagel WC (eds) Superalloys II: high temperature materials for aerospace and industrial power, Chapter 4. Wiley, New York. ISBN: 0-471-01147-9
16. Vanadium supply and demand outlook. The National Academies Press, Washington 1978. <https://doi.org/10.17226/19907>
17. Murray SP, Pusch KM, Polonsky AT, Torbet CJ, Seward GGE, Zhou N, Forsik SAJ, Nandwana P, Kirka MM, Dehoff RR, Slye WE, Pollock TM (2020) A defect-resistant Co–Ni superalloy for 3D printing. *Nat Commun* 11:4975. <https://doi.org/10.1038/s41467-020-18775-0>
18. Press Release, MarketWatch.com, 28 June 2021
19. Report Nickel Superalloy Market 2020, Global Market Insights, Delaware, USA, (n.d.)
20. Eiselstein HL, Tillack DJ (1991) The invention and definition of alloy 625, in: 1991, pp 1–14. https://doi.org/10.7449/1991/superalloys_1991_1_14
21. NACE MR0175/ISO 15156-3, petroleum and natural gas industries—materials for use in H₂S-containing environments in oil and gas production—part 3: cracking-resistant CRAs (corrosion-resistant alloys) and other alloys. Am Natl Stand Inst/NACE Int (2009)
22. Curà F, Mura A, Sesana R (2012) Aging characterization of metals for exhaust systems. *Int J Automot Technol* 13:629–636. <https://doi.org/10.1007/s12239-012-0061-0>

Chapter 2

Phases in Alloy 625



Alloy 625, originally designed as a single-phase solid-solution alloy, contains high concentrations of various alloying elements added primarily to impart desired mechanical and corrosion properties. The high concentrations of elements like chromium, molybdenum and niobium induce the precipitation of multiple phases during solidification, processing and thermal exposure. The precipitation of various phases in the austenite nickel matrix makes the microstructure of the alloy very complex and alters its properties significantly. Precipitation of many phases is associated with cubic to non-cubic transformations, which decide the distribution and morphology of particles in the matrix. Such cubic to non-cubic phase transformations give rise to several physically distinct crystallographic orientations of the precipitating phase called “variants”, whose number depends upon the lattice symmetry reduction due to the transformation. The Chapter briefly introduces crystallographic aspects of various phases in Alloy 625 and lays a foundation for their identification and understanding of phase transformations associated with their evolution.

2.1 Definitions of Phase, Crystal Structure and Solid-solution

A phase is defined as a chemically homogeneous and physically uniform state of matter. A crystalline phase has characteristic chemistry and crystal structure. In a crystalline phase, atoms take positions over geometrically arranged points in a symmetrical pattern termed “lattice”. This arrangement of atoms is called “crystal structure”. The smallest group of atoms, having the crystal symmetry, is called a “unit cell”. A unit cell repeat itself in a three-dimensional space. A crystalline solid containing a uniform mixture of two or more chemical species that share a crystal lattice is called a “solid solution”. The word “solution” signifies the intimate mixing of the species at the atomic level. The species or element present in the highest amount is termed “solvent”, while elements in the lesser concentrations are termed

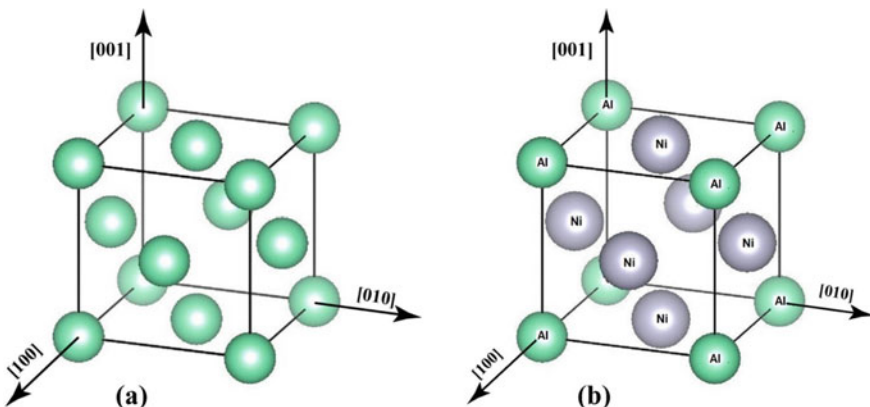


Fig. 2.1 Unit cells of **a** FCC crystal and **b** γ' phase (L1₂ structure)

“solutes”. The solubility limit of a solute in a solid solution is governed by its atomic size and crystal structure compared to the solvent. Some elements readily form solid solutions over a wide range of concentrations, while others may not.

When the solute concentration exceeds the solubility limit, a second phase precipitates at temperatures high enough for diffusion to occur. When atoms of different species are distributed randomly over lattice points, the crystalline structure is called a (chemically) disordered phase. When atoms of various types are distributed in an orderly manner, defined by specific equivalent positions of the lattice, the phase is called an “ordered” phase. The ordered arrangement of two or more atoms gives a covalent character to the metallic bonding of the phase, and such phases are often referred to as intermetallic compounds. The lattice structure of an ordered phase is termed “superlattice”. A superlattice may be regarded as a superimposition of lattices of individual atomic species. For instance, nickel and aluminum atoms in a nickel-13 wt% aluminum alloy are distributed randomly at the corners and face centers of its face-centered cubic (FCC) unit cell with the same probability. This phase is termed the γ phase (Fig. 2.1a). The γ phase orders below 1395 °C to form an ordered FCC structure [1], L1₂ structure, where aluminum atoms occupy all the corners of the unit cell and the face-centered sites are occupied by nickel atoms (Fig. 2.1b). The phase with the L1₂ structure is often termed as the γ' phase because of its similarity with the disordered FCC γ phase.

2.2 Crystal Structures of Phases in Alloy 625

Alloy 625 primarily comprises a nickel-base solid solution as a matrix phase that may contain a variety of intermetallic and carbide phases. Table 2.1 lists crystallographic features of various phases that usually form in Alloy 625 [2–9]. The intermetallic

Table 2.1 Crystallographic details of various phases that may form in Alloy 625

Phase	Common structure type ^a	Pearson's symbol	Space group	Prototype	Formula	Crystal structure	Atoms per unit cell	Lattice parameters ^b (nm)	Angle (°)	References	
Gamma (γ)	A1	cF4	Fm-3 m	Cu	Ni	Face-centered cubic	4	0.3609	0.3609	[2, 4]	
Gamma double prime (γ'')	D0 ₂₂	d8	I4/mmm	Al ₃ Ti	Ni ₃ (Nb, Ti, Al)	Ordered body-centered tetragonal	8	0.362	0.362	[2, 5]	
Ni ₂ (Cr, Mo)	D _{2h} ²⁵	oP6	Pmmm	Pt ₂ Mo	Ni ₂ (Cr, Mo)	Ordered body-centered orthorhombic	6	0.2513	0.7553	0.3580	[2, 8c]
Delta (δ)	D0 _a	oP8	Pmmm	β -Cu ₃ Ti	Ni ₃ Nb	Ordered body-centered orthorhombic	8	0.5116	0.426	0.4565	90° [2]
M ₂₃ C ₆ Carbide	D8 ₄	cF116	Fm-3 m	Cr ₂₃ C ₆	Cr ₂₃ C ₆	Complex cubic	116	1.050–1.070	1.050–1.070	1.050–1.070	[2, 6]
M ₆ C Carbide	E9 ₃	cF112	Fd-3 m	Fe ₃ W ₃ C	(Cr, Mo, Ni) ₆ C	Complex cubic	112	1.091–1.13	1.091–1.13	1.091–1.13	[2–8]
MC Carbide	B1	cF8	Fm-3 m	NaCl	(Nb, Ti)C	Cubic	8	0.430–0.444	0.430–0.444	0.430–0.444	[2–8]
Mu (μ) Phase	D8 ₅	hR13	R-3 m	W ₆ Fe ₇	Mo ₆ Ni ₇	Hexagonal	39	0.48	0.48	2.56	$\gamma = 120^\circ$ [2, 10, 3]
Laves Phase	C14	hP12	P6 ₃ /mmc	Zn ₂ Mg	(Cr, Ni) ₂ (Si, Nb, Mo) Ni ₃ Mo ₂ Si	Hexagonal	12	0.47–0.48	0.47–0.48	0.77–0.78	$\gamma = 120^\circ$ [2, 5, 10, 3]

^aThe “common structure type” is based on the Strukturbericht designation commonly used to describe frequently encountered similar types of crystal structures

^bThe range signifies that the lattice parameter values vary with composition

^cThe reported lattice parameter of the Ni₂(Cr, Mo) phase in a model Ni–Cr–Mo alloy containing Cr and Mo solutes equivalent to the amount present in Alloy 625

phases that may form are $\text{Ni}_2(\text{Cr, Mo})$, gamma double prime (γ'') and the delta (δ) phases, while the carbides phases may be MC , M_{23}C_6 and M_6C . Detrimental phases, like sigma (σ), mu (μ), and Laves phases, may also form in the alloy, particularly during solidification or processing of the alloy. The following describes crystal structures of these phases.

2.2.1 *Gamma (γ) Phase*

The γ phase is a disordered solid solution of nickel-containing other alloying elements and has an FCC structure (Fig. 1a). An FCC unit cell has four atoms at the following coordinate positions:

$$\text{Ni} : 0, 0, 0; 1/2, 1/2, 0; 1/2, 0, 1/2; 0, 1/2, 1/2$$

Each atom at the corner of the cell contributes one-eighth to the unit cell, and each atom at the centers of the faces contributes one-half resulting in four numbers of effective atoms per unit cell (Table 2.1).

2.2.2 *Gamma Double Prime (γ'') Phase*

The γ'' phase is an intermetallic compound of N_3M stoichiometry with an ordered body-centered tetragonal structure. This structure is termed the $\text{D}0_{22}$ structure (Fig. 2.2). A unit cell of the $\text{D}0_{22}$ structure contains eight atoms, two of which are M atoms and six are N atoms, arranged at the following coordinates of the unit cell:

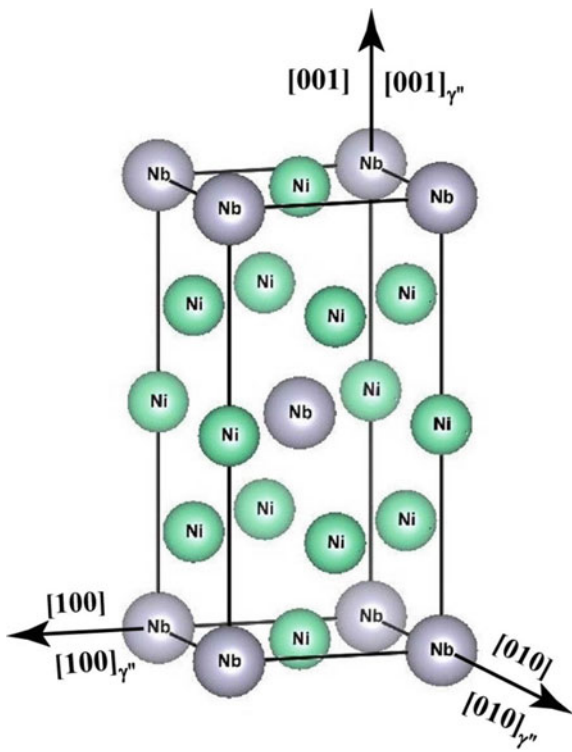
$$M : 0, 0, 0; 1/2, 1/2, 1/2$$

$$N : 0, 0, 1/2; 1/2, 1/2, 0; 0, 1/2, 1/4; 1/2, 0, 1/4; 0, 1/2, 3/4; 1/2, 0, 3/4$$

This arrangement of atoms in the $\text{D}0_{22}$ structure is related to the arrangement of atoms in the $\text{L}1_2$ structure. The former can be visualized as a stacking of two $\text{L}1_2$ unit cells, stacked one above the other, along a $\langle 001 \rangle^1$ direction with a relative displacement of $1/2 \langle 110 \rangle$ perpendicular to the $\langle 001 \rangle$. Because of this closeness to the $\text{L}1_2$ structure, the $\text{D}0_{22}$ phase is termed as γ'' phase. The c parameter of the $\text{D}0_{22}$

¹ Directions and planes are denoted by the standard Miller indices used to describe crystallographic planes and directions of crystal lattices¹¹. This system expresses planes by integers h , k , and l , and directions by integers, usually expressed by u , v and w . Planes and directions expressed as (hkl) and $[uvw]$ notations, respectively, represent specific planes or directions in the crystal basis. In contrast, planes and directions expressed, respectively by $\{hkl\}$ and $\langle uvw \rangle$ notations denote the set of all planes and directions that are symmetrically equivalent to (hkl) and $[uvw]$. All Miller indices are expressed in the cubic crystal system unless otherwise subscripted.

Fig. 2.2 The unit cell of the D0₂₂ structure of the γ'' phase



structure is roughly double the a -parameter. Figure 2.2 shows a unit cell of the D0₂₂ structure of the γ'' phase with Ni_3Nb stoichiometry, which has its lattice parameters as $a = 0.362 \text{ nm}$ and $c = 0.740 \text{ nm}$ [2, 3]. The precipitation of the γ'' phase from the parent γ phase matrix follows a distinct orientation relationship with it, given by

$$(001)_{\gamma''} // \{001\}$$

$$[100]_{\gamma''} // \langle 100 \rangle$$

This orientation relationship implies a matching between $(001)_{\gamma''}$ of the γ'' phase with any one of the $\{001\}$ plane of the γ phase. Since the $[001]_{\gamma''}$ direction of the tetragonal cell may align with any one of the three $\langle 001 \rangle$ axes of the cubic cell, the ordered D0₂₂ phase possesses three mutually orthogonal orientational variants.²

² All the indices for the for non-cubic phases/structures throughout the book are subscripted by the corresponding phase or structure. Indices without subscripts indicate the cubic basis of the γ phase.

2.2.3 $Ni_2(Cr, Mo)$ Phase

The $Ni_2(Cr, Mo)$ phase is an intermetallic compound of Ni_2M stoichiometry with an ordered body-centered orthorhombic structure. The unit cell of the $Ni_2(Cr, Mo)$ phase has a Pt_2Mo type structure that contains six atoms, of which two are M, and four are N atoms, arranged at the following coordinates of the orthorhombic cell.

$$M : 0, 0, 0; 1/2, 1/2, 1/2$$

$$N : 0, 1/3, 0; 0, 2/3, 0; 1/2, 1/6, 1/2; 1/2, 5/6, 1/2$$

The unit cell of the ordered orthorhombic $Ni_2(Cr, Mo)$ phase vis-à-vis the disordered FCC cell is shown in Fig. 2.3. It has lattice parameters $a = 0.2513$ nm, $b = 0.7553$ nm, $c = 0.3580$ nm [11]. When the orthorhombic $Ni_2(Cr, Mo)$ phase precipitates out from the parent γ matrix, it follows an orientation relationship with the matrix, given by:

$$[001]_o // \langle 001 \rangle$$

$$[010]_o // \langle 110 \rangle$$

The C-axis ($[001]_o$) of the orthorhombic cell (the subscript “o” denotes the orthorhombic structure) may align itself with any of the three axes of the cube and the other two orthogonal axes, A ($[100]_o$) and B ($[010]_o$), may direct themselves along appropriate $\langle 110 \rangle$ directions. The two structures follow the following vector relationships.

$$\mathbf{A} = \frac{1}{2}(a_1 + a_2); \quad \mathbf{B} = \frac{3}{2}(-a_1 + a_2); \quad \mathbf{C} = a_3$$

Where a_1 , a_2 and a_3 refer to the three axes of the cubic cell. This relationship results in six independent orientation variants of the $Ni_2(Cr, Mo)$ phase with respect to the γ matrix, defined as per Table 2.2.

Fig. 2.3 The unit cell of the Ni_2Cr phase with Ni_2M stoichiometry

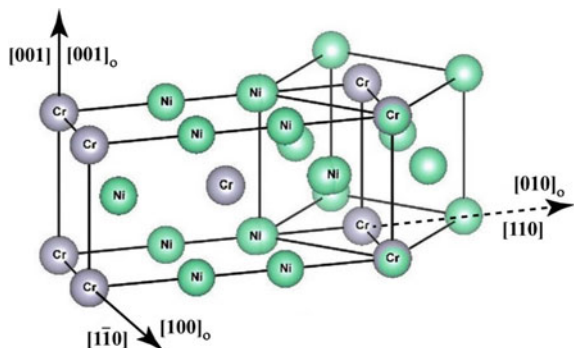


Table 2.2 Lattice correspondence and variant nomenclature of the ordered Ni₂(Cr, Mo) phase in relation to the parent FCC lattice

Variant	(1 0 0) _o	(0 1 0) _o	(0 0 1) _o
1	1/2(1 $\bar{1}$ 0)	3/2(1 1 0)	(0 0 1)
2	1/2(1 1 0)	3/2($\bar{1}$ 1 0)	(0 0 1)
3	1/2(1 0 1)	3/2(1 0 $\bar{1}$)	(0 1 0)
4	1/2(1 0 $\bar{1}$)	3/2($\bar{1}$ 0 $\bar{1}$)	(0 1 0)
5	1/2(0 $\bar{1}$ $\bar{1}$)	3/2(0 1 $\bar{1}$)	(1 0 0)
6	1/2(0 1 $\bar{1}$)	3/2(0 1 1)	(1 0 0)

2.2.4 Delta (δ) Phase

The δ phase has an ordered orthorhombic D0_a (β -Cu₃Ti type) structure with Ni₃Nb stoichiometry. It is the equilibrium phase of the γ'' phase in the binary nickel-niobium system. The δ phase forms during extended thermal exposures above 650 °C. Figure 2.4 shows a unit cell of the D0_a structure of the δ phase. For the N₃M stoichiometry, there are eight atoms in the unit cell of the δ phase, of which two are M atoms, and the remaining six are N atoms. The coordinates of these atoms are:

$$M : 0, 0, 2/3; 1/2, 1/2, 1/3$$

$$N : 0, 1/2, 1/3; 1/2, 0, 2/3; 1/4, 0, 1/6; 3/4, 0, 1/6; 1/4, 1/2, 5/6; 3/4, 1/2, 5/6$$

When the δ phase precipitates out in the γ matrix, it follows the following precipitate-matrix orientation relationship.

$$(001)_{\delta} // \{111\}$$

$$[010]_{\delta} // \langle 1\bar{1}0 \rangle$$

Fig. 2.4 The unit cell of the D0_a structure of the δ phase

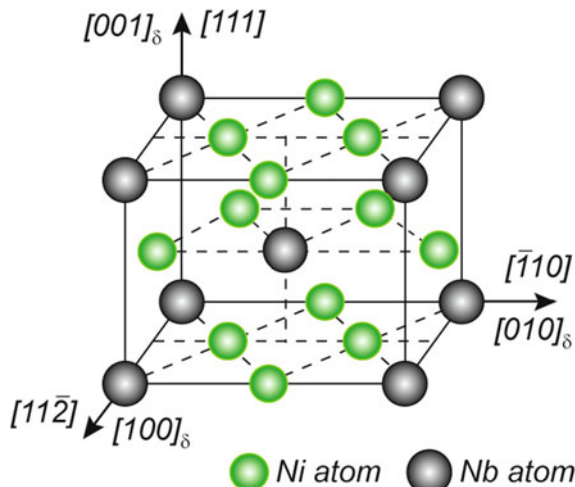


Table 2.3 Lattice correspondence and variant nomenclature of the δ phase in relation to the FCC lattice

Variant	$(1\ 0\ 0)_{\delta}$	$(0\ 1\ 0)_{\delta}$	$(0\ 0\ 1)_{\delta}$
δ_1	$1/2(1\ 1\ \bar{2})$	$(\bar{1}\ 1\ 0)$	$2/3(1\ 1\ 1)$
δ_2	$1/2(1\ \bar{1}\ \bar{2})$	$(1\ \bar{1}\ 0)$	$2/3(1\ \bar{1}\ 1)$
δ_3	$1/2(\bar{1}\ \bar{1}\ \bar{2})$	$(1\ \bar{1}\ 0)$	$2/3(\bar{1}\ \bar{1}\ 1)$
δ_4	$1/2(\bar{1}\ 1\ \bar{2})$	$(\bar{1}\ \bar{1}\ 0)$	$2/3(\bar{1}\ 1\ 1)$
δ_5	$1/2(1\ \bar{2}\ 1)$	$(1\ 0\ \bar{1})$	$2/3(1\ 1\ 1)$
δ_6	$1/2(\bar{2}\ \bar{1}\ 1)$	$(0\ \bar{1}\ \bar{1})$	$2/3(1\ \bar{1}\ 1)$
δ_7	$1/2(\bar{1}\ 2\ 1)$	$(\bar{1}\ 0\ \bar{1})$	$2/3(\bar{1}\ \bar{1}\ 1)$
δ_8	$1/2(2\ 1\ 1)$	$(0\ 1\ \bar{1})$	$2/3(\bar{1}\ 1\ 1)$
δ_9	$1/2(\bar{2}\ 1\ 1)$	$(0\ \bar{1}\ 1)$	$2/3(1\ 1\ 1)$
δ_{10}	$1/2(1\ 2\ 1)$	$(\bar{1}\ 0\ 1)$	$2/3(1\ \bar{1}\ 1)$
δ_{11}	$1/2(2\ \bar{1}\ 1)$	$(0\ 1\ 1)$	$2/3(\bar{1}\ \bar{1}\ 1)$
δ_{12}	$1/2(\bar{1}\ \bar{2}\ 1)$	$(1\ 0\ 1)$	$2/3(\bar{1}\ 1\ 1)$

This orientation relationship implies matching close-packed planes of the precipitate and matrix phases. This orientation relationship gives 12 orientation variants of the δ phase, defined according to Table 2.3.

2.2.5 Carbide Phases

Three types of carbide phases, namely, MC, $M_{23}C_6$ and M_6C , may form in Alloy 625. The MC carbide has an ordered cubic crystal structure of NaCl type (Fig. 2.5). The unit cell of the MC carbide contains four atoms each of M and C type at following coordinates:

$$\begin{aligned} M : & 0, 0, 0; 1/2, 1/2, 0; 1/2, 0, 1/2; 0, 1/2, 1/2 \\ C : & 1/2, 0, 0; 0, 1/2, 0; 0, 0, 1/2; 1/2, 1/2, 1/2 \end{aligned}$$

A unit cell of the MC phase may have a lattice parameter in the range of 0.43–0.444 nm [3, 4], depending upon its composition. The $M_{23}C_6$ and M_6C phases have complex FCC and diamond cubic structures, respectively. Figures 2.6 and 2.7 show unit cells of the $M_{23}C_6$ and M_6C carbides in relation to the unit cell of the parent matrix phase. The $M_{23}C_6$ phase contains 92 M atoms and 24 C atoms in its unit cell, while the M_6C phase contains 96 M atoms and 16 C atoms. Like the MC phase, the unit cells of the $M_{23}C_6$ and M_6C phases may have lattice parameters in the range 1.050–1.070 and 1.091–1.13 nm [5, 8, 6], respectively, which are approximately three times that of the disordered nickel solid-solution matrix. When these carbides (designated by subscript C) precipitate out from a supersaturated matrix, they follow cube to cube orientation relationships with the matrix as

Fig. 2.5 The unit cell of the MC carbide (ordered FCC cubic)

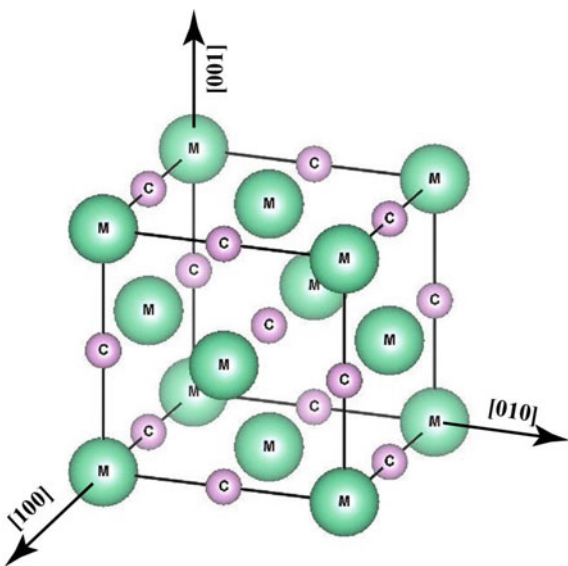
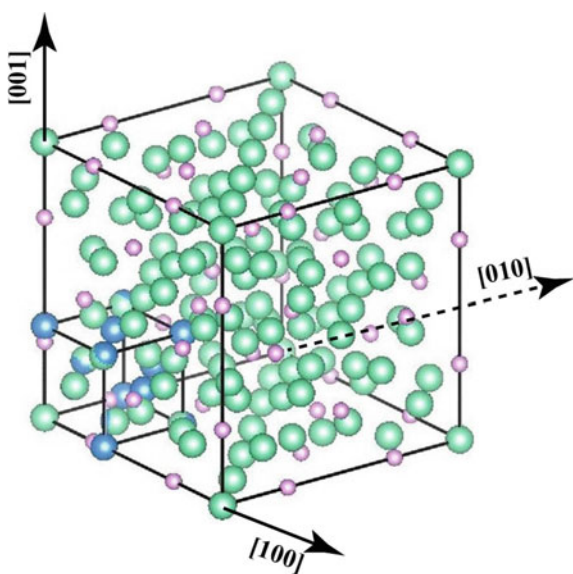


Fig. 2.6 The unit cell of the $M_{23}C_6$ carbide (a complex cubic structure) in relation to an FCC unit cell (smaller cell)

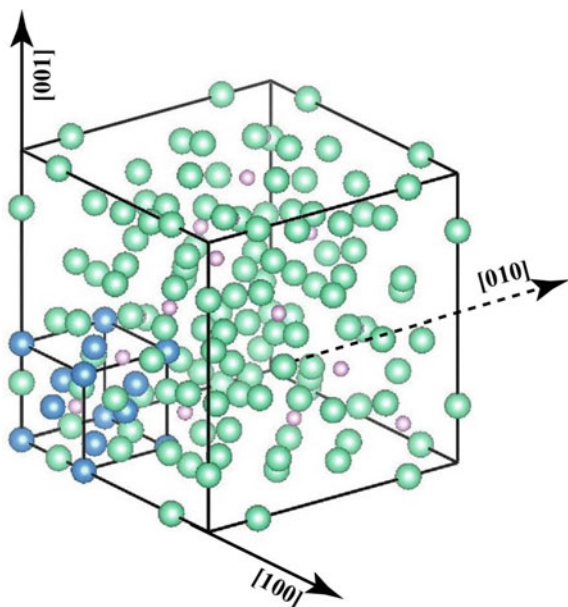


$$\{100\}_C // \{100\}$$

$$\langle 001 \rangle_C // \langle 001 \rangle$$

or

Fig. 2.7 The unit cell of the M₆C carbide (a complex diamond cubic structure) in relation to an FCC unit cell (smaller cell)



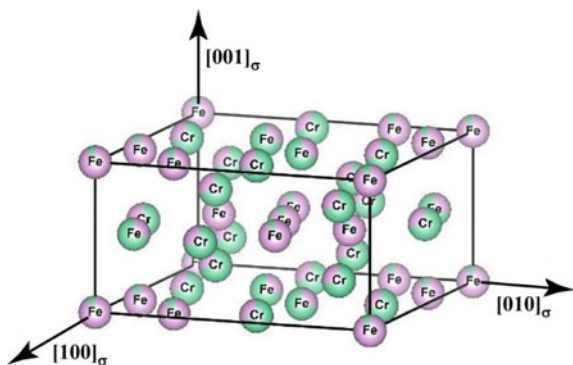
$$\begin{aligned} \{111\}_C // \{111\} \\ \langle 1\bar{1}0 \rangle_C // \langle 1\bar{1}0 \rangle \end{aligned}$$

2.2.6 Topologically Close-Packed Phases

The topologically close-packed (TCP) phases are made of layers of close-packed atomic {111} planes, separated by relatively large distances, unlike the geometrically close-packed phases. The geometrically close-packed phases, like γ and γ'' , are closely packed in all directions. The crystal structures of the TCP phases are quite complex, and their unit cells may contain many atoms. As a consequence, TCP phases display a wide range of compositions. Several TCP phases, like σ , μ , R , χ , G and Laves, are reported in nickel-base alloys containing high concentrations of refractory elements like molybdenum, chromium, tungsten, tantalum, niobium, etc. These phases generally form through electron bonding of the terminal elements that form the phase. Among the elements present in these phases, one or more usually exhibit an electropositive character (e.g., chromium, molybdenum and tungsten).

The TCP phases that may form in Alloy 625 are σ , μ and Laves phases. The μ phase usually forms in alloys with high levels of molybdenum or tungsten and σ forms in alloys containing a high amount of chromium. The Laves usually forms in alloys containing high levels of molybdenum, titanium and tantalum. Unlike the

Fig. 2.8 The unit cell of the tetragonal structure of the $\text{Fe}_2\text{Cr}\sigma$ TCP phase



electron bonding nature of σ and μ phases, the terminal atoms in the Laves phases are bonded by their size factors. Figures 2.8, 2.9 and 2.10 show the unit cells of σ , μ and Laves phases, respectively. The body-centered tetragonal unit cell of the σ phase contains 30 atoms, while the rhombohedral unit cell of the μ phase contains 13 atoms (equivalent hexagonal cell contains 39 atoms). The hexagonal unit cell of the Laves phase contains 12 atoms. Both σ and μ phases are represented by a typical formula A_xB_y , where x and y may vary from 1 to 7. However, the difference in the two phases comes from the atoms involved in their formation. The σ phase usually forms with nearly equal atomic size elements, while the μ phase forms when their atomic size differs significantly [6]. The Laves phases tend to have an A_2B stoichiometry with general formula $(\text{Fe}, \text{Mn}, \text{Cr}, \text{Si})_2(\text{Mo}, \text{Ti}, \text{Nb})$. The close-packed layers of all the TCP phases maintain a high degree of coherency with $\{111\}$ planes of the γ , γ'' and δ phases.

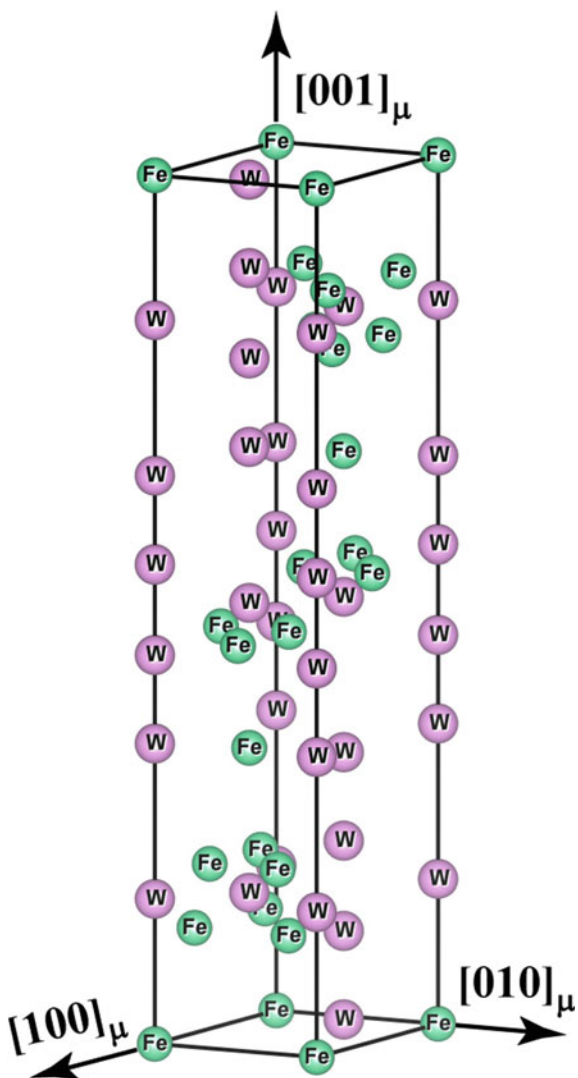
2.3 Basic Concepts of Diffraction and Phase Identification

Various phases can be identified through their diffraction behavior. A summary of principles and concepts of diffraction important for understanding the diffraction behavior of phases in the present context is given below.

2.3.1 Diffraction Behavior of Crystalline Solids and the Bragg's Law

Different phases can be identified from the interaction behavior of x-rays or other electromagnetic radiations with electrons of the atoms. A brief description of this behavior and how it helps identify a phase is discussed considering x-ray radiations, though the same principles apply to all radiations.

Fig. 2.9 The unit cell of the rhombohedral structure of the $\text{W}_6\text{Fe}_7 \mu$ phase



When x-rays interact with atoms in a crystalline lattice, electrons emit x-rays of the same frequency in all directions. However, the emitted waves are not in phase in all directions and cause destructive interference (cancel intensity of one another). Only in certain specific directions the emitted waves are in phase and reinforce the intensity of one another. This specific direction depends upon the angle of the incident x-rays, its wavelength (λ), and the spacing between the reflecting atomic planes (d) that satisfy Bragg's condition $\lambda = 2d\sin\theta$, where θ is the angle of incidence (Fig. 2.11). Such a co-operative scattering (diffraction) of x-rays by all the atoms of the unit cell is analogous to the reflection of x-rays by the atomic plane.

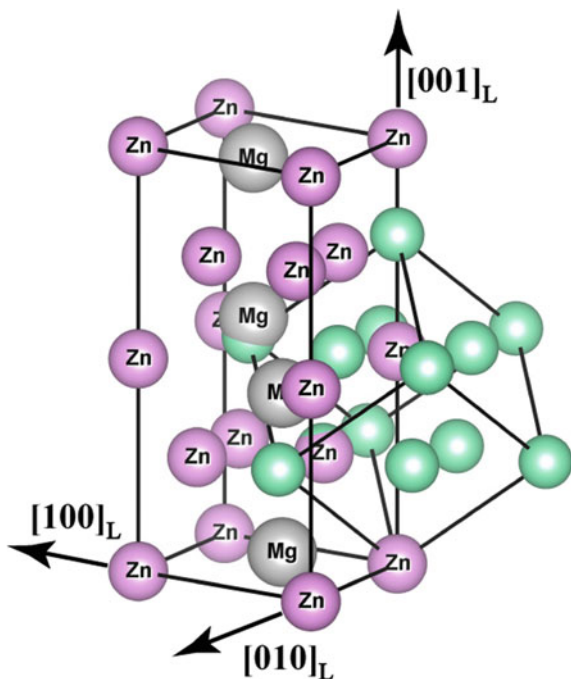


Fig. 2.10 The unit cell of the Zn_2Mg Laves phase in relation to an FCC unit cell (green colored atoms)

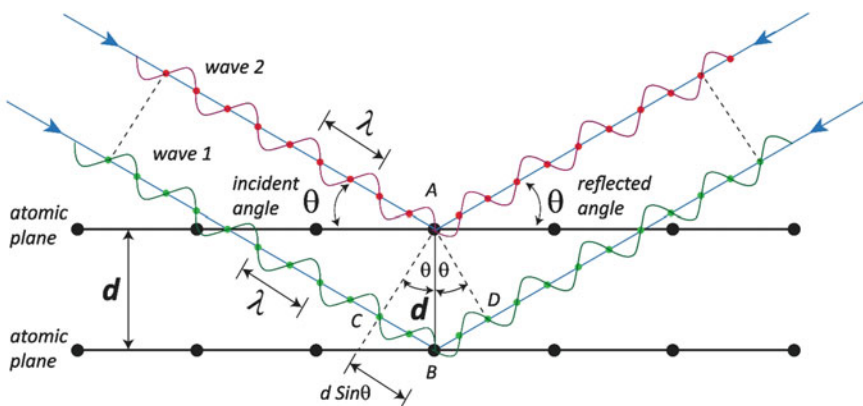


Fig. 2.11 The basic principles of x-ray diffraction and Bragg law

The intensity of a diffracted wave is proportional to the square of its structure factor. The structure factor depends upon the constituent atoms and their arrangements in the unit cell and the Miller indices of the reflecting plane. Each structure factor, F , can be considered a vector (commonly known as a k -vector) in the 3-dimensional space having an amplitude and a phase, and represents the total of waves scattered by all the atoms of the unit cell in the direction of reflection. The structure factor for a given diffracting plane, $\{hkl\}$, is given by [10]

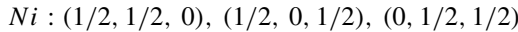
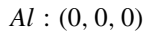
$$F_{hkl} = \sum_1^N f_n \exp[2\pi i(hu_n + kv_n + lw_n)] \quad (2.1)$$

where f_n is the atomic scattering factor/amplitude associated with the n th atom in the unit cell, u_n, v_n, w_n are the fractional coordinates of that atom, and N are the total number of atoms in the unit cell. For example, substituting the positions $(0,0,0)$, $(1/2, 1/2, 0)$, $(1/2, 0, 1/2)$, and $(0, 1/2, 1/2)$ of four atoms of an FCC unit cell in Eq. 2.1 would give its structure factor as

$$F = f[1 + \exp(ihk) + \exp(ihl) + \exp(ikl)] \quad (2.2)$$

In this equation, $\exp(n\pi i) = 1$ when $n = \text{even}$, and $= -1$ when n is odd. Therefore, $F = 4f$ when h, k and l indices are all odd or all even, and $F = 0$ when mixed. Relationship 2.2 implies that only atomic planes with unmixed Miller indices cause constructive reflections from their planes.

This analysis can be further extended to understand the effect of ordering on the structure factor by introducing chemical order in the lattice. Considering the L1₂ ordered phase formed after ordering of the nickel-13% aluminum solid solution. The L1₂ lattice contains nickel and aluminum atoms at specific positions of the FCC unit cell as



Substituting these positions in Eq. 2.1 would give the structure factor relationship for the L1₂ structure as $F_{L1_2} = f_{\text{Al}} + f_{\text{Ni}}[\exp(ihk) + \exp(ihl) + \exp(ikl)]$, and

$$F_{L1_2} = \begin{cases} f_{\text{Al}} + 3f_{\text{Ni}} & (\text{for unmixed } h, k, l) \\ f_{\text{Al}} - f_{\text{Ni}} & (\text{for mixed } h, k, l) \end{cases} \quad (2.3)$$

where f_{Ni} and f_{Al} are atomic scattering factors of Ni and Al atoms, respectively. The structure factor equals $f_{\text{Al}} + 3f_{\text{Ni}}$ when h, k, l are all odd or even, similar to the FCC structure. But it becomes non-zero ($= f_{\text{Al}} - f_{\text{Ni}}$) for the mixed reflections, unlike the forbidden reflections in a face-centered cubic structure. This analysis implies that even for the unmixed reflections, the diffraction peaks will appear for an L1₂ structure, though their intensities would be much less than those with unmixed h ,

k, l reflections. The intense reflections that arise due to the addition of the phase factors of the two types of atoms are termed “fundamental reflections”. In contrast, the chemically sensitive weaker reflections that appear due to the difference in the phase factors are termed “superlattice reflections”.

2.3.2 The Reciprocal Lattice

When striking a photographic plate or a detector, the diffracted waves from a crystal with non-zero structure factors leave their imprints in the form of well-defined spots that form a diffraction pattern. If diffraction occurs from a polycrystalline material containing randomly oriented crystals, these spots appear as rings. Allowed wave vectors that yield diffracted waves constitute the k -space, also known as the “momentum” or “reciprocal” space. The transfer of momentum due to constructive interference of the diffracted waves also forms a lattice termed the “reciprocal lattice”.

A reciprocal lattice, represented by a_1^* , a_2^* and a_3^* axes, is defined by vectors orthogonal to the “real” lattice given by Massalski and Barrett [11]

$$\begin{aligned} \mathbf{a}_1^* &= \frac{(\mathbf{a}_2 \wedge \mathbf{a}_3)}{V} \\ \mathbf{a}_2^* &= \frac{(\mathbf{a}_3 \wedge \mathbf{a}_1)}{V} \\ \mathbf{a}_3^* &= \frac{(\mathbf{a}_1 \wedge \mathbf{a}_2)}{V} \end{aligned} \quad (2.4)$$

where \mathbf{a}_1 , \mathbf{a}_2 and \mathbf{a}_3 represent the “real” (original) lattice basis vectors, $V (= \mathbf{a}_1 \cdot \mathbf{a}_2 \wedge \mathbf{a}_3)$ represents the volume of the direct unit cell, and the symbol \wedge represents the cross product between two vectors. Since each reciprocal lattice axis is the vector product of two (real) lattice axes, a reciprocal lattice axis is perpendicular to the plane defined by the two lattice axes in the real space. The axes of the two lattices are related as follows:

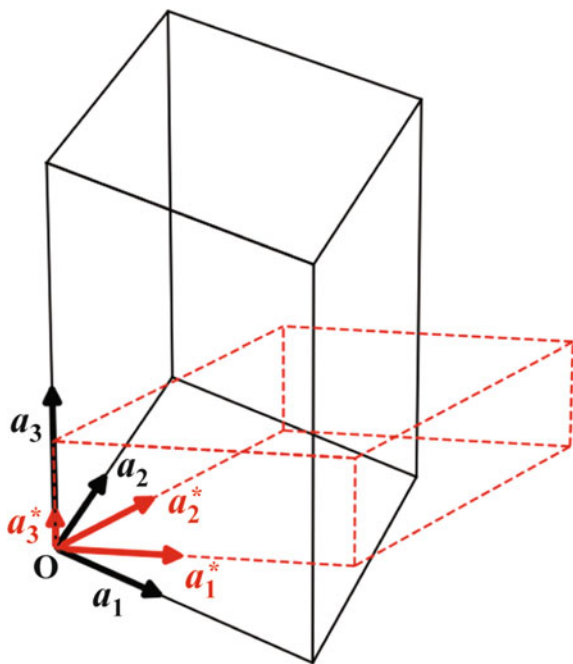
$$\mathbf{a}_1 \cdot \mathbf{a}_1^* = \mathbf{a}_2 \cdot \mathbf{a}_2^* = \mathbf{a}_3 \cdot \mathbf{a}_3^* = 1 \quad (2.5)$$

and

$$\mathbf{a}_1 \cdot \mathbf{a}_2^* = \mathbf{a}_1 \cdot \mathbf{a}_3^* = \mathbf{a}_2 \cdot \mathbf{a}_1^* = \mathbf{a}_2 \cdot \mathbf{a}_3^* = \mathbf{a}_3 \cdot \mathbf{a}_1^* = \mathbf{a}_3 \cdot \mathbf{a}_2^* = 0 \quad (2.6)$$

Figure 2.12 shows the relationship between the real and reciprocal lattices. The unit cell of the real lattice is indicated by solid black lines, while broken red lines draw the unit cell of the corresponding reciprocal lattice. The origin of the reciprocal lattice axes is designated by O . The repeat translation of the reciprocal lattice unit cell in three dimensions forms the complete reciprocal lattice. Each lattice point in the

Fig. 2.12 Relationship between the unit cells of real and reciprocal lattices. Solid black lines show the unit cell of the real lattice, while broken red lines draw the unit cell of the reciprocal lattice



reciprocal space can be represented by a vector, \mathbf{H}_{hkl} , corresponding to a particular set of planes (hkl) of the real lattice according to the relation,

$$\mathbf{H}_{hkl} = h \cdot \mathbf{a}_1^* + k \cdot \mathbf{a}_2^* + l \cdot \mathbf{a}_3^* \quad (2.7)$$

which is normal to the lattice planes (hkl) in the real space. The magnitude of the vector \mathbf{H}_{hkl} is the inverse of the d -spacings of (hkl) planes, $1/d_{hkl}$, from the lattice origin. Therefore, the location of the point in the reciprocal space defines the orientation and d -spacing of lattice planes in the corresponding real space lattice. The farther away a reciprocal lattice point is from the origin, the smaller is the d -spacing of the corresponding lattice planes. Therefore, the reciprocal lattice contains a uniquely defined array of points with the periodicity of the corresponding real lattice. The reciprocal lattice is similar to a “real” lattice but is termed so because all its dimensions are reciprocal length units. Vectors in the reciprocal lattice are usually suffixed by * to distinguish them from the real lattice. The intensity of reciprocal points (in diffraction patterns) is characteristic of a given phase, which can be utilized along with their position ($1/d_{hkl}$) as fingerprints to identify the phase uniquely.

2.3.3 The Ewald Sphere

How the intensity of reciprocal points (reflection spots) depends upon the orientation of the crystal with respect to the incident x-ray beam can be understood from the Ewald sphere concept, which relates wave vectors of the incident x-rays, the diffracted x-rays and the diffraction angle (θ) for a given reflection in the reciprocal space. An Ewald sphere is a geometrical construction of a radius defined by the reciprocal of the wavelength of the incident wave, $1/\lambda$, with the diffracting crystal located at its center, C (Fig. 2.13). Figure 2.13 shows two Ewald spheres of radii $1/\lambda_1$ and $1/\lambda_2$ with corresponding centers as C_1 and C_2 to illustrate the effect of the radiation wavelength, discussed later. However, for the time being, the subscripts can be ignored. The incident beam can be visualized as a vector from I to C . The diffracted beam is the vector from C to P . Both the incident beam and the diffracted beam are at an angle θ from a set of crystal planes, say (hkl) , separated by the d -spacing d_{hkl} . Both incident beam vector, \mathbf{CO} , and the diffracted beam vector \mathbf{CP}

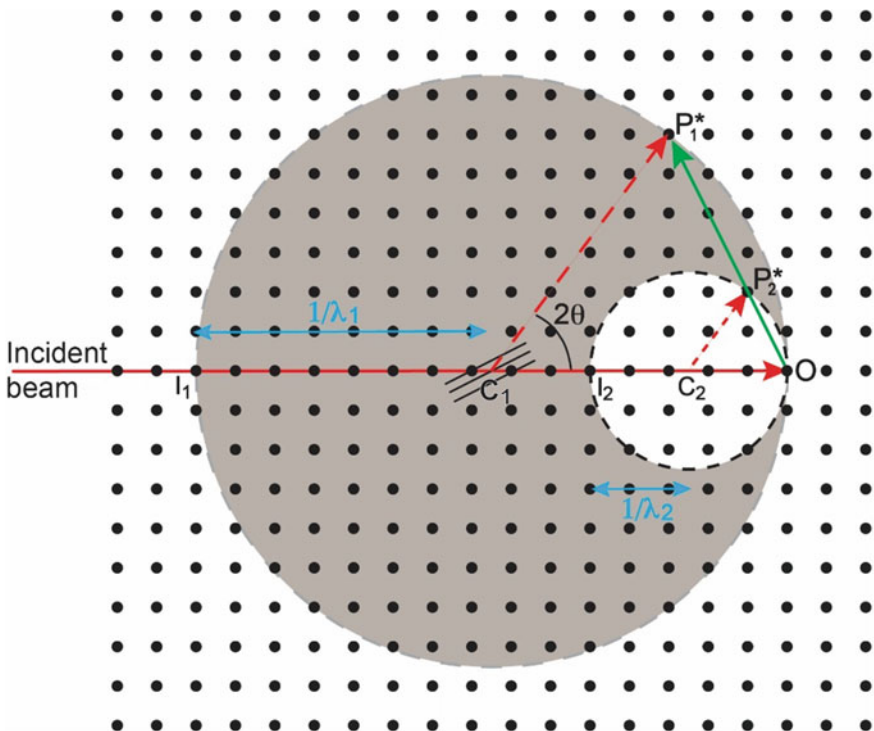


Fig. 2.13 A schematic representation of the Ewald sphere construction, superimposed by a reciprocal lattice. The radius of the sphere is given by $1/\lambda$. The figure shows two Ewald spheres of radii $1/\lambda_1$ and $1/\lambda_2$ to highlight the difference in the number of reciprocal lattice points in contact with the Ewald surface for the two wavelengths. Vector OP represents the diffraction vector, \mathbf{g} , due to constructive interference of the incident beam from the (hkl) plane

start at point C and end at points O and P , respectively, on the surface of the Ewald sphere. The vector from O to P is the reciprocal lattice vector \mathbf{H}_{hkl} and is defined as the diffraction vector \mathbf{g} associated with Bragg's reflection of the (hkl) plane. All the reciprocal lattice points that lie on the surface of the Ewald sphere satisfy the Bragg condition. Therefore, the reciprocal lattice point, P^* , on the sphere's surface represents the constructive interference of the incident beam with the (hkl) . The incident beam passes through the origin of the reciprocal lattice, O , on the Ewald sphere and coincides with the lattice position of the real lattice. By changing the orientation of the reciprocal lattice, all reciprocal lattice points can be mapped and measured. The Ewald sphere construction, combined with the reciprocal lattice, gives a simple way of visualizing the diffraction phenomenon for a single crystal.

A similar diffraction principle is applicable for other radiations like electrons and neutrons. However, the difference in the radiation wavelength would affect the number of reciprocal lattice points on the surface of the Ewald sphere. This is illustrated by Ewald spheres of two different radii $1/\lambda_1$ and $1/\lambda_2$, in Fig. 2.13. This implies that when the wavelength of the radiation is large, e.g., say, of x-rays, the radius of the Ewald sphere would be of the order of the spacing between the reciprocal points and only one reciprocal lattice point would intersect with the surface of the Ewald sphere at a given crystal orientation. But when λ is much small, say, of the order of picometer as in the case of electrons accelerated at about 200 keV, a large number of reciprocal points would intersect with the sphere because the radius of the Ewald sphere would be about two orders larger than that of the lattice spacing.

An Ewald sphere with a large radius has important implications for interpreting the diffraction patterns of a crystal in different zones. A zone represents certain sets of crystal planes that intersect along a common line, and the line of their intersection is termed the "zone axis". In principle, any two non-parallel planes can cross, but a zone contains many different sets of crystal planes. A zone axis, $[uvw]$, thus represents all the planes whose normals are perpendicular to the $[uvw]$ direction. Therefore, for an electron diffraction pattern in a $[uvw]$ zone axis, i.e., when the incident beam is along the $[uvw]$ direction, all the $\{hkl\}$ planes for which $hu + kv + lw = 0$ and which lie on the surface of the Ewald sphere would appear as diffraction spots. For instance, the $[001]$ zone axis of an FCC phase would show reflections from (200) , (020) , (220) and their combinations that satisfy the $hu + kv + lw = 0$ condition.

2.4 Lattice Correspondence Between Cubic and Non-cubic Phases

Consider a transformation from a cubic to non-cubic phase. If Miller indices of directions and planes of a cubic phase are respectively written as column and row matrices as $[u]_C$ and $(h)_C$, the corresponding indices in the non-cubic crystal structure, $[u]_N$ and $(h)_N$, can be obtained by the following matrix relationships.

$$[u]_N = {}_N\Phi^C [u]_C \quad (2.8)$$

$$(h)_N = (h)_C [{}_N\Phi^C]^{-1} \quad (2.9)$$

where ${}_N\Phi^C$ and $[{}_N\Phi^C]^{-1}$ are 3×3 matrices expressing the correspondence relationship between the two bases, so that the columns of the $[{}_N\Phi^C]^{-1}$ matrix are the cube components of the base vectors of the ordered structure (superlattice cell). Using these matrices, it is possible to find the correspondence relationship of any direction or plane between the parent cubic structure and the non-cubic superlattice structure.

2.5 Identification of Phases in Alloy 625

All the phases that form in Alloy 625 are ordered derivatives of the disordered FCC γ phase. However, the slight difference between the atomic structure factors of the ordering elements, e.g., between Ni and Nb of the δ phase and their low volume fractions, does not give a reasonable number of diffraction peaks with sufficient intensity when examined by x-ray diffraction. X-ray diffraction can identify these particles if they are extracted out of the matrix, but such an analysis is associated with its limitations. Electron diffraction by transmission electron microscopy is the best technique for unambiguous identification of such phases. Further, the phase transformations relevant to the precipitating phases in the present context arise due to chemical ordering of the lattice below a specific temperature. Chemical ordering of the disordered lattice breaks cubic symmetry of the disordered matrix as different size of the ordering atoms distorts the lattice slightly in the direction of ordering. Therefore, certain planes and directions of the matrix and the precipitating phase remain parallel or nearly parallel during the ordering transformation, based on orientation relationships between the two. Consequently, the fundamental reflections of the precipitating phase coincide with those of the matrix phase. However, the chemical order in the ordered phase manifests itself as superlattice reflections at characteristic positions, which are otherwise forbidden for the disordered FCC phase. These superlattice reflections help in identifying the nature of the precipitating phase. The superlattice reflections appear at unique positions in a diffraction pattern depending upon the direction of order, i.e., the ordered variant involved. Positions of these superlattice reflections can be identified based on the structure factor and lattice correspondence analysis of the ordered phase. This analysis can be used to simulate electron diffraction patterns for a given zone axis.

2.5.1 Identification of the γ'' Phase

The structure factor for the D0₂₂ structure of the N₃M γ'' phase is given by [12]

$$\begin{aligned} F^{D0_{22}} = & f_M + f_M \exp 2\pi i \left(\frac{h}{2} + \frac{k}{2} + \frac{l}{2} \right) + f_N \exp 2\pi i \frac{l}{2} + f_N \exp 2\pi i \left(\frac{h}{2} + \frac{k}{2} \right) \\ & + f_N \exp 2\pi i \left(\frac{k}{2} + \frac{l}{4} \right) + f_N \exp 2\pi i \left(\frac{h}{2} + \frac{l}{4} \right) \\ & + f_N \exp 2\pi i \left(\frac{k}{2} + \frac{3l}{4} \right) + f_N \exp 2\pi i \left(\frac{h}{2} + \frac{3l}{4} \right) \end{aligned}$$

where f_N and f_M are the atomic scattering factors for N and M atoms, respectively. On rearranging the terms, one gets

$$\begin{aligned} F^{D0_{22}} = & [1 + \exp \pi i(h+k+l)] \\ & \left[f_M + f_N \exp \pi i \frac{l}{2} \left(\exp \pi i h + \exp \pi i k + \exp \pi i \frac{l}{2} \right) \right] \end{aligned} \quad (2.10)$$

All reflections for which $h+k+l$ is odd, the structure factor is zero and the reflections are forbidden. The forbidden reflections arise because of the body-centered nature of the $D0_{22}$ unit cell. For $h+k+l = \text{even}$, the structure factor for fundamental and superlattice reflections, respectively can be thus be expressed as

$$F_f^{D0_{22}} = 2(3f_N + f_M) \begin{cases} \text{for } h, k, l \text{ all even, } l = 4n \\ \text{for } l \text{ even, } h \text{ and } k \text{ odd, } l = 4n+2 \end{cases} \quad n = 0, 1, 2 \dots \quad (2.11)$$

$$F_s^{D0_{22}} = 2(f_M - f_N) \begin{cases} \text{for } h, k, l \text{ all even, } l = 4n+2 \\ \text{for } l \text{ even, } h \text{ and } k \text{ odd, } l = 4n \\ \text{for } l \text{ odd, } h \text{ and } k \text{ mixed} \end{cases} \quad n = 0, 1, 2 \dots \quad (2.12)$$

The subscripts f and s denote the fundamental and superlattice reflections, respectively. The values of the F for different values of h , k and l , are listed in Table 2.4.

Table 2.5 gives lattice correspondence matrices expressing the relationship between the parent FCC structure and three variants of the tetragonal structure of the γ'' phase. Table 2.6 provides the correspondence between planes of the FCC and the $D0_{22}$ structures, calculated using Eq. 2.9. The plane correspondences between the two structures assume an axial ratio of 2 for the $D0_{22}$ structure. Table 2.4 indicates that reflections like $(002)_{\gamma''}^*$, and $(110)_{\gamma''}^*$ and $(011)_{\gamma''}^*$ would appear as superlattice reflections for the $D0_{22}$ variant having the c -axis parallel to [001] of the FCC structure. These reflections are equivalent to $(001)^*$, $(110)^*$ and $(0\ 1\ \frac{1}{2})^*$ reciprocal vectors of the cubic lattice. Similarly, identical superlattice reflections corresponding to the other two variants of the γ'' phase would also appear when all the three variants are present. Therefore, the fundamental reciprocal vectors $\{200\}^*$ and $\{220\}^*$ would be halved by $\{001\}^*$ and $\{110\}^*$ superlattice reflections, and the $\{240\}^*$ reciprocal vectors would be divided into four parts by the $\{1/2\ 1\ 0\}^*$ superlattice reflection when

Table 2.4 Structure factor (F) for different h , k and l values of planes of the D0₂₂ structure with N₃M stoichiometry

$h + k + l$	h	k	l	F	Typical reflections	
					Miller indices in D0 ₂₂ basis	Miller indices in cubic basis
Odd	Odd	Even	Even	0	(100) _{γ''} , (102) _{γ''} , (300) _{γ''}	(100), (101), (300)
	Even	Odd	Even		(010) _{γ''} , (012) _{γ''} , (212) _{γ''}	(010), (011), (211)
	Even	Even	Odd		(001) _{γ''} , (201) _{γ''} , (003) _{γ''}	(0 0 $\frac{1}{2}$), (2 0 $\frac{1}{2}$), (0 0 $\frac{3}{2}$)
	Odd	Odd	Odd		(111) _{γ''} , (311) _{γ''} , (331) _{γ''}	(1 1 $\frac{1}{2}$), (3 1 $\frac{1}{2}$), (3 3 $\frac{1}{2}$)
Even	Even	Even	$l/2$ Even	2(3f_N + f_M)	(220) _{γ''} , (004) _{γ''} , (024) _{γ''} , (404) _{γ''}	(220), (002), (022), (402)
	Odd	Odd	$l/2$ Odd		(112) _{γ''} , (116) _{γ''} , (312) _{γ''} , (136) _{γ''}	(111), (113), (311), (133)
	Even	Even	$l/2$ Odd		(002) _{γ''} , (202) _{γ''} , (042) _{γ''}	(001), (201), (041)
	Odd	Odd	$l/2$ Even	2(f_N - f_M)	(110) _{γ''} , (114) _{γ''} , (130) _{γ''} , (310) _{γ''}	(110), (112), (130), (310)
	Odd	Even	Odd		(101) _{γ''} , (301) _{γ''} , (303) _{γ''} , (321) _{γ''}	(1 0 $\frac{1}{2}$), (3 0 $\frac{1}{2}$), (3 0 $\frac{3}{2}$), (3 2 $\frac{1}{2}$)
	Even	Odd	Odd		(011) _{γ''} , (031) _{γ''} , (013) _{γ''} , (211) _{γ''}	(0 1 $\frac{1}{2}$), (0 3 $\frac{1}{2}$), (0 3 $\frac{3}{2}$), (2 1 $\frac{1}{2}$)

Some illustrative examples of allowed ($F = \text{non-zero}$) and forbidden ($F = 0$) reflections are listed along with their equivalent indices in cubic basis. The orientation of the D0₂₂ structure is assumed to be of Variant 1 of the ordered phase (Table 2.5)

all the three variants of the γ'' phase are present. Therefore, all the diffraction patterns containing {200}*, {220}* and {240}* reflections would show superlattice reflections, as illustrated by the simulated [001] zone axis diffraction pattern (Fig. 2.14). Thus, a <001> zone axis would contain superlattice reflections corresponding to all the three variants of the D0₂₂ phase, which can be imaged individually by dark-field³ imaging in a transmission electron microscope.

³ Bright-field (BF) and dark field (DF) are two diffraction contrast imaging modes in transmission electron microscopy, depending upon whether the transmitted or a diffracted electron beam is chosen for forming the image [14]. In the BF mode, imaged features appear dark in a bright background, while they appear bright in a dark background in the DF mode.

Table 2.5 Lattice correspondence matrices relating the FCC phase to different variants of the D0₂₂ phase

Variant	$T\Phi^C$	$C\Phi^T = [T\Phi^C]^{-1}$
1	$\begin{bmatrix} 1 & 0 & 0 \\ 0 & 1 & 0 \\ 0 & 0 & 2 \end{bmatrix}$	$\frac{1}{2} \begin{bmatrix} 2 & 0 & 0 \\ 0 & 2 & 0 \\ 0 & 0 & 1 \end{bmatrix}$
2	$\begin{bmatrix} 0 & 1 & 0 \\ 0 & 0 & 2 \\ 1 & 0 & 0 \end{bmatrix}$	$\frac{1}{2} \begin{bmatrix} 0 & 0 & 2 \\ 2 & 0 & 0 \\ 0 & 1 & 0 \end{bmatrix}$
3	$\begin{bmatrix} 0 & 0 & 2 \\ 1 & 0 & 0 \\ 0 & 1 & 0 \end{bmatrix}$	$\frac{1}{2} \begin{bmatrix} 0 & 2 & 0 \\ 0 & 0 & 2 \\ 1 & 0 & 0 \end{bmatrix}$

Notation $T\Phi^C$ represents correspondence from tetragonal basis, T , to cubic basis, C

2.5.2 Identification of the Ni₂(Cr, Mo) Phase

For the Pt₂Mo-type phase of N₂M stoichiometry, the structure factor relationship is given by Singh [14]

$$\begin{aligned} F^{N_2M} &= f_M + f_M \exp 2\pi i \left(\frac{h}{2} + \frac{k}{2} + \frac{l}{2} \right) + f_N \exp 2\pi i \left(\frac{k}{3} \right) + f_N \exp 2\pi i \left(\frac{2k}{3} \right) \\ &+ f_N \exp 2\pi i \left(\frac{h}{2} + \frac{k}{6} + \frac{l}{2} \right) + f_N \exp 2\pi i \left(\frac{h}{2} + \frac{5k}{6} + \frac{l}{2} \right) \\ F^{N_2M} &= \left[1 + \exp \pi i (h+k+l) \right] \left[f_M + f_N \left(\exp \pi i \frac{2k}{3} + \exp \pi i \frac{4k}{3} \right) \right] \end{aligned}$$

This relationship simplifies to the form

$$F^{N_2M} = \left[1 + \exp \pi i (h+k+l) \right] \left[f_M + 2f_N \cos \frac{\pi k}{3} \exp \pi i k \right] \quad (2.13)$$

Again, all the reflections for which $h+k+l$ is odd are forbidden because of the body-centered nature of the unit cell. When $h+k+l$ is even, the reflections would be fundamental or superlattice depending upon the value of k , and their structure factors will be

$$F_f^{N_2M} = 2(2f_N + f_M) \quad \text{for } k = 3, 6, \dots \quad (2.14)$$

Table 2.6 Plane correspondence of different variants of the D0₂₂ phase with respect to the FCC lattice

Cubic	D0 ₂₂ phase		
	(100) Variant	(010) Variant	(001) Variant
1 1 1	1 1 2	1 1 2	1 1 2
1 1 1	1 1 2	1 1 2	1 1 2
1 1 1	1 1 2	1 1 2	1 1 2
1 1 1	1 1 2	1 1 2	1 1 2
2 0 0	2 0 0	0 2 0	0 0 4
0 2 0	0 2 0	0 0 4	2 0 0
0 0 2	0 0 4	2 0 0	0 2 0
2 2 0	2 2 0	0 2 4	2 0 4
2 2 0	2 2 0	0 2 4	2 0 4
2 0 2	2 0 4	2 2 0	0 2 4
2 0 2	0 2 4	2 2 0	0 2 4
0 2 2	0 2 4	2 0 4	2 2 0
0 2 2	0 2 4	2 0 4	2 2 0
0 2 4	0 2 8	4 0 4	2 4 0
0 2 4	0 2 8	4 0 4	2 4 0
0 4 2	0 4 4	2 0 8	4 2 0
0 4 2	0 4 4	2 0 8	4 2 0
2 0 4	2 0 8	4 2 0	0 4 4
2 0 4	2 0 8	4 2 0	0 4 4
4 0 2	4 0 4	2 4 0	0 2 8
4 0 2	4 0 4	2 4 0	0 2 8
2 4 0	2 4 0	0 2 8	4 0 4
2 4 0	2 4 0	0 2 8	4 0 4
4 2 0	4 2 0	0 4 4	2 0 8
4 2 0	4 2 0	0 4 4	2 0 8

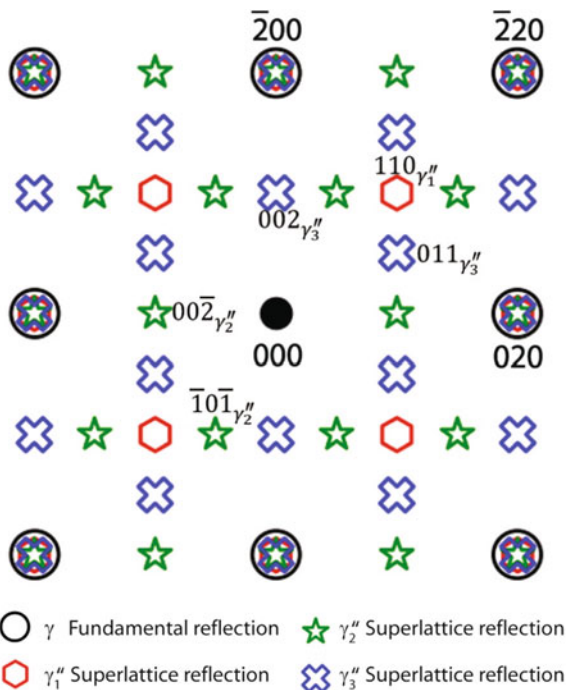
The γ'' phase planes which would show superlattice reflections along their reciprocal vectors are shown in Bold

$$F_s^{N_2M} = 2(f_N - f_M) \quad \text{for } k \neq 3, 6 \dots \quad (2.15)$$

F for different values of h , k and l are listed in Table 2.7.

Lattice correspondence matrices relating the parent cubic structure to different variants of the ordered orthorhombic structure (designated as o) of the Ni₂(Cr, Mo) phase are listed in Table 2.8. Some relevant plane correspondences between the FCC phase and different variants of the Ni₂(Cr, Mo) phase are given in Table 2.9. To simulate the position of superlattice reflections of the orthorhombic phase in electron diffraction patterns, an analysis of its structure factor (Table 2.7) and correspondence of planes with the cubic phase (Table 2.9) can be performed like the one done in

Fig. 2.14 Simulated [001] zone axis pattern of the γ'' phase illustrating the appearance of superlattice reflections due to different variants of the ordered phase. 1, 2 and 3 refers to the [001], [010] and [100] variants of the γ'' phase



Sect. 2.5.1. The reciprocal vectors $\{220\}^*$, $\{113\}^*$ and $\{024\}^*$ of the orthorhombic phase would each be divided into three parts because of superlattice reflections of one or more variants of the ordered phase. Specific variants would show superlattice reflections in particular directions in the reciprocal lattice. These superlattice reflections can identify different variants of the $\text{Ni}_2(\text{Cr}, \text{Mo})$ phase unambiguously. Figure 2.15 shows a set of such simulated electron diffraction patterns.

2.5.3 Identification of the δ Phase

For the δ phase with N_3M stoichiometry, the structure factor is given by Sundararaman [13]

$$\begin{aligned} F^{D0a} = & f_M \left[\exp 4\pi i \frac{l}{3} + \exp 2\pi i \left(\frac{h+k}{2} + \frac{l}{3} \right) \right] \\ & + f_N \left[\exp 2\pi i \left(\frac{k}{2} + \frac{l}{3} \right) + \exp 2\pi i \left(\frac{h}{2} + \frac{2l}{3} \right) + \exp 2\pi i \left(\frac{h}{4} + \frac{l}{6} \right) + \exp 2\pi i \left(\frac{3h}{4} + \frac{l}{6} \right) \right. \\ & \quad \left. + \exp 2\pi i \left(\frac{h}{4} + \frac{k}{2} + \frac{5l}{6} \right) + \exp 2\pi i \left(\frac{3h}{4} + \frac{k}{2} + \frac{5l}{6} \right) \right] \end{aligned} \quad (2.16)$$

Table 2.7 Structure factor (F) for different h , k and l values of planes of the $\text{Ni}_2(\text{Cr},\text{Mo})$ phase

$h + k + l$	h	k	l	F	Typical reflections	
					Orthorhombic basis	FCC basis
Odd	Odd	Even	Even	0	(100) _o , (102) _o , (300) _o	(110), (112), (330)
	Even	Odd	Even		(010) _o , (012) _o , (212) _o	($\frac{1}{3} \frac{1}{3} 0$), ($\frac{1}{3} \frac{1}{3} 2$), ($\frac{5}{3} \frac{7}{3} 2$)
	Even	Even	Odd		(001) _o , (201) _o , (003) _o	(001), (221), (003)
	Odd	Odd	Odd		(111) _o , (311) _o , (331) _o	($\frac{2}{3} \frac{4}{3} 1$), ($\frac{2}{3} \frac{4}{3} 1$), (241)
Even	Even	$K/3$ Even	Even	2(2f_N + f_M)	(002) _o , (200) _o , (202) _o , (060) _o	(002), (220), (222), (220)
	Odd	$K/3$ Odd	Even		(130) _o , (132) _o , (330) _o , (332) _o	(020), (022), (240), (242)
	Odd	$K/3$ Even	Odd		(101) _o , (103) _o , (161) _o , (361) _o	(111), (113), ($\bar{1}31$), (151)
	Even	$K/3$ Odd	Odd		(031) _o , (231) _o , (033) _o , (233) _o	($\bar{1}11$), (131), ($\bar{1}13$), ($\bar{1}33$)
	Even	$K/3$	Even	2(f_M - f_N)	(020) _o , (022) _o , (220) _o , (042) _o	($\frac{2}{3} \frac{2}{3} 0$), ($\frac{2}{3} \frac{2}{3} 2$), ($\frac{4}{3} \frac{8}{3} 0$), ($\frac{4}{3} \frac{4}{3} 2$)
	Odd		Even		(110) _o , (112) _o , (150) _o	($\frac{2}{3} \frac{4}{3} 0$), ($\frac{2}{3} \frac{4}{3} 2$), ($\frac{2}{3} \frac{8}{3} 0$)
	Odd	Non-integral	Odd		(121) _o , (123) _o , (321) _o , (141) _o	($\frac{1}{3} \frac{5}{3} 1$), ($\frac{1}{3} \frac{5}{3} 3$), ($\frac{7}{3} \frac{11}{3} 1$), ($\frac{1}{3} \frac{7}{3} 1$)
	Even	Odd	(011) _o , (013) _o , (211) _o , (051) _o		($\frac{1}{3} \frac{1}{3} 1$), ($\frac{1}{3} \frac{1}{3} 3$), ($\frac{5}{3} \frac{7}{3} 1$), ($\frac{5}{6} \frac{5}{6} 1$)	

Some illustrative examples of allowed ($F = \text{non-zero}$) and forbidden ($F = 0$) reflections are listed along with their equivalent indices in cubic basis. The orientation of the $\text{Ni}_2(\text{Cr},\text{Mo})$ phase is assumed to be of Variant 2 of the ordered phase (Table 2.8)

The values of F for various combinations of h , k and l are listed in Table 2.10. The structure factor is non-zero for all reflections except for which $h + k$ is odd and $l = 3n$, where n is an integer.

The lattice correspondence matrices relating the FCC structure to the orthorhombic structure of the δ phase (designated as δ) are listed in Table 2.11. The plane correspondence between the two phases can be identified using the correspondence matrices. Some relevant plane correspondence relationships between the

Table 2.8 Lattice correspondence matrices relating the FCC phase to different Ni₂(Cr,Mo) phase variants

Variant	$O\Phi^C = [C\Phi^O]^{-1}$	$C\Phi^O = [O\Phi^C]^{-1}$
1	$\frac{1}{2} \begin{bmatrix} 1 & 3 & 0 \\ -1 & 3 & 0 \\ 0 & 0 & 2 \end{bmatrix}$	$\frac{1}{3} \begin{bmatrix} 3 & -3 & 0 \\ 1 & 1 & 0 \\ 0 & 0 & 3 \end{bmatrix}$
2	$\frac{1}{2} \begin{bmatrix} 1 & -3 & 0 \\ 1 & 3 & 0 \\ 0 & 0 & 2 \end{bmatrix}$	$\frac{1}{3} \begin{bmatrix} 3 & 3 & 0 \\ -1 & 1 & 0 \\ 0 & 0 & 3 \end{bmatrix}$
3	$\frac{1}{2} \begin{bmatrix} 1 & 3 & 0 \\ 0 & 0 & 2 \\ 1 & -3 & 0 \end{bmatrix}$	$\frac{1}{3} \begin{bmatrix} 3 & 0 & 3 \\ 1 & 0 & -1 \\ 0 & 3 & 0 \end{bmatrix}$
4	$\frac{1}{2} \begin{bmatrix} 1 & -3 & 0 \\ 0 & 0 & 2 \\ -1 & -3 & 0 \end{bmatrix}$	$\frac{1}{3} \begin{bmatrix} 3 & 0 & -3 \\ -1 & 0 & -1 \\ 0 & 3 & 0 \end{bmatrix}$
5	$\frac{1}{2} \begin{bmatrix} 0 & 0 & 2 \\ -1 & 3 & 0 \\ -1 & -3 & 0 \end{bmatrix}$	$\frac{1}{3} \begin{bmatrix} 0 & -3 & -3 \\ 0 & 1 & -1 \\ 3 & 0 & 0 \end{bmatrix}$
6	$\frac{1}{2} \begin{bmatrix} 0 & 0 & 2 \\ 1 & 3 & 0 \\ -1 & 3 & 0 \end{bmatrix}$	$\frac{1}{3} \begin{bmatrix} 0 & 3 & -3 \\ 0 & 1 & 1 \\ 3 & 0 & 0 \end{bmatrix}$

Notation $O\Phi^C$ represents correspondence from orthogonal basis, O , of the Ni₂(Cr,Mo) phase to the cubic basis, C , of the γ matrix

FCC phase and 12 variants of the δ phase are given in Table 2.12. From Table 2.10, specific planes that exhibit superlattice reflections of the δ phase can be identified based on their structure factor values. However, the superlattice reflections would appear only for a specific variant of the δ phase. For example, the allowed $(200)_\delta^*$ and $(001)_\delta^*$ superlattice reflections of the δ phase appear only along $(400)_\delta^*$ and $(006)_\delta^*$ reciprocal vectors of the δ phase (Table 2.10). As a result, the $(400)_\delta^*$ and $(006)_\delta^*$ reciprocal vectors would be divided into 2 and 6 parts, respectively of the δ phase. The $(400)_\delta$ and $(006)_\delta$ planes are parallel to only some specific planes of the {220} and {224} families of the cubic structure depending upon the ordering direction (i.e., variant) of the δ phase. For instance, the $(400)_\delta$ is parallel to the (2 2 0) FCC plane for δ_1 and δ_4 variants only, while the $(006)_\delta$ planes are parallel to (2 $\bar{2}$ 4) for the δ_7 variant only (Table 2.12). Therefore, zone axes containing (2 $\bar{2}$ 0)* and (2 $\bar{2}$ 4)* reciprocal vectors would exhibit superlattice reflections corresponding

Table 2.9 Plane correspondence of different variants of the Ni₂(Cr,Mo) superlattice with respect to FCC lattice

Cubic	Ni ₂ (Cr,Mo) Phase					
	Variant 1	Variant 2	Variant 3	Variant 4	Variant 5	Variant 6
1 1 1	0 3 1	1 0 1	1 0 1	0 $\bar{3}$ 1	$\bar{1}$ 0 1	0 3 1
$\bar{1}$ 1 1	$\bar{1}$ 0 1	0 3 1	0 $\bar{3}$ 1	$\bar{1}$ 0 1	$\bar{1}$ 0 $\bar{1}$	0 3 $\bar{1}$
1 $\bar{1}$ 1	1 0 1	0 $\bar{3}$ 1	1 0 $\bar{1}$	0 $\bar{3}$ $\bar{1}$	0 $\bar{3}$ 1	$\bar{1}$ 0 1
1 1 $\bar{1}$	0 3 $\bar{1}$	1 0 $\bar{1}$	0 3 1	1 0 1	0 3 1	1 0 1
2 0 0	1 3 0	1 $\bar{3}$ 0	1 3 0	1 $\bar{3}$ 0	0 0 2	0 0 2
0 2 0	$\bar{1}$ 3 0	1 3 0	0 0 2	0 0 2	$\bar{1}$ 3 0	1 3 0
0 0 2	0 0 2	0 0 2	1 $\bar{3}$ 0	$\bar{1}$ $\bar{3}$ 0	$\bar{1}$ $\bar{3}$ 0	$\bar{1}$ 3 0
2 2 0	0 6 0	2 0 0	1 3 2	1 $\bar{3}$ 2	$\bar{1}$ 3 2	1 3 2
$\bar{2}$ 2 0	$\bar{2}$ 0 0	0 6 0	$\bar{1}$ $\bar{3}$ 2	$\bar{1}$ 3 2	$\bar{1}$ 3 $\bar{2}$	1 3 $\bar{2}$
2 0 2	1 3 2	1 $\bar{3}$ 2	2 0 0	0 6 0	$\bar{1}$ $\bar{3}$ 2	$\bar{1}$ 3 2
2 0 $\bar{2}$	1 3 $\bar{2}$	1 $\bar{3}$ $\bar{2}$	0 6 0	2 0 0	1 3 2	1 $\bar{3}$ 2
0 2 2	$\bar{1}$ 3 2	1 3 2	1 $\bar{3}$ 2	$\bar{1}$ $\bar{3}$ 2	$\bar{2}$ 0 0	0 6 0
0 2 $\bar{2}$	$\bar{1}$ 3 $\bar{2}$	1 3 $\bar{2}$	$\bar{1}$ 3 2	1 3 2	0 6 0	2 0 0
3 1 1	1 6 1	2 $\bar{3}$ 1	2 3 1	1 $\bar{6}$ 1	$\bar{1}$ 0 3	0 3 3
$\bar{3}$ 1 1	$\bar{2}$ $\bar{3}$ 1	$\bar{1}$ 6 1	$\bar{1}$ $\bar{6}$ 1	$\bar{2}$ 3 1	$\bar{1}$ 0 $\bar{3}$	0 3 $\bar{3}$
3 $\bar{1}$ 1	2 3 1	$\bar{1}$ $\bar{6}$ 1	2 3 $\bar{1}$	1 $\bar{6}$ $\bar{1}$	0 $\bar{3}$ 3	$\bar{1}$ 0 3
3 1 $\bar{1}$	1 6 $\bar{1}$	2 $\bar{3}$ $\bar{1}$	1 6 1	2 $\bar{3}$ 1	0 3 3	1 0 3
1 3 1	$\bar{1}$ 6 1	2 3 1	1 0 3	0 $\bar{3}$ 3	$\bar{2}$ 3 1	1 6 1
$\bar{1}$ 3 1	$\bar{2}$ 3 1	1 6 1	0 $\bar{3}$ 3	$\bar{1}$ 0 3	$\bar{2}$ 3 $\bar{1}$	1 6 $\bar{1}$
1 $\bar{3}$ 1	2 $\bar{3}$ 1	$\bar{1}$ 6 1	1 0 $\bar{3}$	0 $\bar{3}$ $\bar{3}$	1 $\bar{6}$ 1	$\bar{2}$ 3 1
1 3 $\bar{1}$	$\bar{1}$ 6 $\bar{1}$	2 3 $\bar{1}$	0 3 3	1 0 3	$\bar{1}$ 6 1	2 3 1
1 1 3	0 3 3	1 0 3	2 $\bar{3}$ 1	1 $\bar{6}$ 1	$\bar{2}$ 3 1	$\bar{1}$ 6 1
$\bar{1}$ 1 3	$\bar{1}$ 0 3	0 3 3	1 $\bar{6}$ 1	$\bar{2}$ 3 1	$\bar{2}$ $\bar{3}$ $\bar{1}$	$\bar{1}$ 6 $\bar{1}$
1 $\bar{1}$ 3	1 0 3	0 $\bar{3}$ 3	2 $\bar{3}$ $\bar{1}$	$\bar{1}$ $\bar{6}$ $\bar{1}$	$\bar{1}$ $\bar{6}$ 1	$\bar{2}$ 3 1
1 1 $\bar{3}$	0 3 $\bar{3}$	1 0 $\bar{3}$	$\bar{1}$ 6 1	2 3 1	1 6 1	2 $\bar{3}$ 1

The Ni₂(Cr,Mo) phase planes which would show superlattice reflections along their reciprocal vectors are shown in Bold

to the δ_1/δ_4 and δ_7 variants. Reciprocal vectors corresponding to other planes would show superlattice reflections for other variants. This is illustrated by the simulated [001] and [110] zone axes electron diffraction patterns of the δ phase (Fig. 2.16). It is important to note here that the {111}* and {311}* reciprocal vectors in the

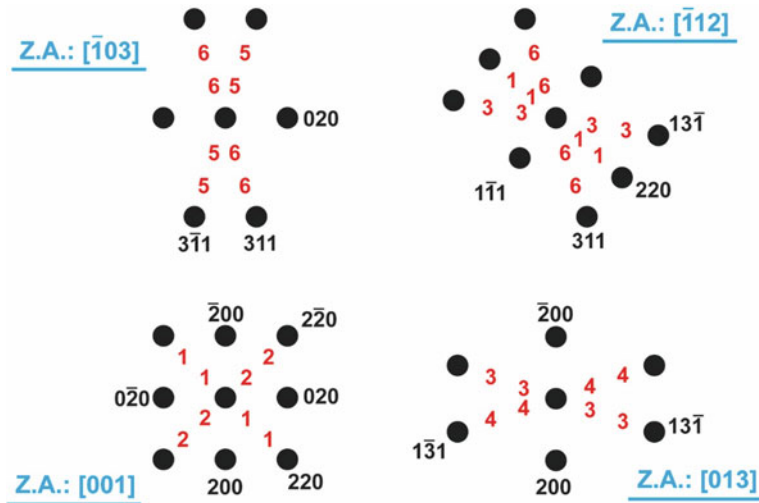


Fig. 2.15 Simulated electron diffraction patterns corresponding to the $\langle 103 \rangle$ and $\langle 112 \rangle$ zone axes in the vicinity of the $[001]$ zone, which can be utilized to identify different variants of the $\text{Ni}_2(\text{Cr},\text{Mo})$ phase. The numbers 1–6 mark the positions of the superlattice reflections corresponding to different variants of the phase. Different zones have been underlined

Table 2.10 Structure factor (F) for different h , k and l values of planes of the δ ($D0_a$) along with some illustrative examples of allowed ($F = \text{non-zero}$) and forbidden ($F = 0$) reflections

h	k	l	F	Examples
Odd	Odd	$l = 3n$	$2(f_M - f_N)$	$(110)_\delta, (133)_\delta, (313)_\delta, (113)_\delta, (330)_\delta$
		$l \neq 3n$	$(f_M - f_N)$	$(111)_\delta, (112)_\delta, (331)_\delta, (132)_\delta$
	Even	$l = 3n$	0	$(100)_\delta, (120)_\delta, (123)_\delta, (323)_\delta$
		$l \neq 3n$	$3(f_M - f_N)$	$(101)_\delta, (121)_\delta, (102)_\delta, (122)_\delta, (321)_\delta$
Even $h/2 = \text{odd}$	Odd	$l = 3n$	0	$(210)_\delta, (213)_\delta$
		$l \neq 3n, l = \text{odd}$	$3(f_M - f_N)$	$(211)_\delta, (231)_\delta$
		$l \neq 3n, l = \text{even}$	$3(f_M - f_N)$	$(212)_\delta$
Even $h/2 = \text{Even}$	Odd	$l = 3n$	0	$(010)_\delta, (013)_\delta, (016)_\delta, (036)_\delta, (410)_\delta$
		$l \neq 3n, l = \text{odd}$	$3(f_M - f_N)$	$(011)_\delta$
		$l \neq 3n, l = \text{even}$	$3(3f_N + f_M)$	$(012)_\delta$
Even $h/2 = \text{odd}$	Even	$l = 3n, l = \text{odd}$	$2(3f_N + f_M)$	$(203)_\delta, (223)_\delta, (243)_\delta, (263)_\delta$
		$l = 3n, l = \text{even}$	$2(f_M - f_N)$	$(200)_\delta, (220)_\delta, (206)_\delta$
		$l \neq 3n, l = \text{odd}$	$(3f_N + f_M)$	$(221)_\delta, (201)_\delta$
		$l \neq 3n, l = \text{even}$	$(f_M - f_N)$	$(222)_\delta, (202)_\delta$
Even $h/2 = \text{Even}$	Even	$l = 3n, l = \text{odd}$	$2(f_M - f_N)$	$(003)_\delta, (023)_\delta, (423)_\delta, (403)_\delta, (043)_\delta$
		$l = 3n, l = \text{even}$	$2(3f_N + f_M)$	$(020)_\delta, (026)_\delta, (426)_\delta, (400)_\delta, (006)_\delta$
		$l \neq 3n, l = \text{odd}$	$(f_M - f_N)$	$(001)_\delta, (005)_\delta, (012)_\delta$
		$l \neq 3n, l = \text{even}$	$(3f_N + f_M)$	$(002)_\delta, (022)_\delta, (004)_\delta, (422)_\delta$

Table 2.11 Lattice correspondence matrices relating the disordered γ phase to different variants of the δ phase

Variant	${}_{\delta} \Phi^C = [{}_{\mathcal{C}} \Phi^{\delta}]^{-1}$	${}_{\mathcal{C}} \Phi^{\delta} = [{}_{\delta} \Phi^C]^{-1}$
δ_1	$\frac{1}{6} \begin{bmatrix} 3 & -6 & 4 \\ 3 & 6 & 4 \\ -6 & 0 & 4 \end{bmatrix}$	$\frac{1}{6} \begin{bmatrix} 2 & 2 & -4 \\ -3 & 3 & 0 \\ 3 & 3 & 3 \end{bmatrix}$
δ_2	$\frac{1}{6} \begin{bmatrix} 3 & 6 & 4 \\ -3 & 6 & -4 \\ -6 & 0 & 4 \end{bmatrix}$	$\frac{1}{6} \begin{bmatrix} 2 & -2 & -4 \\ 3 & 3 & 0 \\ 3 & -3 & 3 \end{bmatrix}$
δ_3	$\frac{1}{6} \begin{bmatrix} -3 & 6 & -4 \\ -3 & -6 & -4 \\ -6 & 0 & 4 \end{bmatrix}$	$\frac{1}{6} \begin{bmatrix} -2 & -2 & -4 \\ 3 & -3 & 0 \\ -3 & -3 & 3 \end{bmatrix}$
δ_4	$\frac{1}{6} \begin{bmatrix} -3 & -6 & -4 \\ 3 & -6 & 4 \\ -6 & 0 & 4 \end{bmatrix}$	$\frac{1}{6} \begin{bmatrix} -2 & 2 & -4 \\ -3 & -3 & 0 \\ -3 & 3 & 3 \end{bmatrix}$
δ_5	$\frac{1}{6} \begin{bmatrix} 3 & 6 & 4 \\ -6 & 0 & 4 \\ 3 & -6 & 4 \end{bmatrix}$	$\frac{1}{6} \begin{bmatrix} 2 & -4 & 2 \\ 3 & 0 & -3 \\ 3 & 3 & 3 \end{bmatrix}$
δ_6	$\frac{1}{6} \begin{bmatrix} -6 & 0 & 4 \\ -3 & -6 & -4 \\ 3 & -6 & 4 \end{bmatrix}$	$\frac{1}{6} \begin{bmatrix} -4 & -2 & 2 \\ 0 & -3 & -3 \\ 3 & -3 & 3 \end{bmatrix}$
δ_7	$\frac{1}{6} \begin{bmatrix} -3 & -6 & -4 \\ 6 & 0 & -4 \\ 3 & -6 & 4 \end{bmatrix}$	$\frac{1}{6} \begin{bmatrix} -2 & 4 & 2 \\ -3 & 0 & -3 \\ -3 & -3 & 3 \end{bmatrix}$
δ_8	$\frac{1}{6} \begin{bmatrix} 6 & 0 & -4 \\ 3 & 6 & 4 \\ 3 & -6 & 4 \end{bmatrix}$	$\frac{1}{6} \begin{bmatrix} 4 & 2 & 2 \\ 0 & 3 & -3 \\ -3 & 3 & 3 \end{bmatrix}$
δ_9	$\frac{1}{6} \begin{bmatrix} -6 & 0 & 4 \\ 3 & -6 & 4 \\ 3 & 6 & 4 \end{bmatrix}$	$\frac{1}{6} \begin{bmatrix} -4 & 2 & 2 \\ 0 & -3 & 3 \\ 3 & 3 & 3 \end{bmatrix}$

(continued)

Table 2.11 (continued)

Variant	${}_{\delta} \Phi^C = [{}_{\delta} \Phi^{\delta}]^{-1}$	${}_{\delta} \Phi^{\delta} = [{}_{\delta} \Phi^C]^{-1}$
δ_{10}	$\frac{1}{6} \begin{bmatrix} 3 & -6 & 4 \\ 6 & 0 & -4 \\ 3 & 6 & 4 \end{bmatrix}$	$\frac{1}{6} \begin{bmatrix} 2 & 4 & 2 \\ -3 & 0 & 3 \\ 3 & -3 & 3 \end{bmatrix}$
δ_{11}	$\frac{1}{6} \begin{bmatrix} 6 & 0 & -4 \\ -3 & 6 & -4 \\ 3 & 6 & 4 \end{bmatrix}$	$\frac{1}{6} \begin{bmatrix} 4 & -2 & 2 \\ 0 & 3 & 3 \\ -3 & -3 & 3 \end{bmatrix}$
δ_{12}	$\frac{1}{6} \begin{bmatrix} -3 & 6 & -4 \\ -6 & 0 & 4 \\ 3 & 6 & 4 \end{bmatrix}$	$\frac{1}{6} \begin{bmatrix} -2 & -2 & 2 \\ 3 & 0 & 3 \\ -3 & 3 & 3 \end{bmatrix}$

Notation ${}_{\delta} \Phi^C$ represents the correspondence matrix for the transformation from the orthorhombic δ phase to the cubic (C) structure

[110] zone axis are shown to be halved by $(010)_{\delta}$ and $(210)_{\delta}$ reflections, respectively, despite their forbidden nature (Table 2.11). The appearance of such forbidden reflections may occur due to the double diffraction⁴ of the diffracted beam.

No single zone axis would show superlattice reflections of all variants of the δ phase. Often the superlattice reflections of more than one variant may be superimposed in a given zone axis. For example, the superlattice reflections of δ_2 and δ_4 variants that divide the $(2\bar{2}0)$ reflection in half (Fig. 2.16a) are superimposed. Therefore, a judicious combination of different zone axes is required to delineate all the variants unambiguously. A [001] zone axis diffraction would show superlattice reflections corresponding to six variants that are superimposed by those of the other six (Fig. 2.16a). Similar limitations would be there for other zone axis diffraction patterns. For instance, $(001)_{\delta}$ superlattice reflections of δ_4 , δ_6 and δ_{11} variants superimpose in the [110] zone axis (Fig. 2.16b). Therefore, imaging of particles using this superlattice reflection would bring particles of all these three variants in bright contrast. In such cases, different variants can be unambiguously identified using a combination of electron diffraction images with specific superlattice reflections and the habit plane analysis of the microstructural features.

⁴ Double diffraction occurs when a diffracted beam travelling through a crystal is diffracted again either within the same crystal or while passing into another crystal [14]. Double diffraction may cause the appearance of otherwise forbidden reflections.

Table 2.12 Plane correspondence between FCC and different variants of the δ phase

FCC phase	δ Phase	δ_1	δ_2	δ_3	δ_4	δ_5	δ_6	δ_7	δ_8	δ_9	δ_{10}	δ_{11}	δ_{12}
111	0 0 2	$\bar{3}\bar{6}2$	$\bar{6}0\bar{2}$	$\bar{3}62$	0 0 2	$\bar{3}62$	602	0 0 2	602	0 0 2	602	$\bar{3}\bar{6}\bar{2}$	$\bar{3}\bar{6}2$
$\bar{1}\bar{1}\bar{1}$	$\bar{3}\bar{6}2$	$\bar{6}0\bar{2}$	$\bar{3}62$	0 0 2	$\bar{3}62$	602	0 0 2	602	$\bar{3}\bar{6}\bar{2}$	0 0 2	602	$\bar{3}\bar{6}\bar{2}$	0 0 2
1 $\bar{1}\bar{1}$	$\bar{3}62$	0 0 2	$\bar{3}\bar{6}2$	$\bar{6}0\bar{2}$	602	0 0 2	$\bar{3}62$	$36\bar{2}$	$\bar{3}\bar{6}2$	0 0 2	602	$\bar{3}\bar{6}\bar{2}$	$\bar{3}\bar{6}\bar{2}$
11 $\bar{1}$	602	$\bar{3}\bar{6}\bar{2}$	0 0 $\bar{2}$	$36\bar{2}$	$\bar{3}62$	602	0 0 $\bar{2}$	$36\bar{2}$	$\bar{3}6\bar{2}$	0 0 $\bar{2}$	$60\bar{2}$	$\bar{0}0\bar{2}$	$\bar{0}0\bar{2}$
200	364	$\bar{3}\bar{6}4$	$\bar{3}\bar{6}\bar{4}$	$3\bar{6}4$	$\bar{6}04$	$\bar{3}6\bar{4}$	$60\bar{4}$	$\bar{6}04$	604	364	$60\bar{4}$	$\bar{3}\bar{6}\bar{4}$	$\bar{3}\bar{6}\bar{4}$
020	$\bar{3}\bar{6}\bar{4}$	$\bar{3}\bar{6}4$	364	$\bar{6}04$	$\bar{3}6\bar{4}$	$60\bar{4}$	$\bar{3}64$	604	364	$60\bar{4}$	$\bar{3}\bar{6}4$	$\bar{3}\bar{6}4$	$\bar{6}04$
002	$\bar{6}04$	$\bar{6}04$	$\bar{6}04$	$\bar{6}04$	364	364	364	364	364	364	364	364	364
220	608	$\bar{0}\bar{4}0$	$\bar{6}08$	0 4 0	$\bar{3}\bar{6}8$	$\bar{3}\bar{2}0$	$36\bar{8}$	$\bar{3}\bar{2}0$	$\bar{3}68$	$\bar{3}\bar{2}0$	320	$\bar{3}\bar{6}\bar{8}$	$\bar{3}\bar{2}0$
$\bar{2}20$	0 4 0	$\bar{6}0\bar{8}$	0 4 0	608	$\bar{3}20$	$36\bar{8}$	$\bar{3}\bar{2}0$	$36\bar{8}$	$\bar{3}68$	$\bar{3}\bar{2}0$	320	$\bar{3}\bar{6}8$	$\bar{3}\bar{2}0$
202	$\bar{3}68$	$\bar{3}\bar{6}8$	$\bar{3}\bar{2}0$	608	$\bar{3}68$	0 4 0	320	$\bar{3}\bar{6}8$	608	320	$\bar{0}40$	$\bar{0}40$	$\bar{0}40$
20 $\bar{2}$	320	$\bar{3}\bar{2}0$	$3\bar{6}\bar{8}$	$\bar{3}\bar{2}0$	$\bar{0}\bar{4}0$	$\bar{3}\bar{2}0$	$\bar{6}0\bar{8}$	$\bar{3}\bar{6}\bar{8}$	$\bar{3}20$	0 4 0	$36\bar{8}$	$\bar{6}0\bar{8}$	$\bar{6}0\bar{8}$
022	$\bar{3}\bar{6}8$	$\bar{3}\bar{2}0$	$\bar{3}20$	$\bar{3}68$	0 4 0	320	608	608	608	$3\bar{2}0$	0 4 0	$\bar{3}\bar{6}8$	$\bar{3}\bar{6}8$
022	$\bar{3}\bar{2}0$	$3\bar{6}\bar{8}$	320	$\bar{3}\bar{2}0$	$\bar{6}0\bar{8}$	$3\bar{6}\bar{8}$	0 4 0	$0\bar{4}0$	$36\bar{8}$	$\bar{6}0\bar{8}$	$\bar{3}\bar{2}0$	$\bar{3}\bar{2}0$	$\bar{3}\bar{2}0$
422	3616	$\bar{3}\bar{1}\bar{8}8$	$\bar{1}\bar{5}\bar{6}\bar{8}$	$\bar{3}60$	$3\bar{6}16$	$\bar{1}\bar{2}\bar{1}\bar{2}8$	$318\bar{8}$	600	$\bar{6}016$	1568	$12\bar{1}\bar{2}\bar{8}$	$\bar{3}\bar{6}0$	$\bar{3}\bar{6}0$

(continued)

Table 2.12 (continued)

FCC phase	δ Phase	δ_1	δ_2	δ_3	δ_4	δ_5	δ_6	δ_7	δ_8	δ_9	δ_{10}	δ_{11}	δ_{12}
$\bar{4}2\bar{2}$	$\bar{3}\bar{6}0$	$\bar{1}\bar{5}6\bar{8}$	$\bar{3}188$	$\bar{3}\bar{6}16$	$\bar{3}\bar{6}0$	$1212\bar{8}$	$15\bar{6}8$	$\bar{6}016$	6 0 0	$3\bar{1}\bar{8}\bar{8}$	$\bar{1}\bar{2}\bar{1}\bar{2}8$	$3\bar{6}16$	
$4\bar{2}2$	$\bar{3}188$	$3\bar{6}16$	$\bar{3}\bar{6}0$	$\bar{1}\bar{5}6\bar{8}$	$15\bar{6}8$	$\bar{6}016$	$\bar{3}60$	$1212\bar{8}$	$\bar{1}\bar{2}\bar{1}\bar{2}8$	$3\bar{6}16$	6 0 0	$\bar{3}\bar{1}\bar{8}\bar{8}$	
$42\bar{2}$	1568	$3\bar{6}0$	$\bar{3}\bar{6}16$	$318\bar{8}$	$\bar{3}\bar{1}\bar{8}8$	6 0 0	$\bar{3}\bar{6}\bar{1}\bar{6}$	$1212\bar{8}$	$\bar{1}\bar{2}\bar{1}\bar{2}8$	$3\bar{6}0$	$601\bar{6}$	$\bar{1}\bar{5}\bar{6}\bar{8}$	
242	$3\bar{6}16$	$\bar{3}\bar{6}0$	$\bar{1}\bar{5}6\bar{8}$	$\bar{3}188$	$\bar{6}016$	360	$1212\bar{8}$	$15\bar{6}8$	$3\bar{6}16$	6 0 0	$3\bar{1}\bar{8}\bar{8}$	$\bar{1}\bar{2}\bar{1}\bar{2}8$	
$\bar{2}42$	$\bar{3}188$	$\bar{1}\bar{5}6\bar{8}$	$\bar{3}60$	$\bar{1}\bar{2}\bar{1}28$	$318\bar{8}$	6 0 0	$3\bar{6}16$	$15\bar{6}8$	$1212\bar{8}$	$\bar{3}\bar{6}0$	$\bar{6}016$	$\bar{6}016$	
242	$\bar{3}60$	3616	$\bar{3}\bar{1}\bar{8}8$	$\bar{1}\bar{5}\bar{6}\bar{8}$	6 0 0	$3\bar{6}16$	$1212\bar{8}$	$318\bar{8}$	$\bar{3}\bar{6}0$	6016	$15\bar{6}8$	$\bar{1}\bar{2}\bar{1}\bar{2}8$	
$24\bar{2}$	$15\bar{6}8$	$3\bar{1}\bar{8}\bar{8}$	$\bar{3}6\bar{1}\bar{6}$	360	$\bar{1}\bar{2}\bar{1}\bar{2}8$	$15\bar{6}8$	$60\bar{1}\bar{6}$	$3\bar{6}0$	$\bar{3}188$	$1212\bar{8}$	$\bar{3}\bar{6}\bar{1}\bar{6}$	6 0 0	
224	$\bar{6}016$	$\bar{1}\bar{2}\bar{1}\bar{2}8$	6 0 0	$\bar{1}\bar{2}\bar{1}28$	3616	$\bar{3}188$	360	$15\bar{6}8$	$3\bar{6}16$	$15\bar{6}8$	$3\bar{6}0$	$\bar{3}\bar{1}\bar{8}\bar{8}$	
$\bar{2}24$	$\bar{1}\bar{2}\bar{1}28$	6 0 0	$\bar{1}\bar{2}\bar{1}28$	$\bar{6}016$	$\bar{3}188$	360	$15\bar{6}8$	3616	$15\bar{6}8$	$3\bar{6}0$	$\bar{3}188$	$3\bar{6}16$	
$2\bar{2}4$	$\bar{1}\bar{2}128$	$\bar{6}016$	$\bar{1}\bar{2}\bar{1}\bar{2}8$	6 0 0	1568	3616	$\bar{3}188$	360	$\bar{3}188$	$3\bar{6}16$	$15\bar{6}8$	$3\bar{6}0$	
$22\bar{4}$	6 0 0	$12\bar{1}\bar{2}8$	$60\bar{1}\bar{6}$	$1212\bar{8}$	$\bar{3}\bar{6}0$	$\bar{1}\bar{5}\bar{6}\bar{8}$	$\bar{3}\bar{6}1\bar{6}$	$318\bar{8}$	$\bar{3}60$	$318\bar{8}$	$\bar{3}\bar{6}1\bar{6}$	$\bar{1}\bar{5}\bar{6}\bar{8}$	

(continued)

Table 2.12 (continued)

FCC phase	δ Phase	\mathbf{g}_1	\mathbf{g}_2	\mathbf{g}_3	\mathbf{g}_4	\mathbf{g}_5	\mathbf{g}_6	\mathbf{g}_7	\mathbf{g}_8	\mathbf{g}_9	\mathbf{g}_{10}	\mathbf{g}_{11}	\mathbf{g}_{12}
4 2 0	3 2 4	3 $\bar{1}\bar{8}4$	$\bar{3}\bar{2}\bar{4}$	$\bar{3}\bar{1}\bar{8}\bar{4}$	$\bar{0}\bar{4}\bar{4}$	$\bar{1}\bar{5}6\bar{4}$	$\bar{0}\bar{4}\bar{4}$	$\bar{1}\bar{5}\bar{6}\bar{4}$	$\bar{3}\bar{2}\bar{4}$	12 12 4	$\bar{3}\bar{2}\bar{4}$	12 12 4	$\bar{1}\bar{2}\bar{1}\bar{2}\bar{4}$
$\bar{4}\bar{2}\bar{0}$	$\bar{3}\bar{1}\bar{8}\bar{4}$	$\bar{3}\bar{2}\bar{4}$	3 18 4	$\bar{3}\bar{2}\bar{4}$	$\bar{1}\bar{2}\bar{1}\bar{2}\bar{4}$	3 2 $\bar{4}$	$\bar{1}\bar{2}\bar{1}\bar{2}\bar{4}$	$\bar{3}\bar{2}\bar{4}$	15 6 $\bar{4}$	$\bar{0}\bar{4}\bar{4}$	$\bar{1}\bar{5}\bar{6}\bar{4}$	0 4 4	$\bar{1}\bar{5}\bar{6}\bar{4}$
2 4 0	3 $\bar{2}\bar{4}$	$\bar{3}\bar{1}\bar{8}\bar{4}$	$\bar{3}\bar{2}\bar{4}$	3 18 4	$\bar{3}\bar{2}\bar{4}$	$\bar{1}\bar{2}\bar{1}\bar{2}\bar{4}$	3 2 $\bar{4}$	$\bar{1}\bar{2}\bar{1}\bar{2}\bar{4}$	0 4 4	12 12 4	0 4 4	15 6 $\bar{4}$	$\bar{1}\bar{5}\bar{6}\bar{4}$
$\bar{2}\bar{4}\bar{0}$	3 $\bar{1}\bar{8}\bar{4}$	$\bar{3}\bar{2}\bar{4}$	$\bar{3}\bar{1}\bar{8}\bar{4}$	3 2 4	$\bar{1}\bar{5}6\bar{4}$	$\bar{0}\bar{4}\bar{4}$	15 6 $\bar{4}$	$\bar{0}\bar{4}\bar{4}$	12 12 4	$\bar{3}\bar{2}\bar{4}$	$\bar{1}\bar{2}\bar{1}\bar{2}\bar{4}$	$\bar{3}\bar{2}\bar{4}$	$\bar{1}\bar{2}\bar{1}\bar{2}\bar{4}$
2 0 4	3 2 4	$\bar{3}\bar{2}\bar{4}$	$\bar{1}\bar{5}\bar{6}\bar{4}$	3 2 4	$\bar{0}\bar{4}\bar{4}$	3 2 4	$\bar{0}\bar{4}\bar{4}$	3 18 4	12 12 4	$\bar{0}\bar{4}\bar{4}$	$\bar{3}\bar{2}\bar{4}$	12 12 4	$\bar{3}\bar{1}\bar{8}\bar{4}$
$\bar{2}\bar{0}\bar{4}$	$\bar{1}\bar{5}\bar{6}\bar{4}$	3 2 4	$\bar{3}\bar{2}\bar{4}$	3 18 4	12 12 4	3 2 4	$\bar{0}\bar{4}\bar{4}$	12 12 4	$\bar{3}\bar{1}\bar{8}\bar{4}$	0 4 4	$\bar{3}\bar{2}\bar{4}$	$\bar{1}\bar{5}\bar{6}\bar{4}$	$\bar{3}\bar{1}\bar{8}\bar{4}$
4 0 2	0 4 4	$\bar{0}\bar{4}\bar{4}$	$\bar{1}\bar{2}\bar{1}\bar{2}\bar{4}$	$\bar{0}\bar{4}\bar{4}$	$\bar{0}\bar{4}\bar{4}$	$\bar{3}\bar{2}\bar{4}$	$\bar{3}\bar{2}\bar{4}$	15 6 $\bar{4}$	$\bar{3}\bar{2}\bar{4}$	3 2 4	$\bar{1}\bar{5}\bar{6}\bar{4}$	$\bar{3}\bar{1}\bar{8}\bar{4}$	$\bar{3}\bar{2}\bar{4}$
$\bar{4}\bar{0}\bar{2}$	$\bar{1}\bar{2}\bar{1}\bar{2}\bar{4}$	$\bar{1}\bar{2}\bar{1}\bar{2}\bar{4}$	$\bar{0}\bar{4}\bar{4}$	$\bar{0}\bar{4}\bar{4}$	$\bar{3}\bar{1}\bar{8}\bar{4}$	$\bar{1}\bar{5}\bar{6}\bar{4}$	$\bar{3}\bar{2}\bar{4}$	3 2 4	$\bar{1}\bar{5}\bar{6}\bar{4}$	$\bar{3}\bar{1}\bar{8}\bar{4}$	$\bar{3}\bar{2}\bar{4}$	$\bar{3}\bar{1}\bar{8}\bar{4}$	$\bar{3}\bar{2}\bar{4}$
0 4 2	0 4 4	$\bar{1}\bar{2}\bar{1}\bar{2}\bar{4}$	$\bar{1}\bar{2}\bar{1}\bar{2}\bar{4}$	$\bar{0}\bar{4}\bar{4}$	$\bar{3}\bar{2}\bar{4}$	$\bar{3}\bar{1}\bar{8}\bar{4}$	15 6 $\bar{4}$	$\bar{3}\bar{2}\bar{4}$	3 2 4	$\bar{1}\bar{5}\bar{6}\bar{4}$	$\bar{3}\bar{1}\bar{8}\bar{4}$	$\bar{3}\bar{2}\bar{4}$	$\bar{3}\bar{1}\bar{8}\bar{4}$
$\bar{0}\bar{4}\bar{2}$	$\bar{1}\bar{2}\bar{1}\bar{2}\bar{4}$	0 4 4	$\bar{0}\bar{4}\bar{4}$	$\bar{1}\bar{2}\bar{1}\bar{2}\bar{4}$	15 6 $\bar{4}$	$\bar{3}\bar{2}\bar{4}$	$\bar{3}\bar{1}\bar{8}\bar{4}$	$\bar{3}\bar{2}\bar{4}$	$\bar{1}\bar{2}\bar{1}\bar{2}\bar{4}$	$\bar{3}\bar{2}\bar{4}$	3 2 4	$\bar{1}\bar{5}\bar{6}\bar{4}$	$\bar{3}\bar{2}\bar{4}$
0 2 4	$\bar{3}\bar{2}\bar{4}$	$\bar{1}\bar{5}\bar{6}\bar{4}$	$\bar{3}\bar{2}\bar{4}$	$\bar{0}\bar{4}\bar{4}$	3 18 4	12 12 4	3 2 4	$\bar{3}\bar{2}\bar{4}$	12 12 4	$\bar{1}\bar{2}\bar{1}\bar{2}\bar{4}$	$\bar{3}\bar{1}\bar{8}\bar{4}$	0 4 4	$\bar{1}\bar{2}\bar{1}\bar{2}\bar{4}$
$\bar{0}\bar{2}\bar{4}$	$\bar{1}\bar{5}\bar{6}\bar{4}$	3 2 4	$\bar{3}\bar{2}\bar{4}$	15 6 $\bar{4}$	12 12 4	3 2 4	0 4 4	3 18 4	$\bar{3}\bar{1}\bar{8}\bar{4}$	0 4 4	3 2 4	12 12 4	$\bar{1}\bar{2}\bar{1}\bar{2}\bar{4}$

The δ phase planes which would show superlattice reflections along their reciprocal vectors are shown in Bold

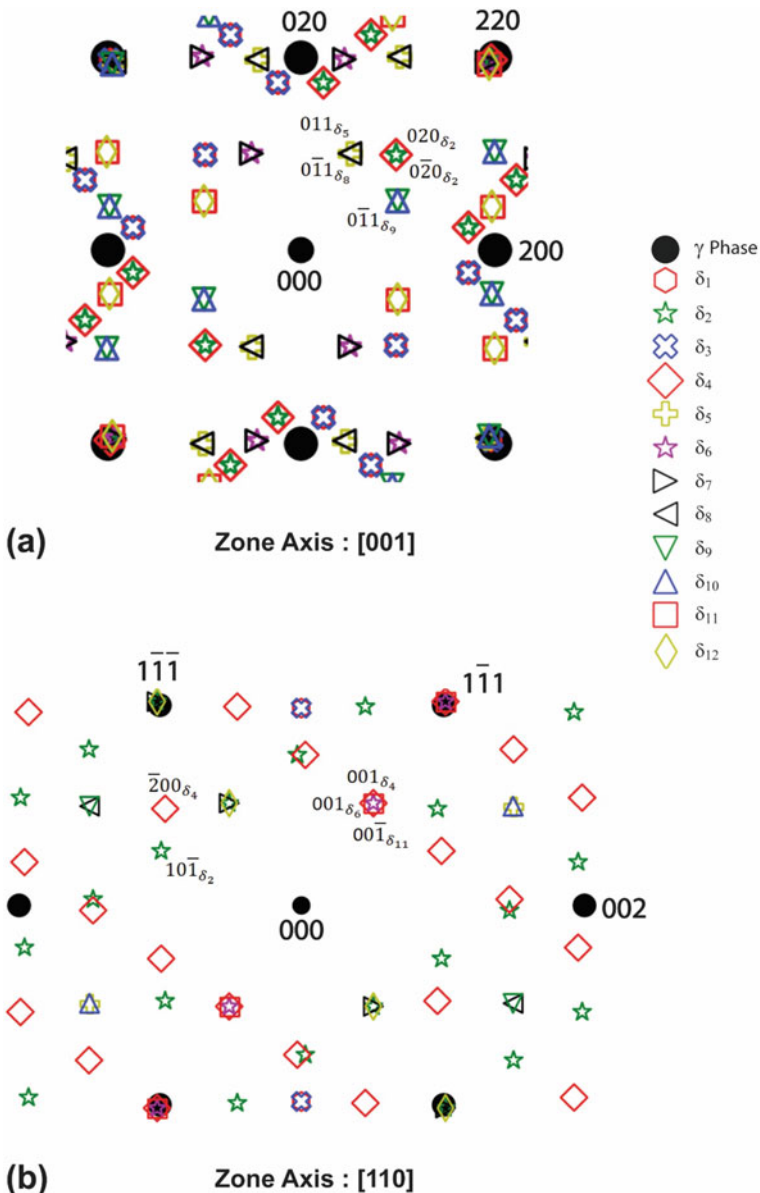


Fig. 2.16 Simulated electron diffraction patterns of the δ phase: **a** [001] zone axis; **b** [110] zone axis

2.5.4 Identification of Carbide Phases

Substituting the coordinates of M and C atoms into the Eq. 2.1 gives the structure factor relationship for the MC phase as

$$F_{MC} = f_M [\exp 2\pi i(0) + \exp \pi i(h+k) + \exp \pi i(h+l) + \exp \pi i(k+l)] \\ + f_C [\exp \pi i(h) + \exp \pi i(k) + \exp \pi i(l) + \exp \pi i(h+k+l)]$$

$$F_{MC} = f_M [1 + \exp \pi i(h+k) + \exp \pi i(h+l) + \exp \pi i(k+l)] \\ + f_C [\exp \pi i(h) + \exp \pi i(k) + \exp \pi i(l) + \exp \pi i(h+k+l)]$$

Where f_M and f_C are atomic scattering factors of M and C atoms, respectively. For the MC phase, the structure factor is again zero for all the reflections for mixed types of indices, and corresponding reflections are forbidden as in a face-centered structure. However, for unmixed reflections, $F_{MC} = 4(f_M \pm f_C)$ and the positive or negative sign would again be dependent upon the index of the plane. The fundamental reflections with $F_{MC} = 4(f_M + f_C)$ would appear only for planes for which h, k, l are all even, while planes with all odd indices would exhibit superlattice reflections with $F_{hkl} = 4(f_M - f_C)$. Figure 2.17 shows simulated [001] and [111] zone axes diffraction patterns for the MC carbide phase.

The depiction of the structure factor calculations for the M_6C and $M_{23}C_6$ phases are beyond this Chapter's scope due to the complexities and the large number of

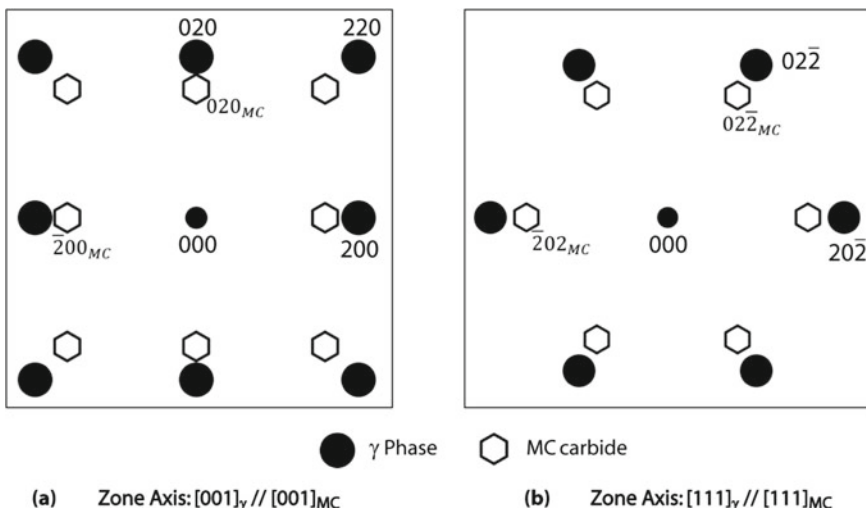


Fig. 2.17 **a** [001] and **b** [111] zone axes simulated diffraction pattern of the MC carbide in relation to the austenite matrix phase. Solid circles represent reflections due to the austenite matrix and hollow hexagonal symbols represent reflections due to the MC carbide phase

atoms per unit cell associated with these phases. However, the similar Bravais lattice and crystal structures of the $M_6C/M_{23}C_6$ phases and the γ phase (Table 2.1) imply that their structure factors would allow reflections identical to the FCC γ phase, see Fig. 2.18 for the case of $M_{23}C_6$.

The electron diffraction pattern mainly identifies the carbide phases. As the lattice parameters of carbide phases are different from the matrix phase (Table 2.1), their interplanar spacings differ. The interplanar spacing of a specific plane in the MC phase is significantly different compared to the corresponding plane of the γ phase. On the other hand, the interplanar spacing in the M_6C and $M_{23}C_6$ phases is about three times of the corresponding plane in the γ phase because of the nearly thrice the lattice parameters of the $M_6C/M_{23}C_6$ phases (Table 2.1). Therefore, the formation of the M_6C and $M_{23}C_6$ phases would subdivide the spacing between the austenite reflections into three equal parts as illustrated by simulated [001] and [111] zone axis electron diffraction patterns of the $M_{23}C_6$ phase (Fig. 2.18). However, it would be rather difficult to distinguish between the M_6C and $M_{23}C_6$ phases because of the commonality between their Bravais lattices and crystal structures and the closeness of their lattice parameter parameters. The lattice parameters of the two differ only by about 4%. The M_6C and $M_{23}C_6$ phases have the same FCC Bravais lattice and differ only in their space groups ($Fd\bar{3}m$ and $Fm\bar{3}m$, respectively) owing to the presence of a diamond glide in the former. However, the two phases can be readily distinguished based on x-ray microanalysis (chemical composition analysis) in conjunction with electron or x-ray diffraction analysis.

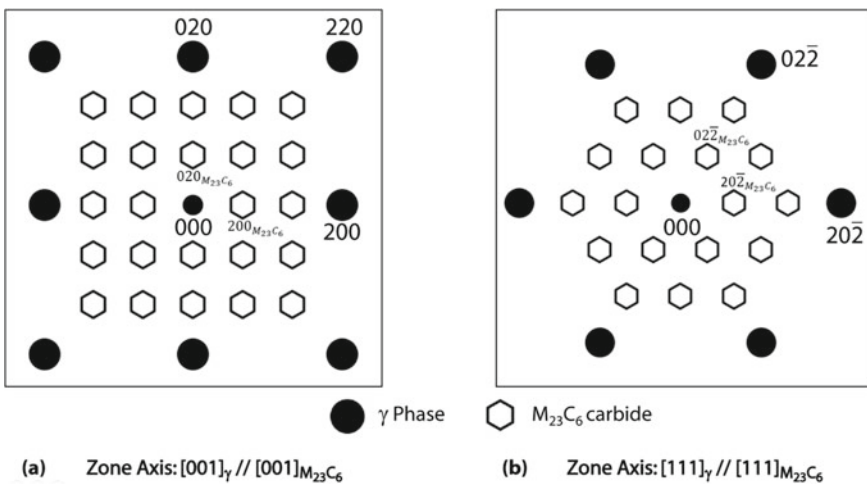


Fig. 2.18 **a** [001] and **b** [111] zone axes simulated diffraction pattern of the $M_{23}C_6$ carbide in relation to the austenite matrix phase. Solid circles represent reflections due to the austenite matrix and hollow hexagonal symbols represent reflections due to the $M_{23}C_6$ carbide phase

2.6 Summary

Alloy 625 comprises a matrix phase, a nickel-rich disordered solid-solution phase of FCC structure, and may contain precipitates of other phases depending upon processing conditions. The precipitating phases may be ordered intermetallic phases, such as γ'' , δ , $\text{Ni}_2(\text{Cr}, \text{Mo})$, μ , Laves, etc. or carbides of MC , M_6C and M_{23}C_6 type, where M represent a metal atom. The size, volume fraction and morphology of these phases determine the final properties of the alloy. These phases can be identified by any diffraction technique that uses x-ray, electrons or neutrons. However, the low volume fractions and closeness in the atomic scattering factors of elements in their compounds make electron diffraction an ideal technique. Further, the formation of most of these phases is associated with cubic to non-cubic phase transformations. Their precipitation gives rise to different orientational variants in the parent cubic matrix.

References

1. Singleton MF, Murray JL, Nash P, Al-Ni phase diagram. (1991) In: Massalski TB (ed in chief) Binary alloy phase diagrams. ASM International Materials Park, p183
2. Villars P, Calvert LD (1986) Pearson's handbook of crystallography data for intermetallic phases, vol 3. ASM, Metals Park
3. Floreen S, Fuchs GE, Yang WJ (1994) The metallurgy of Alloy 625. Superalloys 718, 625, 706 and various derivatives. TMS, Pittsburgh, pp 13–38
4. Radavich JF, Fort A (1994) The metallurgy of alloy 625. Superalloys 718, 625, 706 and various derivatives. TMS Pittsburgh, pp 632–645
5. Tawancy HM (1996) Precipitation characteristics of mu-phase in wrought nickel-base alloys and its effect on their properties. *J Mater Sci* 31:3929–3936
6. Rai SK, Kumar A, Shankar V, Jayakumar T, Bhanu Sankara Rao K, Raj B (2004) Characterization of microstructures in Inconel 625 using X-ray diffraction peak broadening and lattice parameter measurements. *Scripta Mater* 51:59–63
7. Ross EW, Sims CT (1987) In: Sims CT et al (eds) Superalloys II, Chapter.4, New York, Wiley, pp 97–133
8. Verma A, Singh JB, Kaushik SD, Siruguri V (2020) Lattice parameter variation and its effect on precipitation behaviour of ordered $\text{Ni}_2(\text{Cr}, \text{Mo})$ phase in Ni-Cr-Mo alloys. *J Alloys Comp* 813:152–195
9. Tawancy HM (2017) On the precipitation of intermetallic compounds in selected solid-solution-strengthened Ni-base alloys and their effects on mechanical properties. *Metallogr Microstruct Anal* 6:200–215
10. Cullity BD (1959) Elements of X-Ray diffraction. Addison Wesley
11. Massalski TB, Barrett CS (1966) Structure of metals. McGraw-Hill, New York, p 266
12. Singh JB (2002) Ph.D. dissertation. IIT Bombay
13. Sundararaman M (1986) Microstructural studies on the high temperature materials Inconel 718 and Inconel 625 alloys. Ph.D. dissertation, University of Bombay
14. Williams DB, Carter CB (2009) Transmission electron microscopy, 2nd edn. Springer Science, Boston, vol 3

Chapter 3

Physical Metallurgy of Alloy 625



Alloy 625 is designed as a solid-solution alloy with good combinations of mechanical and corrosion properties over a temperature range from room temperature to about 800 °C. It derives its strength from the stiffening of the nickel–chromium matrix due to the addition of molybdenum and niobium. These elements also impart superior resistance to a wide range of corrosive environments as well as oxidation and carburization resistance. However, the alloy develops a highly complex microstructure when different intermetallic phases and various carbides precipitate in the austenite matrix during processing, heat treatments or both. The precipitation of these phases modifies alloy's behavior depending upon their nature, morphology and location of formation. This chapter gives an overview of the alloy's chemistry and its phase transformation behavior. The chapter also briefly describes how the microstructure is modified when various phases evolve.

3.1 Alloying Additions in Alloy 625

In general, alloying additions in superalloys can be categorized into three broad groups [1]. The first group includes elements like nickel, cobalt, iron, chromium, molybdenum, tungsten, and vanadium, which prefer to partition in the nickel lattice and stabilize the face-centered cubic (FCC) phase. The second group of elements, like aluminum, titanium, niobium and tantalum, promotes the formation of intermetallic phases such as $\text{Ni}_3(\text{Al}, \text{Ta}, \text{Ti})$ (γ' phase) and $\text{Ni}_3(\text{Nb}, \text{Ta}, \text{Ti})$ (γ'' phase). The third group includes boron, carbon, magnesium and zirconium, which tend to segregate to grain boundaries. Elements like chromium, molybdenum, niobium and tantalum may also form carbide phases and detrimental topologically closed packed (TCP) phases if their overall composition is not controlled adequately or improper fabrication practices are employed [1]. The alloying elements in Alloy 625 may comprise about 55–62% nickel, about 20–24% chromium, about 7–11% molybdenum, about 3–4.5% niobium plus tantalum, up to about 0.4% of aluminum and titanium, a maximum of

Table 3.1 Nominal composition range of the Alloy 625

Alloy	Ni	Cr	Mo	Nb + Ta	Al	Ti	Fe	C	Si	P	S
Min.	Bal.	20	8	3.15	0.2	0.2	—	—	—	—	—
Max.		23	10	4.15	0.4	0.4	5	0.01	0.5	0.015	0.015

0.1% carbon, up to about 0.5% silicon, up to about 0.5% manganese, up to about 0.015% boron, and the balance iron [2]. The patented design also envisaged up to about 8% tungsten though rarely used in commercial alloys. Over the years, the alloy composition has undergone a small change in the range of various elements. Table 3.1 gives the nominal composition range of Alloy 625. Most commercial alloys contain about 60% nickel, about 22% chromium, about 9% molybdenum, about 4% niobium, about 0.2% aluminum, about 0.15% titanium, about 0.03% carbon and the balance iron. This section presents the role of each element in the design of Alloy 625.

3.1.1 Nickel

The nearly filled 3d electron shell of the nickel allows Alloy 625 to accommodate many alloying elements without phase instability [1]. This provides the nickel-base alloys good solubility for various elements to strengthen its austenite (γ) matrix directly through solid-solution hardening and impart resistance against different environments. Nearly filled third electron shell of the nickel also reduces its propensity to form topologically close-packed phases. Alloy 625 must contain a minimum of about 55% nickel for good high-temperature properties as annealed alloys containing approximately 57% nickel show a peak in stress-rupture strength at about 650 °C (Fig. 3.1) [3].

Fig. 3.1 Effect of the nickel concentration on the rupture strength of alloys annealed for 1 h at 1038 °C and tested at 649 °C for 1000 h. The alloys contained nickel and other elements as 13–21% Cr, 4.25% Nb, 2–3% Mo, 0.1–0.25% Al, 0.1–0.25% Ti, 0.2% Si, 0.2% Mn, 0.02–0.04% C and balance Fe [3]

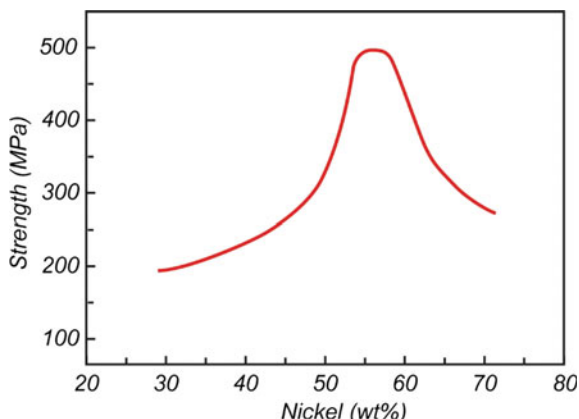
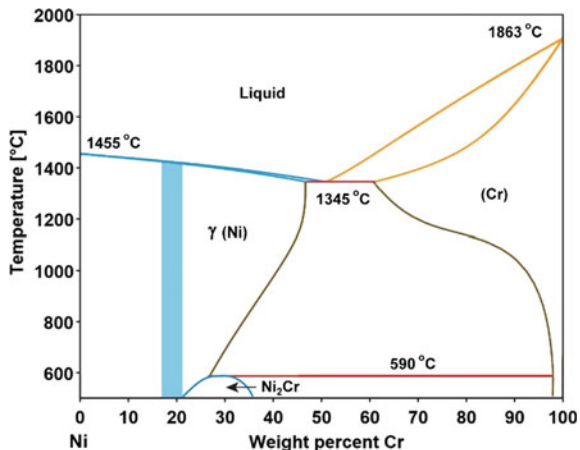


Fig. 3.2 Nickel–chromium binary phase diagram [4]. The nominal range of chromium in Alloy 625 is marked in ‘cyan blue’



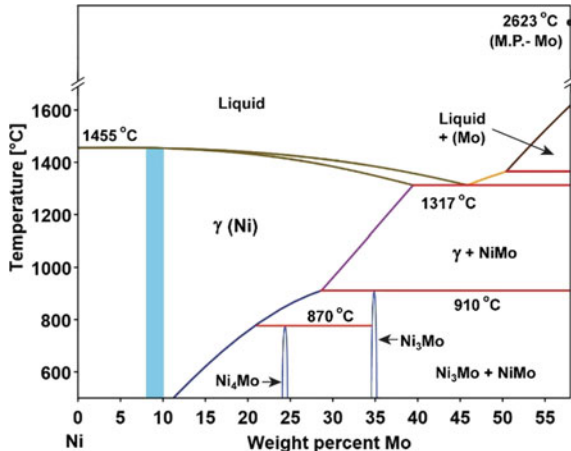
3.1.2 Chromium

Chromium plays an essential role in imparting corrosion resistance and solid-solution strengthening to the nickel matrix. It forms an adherent chromium oxide (Cr_2O_3) surface layer that protects the surface against environmental attack at elevated temperatures [1]. The crystal structure of chromium is body-centered-cubic (BCC), while nickel is face-centered-cubic (FCC). Such a difference in crystal structures thermodynamically results in the eutectic type of phase diagrams with limited solid solubility. However, the nearly filled 3d electron shell of the nickel accommodates a large amount of chromium to accommodate the necessary chromium for Alloy 625 in its solid solution. In Alloy 625, about 20–22% chromium is recommended with a maximum level of 24% chromium as it may cause the formation of undesired deleterious TCP phases beyond 24%. The nominal range of chromium is marked in ‘cyan blue’ on the Ni–Cr phase diagram (Fig. 3.2) [4]. Increasing chromium content from 16 to 22% increases the strength of the nickel matrix without any age-hardening [3]. Higher concentrations may stabilize the Ni_2Cr phase at low temperatures, as depicted in Fig. 3.2. In many alloys, chromium also improves the mechanical strength by precipitation hardening the matrix by forming secondary M_{23}C_6 and M_6C carbides.

3.1.3 Molybdenum

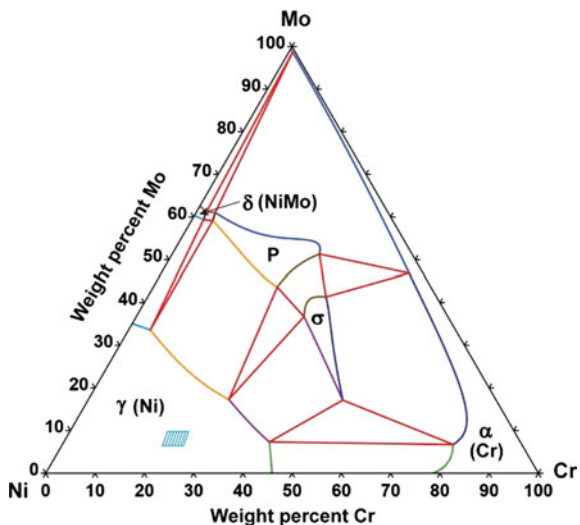
Like chromium, the crystal structure of molybdenum is also BCC and forms a eutectic type Ni-Mo binary phase diagram with a large austenite nickel solid-solution field (Fig. 3.3 [5]). The nominal range of molybdenum in nickel for Alloy 625 is marked in ‘cyan blue’ in Fig. 3.3. Similar crystal structures of molybdenum and chromium

Fig. 3.3 Nickel rich side of the nickel-molybdenum binary phase diagram [5]. The nominal range of molybdenum in Alloy 625 is marked in ‘cyan blue’



make them completely miscible in each other, which is reflected in the precipitation behavior of the $\text{Ni}_2(\text{Cr}, \text{Mo})$ phase. The combined effect of chromium and molybdenum on the phase stability of the austenitic nickel phase can be understood considering their ternary phase diagram. A ternary phase diagram comprises three elements and maps their phase fields in a triangular base as a function of temperature along a vertical axis. The concentration of each element is represented along the three sides of an equilateral triangle, and an isothermal section of the 3-dimensional ternary phase diagram gives the phase fields at a given temperature. Figure 3.4 shows an isothermal section of the Ni–Cr–Mo system taken at 1250 °C temperature. This section was generated using the Thermo-Calc software and the nickel database. The

Fig. 3.4 An isothermal section of the nickel–chromium–molybdenum ternary phase diagram simulated at 1250 °C temperature using the ThermoCalc software and the nickel database. The nominal range of chromium and molybdenum in Alloy 625 is marked in ‘cyan blue’



ternary phase diagram also shows a nickel-rich austenitic phase-field bound by about 45% chromium and about 35% molybdenum of respective binary axes. Beyond these concentrations, the alloy tends to form σ and P topologically close-packed phases. The addition of molybdenum in nickel increases the strength of the γ matrix through solid-solution hardening due to the former's larger atomic size [6]. In addition, molybdenum improves the creep resistance of the alloy because of its low diffusivity. It also imparts good strength when combined with elements like chromium and niobium and increases the alloy's age-hardening response. In combination with chromium, it also provides resistance against corrosion in extremely versatile environments of both oxidizing and reducing chemicals by improving the stability of the Cr_2O_3 film and giving resistance to localized corrosion in aqueous chloride containing media.

3.1.4 Tungsten

Tungsten addition in nickel superalloys plays a similar role as that of molybdenum but provides better solid-solution strengthening than molybdenum due to the larger atomic radius of the former [7]. Tungsten also contributes to room temperature yield strength and creep-rupture strengths of the alloy. However, commercial Alloy 625 rarely contain tungsten, possibly because of niobium that plays a similar role in contributing to the alloy's room temperature yield strength and rupture strength [8].

3.1.5 Niobium and Tantalum

The commercial grades of niobium invariably contain a small proportion of tantalum since the two cannot be separated entirely because of their very similar properties [8]. The nominal composition of Alloy 625 and most other superalloys, therefore, report a combined concentration of niobium plus tantalum. However, niobium is preferred to tantalum because of its lower cost and density. In Alloy 625, the solubility of niobium is about 2.5% and increases with decreasing molybdenum plus chromium content. An increase in niobium content increases the stiffness of the alloy in the annealed condition and exhibits a significant increase in the yield strength in the annealed and aged conditions when present more than 3% (Fig. 3.5) [3]. This increase in strength is due to the formation of the γ'' Ni_3Nb phase in the austenite matrix [8, 9]. In combination with molybdenum and chromium, niobium imparts better creep properties to the alloy (Figs. 3.6 and 3.7) [3]. However, niobium higher than 4% may increase segregation during solidification, leading to poor malleability and lower product yield. This restricts the concentration of niobium plus tantalum in Alloy 625 to 4.5% with a maximum of 4% pure niobium.

Fig. 3.5 Variation in the 0.2% yield strength of Alloy 625 as a function of niobium content [3]. The figure compares the yield strength of the alloy in annealed and annealed and aged conditions

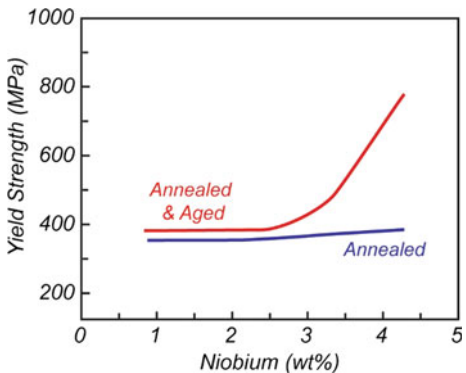


Fig. 3.6 Creep strain as a function of time in Ni–Cr–Mo–Nb alloys tested at 816 °C at 52 MPa [3]

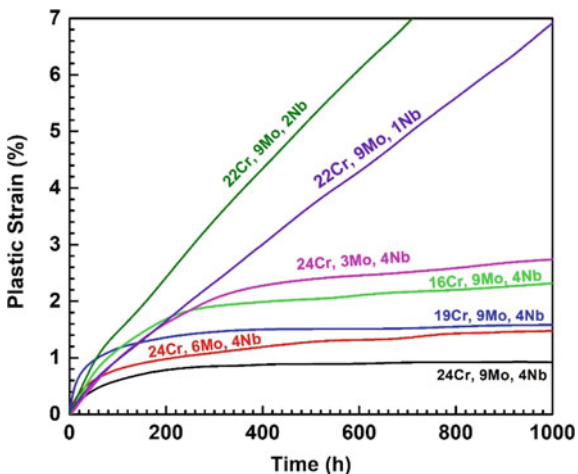
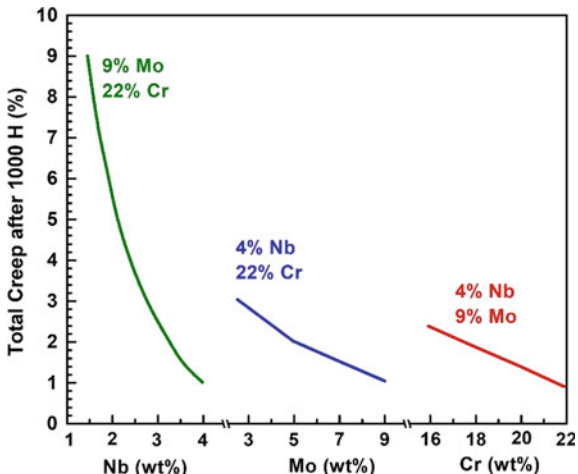


Fig. 3.7 Effect of chromium, molybdenum and niobium concentration on the total creep of forged and annealed alloy, annealed at 1149 °C for 1 h. The alloys were tested at 816 °C at 66 MPa stress [3]



3.1.6 Iron

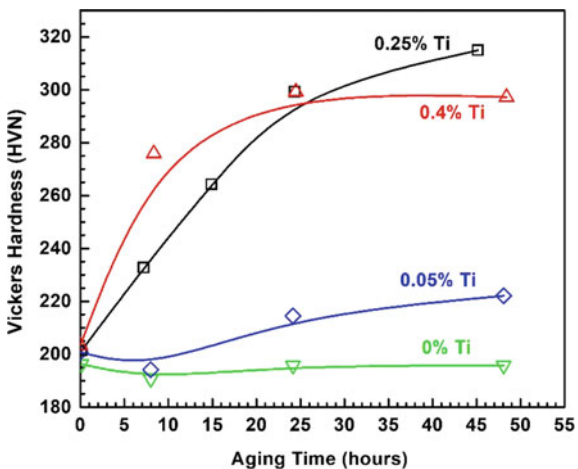
Iron does not play any significant role in Alloy 625. Its presence in most nickel-based superalloys, except in iron-nickel–chromium alloys, is a consequence of the use of ferroalloys for the addition of other elements. On the contrary, iron promotes the formation of TCP phases and the metastable γ'' phase. The maximum limit of iron in Alloy 625 is restricted to about 5%.

3.1.7 Aluminum and Titanium

The addition of aluminum in most superalloys increases their strength and environmental resistance at elevated temperatures. It strengthens the alloy by the precipitation of the well-known γ' phase particles that primarily contains aluminum along with other elements like titanium, niobium, etc. [3]. Aluminum also forms a tenacious and protective Al_2O_3 scale, which restricts the inward diffusion of oxygen and protects the alloy from oxidation. Titanium is generally added to aid the formation of γ' precipitates, which is more effective in raising the solvus temperature of the γ' phase [10]. Titanium further increases the effectiveness of the γ' hardening by increasing the lattice parameter and the antiphase-boundary energy of the γ' phase [7]. Therefore, a large titanium/aluminum ratio imparts higher strength to the alloy even with a relatively low amount of aluminum. In nickel–iron–base superalloys like Alloy 718, titanium promotes the co-precipitation of γ' and γ'' phases, which gives higher strength to alloys over a broader range of temperatures [11]. Titanium also forms MC-type carbide and controls nitrogen levels during solidification as it quickly bonds with nitrogen to form TiN phase particles [12].

Aluminum and titanium in Alloy 625 are primarily used as deoxidizers [2]. Even though the maximum amount of aluminum in the alloy is 0.4%, it can dissolve a much higher amount of titanium. The concentrations of aluminum and titanium are intentionally kept low to avoid age-hardening of the alloy by γ' phase particles. Low levels of aluminum and titanium also improve the weldability and brazeability of the alloy [3]. However, retaining about 0.2% each of aluminum and titanium in the alloy improves creep properties of the alloy considerably compared to an alloy without aluminum and titanium [3]. A small amount of titanium also has a marked effect on age-hardening behavior of the alloy induced by γ'' precipitates. Figure 3.8 shows the influence of titanium on the age-hardening of an Alloy 625 containing about 3.85% Nb [13]. Reducing titanium from 0.4 to 0.05% retards the precipitation of the γ'' phase. An alloy with 0.05% titanium has a hardness value close to 0% titanium. Retaining about 0.2% each of aluminum and titanium also improves the malleability of the alloy [2], which helps in its hot workability. However, the total content of aluminum plus titanium in the alloy must be restricted to a maximum of about 0.4% to avoid age-hardening.

Fig. 3.8 Effect of titanium concentration on γ'' precipitate induced hardening of Alloy 625 at 650 °C. The alloys contained about 3.85% niobium [13]



3.1.8 Carbon

Carbon plays an important role in superalloys. During liquid-phase processing, it acts as a deoxidizer. After deoxidation, the carbon left in the melt combines immediately with refractory elements like titanium, niobium, molybdenum, etc. to form MC carbides that segregate at inter-dendritic regions during solidification. During heat treatment and service exposure, the primary carbides degenerate to form secondary carbides of M₂₃C₆ and M₆C phases at grain boundaries over prolonged exposure [3]. If some carbon is retained in the austenite solid solution due to improper melting practice, the retained carbon may readily form the secondary carbides [14, 15]. Carbon in Alloy 625 must be kept low and not exceed 0.1%.

3.1.9 Nitrogen

Nitrogen is considered harmful for malleability and ductility of the alloy. For a given carbon content, increasing nitrogen contamination reduces the two properties of the alloy. It forms brittle particles of titanium nitride that embrittle grain boundaries and assist the precipitation of MC carbides [12]. Nitrogen can also dissolve in MC and M₆C to form carbonitrides during solidification. However, the formation of carbonitrides may leave excess carbon in the austenite matrix, which can cause premature failure due to the accelerated formation of grain boundary carbides [15] that embrittle the alloy. The Alloy 625 must not contain nitrogen more than about 0.03%.

3.1.10 Sulfur

Sulfur is a detrimental element in iron and nickel alloys [12, 16–18]. Its low solubility in nickel solid solutions causes the formation of a low-melting-point eutectic of 643 °C at grain boundaries. This eutectic compound melts during hot-working of the alloy reducing its workability. Sulfur also reduces fatigue life, creep resistance and adhesion of the protective oxide scales. The addition of small amounts of manganese or magnesium reduces the embrittling effect of sulfur by forming particles of their respective sulfides dispersed in the matrix. In Alloy 625, the amount of sulfur is restricted to a maximum of 0.015%.

3.1.11 Phosphorus

Like sulfur, phosphorus is also considered harmful due to its low solubility in nickel and the formation of a low-melting-point eutectic of 875 °C at grain boundaries [12]. However, it has been reported to strengthen grain boundaries in some alloys when present in small amounts, up to 0.02%, [19, 20]. Segregation of a small amount of phosphorous at grain boundaries impedes the self-diffusion of nickel across grain boundaries, thereby enhancing the creep life [19]. For example, adding 0.008% phosphorous increases the stress-rupture life of Alloy 718 up to 704 °C [21, 22] and improves ductility at 840 °C as compared to the undoped alloy. Like sulfur, phosphorous in Alloy 625 is also restricted up to a maximum of 0.015%.

3.1.12 Grain Boundary Strengthening Elements

Minor additions of elements like boron and zirconium improve creep-rupture resistance of nickel-base superalloys. A small amount of hafnium improves the ductility of grain boundary regions. A synergistic effect of phosphorous and boron in enhancing the creep resistance and stress-rupture life has also been reported in a boron-containing Alloy 718. Addition of 0.011% boron in an Alloy 718 containing 0.005% carbon and 0.022% phosphorous increases its stress-rupture life over 200% at 650 °C [22]. This improvement in creep-rupture properties of the alloy with boron and phosphorus is attributed to their segregation at grain boundaries that improves their cohesion and vacancy pinning capability, which slow down diffusion and reduce particle growth [23]. A maximum of 0.015% of boron may be added for better creep-rupture properties of Alloy 625, although a higher content may reduce hot malleability of the alloy [2].

Table 3.2 Compositions of the Alloy 625 and its LCF variant whose fatigue properties are compared in Fig. 3.9 [3]

Alloy	Ni	Cr	Mo	Nb	Al	Ti	C	Si	Fe	N
625	61.0	21.5	9.0	3.6	0.20	0.20	0.06	0.25	2.5	–
625 LCF	61.0	21.5	9.0	3.6	0.20	0.20	0.03 ^a	0.15 ^a	2.5	0.02 ^a

^aRefers to the maximum concentration

3.1.13 Trace Elements

Commercial superalloys always contain many elements, in minor concentrations, that are not intentionally added but are mostly detrimental to properties. At the same time, some elements are added to control the effects of other elements. For example, silicon, manganese and magnesium are added as refining agents during melting and processing. Silicon is added as a deoxidizer, while manganese and magnesium mitigate the sulfur effect by removing the detrimental low-temperature eutectic phase from grain boundaries [12]. These additions help in getting better mechanical properties of the finished product. In Alloy 625, the concentrations of silicon, manganese and magnesium are restricted to a maximum of 0.5% each to avoid their detrimental effects on high-temperature strength. Likewise, the presence of copper may be limited such that the total of sulfur, copper and phosphorus together does not exceed 0.1% to avoid the loss in mechanical properties or malleability. The presence of such trace elements, intentional or unintentional, may significantly affect the alloy's specific properties, like ductility, fatigue life or environmental resistance. For example, tight control of carbon, silicon, and nitrogen during the manufacturing of Alloy 625 (termed LCF variant), designed for the fatigue limited sheet applications like bellows and expansion joints, significantly increases its fatigue life compared to a standard Alloy 625. Table 3.2 compares the composition, and Fig. 3.9 compares the low-cycle fatigue properties of the Alloy 625 LCF with those of a standard Alloy 625 [3].

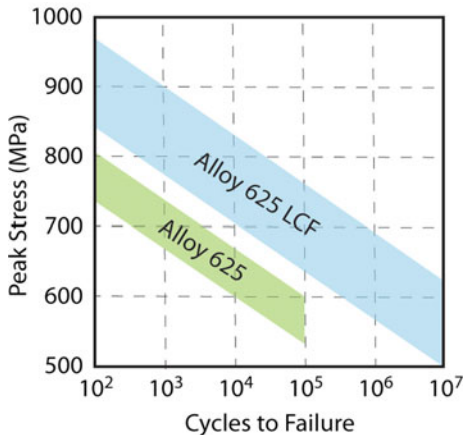
3.2 Characteristic Features of Phases in Alloy 625

The major phases that may be present in Alloy 625 are:

3.2.1 Gamma (γ) Phase

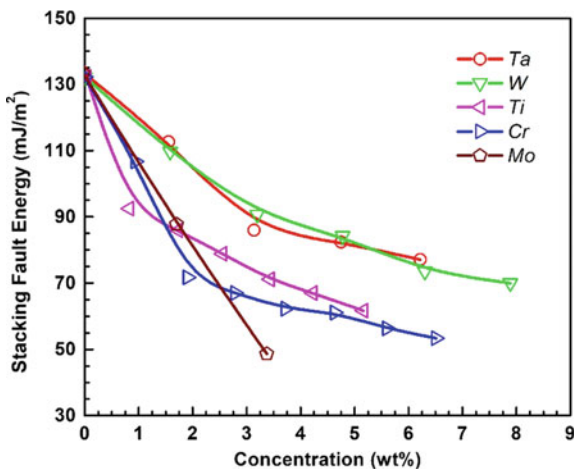
The gamma (γ) phase refers to the continuous FCC nickel matrix of the alloy that contains all the alloying elements dissolved in its disordered solid-solution without

Fig. 3.9 A comparison of the range of low-cycle fatigue strength of 625 and 625 LCF alloys at temperatures over 480–650 °C [3]



causing phase instability. The dissolution of chromium, molybdenum and niobium strengthens the alloy by straining the matrix. These elements have atomic diameters 1–13% and electron vacancy numbers 1–7% different from nickel [1]. The high melting point and slow diffusivity of refractory elements also improve creep resistance of the alloy. Most of these elements also significantly reduce stacking fault energy of the alloy (Fig. 3.10) [24–27], which makes the cross slip of dislocations difficult and, consequently, increases creep resistance of the alloy.

Fig. 3.10 Variation in the stacking fault energy of binary nickel alloys containing various alloying additions [27]

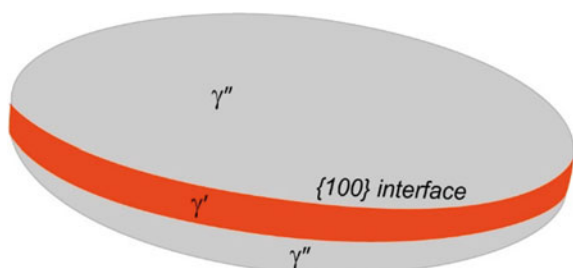


3.2.2 *Gamma Double Prime (γ'') Phase*

The Ni₃Nb based γ'' phase with a D0₂₂ structure is the main hardening phase of niobium bearing nickel–chromium–iron alloys [1] like Alloy 706, Alloy 718, Rene 62 and Udimet 63. However, binary nickel–niobium alloys form a D0_a phase with Ni₃Nb composition rather than the D0₂₂ phase. Formation of the γ'' phase has been attributed to the presence of a small amount of iron, which promotes its formation in alloys containing 2–6% niobium [28]. Further, niobium bearing superalloys invariably contain some amounts of aluminum and titanium also, which promote the co-precipitation of γ'' phase with γ' phase depending upon relative concentrations of the two elements. The γ' phase is the main strengthening phase in most precipitation-hardened nickel-based superalloys [1]. The two phases may precipitate out as separate particles with distinct morphologies, respectively as disk-shaped and cuboidal particles (e.g., Alloy 718 [29, 30]), or form a compact morphology comprising a cuboidal γ' phase particle coated by the γ'' phase (as in Alloy 706 [30]) or as γ' particle sandwich between γ'' phase particles as in Alloy 625 Plus [31] (Fig. 3.11). The difference in the precipitation behavior of the two phases is governed by the concentration of aluminum and titanium with respect to that of niobium. The ratio of niobium to aluminum plus titanium governs the relative rates of nucleation and growth and volume fractions of the two phases. A higher value of Nb/(Al + Ti) ratio for Alloy 718 (about 5% Nb, 0.5% Al, 0.9% Ti) compared to that for Alloy 706 (about 3% Nb, 0.2% Al, 1.7% Ti) favors the precipitation of discrete γ'' particles in the former, while a lower ratio in Alloy 706 favors the precipitation of the γ' phase particles first followed by the nucleation of the γ'' phase on all sides of the γ' phase [30].

In Alloy 625, the γ'' particles form as a metastable phase during thermal exposure over a temperature range 595–760 °C. Floreen et al. [13] have given a formula Ni₃(Nb_{>0.05}Ti_{<0.5}Al_{<0.5}) for the γ'' phase in Alloy 625. Figure 3.12 shows a pair of bright- and dark-field images of ellipsoidal γ'' particles taken by transmission electron microscopy. The particles appear as elongated ellipses due to the projection of the three-dimensional ellipsoid onto a two-dimensional image plane. Inset shows a selected area electron diffraction pattern from the imaged region, which shows streaking of superlattice reflections perpendicular to the thinner direction. Streaking in diffraction is a manifestation of the relaxation in Bragg condition when the crystal

Fig. 3.11 Schematic depicting compact precipitate morphology comprising a γ' phase particle sandwiched between γ'' phase particles



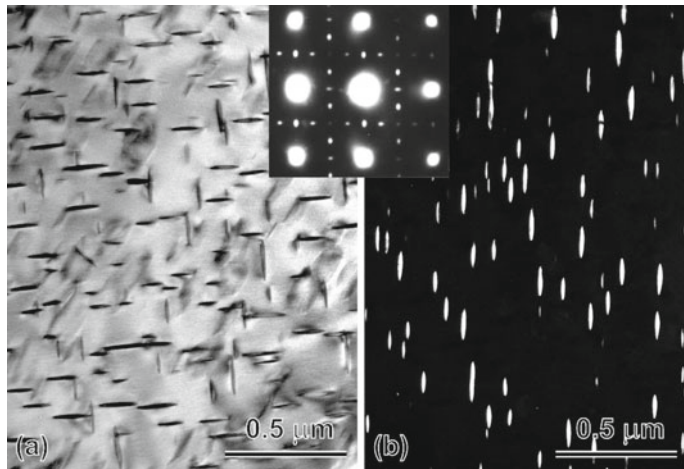


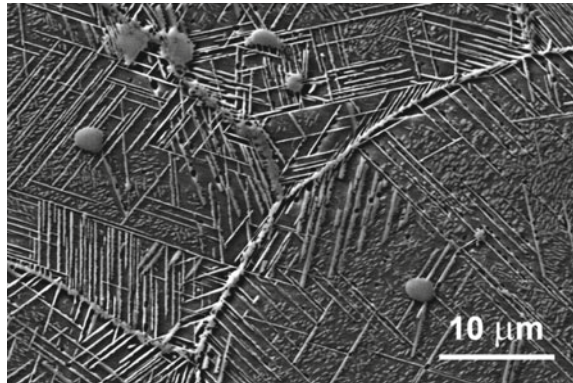
Fig. 3.12 Bright-field and dark-field transmission electron microscopy images of γ'' phase precipitates in an age-hardened Alloy 625. Inset shows a $<001>$ zone-axis electron diffraction pattern showing fine superlattice reflections of the γ'' phase. Note elongation in the superlattice reflections perpendicular to thickness of the ellipsoidal

is very thin and arises in a direction perpendicular to the thickness [32]. These particles are coherent with the austenite matrix. The misfit strain associated with ellipsoidal γ'' particles embedded in the γ -matrix is about 2.9% [33], which is much larger than the maximum γ - γ' misfit strain (~1.2%) in γ' strengthened nickel-base superalloys [1]. Therefore, precipitation of the γ'' phase particles imparts very high strength to the γ'' phase bearing alloys. However, the γ'' phase transforms to its stable δ structure at temperatures above 650 °C. Therefore, careful heat treatment is required to ensure the precipitation of the γ'' phase instead of the δ phase.

3.2.3 Delta (δ) Phase

The δ phase is the equilibrium phase of the γ'' phase. High niobium and silicon and low aluminum contents promote the formation of δ phase while substitution of tantalum for niobium inhibits its formation [34]. The formation of δ precipitates occurs in the temperature range over 750–950 °C [35]. The δ phase particles assume a plate morphology with {111} habit plane (Fig. 3.13), though randomly oriented globular δ particles have also been reported in some cases at the grain boundaries [36]. The globular morphology of δ particles is better than the plate morphology as the latter embrittles the alloy. The δ phase forms by heterogeneous nucleation on grain boundaries and twin boundaries at relatively low temperatures or by intragranular nucleation at relatively high temperatures [37]. The nucleation of the δ phase may occur directly from the supersaturated γ matrix. In addition, the δ phase may form

Fig. 3.13 A scanning electron micrograph of an aged Alloy 625 showing the predominant formation of needle-shaped δ phase particles



from the existing γ'' phase particles in which stacking faults act as nuclei of the δ phase [35]. As shown later in Sect. 4.2, both γ'' and δ phases have the rectangular ordering of niobium atoms in their close-packed planes (Figs. 4.6 and 4.8) and the two phases differ only in the stacking sequences of close-packed planes. The γ'' phase follows a ... $A_1B_1C_1A_2B_2C_2A_1B_1C_1...$ while the δ phase follows a ...ABAB... type stacking sequence of their close-packed planes [35, 37]. The A_1 and the A_2 layers in the γ'' phase, and similarly the B_1 and the B_2 layers and the C_1 and the C_2 layers, represent the same stacking sequence with atom positions (Fig. 4.6), vertically above/below one another, but contain niobium atoms in such a manner that the superimposition of minority atoms occur only after six layers. A missing plane, say B_1 , in the stacking of close-packed planes in the γ'' phase brings stacking of the four layers (say ... $C_1A_2C_2A_1...$) similar to that in the δ phase. Stacking faults in the γ'' phase, therefore, acts as nuclei of the δ phase for the γ'' - δ transformation [35, 37]. All γ'' precipitate strengthened nickel-base alloys are consequently susceptible to the formation of δ phase during processing or service at temperatures above about 650 °C [35]. Although the δ phase particles are known to embrittle the alloy, their controlled precipitation at grain boundaries inhibits grain boundary sliding and may be beneficial for creep-rupture ductility [38].

3.2.4 $Ni_2(Cr, Mo)$ Phase

The $Ni_2(Cr, Mo)$ phase is an equilibrium phase commonly observed in nickel–chromium-molybdenum alloys during thermal exposure at temperatures ~600 °C. The nickel, chromium, and molybdenum constitute major constituent elements of the phase in which the ratio of the nickel to the sum of molybdenum plus chromium content (in atomic per cent) approximately corresponds to $Ni_2(Cr, Mo)$ stoichiometry. In many nickel–chromium–molybdenum alloys, such as Hastelloy C, Hastelloy C276, Hastelloy C4, etc. molybdenum is partially replaced by tungsten to further

enhance the strength at elevated temperatures as well as to improve corrosion resistance in certain media. The thermal stability of the $\text{Ni}_2(\text{Cr}, \text{Mo})$ phase depends upon relative concentrations of chromium and molybdenum in the alloy [39]. The addition of molybdenum increases the thermodynamic stability and the solvus temperature of the $\text{Ni}_2(\text{Cr}, \text{Mo})$ phase [39–41]. The $\text{Ni}_2(\text{Cr}, \text{Mo})$ phase is stable at temperatures up to about 630 °C in Alloy 625 (containing about 26 at% Cr and 6 at% Mo) [42], while it is stable up to about ~775 °C in Haynes 242 (containing about 10 at% Cr and 16 at% Mo) [43]. Besides, an increase in the molybdenum concentration increase kinetics of the precipitation of the $\text{Ni}_2(\text{Cr}, \text{Mo})$ phase [39, 44]. For example, it takes a prolonged thermal exposure of more than 1000 h at 600 °C to form the $\text{Ni}_2(\text{Cr}, \text{Mo})$ phase particles in Alloy 625 [45], while it forms within a few hours at temperatures from 650 to 750 °C in Haynes 242 [43]. The increase in the precipitation kinetics in Haynes 242 is due to a higher diffusivity of the molybdenum than chromium in the nickel matrix [39, 46]. The addition of tungsten enhances the thermal stability of the $\text{Ni}_2(\text{Cr}, \text{Mo})$ phase [47]. This has been exploited by partially replacing molybdenum with tungsten in Haynes 242 alloy to produce Haynes 244 alloy [48]. Recent independent studies have also confirmed the similar effect of W on the thermal stability of the $\text{Ni}_2(\text{Cr}, \text{Mo})$ phase in model Ni–Cr–Mo–X (X = W or/and Ti) [49]. Like γ'' particles, the $\text{Ni}_2(\text{Cr}, \text{Mo})$ phase also form homogeneously with an ellipsoidal morphology (Fig. 3.14a, b) though they are thicker than γ'' particles. Besides, Sundararaman et al. [50] have also reported a snowflake morphology of $\text{Ni}_2(\text{Cr}, \text{Mo})$ precipitates (Fig. 3.14c). Precipitation of the $\text{Ni}_2(\text{Cr}, \text{Mo})$ phase increases the alloy's susceptibility to hydrogen and stress corrosion cracking [51].

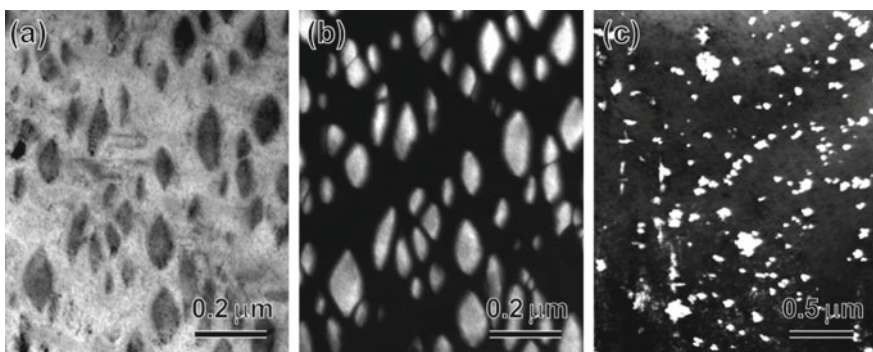


Fig. 3.14 **a** and **b** Bright-field and dark-field transmission electron microscopy images of $\text{Ni}_2(\text{Cr}, \text{Mo})$ precipitates with ellipsoidal morphology in a Ni–Cr–Mo alloy (*Courtesy Dr. Amit Verma*). **c** Snow-flake morphology of $\text{Ni}_2(\text{Cr}, \text{Mo})$ precipitates in a service aged Alloy 625. Reprinted from Ref. [49].

3.2.5 Carbide Phases

Carbide particles of several phases may form in nickel-base alloys containing refractory elements. These alloys may contain carbon in the range of about 0.02–0.2 wt%. The most common carbide phases are MC, M₂₃C₆, M₆C and M₇C₃, where M denotes metal atoms [1]. In general, alloys containing high chromium, titanium and aluminum favor the M₂₃C₆ phase, high molybdenum and tungsten favor the M₆C phase and high niobium, tantalum and titanium favor the MC phase [1]. M₇C₃ forms in alloys with low concentrations of chromium and refractive elements but usually transforms to M₂₃C₆ on aging. In Alloy 625, the formation of carbides of MC, M₂₃C₆ and M₆C phases have been reported during solidification of the melt and during fabrication and service. The carbides that form during solidification are termed “Primary” while those forming during fabrication and service are termed “Secondary”. The MC phase is the most common primary carbide, though the primary carbides of M₆C and M₂₃C₆ type have also been reported (e.g., [52, 53]).

The MC phase forms with refractory elements like niobium, tantalum, hafnium, and titanium. The high stability of the MC with these elements is because of their high (negative) free energy of formation [1]. However, the thermodynamic stability of their MC carbides differs. In decreasing order of stability, it is HfC, TiC, TaC and NbC [2], though they prefer to form in the order as HfC, TaC, NbC and TiC [1]. When multiple refractory elements are present, atoms of different species may substitute for each other, as in (Ti, Nb)C. Partial replacement of titanium, tantalum or niobium by molybdenum or tungsten reduces the stability of the MC phase [1]. The reduced stability makes the MC phase prone to decomposition, which is the primary carbon source for the formation of secondary M₂₃C₆ and M₆C carbides over the temperature range of 700–980 °C [1]. Besides, the secondary carbides may also precipitate directly from the carbon supersaturated austenite matrix.

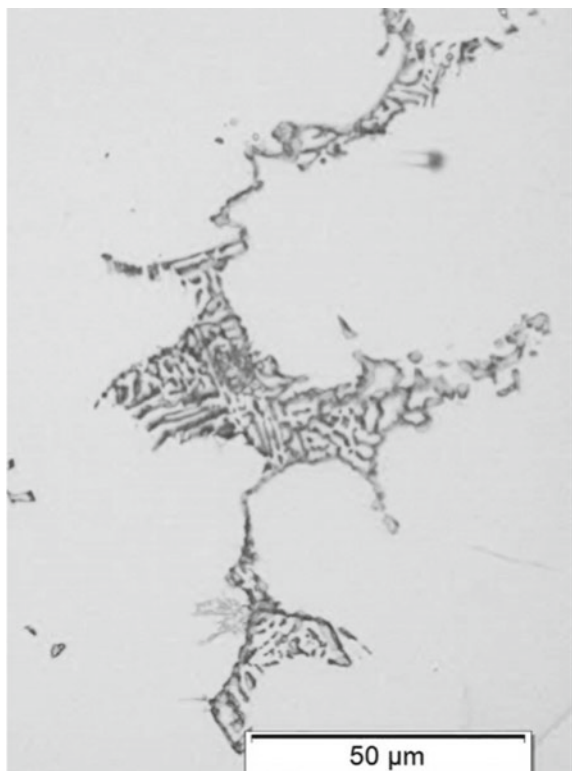
The M₂₃C₆ phase is a chromium-rich carbide. It precipitates abundantly in the temperature range 650–900 °C, mostly as a result of the decomposition of the primary MC carbides in nickel-base superalloys containing moderate to large amounts of chromium [1]. The M₂₃C₆ carbide particles are enriched with chromium and prefer to nucleate at grain boundaries and other defects, like twin boundaries, dislocations and stacking faults [52]. In Alloy 625 the approximate composition of M₂₃C₆ is (Cr_{0.85}Fe_{0.01}Ni_{0.07}Mo_{0.07})₂₃C₆ [13].

The MC carbide may also decompose to form M₆C carbide at about 800–980 °C when molybdenum and tungsten in the alloy is more than 6–8%. Further, M₆C and M₂₃C₆ may interact to form one from the another. For example, pronged thermal exposure of Rene 41 and M-252 alloys converts M₆C to M₂₃C₆, while that of Mar—M 200 converts the M₂₃C₆ to M₆C [1]. Unlike the more rigid M₂₃C₆ phase, the M₆C exhibits a wider composition range. Raghavan et al. [54] have observed that in Ni–Cr–Mo alloys, chromium can substitute for molybdenum up to 30% in the M₆C phase, while in M₂₃C₆, the solubility of molybdenum is only 10%. Moreover, when the ratio of Cr/Mo atoms in the alloy exceeds 3, particles of the M₂₃C₆

carbide nucleate predominantly, while the particles of the M₆C type carbide precipitate when it is less than 3. The approximate composition of the M₆C in Alloy 625 is (Cr_{0.21}Fe_{0.02}Ni_{0.37}Nb_{0.08}Mo_{0.24}Si_{0.08})₆C [13]. In alloys containing molybdenum or tungsten, M₆C may form as grain boundary precipitates along with M₂₃C₆ [1]. The relative abundance of the two types of carbides is determined by the amounts of molybdenum, tungsten and chromium in the alloy.

In Alloy 625, the MC phase forms as discrete particles with coarse cuboidal or “script” morphologies distributed heterogeneously at transgranular and intergranular locations (Fig. 3.15). It is primarily (Nb, Ti)C, with minor amounts of nickel and chromium [13]. The formation of carbide particles may enhance or degrade the mechanical properties of the alloy depending on their morphology and distribution. The secondary carbides may precipitate as continuous grain boundary films or discrete particles at grain boundaries. While continuous films of carbides along grain boundaries severely degrade the impact and rupture properties of the alloy, the formation of discrete carbide particles is beneficial in inhibiting grain boundary sliding during creep.

Fig. 3.15 Formation of primary carbide in Chinese script morphology in cast Alloy 625



3.2.6 Topologically Close-Packed Phases

Nickel–iron base superalloys containing high amounts of transition metals, like tantalum, niobium, chromium, tungsten, and molybdenum, are prone to the formation of topologically close-packed (TCP) phases. Elements like aluminum and silicon promote their formation, while boron and zirconium inhibit their occurrence [1]. The TCP phases are hard and brittle, whose presence may significantly degrade the overall mechanical properties of the alloy [1]. These phases form through non-metallic directional electron bonding of terminal elements. They nucleate at austenite grain boundaries and usually grow as Widmanstätten plates parallel to {111} planes of the γ matrix. The plate morphology promotes crack initiation and easy propagation, which reduces the alloy's ductility and creep-rupture strength, although the yield strength remains unaffected. Further, the TCP phases weaken the matrix as their formation scavenge refractory elements, causing a loss of matrix strength. The precipitation of TCP phases can be minimized and even eliminated by carefully controlling the composition of various refractory elements in the alloy. The TCP phases that may form in Alloy 625 are σ , μ , and Laves, though their occurrence, particularly of the σ phase, has been rarely reported. The σ phase is structurally close to the $M_{23}C_6$ phase because of the similar number of chromium and molybdenum atoms required to form the σ phase. If all the carbon atoms are removed from the $M_{23}C_6$ carbide lattice, the remaining lattice can be converted into the σ phase by a slight shift in atom positions [1]. That is why the σ phase often nucleates on $M_{23}C_6$ particles [1]. Once nucleated, it grows principally in the austenite matrix into the plate morphology. Likewise, the μ phase is structurally similar to the M_6C phase and may form in M_6C bearing alloys, particularly when the concentrations of molybdenum and tungsten are high. The Laves phase in Alloy 625 forms during solidification. It is considerably rich in niobium, molybdenum and silicon compared to the nominal composition of the alloy. However, the composition of each element in the Laves phase may vary significantly depending upon the processing history of the alloy [13, 55].

3.3 Solidification Behavior of Alloy 625

The high concentration of refractory elements in superalloys makes their solidification quite complex compared to materials like aluminum and copper. In general, the phase diagram and heat and mass transport principles govern the solidification behavior, while the solidification kinetics determines the development of the cast microstructure. During solidification of an alloy, first, the solute-lean alloy solidifies, followed by dendritic solidification of the solute-rich liquid. The solidification front grows in the directions of heat and composition gradients. The distribution of solutes in the solidified front is governed by their partitioning coefficient, k . The partitioning coefficient of an element is defined as the ratio of its composition in the

solid to that in the liquid within the solidification temperature range. The k value of an element characterizes its relative thermodynamic tendency to remain in liquid or solid and gives an idea of the extent of micro-segregation expected during solidification of the alloy. A value of k less than unity indicates that dendrite cores will be depleted of the solute relative to the inter-dendritic regions, while a value greater than unity implies enrichment of the dendritic cores. A k value of unity indicates no dendritic micro-segregation will occur. Elements like niobium, molybdenum, titanium, and silicon in nickel solution have $k < 1$ and segregate to inter-dendritic regions, while elements, like iron, have $k > 1$ and tend to partition to dendrite cores. Little chromium enrichment occurs in either of the two regions because of its k value close to zero. This behavior of solutes causes enrichment of nickel and iron in dendrite cores in Alloy 625 and the segregation of niobium, molybdenum and silicon to inter-dendritic regions. This segregation behavior of solutes results in a local variation in the composition at the subgrain level, which may cause the formation of a second phase at the end of the solidification.

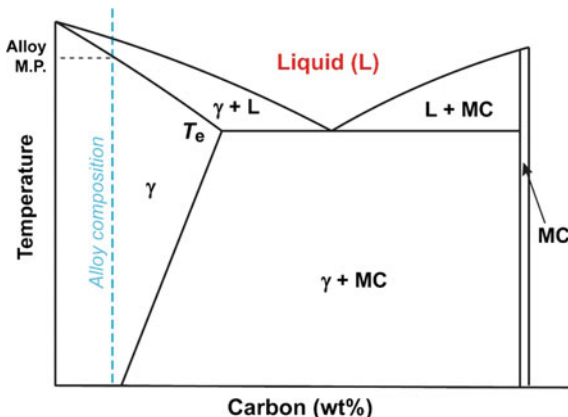
The high concentrations of heavier solutes in superalloys cause their segregation in inter-dendritic regions, which promote the precipitation of TCP phases and carbides during the final stages of solidification. Therefore, the solidification of superalloys requires controlled cooling of the melt. Controlled cooling avoids the formation of continuous channels of heavy solutes rejected during dendrite formation. When such channels solidify, they form continuous TCP phases and carbides, which are highly detrimental to the strength and ductility of the alloy.

The concentration of carbon in Alloy 625 is usually sufficiently high to promote the formation of both carbides and Laves phases at the end of solidification. Like niobium and molybdenum, carbon segregates aggressively to the liquid inducing the formation of eutectic type reactions involving MC-type carbide, Laves phases, or both toward the terminal stages of solidification. The presence of chromium, molybdenum, niobium, iron and silicon promotes the formation of Laves phase in Alloy 625 rather than the Ni_3Nb . Cieslak [55] has studied the effect of niobium, silicon and carbon on the solidification behavior of Alloy 625, containing the three elements in the range ~0–3.6 wt%, ~0.03–0.40 wt%, and ~0.009–0.036 wt%, respectively. Table 3.3 summarizes the phase transformation sequence and terminal reactions in these alloys. He has shown that the terminal liquid that solidifies in the alloy containing high niobium but low carbon and silicon content is enriched with niobium solutes and form the NbC and Laves phases within the γ matrix at inter-dendritic regions. Both NbC and Laves phases are high in niobium, though the two phases may contain other elements in small quantities. The formation of the γ phase in the terminal liquid progresses with a eutectic type $L \rightarrow \gamma + \text{NbC}$ solidification reaction. Figure 3.16 depicts this eutectic reaction in a pseudo-binary phase diagram. Floreen et al. [13] have reported a temperature range of 1190 to 1205 °C for the eutectic reaction in Alloy 625. As the eutectic reaction continues to form the γ/NbC phase, the remaining liquid gets depleted with niobium and carbon. The local liquid composition again shifts back toward the composition where the liquid solidifies to form the γ phase. The eutectic reaction continues until the interfacial composition satisfy the three-phase $L \rightarrow \gamma + \text{NbC}$ non-invariant reaction. This behavior of niobium enrichment

Table 3.3 A summary of the phase transformation sequences and terminal reactions in Alloy 625 containing different amounts of Si and C elements [55, 56]

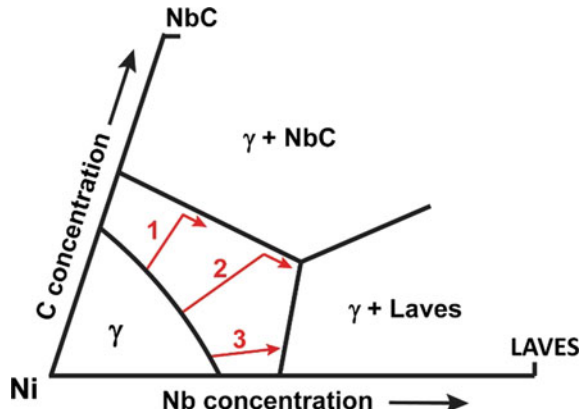
Si and C concentration	Phase transformation sequence	Terminal solidification	
		Reaction	Temperature (°C)
0.03Si, 0.009 C	$L \rightarrow L + \gamma \rightarrow L + \gamma + NbC \rightarrow L + \gamma + NbC + Laves \rightarrow \gamma + NbC + Laves$	$L \rightarrow L + \gamma + Laves$	1150
0.03Si, 0.038 C	$L \rightarrow L + \gamma \rightarrow L + \gamma + NbC \rightarrow \gamma + NbC$	$L \rightarrow L + \gamma + NbC$	1246
0.38Si, 0.008 C	$L \rightarrow L + \gamma \rightarrow L + \gamma + NbC \rightarrow L + \gamma + NbC + M_6C \rightarrow L + \gamma + NbC + M_6C + Laves \rightarrow \gamma + NbC + M_6C + Laves$	$L \rightarrow L + \gamma + Laves$	1148
0.46Si, 0.008 C	$L \rightarrow L + \gamma \rightarrow L + \gamma + NbC \rightarrow L + \gamma + NbC + Laves \rightarrow \gamma + NbC + Laves$	$L \rightarrow L + \gamma + Laves$	1158

Fig. 3.16 A hypothetical pseudo binary phase diagram showing a lower temperature eutectic (T_e) in equilibrium with MC Phase [13]. M. P. represents melting point of the alloy



and depletion in the remaining liquid continues till the last stages of solidification when the last liquid solidifies by a eutectic reaction $L \rightarrow \gamma + Laves$ at ~ 1150 °C. The addition of carbon in niobium bearing alloys promotes the formation of the γ and NbC constituent at the expense of the γ and Laves constituent. This solidification behavior of Alloy 625 is schematically represented as a function of the C/Nb ratio (Fig. 3.17). When C/Nb is high, the alloy forms γ and NbC without Laves phase. At intermediate values of C/Nb, it first forms γ and NbC followed by the formation of Laves phase. When C/Nb is low, it forms γ and Laves phase with no NbC. However, the formation of Laves phases without NbC is not uncommon in Alloy 625 when carbon is less than

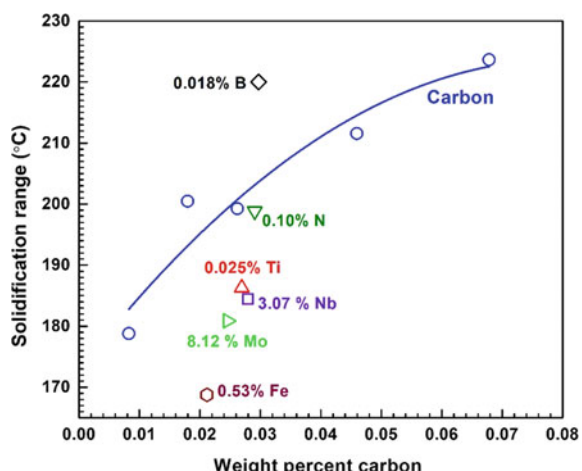
Fig. 3.17 Schematic depicting the effect of carbon and niobium on the solidification path in Alloy 625 [13]. When C/Nb is high, the alloy solidifies to form γ and NbC without Laves phase (Path 1). At intermediate values of C/Nb, it first forms γ and NbC followed by the formation of Laves phase (Path 2). When C/Nb is low, it directly forms γ and Laves phase with no NbC (Path 3)



0.01% [56]. On the other hand, silicon promotes the eutectic formation of the Mo-rich M_6C carbide and enhances the formation of γ /Laves constituents even in Alloy 625 with low levels of carbon. This behavior of silicon is similar to that observed in other superalloys [57]. Independent studies by Bardos et al. [57] supports this role of silicon in promoting the formation of Laves phase. Bardos et al. [57] have reported the formation of Ni_3SiNb_2 phase in a ternary alloy even though a Ni_2Nb Laves phase does not exist. Alloy 625 containing high silicon may therefore have a significantly different solidified microstructure with higher volume fractions of M_6C carbide and Laves phases.

The carbon content also influences the solidification range (i.e., the difference between the liquidus and the solidus temperatures). Figure 3.18 shows a plot of the solidification range during cooling as a function of carbon in a nickel alloy containing 22.1% Cr, 8.9% Mo, 3.6% Nb, 4.3% Fe, 0.27% Al, 0.16% Ti, 0.0015% B, and varying

Fig. 3.18 Plot shows solidification range as a function of carbon in a nickel alloy containing 22.1% Cr, 8.9% Mo, 3.6% Nb, 4.3% Fe, 0.27% Al, 0.16% Ti, 0.0015% B. The figure also shows the individual effects on the solidification range when the amounts of molybdenum, niobium, iron and titanium are reduced close to their lower limits and boron and nitrogen are increased to their highest limits [13]



amounts of carbon [55, 56]. An increase in the carbon content significantly increases the solidification range of Alloy 625. Likewise, silicon and niobium contents significantly increase the solidification range of the alloy. However, the increase in the solidification range due to niobium is much more than carbon or silicon. The solidification range directly influences the formation of the inter-dendritic NbC and Laves phases, as a decrease in the solidification range reduces the amount of segregation. Other elements also individually affect the solidification range of the alloy. For example, reducing the amounts of molybdenum, niobium, iron and titanium close to their lower limits (Table 3.1) tend to reduce the solidification range (Fig. 3.18). Increasing the boron to 0.018% increases the solidification range significantly while increasing the nitrogen content to 0.10% has little effect.

Reducing the solidification range is essential as it reduces the amount of segregation during solidification and, therefore, improves hot workability. Thus, reducing the carbon and niobium contents is beneficial in reducing their quantity available for the formation of NbC or Laves phases and reducing their segregation during solidification. Therefore, the formation of NbC and Laves phase can be reduced by controlling the solute concentration and reducing the solidification range. Likewise, reducing elements like iron, molybdenum and silicon close to their lower limits is beneficial in minimizing the precipitation of the Laves phase [13].

The formation of Laves and NbC phases plays a significant role in the mechanical properties of cast and wrought Alloy 625. Their particles can have detrimental effects on ductility and rupture life if present in excessive or highly localized distributions. Laves phase particle can be eliminated by suitable homogenization treatment, typically annealing for a period of about 15 h at about 1180 °C [58], or by thermo-mechanical treatments. However, the NbC particles are very stable and cannot be eliminated by conventional processing. NbC particles are distributed randomly during subsequent thermo-mechanical processing. Therefore, the Laves phase is usually absent while NbC particles are observed as dispersed particles in wrought products. Improper thermo-mechanical processing may cause the formation of a banded microstructure locally containing a high density of NbC and Laves phase particles in wrought products [13]. The formation of such bands of hard particles degrades the ductility in a direction transverse to the bands. Figure 3.19 shows an example of a banded microstructure with a high local density of Laves phase particles in an Alloy 625 [13]. Alloys with such microstructures display poor ductility when strained perpendicular to the bands.

3.4 Phase Transformations in Alloy 625

Alloy 625 undergo a variety of transformations when exposed to elevated temperatures. These transformations are governed by nucleation and growth of the transforming phase, which are functions of temperature and time. Such transformations are conveniently represented by “C” shape time–temperature-transformation (TTT) curves for a given volume fraction of the transformed phase, where the curve’s nose



Fig. 3.19 Photograph of the banded microstructure formed by the accumulation of NbC and Laves phase particles in a wrought Alloy 625 plate. Reprinted from Ref. [13]. Copyright 1994 by The Minerals, Metals & Materials Society. Used with permission

(or knee) corresponds to the fastest transformation temperature. At temperatures above the nose, the rate of transformation is slow because of the low nucleation rate even though the atomic mobility of solutes is high. On the other hand, at temperatures below the nose where the nucleation rate is high, the transformation rate is slow because the atomic mobility is slow. Further, in alloys like Alloy 625, where multiple phases may form with overlapping fields of time, temperature or both, curves corresponding to different phases may overlap.

Alloy 625 forms various carbides and intermetallic phases during thermal exposures for periods ranging from a few minutes to thousands of hours. Figure 3.20 give the TTT diagram for the beginning of the precipitation of various phases in Alloy 625 in solution annealed condition, drawn based on the diagram proposed by Floreen et al. [13], where all the phases are in the austenite solid solution. The original figure does not contain the precipitation curve for the Ni₂(Cr, Mo) phase, which has been included in Fig. 3.20 based on the literature data. The TTT curves in Fig. 3.20 are for an alloy with nominal composition. A variation in the composition, even within the composition range, may vary their position with respect to time and temperature.

The precipitation of the carbides begins at grain boundaries in the temperature range of about 700–1040 °C. Both MC and M₆C type carbides form at temperatures ranging from about 870–1040 °C, while the M₂₃C₆ phase forms at temperatures in the range of about 700–915 °C. In the overlapping temperature range, all three carbides may form. Figure 3.21 show the formation of all three types of carbides after an exposure of 8 h at about 870 °C [13].

Prolonged exposure in the temperature range of about 700–980 °C may begin the precipitation of both Laves and δ phase. The simultaneous precipitation of the two phases has been attributed to the similar kinetics of their precipitation, which is controlled by the diffusion of niobium solutes. However, the co-precipitation of Laves and δ phase may not always coincide and depends upon the relative concentrations of carbon and niobium solutes, as illustrated by the co-precipitation of carbide and δ

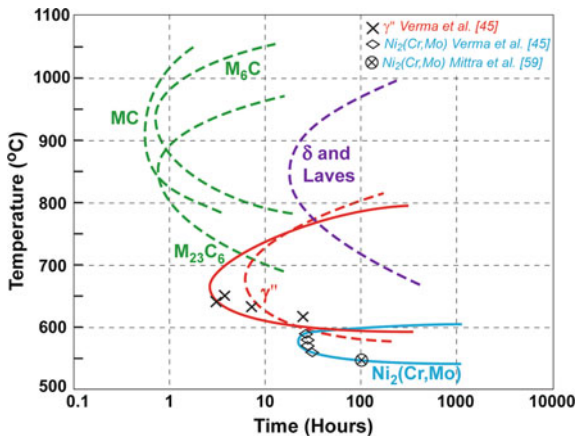
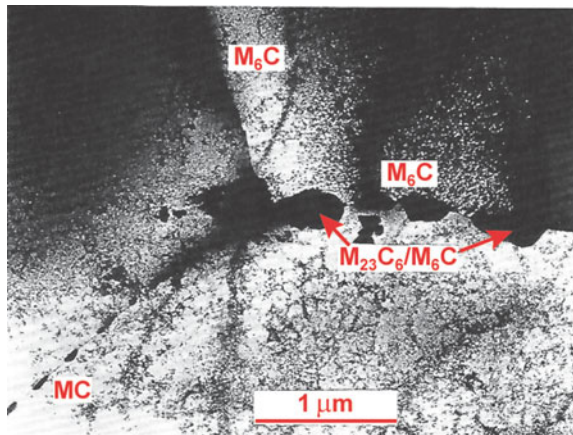


Fig. 3.20 Time–temperature–transformation (TTT) diagram of the beginning of the precipitation of various phases in Alloy 625. The diagram is modified from the TTT diagram proposed by Floreen et al. [13] to include the precipitation of the $\text{Ni}_2(\text{Cr}, \text{Mo})$ phase. Broken lines show the TTT curves proposed by Floreen et al., while solid lines show the new curves for γ'' and $\text{Ni}_2(\text{Cr}, \text{Mo})$ phases drawn based on the new data [45, 59]. The upper and lower bound of the two curves were decided by their temperature stability regimes in the literature

Fig. 3.21 A transmission electron microscopy micrograph of various carbides precipitated at grain boundaries in Alloy 625 after annealing of 8 h at 870 °C. Reprinted from Ref. [13]. Copyright 1994 by The Minerals, Metals & Materials Society. Used with permission



phases during prolonged service exposure of an alloy at around 800 °C (Fig. 3.22). The δ phase typically have an acicular or plate shape morphology, while the Laves phase particles are irregular or blocky shaped, similar in morphology to those of M_6C and M_{23}C_6 carbides [13].

In the temperature range of about 595–760 °C, the γ'' phase forms with its nose at around 650 °C, corresponding to the fastest kinetics. The precipitation of the $\text{Ni}_2(\text{Cr}, \text{Mo})$ phase in Alloy 625 has been reported at a temperature as low as 540 °C after

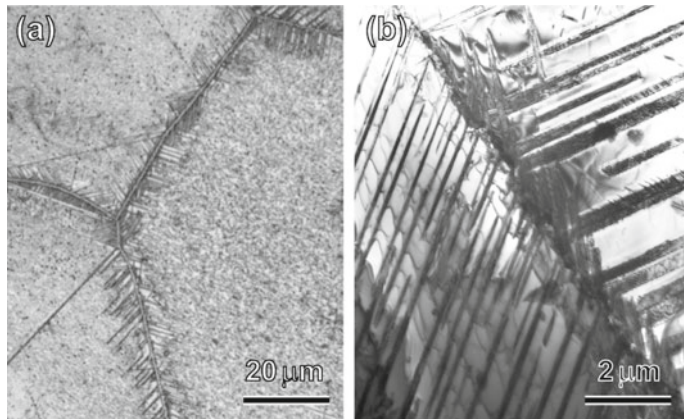


Fig. 3.22 **a** Optical micrograph of a service aged Alloy 625 showing the precipitation of carbide (thin line in light contrast) and needle-shaped δ phase particles at grain boundaries. **b** A transmission electron microscopy image of δ precipitates at a grain boundary

100 h of aging [59]. However, the phase is thermally stable up to about 628 °C and dissolve above it [42].

Plastic deformation may affect the precipitation behavior of all the phases by shifting their curves toward less incubation time and toward lower temperatures [60–62]. This behavior is attributed to three main factors, namely, (i) an increase in the density of nucleation sites due to an increase in the defect density; (ii) an increase in the diffusion coefficient due to the elastic distortions of the lattice; (iii) an increase in diffusion due to dislocation pipe diffusion. Radavich and Fort [61] have reported faster precipitation of the δ phase particles after pre-straining of Alloy 625. Similarly, Suave et al. [62] have reported the precipitation of the δ phase particles at temperatures as low as 650 °C, while that of the γ'' phase at temperature 550 °C in a deformed alloy.

All the phases dissolve at temperatures above their upper-temperature bounds. For example, carbides, δ and Laves phases dissolve into the solution at temperatures above 1100 °C. Carbides dissolve within an hour at 1100 °C, while δ and Laves phases may take much longer time to dissolve completely.

3.5 Microstructural Evolution During Aging of Alloy 625

Solution annealing the alloy in the temperature range 1050–1150 °C does not bring about any appreciable difference in the microstructure [63]. A typical microstructure of wrought alloys subjected to solution annealing at 1150 °C shows equiaxed grains with grain boundaries free of precipitates (Fig. 3.23a) except for the occasional occurrence of randomly distributed blocky precipitates of primary carbides.

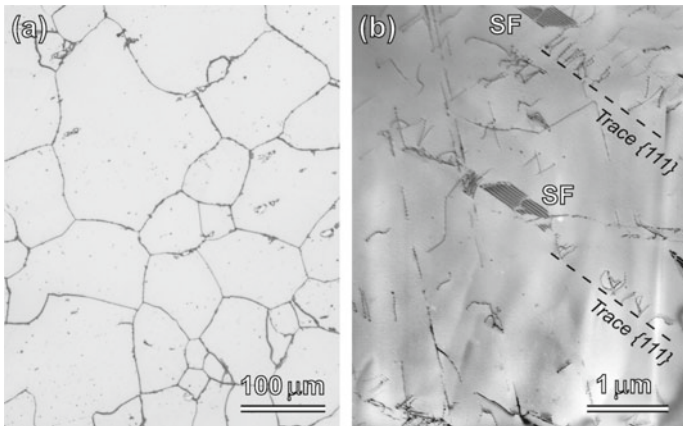


Fig. 3.23 **a** Optical micrograph of a solution annealed Alloy 625. **b** Typical transmission electron microscopy image showing planar arrays of dislocations and stacking faults (SF) in the solution annealed Alloy 625. Broken lines mark the trace of $\{111\}$ glide plane of the dislocation arrays

The alloy exhibit frequent $\{111\}$ annealing twins or stacking faults along with the planar arrangement of dislocations on $\{111\}$ planes (Fig. 3.23b). The frequent observations of the planar arrangement of dislocations and stacking faults is indicative of the low to an intermediate value of the matrix's stacking fault energy (SFE). Alloys, like aluminum alloys, associated with a high SFE (~ 250 – 300 mJ/mm 2) exhibit microstructures with lattice dislocations only without stacking faults or twins (e.g., [64]), while alloys with a low value of SFE (~ 25 – 50 mJ/mm 2) are associated with high incidences of dislocation dissociation and stacking fault formation (e.g., [65]).

3.5.1 Precipitation of the γ'' Phase

As mentioned in Sect. 3.2.2., the γ'' phase precipitates in the temperature range of about 600–760 °C as a metastable phase in Alloy 625. Short time aging of Alloy 625 at temperatures up to 700 °C does not produce any noticeable precipitation of the γ'' phase and the microstructures essentially remain similar to the solution annealed alloy [63]. Aging for 10 h at 650 °C results in the formation of fine γ'' phase particles that are difficult to resolve by transmission electron microscopy but show distinct superlattice reflections in the electron diffraction patterns [63, 66]. Samples aged for 24 h at 650 °C forms distinguishable and homogeneously distributed thin lens shape γ'' particles in the matrix (Fig. 3.24a) [66]. After prolonged annealing, the precipitates assume their characteristic ellipsoidal morphology (Fig. 3.24b). Figure 3.25 shows a three-dimensional drawing of an ellipsoidal particle of thickness t having radii of h and R along the minor and major axes of the ellipse. The habit planes of ellipsoidal

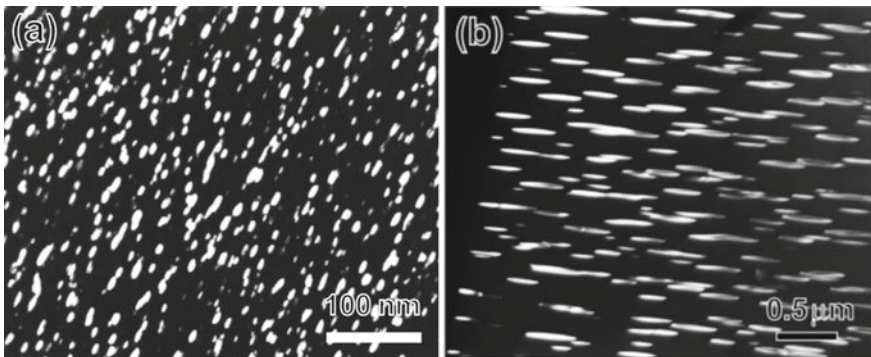
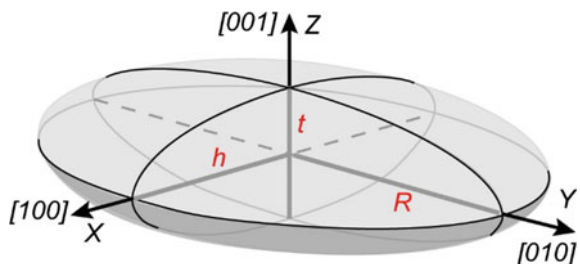


Fig. 3.24 Transmission electron microscopy images (in dark-field) of γ'' phase particles in Alloy 625 after **a** ageing for 24 h at 650 °C, and **b** after a prolonged ageing period

Fig. 3.25 A three-dimensional schematic drawing of an ellipsoidal particle of thickness (height) t and minor and major semi-axes h and R , respectively



particles are parallel to their flat surfaces, which are parallel to {100} planes of matrix and are always perpendicular to c -axis of their unit cell.

Samples aged for prolonged periods also tend to nucleate γ'' particles heterogeneously at structural singularities, like dislocations and twin boundaries. Aging of the alloy at 700 °C for a period of 168 h exhibit homogeneous precipitation of the γ'' particles and their frequent precipitation on matrix dislocations [63, 66]. At still higher aging temperatures, heterogeneous nucleation of γ'' particles preferably occurs at dislocations. Figure 3.26 shows the precipitation of γ'' particles on a planar array of dislocations and twin boundaries in a sample aged at 750 °C for 24 h. The heterogeneous precipitation of the γ'' particles on dislocations resemble “leaves on a stem” morphology with the dislocation line parallel to the “stem” and the ellipsoidal γ'' phase particles appearing “leaves” attached to the “stem” (Fig. 3.27 [63]). The heterogeneous nucleation on dislocations does not entail any change in the habit plane of the γ'' phase particles, but may affect the number density of particles corresponding to a given variant depending upon the strain field of dislocations that provide the nucleation sites for the nucleating variant.

The precipitation of the γ'' particles constrains the matrix due to its non-integral unit cell axial ratio ($c/a = 2.036$), and the constraint strain increases with an increase in the particle size. The ellipsoidal morphology of the γ'' particles is a consequence

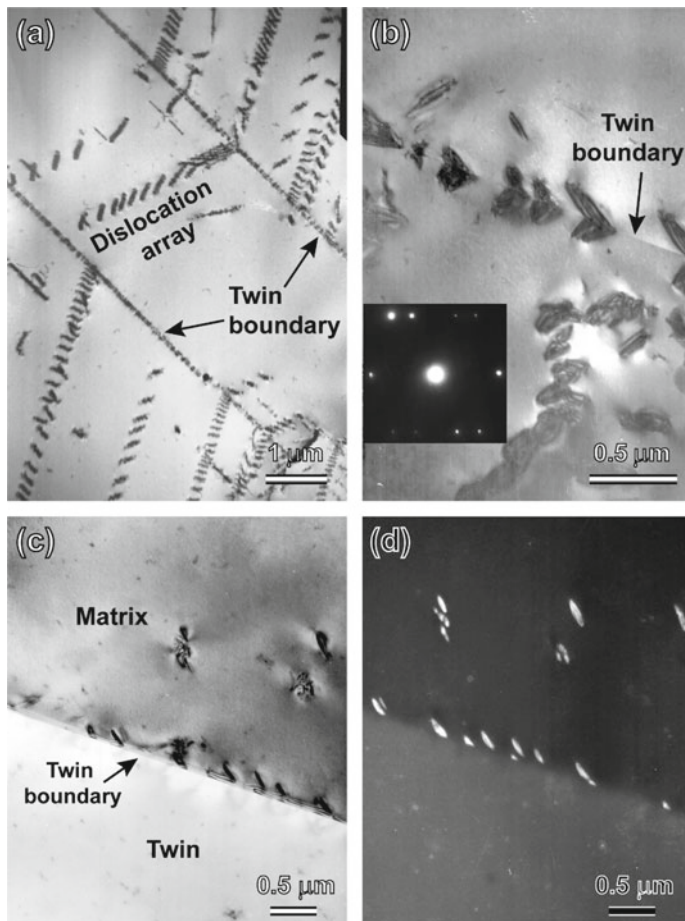


Fig. 3.26 **a** Transmission electron microscopy images of heterogeneous precipitation of γ'' phase precipitates on dislocations and coherent twin boundaries in Alloy 625 aged at 750 °C for 100 h. **b** A magnified image of γ'' precipitates on matrix and twin side of a boundary. **c** and **d** Bright- and dark-field pairs of a few precipitates that nucleated on a twin-boundary and grew into the matrix. Inset in **b** shows a $<110>$ electron diffraction pattern from the twin region. Reprinted from Ref. [63] by permission from Dr. M. Sundararaman

of the minimization of the strain energy arising due to this constraint strain. The constrained strain, ε^C , of an ellipsoidal particle having a tetragonal distortion perpendicular to its habit plane, is related to the stress-free transformation strain ε^T , by the following relationship [67]

$$\varepsilon^C = \left[1 - \frac{(1-2\nu)}{2(1-\nu)} \frac{t}{R} \right] \varepsilon^T \quad (3.1)$$

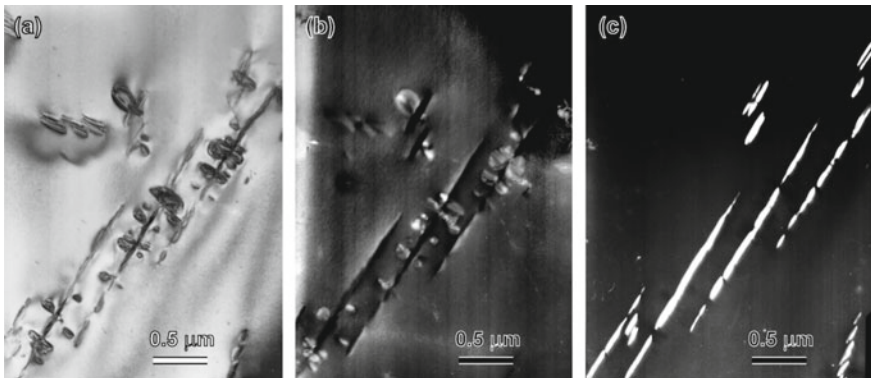


Fig. 3.27 **a** Bright-field transmission electron microscopy image of the “leaves on a stem” morphology of γ'' precipitates nucleated on dislocations during ageing of Alloy 625 at 750 °C. **b** and **c** Dark-field images showing the γ'' precipitates that formed “leaves” and “stem” of the configuration. Reprinted from Ref. [63] by permission from Dr. M. Sundararaman

where $t = 4 h/3$ is the thickness of the ellipsoidal precipitate with major axis R and minor axis h and ν is Poisson’s ratio. As per Eq. 3.1, as the γ'' particles grow (i.e., the aspect ratio R/t increases) with the progress of transformation, the constrained strain ε^C increases and gradually approaches the stress-free transformation strain ε^T .

3.5.2 Precipitation of the δ Phase

The metastable γ'' phase transforms to equilibrium δ phase at temperatures above 650 °C in Alloy 625. Cozar et al. [58] have shown the formation of a few δ phase needles along with profuse γ'' precipitation after aging for 2048 h at 700 °C. At 750 °C, it nucleates on grain boundaries and twin boundaries as well as within grains after the aging of 100 h (Fig. 3.28a) [63], though the number density of δ precipitates remains rather small. At temperatures 800 °C and above, the kinetics of δ precipitation is considerably enhanced. However, at these temperatures, the density of γ'' precipitates reduces significantly (Fig. 3.28b) [63]. Figure 3.28c, d show intragranular and intergranular precipitation of δ precipitates in an Alloy 625 aged at 800 °C for 240 h. Plastic deformation reduces the temperature and the incubation period for the δ phase. Suave et al. [62] have reported the beginning of the nucleation of the δ phase within 10 h at 750 °C in deformed Alloy 625 against its nucleation after 100 h at the same temperature.

The morphological evolution of the δ phase particles in Alloy 625 is similar to that in Alloy 718. Sundararaman et al. [29, 63] have shown that the δ phase particles first nucleate predominantly at austenite grain boundaries and incoherent ledges of twin boundaries and later at coherent twin boundaries. At high temperatures, intragranular

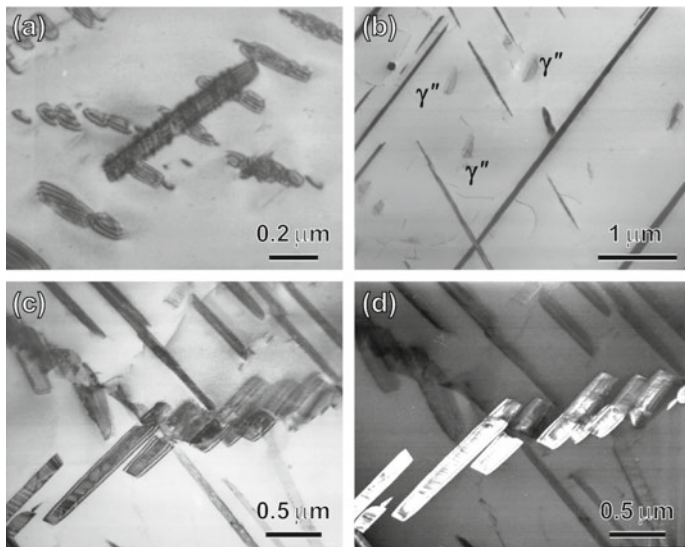
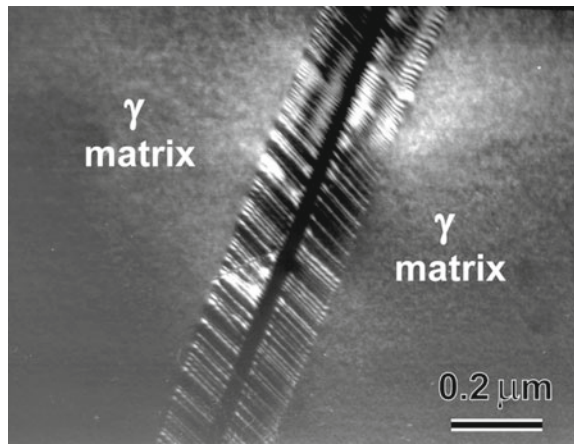


Fig. 3.28 Transmission electron microscopy images of δ phase precipitates in Alloy 625. **a** Intragranular precipitates after ageing of 100 h at 750 °C. **b** Intragranular δ precipitates coexisting with a sparsely distribution of γ'' precipitates after ageing at 800 °C for 240 h. **c** and **d** A bright- and dark-field pair of images showing δ precipitates nucleated at a grain boundary. Reprinted from Ref. [63] by permission from Dr. M. Sundararaman

δ particles may nucleate homogeneously in the supersaturated γ matrix. Alternatively, stacking faults of existing γ'' particles may act as their nuclei, as mentioned in Sect. 3.2.3. The δ precipitates maintain $(010)_\delta \parallel \{111\}_\gamma$ and $[100]_\delta \parallel \langle 011 \rangle_\gamma$ (or $(001)_\delta \parallel \{111\}_\gamma$ and $[010]_\delta \parallel \langle 110 \rangle_\gamma$ depending upon whether the $(010)_\delta$ or the $(001)_\delta$ is considered as the close-packed plane) orientation relationship with the austenite matrix and grow parallel to $\{111\}$ planes of the matrix. During growth, the growing δ precipitates often pass through pre-existing γ'' particles belonging to appropriate variants, while γ'' precipitates belonging to other variants hinders the advancement of the growing δ particles. When sufficiently large, the needle shape δ precipitates assume plate shape morphology and lose its coherency with the austenitic matrix and the γ - δ interface becomes semi-coherent. An array of interfacial dislocations is generated to accommodate the γ - δ misfit (Fig. 3.29). These dislocations have been identified to be $1/2 <110>$ type. On the other hand, the precipitate is fully incoherent in a direction normal to the habit plane, as the stacking sequence along this direction of the γ and δ structures are different.

Fig. 3.29 Transmission electron microscopy image of dislocations at γ - δ interfaces of a δ precipitation in an Alloy 625 aged for 240 h at 800 °C. (Courtesy Dr. M. Sundararaman)



3.5.3 Precipitation of the $\text{Ni}_2(\text{Cr}, \text{Mo})$ Phase

The $\text{Ni}_2(\text{Cr}, \text{Mo})$ phase forms with Ni_2X ($X = \text{Cr}, \text{Mo}$) stoichiometry in alloys that contain nickel, chromium and molybdenum in the ratio that may or may not satisfy the Ni_2X stoichiometry. The thermal stability of the $\text{Ni}_2(\text{Cr}, \text{Mo})$ phase is a function of the relative concentrations of chromium and molybdenum in the phase, where the chromium and molybdenum atoms both take positions of the X atoms in the Ni_2X stoichiometry of the Pt_2Mo type lattice (Sect. 2.2.3). The addition of molybdenum increases the thermodynamic stability and the solvus temperature of the $\text{Ni}_2(\text{Cr}, \text{Mo})$ phase [39 – 41]. For example, the $\text{Ni}_2(\text{Cr}, \text{Mo})$ phase is stable at temperatures up to about 628 °C in Alloy 625 (containing about 26 at% Cr and 6 at% Mo) [42], while it is stable up to about ~775 °C in Haynes 242 (containing about 10 at% Cr and 16 at%) [43]. The increased stability of the $\text{Ni}_2(\text{Cr}, \text{Mo})$ phase in alloys is attributed to its reduced formation energy with higher molybdenum. In binary alloy systems, the Ni_2Cr is stable as its formation energy is -7.095 kJ/mol [51]. In comparison, the Ni_2Mo and Ni_2W phases are respectively barely stable and unstable as their formation energies are nearly zero and $+10 \text{ kJ/mol}$, respectively [51]. The formation energies of binary compounds suggest that a gradual substitution of chromium and molybdenum in Ni–Cr alloys makes the $\text{Ni}_2(\text{Cr}, \text{Mo})$ phase unstable. On the contrary, studies have shown that the substitution of chromium and molybdenum atoms increases its stability by lowering the formation energy of the $\text{Ni}_2(\text{Cr}, \text{Mo})$ phase compared to the Ni_2Cr phase [68, 69]. Another independent study on the stability of the $\text{Ni}_2(\text{Cr}_{1-x}\text{Mo}_x)$ phase has shown that its formation energy decreases up to $x = 0.25$ and starts increasing for $x > 0.25$ indicating the highest stability for the $\text{Ni}_2(\text{Cr}_{0.75}\text{Mo}_{0.25})$ composition of the $\text{Ni}_2(\text{Cr}, \text{Mo})$ phase [40]. On the other hand, the addition of tungsten in Ni–Cr alloys destabilizes the Pt_2Mo type phase as shown by its suppression in Ni–Cr–W alloys [70]. However, in the presence of molybdenum, tungsten addition appears to increase the thermal stability of the Pt_2Mo type phase

[47], as witnessed by their higher thermal stability in Haynes 244 than Haynes 242. An independent study on model Ni–Cr–Mo alloys has also confirmed an increase in the thermal stability of the Pt_2Mo type phase with partial substitution of molybdenum and tungsten [49]. These studies indicate that both Mo and W together increases the thermal stability of the Pt_2Mo type phase in Ni–Cr–Mo–W alloys.

The $\text{Ni}_2(\text{Cr}, \text{Mo})$ phase forms via a disorder to order transformation reaction wherein the chemical ordering of the disordered FCC lattice gives rise to ordered body-centered orthorhombic structure, which may happen via continuous ordering at relatively lower temperatures or by nucleation and growth mechanisms at somewhat higher temperatures. An increase in the molybdenum concentration in Ni–Cr–Mo alloys raises the solvus temperature of the $\text{Ni}_2(\text{Cr}, \text{Mo})$ phase due to higher thermal stability to the phase. An increase in molybdenum concentration also increases the kinetics of the $\text{Ni}_2(\text{Cr}, \text{Mo})$ phase. This effect of molybdenum is reflected in different precipitation kinetics of the $\text{Ni}_2(\text{Cr}, \text{Mo})$ phase in Alloy 625 and Haynes 242. While a significant amount of the $\text{Ni}_2(\text{Cr}, \text{Mo})$ phase forms within 10 h at temperatures ranging from 650 to 750 °C in Haynes 242 [43], it takes about 1000 h at 600 °C for its precipitation in Alloy 625 [45]. This difference in the kinetics is attributed to solute species governing the formation of the $\text{Ni}_2(\text{Cr}, \text{Mo})$ phase. The kinetics is slow when chromium controls the formation of the phase and is fast when molybdenum controls the precipitation as the diffusivity of molybdenum in the nickel lattice is higher than chromium. This is deduced based on activation energy analysis of transformation peaks associated with the formation of the $\text{Ni}_2(\text{Cr}, \text{Mo})$ phase in different model $\text{Ni}_2(\text{Cr}_{1-x} \text{Mo}_x)$ alloys with varying chromium and molybdenum solute concentrations [39, 71]. Further, higher misfit strain energy in alloys containing higher molybdenum concentration due to comparatively bigger atomic size of Mo would also assist in enhancing kinetics of the precipitation of the $\text{Ni}_2(\text{Cr}, \text{Mo})$ phase and the morphology of the phase.

The difference in the kinetics also manifests itself in the morphology of the $\text{Ni}_2(\text{Cr}, \text{Mo})$ phase. The formation of the $\text{Ni}_2(\text{Cr}, \text{Mo})$ phase is mainly reported with an ellipsoidal morphology [45, 72–76]. However, particles with snowflake morphology in service exposed wrought ammonia cracker tubes have also been reported [50]. Interestingly, different morphologies of the $\text{Ni}_2(\text{Cr}, \text{Mo})$ phase in Alloy 625 are reported by the same research group working on ammonia cracker tubes service exposed to similar conditions but procured separately at different periods from different vendors. Ammonia cracker tubes are about 9 mm thick, about 90 mm in outer diameter and 12 m long designed for service exposure of 100,000 h at temperatures in the range of about 650–700 °C. However, local variations in the temperature during service exposure were reported along the tube's length [75]. Chakravarty et al. [75] have reported particles of $\text{Ni}_2(\text{Cr}, \text{Mo})$ phase resembling ellipsoidal morphology in sections of wrought tubes service exposed for 100,000 h at temperatures in between 600 and 650 °C. In contrast, Sundararaman et al. [50] have reported the snowflake morphology in the sections of wrought tubes service exposed for about 70,000 h at temperatures close to but below 600 °C. From these details, it can be safely deduced that temperatures of the tube sections reported by Chakravarty et al. [75] and Sundararaman et al. [50] are likely to differ by about 20–40 °C. This difference in the temperature

is not less considering the narrow temperature window (~ 60 °C) for the precipitation of the Ni₂(Cr, Mo) phase (Fig. 3.20). Ignoring the likely difference in the relative concentrations of chromium and molybdenum, this temperature between the two tubes may bring a significant variation in the kinetics of the Ni₂(Cr, Mo) phase in the two cases. Interestingly, Singh et al. [42] have observed cuboidal/rhombus morphology of Ni₂(Cr, Mo) phase particles in service exposed cast Alloy 625 and found their size much bigger compared to particles of the same phase in the wrought alloys [50, 75]. Such cuboidal/rhombus morphology is the crystallographic manifestation of the coherent faces when two perpendicular axes of the ordered cell do not lie in the foil [76]. The large particle size of the Ni₂(Cr, Mo) phase in cast Alloy 625 could be attributed to local enrichment of molybdenum solutes in the vicinity of inter-dendritic that may have aided the precipitation kinetics.

3.5.4 Precipitation of the Carbide Phases

The austenite phase has low solubility of carbon. Lower levels of carbon in nickel-base alloys are maintained by reducing its content by adding strong carbide forming elements like niobium, tantalum, and titanium [2], which combine with carbon to form MC-type carbides during solidification. The MC carbide particles are commonly observed in most nickel-based superalloys, including Alloy 625 (Fig. 3.30). Carbide particles that form during solidification are termed “primary carbides”. Besides MC carbides, the formation of M₂₃C₆ and M₆C types of primary carbides have also been reported in Alloy 625 [42]. Figure 3.30b shows a micrograph of the M₂₃C₆ primary carbide. All the primary carbides appear as coarse particles, often irregular in shape, distributed randomly within the austenite grains and at grain boundaries and incoherent segments of twin boundaries [52]. The degeneration of the (Nb, Ti)C carbides is the primary source of carbon for the formation of “secondary carbides” that form during alloy processing or thermal exposure.

The precipitation of MC, M₆C and M₂₃C₆ secondary carbides during thermal annealing are reported by various researchers at temperatures ranging from 600 to 1050 °C [13, 52, 54, 77–81]. The M₂₃C₆ carbide primarily precipitates at grain boundaries above 650 °C and usually occurs as irregular, discontinuous, blocky particles or as continuous grain boundary film. The M₆C carbides precipitate at temperatures above 800–850 °C when the M₂₃C₆ becomes unstable. The M₆C carbides also precipitate at grain boundaries along with M₂₃C₆ [1] as a thin film at grain boundaries or in Widmanstätten morphology at intragranular locations [78].

Vernot-Loier and Cortial [78] have reported the formation of the MC carbide particles at 1050 °C, which dissolves at temperatures above 1100 °C. Precipitation of all the carbides follows a cube to cube orientation relationship with the austenite phase.

Chakravarty et al. [75] have reported the precipitation of the M₂₃C₆ type carbide film at a temperature below 600 °C in Alloy 625 service exposed for a prolonged time. Sundararaman et al. [52] have shown the formation of a nearly continuous film

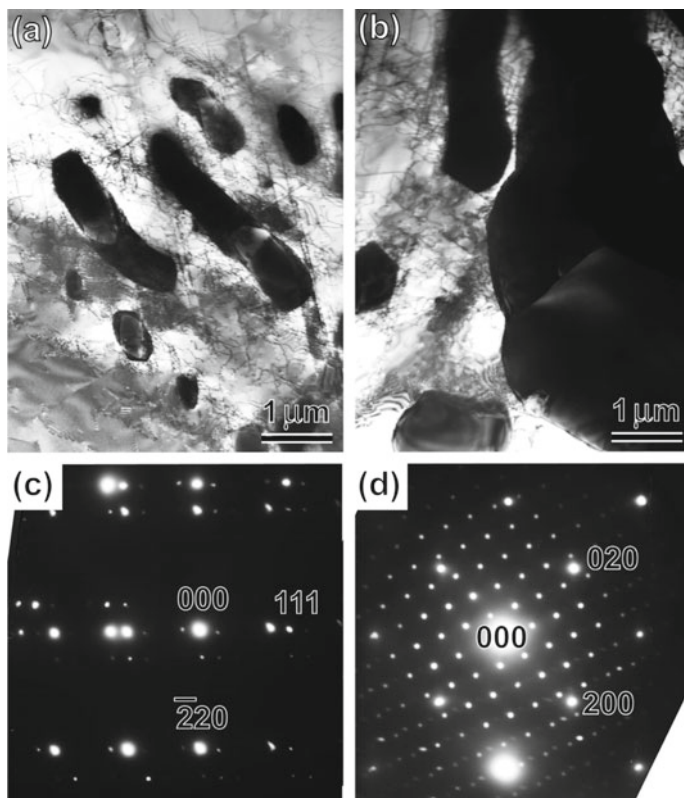


Fig. 3.30 Transmission electron microscopy micrographs of primary **a** MC and **b** $M_{23}C_6$ carbides in cast Alloy 625 alloy. **c** and **d** Electron diffraction patterns from corresponding MC and $M_{23}C_6$ particles. Reprinted from Ref. [42], Copyright (2015), with permission from Elsevier

of the $M_{23}C_6$ phase at many grain boundaries after aging of 90 h at 650 °C and even much thicker film within 24 h at 750 °C. The coalescence of carbide particles formed these films. Figure 3.31a shows the precipitation of $M_{23}C_6$ carbide particles along grain boundaries after a prolonged aging at 650 °C. The extent of carbide precipitation at grain boundaries varies from boundary to boundary depending upon the energy and misorientation of the boundary [80]. When carbide particles form at grain boundaries, particles orient with respect to one of the two austenite grains (Fig. 3.31b). Apart from nucleation at grain boundaries, heterogeneous nucleation of the $M_{23}C_6$ carbides may also occur at dislocations and incoherent segments of annealing twin boundaries (Fig. 3.31c, d). At temperatures of 800 °C and above, co-precipitation of the carbide and the δ phases occur pretty frequently at the grain boundaries (Fig. 3.22) [52]. The secondary carbides first precipitate at intergranular sites, but they precipitate progressively within grains when grain boundaries are saturated. The precipitation of the M_6C carbides at grain boundaries is sensitive to the amount of silicon as it promotes the nucleation of M_6C . The presence of silicon

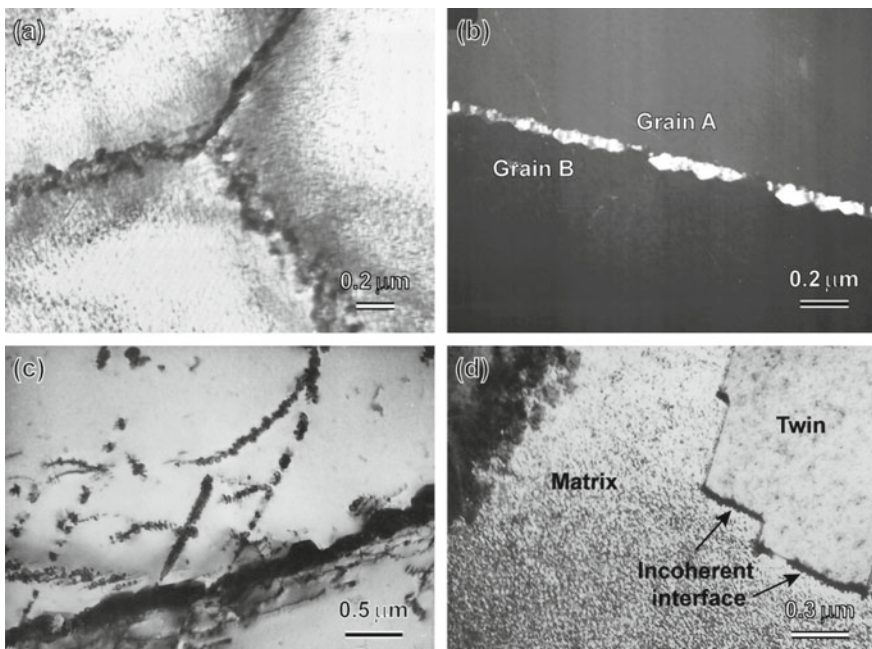


Fig. 3.31 Transmission electron microscopy images depicting the precipitation of $M_{23}C_6$ carbide in Alloy 625 at: **a** grain boundaries during prolonged ageing at about $650\text{ }^{\circ}\text{C}$; **b** a dark-field image showing the growth of carbide particles into grain B after 24 h of ageing at $750\text{ }^{\circ}\text{C}$; **c** and **d** respectively show the precipitation of $M_{23}C_6$ carbide particles at dislocations and incoherent segments of twin boundaries. **c** and **d** Reprinted from Ref. [63] by permission from Dr. M. Sundararaman

as low as less than about 0.15% may significantly retard the precipitation of M_6C carbides, mainly when the carbon is below about 0.035% [13].

The morphology of grain boundary carbides has an important bearing on the overall properties of the alloy. For example, small discrete particles of secondary carbides at grain boundaries increase the creep-rupture life of the alloy. In contrast, precipitation of continuous grain boundary films can severely degrade the impact and rupture properties of the alloy by providing an easy fracture path [15].

3.5.5 Precipitation of the TCP Phases

Alloy 625 is susceptible to the formation of undesirable σ , μ and Laves TCP phases due to the presence of high amounts of metals like niobium, chromium, tungsten, and molybdenum. These phases may form during solidification, processing or service and their precipitation deplete refractory elements in the γ matrix, causing a loss of strength. Proper control of alloy's chemistry and processing conditions can avoid the precipitation of the TCP phases in Alloy 625.

The hexagonal Laves phase is the most frequently observed of the three TCP phases that may form in Alloy 625 [13, 82]. It usually forms as blocky and irregular particles at grain boundaries, similar to the formation of grain boundary M_6C and $M_{23}C_6$ carbide particles. Figure 3.20 shows a single curve for the beginning of the precipitation of the δ and Laves phases. Prolonged thermal exposures at temperatures over the 700–980 °C range may precipitate Laves and δ phases at grain boundary regions that may already contain carbide particles. Identifying the Laves phase in such a configuration may need the support of complete electron diffraction and chemical analysis to delineate it from grain boundary carbides because of their similar morphologies. While the grain boundary carbides may be dissolved by an annealing treatment of about an hour at temperatures about 1100 °C or higher, the dissolution of the δ and Laves particles may require a significantly longer time. For example, Floreen et al. [13] have shown minimum annealing of 24 h at 1100 °C to dissolve even small quantities of Laves and δ phases completely.

Figure 3.32 shows an example of the particles of Laves phase of Ni_3Mo_2Si type precipitated at grain boundaries during aging of 24 h at 760 °C [82]. Silicon appears to stabilize this phase, as evidenced by the EDS spectrum.

The formation of the μ phase in Alloy 625 is reported less frequently than the Laves phase. Evans et al. [83] have reported the μ phase at grain boundaries during creep deformation of thin foils of Alloy 625. Tawancy [84] has reported the precipitation of the μ phase with blocky morphology in Alloy 625 and many other nickel–chromium–molybdenum alloys containing more than 3% iron during prolonged thermal exposures of up to 16,000 h at temperatures over 540–870 °C. The precipitation kinetics increases with increasing temperature in this temperature range and is fastest at 870 °C. The μ -phase particles are characterized by defect structure comprising twins and stacking faults parallel and normal to the basal plane [85] and exhibit a preferential tendency to nucleate at pre-existing molybdenum-rich carbides both within grains and grain boundaries [83]. Tawancy [84] has shown that all nickel–chromium–molybdenum alloys, like Hastelloy C, C-276, C-22, which contain iron more than 3% alloys, exhibit the precipitation of a Mo_6Ni_7 type μ -phase at temperatures over the 540–870 °C range (Fig. 3.33) [82]. In contrast, alloys like Hastelloy C-4, 230, B2 and S, which contain iron less than or equal to 3%, do not show the precipitation of the μ -phase. Alloy 625 also exhibits the precipitation of the μ -phase only when it contains iron more than 3%. The presence of iron stabilizes the otherwise thermodynamically unstable Mo_6Ni_7 type μ -phase [84]. Tawancy [84] has correlated this behavior of the μ -phase precipitation to the concentrations of major solutes and iron and concluded that, for a given combined concentration of molybdenum and tungsten, the tendency to form the μ -phase reduces with an increase in the nickel to iron plus cobalt ratio.

The σ phase is known to form in alloys containing high concentrations of iron and chromium. It may precipitate at grain boundaries, incoherent twin boundaries, or both. Its kinetics is very slow and may take hundreds and sometimes thousands of hours. Very limited cases of the precipitation of the σ phase are reported in Alloy 625. Evans et al. [83] have reported the formation of σ phase precipitates of approximately $Cr_5Ni_3Mo_2$ composition during creep rupture of a thin Alloy 625 foil.

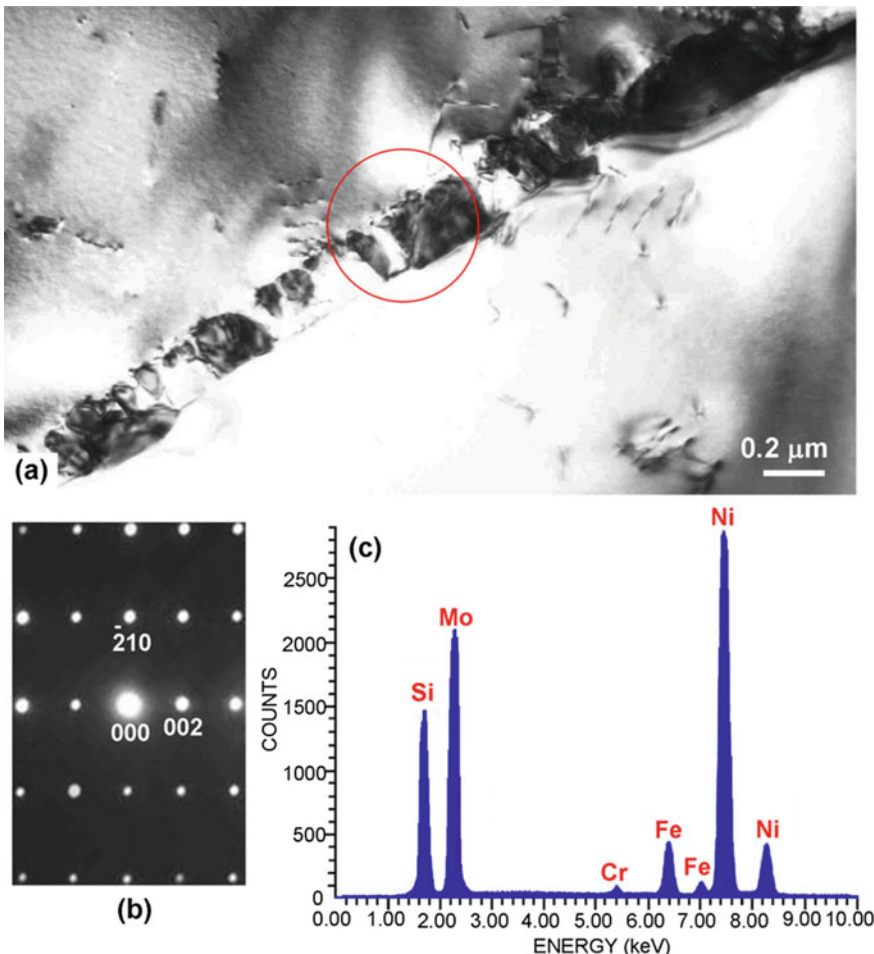


Fig. 3.32 Precipitation of silicon-stabilized Laves phase in Alloy 625 after ageing of 24 h at 760 °C. **a** Bright-field TEM image showing an array of Laves phase particles at grain boundaries. **b** [120] zone axis microdiffraction pattern from the encircled Laves phase particle in **a** consistent with its hexagonal structure. **c** Corresponding EDS spectrum shows the predominant presence of silicon, molybdenum and nickel and minor iron and chromium elements. Reprinted by permission from Springer Ref. [82]. Copyright (2017)

Several studies on ammonia cracker tubes of Alloy 625, service exposed for prolonged periods at temperatures up to about 850 °C, are reported [15, 42, 75, 79, 86]. However, none of these studies reported the formation of any TCP phase. The ammonia cracker tubes operate at temperatures ranging from about 600 °C to 700 °C. Higher temperatures reported in certain portions of tubes were due to local temperature excursions during operation. The no observation of the TCP phases may likely be because of shorter periods of the temperature excursion to the temperature

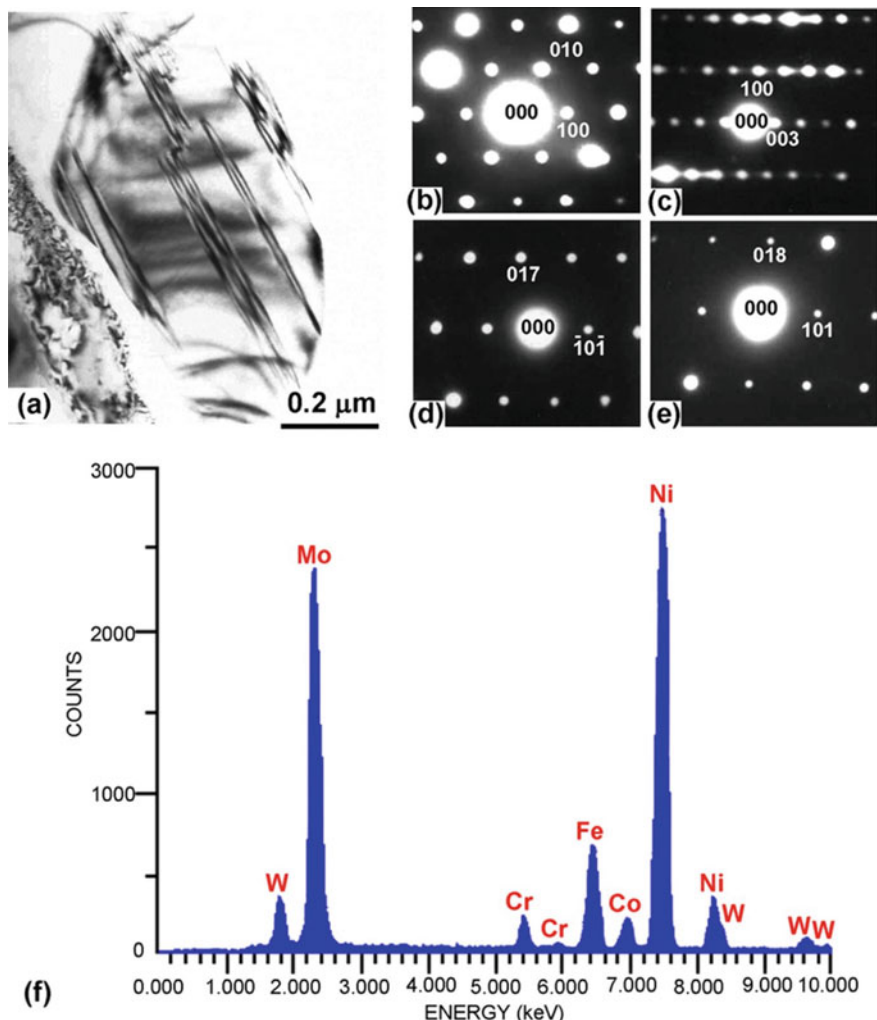


Fig. 3.33 Precipitation of μ phase in Alloy C-276 after ageing of 1 h at 870 °C. **a** Bright-field TEM image showing a blocky particle of μ phase with characteristic internally faulted structure. **b–e** Microdiffraction patterns corresponding to different zone axes **b** [001], **c** [010], **d** [171] and **e** [181] of the μ phase. **f** EDS spectrum showing the elemental composition of the μ phase in the alloy. Reprinted by permission from Springer Ref. [82]. Copyright (2017)

at which the TCP phases form or the low concentrations of elements like Fe and Si that promote their formation.

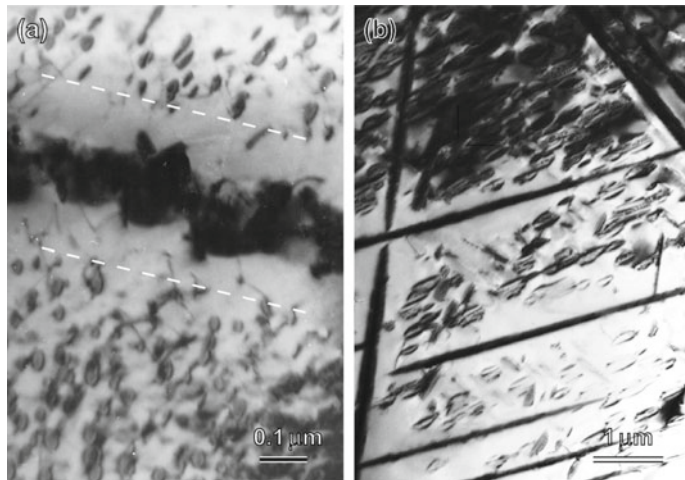


Fig. 3.34 Precipitation free zone around **a** $M_{23}C_6$ carbides precipitated at grain boundaries after ageing at $700\text{ }^{\circ}\text{C}$ for 200 h, and **b** δ precipitates after prolonged ageing at around $750\text{ }^{\circ}\text{C}$. Reprinted **a** from Ref. [63] by permission from Dr. M. Sundararaman. Image **b** Courtesy Dr. M. Sundararaman

3.5.6 Precipitation-Free Zones

Two distinct γ'' precipitate free zones have been observed in Alloy 625. One around the extensively precipitated grain boundary $M_{23}C_6/M_6C$ carbides and the other around large δ precipitates (Fig. 3.34). The formation of the γ'' free zones may be attributed to their dissolution close to carbide and δ precipitates. Conversely, the depletion of solutes impedes further nucleation of γ'' precipitates. Kirman and Warrington [87] have suggested forming precipitate free zones around NbC precipitates in niobium bearing nickel-base alloys due to either vacancy or solute depletion. Vacancy depletion plays a vital role in creating the precipitate free zone around NbC particles in Alloy 718 [52]. A significant difference in the volume misfit between the NbC and the austenite phase generates internal stresses, which are reduced by the migration of vacancies to the growing carbide precipitates. The size/width of such precipitate free zones increases with increasing aging time and the precipitate size [50]. Processing history may affect the extent of precipitation-free zones [13].

The precipitation-free zones in Alloy 625 form due to the depletion of niobium, chromium or molybdenum solutes. Raghavan et al. [54] have shown that the growth of the $M_{23}C_6$ precipitates depletes chromium and molybdenum from the adjacent austenite matrix, while that of the M_6C particles depletes molybdenum. Sundararaman et al. [50] have argued that the γ'' free zones in the vicinity of grain boundary carbides are mainly due to solute depletion. The vacancy depletion plays a minor role because the misfit between the austenite and the $M_{23}C_6$ or M_6C carbide in Alloy 625 is not very large (Sect. 2.2). Therefore, precipitation of the two carbides would not create much internal stress. On the other hand, the precipitation of either of

the carbide phases would deplete the adjacent region of chromium or molybdenum. The depletion of chromium or molybdenum would enhance the solubility of γ'' precipitates in the vicinity of carbides, resulting in precipitate free zones. Similarly, the precipitation of δ precipitates forms precipitates free zones around them.

The precipitate free zones are more ductile than the matrix. Small size precipitation-free zones may be beneficial in improving the creep life of precipitation-hardened alloys containing a high-volume fraction of precipitates. A thin precipitate free zone helps relieve the stress concentrations due to the accumulation of dislocations during creep. However, when the precipitate free zone is too broad, it may cause easy failure due to the weakening of the matrix there.

3.6 Summary

Alloy 625 is designed to be a solid solution strengthened alloy. However, processing and heat treatment of Alloy 625 at temperatures above 550 °C precipitate out ordered intermetallic phases γ'' , δ and Ni₂(Cr, Mo) and various carbides in the disordered nickel matrix. These phases form due to the interaction of multiple solutes present in high concentrations. Each phase has unique characteristics and morphology and evolves depending on the exposure time and temperature. Deformation accelerates the kinetics of precipitation. The precipitation of these phases would modify the alloy's mechanical, corrosion, and welding behavior. The broad composition range of the alloy allows a variation in its composition range. Such a variation may affect some properties strongly. Tighter control of a few elements may improve some alloy properties significantly. However, this improvement in properties by a composition adjustment may be a trade-off with other properties.

References

1. Ross EW, Sims CT (1987) Chapter 4. In: Sims CT (ed) Superalloys II. Wiley, New York, pp 97–133
2. Eiseltstein HL, Gadet J (1964) Matrix stiffened alloy. US Patent no. 3160500
3. Eiseltstein HL, Tillack DJ (1991) The invention and definition of alloy 625. Superalloys 718(625):1–14 (Var, Deriv)
4. Nash P (1991) Ni-Cr system. In: Nash P (ed) Phase diagrams Bin. Nickel alloy. ASM International, Materials Park, pp 75–84
5. Singleton P, Nash MF (1991) Ni-Mo system. In: Nash P (ed) Phase diagrams Bin. Nickel Alloy., ASM International, Materials Park, pp 207–212
6. MacKay RA, Nathal MV, Pearson DD (1990) Influence of molybdenum on the creep properties of nickel-base superalloy single crystals. Metall Trans A 21:381–388
7. Collier JP, Keefe PW, Tien JK (1986) The effects of replacing the refractory elements tungsten, niobium, and tantalum with molybdenum in nickel-base superalloys on microstructural, microchemistry, and mechanical properties. Met Trans A 17:651–661

8. Kumar P (1994) Role of niobium and tantalum in superalloys. In: Koul AK (ed) Advanced high temperature structure material protection coatings. National Research Council of Canada, Ottawa, pp 73–94
9. Smith GD, Patel SJ (2005) The role of niobium in wrought precipitation-hardened nickel-base alloys. In: Loria EA (ed) Superalloys 718, 625, 706 derivatives. The Minerals, Metals, and Materials Society, pp 135–154
10. Loomis WT, Freeman JW, Sponseller DL (1972) The influence of molybdenum on the γ' phase in experimental nickel-base superalloys. Metall Mater Trans B 3:989–1000
11. Shibata T, Shudo Y, Yoshino Y (1996) Effects of aluminum, titanium and niobium on the time-temperature-precipitation behavior of alloy 706. Superalloys 1996:153–162
12. Holt RT, Wallace W (1976) Impurities and trace elements in nickel-base superalloys. Int Met Rev 21:1–24
13. Floreen S, Fuchs GE, Yang WJ (1994) The metallurgy of alloy 625. Superalloys 718(625, 706) and Various Derivatives: 13–37
14. Wahl JB, Harris K, Moore TL (2002) Grain boundary strengthened single crystal superalloys. Adv Mater Process Gas Turbines:129–135
15. Singh JB, Verma A, Paul B, Chakravartty JK (2013) Failure of alloy 625 tube stub ends—effect of primary nitrides. Eng Fail Anal 32:236–247. <https://doi.org/10.1016/j.engfailanal.2013.03.018>
16. Gordon JE (1968) The new science of strong materials, or why you don't fall through the floor. Pelican
17. Stoughton B (1908) The metallurgy of iron and steel by Bradley Stoughton, Hill. <https://books.google.co.in/books?id=baftAQAAQAAJ>
18. Merica PD, Waltenberg R (1925) The malleability of nickel. Trans AIME 71:709–719
19. Liu X, Dong J, Tang B, Hu Y, Xie X (1999) Investigation of the abnormal effects of phosphorus on mechanical properties of INCONEL718 superalloy. Mater Sci Eng A 270:190–196. [https://doi.org/10.1016/S0921-5093\(99\)00153-7](https://doi.org/10.1016/S0921-5093(99)00153-7)
20. Hu ZQ, Song H, Guo SR, Sun W (2001) Role of P, S and B on creep behavior of alloy 718. J Mater Sci Technol 17:399–402
21. Cao WD, Kennedy RL, Thomas WM (1996) Stress-rupture strength of alloy 718. Adv Mater Process 149:33–36
22. Cao WD, Kennedy RL (2001) Improving stress rupture life of alloy 718 by optimizing Al, Ti, P and B contents. In: International symposium superalloys various derivates, 477–488
23. Miller MK, Horton JA, Cao WD, Kennedy RL (1996) Characterization of the effects of boron and phosphorus additions to the nickel-based superalloy 718. J Phys IV 6:241–246
24. Deléhouzée L, Deruyttere A (1967) The stacking fault density in solid solutions based on copper, silver, nickel, aluminium and lead. Acta Metall 15:727–734. [https://doi.org/10.1016/0001-6160\(67\)90353-7](https://doi.org/10.1016/0001-6160(67)90353-7)
25. Beeston BEP, France LK (1968) J Inst Met 96:105
26. Gallagher PCJ (1970) The influence of alloying, temperature, and related effects on the stacking fault energy. Metall Trans 1:2429–2461
27. Yang W, Qu P, Sun J, Yue Q, Su H, Zhang J, Liu L (2020) Effect of alloying elements on stacking fault energies of γ and γ' phases in Ni-based superalloy calculated by first principles, Vacuum 181:109682
28. Quist WE, Taggart R, Polonis DH (1971) The influence of iron and aluminum on the precipitation of metastable Ni_3Nb phases in the Ni-Nb system. Metall Trans 2:825–832
29. Sundararaman M, Mukhopadhyay P, Banerjee S (1992) Some aspects of the precipitation of metastable intermetallic phases in INCONEL 718. Metall Trans A 23:2015–2028. <https://doi.org/10.1007/BF02647549>
30. Cozar R, Pineau A (1973) Morphology of γ' and γ'' precipitates and thermal stability of inconel 718 type alloys. Metall Trans 4:47–59. <https://doi.org/10.1007/BF02649604>
31. Yu L-J, Marquis EA (2019) Precipitation behavior of Alloy 625 and Alloy 625 plus. J Alloys Compd 811:151916. <https://doi.org/10.1016/j.jallcom.2019.151916>

32. Thomas G, Goringe MJ (1979) Transmission electron microscopy of materials, vol 80. Wiley, NY
33. Chaturvedi MC, Han Y (1983) Met Sci 17:145
34. Merrick HF (1978) Precipitation processes in solids. In: Russel KC, Aaronson HI (eds) TMS-AIME. Warrendale
35. Sundararaman M, Mukhopadhyay P, Banerjee S (1988) Precipitation of the δ -Ni₃Nb phase in two nickel base superalloys. Metall Trans A 19:453–465. <https://doi.org/10.1007/BF02649259>
36. Muzyka DR, Maniar GN (1969) Effects of solution treating temperature and microstructure on the properties of hot-rolled 718 alloy. Met Eng Quart 9:23–37
37. Kirman I (1969) J Iron Steel Inst 207:1612–1618
38. Moll JH, Maniar GN, Muzyka DR (1971) Met Trans 2:2153–2160
39. Verma A, Singh JB, Wanderka N, Chakravarty JK (2015) Delineating the roles of Cr and Mo during ordering transformations in stoichiometric Ni₂(Cr_{1-x}, M_{ox}) alloys. Acta Mater 96:366–377
40. Hu R, Cheng GM, Zhang JQ, Li JS, Zhang TB, Fu HZ (2013) First principles investigation on the stability and elastic properties of Ni₂Cr_{1-x}M_x (M=Nb, Mo, Ta, and W) superlattices. Intermetallics 33:60–66. <https://doi.org/10.1016/j.intermet.2012.09.017>
41. Karmazin L, Krejčí J, Zeman J (1994) γ phase and Ni₂Cr-type long-range order in Ni-rich NiCrMo alloys. Mater Sci Eng A 183:103–109. [https://doi.org/10.1016/0921-5093\(94\)9094-X](https://doi.org/10.1016/0921-5093(94)9094-X)
42. Singh JB, Verma A, Jaiswal DM, Kumar N, Patel RD, Chakravarty JK (2015) Rejuvenation of service exposed ammonia cracker tubes of cast Alloy 625 and their re-use. Mater Sci Eng A 644:254–267. <https://doi.org/10.1016/j.msea.2015.06.098>
43. Kumar M, Vasudevan VK (1996) Ordering reactions in an Ni-25Mo-8Cr alloy. Acta Mater 44:1591–1600
44. Verma A, Singh JB, Kaushik SD, Siruguri V (2020) Lattice parameter variation and its effect on precipitation behaviour of ordered Ni₂(Cr,Mo) phase in Ni-Cr-Mo alloys. J Alloys Compd 813:152195. <https://doi.org/10.1016/j.jallcom.2019.152195>
45. Verma A, Singh JB, Resistivity and hardness studies on the precipitation behavior of Alloy 625 in the temperature range from 540 to 700 °C, Un-published work
46. Janotti A, Krcmar M, Fu CL, Reed RC (2004) Solute diffusion in metals: larger atoms can move faster. Phys Rev Lett 92:85901. <https://doi.org/10.1103/PhysRevLett.92.085901>
47. Fahrmann M, Srivastava SK, Pike LM (2012) In: International symposium superalloys, pp 769–777
48. HAYNES® 244® alloy Data sheet, 2020., 2020 Haynes Int. <http://haynesintl.com/docs/default-source/pdfs/new-alloy-brochures/high-temperature-alloys/brochures/244-brochure.pdf>
49. Karri M, Verma A, Singh JB, Un published work
50. Sundararaman S, Mukhopadhyay M, Banerjee P (2001) Influence of intermetallic phase precipitation during prolonged service in alloy 625 on its properties. In: Loria EA (ed) Superalloys 718, 625,706 various Derivates, the minerals. Metals and Materials Society, pp 367–378
51. Turchi PEA, Kaufman L, Liu Z-K (2006) Modeling of Ni-Cr-Mo based alloys: part I—phase stability. Calphad 30:70–87. <https://doi.org/10.1016/j.calphad.2005.10.003>
52. Sundararaman M, Mukhopadhyay P, Banerjee S (1997) Carbide precipitation in nickel base superalloys 718 and 625 and their effect on mechanical properties. In: Loria EA (ed) Superalloys 718,625,706 various derivate. The Minerals, Metals and Materials Society, pp 367–378
53. Lewis MK, Hattersley B (1965) Precipitation of M₂₃C₆ in austenitic steels. Acta Metall 13:1159–1168. [https://doi.org/10.1016/0001-6160\(65\)90053-2](https://doi.org/10.1016/0001-6160(65)90053-2)
54. Raghavan M, Mueller RR, Klein CF, Vaughn GA (1983) Carbides in Ni-Cr-Mo system. Scr Metall 17:1189–1194. [https://doi.org/10.1016/0036-9748\(83\)90281-8](https://doi.org/10.1016/0036-9748(83)90281-8)
55. Cieslak MJ (1991) Excellence sought and found. Weld J 70:49s
56. Cieslak MJ, Headley TJ, Romig AD, Kollie T (1988) A melting and solidification study of alloy 625. Metall Trans A 19:2319–2331. <https://doi.org/10.1007/BF02645056>
57. Bardos DI, Gupta KP, Beck PA (1961) Ternary Laves phases with transition elements and silicon, vol: 221:10. <https://www.osti.gov/biblio/4833536>

58. Cozar R, Rouby M, Mayonobe B, Morizot C (1991) Mechanical properties, corrosion resistance and microstructure of both regular and titanium hardened 625 alloys. *Superalloys*: 423–436
59. Mittra J, Dubey JS, Kulkarni UD, Dey GK (2009) Role of dislocation density in raising the stage II work-hardening rate of Alloy 625. *Mater Sci Eng A* 512:87–91. <https://doi.org/10.1016/j.msea.2009.02.053>
60. Clavel M, Fournier D, Pineau A (1975) Plastic zone sizes in fatigued specimens of INCO 718. *Metall Mater Trans A* 6:2305–2307. <https://doi.org/10.1007/BF02818660>
61. Radavich A, Fort JF (1994) The metallurgy of alloy 625. In: *Superalloys 718, 625, 706 various derivates*. The Minerals, Metals & Materials Society, Pittsburgh, pp 632–645
62. Suave LM, Cormier J, Villechaise P, Soula A, Hervier Z, Bertheau D, Laigo J (2014) Microstructural evolutions during thermal aging of alloy 625: impact of temperature and forming process. *Metall Mater Trans A* 45:2963–2982. <https://doi.org/10.1007/s11661-014-2256-7>
63. Sundararaman M (1986) Microstructural studies on the high temperature materials inconel 718 and inconel 625 alloys. Ph.D. Dissertation, University of Bombay
64. Karri M, Singh JB, Manikrishna KV, Kumawat BK, Kumar N, Srivastava D (2017) On the suitability of peak profile analysis models for estimating dislocation density. *Mater Sci Eng A* 700:75–81. <https://doi.org/10.1016/j.msea.2017.05.103>
65. François A, Hug G, Veyssiére P (1992) The fine structure of dislocations in Ni₃V. *Philos Mag A* 66:269–288
66. Sundararaman M, Kishore R, Mukhopadhyay P (1994) Some aspects of the heterogeneous precipitation of the metastable γ'' phase in alloy 625. In: Loria EA (ed) *Superalloys 718, 625, 706 various derivates*. The Minerals, Metals, and Materials Society, Pittsburgh, pp 405–417
67. Ashby MF, Brown LM (1963) On diffraction contrast from inclusions. *Philos Mag A J Theor Exp Appl Phys* 8:1649–1676. <https://doi.org/10.1080/14786436308207329>
68. Chan KS, Pan Y-M, Lee Y-D (2006) Computation of Ni-Cr phase diagram via a combined first-principles quantum mechanical and CALPHAD approach. *Metall Mater Trans A* 37:2039–2050. <https://doi.org/10.1007/BF02586124>
69. Arya A, Dey GK, Vasudevan VK, Banerjee S (2002) Effect of chromium addition on the ordering behaviour of Ni–Mo alloy: experimental results vs. electronic structure calculations. *Acta Mater* 50:3301–3315. [https://doi.org/10.1016/S1359-6454\(02\)00093-9](https://doi.org/10.1016/S1359-6454(02)00093-9)
70. Chen Y, Hu R, Kou H, Zhang T, Li J (2014) Precipitation of nanosized DO₂₂ superlattice with high thermal stability in an Ni–Cr–W superalloy. *Scr Mater* 76:49–52. <https://doi.org/10.1016/j.scriptamat.2013.12.013>
71. Verma A (2015) Order evolution in Ni–Cr–Mo alloys. Ph.D. Dissertation, HBNI, Mumbai
72. Song J, Field R, Clarke A, Fu Y, Kaufman M (2019) Variant selection of intragranular Ni₂(Mo,Cr) precipitates (γ') in the Ni–Mo–Cr–W alloy. *Acta Mater* 165:362–372. <https://doi.org/10.1016/j.actamat.2018.11.063>
73. Tawancy HM, Abelfotoh MO (2008) High strength and high ductility in a nanoscale superlattice of Ni₂(Cr,Mo) deformable by twinning. *Scr Mater* 59:846–849. <https://doi.org/10.1016/j.scriptamat.2008.06.026>
74. Yuan L, Hu R, Zhang T, Han Y, Xue X, Li J (2014) Precipitation behavior of Pt₂Mo-type superlattices in hastelloy C-2000 superalloy with low Mo/Cr Ratio. *J Mater Eng Perform* 23:3314–3320. <https://doi.org/10.1007/s11665-014-1126-1>
75. Chakravarthy JK, Singh JB, Sundararaman M (2012) Microstructural and mechanical properties of service exposed Alloy 625 ammonia cracker tube removed after 100 000 h. *Mater Sci Technol* 28:702–710. <https://doi.org/10.1179/1743284711Y.0000000118>
76. Tanner LE (1972) The ordering transformation in Ni₂V. *Acta Metall* 20:1197–1227. [https://doi.org/10.1016/0001-6160\(72\)90168-X](https://doi.org/10.1016/0001-6160(72)90168-X)
77. Shoemaker LE (2005) In: Loria EA (ed) *Superalloys 718, 625, 706 derivates*. The Minerals, Metals, and Materials Society, Pittsburgh, pp 409–418
78. Vernot-Loier C, Cortial F (1991) In: Loria EA (ed) *Superalloys 718, 625 various derivates*. The Minerals, Metals, and Materials Society, Pittsburgh, pp 409–422
79. Shankar V, Valsan M, Bhanu Sankara Rao K, Mannan SL (2001) Room temperature tensile behavior of service exposed and thermally aged service exposed alloy 625. *Scr Mater* 44:2703–2711. [https://doi.org/10.1016/S1359-6462\(01\)00965-4](https://doi.org/10.1016/S1359-6462(01)00965-4)

80. Unwin PNT, Lorimer GW, Nicholson RB (1969) The origin of the grain boundary precipitate free zone. *Acta Metall* 17:1363–1377. [https://doi.org/10.1016/0001-6160\(69\)90154-0](https://doi.org/10.1016/0001-6160(69)90154-0)
81. Cortial F, Corrieu JM, Vernot-Loier C (1995) Influence of heat treatments on microstructure, mechanical properties, and corrosion resistance of weld alloy 625. *Metall Mater Trans A* 26:1273–1286. <https://doi.org/10.1007/BF02670621>
82. Tawancy HM (2017) On the precipitation of intermetallic compounds in selected solid-solution-strengthened Ni-base alloys and their effects on mechanical properties. *Metallogr Microstruct Anal* 6:200–215. <https://doi.org/10.1007/s13632-017-0352-y>
83. Evans ND, Maziasz PJ, Shingledecker JP, Yamamoto Y (2008) Microstructure evolution of alloy 625 foil and sheet during creep at 750 C. *Mater Sci Eng A* 498:412–420
84. Tawancy HM (1996) Precipitation characteristics of μ -phase in wrought nickel-base alloys and its effect on their properties. *J Mater Sci* 31:3929–3936. <https://doi.org/10.1007/BF00352653>
85. Massalski CS, Barrett TB (1966) In: *Structure of metals*. McGraw-Hill, New York, p 266
86. Raman VV, Prasad GE, Das Gupta P (1987) Deformation behaviour of Inconel 625 at various temperatures. *Trans Indian Inst Met* 40:113–120
87. Kirman I, Warrington DH (1970) The precipitation of Ni₃Nb phases in a Ni-Fe-Cr-Nb alloy. *Metall Trans* 1:2667–2675

Chapter 4

Mechanical Behavior of Alloy 625



Alloy 625 contains substantial alloying elements that impart excellent strength and creep resistance in solid-solution conditions. As noted in Chap. 3, these elements may cause the precipitation of different intermetallic and carbide phase particles during thermo-mechanical processing. Precipitation of these phases affects mechanical behavior of the alloy. The ordered intermetallic phases form as small and coherent particles distributed homogenously throughout the matrix. Twinning plays an essential role in the continuity of deformation across intermetallic phase particles during the alloy's deformation. This chapter discusses various factors that govern the mechanical behavior of Alloy 625.

4.1 Fundamentals of Plastic Deformation of Crystalline Solids

Plastic deformation occurs by the movement of dislocations when the shear stress exceeds a critical value, known as “critical resolved shear stress”. It occurs primarily by two modes, namely, slip and twinning.

4.1.1 Deformation by Slip

Slip is the most commonly observed deformation mode. Slip deforms metals by sliding a part of the crystal, over the remaining, along definite crystallographic planes called “slip planes”. Slip is generally confined to the low-index planes as they contain a high density of atoms per unit area, thereby providing the least lattice friction (Peierls stress) to the motion of dislocations. The translational symmetry of the crystal lattice perfectly restores the crystal structure after the slip. A slip plane containing a slip direction defines a “slip system”. For example, in the face-centered cubic

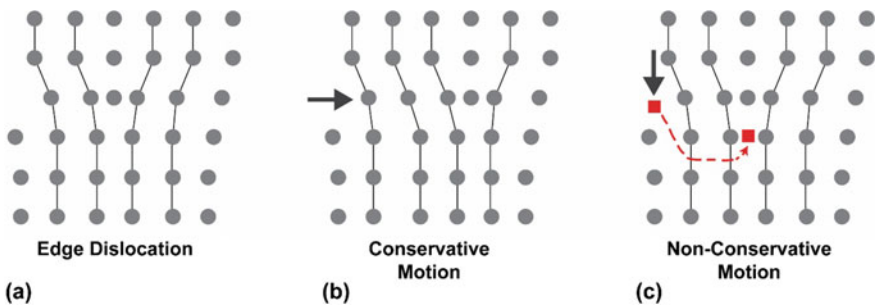


Fig. 4.1 **a** Schematic arrangement of atoms depicting an edge dislocation; **b** Conservative motion of an edge dislocation within the glide plane in the direction of slip (arrow mark); **c** Non-conservative motion of dislocation by a climb in a direction perpendicular to the slip plane. Square symbol represents the row of atoms that moved from one location to another as a result of climb.

structure, four independent {111} octahedral planes, each having three independent $<110>$ close-packed directions, together give 12 independent slip systems.

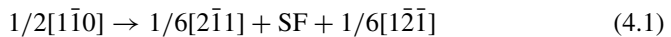
Slip occurs most readily in specific directions on certain close-packed crystallographic planes, and the displacement that defines the magnitude and direction of the movement of atoms is called Burgers vector (\mathbf{b}) of the dislocation. Dislocations are linear crystallographic defects or singularities in a crystalline lattice where extra atoms are arranged linearly within the body of the crystal. Dislocations are basically of two types, edge and screw dislocations, though a combination of the two, called “mixed dislocations”, is most commonly observed. In an “edge dislocation”, the extra atoms are arranged in a row of mismatched atoms along a straight line as an extra half-plane (Fig. 4.1a) within the crystal, while extra atoms in a “screw dislocation” trace a spiral path around the dislocation line with a pitch of one interplanar distance within the crystal.

Dislocation motion is generally of two types, conservative and non-conservative, depending on whether the number of atoms in the neighborhood of a dislocation core changes due to the motion [1, 2]. When a dislocation moves in the glide plane in the direction of slip, its movement is termed “conservative”. When a dislocation moves by climbing in a direction normal to the slip plane, it is termed “non-conservative”. Figure 4.1b, c, respectively show the conservative and non-conservative movements of the edge dislocation shown in Fig. 4.1a. The climb usually occurs when deformation is assisted by thermal activation of atoms at elevated temperatures or when the crystal possesses a density of interstitials and vacancies, which are attracted toward dislocation cores by their interacting stress fields [1, 2].

When the slip associated with dislocations displaces atoms into their coincidence positions, dislocations are termed “perfect dislocations”. Perfect dislocations move atoms by integral multiple of atomic distances in a specific direction along the slip plane (Fig. 4.1). Dislocations with Burgers vector $1/2<110>$ in a face-centered cubic crystal move atoms by one atom distance are called “unit dislocations”. Dislocations with Burgers vectors having magnitudes larger than unity are also possible. But,

they are unstable and tend to dissociate into two or more dislocations of smaller Burgers vector as per the dislocation dissociation reaction $\mathbf{b}_1 \rightarrow \mathbf{b}_2 + \mathbf{b}_3$ provided the reaction satisfies the condition, $b_1^2 > b_2^2 + b_3^2$, where \mathbf{b}_1 is the Burgers vector of the un-dissociated dislocations, and \mathbf{b}_2 and \mathbf{b}_3 are Burgers vectors of dissociated dislocations. The driving force for such dissociation reactions comes from a reduction in strain energy of the dislocation, which is proportional to the square of its Burgers vector.

If the magnitude of the Burgers vector is not equal to a crystal's translation vector, the dislocation is called a "partial dislocation". The movement of partial dislocations causes a local error (fault) in the stacking sequence on the dislocation slip plane. Such stacking faults (SFs) are common in face-centered cubic (FCC) materials like nickel and copper alloys due to their low stacking fault energies. In these alloys, a perfect dislocation, say $1/2[1\bar{1}0]$, may dissociate into two partial dislocations of $1/6<112>$ type as per the dissociation reaction:



In FCC structures, dislocations of $1/6<112>$ type are commonly called "Shockley partials".

4.1.2 *Deformation by Twinning*

Twinning generally occurs when the slip is restricted due to fewer operable slip systems or when the slip's critical resolved shear stress is more than the twinning stress. It is commonly observed at low temperatures or high strain rates (e.g., shock loading) in metals with body-centered cubic (BCC) and hexagonal close-packed (HCP) crystal structures. Twinning is also common in many FCC metals and alloys with low stacking fault energy (SFE). Twinning occurs when atoms in a portion are homogeneously sheared to orientations that are mirror related to atoms in the un-twinned lattice across a plane called the 'twinning plane' (Fig. 4.2a). Twinning occurs in a definite direction, called the 'twinning direction', on a specific crystallographic plane. Twinning is characterized by four essential elements, namely, the twinning plane, K_1 , the twinning direction, η_1 , an undistorted plane (other than the K_1), K_2 , and a second twinning direction, η_2 ; the last two elements essentially arise from the condition of homogeneous shear (Fig. 4.2b).

Twinning differs from slip mainly in the following respects: (1) The orientation of the crystal above and below the slip plane remains the same after the slip, while in twinning, the orientation of the twinned crystal is different across the twin plane; (2) In slip, the deformation usually occurs in discrete multiples of the atomic spacing, while in twinning the atom's movement is much less than a translation vector of the lattice; (3) In slip, the deformation occurs on relatively widely spread planes, while in twinning every atomic plane in the twinned region is involved in the deformation; (4) A large amount of the bulk plastic deformation can be produced by slip, while

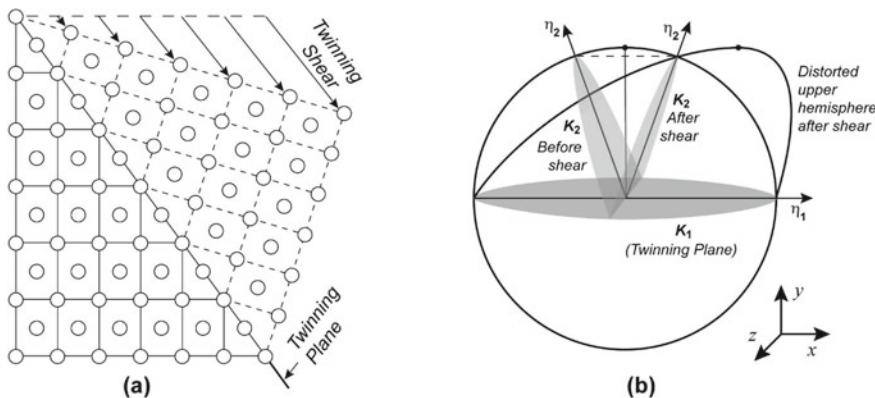


Fig. 4.2 **a** Illustrates twinning of the lattice under the action of twinning shear; **b** Schematic illustrating the geometric relationship between different twinning elements when an upper hemisphere of a solid sphere is brought into a twin relationship with the lower hemisphere across the twinning plane (K_1). A second plane, the K_2 plane, remains undistorted but rotated in the distorted upper hemisphere. The shear plane is parallel to the plane of the paper

the twinning produces comparatively a small amount. However, the twinning may aid slip by reorienting crystals to orientations favorable for the slip relative to the stress axis.

Stacking faults influence the plastic deformation of metal significantly. Stacking faults are errors in the stacking sequence of close-packed planes, which can be produced in many metals by plastic deformation or annealing. The atomic arrangement of atoms on the close-packed {111} plane of an FCC structure and the close-packed {0001} plane of an HCP structure is similar, but the two structures have a different stacking sequence of their close-packed planes. An FCC structure is obtained when the close-packed planes are stacked as ...ABCABCABC... On the other hand, a stacking sequence of ...ABABAB... type produces an HCP structure (Fig. 4.3). Therefore, a fault in the stacking sequence in the FCC structure makes four layers of the HCP structure. Such a fault can be created in an FCC crystal if atoms, say above the B plane, are moved by the glide of a Shockley partial dislocation $(1/6<112>)$ [1]. Such a movement of atoms would bring the C layer directly over the A layer and thus produces a local HCP sequence. A stacking fault can be viewed as an “extended dislocation” comprising a thin HCP region bounded by partial dislocations. Since stacking fault is not the equilibrium structure of the crystal, it raises the crystal’s energy. This energy is called stacking fault energy (SFE). Stacking fault energy can be treated as the surface tension of the stacking fault that pulls the partial dislocations together, which repel each other due to their nearly parallel line directions. The lower the stacking fault energy, the greater the separation between the partial dislocations and the wider the stacking fault.

The stacking fault energy plays a vital role in the deformation of the metal. Stacking faults in FCC metals can also be considered sub-microscopic twins of four

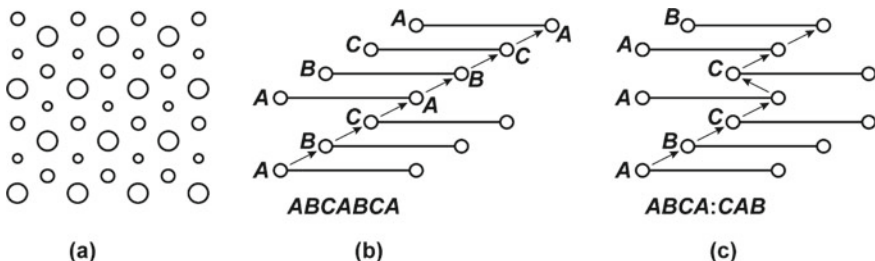


Fig. 4.3 Schematic showing the stacking of close-packed layers of atoms in an FCC lattice. **a** A three-layer stacking of the close-packed $\{111\}$ plane viewed along the plane normal. Layers A, B and C, respectively, are shown by circles of decreasing diameter. **b** Stacking of the $\{111\}$ plane viewed perpendicular to the plane. **c** Formation of an HCP region after introducing a stacking fault in the FCC stacking sequence

atom thicknesses. Deformation twinning is therefore favored in metals with low SFE, dislocation-slip in metals with high SFE. Metals with high SFE, such as aluminum, have a deformation substructure of dislocation tangles and cells. In contrast, metals with low SFE are characterized by stacking faults or banded substructures comprising planar arrays of dislocations that make cross slip and climb of dislocations difficult.

4.1.3 Deformation in Superlattice Compounds

The directional nature of bonding in ordered intermetallic phases necessitates the displacements of large magnitudes to bring the ordered lattice back into coincidence with itself. Burgers vectors of large magnitudes are illustrated by considering the arrangement of N and M atoms in a close-packed $\{111\}$ plane of an N_3M compound with an $L1_2$ structure (Sect. 2.1). On each $\{111\}$ plane of the $L1_2$ structure,¹ two $1/2<110>$ displacements in each close-packed direction are required. Figure 4.4a shows the arrangement of atoms on the (111) plane of an N_3M compound with the $L1_2$ structure. It can be noticed that the movement of a minority atom M by $<110>$ displacement in all the three close-packed directions brings it into coincidence with itself. Dislocations with such large Burgers vector are called superlattice dislocations (or simply “superdislocations”), and the $1/2<110>$ dislocations are called “superpartial dislocations” of the superlattice. The total Burgers vector of a superdislocation must necessarily be equal to an integral multiple of the superpartial translation vector. The movement of superpartials of $1/2<112>$ type in the ordered structure breaks its order in the slip plane as illustrated in Fig. 4.4b. This destruction of the chemical order is associated with extra boundary energy, called anti-phase boundary (APB) energy. Therefore, the superpartial dislocations move in pairs separated by a

¹ Indices for all the phases, throughout the chapter, are expressed in the FCC basis unless and otherwise specifically mentioned or subscripted with a lattice notation.

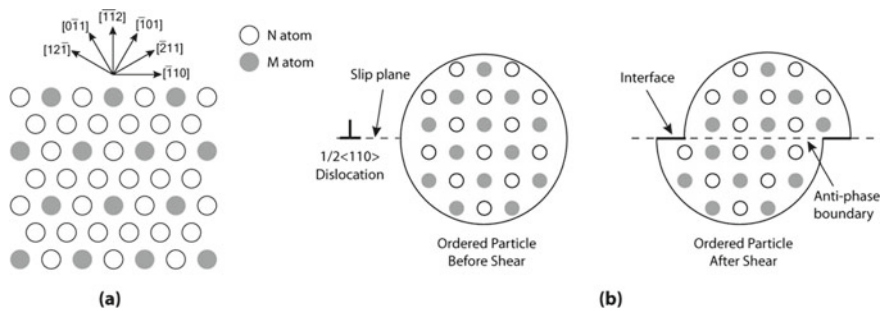


Fig. 4.4 **a** Arrangement of atoms on (111) plane of the ordered $L1_2$ structure (N_3M stoichiometry). **b** Schematic showing the creation of anti-phase boundary when a dislocation passes through an ordered phase precipitate

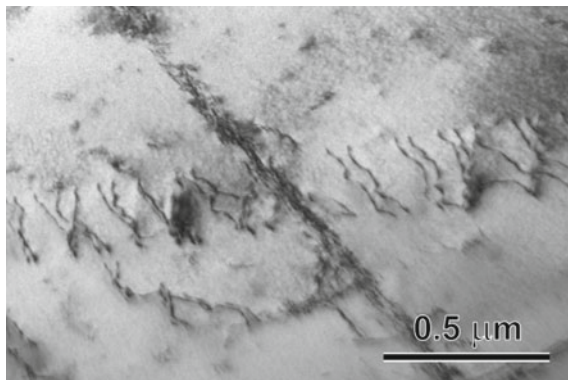
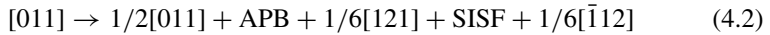


Fig. 4.5 A TEM micrograph showing pairs of $1/2<110>$ dislocations in a deformed Alloy 693 containing fine precipitates of γ' phase

ribbon of APB. Figure 4.5 shows a transmission electron microscopy (TEM) image of dislocation pairs of $1/2<110>$ dislocations observed in lightly deformed Alloy 693 containing fine precipitates of the hardening γ' phase. Further, the $1/2<110>$ superpartial dislocations may decompose into Shockley partial dislocations depending upon the stacking fault energy of the alloy. The creation of stacking faults in ordered structures may or may not disturb the long-range order of the lattice. When they do not disturb the chemical order of the lattice, they are termed superlattice intrinsic stacking faults (SISFs) or simply geometric stacking faults (GSFs). When stacking faults destroy the chemical order locally, they are termed complex stacking faults (CSFs) and are associated with very high energy. For this reason, CSFs are usually not observed. On the other hand, SISFs are commonly observed in intermetallic compounds with low stacking fault energies. In such alloys, the dissociation of a superdislocation into Shockley partial dislocations may be represented by a reaction like:



where SISF represents the stacking fault bounded by Shockley partials. Such a configuration of superdislocations involving an APB and a stacking fault is quite common in ordered L1₂ structures [3]. At high temperatures, such decomposition reactions allow the APB to be located on the low energy {001} plane while the SISF remains on the {111} plane. This results in a sessile dislocation configuration known as Kear and Wilsdorf lock [4].

4.2 Deformation Crystallography of Hardening Phases in Alloy 625

As presented in Chap. 3, various intermetallic and carbide phases may form in Alloy 625 depending upon the temperature and time of exposure. The primary hardening in age-hardened conditions of the alloy comes from γ'' and Ni₂(Cr,Mo) phase particles, and comparatively much lesser from the δ phase particles. Carbide phases behave as non-deformable particles but contribute little to hardening in this alloy. This section is therefore restricted to understanding dislocations and defect structures in γ'' , Ni₂(Cr,Mo) and δ phases. Further, due to the non-cubic nature of these phases, their deformation behavior depends on the orientation of their variants with respect to the stress axis.

4.2.1 γ'' Phase

The deformation characteristics of the γ'' phase are illustrated considering a particle whose *c*-axis is oriented along the [001] direction of the matrix. Figure 4.6 shows the arrangement of atoms on (111) closed-packed plane of the D0₂₂ structure when its *c*-axis is oriented along the [001] direction of the matrix. Neglecting distortions due to tetragonality, FCC (111) plane would become (112) _{γ''} of the D0₂₂ structure. All the four {111} planes of the disordered lattice would become {112} _{γ''} planes of the D0₂₂ structure and have similar arrangements of N and M atoms. The minority element atoms (M atoms) would be arranged in a rectangular array in the closed-packed plane, and each layer maintains the N₃M stoichiometry. Such an arrangement of minority atoms destroys the three-fold rotational symmetry of the FCC {111} planes in the D0₂₂ structure. That is why the close-packed <110> directions of the FCC structure (e.g., [110], [101] and [011] in Fig. 4.6) are not equivalent in the D0₂₂ structure.

The stacking of six close-packed layers, one above the other as ...A₁B₁C₁A₂B₂C₂A₁B₁C₁... in a manner that every successive layer is displaced by a vector 1/3[121] (or 1/3[211]) with respect to the previous layer would make up the D0₂₂ structure. For example, layer B₁ is displaced with respect to layer A₁

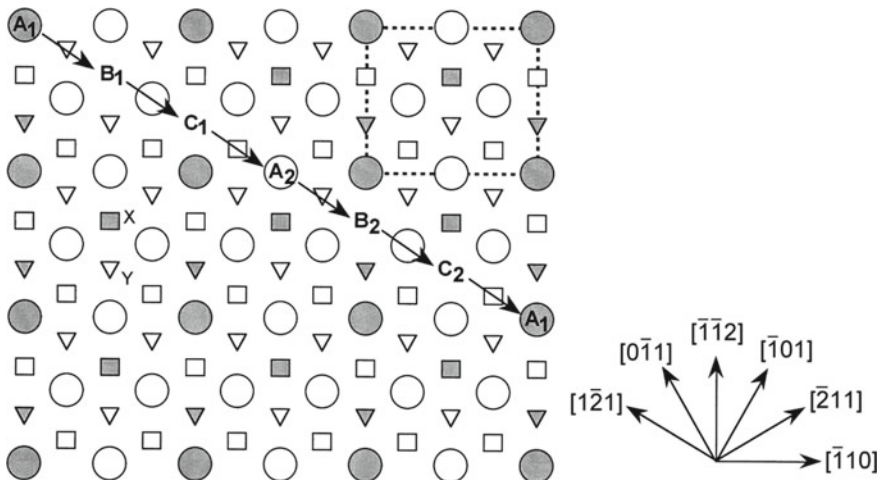


Fig. 4.6 The atomic arrangement on (111) planes and their stacking sequence in the D0₂₂ lattice. The arrows shown represent the displacement vector. Circles, squares and triangles represent the atom positions on the 1st, 2nd and 3rd layers. Atom positions on the 4th, 5th and 6th layers coincide with those of the 1st, 2nd and 3rd layers such that superimposition of minority atoms occur only after every six layers. The open and grey symbols represent N and M atoms of the N₃M D0₂₂ phase. Delineated rectangle shown by broken lines indicates the rectangular ordering nature in D0₂₂ structures

by a vector $1/3[\bar{1}2\bar{1}]$, layer C₁ is displaced by the same vector with respect to the B₁ layer, etc. A₁ and A₂ layers (and similarly B₁ and B₂ layers as well as C₁ and C₂ layers) contain atom positions vertically above (or below) one another along the [111] direction in such a way that the superimposition of the minority atom occurs only after six layers.

Different dislocations that can be encountered in the γ'' phase can be inferred from an inspection of the possible lattice translation vectors on the (111) plane of the [001] variant of the D0₂₂ structure (Fig. 4.6) and are listed in Table 4.1. The table also lists dislocations in other octahedral planes and for all the planes for the other two variants of the γ'' phase (Table 2.5). For the [001] variant, the Burgers vectors of perfect dislocations are $1/2[1\bar{1}\bar{2}]$, $[\bar{1}10]$, $[2\bar{0}\bar{2}]$, $[0\bar{2}\bar{2}]$, $[2\bar{4}\bar{2}]$ and $[\bar{4}2\bar{2}]$, and listed in the ascending order of their magnitudes. The shortest perfect dislocations in the D0₂₂ structure (Fig. 2.2) are [100] and [010], but they do not lie on the close-packed plane.

The superdislocations $[\bar{1}10]$ and $<\bar{1}01>^2$ comprise doublet or quadruplets of $1/2<110>$ of superpartials. Therefore, superdislocations may split into pairs of superpartials bounding an APB. Likewise, the perfect dislocation $1/2[1\bar{1}\bar{2}]$ may split into three $1/6[11\bar{2}]$ Shockley partials to reduce its energy. All the three types of dislocation

² Mixed parenthesis notation used for directions and planes in the text represents that all permutations are possible only on the first two indices while the third index is fixed. For example, in the present case, $<\bar{1}01>$ represents $[\bar{1}01]$ as well as $[0\bar{1}1]$ directions.

arrangements have been observed in the Ni₃V phase, which is iso-structural to the γ'' phase and has the lattice parameters very close to it [5–8]. Since the stacking fault energy of the γ'' phase is low, the $1/2<110>$ superpartial dislocations may further dissociate into Shockley partials depending upon whether the splitting would create a superlattice intrinsic stacking fault. For example, a minority atom, M, at a site, say X in Fig. 4.6, in a plane above (111) plane would be shifted to a site Y corresponding to the next layer, by a displacement equal to $1/6[1\bar{1}\bar{2}]$. This displacement corresponds to the shortest Burgers vector of the partial dislocation (Table 4.1). This

Table 4.1 Burgers vectors of possible perfect and partial dislocations in the D0₂₂ structure on the four octahedral planes. [100], [010] and [001] represent variants of the D0₂₂ structure whose *c*-axis is oriented along these directions. Note that the perfect translation vectors are applicable in their opposite directions also

Glide plane	Dislocation burgers vectors in different variants of the γ'' phase					
	Perfect translations			Shortest burgers vectors of partials bounding a pure stacking fault		
	[100]	[010]	[001]	[100]	[010]	[001]
$(\bar{1} \ 1 \ \bar{1})$	$1/2[21\bar{1}]$	$1/2[\bar{1}\bar{2}\bar{1}]$	$1/2[\bar{1}12]$	$1/6[21\bar{1}]$	$1/6[\bar{1}\bar{2}\bar{1}]$	$1/6[\bar{1}12]$
	$[0\bar{1}\bar{1}]$	$[10\bar{1}]$	$[\bar{1}\bar{1}0]$	$1/3[21\bar{1}]$	$1/3[121]$	$1/3[1\bar{1}\bar{2}]$
	$2[\bar{1}\bar{1}0]$	$2[0\bar{1}\bar{1}]$	$2[10\bar{1}]$	$2/3[\bar{1}12]$	$2/3[\bar{1}\bar{2}1]$	$2/3[\bar{1}12]$
	$2[10\bar{1}]$	$2[\bar{1}\bar{1}0]$	$2[0\bar{1}1]$	$2/3[21\bar{1}]$	$2/3[21\bar{1}]$	$2/3[21\bar{1}]$
	$2[\bar{1}12]$	$2[21\bar{1}]$	$2[\bar{1}\bar{2}\bar{1}]$	$2/3[\bar{1}\bar{2}\bar{1}]$	$2/3[\bar{1}\bar{2}\bar{1}]$	$2/3[\bar{1}\bar{2}\bar{1}]$
	$2[\bar{1}\bar{2}\bar{1}]$	$2[\bar{1}12]$	$2[21\bar{1}]$			
$(1\bar{1}\bar{1})$	$1/2[\bar{2}\bar{1}\bar{1}]$	$1/2[12\bar{1}]$	$1/2[1\bar{1}2]$	$1/6[\bar{2}\bar{1}\bar{1}]$	$1/6[12\bar{1}]$	$1/6[1\bar{1}2]$
	$[0\bar{1}1][0\bar{1}1]$	$[\bar{1}0\bar{1}]$	$[\bar{1}\bar{1}0]$	$1/3[211]$	$1/3[\bar{1}\bar{2}1]$	$1/3[1\bar{1}\bar{2}]$
	$2[\bar{1}\bar{1}0]$	$2[0\bar{1}1]$	$2[\bar{1}0\bar{1}]$	$2/3[1\bar{1}2]$	$2/3[\bar{1}\bar{1}2]$	$2/3[1\bar{1}2]$
	$2[\bar{1}0\bar{1}]$	$2[\bar{1}\bar{1}0]$	$2[0\bar{1}1]$	$2/3[12\bar{1}]$	$2/3[12\bar{1}]$	$2/3[12\bar{1}]$
	$2[\bar{1}\bar{1}2]$	$2[\bar{2}\bar{1}\bar{1}]$	$2[12\bar{1}]$	$2/3[\bar{2}\bar{1}\bar{1}]$	$2/3[\bar{2}\bar{1}\bar{1}]$	$2/3[\bar{2}\bar{1}\bar{1}]$
	$2[12\bar{1}]$	$2[1\bar{1}2]$	$2[\bar{2}\bar{1}\bar{1}]$			
$(\bar{1}\bar{1}1)$	$1/2[\bar{2}\bar{1}1]$	$1/2[\bar{1}21]$	$1/2[\bar{1}\bar{1}\bar{2}]$	$1/6[\bar{2}\bar{1}1]$	$1/6[\bar{1}21]$	$1/6[\bar{1}\bar{1}\bar{2}]$
	$[0\bar{1}1]$	$[\bar{1}0\bar{1}]$	$[\bar{1}10]$	$1/3[\bar{2}\bar{1}1]$	$1/3[\bar{1}\bar{2}1]$	$1/3[112]$
	$2[\bar{1}10]$	$2[0\bar{1}\bar{1}]$	$2[\bar{1}0\bar{1}]$	$2/3[2\bar{1}1]$	$2/3[2\bar{1}1]$	$2/3[2\bar{1}1]$
	$2[\bar{1}0\bar{1}]$	$2[\bar{1}\bar{1}0]$	$2[0\bar{1}1]$	$2/3[\bar{1}21]$	$2/3[\bar{1}21]$	$2/3[\bar{1}21]$
	$2[\bar{1}\bar{1}\bar{2}]$	$2[\bar{2}\bar{1}1]$	$2[\bar{1}21]$	$2/3[\bar{1}\bar{1}\bar{2}]$	$2/3[\bar{1}\bar{1}\bar{2}]$	$2/3[\bar{1}\bar{1}\bar{2}]$
	$2[\bar{1}21]$	$2[\bar{1}\bar{1}\bar{2}]$	$2[2\bar{1}1]$			
(111)	$1/2[\bar{2}11]$	$1/2[\bar{1}\bar{2}1]$	$1/2[11\bar{2}]$	$1/6[\bar{2}11]$	$1/6[\bar{1}\bar{2}1]$	$1/6[11\bar{2}]$
	$[0\bar{1}1]$	$[\bar{1}0\bar{1}]$	$[\bar{1}10]$	$1/3[\bar{2}\bar{1}\bar{1}]$	$1/3[\bar{1}\bar{2}\bar{1}]$	$1/3[11\bar{2}]$
	$2[\bar{1}10]$	$2[0\bar{1}\bar{1}]$	$2[10\bar{1}]$	$2/3[1\bar{2}1]$	$2/3[\bar{1}\bar{2}1]$	$2/3[1\bar{2}1]$
	$2[10\bar{1}]$	$2[\bar{1}10]$	$2[0\bar{1}1]$	$2/3[\bar{2}11]$	$2/3[\bar{2}11]$	$2/3[\bar{2}11]$
	$2[\bar{1}\bar{2}1]$	$2[\bar{2}\bar{1}1]$	$2[\bar{1}21]$	$2/3[\bar{1}\bar{1}\bar{2}]$	$2/3[\bar{1}\bar{1}\bar{2}]$	$2/3[\bar{1}\bar{1}\bar{2}]$
	$2[11\bar{2}]$	$2[11\bar{2}]$	$2[\bar{2}11]$			

shift does not produce any first nearest neighbor bond violation in the ordered lattice but disturbs only the stacking sequence. On the other hand, the passage of partials with Burgers vectors $1/6[1\bar{2}1]$ and $1/6[\bar{2}11]$ on the (111) plane (Fig. 4.6) would result in first nearest neighbor bond violations compared to the perfect lattice, which would create a stacking fault as well as violate the nearest neighbor bond. Such faults are termed complex stacking faults (CSFs) and are associated with very high energy. Nonetheless, if the displacement vectors of the three partials are quadrupled, as $2/3[\bar{2}11]$, $2/3[1\bar{2}1]$ and $2/3[11\bar{2}]$, all the three partials can glide in all the three orientations of the γ'' phase without violating the nearest neighbor bonds (see Table 4.1). Even though such partials are associated with high self-energies, their operation has been reported in the deformed Ni₃V phase [9].

The passage of $1/6[11\bar{2}]$ dislocations on every (111) plane generate a true crystallographic twin, and the new stacking sequence would be ...A₁B₁C₁A₂B₂C₂A₁C₂B₂A₂C₁B₁A₁.... (Fig. 4.7). A true twin retains the long-range order of the parent crystal within the twinned crystal such that minority atoms are also in mirror reflection across the twin plane. On the other hand, other partial dislocations bring lattice sites in twin positions incorrectly occupied by different atom species, breaking the long-range order. Such twins are called pseudo twin [10, 11]. Out of the 12 twinning modes of the disordered structure, only four modes transform the γ'' phase lattice to true twinning modes. The remaining eight modes transform to pseudo twinning modes. As a consequence, two of the {110} planes of shear become $\{110\}_{\gamma''}$ planes for the true twinning modes of the superlattice while the remaining four {110} become $\{102\}_{\gamma''}$ planes for the pseudo twinning modes of the D0₂₂ structure. Table 4.2 gives characteristic twinning elements of the two modes of twins. The following provides a brief description of the formation of the true twins in the D0₂₂ structure with *c*-axis along [001] direction of the FCC structure. For more details, the reader is referred to references [12, 13].

Orienting the superlattice in a manner that orients the twinning plane (111) (i.e., $(112)_{\gamma''}$ plane) in edge-on orientation would bring the shear plane (110) parallel to the plane of the paper. Projection of the N₃M superlattice onto the shear plane (plane of the paper) is shown in Fig. 4.7. A repeating four shearing plane sequence of ...01230... type, each containing N and M atoms in an order

Table 4.2 Twinning elements for different twinning modes in γ'' and Ni₂(Cr,Mo) phases, given in terms of corresponding ordered unit cell indices

Twin type	K_1	K_2	η_1	η_2
<i>γ'' phase</i>				
Combined	(1, 1, 2)	(1, 1, $\bar{2}$)	[1, 1, $\bar{1}$]	[1, 1, 1]
Pseudo	($\bar{1}$, 1, 2)	($\bar{1.077}$, $\bar{1.039}$, 2)	[2.31 $\bar{5}$, 4.31 $\bar{5}$, 1]	[$\bar{2}$, 4, 1]
<i>Ni₂(Cr,Mo) phase</i>				
Combined	(1, 0, 1)	(1, 0, $\bar{1}$)	[1, 0, $\bar{1}$]	[1, 0, 1]
Type I-II	(0, 3, 1)	($\bar{0.966}$, 0.034 , 1)	[8.344, $\bar{1}$, 3]	[1, 1, 1]
Pseudo	(0, $\bar{3}$, 1)	(0, $\bar{3}$, $\bar{1}$)	[0, $\bar{1}$, $\bar{3}$]	[0, $\bar{1}$, 3]

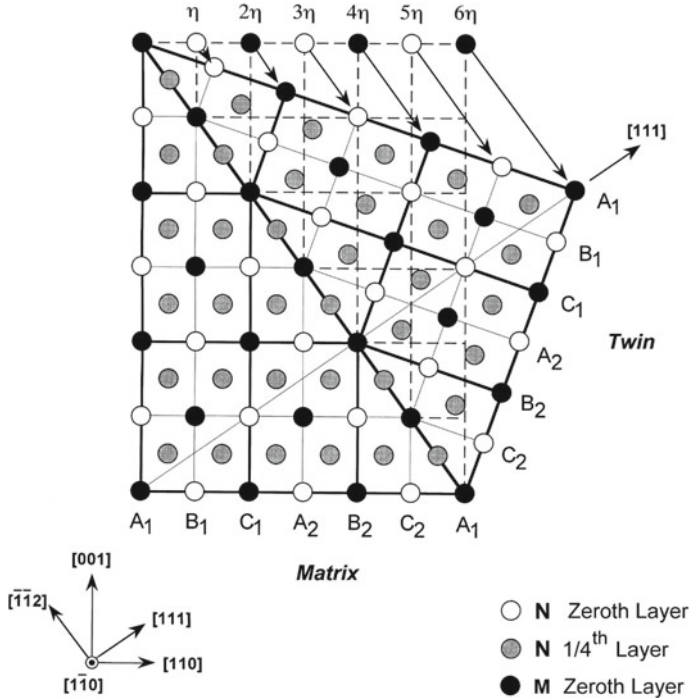


Fig. 4.7 Schematic drawing illustrating the projection of N_3M lattice onto the shear plane $(1\bar{1}0)$. A repeating four-layer shear plane stacking of type ...01230... constitutes the D_{022} structure. A twinning shear, η , of $1/6[11\bar{2}]$ on every (111) (i.e., $(112)_{D_{022}}$) plane generates a true crystallographic twin. Note that only the zeroth and the $1/4$ th layers are shown, as the $1/2$ and $3/4$ th layer positions coincide with those of the previous two layers in such a way that the minority atoms coincide only after four layers

... $(N_{1/2}M_{1/2})N(M_{1/2}N_{1/2})N\dots$, constitutes the N_3M lattice. The 1st and the 3rd layers contain only N atoms, whereas the zeroth and 2nd layers contain N and M atoms in an equal proportion, with the two atoms switching their positions in the two layers. It is to be noted that, in terms of the FCC notation, even-numbered planes correspond to zeroth layer projection of the shear plane in an FCC structure, whereas odd-numbered layers correspond to that of the half layer projection. The tetragonal axis in this projection lies within the plane of paper along $[001]$ direction. In contrast, the a - and b -axis are pointing, respectively outward and inward from the plane of the paper in such a way that the projection of both the axes in the plane of paper lie along $[110]$ direction. It can be seen that a shear of $1/6[11\bar{1}]_\gamma$ (i.e., $1/6[11\bar{2}]$) magnitude on this plane would bring the lattice points occupied by the right kind of atoms at twin positions with respect to the matrix (un-twinned lattice). Since the repeat vector along $[111]$ direction is six times the interplanar spacing, shear of such a magnitude would be required on at least six consecutive (111) planes to restore the twinned lattice with respect to the matrix. This type of twinning, along with a slip of

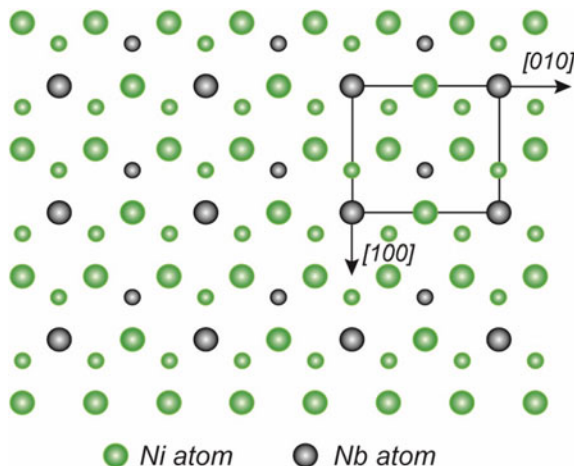
$<110]$ and $<100]$ at higher temperatures (in the [001] domain), has been observed in the Al_3Ti phase with $\text{D}0_{22}$ structure [14].

4.2.2 δ Phase

The ordered arrangement of atoms in the $\text{D}0_a$ structure strongly influences its deformation behavior. The unit cell of the orthorhombic $\text{D}0_a$ structure is shown in Fig. 2.4. $(001)_\delta$ is its close-packed plane (Fig. 4.8) and has the same arrangement of atoms as that in the close-packed plane of the γ'' phase (Fig. 4.6). However, the stacking sequence of the close-packed plane in the $\text{D}0_a$ structure is ...ABABAB... type. This stacking sequence is similar to that encountered in hexagonal-close packed (HCP) structures. When a GSF is introduced in the $\text{D}0_{22}$ structure, it brings its four layers to the $\text{D}0_a$ type stacking sequence. Therefore, this structure is very similar to the HCP structure with its close-packed $(001)_\delta$ plane identical to that of the (0001) plane in a hexagonal lattice. However, the ordering of M atoms in the N_3M stoichiometry distorts the hexagonal symmetry to form the orthorhombic structure. For that reason, the $\text{D}0_a$ structure of the δ phase can also be regarded as an ordered structure based on the HCP lattice. Therefore, the deformation behavior of the δ phase has many commonalities compared to $\text{D}0_{22}$ and HCP phases. As in a $\text{D}0_{22}$ structure, faults like APB, GSF and CSF may occur on close-packed planes of the $\text{D}0_a$ structure also. Amelinckx [15] has proposed four-fold and eight-fold dissociation of dislocations with Burgers vectors parallel to the close-packed directions involving these faults.

The deformation behavior of the δ phase is illustrated considering the δ_1 variant orientation of the phase (Table 2.3). In this orientation of the δ phase, the $(010)_\delta$ plane of the orthorhombic structure is the close-packed plane. Several types of slip and twinning systems, such as $(001)_\delta[100]_\delta$ and $(001)_\delta[010]_\delta$ slip systems and $\{011\}_\delta$

Fig. 4.8 Projection of atoms on close-packed $(001)_\delta$ plane of the δ phase. The bigger circles represent the position of A layer atoms, while the small circles represent the projections of B layer atoms



$\{0\bar{1}1\}_{\delta}$, $\{211\}_{\delta}<\bar{1}0\ 7\ 13>_{\delta}$ and $\{012\}_{\delta}<0\bar{2}1>_{\delta}$ twinning systems [16–22], may get activated depending on crystal orientation. The twins in the Ni₃Nb D0_a phase have similar characteristics to those reported in many pure HCP metals [23].

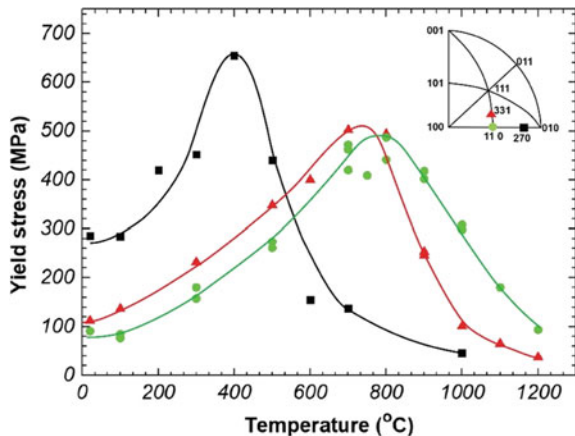
Fukuchi and Watanabe [24] have shown that Ni₃Nb single crystals can be deformed to extensive strains even at room temperature by controlling the stress axis even though the D0_a structure has low crystal symmetry. The D0_a Ni₃Nb alloy exhibits sufficient compressive ductility mainly because of the slip on the $(001)_{\delta}$ plane by $[100]_{\delta}$ or $[010]_{\delta}$ dislocations in all orientations except for the $[001]_{\delta}$ orientation. In the $[001]_{\delta}$ orientation, it exhibits numerous $\{211\}_{\delta}$ twins. However, the $\{211\}_{\delta}$ twins cause brittle failure of the alloy in tension along the twinning planes even at 500 °C.

The $\{011\}_{\delta}<0\bar{1}1>_{\delta}$ twins are similar to the $\{1\ 0\ \bar{1}\ 2\}<1\ 0\ \bar{1}\ \bar{1}\>$ reported in many pure HCP metals [23]. The twinning planes of $\{211\}_{\delta}$ and $\{012\}_{\delta}$ twins in Ni₃Nb correspond to $\{1\ 0\ \bar{1}\ 1\}$ in the HCP notation. The $\{1\ 0\ \bar{1}\ 1\}$ twins are reported in metals like magnesium, titanium and zirconium [23]. However, the formation of the $\{10\ \bar{1}\ 1\}$ twins in HCP structures is associated with $<\bar{1}\ 0\ 1\ 2>$ type shear, which is different from an equivalent shear of $<\bar{1}0\ 7\ 13>_{\delta}$ in the orthorhombic structure required to produce $\{211\}_{\delta}$ twins in Ni₃Nb. The irrational index close to the $<\bar{1}0\ 7\ 13>_{\delta}$ shear direction in the HCP structure is $<\bar{2}\ 3\ \bar{1}\ 1>$. This gives a relatively small magnitude of shear (= 0.40) but does not disturb the order symmetry [22].

At low temperatures, the slip is predominantly by the $(001)_{\delta}[100]_{\delta}$ and $(001)_{\delta}[010]_{\delta}$ dislocations because of their low CRSS. The pyramidal slip, similar to the *c* + *a* dislocations in HCP crystals, is not operative. The limited-slip systems necessitate deformation twinning to provide strains along the *b*-axis. That is why the three twinning systems are operative even at room temperature despite high CRSS values. The CRSS rapidly decreases with increasing temperature from a temperature of around 200 °C for the $\{011\}_{\delta}$ twin and from a temperature around 400 °C for the $\{211\}_{\delta}$ twin. However, deformation twins may induce fracture. The CRSS showed orientation dependence and no significant strain rate dependence in the temperature range for anomalous strengthening.

The δ phase exhibits anomalous strengthening at elevated temperatures when deformed by $(001)_{\delta}[010]_{\delta}$ slip [25]. The CRSS for the $(001)_{\delta}[010]_{\delta}$ slip increases with increasing temperature showing a peak between 400 and 800 °C depending upon the crystal orientation (Fig. 4.9). This anomalous increase in the CRSS is similar to that observed in many L1₂ compounds due to the formation of Kear-Wilsdorf type of locks (Sect. 4.1). The $[010]_{\delta}$ superlattice dislocation dissociated into two $1/2[010]_{\delta}$ superpartials bound by an anti-phase boundary (APB). The $1/2[010]_{\delta}$ superpartial easily cross slip from the primary $(001)_{\delta}$ to the $(100)_{\delta}$ plane due to its lower APB energy on the $(100)_{\delta}$ plane as no violation of the first nearest neighbor atoms occurs. However, the yield stress decreases rapidly at temperatures above the anomalous peak temperature due to a transition of the $(001)_{\delta}[010]_{\delta}$ slip from the $(001)_{\delta}[010]_{\delta}$ slip to either $\{211\}_{\delta}<\bar{1}0\ 7\ 13>_{\delta}$ twinning or $(100)_{\delta}[010]_{\delta}$ slip depending upon the crystal orientation.

Fig. 4.9 Temperature dependence of the yield strength of Ni_3Nb single crystals with different orientations



4.2.3 $\text{Ni}_2(\text{Cr},\text{Mo})$ Phase

Two types of close-packed planes, $(101)_o$ and $(031)_o$ types, exist in the N_2M superlattice of the $\text{Ni}_2(\text{Cr},\text{Mo})$ phase. The subscript “o” refers to the orthorhombic structure. Upon ordering, the four equivalent closed-packed $\{111\}$ planes of the disordered FCC phase get converted into two each of the $(101)_o$ type and the $(031)_o$ type planes of the ordered phase. Both the planes maintain the N_2M stoichiometry of the superlattice. However, the ordering reduces the six-fold symmetry of the FCC octahedral planes to half (i.e., to three-fold) of the $\{101\}_o$ planes (Fig. 4.10a) and to one third (i.e., to two-fold) of the $\{031\}_o$ planes (Fig. 4.11a). Due to the difference in the arrangement of N and M atoms in the two types of planes, the stacking sequence of the planes (which constitute the N_2M lattice) is different. Figures 4.10b and 4.11b illustrates the stacking of $(101)_o$ and $(031)_o$ closed-packed planes for an orientation corresponding to variant 2 of the $\text{Ni}_2(\text{Cr},\text{Mo})$ phase. A three-layer sequence of the $\{101\}_o$ type planes as ...ABCABC... makes the $\text{Ni}_2(\text{Cr},\text{Mo})$ structure. On the other hand, a nine-layer sequence of the $\{031\}_o$ type planes as ...ABCDEFGHIA... (or as..1234567891...), such that the superposition of atoms take place after every three layers but the superposition of M atoms occurs every nine layers only, makes the $\text{Ni}_2(\text{Cr},\text{Mo})$ structure. Consequently, the smallest repeat vector, which brings an atom to its correct position in the superlattice, is different in the two types of planes. Table 4.3 lists the Burgers vectors of possible perfect and partial dislocations on $(101)_o$ and $(031)_o$ planes of an N_2M superlattice oriented as variant 2.

In the $\{101\}_o$ plane (Fig. 4.10), the three close-packed directions are equivalent and perfect superdislocations in all three directions, and would comprise triplets of $1/2<110]$ superpartials containing anti-phase boundaries (APBs). Further splitting the individual superpartials into Shockley partials would lead to complex stacking faults. The smallest perfect dislocation is of $1/2<112>$ type. On the $\{031\}_o$ plane, the glide of a unit dislocation $1/2<110>$ is possible parallel to the row of Mo atoms

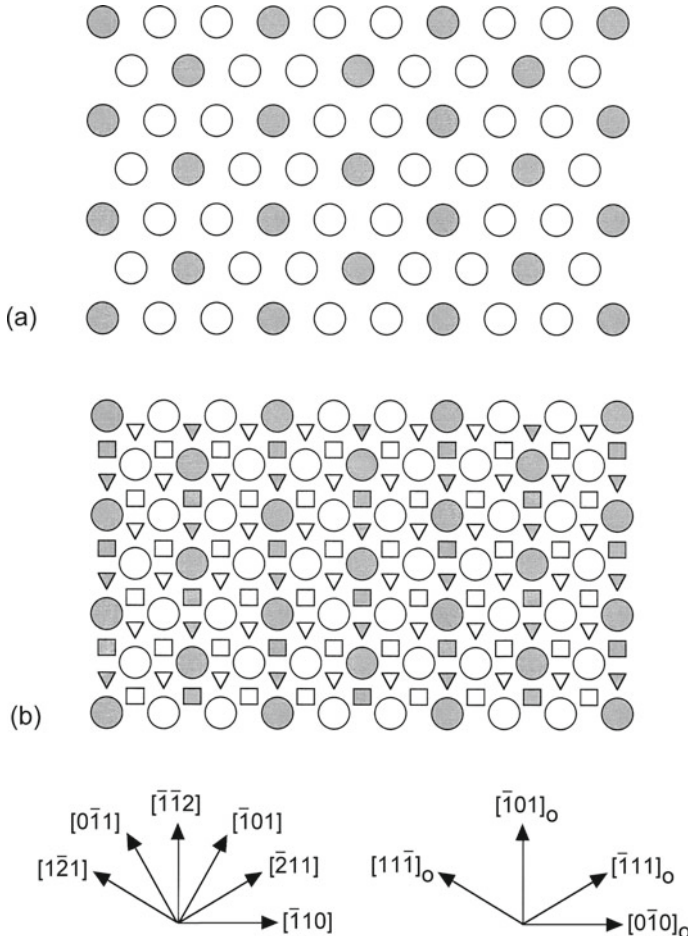


Fig. 4.10 **a** Drawing illustrating how the close-packed (111) plane of the FCC structure on ordering becomes the (101)_o plane of variant 2 of the N₂M phase. **b** Projection of the N₂M lattice onto the (101)_o plane illustrating that a stacking of three (101)_o planes in a sequence ...ABCABC... constitutes the N₂M lattice. Open and shaded symbols represent N and M atoms, respectively. Atoms lying in the first (A) layer are represented by circles, while squares and triangles represent atoms in the second (B) and third (C) layers

(i.e., [1̄10] direction in Fig. 4.11). Still, superdislocations in the other two close-packed directions would comprise triplets of the unit dislocations. Likewise, perfect dislocations of type 3/2 <112> are possible in the {031}_o plane. In addition, a perfect translation exists along the C-axis also ([001] for variant 2) though it does not lie in the octahedral plane. Similar glide planes and displacement vectors of dislocations in other phase orientations can be obtained using the correspondence relationships given in Eq. 2.8 and 2.9 in Chap. 2.

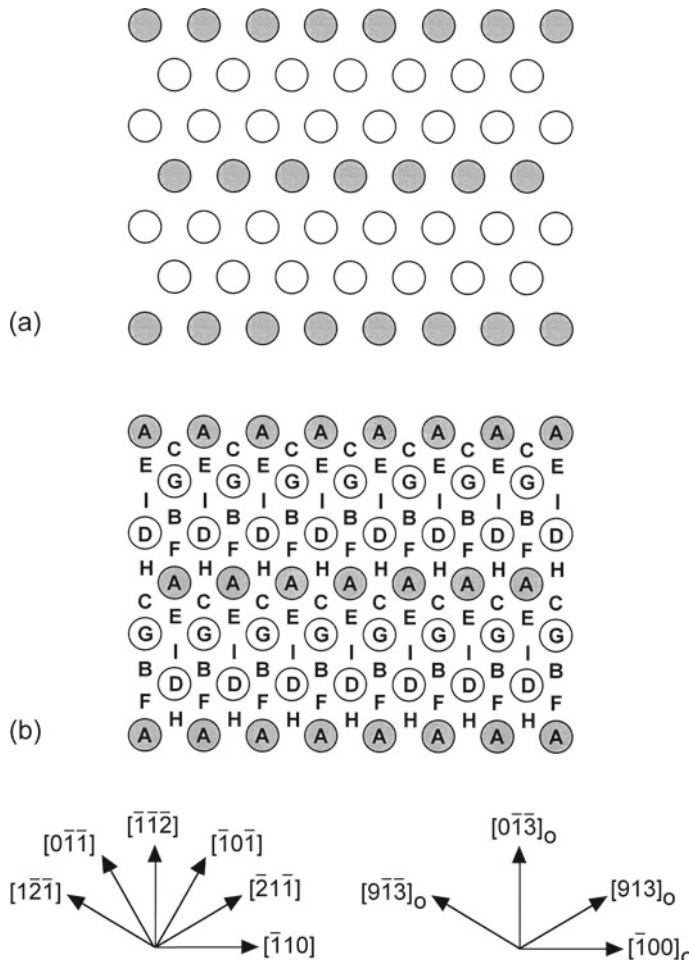


Fig. 4.11 **a** Drawing illustrating how the close-packed $(\bar{1}11)$ plane of the FCC structure on ordering becomes the $(031)_o$ plane of variant 2 of the N_2M phase. **b** Projection of the N_2M lattice onto the $(031)_o$ plane illustrating that a nine-layer stacking sequence of $(031)_o$ planes in a sequence ...ABCDEFIGHIA... constitutes the N_2M lattice. Open and shaded symbols represent N and M atoms, respectively. A, B, C, ... G, H, I represent positions of M atoms on the 1st, 2nd, 3rd, ... 7th, 8th, 9th layers, stacking of which constitute the N_2M structure

Twinning in the N_2M superlattice can take place in four different modes. As a result of the cubic to orthorhombic transformation, out of the twelve $\langle 112 \rangle \{111\}$ twinning systems of the FCC structure, only ten twinning systems transform to twinning modes that give true twins in the N_2M structure. The remaining two twinning systems produce pseudo twins in the N_2M lattice. Among the ten true twinning modes, two twinning systems make true twins by “Combined” twinning mode, and the remaining eight gets converted into four equivalent conjugate pairs of “Type I”

and “Type II” modes of the ordered lattice. This classification of twinning modes is based on the classification proposed by Christian and Laughlin [26]. Table 4.2 also lists characteristic crystallographic features of different twinning modes in the N₂M superlattice. The crystallography of the formation of true twins is illustrated by taking one example of each of the three modes of variant 2 of N₂M superlattice (Table 2.8). For more details, readers are referred to references [13, 27].

The combined mode of twinning is operative when both the twinning planes, K₁ and K₂ are of (101)_o type and the shear acts along <10̄1>_o direction. The shear plane for this mode is (010)_o. Projection of the superlattice on (010)_o (i.e., (1̄10)) shear plane would orient the twinning plane (111) (i.e., (101)_o) in edge-on orientation as illustrated in Fig. 4.12. A six-layer stacking sequence of the shear plane (010)_o as ...0123450... constitute the N₂M lattice. In this orientation, only one atom species is present in each layer with zeroth and the 3rd layer containing only M atoms and 1st, 2nd, 4th and 5th layers containing only N atoms. These layers are arranged in such a way that atom positions in an even-numbered layer coincides with another even-numbered layer, and an odd-numbered layer coincides with another odd-numbered layer, or the coincidence of M atoms occurs only after six layers. The orthorhombic axes **A** and **C** would lie within the projection plane (plane of the paper), whereas **B** would be parallel to its normal. It is also apparent from atom positions on the (101)_o plane (Fig. 4.10) that there are only one species of atoms (i.e., N or M) along the shear directions [10̄1]_o. It can be seen that an operation of shear of 1/3[10̄1]_o (i.e., 1/6[11̄2]) on a plane (say B in Fig. 4.12) would restore the lattice across the projection of the twinning plane with the right kind of atoms in twinned positions with respect to the matrix. Displacement of such a magnitude would need to take place on at least three consecutive planes to repeat the stacking sequence with respect to the matrix. It is to be noted that the same twinned positions can be obtained both by reflection across the twin plane and by rotation about the twinning (shear) axis. As the twin and the conjugate twin plane and the twinning direction and its conjugate

Table 4.3 Burgers vectors of possible perfect and partial dislocations on (101)_o and (031)_o planes of a N₂M crystal oriented according to variant 2 with respect to the FCC structure

	(1 0 1) _o // (1 1 1) _{fcc}	(0 3 1) _o // (1̄1 1) _{fcc}
Perfect translations	1/2[11̄2]	1/2[110]
	1/2[1̄21]	3/2[101]
	1/2[211]	3/2[01̄1]
	3/2[1̄10]	3/2[211]
	3/2[10̄1]	3/2[1̄12]
	3/2[011]	3/2[1̄21]
Shortest burgers vectors of partials bounding a pure stacking fault	1/6[11̄2]	1/6[211]
	1/6[1̄21]	1/6[1̄21]
	1/6[211]	
	1/3[1̄12]	

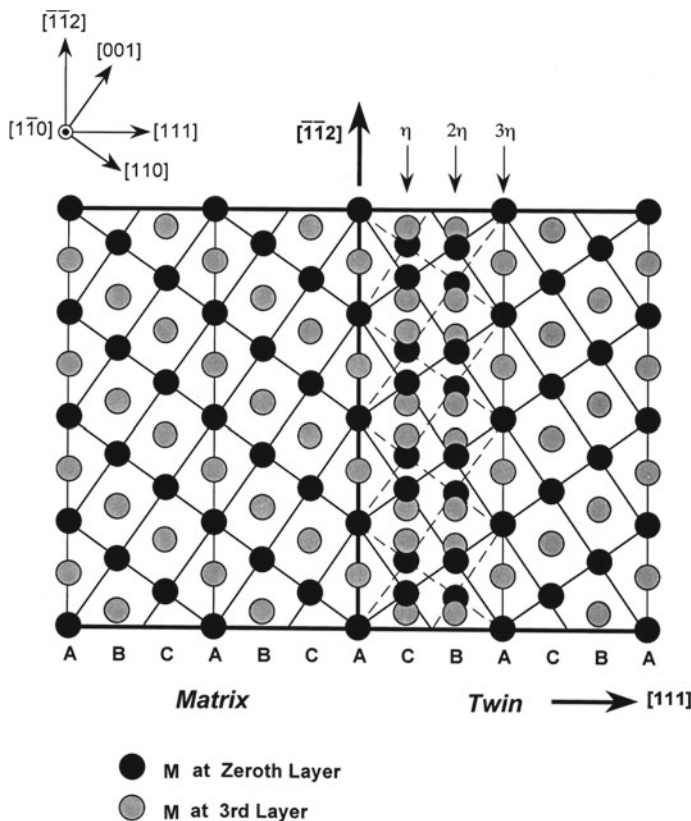


Fig. 4.12 Schematic drawing showing the shear plane projection for the Combined mode of twins in N_2M lattice. N_2M lattice comprises a six-layer stacking sequence of type ...0123450... of the shear plane $(010)_o$ arranged in such a way that atom positions in an even-numbered layer coincides with another even-numbered layer, and an odd-numbered layer overlaps with another odd-numbered layer. The coincidence of M atoms occurs only after six layers. Different layers have been represented with respect to the position of M atoms in each layer. A twinning shear, η , of $1/6[11\bar{2}]$ on every (111) (i.e., $(101)_o$) plane generates a true crystallographic twin

are crystallographically equivalent and rational, the derived mode for the ordered structure gives the same results as the compound twinning mode of the disordered FCC lattice [26].

The type I mode of twinning is operative when the K_1 plane is of $(031)_o$ type and K_2 is of $(101)_o$ type. The corresponding twinning shear directions are of $\eta_1 = [9\bar{1}3]_o$ and $\eta_2 = [\bar{1}11]_o$ type. The associated conjugate mode (Type II) is obtained by interchanging K_1 and K_2 , and η_1 and η_2 .

Projection of the superlattice on the shear plane $(13\bar{2})_o$ (i.e., $(01\bar{1})$) would reveal that a stacking of six layers of the shear planes as ...0123450... is required to construct the superlattice (Figs. 4.13 and 4.14). The stacking arrangement of this shear plane would such that an even-numbered layer would coincide with another even-numbered

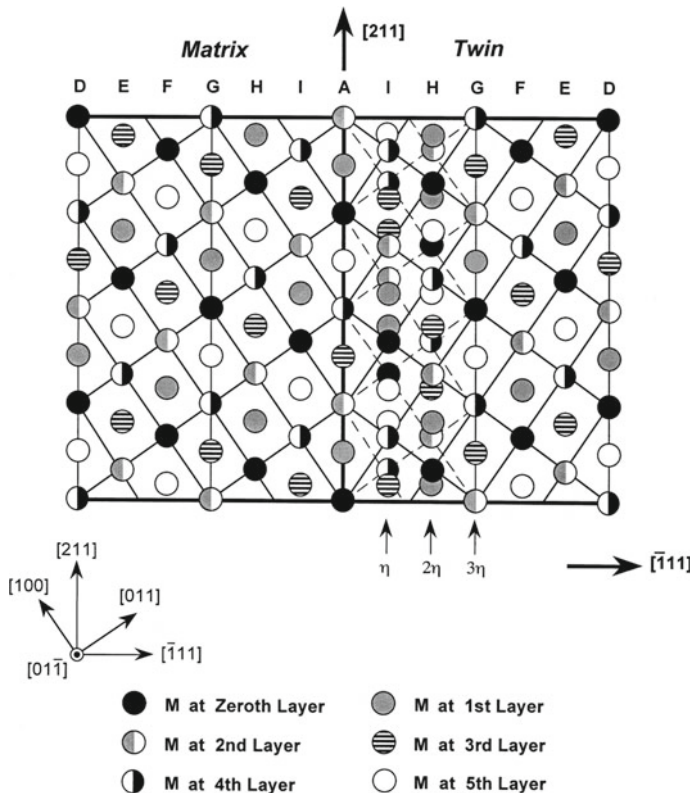


Fig. 4.13 Schematic drawing shows the projection plane for Type I mode of twins in the N_2M lattice. A six-layer stacking of the shear plane $(0\bar{1}\bar{1})$ (i.e., $(1\bar{3}2)_0$) would constitute the N_2M lattice. Different layers have been represented with respect to the position of M atoms in each layer. A twinning shear of $1/6[211]$ on every $(\bar{1}11)$ (i.e., $(031)_0$) plane generates a true crystallographic twin

layer, and an odd-numbered layer would coincide with another odd-numbered layer. The coincidence of M atoms would occur only after every six layers. Each layer would contain both the species of atoms. This projection would bring the $(031)_0$ (i.e., $(\bar{1}11)$) and the $(101)_0$ (i.e., (111)) planes in the edge-on orientation. The A-axis would be pointing outward from the plane of the paper at an angle of 30° , and its projection in the plane of the paper would lie along $[211]$ direction. In contrast, the C-axis would point downward at 45° with the plane of paper such that its projection lies along $[01\bar{1}]$ direction. A nine-layer stacking of $(\bar{1}11)$ planes, as ...ABCDEF G HIA... (Fig. 4.11b), or a three-layer stacking of (111) planes, as ...ABC A ... (Fig. 4.10b), make variant 2 of this superlattice. This stacking sequence can also be inferred from Figs. 4.13 and 4.14. It can be seen that a twinning shear of $1/36[9\bar{1}3]_0$ (i.e., $1/6[211]$) on consecutive $(031)_0$ (i.e., $(\bar{1}11)$) planes would bring the sheared lattice at twin position by Type I mode with right kind of atoms occupying the lattice positions with respect to the matrix. Similarly, a shear of $1/6[\bar{1}11]_0$ (i.e., $1/6[\bar{2}11]$) magnitude

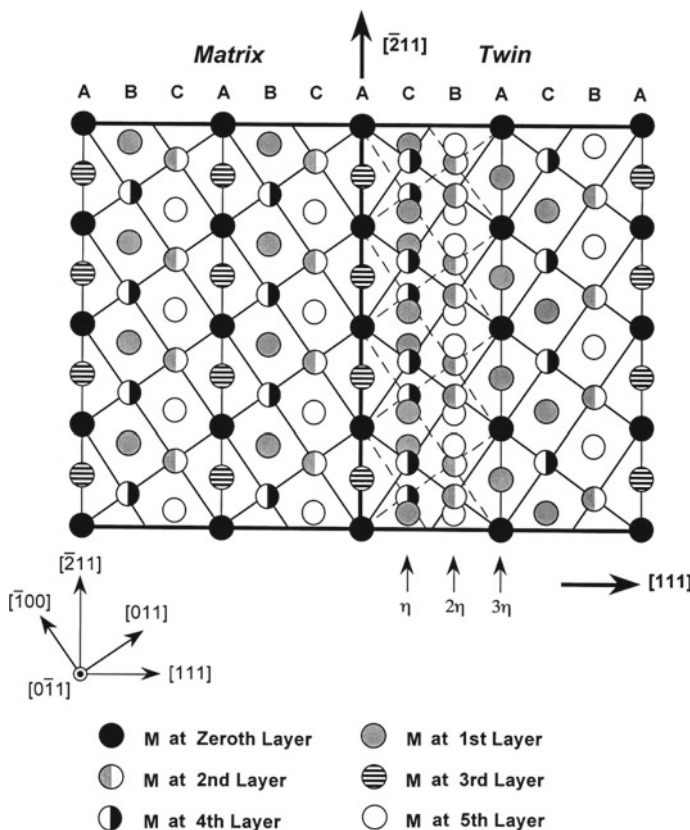


Fig. 4.14 Schematic drawing showing the plane of projection for the Type II mode of twins in N_2M lattice. A six-layer stacking of the shear plane (011) (i.e., $(13\bar{2})_0$) would constitute the N_2M lattice. Different layers have been represented with respect to the position of M atoms in each layer. A twinning shear of $1/6[\bar{2}11]$ on every (111) (i.e., $(101)_0$) plane would bring the lattice points at twin position, on which a true crystallographic twin can be generated by a rotation of 180° about the twinning axis

on consecutive $(101)_0$ (i.e., (111)) planes would also bring the lattice to twin position. The identical twin structure could be achieved by a rotation of 180° about the twinning axis $[\bar{2}11]$. Shears of such magnitude are required on at least nine consecutive planes for Type I twins and at least three successive planes for Type II twins to restore the lattice.

4.3 Strengthening of Alloy 625

Superalloys, in general, are strengthened by solid-solution hardening, precipitation hardening, or dispersion strengthening. Dispersion strengthening may include strengthening by carbides or oxide particles. Other strengthening mechanisms, such as grain size refinement and cold working, usually do not play much role due to intended applications of superalloys at elevated temperatures. Alloy 625 achieves its strength primarily from solid-solution hardening, but service exposure precipitates out particles of various intermetallic phases, which age hardens the alloy. These precipitates directly bear the temperature/stress capabilities of Alloy 625 components. This section briefly describes the solid-solution and precipitation hardening mechanisms that primarily govern the Alloy 625 strength.

4.3.1 Solid-Solution Strengthening

Solid-solution hardening is mainly related to the difference in the atomic size of solute and solvent atoms. It is a measure of the lattice parameter (a) change of the austenite matrix [28]. Substitutional elements whose atomic diameter differs from nickel by about 1 to 13% solid solution harden the alloy by straining the nickel matrix [29]. Besides, a change in the electron vacancy number (N_v) also changes the yield stress of the nickel-base superalloys. The position of solutes in the periodic table governs their N_v values, which may differ by 1 to 7% for various solutes. For the same lattice strain, the extent of hardening increases with an increase in the value of N_v . That is why the strengthening is more potent for aluminum, tungsten, molybdenum and chromium and least effective for elements like cobalt, iron, titanium and vanadium. However, the tendency of these alloys to form topologically close-packed (TCP) phases limit the extents of tungsten, molybdenum and chromium additions. Solid-solution strengthening in Alloy 625 is due to chromium, molybdenum, aluminum and titanium. Niobium does not contribute much to the solid-solution hardening. Still, it strengthens the alloy along with molybdenum at elevated temperatures by virtue of their high melting points when the matrix strength is diffusion dependent.

A part of the solid-solution strength of Alloy 625 can also be attributed to the low stacking fault energy (SFE) of its austenite phase. A strong correlation between N_v of the solute and a reduction in the SFE has been well documented [30, 31]. Pure Ni has a high SFE ($\sim 150 \text{ mJ/m}^2$) [1]. The addition of solutes like chromium, molybdenum, tantalum, titanium, etc. in nickel decrease the SFE of the austenite nickel phase (Fig. 3.10). Further, the effect of solute elements on SFE is not the same for binary and multicomponent alloys [32]. Therefore, alloying additions in nickel lower the SFE of the solid solution. A low SFE leads to planar arrays of dislocations, which inhibits the cross slip.

Other solid-solution strengthening mechanisms such as difference in the shear moduli of solute and the solvent atoms [30] and the presence of short-range order

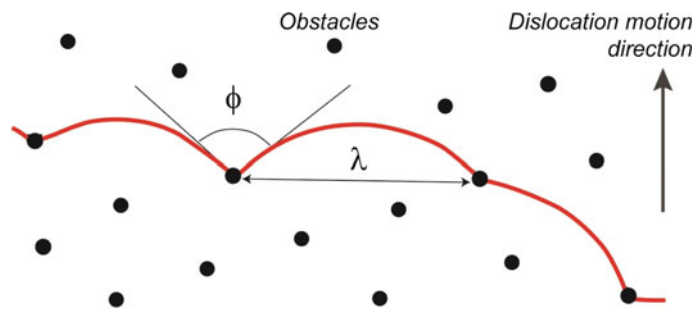


Fig. 4.15 A schematic illustration of the interaction of a dislocation with obstacles

[29] may also contribute to solid-solution strengthening. However, the short-range order has never been reported in Alloy 625 though it is known to exist in many nickel–chromium-molybdenum alloys.

4.3.2 Precipitation Strengthening

Second phase particles increase strength of the alloy by acting as barriers to dislocation motion. When a dislocation encounters obstacles, it bows between them. The extent to which dislocations can bend is governed by the strength of barriers (Fig. 4.15). Shear stress, τ , required to bend dislocations to an angle ϕ is given by [33],

$$\tau \cong \frac{Gb}{\lambda} \cos \frac{\phi}{2} \quad (4.3)$$

where G is the shear strength of obstacles, b is the Burger's vector of dislocations and λ is spacing between two obstacles in a slip plane. The angle ϕ is inversely related to the obstacle strength. As the strength of barriers increases, ϕ approaches zero because the dislocation doubles back on itself when particles behave like impenetrable obstacles (particle bypassing). On the other hand, for values of $\phi > 0$, the particles can be sheared by the glide of dislocations. For weak obstacles, ϕ is very large and tend to approach 180°. λ is another critical parameter as a decrease in its value would also reduce ϕ for a given stress.

In general, strengthening by ordered phase precipitates is governed by one or more of the following factors:

1. order hardening due to the additional energy associated with the creation of anti-phase boundary when ordered particles are sheared;
2. coherency strain hardening;

3. modulus hardening due to the difference between the elastic moduli of the matrix and the precipitate phases, which results in different elastic energies around dislocations in precipitates and the matrix;
4. difference between the stacking fault energies of the precipitate and the matrix phases;
5. surface hardening due to the energy required to create additional particle/matrix interfaces when dislocations shear the particles.

The precipitation strengthening in Alloy 625 is brought about mainly by the formation of the γ'' and Ni₂(Cr,Mo) phase particles. Both phases form in ellipsoidal morphology due to their cubic to non-cubic transformations (Sect. 3.5). The significant contribution comes from the coherency hardening and the order hardening associated with the two phases. Hence, the analysis of the precipitation strengthening here is restricted only to these two mechanisms.

4.3.2.1 Order Strengthening

The ordered precipitates impede dislocations' movement as their passage destroys their order structure and creates anti-phase boundaries. Passage of multiple dislocations of the disordered matrix is required to restore the ordered state. Therefore, dislocations in an ordered structure often glide in pairs bound by an anti-phase boundary (Sect. 4.1.3). Consequently, there is a net enhancement in the alloy's shear strength when ordered phase precipitates are present. Ordering asymmetry in the close-packed directions of the γ'' phase necessitates the passage of two dislocations in one close-packed direction and four dislocations in the other two close-packed directions on a {111} plane. When the γ'' phase particles are sheared by four, two and single $1/2\langle 110 \rangle$ dislocations, the increase in the strength of the alloy is given by [34]:

- (a) When particles are sheared by a quadruplet of $1/2\langle 110 \rangle$ dislocations,

$$\Delta\tau_4 = \left[\frac{\Gamma}{4b} \right] \left[\left\{ \frac{4\Gamma f R}{\pi T} \left(\frac{\sqrt{6}}{3A} \right)^{1/2} \right\}^{1/2} - f \right] \quad (4.4)$$

- (b) When particles are sheared by a pair of $1/2\langle 110 \rangle$ dislocations,

$$\Delta\tau_2 = \left[\frac{\Gamma}{2b} \right] \left[\left\{ \frac{4\Gamma f R}{\pi T} \left(\frac{\sqrt{6}}{3A} \right)^{1/2} \right\}^{1/2} - \beta f \right] \quad (4.5)$$

and

- (c) When particles are sheared by a single $1/2\langle 110 \rangle$ dislocation,

$$\Delta\tau_1 = \left[\frac{\Gamma}{b} \right] \left[\frac{4\Gamma f R}{\pi T} \left(\frac{\sqrt{6}}{3A} \right)^{1/2} \right]^{1/2} \quad (4.6)$$

where $\Delta\tau$ stands for the increment in the flow stress due to precipitate shearing, subscripts 4, 2 and 1, respectively represent the number of dislocations, b is the magnitude of the Burgers vector, A is the aspect ratio given by the ratio of the major and the minor axes of γ'' particles and R is the semi-major axis (see Fig. 3.25), T is the dislocation line tension, β represents the fraction of γ'' particles in which the passage of dislocation pairs restores the order, Γ is the APB energy per unit area of the γ'' phase and f is its volume fraction. It should be noted that in the original work of Oblak et al. [34] R was taken as the mean of the semi-minor and semi-major axes of the ellipsoid, while Kelly [35] assumed R as the semi-major axis for estimating the particle bypassing strength. For the sake of simplicity, Kelly's assumption has been used for particle size in the present text. Such an assumption would not result in any significant error in the shear strength measurement. When all the three variants of the γ'' precipitates are present, $\beta = 1/3$. An important feature of the strengthening by particles of the γ'' phase is that $\Delta\tau$ is sensitive to the specific variant of the γ'' phase.

Oblak et al. [34] relationships for the contribution of order hardening by ellipsoidal γ'' phase precipitates are equally applicable for treating the ordering hardening by Ni₂(Cr,Mo) precipitates. For the Ni₂(Cr,Mo) phase $\beta = 1/6$, assuming all its variants precipitate homogeneously throughout the matrix.

4.3.2.2 Coherency Strengthening

Tetragonality associated with coherent γ'' precipitates produce distortions in the matrix around them. Dislocations interacts with the strain field surrounding the particles. Oblak et al. [34] have derived an expression for the increase in the critical resolved shear stress due to the interaction of edge dislocations with the coherency strain associated with ellipsoidal shape particles.

$$\Delta\tau = 1.7\mu\varepsilon^{3/2} \left[\frac{fR}{2A^2b} (1 - \beta) \right]^{1/2} \quad (4.7)$$

where ε is the tetragonal misfit strain and β is the fraction of particles whose c -axis is normal to b . $\beta = 1/3$ when all the three precipitate variants of γ'' are present. The coherency contribution is directly proportional to the shear modulus μ . Therefore, the coherency strength decreases with increasing temperature. Coherency hardening effects may also depend strongly on the alloy composition as the lattice mismatch between the matrix and the precipitate changes with composition. Oblak et al. [34] have shown the contribution of the coherency strengthening (~221 MPa) due to γ'' phase particles is more than their order strengthening (~183 MPa) in Alloy 718.

4.3.2.3 Particle Bypassing

Particle bypassing by dislocations limits the strength achievable by precipitation. Bypassing occurs beyond a specific particle size by either forming dislocation loops (Orowan looping) or by a climb of dislocations at the matrix-precipitate interface. Kelly [35] has derived an expression for the stress necessary to initiate the bypassing process for plate-shaped particles of a given orientation in the matrix:

$$\Delta\tau = \frac{0.85\mu b}{2\pi(1-\nu)^{1/2}} \frac{C}{2R\left[1 - \frac{\pi}{2A}C\right]} \ln\left(\frac{4R}{r_0}\right) \quad (4.8)$$

where $\Delta\tau$ is the shear stress increment associated with precipitate bypassing, ν is the Poisson ratio for the matrix, r_0 is the dislocation core radius, R is the semi-major axis of the ellipsoidal, and the following relation gives the value of C:

$$C = \left[(fA)^{1/2} + \left(\frac{2}{\pi} - \frac{\pi}{2A}\right)fA \right] \quad (4.9)$$

Other terms have the usual significance. The stress required for the onset of the particle bypassing mechanisms decreases with increasing particle size. Kelly has shown that the stress necessary for Orowan bypassing to operate is much higher for needle-shaped and plate-shaped precipitates than for spherical ones. When the Orowan process operates, the alloy work hardens rapidly because every dislocation passing the particles leaves a loop around them, decreasing the effective interparticle spacing λ .

Equation 4.8 is valid only at low temperatures. At high temperatures, dislocations' climb over particles becomes the rate-controlling mechanism for the dominant creep phenomenon [36]. At stresses $\sigma > \mu b/\lambda$, dislocations move past particles by Orowan looping. Built-up dislocation loops exert back-stresses to prevent further looping until they climb to the nearest particle. When this process occurs, the creep rate, $\dot{\epsilon}$, is given by

$$\dot{\epsilon} = \frac{\pi\sigma^4\lambda^2D}{R\mu^3kT} \quad (4.10)$$

where σ is the stress applied, D is the self-diffusion coefficient, k is the Boltzmann constant, and T is temperature. At $\sigma < \mu b/\lambda$, dislocation can climb over the particles without piling up or bowing, and the corresponding creep rate is given by:

$$\dot{\epsilon} = \frac{\pi\sigma b^3 D}{8kTR^2} \quad (4.11)$$

A decrease in the diffusivity and an increase in the size of the second phase particle reduce the creep rate. In addition, a low value of λ reduces the creep rate at high stresses. These parameters are usually achieved by adding slow diffusing species,

like molybdenum, niobium, etc. in the alloy and by increasing the volume fraction and size of precipitates by suitable aging treatments.

4.4 Deformation Micromechanisms in Alloy 625

Several studies on the deformation behavior of alloys containing ordered strengthening phases of tetragonal or orthorhombic symmetry [12, 37, 38] show a transition in the deformation mode from slip to twinning in ordered particles owing to their low symmetry and low stacking fault energies. Such a transition implies that the deformation mode changes from the glide of unit dislocations (or superdislocations) to the movement of Shockley partials when they enter the ordered phase precipitates and vice versa. The slip to twinning transition is governed by the stacking fault energy of the ordered phases.

The main hardening phases in Alloy 625, namely γ'' and $\text{Ni}_2(\text{Cr},\text{Mo})$ phases, have properties similar to those studied by Sundararaman et al. [12] in Inconel 718 and by Kumar and Vasudevan in Haynes 242 [38], respectively. Frequent observation of stacking faults within γ'' precipitates in deformed and un-deformed Alloy 718 has been reported by many workers. The frequent observations of stacking faults indicate that the stacking fault energy (SFE) of the γ'' phase is relatively low. Ni_3V phase is the only equilibrium $D0_{22}$ structure with lattice parameters very close to that of the γ'' phase. The SFE of the Ni_3V phase is reasonably low ($\sim 22 \text{ mJ/m}^2$ [39]) and frequently exhibits stacking faults without disturbing the long-range order [13, 40, 41]. The low stacking fault energy of the metastable γ'' phase is also consistent with SFE of the Ni_3V phase as the two phases are isostructural and niobium and vanadium belong to the same group (VB) in the periodic table.

Figure 3.10 shows that adding chromium and molybdenum to nickel reduces its stacking fault energy. The SFE of the Ni_2Mo phase lies in the range of 20 to 30 mJ/m^2 [42]. It is, therefore, reasonable to deduce that the $\text{Ni}_2(\text{Cr},\text{Mo})$ phase has very low SFE. The low SFE of the $\text{Ni}_2(\text{Cr},\text{Mo})$ phase is consistent with the observation of frequent splitting of unit dislocations into partials in Alloy 625 containing a high density of uniformly distributed γ'' and $\text{Ni}_2(\text{Cr},\text{Mo})$ precipitates [43]. This observation also agrees with frequent twinning and stacking faults within $\text{Ni}_2(\text{Cr},\text{Mo})$ precipitates reported by Kumar and Vasudevan [38].

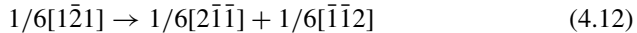
As mentioned in Sect. 4.2, the two phases are sheared by pairs of unit dislocations. The dislocation pairs may further dissociate into Shockley partials by reactions like Eq. 4.2. Each pair of partials is connected by a superlattice intrinsic stacking fault (SISF) in the appropriate variant and a complex stacking fault in others. The formation of SISF in the two phases energetically favors the deformation process due to their low stacking fault energies. The formation of the SISF neither violates the nearest neighbor bonds nor disturbs the long-range order of the phase. Therefore, the unit dislocations tend to dissociate and create SISFs in the ordered phase. Sundararaman et al. [12] and Kirman and Warrington [44] have reported the frequent occurrence of stacking faults within γ'' precipitates in deformed Alloy 718. Such stacking faults,

lying on adjacent glide planes, eventually lead to the formation of twins within the precipitates. The following discusses, in brief, the transition in the deformation mode from slip to twinning in such ordered particles. This behavior is examined considering the case of γ'' particles, but the same principles are applicable for the $\text{Ni}_2(\text{Cr},\text{Mo})$ particles also owing to similar crystallography of their deformation noted in Sect. 4.2.

4.4.1 *Deformation of Particles by Shearing and Twinning*

The creation of SFs within γ'' phase precipitates is energetically favorable owing to its low SFE, which in turn promote the formation of true deformation twins within γ'' particles. Sundararaman et al. [12] have shown profuse deformation twinning in particles of size larger than 10 nm in deformed Alloy 718, indicating twinning to be the predominant mode of deformation in γ'' particles of size larger than 10 nm. Though deformation in the γ phase can occur in any of the four $\{111\}$ plane favored by Schmid factor values, the crystallography of the ordered phase constrains the continuity of deformation by twinning in the ordered precipitates without disturbing their order. For a given shear on a specific $\{111\}$ plane in the matrix, true twins on that plane in the γ'' phase would form only in a particular variant of the γ'' phase, which has the twinning shear compatible with the shear direction in the matrix. The compatibility of the shear is required because true twins on a given $\{111\}$ plane in the $\text{D}0_{22}$ structure form only by one specific $1/6<112>$ shear while the other two shears destroy the chemical order (Sect. 4.2). Therefore, a precipitate would be easily sheared by twinning if its orientation were favorable to the incoming shear. This mode of deformation would thus create different types of twins (i.e., with a different twinning plane and shear) in different precipitate variants for a given tensile stress direction. Such twins nucleate when the stress concentration at the precipitate-matrix interface exceeds critical stress, followed by easy growth as the ordered structure is retained.

Despite this restriction, the twinning along different $\{111\}$ planes of γ'' particles corresponding to all variants of the phase has been shown to occur to give homogeneous macroscopic deformation. Sundararaman et al. [12] have rationalized this observation considering dislocation decomposition reactions at the particle/matrix interface. In principle, twins on any specific $\{111\}$ plane can propagate through all the γ'' variants, though the directions of the twinning shear would be different in precipitates belonging to other variants. As a result, the orientations of the twinned crystals formed in different variants would also be different. The difference essentially arises because of the direction of ordering in each particle. If the ordered atomic arrangement is ignored, the underlined lattice is identically twinned in all variants. Therefore, for the deformation to propagate by twinning on a specific $\{111\}$ plane across particles of all orientations, appropriate shear directions compatible with orientations of the precipitate variants are required to conserve the $\text{D}0_{22}$ ordering within twin bands. Shear compatible with different variants can be created if dislocation dissociation reactions of the following type are assumed to occur at the particle/matrix interface:



where an incoming shear front consisting of a set of incompatible $1/6[1\bar{2}1]$ dislocations on every plane split into sessile $1/6[2\bar{1}\bar{1}]$ and glissile (compatible) $1/6[\bar{1}\bar{1}2]$ components at the precipitate-matrix interface. The glissile partials with the appropriate shear vector would glide through a precipitate, leading to the formation of a twin within it. Even though such dislocation reactions are energetically not favorable, they are feasible under externally applied stress. The energy savings accrued by preserving the order during the propagation of deformation twin outweigh the energy spent in creating a set of sessile partials at the precipitate-matrix interface.

Shearing by deformation twinning is associated with a drop in the work hardening because these twins, once nucleated, form an easy passage of the shear across the matrix-precipitate interface. Deformation twinning, therefore, does not increase the dislocation density at the interface and consequently does not work-harden the matrix. Moreover, since the deformation twins in γ'' particles remain confined within precipitate particles on only one crystallographic plane, work hardening associated with the interaction of twins on different planes is also not there [1, 45].

4.4.2 Effect of Particle Size on the Deformation Mode

During the deformation of two-phase aggregates comprising a homogeneous distribution of hard particles in a softer matrix, two distinct deformation modes, particle shearing and particle bypassing, are commonly observed. The dislocations bypass overaged precipitates by creating loops around them. However, alloys containing overaged ordered precipitates of tetragonal or orthorhombic crystal symmetry do not show dislocation looping around them. Sundararaman et al. [12] have explained this type of behavior by invoking the order hardening and particle bypassing models for the interaction of dislocations with ordered particles in conjunction with deformation by twinning.

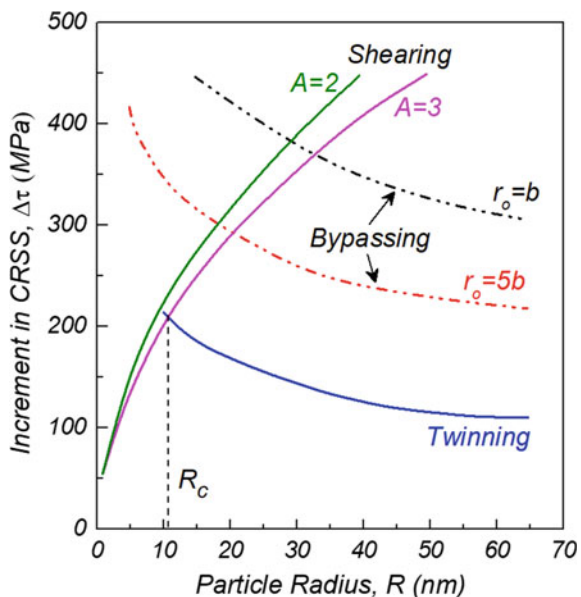
Equation 4.5 gives increase in the shear strength of the alloy when a pair of dislocations shear ordered particles. As noted earlier, a pair of the matrix dislocations can shear γ'' and $\text{Ni}_2(\text{Cr},\text{Mo})$ phase particles without disturbing their order. Figure 4.16 shows the functional dependence of the critical resolved shear stress (CRSS) as a function of particle size for the different deformation mechanisms. This dependence indicates that the stress required for shearing of particles increases with increasing particle size, which is directly related to an increase in the destruction of the order within particles. On the other hand, the stress associated with particle bypassing decreases with increasing particle size for a constant volume fraction. An increase in the mean particle size accompanies a concomitant increase in the interparticle spacing. Therefore, the stress necessary to initiate bypassing decreases according to the relation given by Eq. 4.8. A crossover point is observed in terms of the size of the precipitates. Operation of the bypassing mechanism has a lower stress requirement

than the shearing mechanism beyond a critical precipitate size. Yet these alloys do not show dislocation looping around the precipitate particles.

As mentioned earlier, shearing of particles by deformation twinning occurs only for particles of size bigger than a critical size. These twins are true twins of respective ordered phases as the twinned lattice retains their original order. For this mode of particle shearing to begin operating, the stress concentration at the precipitate-matrix interface should exceed the resolved shear stress required to propagate Shockley partial dislocations and nucleate deformation twins within the ordered particles. These Shockley partials create SISFs, which act as nuclei of the true twins. Once nucleated, the growth of the twin nuclei does not disturb the order and, hence, does not require stresses greater than that required for their nucleation. This implies that once the required threshold stress concentration builds up, the shear propagates through the precipitate catastrophically. A stress concentration above the threshold can easily build due to dislocation piling at the particle/matrix interface in alloys characterized by planar slip. An approximate estimation of the stress necessary for nucleation of deformation twin within an ordered precipitate can be made by equating the critical stress required for twinning, τ_T , to the critical stress, τ_C , generated at the interface by a pile-up of dislocations of pile-up length λ . This critical stress can be expressed as [46].

$$\tau_a = \mu \left[\frac{\tau_C}{\pi \alpha \mu} \right]^{1/2} \left[\frac{\lambda}{b} \right]^{-1/2} \quad (4.13)$$

Fig. 4.16 Theoretical increment in the shear stress, $\Delta\tau$, as a function of γ'' precipitate size for different deformation mechanisms in Inconel 718 [12]. R_c is the critical radius above which the particle's deformation mechanism changes from shearing to twinning



where τ_a is the applied shear stress and α is a geometrical factor which assumes a value of 1 for a screw dislocation pile-up or $(1-\nu)$ for an edge dislocation pile-up. Expressing in terms of R , A and f , and putting $\tau_C = \tau_T$, relation 4.13 can be expressed as [35]:

$$\tau_a = \mu \left[\frac{15b\tau_T}{16\pi\mu} \right]^{1/2} \left[\frac{fA}{2R^2} \left(\frac{\pi}{2} \right)^{1/2} \right]^{1/4} \quad (4.14)$$

For fixed values of b , μ , τ_T , f and A , τ_a becomes inversely proportional to $R^{1/2}$. This dependence of the shear stress increase for twinning as a function of precipitate size is also shown in Fig. 4.16, along with the shear stress increase for shearing and bypassing. This analysis shows that, like particle bypassing, the twinning shear is also size-dependent. There is a critical particle size above which the stress required for deforming ordered precipitates by twinning is lower than the stress by unit dislocations shearing. Besides, the twinning stress for ordered particles is always lower than the bypassing/looping stress for all the particle sizes.

4.5 Tensile Behavior of Alloy 625

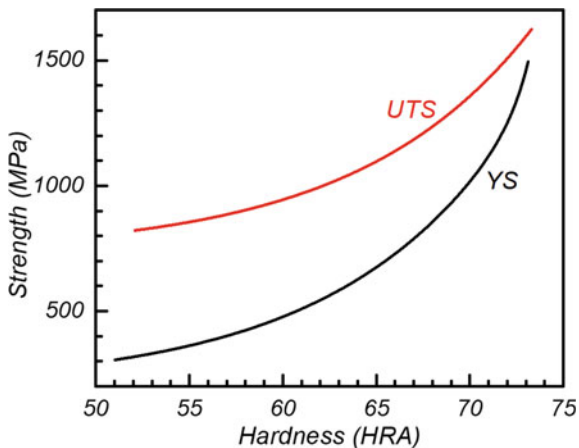
The tensile behavior of Alloy 625 may change significantly depending upon its thermal history. This change is due to the dominant hardening mechanisms associated with the microstructural condition. This section gives a brief account of the tensile properties of the alloy in different microstructural states. As the alloy does not exhibit a well-defined yield point phenomenon, the reported yield strength values correspond to 0.2% proof stress.

4.5.1 Solution Annealed Alloy

The tensile properties of the annealed alloy may vary significantly depending upon the annealing condition and the product form. The alloy possesses a minimum room temperature yield strength of about 276 MPa in fully solution annealed conditions. However, a minimum room temperature yield strength of 414 MPa is achievable in cross-sections up to 100 mm and 345 MPa in cross-sections from 100–250 mm without extensive mechanical working. Table 4.4 gives nominal room temperature tensile properties of wrought Alloy 625 in different conditions [47, 48]. The inherent solid-solution nature of Alloy 625 limits its hardness³ below about 100 HRB (~240

³ The hardness of a material refers to its ability to resist local plastic deformation during indentation or scratch. Its value depends highly upon the type and geometry of the indenter tool being used and the applied load range [1]. Many hardness testing techniques are available, and all have their scale to rate the hardness based on the type of indenter and the capacity of the load that is applied. Each scale

Fig. 4.17 A correlation between the hardness and strength of the Alloy [47].
YS = Yield strength; UTS = Ultimate tensile strength



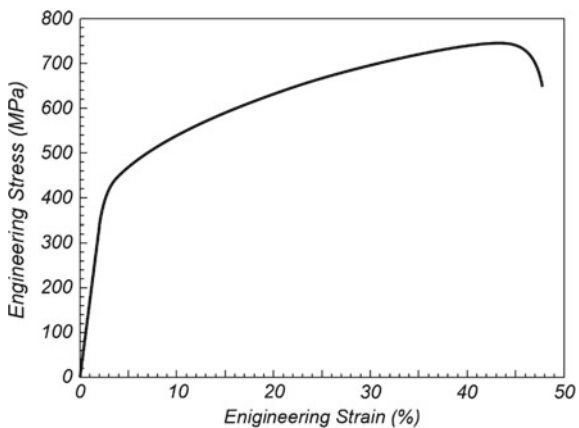
BHN) [47, 48], which can only be increased further by prolonged aging or by cold or warm working. Cold working can increase the hardness of Alloy 625 up to about 45 HRC with a drastic decrease in ductility to about 5% [48]. Warm or cold working may be combined with prolonged aging to age harden the alloy, but such warm or cold working operations becomes less practical as the cross-section of the working piece increases. Figure 4.17 shows a direct correlation between the hardness and strength of the alloy [47]. The plots in Fig. 4.17 can be used for engineering relationships correlating alloy's hardness with yield and ultimate tensile strengths:

$$\text{YS(MPa)} = 200 + 3.65 \times 10^{-5} \exp\left[\frac{(H - 59.84)}{0.87}\right] + 272.6 \exp\left[\frac{(H - 59.84)}{9.31}\right] \quad (4.15)$$

$$\text{UTS(MPa)} = 730.24 + 0.34 \exp\left(\frac{H}{9.31}\right) \quad (4.16)$$

gives a hardness value using a particular indentation tool under specific loading conditions. The use of a particular scale depends upon the material's strength, its work hardening behaviour and the employed test technique. The most commonly used hardness tests are Rockwell hardness, Vickers hardness, Brinell hardness and the Knoop hardness. The Rockwell hardness tests can measure hardness over a wide range and rate it on multiple scales depending upon the load required. Each Rockwell hardness scale is identified by a letter indicating A, B, C, D, etc. depending on the size and type of the indenter and the load applied during measurement. For example, HRA refers to Rockwell hardness scale A, HRB refers to Rockwell hardness scale B, and so forth, which are being used in the increasing hardness order. However, no direct relationship between different hardness scales exists because (i) hardness represents the local strength of a material and (ii) all the tests use different types of indenters. Nonetheless, some empirical hardness conversion relationships have been developed for some scales, particularly for hard steels. For the ease of the readers, standard hardness conversion tables at various sources are summarized in Appendix E. For more details, readers are referred to reference [1].

Fig. 4.18 Engineering stress-engineering strain plot of a solution annealed Alloy 625

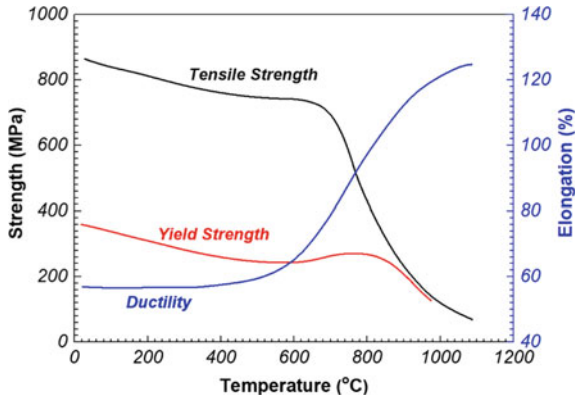


where YS and UTS refer to yield and ultimate tensile strengths of the alloy (in MPa), respectively and H is the hardness of the alloy on the Rockwell A scale [47].

Figure 4.18 shows the engineering stress versus engineering strain curve of Alloy 625 in solution annealed condition. Alloy's typical stress-strain curve is characterized by rapid strain hardening due to predominant planar slip in the alloy (see Fig.3.23b). Sundararaman [49] has studied the deformation microstructure of the alloy in solution-treated conditions and shown that dislocations invariably remain in planar arrays confined within the primary slip plane even after extensive deformation. The planar arrangement of dislocations causes rapid strain hardening of the alloy. Features like cross slip of dislocations, tangling of dislocations, and cell formation are primarily absent in deformed annealed alloys. However, dislocations do not show any resolvable splitting into partials. Such a deformation microstructure is a typical feature of alloys with low stacking fault energy (SFE) or when alloys exhibit short-range order (SRO) or both. As no SRO is reported in Alloy 625, the observed deformation behavior of the alloy in solution annealed condition can be attributed to its low stacking fault energy. Based on the effects of adding elements like chromium, molybdenum, aluminum and titanium on the SFE of nickel reported by different researchers [31, 50–53], the SFE of Alloy 625 is expected to be between 50 and 75 mJ/mm². This range of the stacking fault energy is consistent with the values estimated by Yang et al. [54] for various nickel binary alloys using the first-principle calculations (Fig.3.10).

Figure 4.19 shows the yield strength, ultimate tensile stress, and elongation properties of Alloy 625 in solution annealed condition as a function of temperature, tested over a temperature range from room temperature to 1000 °C [47]. The yield strength falls slightly up to about 600 °C, followed by an increase up to 700 °C. Above 700 °C, the yield strength decreases again. The ultimate tensile strength follows a uniform behavior of a slight decrease up to the test temperature of 600 °C followed by a sharp reduction at temperatures above 700 °C. The ductility remains almost constant up

Fig. 4.19 High-temperature tensile properties of a hot-rolled Alloy 625 rod in solution annealed condition [47]



to about 550 °C, after which it increases sharply till a maximum of about 120% is reached.

A peak and a plateau in the yield and ultimate tensile strength of an alloy at elevated temperatures are manifestations of dynamic strain aging (DSA). DSA is characterized by a jerky/serrated flow behavior, known as Portevin–Le Chatelier (PLC) effect. Such a deformation behavior in the intermediate temperature range is commonly observed in many alloys [54–64]. Many authors have reported DSA in Alloy 625 at temperatures over 250–600 °C and strain rates ranging from 10^{-5} to 10^{-3} s^{-1} [56, 65–68]. This DSA behavior is observed in the solution annealed as well as aged Alloy 625. The alloy exhibits a normal PLC behavior at lower temperatures due to locking of dislocations by interstitial carbon atoms, and an inverse PLC behavior at higher temperatures because of the pinning of dislocations by molybdenum atoms. In the DSA regime, the alloy exhibits negative strain rate sensitivity [56].

4.5.2 Age-Hardened Alloy

Alloy 625 can be age-hardened to achieve higher levels of strength. But the alloy's age-hardening response is sluggish and sensitive to the annealing temperature. In smaller cross-section specimens, a higher annealing temperature makes the alloy less responsive to direct aging. For example, hot-rolled bars of diameter larger than 100 mm, annealed at 1149 °C for 1 h, can be age-hardened directly by subjecting them to aging treatment at about 650 °C. However, bars of diameters less than 100 mm require an intermediate treatment of 1 h at about 760 °C before the same age-hardening treatment. Even for a prolonged time, direct treatment is not sufficient to induce age hardening at 649 °C [69]. Figure 4.20a shows a comparison of the age-hardening response of a hot-rolled bar annealed at about 1150 °C for 1 h. Samples that did not receive an intermediate nucleation treatment did not show any increase in the hardness even after 96 h of aging at 649 °C. On the contrary, the hardness of the

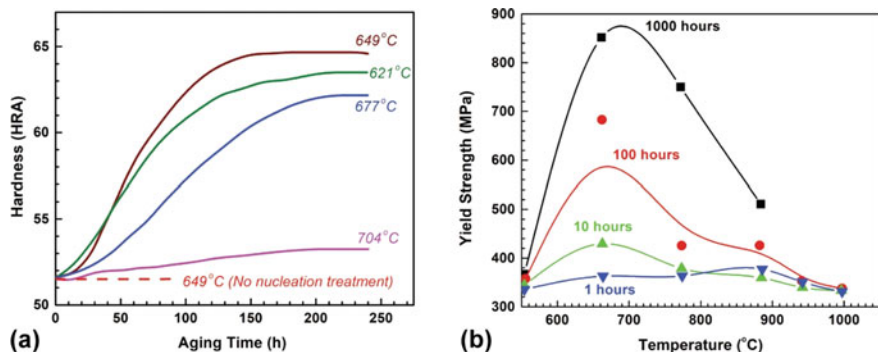


Fig. 4.20 **a** Age hardening response of an Alloy 625 solution treated at 1149 °C for 1 h and a subsequent nucleation treatment at 760 °C for 1 h [69]. **b** Effect of annealing on the yield strength of the alloy at intermediate temperatures for different periods [69]

samples with intermediate annealing increased by about 11 HRA points within 96 h of aging at 649 °C [69]. This difference in the age-hardening response of different size rods is because of the slower cooling rate experienced by the thicker section alloy from the annealing temperature. The slower cooling allows the alloy to dwell more to nucleate γ'' particles in the intermediate temperature range. The nucleation of γ'' particles allow faster growth of subcritical γ'' nuclei permitting their normal, though slow, precipitation during subsequent treatment at about 650 °C. Eiseilstein and Tillack [69] have noted that a time between 2–4 min in the critical temperature range of 760–788 °C is necessary to cause more rapid aging at 649 °C.

The age-hardening response of Alloy 625 is the fastest in a narrow window, around 650 °C, with the highest response within 48 h [69]. Figure 4.20b shows a plot of room temperature yield strength of an Alloy 625 bar subjected to annealing at 1149 °C for 1 h followed by aging treatments at intermediate temperatures for various times up to 1000 h. Age hardening in the temperature range 780–925 °C for about 100 h imparts a minimum yield strength of 414 MPa, while an aging treatment of approximately 10 h is sufficient at about 650 °C. At 650 °C, the age hardening can achieve a minimum yield strength of 552 MPa within 24–48 h [69]. Warm working accelerates the age-hardening response, but the inhomogeneous strain may cause considerable variation in the properties across the cross-section.

Figure 4.21 depicts the tensile properties of Alloy 625 age-hardened at 540, 700 and 850 °C temperatures for periods ranging from 10 to 1200 h. Microstructures of the aged alloys showed the predominant formation of $\text{Ni}_2(\text{Cr},\text{Mo})$, γ'' and δ phases, respectively at 540, 700 and 850 °C [70]. At all the three aging temperatures, the room temperature yield and ultimate tensile strengths increased with aging time and a concomitant decrease in ductility, albeit with different trends at the three temperatures. Interestingly, increase in the strength was maximum at 540 °C and least at 850 °C. The alloy aged at 540 °C exhibited more ductility than those aged at 700 and 850 °C. Moreover, unlike the monotonous decrease in the ductility of alloys aged up to 1200 h at 700 and 850 °C, the alloy's ductility at 540 °C increased

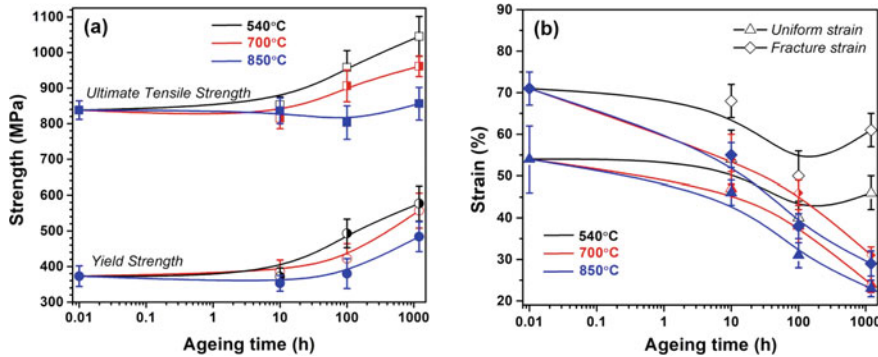


Fig. 4.21 Variation in the tensile properties of Alloy 625 with ageing time: **a** yield and ultimate tensile strength; **b** Uniform and fracture strain [70]

after aging for 1200 h, apparently due to growth and coarsening of precipitates. This behavior of the alloy indicates that the precipitation of the $\text{Ni}_2(\text{Cr},\text{Mo})$ phase is most effective in increasing the alloy's strength, while the formation of δ phases particles is the least.

Chakravarthy et al. [71] have studied the tensile behavior of the alloy as a function of microstructure developed during service exposure for prolonged periods. These studies were carried out over a temperature range from room temperature to 700 °C. Figure 4.22 shows three microstructures of the alloy developed along with a 12 m long tube service exposed at temperatures over a range of about 600 to 750 °C for a prolonged period. The three microstructures, respectively contained: (1) a uniform distribution of fine precipitates of γ'' as well as $\text{Ni}_2(\text{Cr},\text{Mo})$ phases in comparable volume fractions (Fig. 4.22a); (2) coarse γ'' particles distributed uniformly within the γ matrix (Fig. 4.22b); (3) very coarse γ'' particles (Fig. 4.22c) along with δ particles predominantly at grain boundaries (Fig. 4.22d). The three microstructures were designated as Top, Middle and Bottom, respectively according to regions of the tube in which they formed. A detailed description of the development of this microstructure is given later in Sect. 8.6.1 of Chap. 8.

All microstructures showed uniform distribution of three variants of the γ'' phase and six variants of the $\text{Ni}_2(\text{Cr},\text{Mo})$ phase precipitates (only in Fig. 4.22a). Table 4.5 shows the average size of the γ'' and $\text{Ni}_2(\text{Cr},\text{Mo})$ phase particles in the three samples. Particles of both the phases maintained coherency with the matrix even when they grew to large sizes. Precipitation of these phases significantly increased the alloy's yield and ultimate tensile strengths with an enormous reduction in the attendant ductility and impact toughness compared to the alloy in solution annealed condition.

Figure 4.23 shows the flow stress behavior of this service exposed alloy at different test temperatures. The Top samples showed a much larger elongation, particularly at 25 and 300 °C temperatures, than those in the Middle and Bottom samples. The Bottom specimens exhibited the lowest properties in terms of both strength and

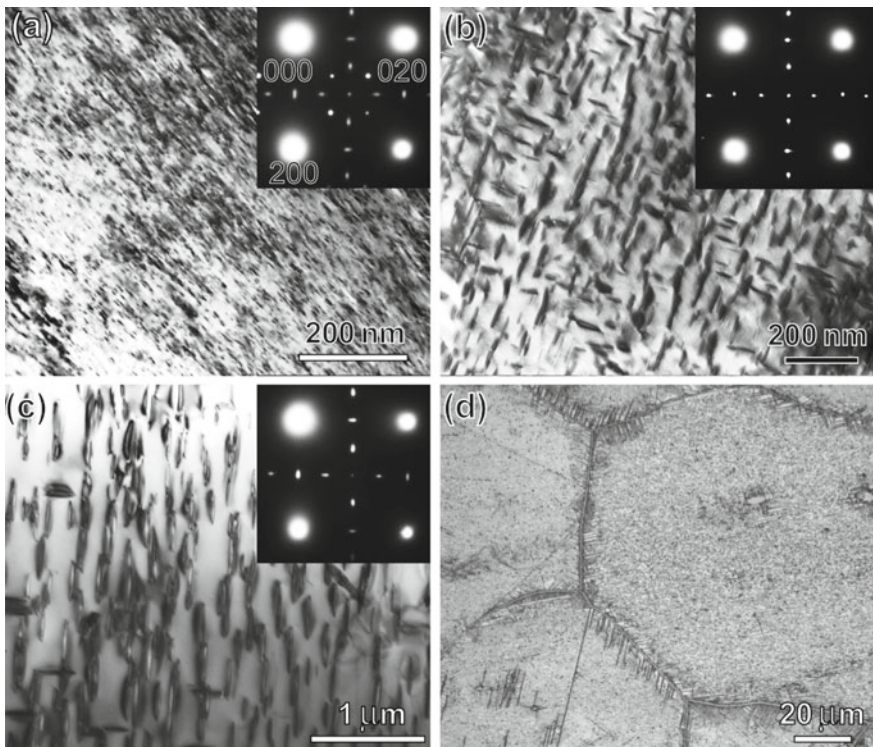


Fig. 4.22 Microstructures of the service aged samples. **a–c** TEM micrographs of Top, Middle and Bottom samples showing the formation of γ'' and $\text{Ni}_2(\text{Cr},\text{Mo})$ (only in Top sample) phase particles in the three microstructures and corresponding electron diffraction patterns in their insets. **d** Optical micrograph of the Bottom sample showing the formation of δ phase particles along grain boundaries. Reprinted from Ref. [72], Copyright (2013), with permission from Elsevier

elongation. Variations in tensile properties of the three samples, as a function of the test temperature, are shown in Fig. 4.24. While the UTS of Bottom and Middle specimens showed similar trends of slight increase with test temperature up to 600 °C followed by a sharp drop, the Top specimens showed a slight decrease up to about 450 °C before its sharp drop. In general, the YS of all the samples showed a decreasing trend with increasing test temperature except in the temperature range 300–550 °C where it showed either a plateau or a slight increase within the temperature range. However, the ductility first improved gradually with temperature, followed by a rapid rise for all the samples. The Top sample showed a much higher elongation, particularly at 25 and 300 °C, than Bottom and Middle specimens. The Bottom specimen showed the lowest properties in terms of both strength and elongation.

The three samples exhibited relatively low Charpy impact energies, in the range of 10–40 J, at room and 300 °C temperatures compared to a typical value of about 110–150 J for the virgin wrought Alloy 625 [47]. Thomas and Tait [73] reported similar low impact values for superheaters tubes of Alloy 625 service exposed at

Table 4.4 Nominal room temperature mechanical properties of Alloy 625 in different product forms and thermal conditions [47]

Alloy product and condition	Yield strength ^a (MPa)	Ultimate tensile strength (MPa)	Ductility (%)		Brinell hardness (BHN)
			Elongation	Area reduction	
<i>Rod, Bar, Plate</i>					
As-rolled	414–758	827–1103	60–30	60–40	175–240
Annealed	414–655	827–1034	60–30	60–40	145–220
Solution annealed	290–414	724–896	65–40	90–60	116–194
<i>Sheet and strip</i>					
Annealed	414–621	827–1034	55–30	-	145–240
<i>Cold-drawn tube and pipe</i>					
Annealed	414–517	827–965	55–30	-	-
Solution annealed	276–414	689–827	60–40	-	-

^a0.2% offset value

Table 4.5 Average size of particles in Top, Middle and Bottom samples shown in Fig.4.22 [71]

Sample	γ'' particles	Ni ₂ (Cr,Mo) particles
Top	13 ± 21.8 nm	20.2 ± 25 nm
Middle	38.9 ± 65.6 nm	-
Bottom	206.7 ± 177 nm	-

temperatures between 480 and 560 °C. The service exposed alloys also exhibited very low resistance to crack propagation, particularly in the Bottom samples as reflected in its very low fracture toughness, K_{IC} , (in the range 35–40 MPa \sqrt{m}) for the fatigue pre-cracked sample at room temperature. However, the K_{IC} value recovered to about 140 MPa \sqrt{m} at 600 °C.

The plastic flow in the temperature range 250–550 °C exhibits a plateau or an increase in the yield strength due to the dynamic strain aging (DSA) [56]. The flow behavior in this temperature range is characterized by serrated plastic flow. The alloy exhibits a transition from a normal to an inverse PLC behavior at a temperature above 350 °C. Deformation microstructure of the Top samples showed shearing of precipitates due to the passage of dislocation pairs (Fig. 4.25a) in the normal PLC regime and a high density of shear bands in the inverse PLC regime (Fig. 4.25b). On the other hand, deformation microstructure of Middle and Bottom samples showed similar features comprising shear bands with a high density of dislocations (Fig. 4.25c) and twinning (Fig. 4.25d) in the inverse PLC regime.

The change in the deformation mechanism from shearing in the Top samples to twinning in the Bottom samples appears to result from the difference in their microstructure. The Top samples contained very fine particles of γ'' and Ni₂(Cr,Mo)

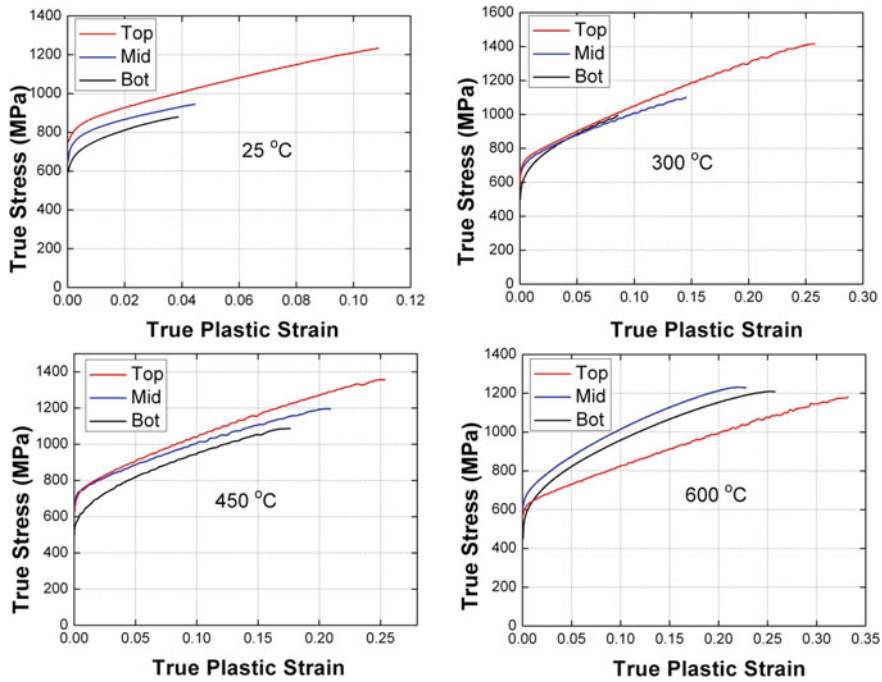


Fig. 4.23 True stress versus true plastic strain plots of Top, Middle (Mid) and Bottom (Bot) samples at 25, 300, 450 and 600 °C test temperatures. Reprinted from Ref. [72], Copyright (2013), with permission from Elsevier

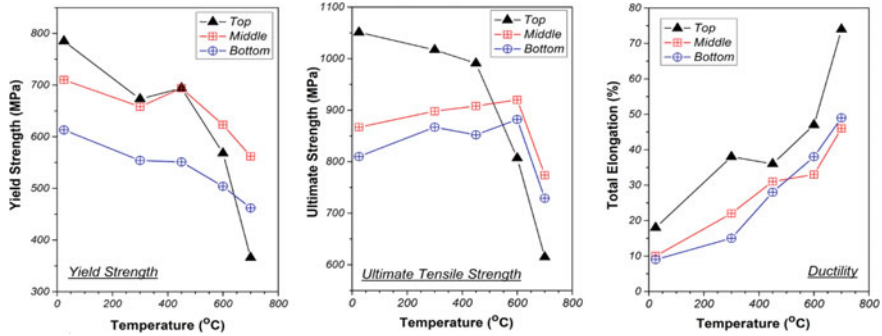


Fig. 4.24 Tensile behaviour of Top, Middle and Bottom samples as a function of the test temperature

phases, while the Middle and Bottom samples both contained coarse particles of the γ'' phase in the matrix. As noted in Sect. 4.2, alloys containing γ'' and $\text{Ni}_2(\text{Cr},\text{Mo})$ phase particles exhibit a transition in the deformation mode from slip to twinning above a critical precipitate size. Independent studies on the deformation behavior of Inconel 718 by Sundararaman et al. [12] and on Haynes 242 alloy by Kumar

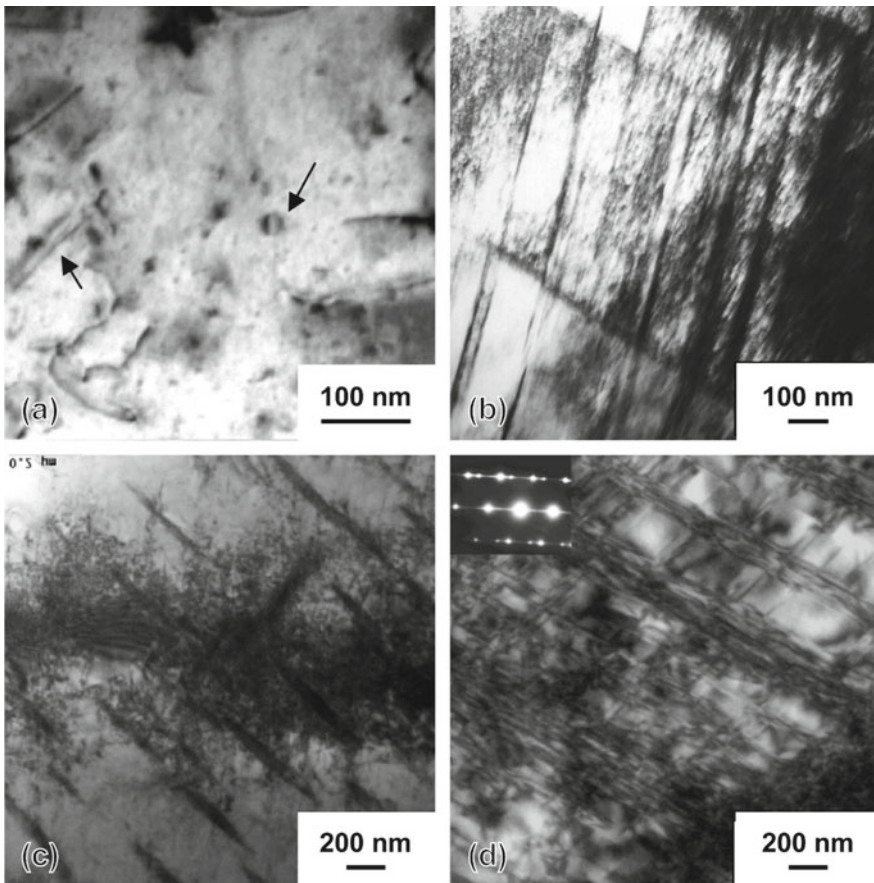


Fig. 4.25 Deformation microstructures of service aged alloys in different PLC regimes. **a** shows pairs of dislocations and **b** heavy shearing in Top samples in normal and inverse PLC regimes, respectively. **c, d** samples show heavy deformation by twinning in Bottom samples in the inverse PLC regime. Inset in **(d)** shows an electron diffraction pattern from twins in the region. Reprinted by permission from Springer Ref. [56]. Copyright (2015)

and Vasudevan [38] have shown that the two alloys exhibit a transition from shear to the twinning mode when the sizes of γ'' and $\text{Ni}_2(\text{Cr},\text{Mo})$ particles in the two alloys are above 10 nm and 70 nm, respectively. Indeed, the critical size of the particle would be a function of many factors like anti-phase boundary energy, shear modulus, stacking fault energy, etc., which are directly related to the composition of the phase. The composition (in atomic per cent) of the $\text{Ni}_2(\text{Cr},\text{Mo})$ in the Top sample was Ni-22%Cr-10.5%Mo-3%Fe-1.4%Nb, while that of the γ'' precipitates in the Middle samples was Ni-9%Nb-8%Mo-5.6%Cr-1.5%Ti-1%Al-0.9%Fe [74]. The composition of the $\text{Ni}_2(\text{Cr},\text{Mo})$ phase is very close to that in Haynes 242 alloy studied by Kumar and Vasudevan [38]. Therefore, the critical size of the $\text{Ni}_2(\text{Cr},\text{Mo})$

precipitates in Alloy 625 can also be assumed to be 70 nm. However, the composition of the γ'' phase particles in Alloy 718 contain about 19% niobium [75], significantly different from its composition in Alloy 625. This difference in the composition of the γ'' phase in Alloy 625 and 718 would affect stacking fault energy of the γ'' phase in the two alloys. Such a difference in the stacking fault energy of the γ'' phase was suggested by Sundararaman [49] who reported the formation of profuse faults and twins within γ'' phase particles in Alloy 718 and very few in γ'' phase of Alloy 625. A difference in the stacking fault energy of the γ'' phase particles in the two alloys would affect their critical size in the two alloys above which their deformation mode would change from shearing to twinning. This change in the critical size agrees with the deformation microstructure of an Alloy 625 (aged for 200 h at 650 °C), subjected to 29% deformation [49]. The aged alloy contained γ'' particles of about 60 nm diameter (Fig. 4.26). The deformation microstructure exhibited the formation of extensive deformation bands containing a high density of dislocations due to the slip activity. Dark-field transmission electron microscopy imaging revealed the presence of very few γ'' particles within the bands (Fig. 4.26c),

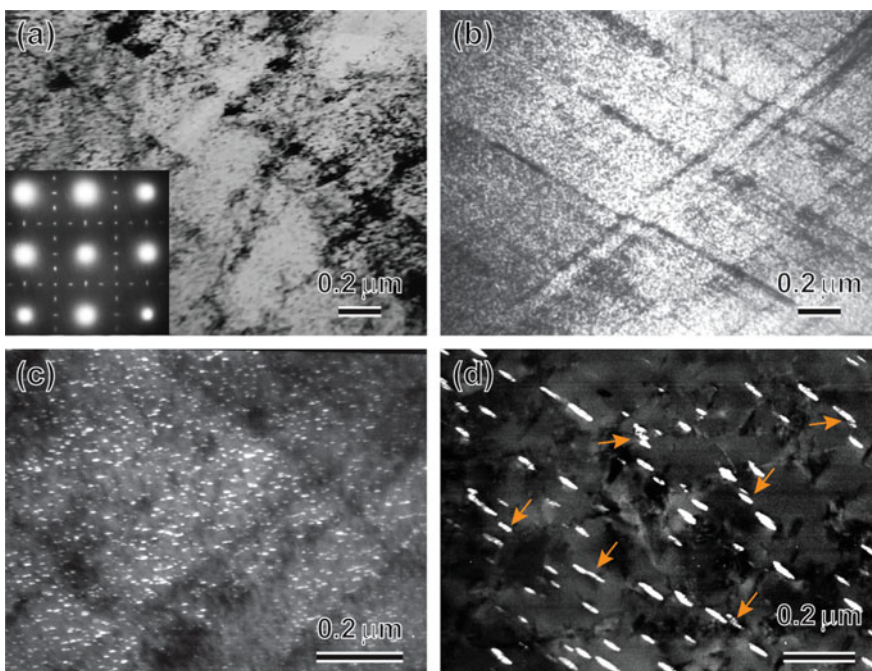


Fig. 4.26 Deformation microstructure of an Alloy 625 aged at 650 °C for 200 h showing deformation by shearing [49]. **a, b**, Respectively are bright field and dark field TEM micrographs of a deformed region. Inset in (a) shows an electron diffraction pattern showing superlattice reflections of the γ'' particles. **c** Shows near absence of γ'' particles within deformation bands with heavy deformation. **d** A high magnification image of sheared γ'' particles. Reprinted from Ref. [49] by permission from Dr. M. Sundararaman

which indicated that the deformation within the band sheared particles to such an extent that either their order was nearly destroyed or their orientation was changed that they did not image in the dark-field mode (Fig. 4.26d).

4.5.3 Work-Hardening Behavior

The flow stress of a material can be correlated with strain hardening parameter, n , by the Crussard – Jaoul formulation, given by [76]:

$$\sigma_t = \sigma_0 + k \varepsilon_t^n \quad (4.17)$$

where σ_t and ε_t are true stress and true plastic strain, respectively, σ_0 is the true stress at $\varepsilon_t = 0$ and k is a constant.

In their studies, both Sundararaman et al. [12] and Kumar and Vasudevan [38] have correlated the dominant deformation mechanisms with n . They have shown that the shearing of precipitates by dislocations is accompanied by a high value of n (~0.85–0.95).

In contrast, a change in the deformation mechanism from shearing to the twinning of particles above the critical size is accompanied by a significant drop in the value of n (<0.57). This is because the passage of deformation by twinning through large precipitates is controlled by the nucleation of twins, which occurs at a stress value higher than that required for their growth. Therefore, nucleation of twins is immediately followed by a “burst” of flow resulting in the easy propagation of deformation twins across the precipitates (Sect. 4.4).

Table 4.6 Work-hardening parameters obtained by fitting flow stress curves to the Crussard and Jaoul's formulation

		25 °C	300 °C	450 °C	600 °C
Top sample	σ_0 (MPa)	808	700	713	597
	K (MPa)	2325	2142	1908	1415
	n	0.761	0.785	0.761	0.788
Middle sample	σ_0 (MPa)	708	682	702	600
	K (MPa)	1118	1650	1537	1517
	n	0.499	0.707	0.707	0.564
Bottom sample	σ_0 (MPa)	569	537	528	480
	K (MPa)	1070	1492	1445	1469
	n	0.379	0.485	0.535	0.486
Solution treated	σ_0 (MPa)	423			
	K (MPa)	1305			
	n	0.792			

Singh et al. [72] have analyzed the work-hardening behavior of service aged samples shown in Fig. 4.22. Table 4.6 gives the values of σ_0 , k and n obtained by fitting the flow curves in Fig. 4.23 to Eq. 4.17. The Top specimens showed a much higher value of n than that in Middle and Bottom samples, except for the values at 300 and 450 °C temperatures for the Middle sample. The values of n indicate that the Top samples were sheared by the passage of dislocations across particles, while Middle and Bottom samples were sheared by deformation twinning. Interestingly, n for the Top sample at room temperature was close to solution-treated alloy (Table 4.6). A drop in the value of n to about 0.57 in Middle and Bottom samples indicated a transition of the deformation mechanism from the shearing of particles by dislocations to particle twinning. The low value of n also ruled out particle bypassing as the mechanism in these samples because it is always accompanied by an abrupt increase in the work-hardening rate because of the accumulation of geometrically necessary dislocations in the vicinity of particles [77, 78]. The values of n are consistent with the deformation microstructures of the three samples (Fig. 4.25). In addition, they agree with those reported by Sundararaman et al. [12] for Alloy 718 and by Kumar and Vasudevan [38] for Haynes 242.

4.6 Fatigue Behavior of Alloy 625

Fatigue in materials may be defined as progressive, localized, permanent microstructural damage occurring under cyclic stresses and strains arising due to thermal or mechanical loading conditions. The fatigue process is believed to begin at internal or surface flaws where stresses are concentrated and the initial shear is along slip planes. The repetitive tensile and compressive loading cycles generate slip intrusions and extrusions at which cracks nucleate. A crack may initially propagate along one of the original slip planes but may turn to propagate transversely to the principal normal stress (Fig. 4.27). Growth of the crack to the critical size may cause fracture after a certain number of cycles. The path to failure of a material under fatigue conditions may, therefore, be divided into the following processes [79]: (1) crack initiation due to the early development of fatigue damage; (2) slip band crack growth due to deepening of the initial crack on planes of high shear stress; (3) crack growth on planes of high stress in a direction normal to the maximum tensile stress; and, (4) failure, when the crack grows to a length beyond which the cross-section cannot support the applied load.

$S-N$ diagrams are the simplest way to express the fatigue behavior of materials. An $S-N$ diagram depicts the number of cycles (N) required to fail a specimen at a constant cyclic stress amplitude (S) (Fig. 4.28). The number of cycles to failure at a given stress amplitude is known as fatigue life at that stress amplitude level. In contrast, the minimum stress amplitude that can fail the material for a given number of cycles represents its fatigue strength. The value of the S decreases with increasing N and tend to flatten out eventually to a stress level below which failure does not occur. This stress level is termed as fatigue “endurance limit” or simply “fatigue limit”

Fig. 4.27 Crack initiation and propagation under fatigue loading

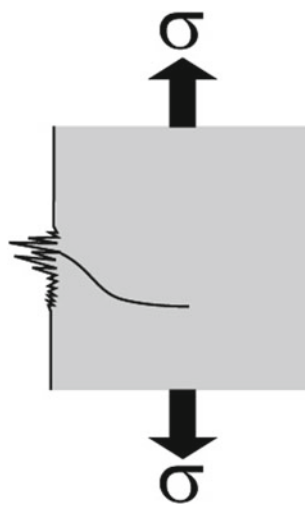
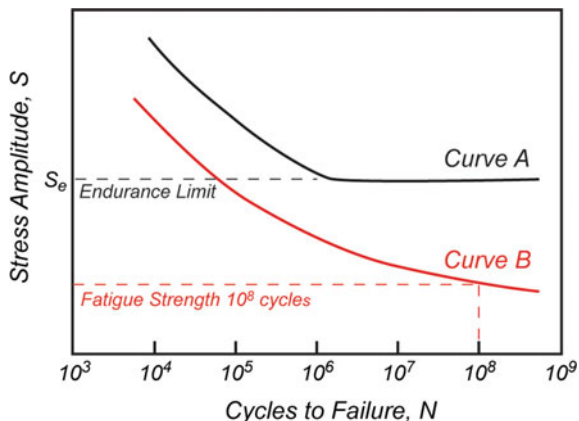


Fig. 4.28 Typical $S-N$ curves for materials with and without endurance limit



of the material. Certain materials, like carbon steels and titanium, have a fatigue limit below which they do not fail and can be cycled infinitely (Curve A). However, many non-ferrous metals and alloys, like aluminum, copper and magnesium alloys, do not exhibit well-defined endurance limits. These materials, instead, display a continuously decreasing $S-N$ response (Curve B). However, a practical endurance limit may be defined, typically at 10^8 cycles (Fig. 4.28).

Factors like mean stress, specimen temperature, surface roughness and stress concentration significantly affect the fatigue life [80]. Stress concentration affects fatigue strength too. Stress concentrations may arise due to a change in the configuration of a component, surface discontinuities like scratches and notches or inherent metallurgical discontinuities like inclusions and micro cracks. An increase in the surface area increases the probability of fatigue crack initiation.

The fatigue loading conditions may involve a combination of tensile and compressive stresses to impose a completely reversed cycle with a zero mean stress value (Fig. 4.29a). However, the loading cycles are often repeated between a maximum stress, σ_{\max} , and a minimum stress, σ_{\min} , with a non-zero mean stress, σ_m ($= (\sigma_{\max} + \sigma_{\min})/2$), and a stress ratio R given by $\sigma_{\min}/\sigma_{\max}$ (Fig. 4.29b). For a fully reversed loading cycle, $R = -1$. The R -value strongly affects the fatigue life of a material, which decreases with increasing mean stress [1]. Figure 4.29b also illustrates that the maximum and the minimum stresses can be both tension or compression in nature. In practical situations, a stress cycle may be rather complicated, which can be approximated to a sinusoidal cycle superimposed on a mean stress.

Fatigue can be classified into high-cycle fatigue (HCF) and low-cycle fatigue (LCF) depending upon the number of stress cycles to failure being more than or less than 10^4 cycles. In principle, there is no fundamental differences between the mechanisms of the two processes as the $S-N$ curves for the two processes are similar. However, the important distinction between the two comes from the dominant part of the fatigue life spent in the damage process. In HCF, most of the fatigue life is spent in the initiation of cracks, whereas most of the fatigue life in LCF is spent in the crack propagation. In LCF, cracks may nucleate within 3–10% of the fatigue life [80]. The LCF condition is of more concern because the failures occur at relatively high stresses and a low number of cycles. It is characterized by a high plastic strain that fails the sample within about 10^4 cycles. Moreover, the HCF exposure is usually accommodated during the design of a component itself. The LCF loadings in a plant may arise from the fluctuating workload due to power transients and temperature-gradient induced thermal strain during its operation and start-ups and shut-downs. The low-cycle fatigue failure considerations are essential in designing critical components like nuclear pressure vessels, steam turbines, and other power machinery.

Figure 4.30 shows the fatigue behavior of Alloy 625 as a function of stress concentration and temperature [80]. An increase in temperature reduces its fatigue limit as

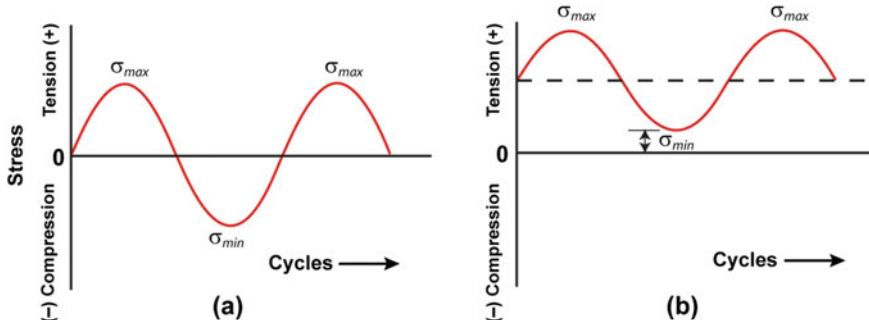
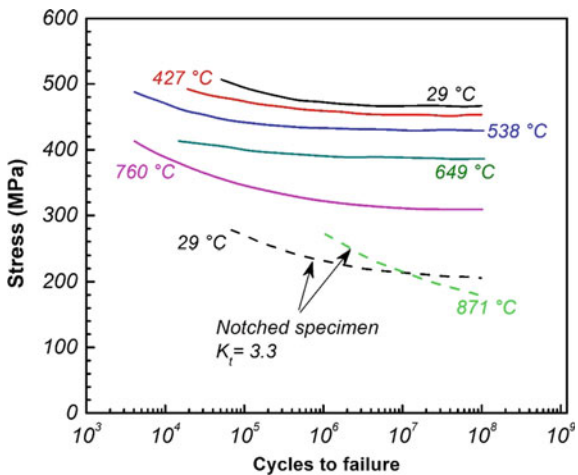


Fig. 4.29 Typical fatigue stress cycles under **a** reversed stress loading and **b** repeated stress loading [1]

Fig. 4.30 $S-N$ curves of Alloy 625 subjected to fatigue at different temperatures [80]



well as fatigue strength. The presence of a notch further reduces fatigue limit of the alloy significantly.

As the LCF involves cyclic plasticity, the material may respond by hardening or softening under cyclic loads when the strain amplitude is changed at a given temperature. The hardening or softening would cause an increase or decrease in the stress amplitude, respectively. In general, under strain-controlled conditions, an alloy subjected to a cyclic stress response (CSR) test initially hardens during early fatigue cycles. Still, it may reach a period of either cyclic saturation or cyclic softening later, depending upon the microstructure, temperature and total strain range. Well annealed polycrystalline metals of high purity usually show cyclic hardening due to dislocation multiplication. At the same time, work-hardened materials undergo cyclic softening due to rearrangement of pre-strain induced dislocation networks with the fatigue cycles [1].

Bashir et al. [81] have shown a continuous hardening before failure and a decrease in the fatigue life with increasing temperature in cast Alloy 625 subjected to LCF at room and elevated temperatures (Fig. 4.31). Suave et al. [82] have subjected Alloy 625 to fully reversed, strain-controlled stress cycles of 0.5 Hz frequency at 600 °C to study the effect of the precipitation of the γ'' phase particles on LCF behavior of the alloy at elevated temperatures (Fig. 4.32). They have studied this behavior at 0.29, 0.34 and 0.36% strain amplitudes. The alloy exhibited limited cyclic hardening for about initial 10 cycles at all three strain amplitudes. For about 10–300 cycles, the alloy exhibited a plateau followed by significant secondary hardening up to the final failure after a strain amplitude of about 0.35%. The initial hardening of the alloy can be attributed to dislocation multiplication and accumulation within the slip band. In contrast, the secondary hardening has been attributed to the faster formation of the γ'' phase particles observed under cycling at the test temperatures. Suave et al. [82] have shown that the kinetics of the formation of the γ'' phase is dependent on the applied strain amplitude. The LCF enhances precipitation kinetics due to the accumulation

Fig. 4.31 Effect of temperature on the cyclic stress response of Alloy 625 at 0.4% strain amplitude [81]

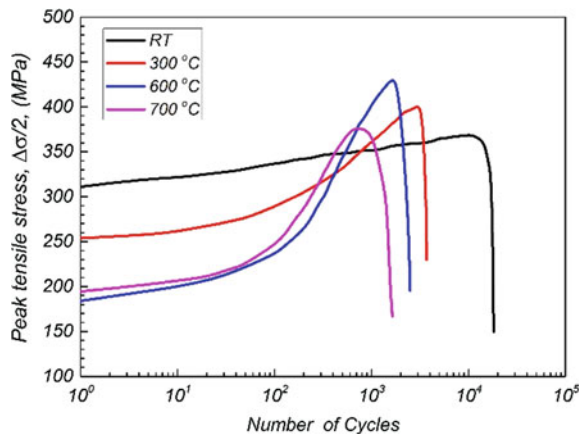
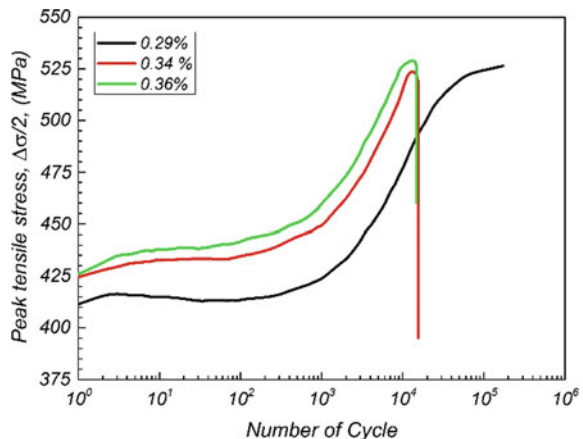


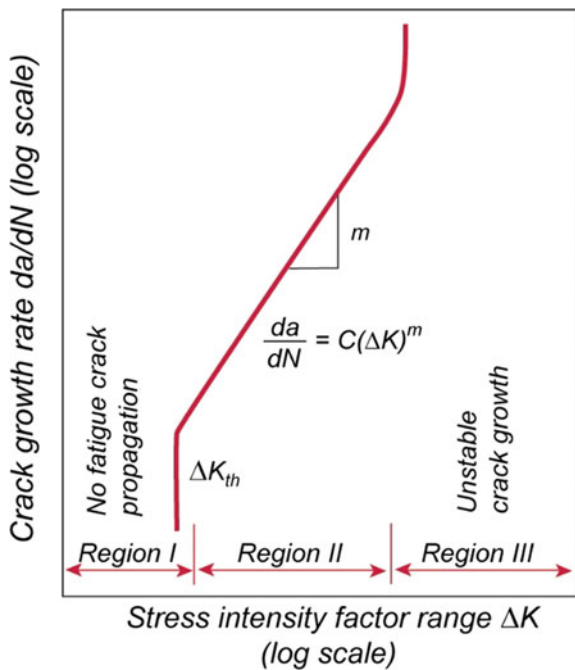
Fig. 4.32 Cyclic stress response of Alloy 625 at 600 °C under fully reversed strain-controlled mode [82]



of plastic strain, which provides numerous sites for nucleating γ'' particles and faster diffusion than that in pure thermal exposure. For instance, the δ particles formed after LCF cycling were bigger than those formed after pure thermal aging of 2000 h at 650 °C. The enhanced kinetics of the γ'' to δ transformation is attributed to extensive deformation induced during LCF. The drastic decrease in CSR after the secondary hardening could be attributed to the catastrophic propagation of microcracks under the applied load.

The flaw tolerance behavior of an alloy under cyclic loading conditions can be understood from the crack growth rate, which is a function of: (1) the stress intensity factor range, $\Delta K = K_{\max} - K_{\min}$; (2) the stress ratio, $R = K_{\min}/K_{\max}$ ($=\sigma_{\min}/\sigma_{\max}$); and (3) history of stress in the material, where K_{\max} and K_{\min} refer to the maximum and minimum stress intensities for each cycle. Figure 4.33 shows the relationship between fatigue crack growth rate and ΔK . The curve follows a sigmoidal behavior, divided into three regions. In region I, when ΔK is small, the crack growth rate is low or below

Fig. 4.33 Schematic diagram showing the primary fracture mechanisms associated with the sigmoidal variation of fatigue crack propagation rate (da/dN) with alternating stress intensity (ΔK)



the threshold crack growth region. In this region, the crack propagation depends on the material's microstructure, flow properties, and environmentally induced fracture modes.

For intermediate magnitudes of ΔK (region II), the crack growth rate is governed by a power-law relationship given by [83],

$$\frac{da}{dN} = C\Delta K^m \quad (4.18)$$

where C and m are assumed to be material constants, da/dN is the fatigue crack growth rate per cycle. In region II, the crack growth is stable and follows a linear relationship between $\log da/dN$ and $\log \Delta K$ and is commonly known as the Paris' Law [83]. The crack growth rate is largely insensitive to the microstructure and the stress ratio R [84, 85]. The failure generally occurs by a transgranular ductile striation mechanism [86]. In region III, at very high values of ΔK , the striation growth of crack is replaced by a high crack growth rate till the fracture occurs [84, 86, 87]. The superimposition of multiple static damage mechanisms, like cleavage, intergranular and microvoid coalescence, accelerate the crack growth rate. This behavior of fracture is somewhat sensitive to microstructure and flow properties of the material.

Figure 4.34 illustrates the difference between regions II and III of the fatigue fractur in an Alloy 625 sample [88]. Figure 4.34a shows the surface corresponding to region II characterized by fatigue striations formed during the stable crack growth.

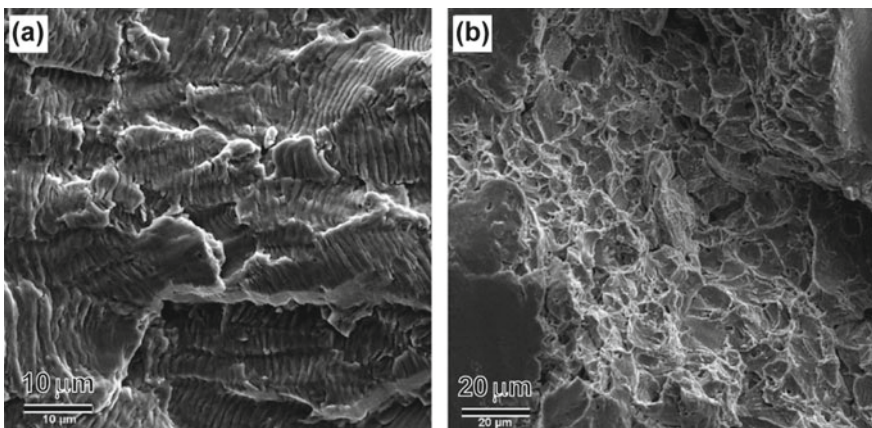


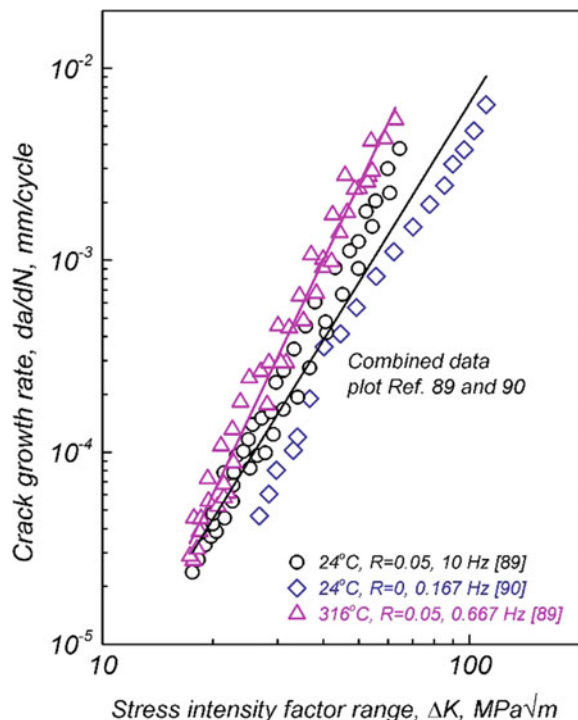
Fig. 4.34 Fractographs of a fatigue fractured Alloy 625 sample failed after 1,10,067 cycles under maximum stress of 472 MPa: **a** fractured surface characterized by the propagation of stable crack growth (region II); **b** fractured surface characterized by accelerated crack growth in region III. Reprinted from open-source Ref. [88] under the terms of Creative Commons CC by license

Striations are formed due to the opening and blunting of the crack with the progression of the fatigue cycle. Each time the crack is opened by a stress cycle, the crack's tip deforms plastically and blunts the region that appears as a striation on the ruptured surface. Figure 4.34b shows the fatigue fractured surface corresponding to region III, characterized by the coalescence of microvoids, and the sample failed by intergranular cleavage when it could no longer sustain the load.

James [89, 90] has studied the fatigue crack propagation behavior in Alloy 625 and compared it with that in Alloy 600 and Alloy 718 over the temperature range of 24–703 °C [91–93]. He has shown that the fatigue crack propagation rate increases with increasing temperature (Fig. 4.35). Most alloys exhibit similar behavior. Figure 4.36 shows da/dN vs ΔK plots of the Alloy 625 at different temperatures and compared with the results of Alloy 600 and Alloy 718 for comparison [92, 93]. James [89] has also studied the effect of the stress ratio, R , on the crack propagation rate in the stress ratio range $0.05 < R < 0.667$. Although the slope of all the plots is nearly parallel for different stress ratios (Fig. 4.37), an increase in the fatigue crack propagation rate with increasing stress ratio is observed. Still, the effect diminishes at higher values of R . This has been attributed to the decreasing influence of crack closure with an increase in the stress ratio [94]

Long [95] has studied the fatigue crack growth rate in welded metal in air and artificial seawater (3.5% NaCl solution) (Fig. 4.38). The study has shown that the fatigue crack resistance in Alloy 625 weld metal depends on grain size and its orientation. The resistance to crack growth increases with decreasing grain size in the plane of crack propagation. It also increases when the crack propagates at the transverse direction of the dendritic structure rather than along the dendritic structure (Fig. 4.39). This indicates that finer grain size improves the fatigue crack growth resistance in

Fig. 4.35 Fatigue crack propagation rate in annealed Alloy 625 in air at 24 and 316 °C



Alloy 625. In addition, the crack growth rate under fatigue loading is sensitive to the morphology and volume fraction of second phase particles. The presence of inclusions, like carbide and TCP phase particles and other microstructural abnormalities that restricts the plastic flow, reduces the fatigue life. At such inclusions, cracks may form due to the accumulation of dislocations induced during the cyclic loading.

4.7 Creep Behavior of Alloy 625

Creep is time-dependent plastic deformation at constant load/stress and is a crucial design consideration at high temperatures ($T/T_m > 0.5$), where T_m is the melting point temperature in Kelvin. A creep curve (creep strain vs. time) consists of three distinct regimes caused by two competing factors: hardening due to strain and softening due to recovery. In the primary regime, hardening dominates over recovery and strain rate decreases with time. The hardening process is balanced by a recovery process in the secondary regime, and nearly a constant creep strain rate (or steady-state creep rate) is observed. A general expression for the steady-state creep can be given as a power-law relation between the applied stress (σ) and minimum creep rate ($\dot{\epsilon}_{min}$) as:

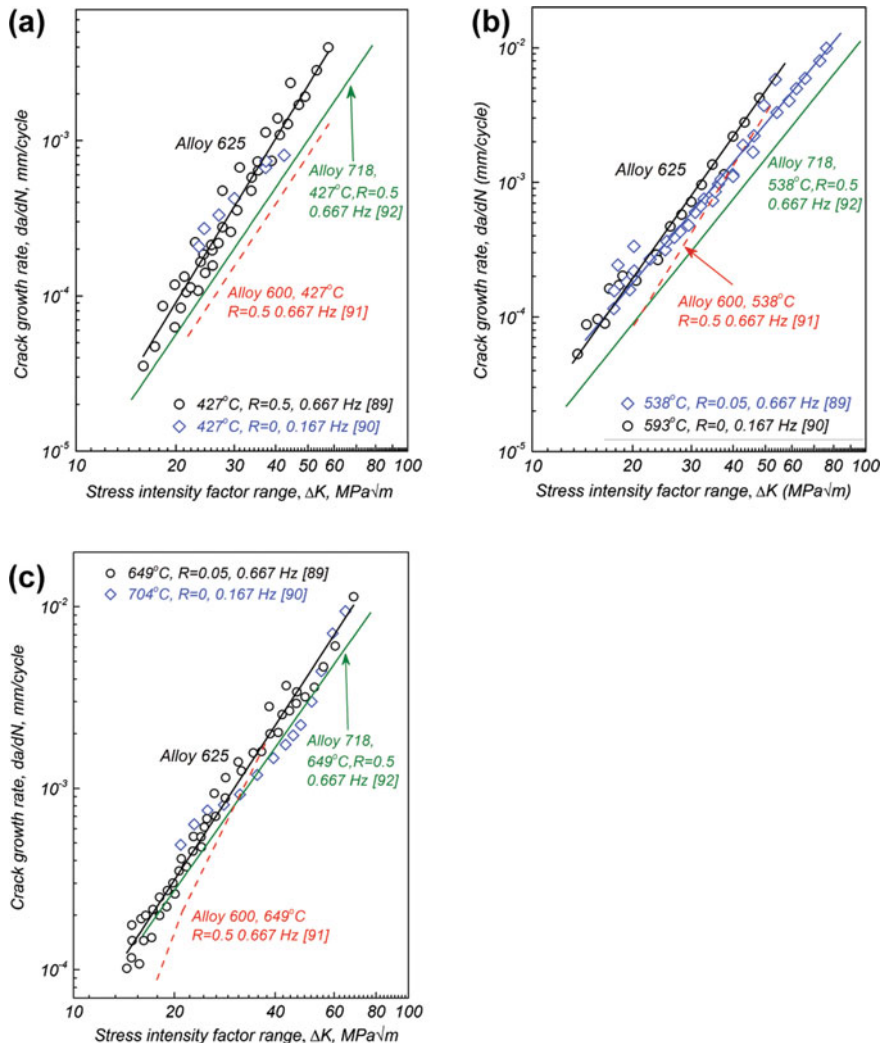


Fig. 4.36 The fatigue crack propagation rate, da/dN , as a function of ΔK in annealed Alloy 625 in air at **a** 427°C , **b** 538 and 593°C and **c** 649 and 704°C [89–91] in comparison to the crack propagation rates in Alloy 600 and Alloy 718 [92, 93]

$$\dot{\epsilon}_{\min} = A\sigma^n \exp\left(\frac{-Q_C}{RT}\right) \quad (4.19)$$

where A is a constant, n is the stress constant, Q_C is the activation energy for creep deformation, R is the universal gas constant, and T is the temperature. Usually, at $T > 0.5T_m$, Q_C corresponds to the activation energy for self-diffusion. The value of n may vary considerably with temperature as creep mechanisms change

Fig. 4.37 The effect of stress ratio R on the crack propagation rate in annealed Alloy 625 fatigue tested in air at 538 °C and 6.67 Hz [90]

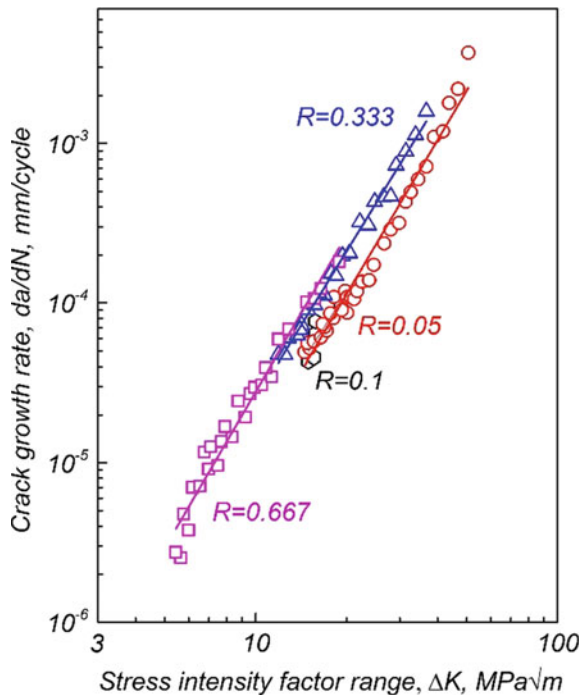


Fig. 4.38 Crack growth resistance curve (da/dN vs. ΔK) of an Alloy 625 plate fatigue tested in air and 3.5%NaCl solution [95]

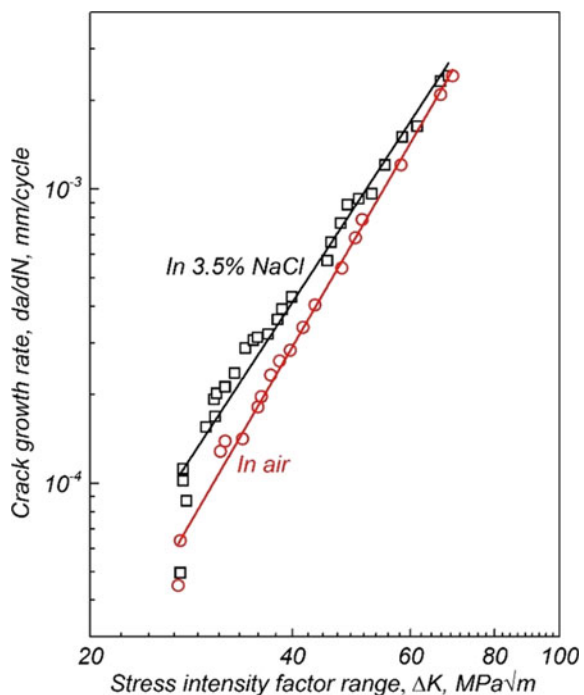
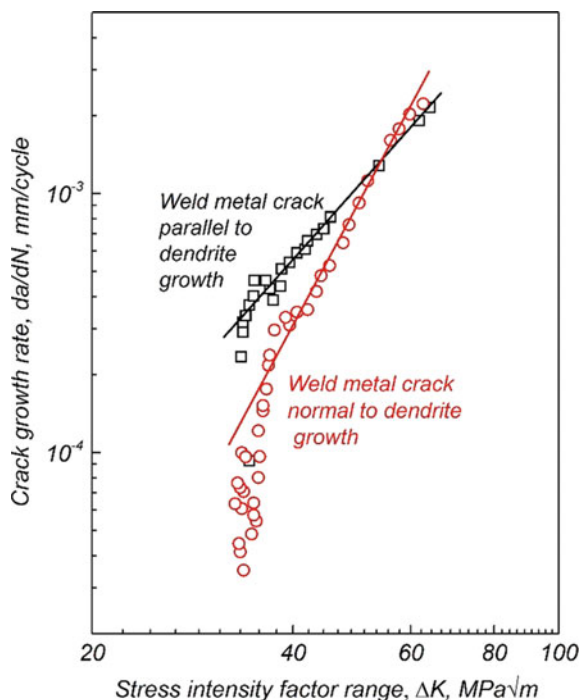


Fig. 4.39 Growth rate (da/dN vs. ΔK) of weld metal cracks parallel and normal to the dendrite growth direction in a welded Alloy 625 metal sample in air [95]



The creep phenomenon can be classified into two broad categories, diffusion creep and dislocation creep, depending upon the controlling mechanism. Diffusion creep involves the migration of atoms and vacancies under the influence of applied stress. It becomes rate-controlling at high temperatures and relatively lower stresses ($\sigma/G < 10^{-4}$, where σ is the applied stress and G is the shear modulus). Diffusion creep can be further classified into two mechanisms: (1) Nabarro-Herring (N–H) creep [96, 97], when the migration of atom is through the crystal lattice; and (2) Coble creep [98] when the migration of atom is through grain boundaries. On the other hand, dislocation creep is controlled by the climb of dislocations and typically follow a power-law behavior between the minimum creep rate and the applied stress. Dislocation creep may start at $T > 0.4T_m$ and at intermediate to high stresses ($10^{-4} < \sigma/G < 10^{-2}$). At higher stresses ($\sigma/G > 10^{-2}$), the power-law breaks down due to the transition from dislocation climb controlled to dislocation glide-controlled process.

Limited work is reported on the creep behavior of Alloy 625. Mathew et al. [99] have studied the creep behavior of a service exposed Alloy 625 after subjecting it to a solution annealing treatment. These studies were over the temperature range 600–950 °C at stresses ranging from 50 to 290 MPa. The creep damage in Alloy 625 occurs predominantly in the form of microstructural changes rather than the mechanical damage in the form of cracks and cavities. The rate-controlling deformation mechanism is dislocation creep.

Typical creep curves obtained at a stress level of 105 MPa at 760, 800 and 815 °C are shown in Fig. 4.40. However, Alloy 625 exhibits a two-slope behavior with a slope change at temperatures around 800 °C, around which formation of the δ-phase dominates. Figure 4.41 shows an iso-stress plot of the rupture life versus temperature at 105 MPa with a change in the slope at 802 °C [99]. The alloy also exhibits a minimum rupture elongation at around 777 °C for all the stress and temperature test conditions (Fig. 4.42). The rupture ductility exhibits a minimum with 10 and 20% at around 777 °C, after which it increases significantly to reach a value as high as 65% at 875 °C. This minimum in the rupture ductility is observed around the same temperature at which the iso-stress plot of temperature versus rupture life showed a change in the slope (Fig. 4.41).

This behavior of the rupture ductility is related to the precipitation behavior of γ'' and δ phases. The γ'' precipitation occurs below 727 °C and above this temperature

Fig. 4.40 Typical creep curves of solution annealed alloy obtained at a stress of 105 MPa [99]

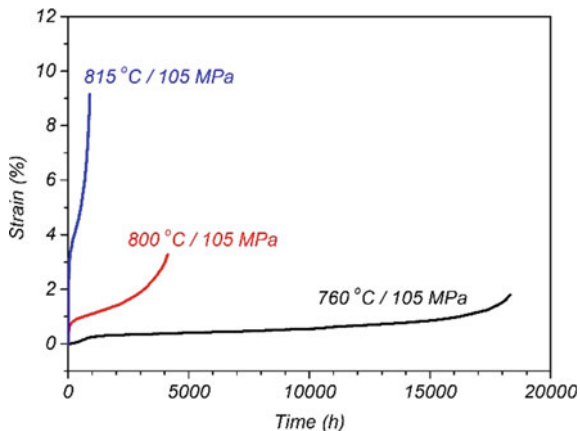


Fig. 4.41 Iso-stress plots of the alloy in solution annealed condition [99]

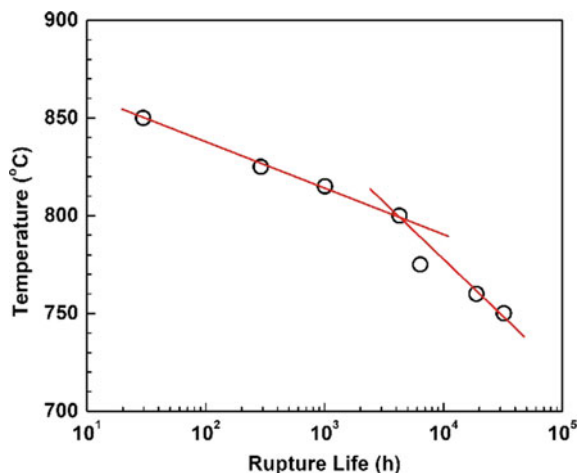
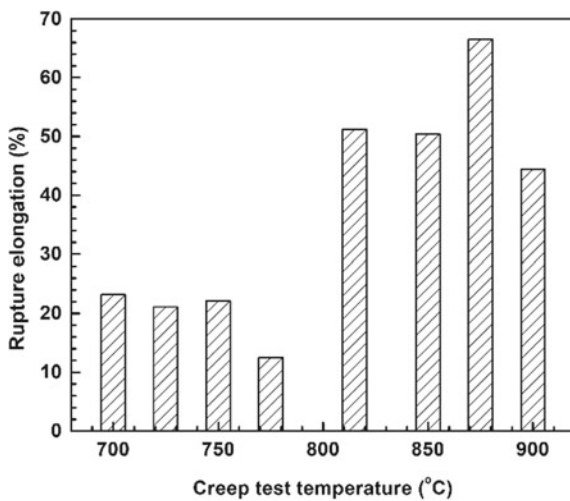


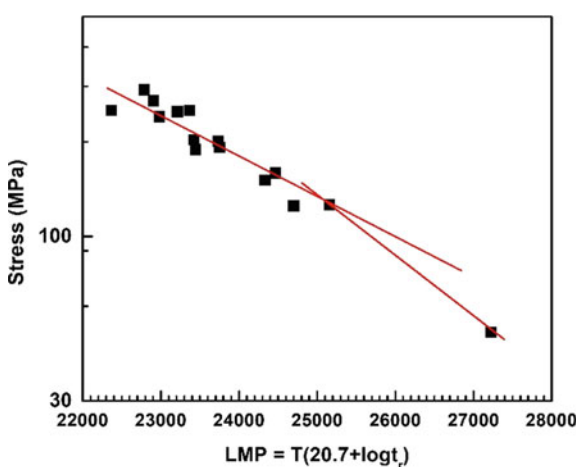
Fig. 4.42 Plots showing the rupture ductility as a function of test temperature [99]



transforms to the δ phase. The size and morphology of the δ -phase particles increases with an increase in temperature. The γ'' phase fully dissolves in the matrix at high temperatures. The temperature range of precipitation of the γ'' phase and its transformation to the δ phase also depend on the duration of aging. In addition, it is a function of applied stress as it controls the rate at which defects are created, which in turn helps in diffusional transformations. The alloy exhibits a peak in the hardness and tensile strength at round 727 °C. Above 727 °C, both hardness and tensile strength decrease with an increase in aging temperature due to γ'' particle coarsening and the δ phase precipitation [100] (Sect. 4.5.2).

Figure 4.43 compares the rupture life of the solution annealed alloy with that of the

Fig. 4.43 LMP data of the solution annealed alloy [99] superimposed on the LMP plot of the virgin annealed alloy [47]



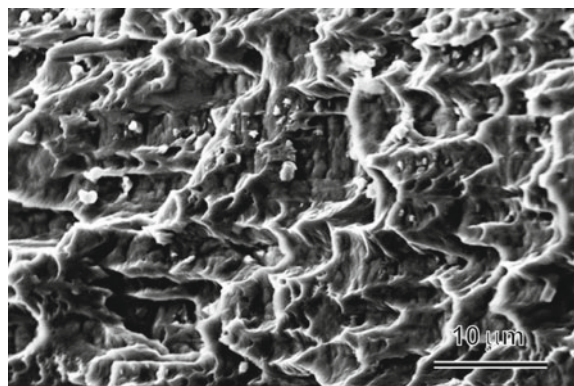
virgin alloy (in annealed condition) using the Larson–Miller parameter (LMP) relationship. A value of 20.7 has been used for the constant C in the LMP equation [101], $LMP = T(C + \log t_r)$, where t_r is the rupture life in hours, and T is the test temperature in Kelvin. The solid line in Fig. 4.43 represents the stress versus LMP plot of the virgin alloy plotted using Alloy 625 datasheet of the Special Metals Corporation, USA [47]. The experimental data of the solution annealed service exposed material is shown separately. The creep data of the solution annealed service exposed material falls within a scatter band of $\pm 20\%$ of the rupture strength of the virgin material.

4.8 Fracture Behavior of Alloy 625

The fracture behavior of Alloy 625 changes significantly with microstructural conditions. In solution annealed condition, the alloy exhibits transgranular ductile behavior typically observed in most face-centered cubic metals. The fractured surface of solution annealed samples is characterized by locally very high plastic deformation visible as large dimples (Fig. 4.44) that form due to the nucleation, growth, and coalescence of voids during deformation culminating into fracture. The voids may nucleate by the cracking of inclusions like blocky primary-carbides or debonding of the particle–matrix interface when dislocations in the matrix accumulate in the vicinity of the interface due to strain incompatibility between the two. With the build-up of dislocations, the interfacial stress peaks near the particle/matrix interface, which causes fracture when the stresses become large enough to cause decohesion of particles from the matrix.

The fractured surfaces of the aged alloy containing fine precipitates of coherent γ'' and $Ni_2(Cr,Mo)$ phase are characterized by shear facets, reduction in the depth, and the sizes of the dimples. Precipitation of coherent γ'' and $Ni_2(Cr,Mo)$ particles enhances the planar slip. This manifests itself in shallow dimples and micro cracks on fractured surfaces due to the high density of flow localization. Figure 4.45a show

Fig. 4.44 A typical ductile fracture of an Alloy 625 in solution annealed condition



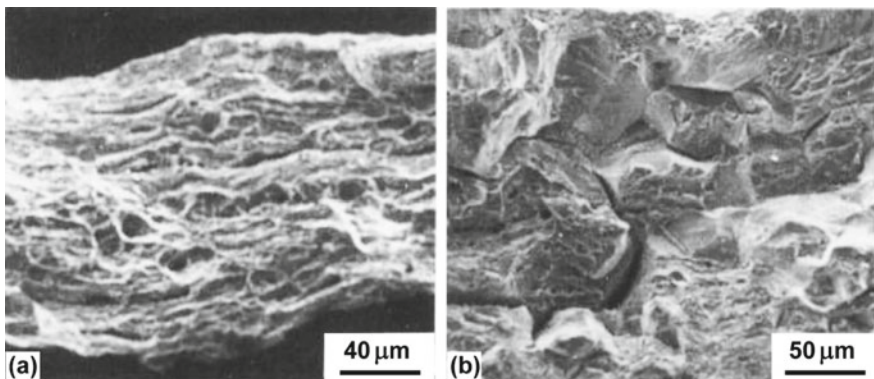


Fig. 4.45 Fractographs showing transition in the fracture mode from ductile to transgranular cleavage with the coarsening of γ'' particles in Alloy 625 aged at 650 °C for **a** 6 h; **b** 96 h. Reprinted from Ref. [102]. Copyright 1997 by The Minerals, Metals & Materials Society. Used with permission

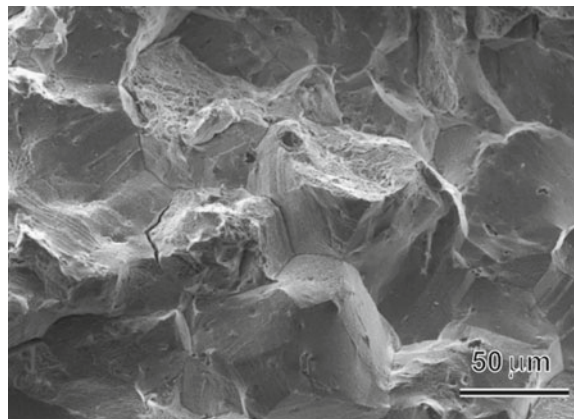
a typical fractograph of the fractured surface of the alloy containing fine particles of the γ'' phase [49, 102]. With the growth of the γ'' particles, the faceted region increases and the dimpled regions decrease, and the fracture mode gradually shifts from ductile to transgranular cleavage fracture (Fig. 4.45b) [49, 102]. When the γ'' phase particles are large, the fractured surface becomes prominently faceted with some dimple-regions because the alloy fractures only after a considerable amount of deformation in the matrix. The faceted fractured surface with uniform micro-dimples characterizes the rupture of the alloy containing predominantly the δ phase particles (Fig. 4.46). Mittra et al. [70] have shown these facets to be along {111} planes.

The formation of carbide precipitates at the grain boundaries significantly influences fracture behavior of the alloy. As noted above, carbide particles are very hard and behave as nondeformable inclusions. These particles have little effect on the

Fig. 4.46 Typical fractured surface of Alloy 625 containing predominantly the δ phase particles



Fig. 4.47 Intergranular failure of Alloy 625 with a continuous or near-continuous layer of carbides at grain boundaries



fracture mode when they are discrete and fine in size. The fracture mode remains predominantly transgranular even when the δ phase particles co-precipitate with discrete particles of the carbide phase at the grain boundaries. However, the precipitation of grain boundary carbides as a continuous or near-continuous layer changes the fracture mode from transgranular to predominantly intergranular (Fig. 4.47). The carbide films act as nucleation sites for the initiation of microcracks due to the localization of the slip, which causes the intergranular fracture. The frequency of the occurrence of microcracks associated with such intense, localized slip is nearly independent of the orientation of the grain boundary with respect to the axis of straining. Many researchers have shown the formation of such microcracks around the points of impingement of deformation bands on grain boundary carbide particles in heavily deformed Alloy 625 and other alloys [102, 103]. When the carbide particles are very closely spaced, the distances separating neighboring microcracks are very small. These microcracks can join up to facilitate an easy intergranular fracture path, similar to when the film is continuous.

Under fatigue loading conditions, the repeated cyclic straining leads to different amounts of net slip on other glide planes responsible for fatigue crack initiation and further slipping [1]. Carbide particles near the surface acts as a stress raiser and aid the initiation of fatigue cracks. Figure 4.48a, c depicts the fracture behavior of a wrought Alloy 625 subjected to high-cycle fatigue at 650 °C [104]. Multiple crack initiation was observed in specimens tested under high stressed conditions, whereas the specimen failed by initiating and propagating a single crack at low-stress levels. In addition, carbide fracture occurs more easily in cyclic stress conditions [104]. Fracturing and debonding of brittle carbides from the nickel matrix reduces the fatigue life.

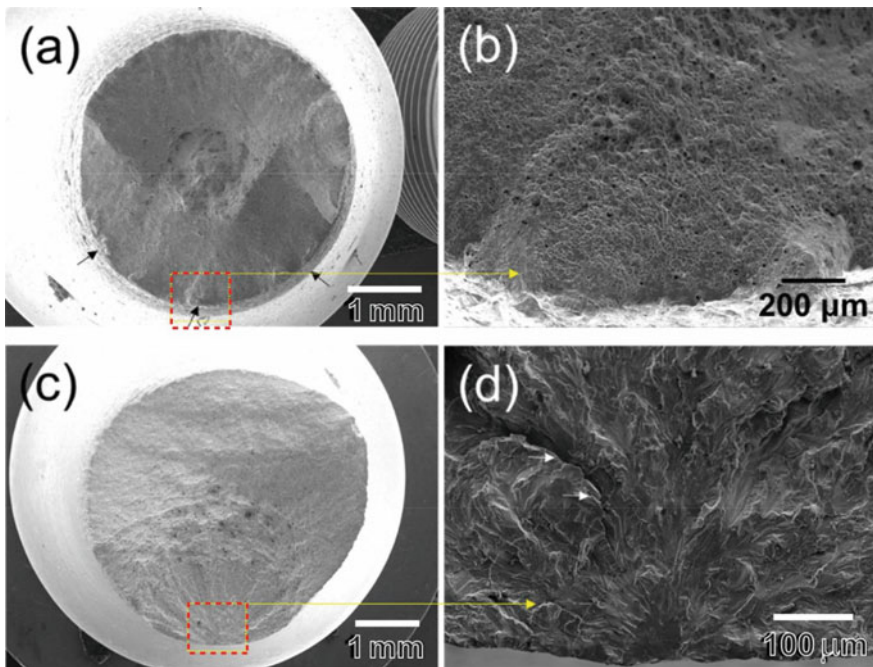


Fig. 4.48 High cycle fatigue fractured surfaces of wrought Alloy 625 at 650 °C; **a–b** 600 MPa(14,761 cycles) and **c–d** 575 MPa (38,563 cycles). Sites of fatigue crack initiation are pointed by black arrows. Reprinted from Ref. [104], Copyright (2020), with permission from Elsevier

The fractured surface of samples subjected to creep at intermediate temperatures exhibits wedge type of cracks [99]. Figure 4.49a, b shows typical creep damage, and the fractured surface of a sample crept at 750 °C that ruptured after a period of 170 h.

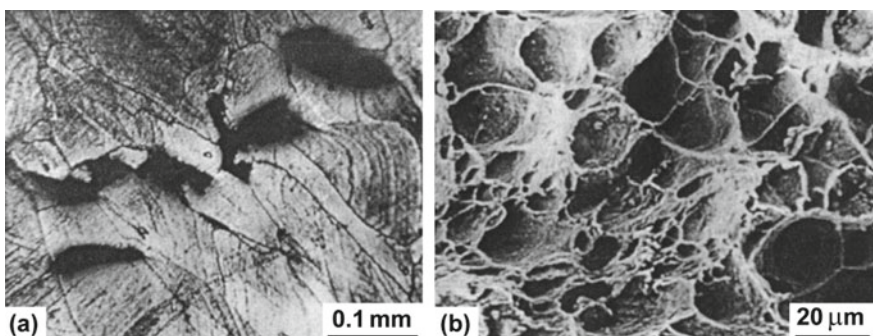


Fig. 4.49 Micrographs of a creep tested Alloy 625 sample tested at 650 °C for 170 h: **a** typical creep damage; **b** fractured surface. Reprinted from Ref. [99], Copyright (2004), with permission from Elsevier

The fracture during creep occurs due to the growth and linkage of microcracks leading to plastic instability or ligament tearing between the intergranular cracks [99].

4.9 Summary

Alloy 625 has an excellent combination of strength and ductility in the annealed condition. The strength of the alloy in the annealed condition is due to the solid-solution effects of various alloying additions. However, thermal exposure at intermediate temperatures causes significant hardening and concomitant loss in ductility and toughness. This alloy's hardening is mainly due to the formation of precipitates of γ'' and $\text{Ni}_2(\text{Cr},\text{Mo})$ precipitates, while the precipitation of δ and carbide phases harden to a lesser extent though their precipitation weaken grain boundaries considerably. γ'' and $\text{Ni}_2(\text{Cr},\text{Mo})$ precipitates form as small and coherent particles, distributed homogeneously throughout the matrix. The ordered nature of precipitates imposes restrictions on the continuity of deformation across them. These restrictions cause a loss in the alloy's ductility. The alloy exhibits a change in the precipitate deformation mechanism from shearing of particles to twinning above a critical particle size. The twinning of intermetallic precipitates allows the passage of deformation without disturbing the ordered atomic arrangement in precipitates. Energetically, the twinning of large ordered precipitates by dislocation movement is favored over looping. The transition of the deformation mechanism from particle shearing to particle twinning is accompanied by a significant drop in the work-hardening exponent.

References

1. Dieter GE (1988) Mechanical metallurgy. McGraw-Hill, London. ISBN 0-07-100406-8
2. Bulatov V, Cai W (2006) Computer simulations of dislocations, vol 3. Oxford University Press, Oxford
3. Yamaguchi M, Umakoshi Y (1990) The deformation behaviour of intermetallic superlattice compounds. Prog Mater Sci 34:1–148. [https://doi.org/10.1016/0079-6425\(90\)90002-Q](https://doi.org/10.1016/0079-6425(90)90002-Q)
4. Kear BH, Wilsdorf HG (1962) No title. Trans Met Soc AIME 224:382
5. Moreen HA, Polonis DH, Taggart R (1971) Superdislocations in Ni_3V . J Appl Phys 42:2151–2152. <https://doi.org/10.1063/1.1660513>
6. Vanderschaeve G, Escaig B (1973) A plastic deformation mode for long-period ordered alloys. Phys Status Solidi 20:309–319. <https://doi.org/10.1002/pssa.2210200131>
7. Vanderschaeve G, Escaig B (1978) Dissociation of $1/2<112>$ perfect dislocations and nature of slip dislocations in ordered Ni_3V . J Phys Lettres. 39:74–77
8. Vanderschaeve G, Sarrazin T (1977) On the nature of deformation twins in ordered Ni_3V . Phys Status Solidi 43A:459
9. Vanderschaeve G, Sarrazin T, Escaig B (1979) Effect of domain size on the mechanical properties of ordered Ni_3V . Acta Metall 27:1251–1260. [https://doi.org/10.1016/0001-6160\(79\)90141-X](https://doi.org/10.1016/0001-6160(79)90141-X)
10. Laves F (1966) What is a twin and what is a “twin”? Acta Metall 14:58. [https://doi.org/10.1016/0001-6160\(66\)90273-2](https://doi.org/10.1016/0001-6160(66)90273-2)

11. Goo E, Duerig T, Melton K, Sinclair R (1985) Mechanical twinning in Ti₅₀Ni₄₇Fe₃ and Ti₄₉Ni₅₁ alloys. *Acta Metall* 33:1725–1733. [https://doi.org/10.1016/0001-6160\(85\)90167-1](https://doi.org/10.1016/0001-6160(85)90167-1)
12. Sundararaman M, Mukhopadhyay P, Banerjee S (1988) Deformation behaviour of γ' strengthened inconel 718. *Acta Metall* 36:847–864. [https://doi.org/10.1016/0001-6160\(88\)90139-3](https://doi.org/10.1016/0001-6160(88)90139-3)
13. Singh JB (2002), Ph.D. Dissertation, IIT Bombay
14. Yamaguchi M, Umakoshi Y, Yamane T (1987) Plastic deformation of the intermetallic compound Al₃Ti. *Philos Mag A* 55:301–315. <https://doi.org/10.1080/01418618708209869>
15. Amelinckx S (1979), Dislocations in solids. In: Nabarro FRN (ed). North-Holland Publishing Co.
16. Hoover WR, Hertzberg RW (1971) The mechanical response of the Ni–Ni₃ Nb eutectic composite: Part I. Monotonic behaviour. *Metall Trans* 2:1283–1288
17. Grossiord C, Turpin M (1973) Deformation twins in the Ni₃ Nb phase. *Metall Trans* 4:1415–1416
18. Bhowal PR, Metzger M (1978) Deformation substructure and slip systems in directionally solidified Ni₃Al(γ')-Ni₃Nb(δ). *Metall Trans A* 9:1027–1038. <https://doi.org/10.1007/BF02652207>
19. Bhowal PR, Prewo KM, McEvily AJ (1978) The role of twinning in the cyclic stress-strain behavior of directionally solidified γ/γ'-δ. *Metall Trans A* 9:747–751. <https://doi.org/10.1007/BF02649783>
20. Grossiord C, Lesoult G, Turpin M (1972) Electron microscopy and structure of materials. University of California Press. [https://doi.org/10.1016/0047-7206\(71\)90049-5](https://doi.org/10.1016/0047-7206(71)90049-5)
21. Haghjara K, Nakano T, Umakoshi Y (2000) Plastic deformation behaviour and operative slip systems in Ni₃Nb single crystals. *Acta Mater* 48:1469–1480
22. Haghjara K, Nakano T, Umakoshi Y (2001) Deformation twins in Ni₃Nb single crystals with D0a structure. *Mater Res Soc Symp Proc* 646:5–11. <https://doi.org/10.1557/proc-646-n5.23.1>
23. Yoo MH (1981) Slip, twinning, and fracture in hexagonal close-packed metals. *Metall Trans A* 12:409–418. <https://doi.org/10.1007/BF02648537>
24. Fukuchi M, Watanabe K (1986) On the plastic deformation of a Ni₃Nb single crystal. *Trans Jpn Inst Met* 27:434–440. <https://doi.org/10.2320/matertrans1960.27.434>
25. Haghjara K, Nakano T, Umakoshi Y (1998) Plastic deformation of Ni₃Nb single crystals. In: MRS proceedings, vol 552, KK10.7.1. <https://doi.org/10.1557/PROC-552-KK10.7.1>
26. Christian JW, Laughlin DE (1988) Overview no. 67 the deformation twinning of superlattice structures derived from disordered B.C.C. or F.C.C. solid solutions. *Acta Metall* 36:1617–1642. [https://doi.org/10.1016/0001-6160\(88\)90230-1](https://doi.org/10.1016/0001-6160(88)90230-1)
27. Kumar M, Vasudevan VK (1997) Crystallographic analysis and observations of true twinning modes in the Ni₂Mo superlattice phase contained in a Ni-25Mo-8Cr alloy. *Acta Mater* 45:3203–3222. [https://doi.org/10.1016/S1359-6454\(97\)00007-4](https://doi.org/10.1016/S1359-6454(97)00007-4)
28. Pelloix RMN, Grant NJ (1960) Solid solution and second phase strengthening of nickel alloys at high and low temperatures. *Trans TMS-AIME* 218:232
29. Stoloff NS (1987) Superalloys II. Sims CT, Stoloff NS, Hagel WC (eds). Wiley, New York, US. <https://www.osti.gov/biblio/5452409>
30. Beeston BEP, Dillamore IL, Smallman RE (1968) The stacking-fault energy of some nickel-cobalt alloys. *Met Sci J* 2:12–14. <https://doi.org/10.1179/030634568790443468>
31. Beeston BEP, France LK (1968) The stacking-fault energies of some binary nickel alloys fundamental to the nimonic series. *J Inst Met* 96:105–107
32. Douglass DL, Thomas G, Roser WR (1964) Ordering, stacking faults and stress corrosion cracking in austenitic alloys. *Corrosion* 20:15–28. <https://doi.org/10.5006/0010-9312-20.1.15t>
33. Courtney TH (2005) Mechanical behavior of materials. Waveland Press, pp 175–243
34. Oblak JM, Duval DS, Paulonis DF (1974) *Metall Trans* 5:143–153
35. Kelly PM (1972) The effect of particle shape on dispersion hardening. *Scr Metall* 6:647–656. [https://doi.org/10.1016/0036-9748\(72\)90120-2](https://doi.org/10.1016/0036-9748(72)90120-2)
36. Ansell GS, Weertman J (1959) Creep of a dispersion-hardened aluminum alloy. No. NRL-5176. Naval Research Lab., Washington, DC, 1958.

37. Nesbit LA, Laughlin DE (1980) The deformation microstructure of the NiNi₄Mo system. *Acta Metall* 28:989–998. [https://doi.org/10.1016/0001-6160\(80\)90117-0](https://doi.org/10.1016/0001-6160(80)90117-0)
38. Kumar M, Vasudevan VK (1996) Mechanical properties and strengthening of a Ni-25Mo-8Cr alloy containing Ni₂(Mo,Cr) precipitates. *Acta Mater* 44:4865–4880. [https://doi.org/10.1016/S1359-6454\(96\)00092-4](https://doi.org/10.1016/S1359-6454(96)00092-4)
39. François A, Hug G, Veyssiére P (1992) The fine structure of dislocations in Ni₃V. *Philos Mag A* 66:269–288
40. Singh JB, Sundararaman M, Mukhopadhyay P (2000) Propagation of stacking faults across domain boundaries in Ni–V and Ni–V–Nb alloys with D0₂₂ structure. *Philos Mag A* 80:1983–2010. <https://doi.org/10.1080/01418610008212147>
41. Singh JB, Sundararaman M, Mukhopadhyay P (2004) Propagation of twins across Ni₂V/Ni₃V coherent interfaces in a two phase Ni–29at%V alloy. *Scr Mater* 51:693–698. <https://doi.org/10.1016/j.scriptamat.2004.06.009>
42. Nosava G, Polyakova W (1971) Effect of ordering on the critical shearing stresses in Ni₂Cr alloy. *Phys Met Metallgr* 32:825
43. Sundararaman M, Kumar L, Prasad GE (1999) Precipitation of an intermetallic phase with Pt₂Mo-type structure in alloy 625. *Metall Mater Trans A* 30, 41–52. <https://doi.org/10.1007/s11661-999-0194-6>
44. Kirman I, Warrington DH (1970) The precipitation of Ni₃Nb phases in a Ni–Fe–Cr–Nb alloy. *Metall Trans* 1:2667–2675. <https://doi.org/10.1007/BF03037800>
45. Garde AM, Aigeltinger E, Reed-Hill RE (1973) Relationship between deformation twinning and the stress-strain behavior of polycrystalline titanium and zirconium at 77 K. *Metall Trans* 4:2461–2468. <https://doi.org/10.1007/BF02669391>
46. Embury JD (1971) Strengthening methods in crystals. In: Kelly A, Nicholson RB (1971)
47. Inconel alloy 625 Data Sheet (2021). <https://www.specialmetals.com/documents/technical-bulletins/inconel/inconel-alloy-625.pdf>
48. Haynes 625 alloy Data sheet (2021) https://www.haynesintl.com/docs/default-source/pdfs/new-alloy-brochures/high-temperature-alloys/brochures/625-brochure.pdf?sfvrsn=967229d4_26
49. Sundararaman M (1986) Ph.D. thesis, University of Bombay
50. Deléhouzée L, Deruyttere A (1967) The stacking fault density in solid solutions based on copper, silver, nickel, aluminium and lead. *Acta Metall* 15:727–734. [https://doi.org/10.1016/0001-6160\(67\)90353-7](https://doi.org/10.1016/0001-6160(67)90353-7)
51. Kotval PS (1968) Carbide precipitation on imperfections in superalloy matrices. <https://www.osti.gov/biblio/4492243>
52. Gallagher PCJ (1970) The influence of alloying, temperature, and related effects on the stacking fault energy. *Metall Trans* 1:2429–2461. <https://doi.org/10.1007/BF03038370>
53. Fournier D, Pineau A (1977) Low cycle fatigue behavior of inconel 718 at 298 and 823 K. *Metall Trans A* 8:1095–1105. <https://doi.org/10.1007/BF02667395>
54. Yang W, Qu P, Sun J, Yue Q, Su H, Zhang J, Liu L (2020) Effect of alloying elements on stacking fault energies of γ and γ' phases in Ni-based superalloy calculated by first principles. *Vacuum* 181:109682. <https://doi.org/10.1016/j.vacuum.2020.109682>
55. Hale CL, Rollings WS Weaver ML (2001) Activation energy calculations for discontinuous yielding in Inconel 718SPF. *Mater Sci Eng A* 300:153–164. [https://doi.org/10.1016/S0921-5093\(00\)01470-2](https://doi.org/10.1016/S0921-5093(00)01470-2)
56. Chatterjee A, Sharma G, Tewari R, Chakravarty JK (2015) Investigation of the dynamic strain aging and mechanical properties in alloy-625 with different microstructures. *Metall Mater Trans A* 46:1097–1107. <https://doi.org/10.1007/s11661-014-2717-z>
57. Fournier L, Delafosse D, Magnin T (2001) Oxidation induced intergranular cracking and Portevin–Le Chatelier effect in nickel base superalloy 718. *Mater Sci Eng A* 316:166–173. [https://doi.org/10.1016/S0921-5093\(01\)01224-2](https://doi.org/10.1016/S0921-5093(01)01224-2)
58. Nalawade SA, Sundararaman M, Kishore R, Shah JG (2008) The influence of aging on the serrated yielding phenomena in a nickel-base superalloy. *Scr Mater* 59:991–994. <https://doi.org/10.1016/j.scriptamat.2008.07.004>

59. Rahman MS, Priyadarshan G, Raja KS, Nesbitt C, Misra M (2009) Characterization of high temperature deformation behavior of INCONEL 617. *Mech Mater* 41:261–270. <https://doi.org/10.1016/j.mechmat.2008.10.003>
60. Wright JK, Carroll KJ, Cabet C, Lillo TM, Benz JK, Simpson JA, Lloyd WR, Chapman JA, Wright RN (2012) Characterization of elevated temperature properties of heat exchanger and steam generator alloys. *Nucl Eng Des US* 252–260. <https://doi.org/10.1016/j.nucengdes.2011.10.034>
61. Mo K, Lovicu G, Chen X, Tung H-M, Hansen JB, Stubbins JF (2013) Mechanism of plastic deformation of a Ni-based superalloy for VHTR applications. *J Nucl Mater* 441:695–703. <https://doi.org/10.1016/j.jnucmat.2013.03.083>
62. Tian C, Cui C, Xu L, Gu Y, Sun X (2013) Dynamic strain aging in a newly developed Ni–Co-base superalloy with low stacking fault energy. *J Mater Sci Technol* 29:873–878. <https://doi.org/10.1016/j.jmst.2013.04.012>
63. Hrutkay K, Kaoumi D (2014) Tensile deformation behavior of a nickel based superalloy at different temperatures. *Mater Sci Eng A* 599:196–203. <https://doi.org/10.1016/j.msea.2014.01.056>
64. Kaoumi D, Hrutkay K (2014) Tensile deformation behavior and microstructure evolution of Ni-based superalloy 617. *J Nucl Mater* 454:265–273. <https://doi.org/10.1016/j.jnucmat.2014.08.003>
65. Kim IS, Chaturvedi MC (1987) Serrated flow in Inconel 625. *Trans Jpn Inst Met* 28:205–212. <https://doi.org/10.2320/matertrans1960.28.205>
66. Shankar V, Valsan M, Rao KBS, Mannan SL (2004) Effects of temperature and strain rate on tensile properties and activation energy for dynamic strain aging in alloy 625. *Metall Mater Trans A* 35:3129–3139
67. Ziaja W, Poręba M, Motyka M (2017) Plasticity of nickel-based superalloy 625 at elevated temperature. *Adv Manuf Sci Technol* 41:41–49. <https://doi.org/10.2478/amst-2017-0021>
68. Maj P, Zdunek J, Mizera J, Kurzydlowski KJ, Sakowicz B, Kaminski M (2017) Microstructure and strain-stress analysis of the dynamic strain aging in inconel 625 at high temperature. *Met Mater Int* 23:54–67. <https://doi.org/10.1007/s12540-017-6264-1>
69. Eiselstein HL, Tillack DJ (2012) The invention and definition of alloy 625. 1–14. https://doi.org/10.7449/1991/superalloys_1991_1_14
70. Mittra J, Banerjee S, Tewari R, Dey GK (2013) Fracture behavior of Alloy 625 with different precipitate microstructures. *Mater Sci Eng A* 574:86–93. <https://doi.org/10.1016/j.msea.2013.03.021>
71. Chakravarty JK, Singh JB, Sundararaman M (2012) Microstructural and mechanical properties of service exposed Alloy 625 ammonia cracker tube removed after 100,000 h. *Mater Sci Technol* 28:702–710. <https://doi.org/10.1179/1743284711Y.0000000118>
72. Singh JB, Chakravarty JK, Sundararaman M (2013) Work hardening behaviour of service aged Alloy 625. *Mater Sci Eng A* 576:239–242. <https://doi.org/10.1016/j.msea.2013.03.091>
73. Thomas C, Tait P (1994) The performance of Alloy 625 in long-term intermediate temperature applications. *Int J Press Vessel Pip* 59:41–49. [https://doi.org/10.1016/0308-0161\(94\)90140-6](https://doi.org/10.1016/0308-0161(94)90140-6)
74. Verma A, Singh JB (n.d.) Atom probe tomography analysis of Alloy 625 with different microstructures. Unpublished work
75. Miller MK, Babu SS, Burke MG (2002) Comparison of the phase compositions in Alloy 718 measured by atom probe tomography and predicted by thermodynamic calculations. *Mater Sci Eng A* 327:84–88. [https://doi.org/10.1016/S0921-5093\(01\)01881-0](https://doi.org/10.1016/S0921-5093(01)01881-0)
76. Crussard C, Jaoul B (1950) Contribution à l'étude de la forme des courbes de traction des métaux et à son interprétation physique. *Rev Métallurgie* 47:589–600. <https://doi.org/10.1051/metal/195047080589>
77. Raynor D, Silcock JM (1970) Strengthening mechanisms in γ' precipitating alloys. *Met Sci J* 4:121–130. <https://doi.org/10.1179/msc.1970.4.1.121>
78. Martens V, Nembach E (1975) Strengthening of the nimonic alloy PE 16 by ordered particles of $\text{Ni}_3(\text{Al}, \text{Ti})$. *Acta Metall* 23:149–153. [https://doi.org/10.1016/0001-6160\(75\)90178-9](https://doi.org/10.1016/0001-6160(75)90178-9)

79. Plumbridge WJ, Ryder DA (1969) The metallography of fatigue. *Metall Rev* 14:119–142. <https://doi.org/10.1179/mtrl.1969.14.1.119>
80. Viswanathan R (1989) Damage mechanisms and life assessment of high-temperature components. ASM international. <https://doi.org/10.31399/asm.tb.dmlahtc.9781627083409>
81. Bashir M, Kannan R, Sandhya R, Harmain GA (2020) Low Cyclic Fatigue Behavior of Alloy 625 at ambient and elevated temperatures. In: Structural integrity assessment. Springer, pp 653–661
82. Suave LM, Cormier J, Bertheau D, Villechaise P, Soula A, Hervier Z, Hamon F (2016) High temperature low cycle fatigue properties of alloy 625. *Mater Sci Eng A* 650:161–170
83. Paris P, Erdogan F (1963) A critical analysis of crack propagation laws
84. Richards CE, Lindley TC (1972) The influence of stress intensity and microstructure on fatigue crack propagation in ferritic materials. *Eng Fract Mech* 4:951–978. [https://doi.org/10.1016/0013-7944\(72\)90028-8](https://doi.org/10.1016/0013-7944(72)90028-8)
85. Ritchie RO, Knott JF (1973) Mechanisms of fatigue crack growth in low alloy steel. *Acta Metall* 21:639–648. [https://doi.org/10.1016/0001-6160\(73\)90073-4](https://doi.org/10.1016/0001-6160(73)90073-4)
86. Ritchie RO, Knott JF (1974) Micro cleavage cracking during fatigue crack propagation in low strength steel. *Mater Sci Eng* 14:7–14. [https://doi.org/10.1016/0025-5416\(74\)90118-9](https://doi.org/10.1016/0025-5416(74)90118-9)
87. Pelloux RMN (1970) Crack extension by alternating shear. *Eng Fract Mech* 1:697–704. [https://doi.org/10.1016/0013-7944\(70\)90008-1](https://doi.org/10.1016/0013-7944(70)90008-1)
88. Lima Pereira FG, Lourenço JM, Nascimento RM, Castro NA (2018) Fracture behavior and fatigue performance of inconel 625. *Mater Res* 21. <https://doi.org/10.1590/1980-5373-MR-2017-1089>
89. James LA (1991) The effect of temperature upon the fatigue crack propagation behavior of Alloy 625. In: Loria EA (ed) Proceedings of conference on superalloys 718, 625 and various derivatives. The Minerals, Metals & Materials Society, pp 501–508
90. James LA (1977) Effect of temperature upon the fatigue-crack propagation behavior of Inconel 625. United States. <https://doi.org/10.2172/7257141>
91. Shahinian P (1978) Fatigue crack growth characteristics of high-temperature alloys. *Met Technol* 5:372–380. <https://doi.org/10.1179/mt.1978.5.1.372>
92. James LA (1977) Fatigue-crack propagation behaviour of Inconel 600. *Int J Press Vessel Pip* 5:241–259. [https://doi.org/10.1016/0308-0161\(77\)90006-0](https://doi.org/10.1016/0308-0161(77)90006-0)
93. James LA, Mills WJ (1985) Effect of heat-treatment and heat-to-heat variations in the fatigue-crack growth response of alloy 718. *Eng Fract Mech* 22:797–817. [https://doi.org/10.1016/0013-7944\(85\)90109-2](https://doi.org/10.1016/0013-7944(85)90109-2)
94. Elber W (1971) The significance of fatigue crack closure. In: Toler D (ed). Aircraft structures. ASTM International
95. Long T (1972) A comparison of fatigue crack propagation in Inconel 625 and 3.25 Ni steel. <http://calhoun.nps.edu/public/handle/10945/16029>
96. Nabarro FRN (1948) Deformation of crystals by motion of single ions. In: Rep. A conference strength solids, The Physical Society
97. Herring C (1950) Diffusional viscosity of a polycrystalline solid. *J Appl Phys* 21:437–445
98. Coble RL (1963) A model for boundary diffusion controlled creep in polycrystalline materials. *J Appl Phys* 34:1679–1682
99. Mathew MD, Bhanu Sankara Rao K, Mannan SL (2004) Creep properties of service-exposed Alloy 625 after re-solution annealing treatment. *Mater Sci Eng A* 372:327–333. <https://doi.org/10.1016/j.msea.2004.01.042>
100. Mathew MD, Murty KL, Rao KBS, Mannan SL (1999) Ball indentation studies on the effect of aging on mechanical behavior of alloy 625. *Mater Sci Eng A* 264:159–166. [https://doi.org/10.1016/S0921-5093\(98\)01098-3](https://doi.org/10.1016/S0921-5093(98)01098-3)
101. Ferrer L, Pieraggi B, Uginet JF (1991) Superalloys 718, 625 and various derivatives. In: Loria EE (ed) Minerals, Materials & Society, p 217
102. Sundararaman M, Mukhopadhyay P, Banerjee S (1997) Superalloys 718, 625, 706 and various derivatives. In: Loria EA (ed), Minerals, Materials & Society, pp 367–378

103. Shiozawa K, Weertman JR (1983) Studies of nucleation mechanisms and the role of residual stresses in the grain boundary cavitation of a superalloy. *Acta Metall* 31:993–1004. [https://doi.org/10.1016/0001-6160\(83\)90194-3](https://doi.org/10.1016/0001-6160(83)90194-3)
104. Kim K-S, Kang T-H, Kassner ME, Son K-T, Lee K-A (2020) High-temperature tensile and high cycle fatigue properties of inconel 625 alloy manufactured by laser powder bed fusion. *Addit Manuf* 35:101377. <https://doi.org/10.1016/j.addma.2020.101377>

Chapter 5

Alloy 625 PLUS



Alloy 625 PLUS alloy is developed as an age-hardenable variant of Alloy 625 to impart strength superior to Alloy 718 but retaining excellent corrosion resistance and welding properties of Alloy 625 [1–6]. The sluggish aging response of Alloy 625 constrains it for deformation-induced strengthening and precipitation for higher strength levels. M/s Carpenter Technology, USA, patented Alloy 625 PLUS vide a US Patent number 5556594 and market as “Custom Age 625 PLUS” alloy [6]. Alloy 625 PLUS is a highly corrosion-resistant, cobalt-free, alloy developed to be age-hardened by the precipitation of γ'' phase particles to achieve high strength levels without warm or cold working. The nominal composition of the alloy is given in Table 5.1. The corrosion resistance of Alloy 625 PLUS is similar to Alloy 625 and superior to Alloy 718 in many environments. The alloy is designed for applications in deep sour wells or environments containing chlorides, hydrogen sulfide and carbon dioxide at elevated temperatures and pressures. These applications require good resistance against pitting and crevice corrosion and stress-corrosion cracking, combined with high strength and ductility.

5.1 Chemistry of Alloy 625 PLUS

The chemistry of alloying additions in Alloy 625 PLUS is adjusted to accelerate the precipitation of γ'' particles for age hardening after a short incubation period. Yield strength of about 825 MPa or above can be obtained within 24 h of aging [5], while much longer aging times (>70 h) are required to obtain similar strength levels in annealed Alloy 625 (Sect. 4.5.2). The amount of titanium in Alloy 625 PLUS is increased to about 1.3 wt%, compared to a maximum of 0.4 wt% in Alloy 625. In addition, the carbon content is reduced to about 0.01 wt% compared to a maximum of 0.10 wt% in Alloy 625 [5]. An increase in the titanium, along with niobium and aluminum, promotes the γ'' induced age hardening of the alloy. The best combination of properties is obtained using 2.75–4.25% Nb and 0.75–1.5% Ti

Table 5.1 The nominal composition of Alloy 625 PLUS

	Ni	Cr	Mo	Nb	Al	Ti	C	Si	Fe
Min.	59.0	19.0	7.0	2.75	—	0.75	—	—	—
Max.	63.0	22.0	9.5	4.0	0.35	1.5	0.03	0.2	Bal

[5]. The amount of niobium and titanium elements are balanced to achieve alloy's hardness in the range of about 35–40 HRC using a double-aging treatment similar to the one commonly given to Alloy 718. Even though aluminum also promotes the age-hardening reaction in most γ' bearing superalloys, it has little role in strengthening γ'' bearing alloys. Niobium and titanium promotes the precipitation of the γ'' phase while aluminum stabilizes the γ' phase. The concentration of aluminum is therefore restricted to a maximum of 0.35%. The minimum levels of 2.75% and 0.75% of niobium and titanium, respectively are required to achieve a yield strength of about 825 MPa. Higher levels of the yield strength, up to about 965 MPa and even higher, can be achieved by increasing the niobium and titanium contents, but an increase in the titanium content reduces the resistance to stress-corrosion cracking [5]. This effect of titanium restricts its concentration to a maximum of 1.5% titanium. On the other hand, alloys containing less than about 0.75% titanium exhibits much lower resistance to crevice corrosion than alloys with higher titanium contents.

Minimum levels of chromium and molybdenum are retained to preserve the excellent corrosion resistance of Alloy 625. An excellent combination of properties is obtained using 18–22% chromium and 7.5–11% molybdenum, provided that the sum of the two elements does not exceed 31%. However, excessive chromium and molybdenum may promote the formation of TCP phases (Chap. 3), which reduce corrosion resistance, hot workability and toughness. A minimum of 60.5% nickel is required for good resistance to stress-corrosion cracking in boiling 45% $MgCl_2$. The carbon content is reduced to a maximum of 0.03% for the best combination of strength and corrosion resistance and to minimize the precipitation of intergranular carbides during aging. Low carbon and nitrogen contents reduce the formation of niobium- and titanium-rich primary carbonitride particles ((Nb, Ti)(C, N)) during solidification. However, even with a very low amount of carbon in the alloy, high activities of chromium and molybdenum may cause the precipitation of undesirable chromium and molybdenum-rich carbides ($M_{23}C_6$, M_6C) during a subsequent aging treatment at temperatures about 730 °C or above, which can sensitize the alloy for intergranular corrosion. As noted later in Sect. 7.4.3, precipitation of the niobium/titanium-rich carbide ((Nb, Ti)C) particles at temperatures above 980 °C minimize the intergranular precipitation of $M_{23}C_6$ and M_6C carbides and improves the resistance against intergranular corrosion. With this chemistry, Alloy 625 PLUS gives corrosion resistance, in solution annealed condition, similar to Alloy 625 and can be age-hardened to achieve a strength better than Alloy 718, to a value of 825 MPa and more [5].

5.2 Mechanical Properties of Alloy 625 PLUS

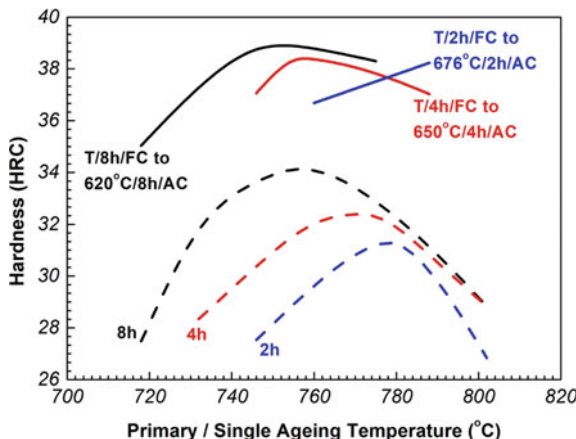
Alloy 625 PLUS is solution annealed at temperatures in the range of about 1025 - 1050 °C to dissolve hardening precipitates and recrystallize the deformed grains to achieve uniform properties [7, 8]. A solution annealing treatment at temperatures above 1050 °C may coarsen the grains. On the other hand, an annealing treatment at temperatures below 980 °C may leave some grains un-recrystallized and result in mixed grain structures. Typical mechanical properties of Alloy 625 PLUS in fully solution annealed condition are listed in Table 5.2 [7].

Unlike Alloy 625, solution annealed Alloy 625 PLUS can be age-hardened to achieve hardness up to about 50 HRC [7]. The inherent solid-solution nature of Alloy 625 limits its hardness below about 100 HRB [9, 10], which can only be increased further by prolonged aging, as noted in Chap. 4, or by cold or warm working. Cold working can increase the hardness of Alloy 625 up to about 45 HRC with a drastic decrease in ductility to about 5% [10]. Warm or cold working combined with prolonged aging may, therefore, be used to strengthen Alloy 625, but such warm or cold working operations becomes less practical as the cross-section of the working piece increases. On the other hand, the Alloy 625 PLUS can be age-hardened easily without cold or warm deformation using standard age-hardening treatments to impart higher mechanical properties across a broad section thickness range. Frank has studied the age-hardening behavior of 625 PLUS alloy [5]. Figure 5.1 shows variation in the hardness of the Alloy 625 PLUS as a function of time and temperature after single- and double-aging treatments. The lower curves depict the hardness

Table 5.2 Typical room-temperature tensile properties of solution annealed Alloy 625 PLUS [7]

YS (MPa)	UTS (MPa)	Elongation (%)	Reduction in area (%)	Hardness (HRB)
379	834	61	73	88

Fig. 5.1 Variation in the hardness of the Alloy 625 PLUS as a function of time and temperature after single-ageing (broken curves) and double-ageing (solid curves) treatments [5]. “T” in upper curves refers to the first (primary) ageing temperature, while FC and AC refer to the furnace- and air-cooled, respectively



of the single-step aging. The upper curves show the hardness after the double-aging treatments, where “T” in the labels refers to the first (or the primary) aging temperature. During the double-aging treatment, the samples were furnace cooled (FC) from the primary temperature to the second aging temperature (620, 650 or 676 °C) at a rate of about 50 °C/h to reach the second temperature in 2 h. The samples were air-cooled (AC) after the second aging treatment. It is evident from Fig. 5.1 that the second aging in a double-aging treatment increases the hardness of the alloy by about 5–6 HRC points over the hardness achieved by the single (primary) aging treatment for a given aging time and temperature with little or no additional intergranular carbides. Further, the double 8-h cycle provides slightly higher hardness than the double 4- or 2-h cycles. Under-aging during the primary-aging treatment minimizes the intergranular carbide precipitation [5]. This study established that a double-aging treatment of 730 °C/8 h/FC to 620 °C/8 h/AC gives the highest hardness with minimal intergranular precipitation [5]. This 18-h double-aging treatment is very close to the double-age-hardening treatment usually employed for hardening of aerospace-grade Alloy 718 as per the AMS 5662 standard [11]. The AMS 5662 treatment involves a solution treatment at about 980 °C for 1 h, followed by air cooling, and a subsequent 18-h double-aging treatment involving 720 °C/8 h/FC and 620 °C/8 h/AC cycles.

The aging treatments mentioned above can be used to achieve a yield strength in the range of over 690 to 1035 MPa without cold or warm working [5, 7]. Table 5.3 gives room-temperature tensile properties of the alloy age-hardened by a few single- and double-aging treatments [7]. An 18-h double-aging treatment of 732 °C/8 h/FC to 620 °C/8 h/AC imparts about 900 MPa of yield strength to the 625 PLUS alloy without the cold or warm deformation.

Table 5.4 compares the room-temperature tensile properties of the double-age-hardened 625 PLUS alloy with those of age-hardened 625 and 718 alloys [5]. The age-hardened Alloy 625 PLUS also exhibits good hardenability as evidenced by similar tensile properties of the annealed alloy bars of various diameters subjected to the double-aging of 730 °C/8 h/FC to 620 °C/8 h /AC (Table 5.5) [7]. The solution

Table 5.3 Age-hardening effect on room-temperature tensile properties of a solution annealed Alloy 625 PLUS solution annealed at 1038 °C/2 h/AC [7]

Aging treatment	YS (MPa)	UTS (MPa)	Elongation (%)	Reduction in area (%)	Hardness (HRC)
732 °C/4 h/AC	710	1117	48	63	30
732 °C/8 h/AC	779	1145	41	59	34
718 °C/8 h/FC to 620 °C/8 h/AC	827	1220	37	57	35.5
732 °C/8 h/FC to 620 °C/8 h/AC	896	1248	32	54	38
746 °C/8 h/FC to 620 °C/8 h/AC	952	1269	32	51	39.5

Table 5.4 A comparison of room-temperature tensile properties of Alloy 625, Alloy 625 PLUS and Alloy 718 [5]

Alloy	Solution treatment	Aging treatment	YS (MPa)	UTS (MPa)	Elongation (%)	Reduction in area (%)
Alloy 625	925 °C/1 h/AC	640 °C/64 h/AC	552	972	46	58
	885 °C/1 h/AC	650 °C/70 h/AC	869	1186	31	37
	1150 °C/0.5 h/AC	Cold Rolled 25% (No Age)	889	1048	29	59
Alloy 625 PLUS	1040 °C / 2 h/AC	730 °C /8 h/FC to 620 °C/8 h/AC	917	1262	32	53
Alloy 718	1025 °C/2 h/WQ	788°C/8 h/AC	910	1227	26	33
	970 °C/1 h/AC	720 °C/8 h/FC to 620 °C/8 h/AC	1200	1400	16	30

Table 5.5 Room-temperature tensile properties of bars of various diameters of Alloy 625 PLUS alloy subjected to a double ageing treatment of 730 C/8 h/FC to 620 °C/8 h/AC after an annealing treatment 1040 °C/2 h/AC

Bar diameter (mm)	YS (MPa)	UTS (MPa)	Elongation (%)	Reduction in area (%)
25	917	1310	33	55
38	896	1282	31	56
70	862	1250	35	53
102	924	1282	33	54
127	931	1262	32	53
152	917	1262	32	53
184	910	1276	32	51

annealed and age-hardened 625 PLUS alloy exhibit similar tensile properties and impact energies in the longitudinal and transverse orientations [7].

A hardness of over 50 HRC can be achieved within 4 h of single-aging in the temperature range 675 to 690 °C (Fig. 5.2) [12]. A secondary aging treatment for 4 h at about 580 °C results in a further increase in the hardness. Cold working the alloy before age-hardening significantly improves its strength. Tensile strengths above 1790 MPa, along with good ductility, has been reported in the 38% cold-worked alloy subjected to direct aging for 4 h at 732 °C [12]. Cold working of the alloy before aging nearly doubles the yield strength. It increases the ultimate tensile strength by about 550–620 MPa compared to the solution-treated and double-aged conditions [2]. Table 5.6 gives room-temperature tensile properties of a cold-worked 625 PLUS alloy subjected to various single and double-aging treatments [12]. A single age-hardening treatment to the cold-worked alloy results in about 180–240 MPa increase in the tensile strength of the cold drawn bar of 625 PLUS alloy. Tensile strengths of over 1790 MPa can be obtained with about 9% elongation. A second (final) aging

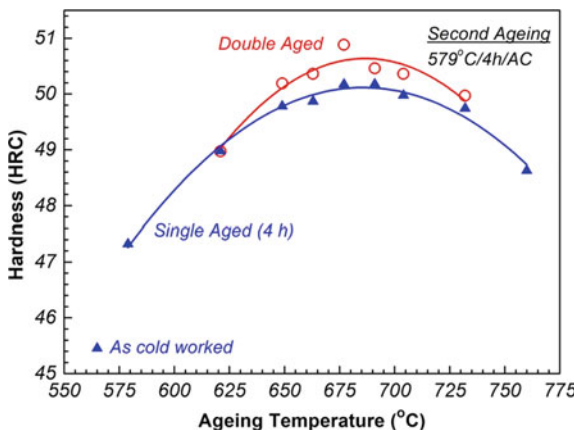


Fig. 5.2 Effect of single-and double-ageing on the hardness of 38% cold-worked Alloy 625 PLUS [12]

Table 5.6 Room-temperature tensile properties of cold-worked Alloy 625 PLUS Alloy after various age-hardening treatments

Age treatment	YS (MPa)	UTS (MPa)	Elongation (%)	Reduction in area (%)	Hardness (HRC)
As cold drawn	1269	1613	12.5	52	45.5
649 °C/4 h/AC	1772	1820	9.4	39	50
691 °C/4 h/AC	1793	1848	8.8	38	50
732 °C/4 h/AC	1724	1793	9.1	33	50
649 °C/4 h/FC to 579 °C/4 h/AC	1820	1862	9.0	37	50
677 °C/4 h/FC to 579 °C/4 h/AC	1855	1896	8.4	35	51
718 °C/8 h/FC to 621 °C/8 h/AC	1806	1869	8.2	32	51

FC = Furnace cooled at rate of 56 °C per hour; AC = Air-cooled
The alloy was given 38% cold drawn before ageing treatments [12]

treatment increases its strength by an additional 35–70 MPa without significantly reducing ductility. A double-aging treatment of 650 °C/4 h/FC to 580 °C/4 h/AC to a 38% cold-worked 625 PLUS alloy produces high tensile strength of about 1862 MPa and maximum ductility of 9%. Similar strength levels are obtained in Alloy 718 solution annealed at 1025 °C alloy followed by an over-aging treatment at about 790 °C as per NACE MR0175 specifications [11]. This treatment of Alloy 718 provides better uniformity and toughness compared to that obtained by the standard aerospace double-aging treatment of 720 °C/8 h/FC to 620 °C/8 h/AC. However, the over aging of Alloy 718 at 790 °C imparts relatively a lower strength than that

Table 5.7 Effects of prolonged thermal exposure on the room-temperature tensile properties of cold-worked and aged Alloy 625 PLUS at various intermediate temperatures [12]

Thermal exposure	YS (MPa)	UTS (MPa)	Elongation (%)	Reduction in area (%)	Hardness (HRC)
As aged	1820	1862	9.0	37	50
427 °C/1000 h	1841	1882	8.8	36	50
482 °C/1000 h	1889	1917	8.3	37	50.5
538 °C/1000 h	1875	1931	8.0	35	51
538 °C/2000 h	1903	1944	7.7	34	51
593 °C/1000 h	1924	1979	6.7	29	51.5
649 °C/1000 h	1827	1924	7.0	27	50.5

FC = Furnace cooled at rate of 56 °C per hour; AC = Air cooled

The alloy was 38% cold drawn and aged 649 °C/4 h/FC to 579 °C/4 h/AC

by the AMS 5662 treatment [11, 13]. Pronged thermal exposure of the double-aged Alloy 625 PLUS further enhanced its tensile strength by about 125 MPa (Table 5.7), particularly at temperatures in between about 500–600 °C, which is the temperature range known to form Ni₂(Cr, Mo) phase particles in Alloy 625 (Sect. 3.5.3).

A 10-h double-aging cycle of 650 °C/4 h/FC to about 580 °C/4 h/AC gives Alloy 625 PLUS the best combination of strength and ductility. This combination of strength and ductility is better than about 1731 MPa strength and about 10% ductility of the age-hardened cold-worked Alloy 718 aged by an 18-h long 720/620 °C double-aging cycle [12]. Increased grain boundary precipitation, which occurs with primary-aging temperatures above 650 °C, may be responsible for the lower ductility levels. The impact energy of the double-aged 625 PLUS alloy showed a higher value (~19.4 J) compared to ~10 J of Alloy 718 [12]. The elevated temperature tensile properties of the two alloys show a similar trend of a slight reduction in the strength with increasing temperature and a ductility minimum at about 538 °C (Fig. 5.3).

5.3 Microstructure of Alloy 625 PLUS

Alloy 625 Plus is likely to possess all the phases of Alloy 625 noted in Chap. 2. However, the increased titanium concentration in Alloy 625 PLUS affects the precipitation behavior and composition of titanium-containing phases. Thermo-dynamic computations using the MatCalc 6.03 Pro software and accompanied nickel-database (ME-Ni 1.3) predict increased titanium partition in niobium bearing phases, which may, in turn, affect their lattice parameters and thermal stability. For example, the thermodynamic calculations predict the composition of the γ'' phase to be Ni₃(Nb_{0.60}Ti_{0.27}Mo_{0.04}) in Alloy 625 PLUS against its composition of Ni₃(Nb_{0.69}Ti_{0.05}Mo_{0.12}Al_{0.03}) in Alloy 625, while its thermal stability increased up to about 900 °C in the former against up to about 725 °C in the latter. In addition,

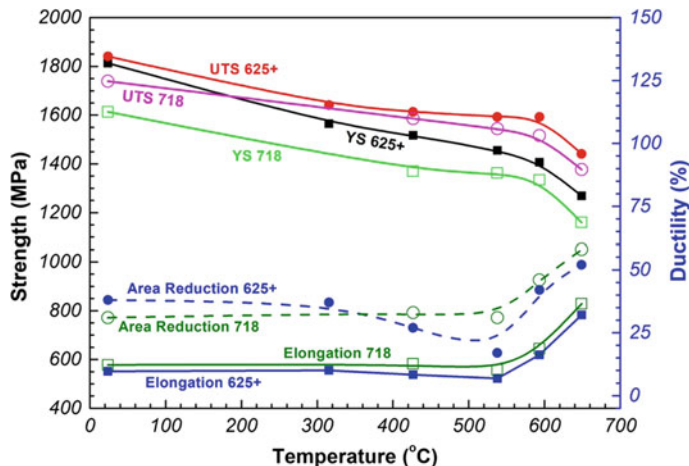
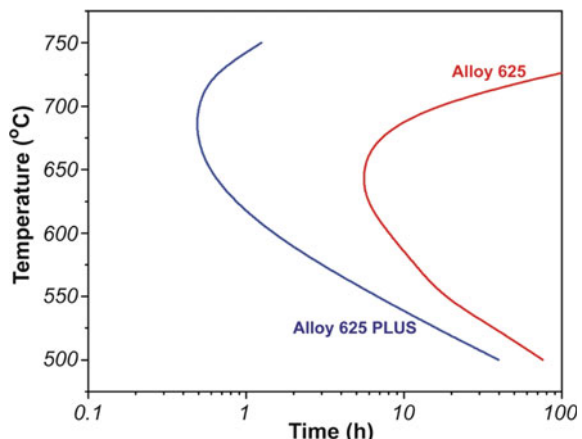


Fig. 5.3 A comparison of the elevated-temperature tensile behaviour of 625 PLUS and 718 alloys subjected to double ageing treatments [7]. Alloy 625 PLUS was subjected to a 10-h long double-ageing 650 °C/4 h/FC to 580 °C/4 h/AC cycle while Alloy 718 was subjected to its standard 18-h 720 °C/8 h/FC to 620 °C/4 h/AC cycle

increased titanium enhances the precipitation kinetics of the γ'' phase in the former as reflected by its Time-Temperature-Transformation (TTT) curves in the two alloys (Fig. 5.4).

The limited reports available on microstructure-properties relationships for the Alloy 625 PLUS pertains to the formation and evolution of the γ'' phase because of its primary contribution to the age hardening of the alloy. Most of the studies above are related to the effect of the formation of the γ'' phase on mechanical and corrosion properties of the alloy subjected to various heat treatments. Apart from the γ'' phase, Yu and Marquis [14] have reported the precipitation of the titanium and

Fig. 5.4 Calculated time-temperature-transformation curves for the precipitation of γ'' phase in Alloy 625 and Alloy 625 PLUS. The curves represent a 5% volume fraction of the γ'' phase

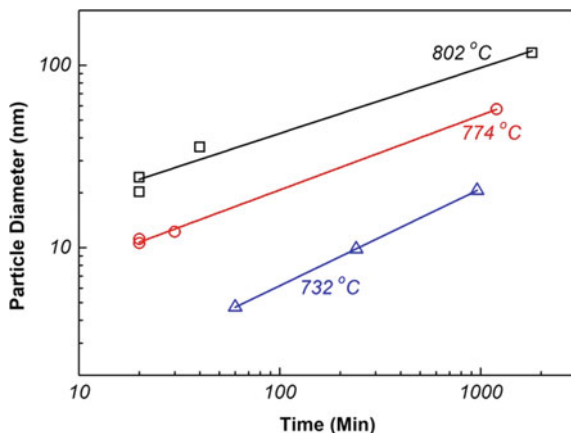


aluminum rich γ' phase particles after aging of more than 300 h at 650 °C. They have argued that the formation of the γ' phase after prolonged aging is due to reduced concentration of the niobium in the matrix because of $\text{Ni}_3(\text{Nb}, \text{Ti})\gamma''$ precipitation. The formation of the γ'' phase increases the concentration ratio of (Al + Ti) to Nb, which promotes its precipitation similar to that reported in Alloy 718 [15, 16]. A higher (Al + Ti)/Nb ratio in Alloy 625 Plus (~0.9) compared to Alloy 625 (~0.3) appears to stabilize the γ' phase. The γ'' and γ' phases in Alloy 625 PLUS form with compositions close to $\text{Ni}_3(\text{Nb}_{0.39}\text{Ti}_{0.26}\text{Mo}_{0.22}\text{Al}_{0.02})$ and $\text{Ni}_3(\text{Ti}_{0.4}\text{Al}_{0.4}\text{Nb}_{0.2})$, respectively [14], which are in close agreement with $\text{Ni}_3(\text{Nb}_{0.60}\text{Ti}_{0.27}\text{Mo}_{0.04})$ and $\text{Ni}_3(\text{Ti}_{0.49}\text{Al}_{0.28}\text{Nb}_{0.23})$ compositions predicted for the two phases by thermodynamic calculations using the MatCalc 6.03 Pro software.

Vander Voort et al. [8] have studied the growth/coarsening of ellipsoidal shaped γ'' phase particles in Alloy 625 PLUS solution annealed at 1038 °C for 2 h, followed by single-aging or double-aging treatments. Figure 5.5 shows variation in the length (diameter) of γ'' particles (Fig. 3.20) as a function of time in Alloy 625 PLUS aged at 732, 774 and 802 °C for periods ranging from 20 to 1800 min. The growth of the γ'' particles is a function of temperature and time, though the effect of the time on the size reduces somewhat with an increase in the aging temperature. An 18 h double-aging treatment involving 732 °C/8 h/FC and 620 °C/8 h/AC aging produced particles of average diameter 14.9 ± 1.3 , which increased to 26.5 ± 1.7 nm during a subsequent prolonged exposure of 500 h at 650 °C [8]. Over aging during the first aging produces much bigger particles. For instance, a double-aging treatment involving the first aging of 8 h at a higher temperature of 788 °C, followed by furnace cooling to 620 °C for the second aging of 8 h, producing particles of average size 55.2 ± 3.7 nm [8].

Yu and Marquis [14] have reported the formation of γ'' precipitates after aging for 8 h at 650 °C, which increased in the size with increasing aging time, in agreement with Vander et al. [8]. However, Yu and Marquis have also reported the formation of the γ' phase particles after aging of more than 300 h, though their density was

Fig. 5.5 Variation in the size of γ'' particles as a function of time during single ageing at different temperatures [8]



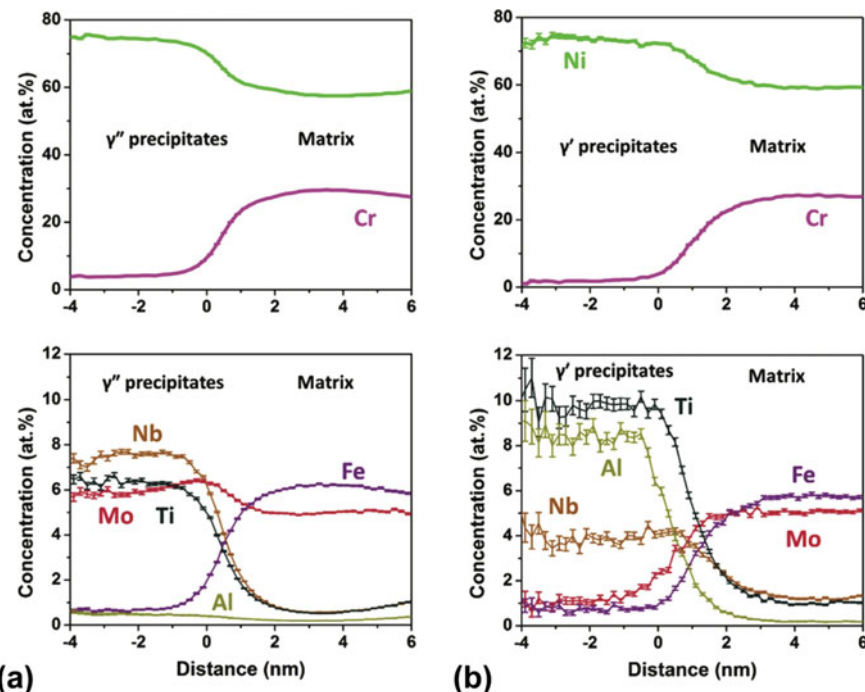
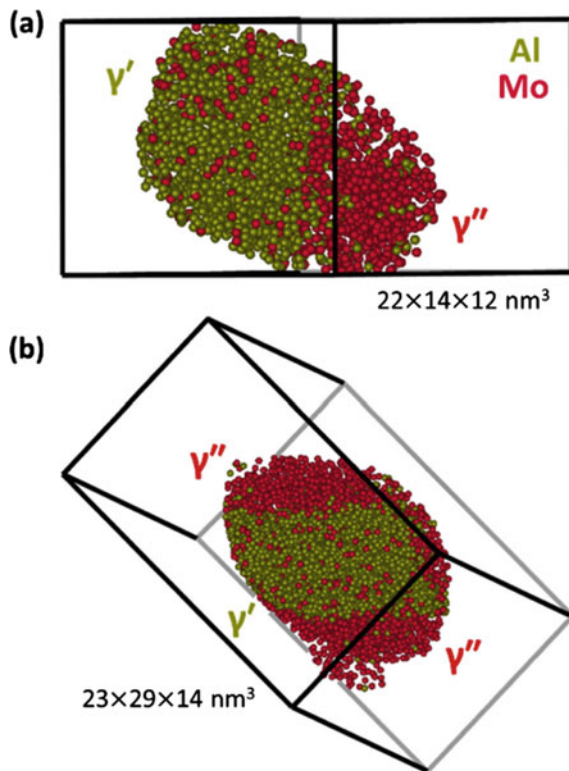


Fig. 5.6 Proxigrams showing partitioning behaviour of different solutes in **a** γ'' - γ phase, and **b** γ' - γ phase in the 625 PLUS alloy after ageing for 1000 h at 650 °C. Reprinted from Ref. [14], Copyright (2019), with permission from Elsevier

much lower than the γ'' particles [14]. Figure 5.6 shows the partitioning behavior of different constituent species in γ'' - γ and γ' - γ phases [14]. It is clear from Fig. 5.6 that nickel, niobium and titanium partitioned to γ'' precipitates while chromium and iron remained in the γ matrix. Aluminum partitions strongly to the γ' phase compared to slight enrichment in the γ'' phase. Molybdenum significantly depletes from the γ' phase, while its distribution remains unchanged in the γ'' phase. The cuboidal γ' phase particles forms on the flat surface of the disk-shaped γ'' phase particles in two configurations as γ'' - γ' doublets and γ'' - γ' - γ'' triplets comprising two γ'' particles bounding a γ' particle (Fig. 5.7), though doublets are observed more frequently. The formation of the “piggyback” configuration of γ'' and γ' phase particles have been attributed to the low energy of the coherent γ'/γ'' interface owing to good atomic matching between the {100} planes of the L1₂ structure of the γ' phase and the (001) plane of the D0₂₂ structure of the γ'' phase [15]. The γ''/γ' interface favors the heterogeneous nucleation due to smaller lattice misfit than the γ''/γ interface. Similar arrangements of γ'' and γ' precipitates have been reported in many studies on Alloy 718 [15–21]. Theska et al. [18] have also reported γ' - γ'' - γ' triplets in addition to γ'' - γ' - γ'' triplets in Alloy 718 under different aging conditions.

Fig. 5.7 Atom probe tomography reconstructed maps illustrating the formation of γ' - γ' duplets and γ'' - γ' - γ'' triplets in Alloy 625 PLUS. Reprinted from Ref. [14], Copyright (2019), with permission from Elsevier



In principle, either of the two phases can heterogeneously nucleate on the other depending upon the relative precipitation kinetics of the two. Unlike the present case, heterogeneous nucleation of the γ'' phase particles on pre-existing γ' has been reported in some cases where the γ' particles form first [15, 16, 19]. However, the formation γ'' - γ' - γ'' triplets in Alloy 625 PLUS is rather surprising as the γ'' phase forms first in Alloy 625 PLUS, while the γ' phase particles nucleate much later, as observed only after about 300 h of aging [14]. Therefore, it is reasonable for the γ' phase particles to form γ'' - γ' doublets by nucleating onto the existing γ'' particles to reduce the interfacial and elastic strain energy. Similar nucleation sequence involving the nucleation of the γ'' phase followed by that of the γ' phase has been reported earlier [17, 20]. Miller [17] has postulated that aluminum rejection in the adjacent matrix during the formation of the pre-existing γ'' precipitates favor the nucleation of γ' precipitates by increasing the $(\text{Al} + \text{Ti})/\text{Nb}$ ratio. However, the low amount of aluminum and its slight partitioning in the γ'' precipitates in Alloy 625 Plus appears less convincing for the formation process of γ'' - γ' - γ'' triplet. Alternatively, such configurations may form as a result of the impingement of independently nucleated adjacent γ'' and γ' precipitates as suggested by Sundararaman et al. [20]. Nonetheless, the formation of the γ' phase particles during prolonged aging may be the reason for

further increase in the strength of the alloy, as reported by Frank and Grimes [12] (Table 5.7).

The γ'' phase in Alloy 625 PLUS also exhibits different composition and precipitation behavior than Alloy 625. The main difference in the composition of the γ'' phase in two alloys is the concentration of niobium and titanium. The amount of niobium is reduced to about 9.5 at% in Alloy 625 Plus compared to about 13 at% in Alloy 625. In contrast, the titanium concentration increased significantly to about 7 at% in Alloy 625 Plus compared to about 1.5 at% in Alloy 625 [14].

Figure 5.8 illustrates the partitioning behavior of constituent elements in γ'' and γ phases during aging at 650 °C up to 1000 h [21]. The figure depicts the difference in the composition of various elements in the γ'' phase ($C_{\gamma''}$) and γ matrix (C_γ) along the x -axis, against the difference in their compositions in the matrix compared to the average alloy composition (C_n) on the y -axis. Figure 5.8 indicates that nickel and niobium preferentially partition to the γ'' phase and the phase becomes richer in nickel and niobium during their evolution with increasing aging time. The titanium also partitions to the γ'' . However, its concentration in the phase remains more or less unchanged with time. This partitioning of titanium is consistent with the composition of the γ'' phase, $\text{Ni}_3(\text{Nb}_{>0.5}\text{Ti}_{<0.5}\text{Al}_{<0.5})$, proposed much earlier by Floreen et al. [22] (Sect. 3.2.2). On the other hand, molybdenum initially partitions to the γ'' phase, but the phase tends to reject it during prolonged aging, consistent with Yu and Marquis [14] (Fig. 5.6). This result is also in agreement with a small amount of molybdenum (~6 at%) in the γ'' phase reported by Floreen et al. [22]. Aluminum has a slight preference for the partitioning to the γ'' phase. On the contrary, chromium and iron partition to the γ matrix and enrich the phase with time. Notwithstanding that, Floreen et al. [22] reported a small amount of chromium (~4 at%) in the γ'' phase. In Alloy 625 Plus, however, chromium reduces to nearly half, ~2 at% [14], indicating its enhanced partitioning to the matrix phase in Alloy 625 Plus.

The γ' phase in Alloy 625 Plus forms with a composition close to $\text{Ni}_3(\text{Ti}_{0.4}\text{Al}_{0.4}\text{Nb}_{0.2})$. The partitioning of nickel, titanium, aluminum and niobium solutes to the γ' in Alloy 625 Plus agrees with that reported for Alloy 718. However, the γ' phase in Alloy 625 Plus contains slightly higher titanium and less niobium than their concentrations in the same phase in Alloy 718. The composition of the γ' phase in Alloy 718 is reported as $\text{Ni}_3(\text{Ti}_{0.24\sim0.36}\text{Al}_{0.36\sim0.43}\text{Nb}_{0.22\sim0.36})$ [16, 23, 24].

Yu and Marquis [14] have also compared the evolution of the γ'' precipitates in Alloy 625 Plus and Alloy 625 and have shown that the volume fraction and the number density of the γ'' phase precipitates are nearly an order of magnitude higher in the former for the same aging conditions for the two alloys [14]. The coarsening rate of γ'' precipitates are slower in Alloy 625 Plus than Alloy 625, owing to the higher partition coefficients of niobium and titanium in the former [14]. A high partition coefficient reduces the coarsening rate [25]. The precipitation of the γ' phase particles do not significantly influence the coarsening kinetics of γ'' precipitates, as the γ' phase forms after a prolonged period and in low volume fraction and number density [14].

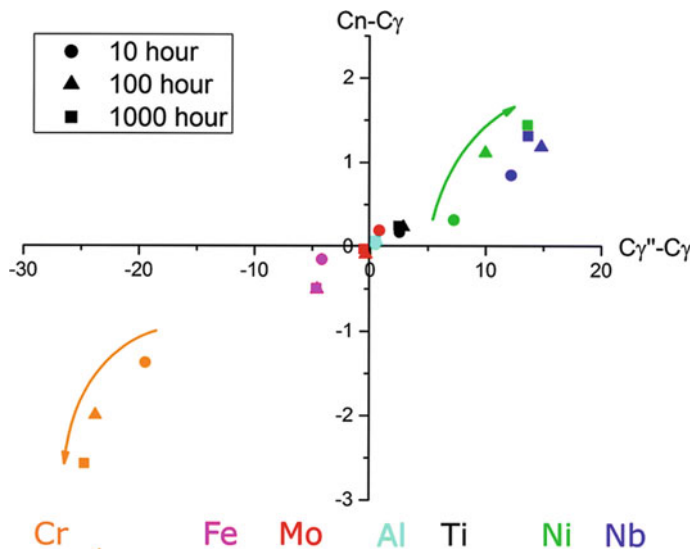


Fig. 5.8 Lever rule plots depicting partitioning behaviour of constituent elements in the γ'' and γ phases during ageing of Alloy 625 at $650\text{ }^{\circ}\text{C}$ for 10, 100 and 1000 h. The figure shows the difference in the composition of various elements in γ'' phase ($C_{\gamma''}$) and the γ matrix (C_{γ}) along the x-axis against the difference in their composition in the γ matrix with respect to average composition (C_n) of the analysed volume along the y-axis. Reprinted from open-source Ref. [21] under the terms of Creative Commons CC by license

5.4 Summary

Even though Alloy 625 age hardens significantly at elevated temperatures, its sluggish aging response constraints it to exploit commercially. Alloy 625 Plus differs from Alloy 625 by about 1% extra titanium. Increasing the titanium concentration in Alloy 625 to about 1.3% significantly increases the alloy's age-hardening response by γ'' precipitates. This allows Alloy 625 Plus to achieve higher strength levels without warm or cold working. Age-hardened Alloy 625 Plus shows mechanical properties better than Alloy 718 with equivalent ageing treatment.

References

- Frank RB, DeBold TA (1986) Custom age 625 PLUS—A new age-hardenable, corrosion-resistant alloy. In: ASM materials conference, Orlando
- Frank RB, DeBold TA (1988) Properties of an age-hardenable, corrosion-resistant, nickel-based alloy. Mater Perform 27:59–66
- Frank RB, DeBold TA (1990) Heat treatment of an age-hardenable, corrosion-resistant alloy—UNS NO7716. In: Paper No. 59, NACE corrosion conference, Las Vegas, NV
- Cieslak MJ, Headley TJ, Frank RB (1989) Welding metallurgy of custom age 625 PLUS alloy. Weld J (Miami, FL) 68

5. Frank RB (1991) Customage 625 plus alloy—a higher strength alternative to alloy 625. Loria EA (ed) Superalloys 718,625 various derivative
6. Frank RB, DeBold TA, Widge S, Martin JW (1996) Corrosion resistant age hardenable nickel-base alloy. US Patent no. 5556594
7. Data Sheet Custom Age 625 PLUS. <https://f.hubspotusercontent20.net/hubfs/7407324/Material%20Saftey%20Data%20Sheets/625%20Plus.pdf>; Data Sheet Custom Age 625PLUS alloy
8. Vander Voort G, Bowman JW, Frank RB (1994) Microstructural characterization of Custom Age 625 Plus alloy. https://doi.org/10.7449/1994/Superalloys_1994_489_498
9. Data Sheet Inconel alloy 625, Special Metals Corporation (2013) <https://www.specialmetals.com/documents/technical-bulletins/inconel/inconel-alloy-625.pdf>
10. Data Sheet HAYNES ® 625 alloy, HAynes International (2020) https://www.haynesintl.com/docs/default-source/pdfs/new-alloy-brochures/high-temperature-alloys/brochures/625-brochure.pdf?sfvrsn=967229d4_26#:~:text=HAYNES%C2%AE%20625%20alloy%20UNS,other%20solid%20solution%20strengthened%20alloys.
11. Data Sheet Inconel alloy 718, Special Metals Corporation (2007) <https://www.specialmetals.com/documents/technical-bulletins/inconel/inconel-alloy-718.pdf>; Special Metals Corporation, Publication No. SMC-045
12. Frank RB, Grimes R (1994) Properties of ultra-high-strength Custom Age 625 Plus alloy. Superalloys. 718:625–706
13. Onyewuenyi OA (2012) Alloy 718: alloy optimization for applications in oil and gas production. 345–362. https://doi.org/10.7449/1989/superalloys_1989_345_362
14. Yu LJ, Marquis EA (2019) Precipitation behavior of alloy 625 and alloy 625 plus. J Alloys Compd 811:151916. <https://doi.org/10.1016/j.jallcom.2019.151916>
15. Cozar R, Pineau A (1973) Morphology of γ' and γ'' precipitates and thermal stability of inconel 718 type alloys. Metall Trans 4:47–59. <https://doi.org/10.1007/BF02649604>
16. Detor AJ, DiDomizio R, Sharghi-Moshtaghin R, Zhou N, Shi R, Wang Y, McAllister DP, Mills MJ (2018) Enabling large superalloy parts using compact coprecipitation of γ' and γ'' . Metall Mater Trans A 49:708–717
17. Miller MK (2001) Contributions of atom probe tomography to the understanding of nickel-based superalloys. Micron 32:757–764. [https://doi.org/10.1016/S0968-4328\(00\)00083-4](https://doi.org/10.1016/S0968-4328(00)00083-4)
18. Theska F, Stanojevic A, Oberwinkler B, Ringer SP, Primig S (2018) On conventional versus direct ageing of Alloy 718, Acta Mater 156:116–124. <https://doi.org/10.1016/j.actamat.2018.06.034>
19. Shi R, McAllister DP, Zhou N, Detor AJ, DiDomizio R, Mills MJ, Wang Y (2019) Growth behavior of $\gamma\$$ / $\gamma''$$ coprecipitates in Ni-base superalloys. Acta Mater 164:220–236
20. Sundararaman M, Mukhopadhyay P, Banerjee S (1992) Some aspects of the precipitation of metastable intermetallic phases in INCONEL 718. Metall Trans A 23:2015–2028. <https://doi.org/10.1007/BF02647549>
21. Gardner H, Pedrazzini S, Douglas JO, De Lille D, Moody MP, Bagot PAJ (2019) Atom probe tomography investigations of microstructural evolution in an aged nickel superalloy for exhaust applications. Metall Mater Trans A 50:1862–1872. <https://doi.org/10.1007/s11661-018-5098-x>
22. Floreen S, Fuchs GE, Yang WJ (1994) The metallurgy of alloy 625. In: Superalloys 718, 625, 706 various derivative. The Minerals, Metals & Materials Society, Pittsburgh, PA, USA, pp 13–38
23. Drexler A, Oberwinkler B, Primig S, Turk C, Povoden-Karadeniz E, Heinemann A, Ecker W, Stockinger M (2018) Experimental and numerical investigations of the γ'' and γ' precipitation kinetics in alloy 718, Mater Sci Eng A 723:314–323. <https://doi.org/10.1016/j.msea.2018.03.013>
24. Lawitzki R, Hassan S, Karge L, Wagner J, Wang D, von Kobylinski J, Krempaszky C, Hofmann M, Gilles R, Schmitz G (2019) Differentiation of γ' - and γ'' -precipitates in Inconel 718 by a complementary study with small-angle neutron scattering and analytical microscopy. Acta Mater 163:28–39. <https://doi.org/10.1016/j.actamat.2018.10.014>
25. Kuehmann CJ, Voorhees PW (1996) Ostwald ripening in ternary alloys. Metall Mater Trans A 27:937–943. <https://doi.org/10.1007/BF02649761>

Chapter 6

Fabrication



Superalloy ingots are usually fabricated into sheets, bars, tubes, and various other wrought products and shapes. Standard fabrication techniques involve casting, metal-forming, machining, welding, etc. Some superalloys of highly alloyed compositions, like IN-100, Rene 95, Stellite 31, etc. or oxide-dispersion strengthened alloys that are difficult or impractical to fabricate by the conventional techniques are generally processed into wrought shapes by powder metallurgy processing. Advancements in powder metallurgy and laser technologies have evolved a new approach commonly known as “additive manufacturing” as an alternative to conventional fabrication. The significant advantage of additive manufacturing is it lowers the production cost by reducing the input weight of expensive raw materials and the number of secondary machining operations. This chapter gives an overview of essential fabrication techniques used to fabricate Alloy 625 products.

6.1 Hot Forming of Metals

Forming of metals and alloys refers to the processes involved in their plastic deformation to affect changes to achieve desired shape and properties. When the deformation is performed at a temperature above which recrystallization occurs, the process is termed as “hot working”. Deformation at low temperatures is called “cold working”. Hot-working allows imparting large deformation in successive steps because the metal remains soft and ductile, requiring less deformation energy. But, most metals experience some surface oxidation that results in metal loss and a poor final surface finish. The strain accumulated during hot deformation is removed by recrystallization of the grains. On the other hand, cold-working operations work hardens the material and significantly reduce ductility. Yet, cold-working produces the finished product with a closer dimensional control and a higher quality surface finish.

Hot-working is usually done at temperatures above about $0.5T_m$ (T_m is melting temperature in Kelvin). Most hot working operations involve forging, rolling, extrusion or drawing, which differ in how they impose stress on the workpiece. During forging, the shape change is achieved by applying successive blows or continuous squeezing. Forged products have outstanding grain structures and the best combination of mechanical properties. Rolling is usually used for reducing thickness under compressive stresses when a piece of metal is passed between two rolls. In an extrusion process, a metal bar is forced through a die orifice to reduce its cross-section by a compressive force applied through a ram. On the other hand, a metal piece in a drawing operation is pulled through the die with a tapered bore, using a tensile force applied on the exit side. These techniques have inherent limitations and advantages, as well as the ability to produce specific products.

The main objectives of all hot forming processes are to optimize properties of the alloy in all sections of the component by achieving (i) uniform grain refinement; (ii) control of second-phase particles; (iii) controlled plastic flow; (iv) structurally sound components. A necessary requirement of successful operations of all hot deformation processes is the uniform flow of the metal and the complete recrystallization of grains of desired size. The nonuniform or inhomogeneous flow of the metal may lead to failure. Recrystallization of grains is required to obtain the strain-free grains.

6.1.1 Rate Controlling Phenomenon

A crystalline material starts deforming plastically when the shear stress due to the applied force reaches a value above the yield stress. At elevated temperatures, dislocations overcome obstacles under the combined applied stress and thermal energy. When the external stress is low, the energy required to overcome the barriers (activation energy) comes from the thermal energy, and the thermally activated climb alone dominates the deformation. At high temperatures, the lattice-diffusion controls the climb of dislocations for which the activation energy is high. In contrast, the diffusion through the dislocation's cores controls the climb at low temperatures for which the activation energy is less. The influence of the stress (σ) and temperature on the strain rate ($\dot{\varepsilon}$) can be represented by a constitutive equation of the type [1]

$$\dot{\varepsilon} = A[\sinh(\alpha\sigma)]^n \exp(-Q/RT) \quad (6.1)$$

where A and α are material constants, α is the stress multipliers, Q is the deformation activation energy, R is the universal gas constant, T is the absolute temperature, and n is the stress exponent. In principle, A and Q are independent of temperature, but their independence is restricted to the temperature range of no phase transformation.

Dislocation climb plays a significant role in the plastic flow of the material at high temperatures. Even though dislocation glide produces almost all the plastic strain, the climb controls their velocity at high temperatures because climb allows them to

surmount obstacles whenever they obstruct the glide. The mechanism that controls the climb process is governed by the Power-law creep (Eq.4.19, Chapter 4). At high temperatures ($\geq 0.6 T_M$), the deformation may be accompanied by repeated waves of recrystallization [2]. Each wave removes or drastically changes the dislocation substructures allowing a period of primary creep so that the strain rate oscillates at a constant load. At higher strain rates and temperatures, the power-law breaks down when a recovery process different from that of the climb-controlled creep occurs. When the power-law breaks down, the activation energy may exceed that of the self-diffusion.

Though hot working shares many commonalities with a creep phenomenon, it differs significantly from creep because of:

- (i) the stress, which is a function of both strain rate and strain, unlike in creep where it is a function of strain rate only;
- (ii) the strain rate or the total energy of deformation controls the stress applied, which can vary with the strain, unlike in creep, where a fixed stress is applied.
- (iii) much higher strain rates during hot working (typically 10^{-3} to 10^3 s^{-1}) compared to that in creep ($\sim 10^{-8}$ to 10^{-5} s^{-1}), which results in higher flow stresses, and in turn, alters microstructure significantly;
- (iv) the working stresses are relatively high in hot working.

6.1.2 *Microstructural Changes during Hot Deformation*

The alloy undergoes dynamic recovery or recrystallization of grains during hot working. Recovery refers to removing work-hardening defects without disturbing the high-angle grain boundaries. In contrast, recrystallization refers to forming new, strain-free grains from the existing deformed grains containing work-hardening defects. The prefix “dynamic” refers to the recovery/recrystallization coinciding with hot working. Figure 6.1 depicts the structural changes occurring during a typical hot-working process. During hot-working, either dynamic recovery, or dynamic recrystallization, or both may occur depending upon the stress and strain rates. For materials, like Alloy 625, with a low or intermediate stacking fault energy, the dynamic recovery process is slow as the low stacking fault energy resist the climb of dislocations. The slow recovery process reduces the recovery rate, and grains attain a sufficiently high density of dislocations within a short period to initiate dynamic recrystallization.

Immediately after hot working, the dynamic recovery is followed by static recrystallization before quenching. This static recrystallization commences without any incubation period, and dynamically recrystallized grains continue to grow at the expense of unrecrystallized grains [3]. This process is termed “meta-dynamic” recrystallization. The meta-dynamic recrystallization is extremely quick and can cause the rapid growth of recrystallized grains.

During dynamic recovery, the overall level of the flow stress increases with an increase in the strain rate and decreases in temperature, or both, because of the build-up of dislocation networks and small-angle grain boundaries till a steady state in

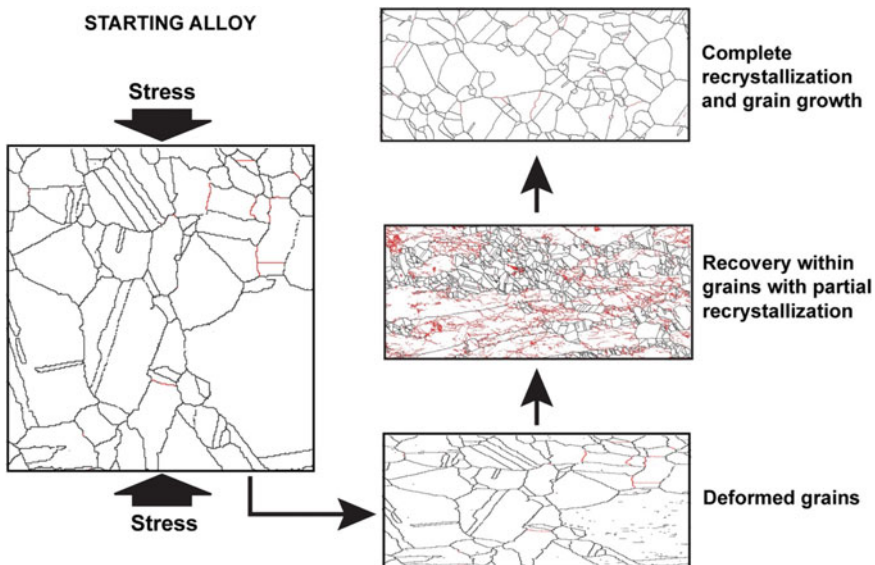


Fig. 6.1 A schematic illustrating the structural changes occurring during a typical hot-working operation. Boundaries in black represent grain boundaries, while boundaries in red represent small-angle boundaries that form due to the dynamic recovery process

the stress value is reached (σ_{ss}). The steady-state microstructure is characterized by grains elongated in the primary direction of strain and contracted in other directions. The substructure of these grains comprised equiaxed sub-grains whose size decreases with increasing stress.

The material's response during dynamic recrystallization depends upon the temperature of deformation or the strain rate applied. At higher strain rates (or lower temperatures), the overall flow stress level is higher than at lower strain rates (or higher temperatures). At higher strain rates, the flow stress increases after yielding till a maximum value (σ_{max}) is reached, after which the stress decreases and eventually attains a steady-state value (σ_{ss}). The dynamic recovery occurs until the σ_{max} is reached. The stress level drops after the σ_{max} as dynamic recrystallization starts dominating. On the other hand, at low strain rates and higher temperatures, the overall level of the flow stress is less because of the dominance of the dynamic recrystallization soon after yielding. In addition, the stress-strain curve may exhibit oscillatory behavior, cycling above and below an approximate steady-state stress, which tends to dampen out at larger strains.

The difference in the flow stress behavior is the manifestation of the development of different substructures during dynamic recovery and recrystallization. For recrystallization to begin, a critical dislocation substructure needs to be developed within a grain. Deformation at a high strain rate (and the correspondingly high stress) or low temperature causes the heterogeneous distribution of deformation levels within different grains. Because of the high strain rate (and higher stress), the time needed

to attain the critical structure is short for an individual grain. As a result, grains possessing a well-developed substructure with a high density of dislocations recrystallize while other grains continue to deform. This substructure is invariant to the strain even though the structure within each grain is continuously changing. By the time the deformed grains recrystallize, other grains accumulate sufficient dislocations for recrystallization. Simultaneously, the dislocation density in just recrystallized grains reaches a low value, continuing the process. This process of dynamic recrystallization of some grains is stochastic but develops a steady-state structure throughout the material volume. On the other hand, the deformation at low strain rates, at a given time, is uniform with approximately the same substructure within all grains throughout the material because the low strain rates provide sufficiently long time and greater strain to accumulate the critical dislocation density within grains to begin recrystallization. The uniform recrystallization reduces the stress levels to deform the strain-free new grains. Thus the flow curve is characterized by oscillatory stress where the accumulation of dislocations harden and the dynamic recrystallization softens the flow. The repeated wave of recrystallization continuously removes or drastically changes the dislocations substructures within the individual grain. Each local minimum in the stress level represents the end of a recrystallization wave when a low density of dislocations characterizes individual grains.

6.1.3 Hot Working of Alloy 625

The hot deformation behavior of Alloy 625 has been studied by different research groups over the temperature range of 900–1200 °C at constant strain rates ranging from 0.001 to 80 s⁻¹ [4–9]. Experimental details of individual work are listed in Table 6.1. The flow stress behavior of the alloy compares well among different groups and follows typically a thermally induced behavior discussed above. The flow stress increases with increasing strain rate and decreasing temperature. An increase in

Table 6.1 Experimental details of hot deformation experiments and the kinetic parameters estimated during studies on hot deformation of Alloy 625

Authors	Temperature range (°C)	Strain rate range (s ⁻¹)	α (MPa ⁻¹)	A (s ⁻¹)	Q (kJ/mol)	n	Reference
Lopez and Urcola	950–1150	0.17–5.3	0.0036	2.65×10^{15}	400	4.0	[4]
Zhou et al. [6]	950–1150	0.001–5	0.0044	1.05×10^{15}	421	3.92	[6]
Jia et al. [8]	900–1200	0.01–10	0.0033	5.82×10^{17}	474	4.87	[8]
Sun et al. [7]	950–1200	0.1–80	0.0023	1.35×10^{18}	680	7.65	[7]

the strain rate at low temperatures results in flow softening. A fully dynamically recrystallized microstructure is achieved at a temperature above 1050 °C.

Figure 6.2 shows the typical flow behavior of Alloy 625 at temperatures above 950 °C for strain rates between 0.1 and 5.5. The alloy achieves steady-state flow stress at strains between 1 and 1.5 [4, 9]. Figure 6.3 shows the variation of the peak stress with temperature and strain rate. The peak stress increases with decreasing temperature and increasing strain rate. The amount of strain is uniquely related to the peak flow stress, which increases with decreasing temperature and increasing strain rate. This behavior is similar to many other alloys ([for example, Alloy 718 [10], Alloy 693 [11]) and is attributed to an increase in grain boundary mobility and a decrease in the critical dislocation density for dynamic recrystallization with increasing temperature, resulting in a reduction of the peak strain [9]. An increase in the strain rate has the opposite effect. All the authors in Table 6.1, except Sun

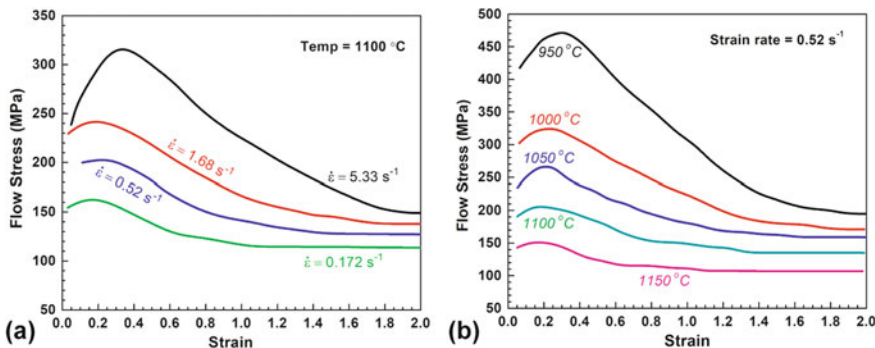
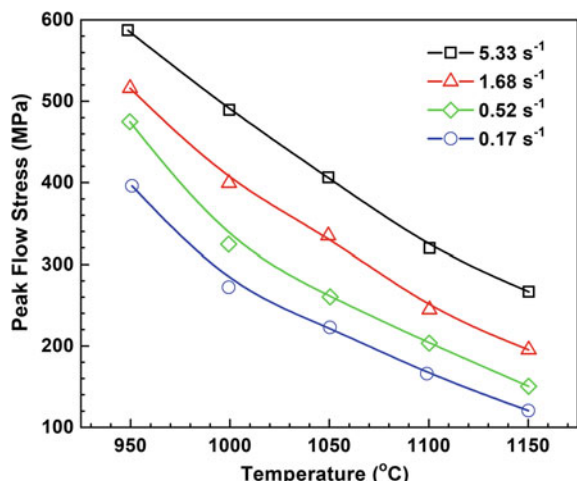


Fig. 6.2 Stress–strain flow curves of Alloy 625 as a function of temperature and strain rates: **a** at a fixed temperature of 1100 °C; **b** at a fixed strain rate of 0.52 s⁻¹ [4]

Fig. 6.3 Dependence of peak flow stress on the temperature at a given strain rate [4]

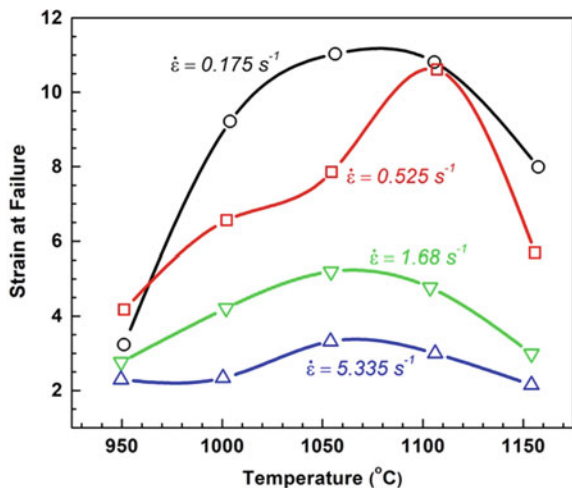


et al. [7], reported similar kinetic behavior of the alloy during hot deformation and estimated the values of Q in the range 400–474 kJ/mol and n in between 3.9 and 4.9, indicating that the climb-plus-glide power-law creep controls the hot deformation behavior of Alloy 625. Table 6.1 also lists the kinetic parameters (Eq. 6.1) estimated by these authors. However, the power-law mechanism appears to break down under the processing conditions used by Sun et al. [7], as indicated by high values of the Q and n . The breakdown of the power-law mechanism is possible due to the high strain rate, which requires higher stress for deformation.

The fraction of dynamically recrystallized grains increases with temperature. The alloy exhibits nearly complete recrystallized microstructure at temperatures above 1050 °C. At lower temperatures, the recrystallization is usually incomplete. The size of the dynamically recrystallized grain, d_{rex} , is related to fracture stress σ_f by a relationship given by $\sigma_f \propto d_{\text{rex}}^{-0.75}$ [4].

For a given strain rate, the alloy exhibits maximum ductility at temperatures between 1050 and 1100 °C, followed by a rapid decrease at higher temperatures (Fig. 6.4). An increase in the strain rate decreases the ductility and shifts the ductility maxima to lower temperatures. This strain rate effect on the ductility is consistent with other superalloys [12]. McQueen et al. [12] have associated the highest ductility to the optimum conditions for the occurrence of significant recovery and recrystallization without encountering grain growth. Low ductility at lower temperatures is attributed to increased work-hardening and the material's inability to recover or recrystallize dynamically. On the other hand, the reduced ductility at temperatures above 1100 °C is due to the grain coarsening effect. At much higher temperatures, close to the incipient melting, the synergistic effects of grain coarsening and grain boundary embrittlement appear to reduce the ductility further [12].

Fig. 6.4 Variation in ductility of Alloy 625 with the temperature at a given strain rate [4]



6.2 Heat Treatments

Heat treatment refers to heating or cooling the alloy to obtain desired properties by removing internal stress, changing microstructure, precipitating or dissolving the second-phase particles. Heat treatment of nickel-based alloys is typically performed in reducing atmosphere. The terminology of different heat treatments may vary among shop floors, but the purpose remains mostly the same, as noted in this section. This section briefly describes various heat treatments Alloy 625 may undergo during processing or fabrication. Representative annealing temperatures, holding times, and cooling procedure for Alloy 625 are listed in Table 6.2 [13]. Primary carbides in the alloy are usually not affected by any heat treatment though some dissolution may occur during the homogenization treatment.

6.2.1 Types of Heat Treatments

6.2.1.1 Stress Equalizing Treatment

Stress equalizing treatment balances stresses in work-hardened alloys. It is a low-temperature heat treatment, usually in the temperature range of 260–370 °C [1]. Stress equalizing is by partial recovery of the cold-worked material without detectable microscopic structural changes. This treatment results in a slight increase in the hardness, yield strength and tensile strength with little change in the ductility.

6.2.1.2 Stress Relieving Treatment

Stress-relieving treatment reduces stresses in the work-hardened alloy without producing a recrystallized grain structure. This treatment removes more internal stresses than are released by the stress equalizing treatment without appreciably decreasing the strength. The stress-relieving temperature is usually below the annealing temperature. The typical stress relieving temperature for Alloy 625 is

Table 6.2 Typical heat treatment temperatures for Alloy 625 [13]

Heat treatment	Temperature ^a (°C)	Time ^b (h)
Stress relieving	870	1
Annealing	980	1
Solution annealing	1150	2

^a To provide an adequate quench after the treatment, it is necessary to cool below about 600 °C rapidly enough to prevent sensitization of the alloy

^b Holding time per inch of section

about 870 °C (Table 6.2). However, it may vary depending on the alloy's microstructure and the magnitude of stresses accumulated during thermo-mechanical treatment. Stress-relieving requires careful control of time and temperature. The stress-relieving treatment may cause slight decreases in yield strength, tensile strength and hardness, and a slight increase in elongation.

6.2.1.3 Annealing Treatment

Annealing refers to a heat treatment at a suitable temperature, followed by cooling at a suitable rate. An annealing treatment is given to soften a work-hardened material. The treatment is used to increase alloy's ductility for forming or machining, relieve stresses before and after welding and simultaneously produce other desired properties and changes. The treatment involves alloy's exposure to an elevated temperature to cause recrystallization of the work-hardened microstructure. Recrystallization removes all the stresses and softens the material but decreases the mechanical strength. The typical annealing temperature for Alloy 625 is about 980 °C (Table 6.2). However, it may vary considerably as the recrystallization temperature depends on time, temperature, and the amount of cold work. Figure 6.5 illustrates a typical variation in the recrystallization temperature of Alloy 600 with the amount of cold work [14]. The annealing time and temperature of the alloy must be controlled carefully. Otherwise, grain growth may occur if the temperature and time exceed those required for recrystallization.

Alloys with coarse grains are less desired for many cold-forming operations and service conditions requiring good fatigue strength. If grains coarsen, a repeat of

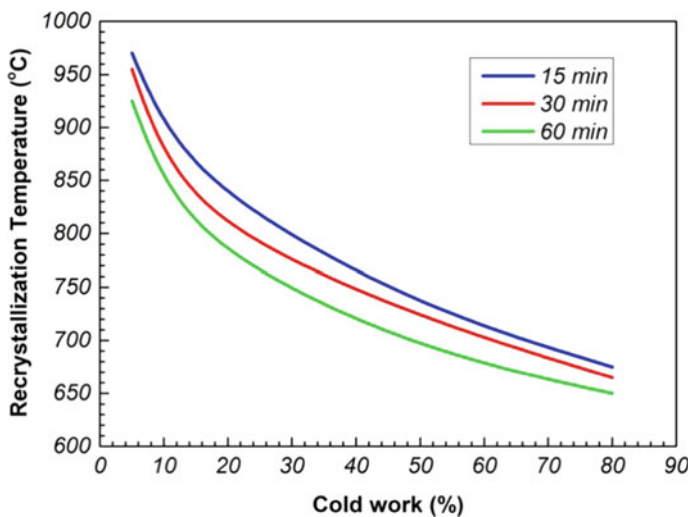
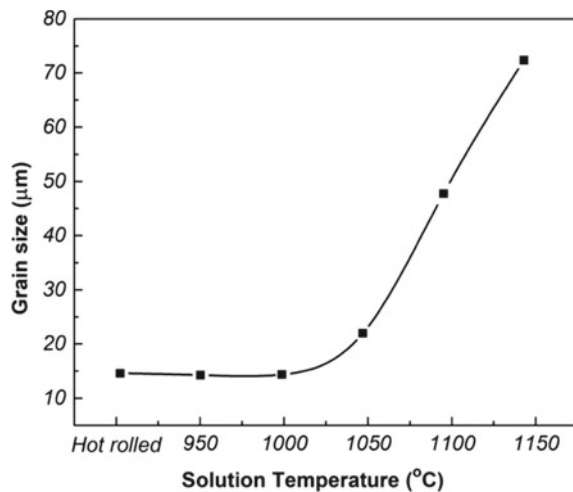


Fig. 6.5 Variation in the recrystallization temperature of Alloy 600 with percentage cold work [14]

Fig. 6.6 Grain size of a hot rolled Alloy 625 annealed at different annealing temperatures for 10 min [15]



the cold working, followed by a recrystallization treatment on the alloy is the only solution to produce a fine-grained structure. The average grain size of Alloy 625 does not change significantly when the alloy is annealed for 10 min at temperatures up to 1000 °C (Fig. 6.6) [15]. The grain size increases at temperatures above 1000 °C as the grain boundary carbides dissolve above this temperature. Above 1100 °C, the grains grow considerably. The beginning of the grain growth at temperatures above 1000 °C coincides with the maximum temperature (1040 °C) up to which carbides are stable (Sect. 3.2.5 and 3.5.4). Sometimes, imprecise terms like “final annealing” and “full annealing” are used to describe specific annealing conditions. “Final annealing” refers to the last annealing treatment given to the alloy before the shipment. “Full annealing” refers to the annealing cycle that produces alloy with entirely recrystallized microstructure and the lowest hardness and strength.

6.2.1.4 In-Process Annealing Treatment

Cold working markedly increases the strength and lowers the ductility of the alloy. Therefore, imparting a high cold working often requires intermediate annealing operations. The intermediate annealing reduces the stress and improves ductility for adequate formability of the metal. However, the in-process annealing temperatures may vary widely depending on working operations. Even during hot working, most nickel-based superalloys begin to accumulate defects, particularly toward the final stages of deformation, that are removed by intermediate heating the alloy for subsequent deformation. Similar in-process annealing treatments are required even during multistep forging, except for isothermal operations. The heat supplied to maintain the constant temperature is sufficient to cause the annealing of the forged alloy simultaneously with forging. In general, in-process annealing is usually done for complete or

nearly complete recrystallization of grains and the dissolution of all or most secondary phases. However, temperature control is critical when varying degrees of recrystallization are desired during the final stage properties. The in-process annealing is restricted to temperatures that do not dissolve all secondary phases but retains some to pin the grain boundaries to limit the grain growth during the final steps of the desired product.

6.2.1.5 Solution Annealing Treatment

The solution annealing temperature is higher than the annealing temperature. Solution heat treatment refers to heating an alloy to a suitable temperature and holding for a time that causes the dissolution of one or more of the “second-phase” particles into the matrix solid solution. A solution heat treatment is followed by cooling the alloy rapidly enough to retain the constituents of the dissolved phases in the solid solution. The solution annealing aims to produce a fully disordered microstructure for maximum corrosion resistance or prepare the alloy for subsequent aging. The typical solution annealing temperature for Alloy 625 is carried out at about 1150 °C (Table 6.2). A higher solution treating temperature will result in grain growth in wrought alloys.

Solution annealing treatment is sometimes confused with the “full annealing” treatment. The two treatments appear identical but are distinguished based on their purpose. Solution treating intends to dissolve the second-phase precipitate particles and applies to age-hardened materials. In contrast, full annealing refers to the annealing cycle that produces the fully recrystallized microstructure.

6.2.1.6 Homogenization Treatment

Homogenization treatment eliminates or decreases chemical segregation by diffusion when the alloy is heat treated at temperatures above the solution annealing temperature. However, the homogenization temperature must be restricted below the alloy’s incipient melting temperature. The incipient temperature is governed by equilibrium and non-equilibrium phases formed by segregating elements during solidification. The incipient melting temperature of Alloy 625 is 1288 °C and its homogenization are recommended at about 1200–1250 °C. The inhomogeneity level decides the period of homogenization. However, homogenization becomes increasingly uneconomical with a temperature above 1200 °C. The homogenization is explicitly done on the cast structures where thermo-mechanical processing is impossible.

6.2.1.7 Precipitation/Age-hardening Treatment

Precipitation treatments are intended to precipitate desirable strengthening phases from the supersaturated matrix and control carbide phases. Unlike other heat treatment temperatures mentioned above, selecting the precipitation temperature and periods for a given alloy may vary significantly, depending on the size, distribution, volume fraction, and density of precipitating phase particles. When more than one phase precipitates from the matrix, as in Alloy 625, judicious selection of an aging temperature is essential.

As per the design of the alloy, Alloy 625 is a solid-solution strengthened alloy. However, as noted in Chaps. 3 and 4, precipitation of various hardening phases occurs at intermediate temperatures. These phases precipitate out homogeneously as sub-microscopic particles throughout the grains and cause a substantial increase in the hardness and strength. Precipitation reactions and their temperature range for the formation of various phases in Alloy 625 are summarized in Table 6.3. Unlike many γ' strengthened alloys, such as Alloy 693 [16], precipitation of the hardening phases in Alloy 625 is delayed because of their large incubation periods. Nonetheless, their incubation time and precipitation temperature can be reduced by deforming the alloy before precipitation (Sect. 3.4).

6.2.2 Prevention of Contamination

Like other nickel alloys, Alloy 625 is also susceptible to embrittlement by sulfur, phosphorus, lead, zinc, and other low melting-point or eutectic forming elements. These elements may be present in lubricants, marking crayons and inks, paints, pickling liquids, dirt accumulated on the alloy during storage, furnace slag and cinder, or temperature-indicating sticks, pellets, lacquers, etc. It is therefore important that the alloy be cleaned before heating. In addition, the alloy must be protected from

Table 6.3 Precipitation sequence of different intermetallic phases in Alloy 625

Temperature range	Precipitation reaction	Aging duration
$T \leq 600 \text{ }^{\circ}\text{C}$	$\gamma_s \rightarrow \gamma + \text{Ni}_2(\text{Cr, Mo})$	Prolonged aging
$600 \text{ }^{\circ}\text{C} < T \leq 650 \text{ }^{\circ}\text{C}$	$\gamma_s \rightarrow \gamma + \text{Ni}_2(\text{Cr, Mo}) + \gamma''$	Prolonged aging
$650 \text{ }^{\circ}\text{C} < T < 750 \text{ }^{\circ}\text{C}$	$\gamma_s \rightarrow \gamma + \gamma''$	Short aging
$650 \text{ }^{\circ}\text{C} < T < 750 \text{ }^{\circ}\text{C}$	$\gamma_s \rightarrow \gamma + \gamma'' + \delta$	Prolonged aging
$750 \text{ }^{\circ}\text{C} < T < 800 \text{ }^{\circ}\text{C}$	$\gamma_s \rightarrow \gamma + \gamma'' + \delta$	Short aging
$750 \text{ }^{\circ}\text{C} < T < 800 \text{ }^{\circ}\text{C}$	$\gamma_s \rightarrow \gamma + \delta$	Prolonged aging
$T > 800 \text{ }^{\circ}\text{C}$	$\gamma_s \rightarrow \gamma + \delta$	Short aging

γ_s Refers to supersaturated γ phase

contamination while in the furnace by placing in metal baskets or on a metal floor, trays, rider bars or any other material that avoid the alloy's direct contact with the refractory heart.

6.2.3 Fuels

In general, gaseous fuels are preferred for heating nickel-based alloys because of: (i) their high calorific values and good heating; (ii) their easy mixing with air; (iii) better control of their supply. However, any low sulfur gaseous and oil fuel or electricity can be used to heat Alloy 625. Natural gas is the best fuel as it is free of sulfur compounds and primarily contains methane and smaller amounts of ethane, propane, and butane. Manufactured gases produced from coal or oils may contain substantial amounts of sulfur. Manufactured gases should, therefore, be used only after reducing their sulfur compounds to an acceptable level. Oil is a good fuel for heating the alloy if its sulfur content is not more than 0.5% by weight of sulfur [14]. When the use of a high-sulfur fuel cannot be avoided, the detrimental effect of sulfur can be minimized by maintaining a slightly oxidizing atmosphere of the furnace. However, this may cause some oxidation of the alloy surface. Solid fuels like coal and coke are not preferred because of their excessive sulfur content, comparatively low calorific values and poor heating control.

6.2.4 Protective Atmosphere

A protective atmosphere for annealing is required for all materials to maintain a reducing environment for a bright surface of the annealed alloy. Protective atmospheres of helium, nitrogen or dissociated ammonia gas is generally used for treating nickel-based alloys. However, these gases must be dry for the bright finish of the heat-treated surface. Water vapor present in gases decomposes into hydrogen and oxygen at high temperatures when they come into contact with hot metal surfaces. The oxygen produced oxidizes the surface resulting in the loss of brightness. Therefore, the water content in gas must be reduced to an acceptable level.

Dew point gives a measure of the moisture in natural gases. Dew point is the temperature and pressure at which the first drop of the water vapor condenses into a liquid. With a decrease in the amount of water vapor, the dew point of the gas decreases. At lower temperatures, lower dew points are required.

Chromium, molybdenum and niobium are the main oxides forming elements in Alloy 625. The best protective atmosphere for Alloy 625 is a dry 100% hydrogen environment. If the hydrogen is prepared by catalytic gas reactions instead of electrolysis, residual hydrocarbons, such as methane, must be limited to about 50 ppm to prevent carburizing [14]. The significance of the dew point of the gas in controlling the oxidation of the surface can be understood considering the oxidation behavior

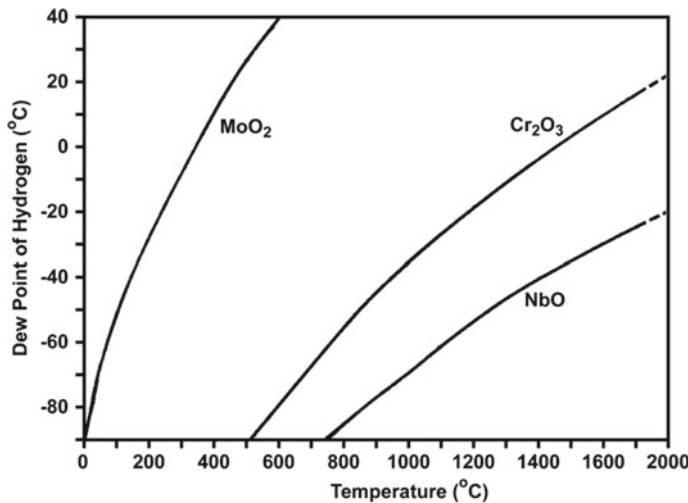


Fig. 6.7 The metal/metal oxide equilibria of chromium, molybdenum and niobium elements in hydrogen atmospheres as a function of temperature and dew point [14]

of chromium in a 100% hydrogen atmosphere. Figure 6.7 shows the metal/metal-oxide equilibria of chromium, molybdenum and niobium elements in hydrogen atmospheres as a function of temperature and dew point. The area on the left of each curve is the oxidized condition, and on the right is the reduced condition. At a temperature of 1100 °C, a dew point of less than –30 °C of the hydrogen gas is required to reduce chromium oxide to chromium. For example, at 800 °C, the dew point must be below –50 °C. Though this dew point is for the chromium element, the same would avoid molybdenum oxidation also because of its higher dew point. Though a lower dew point of the gas is required to prevent niobium oxidation, it would play an insignificant role due to niobium's much lower concentration. Though these dew point values are derived from the thermodynamic relationships of pure metals and their oxides at thermal equilibrium, the same has been shown to work as a guide to the oxidizing behavior of complex alloys under non-equilibrium conditions [14]. Therefore, a protective environment of 100% hydrogen gas of dew point –50 °C or lower is required for bright annealing of Alloy 625. As the dew point decreases at lower temperatures, the alloy must be cooled rapidly in the protective atmosphere to minimize its oxidation during cooling. Environments like nitrogen or dissociated ammonia may not protect Alloy 625 adequately because it tends to form nitride.

It is important to note that the protective atmosphere of hydrogen within the heating chamber or the furnace must be maintained at a positive pressure throughout heating and cooling. Hydrogen forms explosive mixtures with air over a wide range of compositions. Any infiltration of the air at high temperatures may cause severe fires or explosions. The same precautions are also required while preparing the atmosphere for heat treatment. The chamber must be thoroughly purged with an inert gas to remove all air before heating.

6.3 Machining of Alloy 625

6.3.1 Conventional Machining

The machining behavior of Alloy 625 in conventional machining processes is governed by its rapid work-hardening characteristics (Sect. 4.5.1). The machining properties are similar to those of other nickel-base alloys like Inconel 901, 900, 617, 706, 718, X 750, Nimonic 75 and 80 A, Waspaloy, etc. [17].

During the machining process, intense friction is generated at the tool-workpiece interface. This friction causes localized severe plastic deformation of the workpiece and generates excessive heat. This heat coupled with work-hardening may cause debonding of the tool substrate. Debonding of the tool may lead to machining related failures like poor surface finish, excessive tool wear, frequent tool change, productivity loss, high power consumption, etc. all of which makes machining of the Alloy 625 less economical. Moreover, the high pressures developed during machining work hardens the alloy surface rapidly, which retards further machining. The work-hardening produces stresses even under optimum machining conditions and, subsequently, may distort the workpiece, particularly parts with small cross-sections. High temperature and mechanical stresses at the tip of the tool in contact with the hardened machined surface layer may cause notch wear of both the flank and the rake of the tool. The predominant mechanisms of wear during machining are abrasive and diffusive [18]. Such wear may result in chipping, formation of the built-up edge (BUE) and built-up layer (BUL) and even fracture the tool. An increase in the cutting speed, cutting temperature or cutting depth tends to increase the tool wear rate. The tool's wear causes deterioration in the quality of the machined surface and increases the surface roughness. Due to these limitations of Alloy 625, only a low cutting speed is used in a chip-removing operation for acceptable machined surface quality and reduced tool wear [19]. In addition, the machining of the alloy produces long and continuous chips independent of the cutting conditions. Therefore, the machining process has to be interrupted often to remove the long chips from the process zone. Automatization of conventional machining is, therefore, rather difficult for Alloy 625. Despite these limitations, conventional chip-making processes are often employed because they offer much higher metal removal rates.

During machining, the work-hardening effects can be reduced by using work-hardened and stress-relieved material or using sharp tools with positive rake angles. Tools with a positive rake angle cut the metal instead of pushing it, as occurs with the negative rake angle. For example, it is easier to machine the alloy in a hot-rolled condition than an annealed one. Tools with positive rake angles help to avoid rubbing the work. Hot machining is another approach to improve the machinability of Alloy 625. In hot machining, the machining is performed at a raised temperature, which does not affect the material's metallurgical properties [20]. The material may be heated before or during the machining operation. Heating the material reduces its shear strength and allow easy machining without affecting the metallurgical behavior of the material [20]. Hot machining prevents material's strain hardening, reduces the

cutting force and tool wear, and improves the material removal rate and the surface finish.

Cutting fluids play an important role in machining operations. They reduce friction and power consumption, chip removal, and cool and lubricate the cutting zone. These benefits of cutting fluids improve the efficiency of chip removal operations. Other benefits of cutting fluids include protecting the cutting tools from oxidation. Due to these benefits, cutting fluids is vital during the turning operation of Alloy 625. Almost all cutting fluids can be used in the machining of Alloy 625. Cutting fluids also help in improving the cutting tool life. Another way to enhance the life of the cutting tool is to select a suitable cutting tool geometry.

Judicious control of the cutting parameters helps reduce the limitation of Alloy 625 machining. The rake angle of the main tool's cutting edge substantially affects its notch wear. An angle of 45° evenly distributed the mechanical force in three directions, which improves the tool's life [21]. Using the minimum quantity lubrication (MQL) technique has also been shown to be quite effective in reducing the tool's wear when turning Alloy 625. In the MQL system, the cutting fluid/oil at an average flow rate of 10–100 ml/h is mixed with air and sent to the tool-work region as an aerosol [22]. The cutting oil provides lubrication, while the cooling is achieved by the compressed air at high pressure.

Hacksawing of Alloy 625 is somewhat difficult by standard hand and power hacksaw tools. Blades made of high-speed tool steel with 14 to 18 teeth per inch (TPI) raker set may be used for general hand saw works. Blades with 24 to 32 TPI wavy set are used for sawing thin-wall tubes. The band saw can be used to cut the alloy sections to a certain thickness. A cutting speed of about 18 m/min can be used as a guide for bandsawing the alloy using blades containing 32 TPI at medium feeding pressures. The saw should constantly bite into the work; otherwise, the blade may work harden the material. The blade and workpiece should be flooded with soluble oil.

Cutting speed is most significant for the surface roughness parameter followed by the feed rate. An increase in the cutting speed increases the surface roughness. The depth of cut has an insignificant effect on the surface roughness [23]. The feed rate and the depth of the cut affect the cutting force most, while the cutting speed has a minor effect. A medium level of cutting speed (~ 75 m/min) is preferred for a good surface finish (low roughness value and low peak-to-valley height) in the machining of Alloy 625 using a TiAlN/TiN coated carbide tool. MQL also contributes to the improvement of surface roughness. For maximum dimensional stability, it is best to rough out the part almost to the size, stress relieve, and then finish it to the final size. Stress-relieving remove stresses with little effect on dimensions which, in turn, ease the final machining.

Conventional machining methods that are most commonly used are: turning, grinding, milling and broaching. Other methods may include planning, drilling, screw machining and tapping. Single point turning is the most frequently used machining process for superalloys.

Carbide tools are recommended for uninterrupted cuts for most turning operations and the high cutting rates. High-speed steel tools should be used for machining, like

Table 6.4 Typical machining parameters for different types of machining operations on Alloy 625[17] (sfm = surface feet per minute)

Machining operation	Roughing speed		Finishing speed		Feed	
	m/min	sfm	m/min	sfm	mm/rev	in/rev
Turning by HSS	8	20	8	25	—	—
Turning by carbide brazed	15	50	27	90	—	—
Turning by carbide indexable	18	60	30	100	—	—
Drilling by twist drill	6	20	—	—	0.04–0.1	0.002–0.004
Drilling by carbide gun drill	24	80	—	—	—	—
Reaming by HSS	6	20	4.5	15	0.075–0.4	0.003–0.015
Reaming by carbide tools	12	40	8	25	0.075–0.4	0.003–0.015
Thread milling by HSS	6	20	—	—	0.038	0.0015

roughening uneven surfaces. They are also used for cutting with the least work-hardening and finishing operations to close tolerances and the smoothest surfaces.

Recommended feeds and speeds for everyday machining operations of Alloy 625 are given in Table 6.4 [17]. The centers of the ranges in Table 6.4 may be used as starting points in establishing the best conditions for specific jobs.

Tapping of the alloy is recommended with serial taps using a surface speed in the range of 1.5–3 m/min with 50% thread engagement. Serial taps are similar to standard taps with modified diameters to increase the thread diameter proportionately with each successive tap. Lathe tools for thread-cutting are ground as per the principles of turning tools, but the angles on threading tools are kept smaller than those on turning tools to support their small nose. Because of the limitation of the tool nose to dissipate heat, threading using single-point tools must be done at lower speeds and feeds than those used for turning. The threading speed for Alloy 625 is recommended to be 0.9–1.1 m/min.

The essential requirements of milling are accuracy and a smooth finish. High-speed tool steel sharp cutters and rigid machines and fixtures are recommended for interrupted milling of Alloy 625. Recommended feeds and speeds for milling by high-speed steel (HSS) cutters are also listed in Table 6.4. It must be ensured that the feed should not be too light, like just rubbing the surface, as it may generate an excessively work-hardened layer. Down milling is more advantageous for tool life than conventional up milling because the cutting tool can withstand impacts better than friction. In down milling, the cutting conditions that generated the lowest impact energy favored tool life [18]. In addition, the downward motion of the cut assist rigidity and reduces the chatter. Face milling is preferred to slab milling because the former reduces the work-hardening and chatter. The chip problem and the tool wear during milling of Alloy 625 are similar to those in a turning operation. A standard milling cutter with adequate clearance for chips can be used for milling Alloy 625.

Aluminum oxide wheels or grinding belts are recommended for surface grinding of Alloy 625. Rough grinding can be done dry, but a lubricant based on a machine oil of high-flowing characteristic is recommended. For semi-finish and finish grinding,

cottonseed oil or a similar lubricant, with the addition of kerosene oil, may be used. The addition of kerosene imparts a high-flowing characteristic to the oil.

Heavy-duty high-speed steel drills with a heavy web are recommended for drilling Alloy 625 using steady feed rates. Care must be taken not to allow the drill to dwell for long to avoid excessive work-hardening of the alloy at the bottom of the hole. Excessive hardening may cause jamming of the drill, which would make it difficult to resume cutting and may break the drill. Thinning the web at the chisel point reduces the cutting pressures and maintain an effective positive rake angle. An increase in the point angle to 135° is beneficial. Recommended speed and feed rates for drilling by twist drill and carbide gun drill are given in Table 6.4.

Reaming should be done at about two-thirds the speed for drilling (Table 6.4). Standard fluted reamers of high-speed tool steel characterized by the right-hand cut positive axial rake (right-hand helix) and positive radial rake are recommended for reaming of Alloy 625. The reamer feed should be 0.038–0.1 mm per flute per revolution. Too low a feed rate may glaze the workpiece and wear the tool excessively. On the other hand, an excessive feed rate may reduce the accuracy of hole dimensions and the quality of the finish. Conventional fluted reamers and flat solid reamers are recommended for reaming the alloy. In addition, insert tools for built-up reamers made of high-speed tool steel and composite tools having steel shanks tipped with carbide can also be used. Speeds of about two-thirds of those turning with similar tools and feeds of 0.20–0.25 mm/rev are recommended for starting the operation.

6.3.2 Hot Machining of Alloy 625

Hot machining of Alloy 625 may reduce many machining problems associated with alloy work-hardening. It prevents strain hardening and improves machining and surface finish. In hot machining, the material is heated before or during machining to reduce its shear strength, allowing easy machining. Parida et al. [19] have studied the effect of hot machining on various machining parameters of different nickel-based superalloys and reported significant ease in the machining at elevated temperatures. Table 6.5 gives the improvement across multiple machining parameters during hot turning of Alloy 625 at 30, 300 and 600 °C, using a cutting speed of 100 m/min, a feed rate of 0.13 mm/rev and 0.3 mm depth of cut. The hot machining significantly enhances the tool life, apparently due to the softening of the alloy and hard carbide particles that cause abrasive wear by exerting more pressure on the tool during the cutting operation. The alloy machined at high temperatures exhibits a softened thin layer beneath the machined surface. Alloy's hardness beneath the machined surface decreases with an increase in the machining temperature due to the annealing of the defects. However, it increases beyond a certain distance away from the surface due to strain hardening. Machining at much higher temperatures may cause grain growth, as reported at 600 °C [19, 24]. The chip morphology changes from discontinuous and helical at room temperature to continuous and spiral at elevated temperature (Fig. 6.8).

Table 6.5 Change in the tool life, cutting force, feed force, radial force and surface finish of the machined alloy during hot machining of Alloy 625 at 600 °C compared to those at 30 °C, when machined using a cutting speed of 100 m/min, feed rate of 0.13 mm/rev and 0.3 mm depth of cut. “+” and “–” refer to an increase and decrease in the parameter

Parameter	Change (%)
Tool life	+ 238
Cutting force	– 29
Feed force	– 28
Radial force	– 36
Surface roughness	– 42



Fig. 6.8 The morphology of chips formed during hot machining of Alloy 625. Reprinted from [19], Copyright (2018), with permission from Elsevier

6.3.3 Non-conventional Machining

Most conventional means of improving machinability are not effective with Alloy 625 and most other superalloys. Several non-conventional, electrically assisted machining techniques have evolved, which are more effective in shaping superalloys than by conventional methods. These techniques are termed “non-conventional” because they do not employ conventional tools for metal cutting. Instead, they directly utilize the machining energy for machining. The machine energy may be mechanical, electrochemical, chemical, or thermoelectric. Some non-conventional machining operations are electrical discharge machining (EDM), electrochemical machining (ECM), photochemical machining (PCM), electron-beam machining, laser beam machining and plasma-arc cutting. Some of them even supplement the conventional machining practices for the alloy. Some of the advantages of non-conventional techniques include high accuracy of machining, no tool wear, no burrs, good surface finish and no stresses on the worked surface. However, advantages like no stresses may be attended with disadvantages for some applications compared to conventional machining. For example, ECM of a nickel-base superalloy after conventional turning reduces the fatigue endurance stress capability by about 50% because the conventional turning introduces favorable compressive stresses on the machined surface. However, all the

non-conventional techniques are limited by the low metal removal rates. Of the non-conventional machining techniques, electric discharge machining (EDM) is the most effective machining to overcome the constraints of the conventional processes and can machine all sorts of difficult to machine tough and hard electrically conductive materials.

6.3.3.1 Electric Discharge Machining

Electrical discharge machining is an electro-thermal process in which material is removed from the workpiece by a series of continuous sparks between the tool (wire) and the workpiece. There is no mechanical contact between the wire and the workpiece in EDM. The gap between the wire and the workpiece usually ranges from 0.025 to 0.050 mm and is continuously maintained by a computer-controlled positioning system. De-ionized water floods the gap between the wire and the workpiece. The de-ionized water acts as a dielectric and flushes the eroded particles. The material removal mechanism is based on the melting and evaporation of materials by a series of electrical discharges (or spark erosion) by voltage pulses generated by a pulse generator. The electrode (a thin wire of diameter ranging from 0.05 to 0.35 mm) continuously moves on a spool, feeds through the workpiece, and wound on a second spool. The wire electrode may be copper, brass or zinc coated. The wire is kept straight by a mechanical tensioning device and is fed into the workpiece by a numerically controlled mechanism or a microprocessor.

Several workers have demonstrated satisfactory machining response of the EDM for material rate removal, cutting speed, optimum surface roughness and economical cutting of Alloy 625 and many other superalloys [25–27]. Table 6.6 gives typical machining parameters for optimum cutting speed and low surface roughness of Alloy 625 [27]. Singh and Singh [28] have demonstrated the effect of peak current (I_p), pulse on time (T_{on}), wire feed rate, and wire tension on the performance of material removal rate and surface roughness during EDM of Inconel 625. They have concluded that T_{on} time is the most controllable influential factor, followed by peak current, wire feed rate, and wire tension.

Table 6.6 Optimum EDM machinability parameters for cutting speed and low surface roughness of the machining of Alloy 625 [27]

Parameters	High cutting speed	Minimum R_a	Both high cutting speed and minimum R_a
Wire tension	10 N	10 N	10 N
Wire speed	110 mm/s	305 mm/s	305 mm/s
Flushing pressure,	16 kg/mm ²	8 kg/mm ²	16 kg/mm ²
Discharge current	7A	7A,	21 A,
Spark time on (T_{on})	28 μ s	14 μ s	28 μ s

Garg et al. [26] have studied the effect of pulse on time, pulse off time, spark gap voltage (SV) and wire feed (WF) parameters on cutting speed (CS), gap current (I_g), and surface roughness (R_a) of the machined surface. An increase in T_{on} from 0.85 to 1.35 μs increases the cutting speed by about 80%. On the contrary, a decrease in T_{off} from 36 to 18 μs increases by 85%. The cutting speed increases marginally with a decrease in the SV. Garg et al. achieved a maximum cutting speed of 1.27 mm/min with parameters $T_{on} = 1.35 \mu\text{s}$, $T_{off} = 18 \mu\text{s}$, SV = 45 V, and WF = 5 m/min.

6.3.3.2 Electrochemical Machining

Electrochemical machining (ECM) removes metal by an electrochemical process. It involves electrolytic “deplating” or “reverse electroplating” of the workpiece [29]. A high current is passed between the workpiece (anode) and a tool (cathode) through a conductive fluid (electrolyte) to selectively dissolve (machine) the workpiece submerged in the electrolyte by the electrochemical reaction of the type.



where M refers to the metal of valency 2. The electrons (e^-) lost by the dissolution of M atoms travel to the cathode, where it reacts with water molecules forming gaseous hydrogen and hydroxyl ions (anions) as per the reaction



The cations and the anions react in the aqueous solution to form insoluble metal hydroxide



The flowing electrolyte removes the insoluble hydroxide.

During ECM, the tool is moved into the workpiece at the machined area, and the pressurized electrolyte is injected at a set temperature. The gap between the tool and the workpiece typically varies within 80–800 μm [30]. As electrons cross the gap, material from the workpiece is dissolved, as the tool is guided along the desired path close to the work. No tool wear occurs in ECM [30] because the cutting tool does not touch the workpiece. For nickel alloys, salt solutions of sodium or potassium nitrate or chloride or dilute sulfuric acid may be used as electrolytes. The high corrosion resistance of Alloy 625 does not seem to retard its electrochemical dissolution. However, alloy's high corrosion resistance may cause a voltage drop during ECM and necessitate higher power and electrolyte heating. The ECM can be used for machining intricate and odd-shaped angles and cavities in materials of varying strength and hardness, usually complicated to machine using conventional methods [30]. However, the technique is limited to electrically conductive materials.

6.3.3.3 Chemical and Photochemical Machining

Chemical and photochemical machining (PCM) is a chemical milling process using a photoresist and corrosive etchants to machine away selected areas by selective etching. The tooling is inexpensive and can be quickly produced. The machining maintains dimensional tolerances and does not create burrs or sharp edges. However, the high corrosion resistance of Alloy 625 requires strong acids for metal removal, which can cause intergranular attack if not correctly used. The process is an economical alternative to stamping, punching, laser or water jet cutting, etc. for thin gauge precision parts and can accurately produce highly complex components with minute details. However, it is limited to materials with a thickness of 0.013 to 2.032 mm [31]. It also lowers the fatigue life slightly even under optimum conditions.

6.3.3.4 Plasma Cutting

Plasma cutting is a process that utilizes an accelerated jet of hot plasma (ionized gas) to cut electrically conductive materials. When compressed gas is blown through a focused nozzle at high speed toward the workpiece, an electrical arc forms within the gas between an electrode and the workpiece itself. The electrode may be placed very near or integrated into the gas nozzle. The electrical arc ionizes the gas, creating an electrically conductive hot plasma channel. The plasma channel forms a complete electrical circuit from the plasma cutter through the workpiece and back to the plasma cutter through a grounding clamp. The electricity from the cutter torch travels down the plasma to melt the workpiece at the point of contact. At the same time, the high-velocity plasma and compressed gas blow away the hot molten metal from the workpiece. Plasma-arc torches can cut thick and thin sections of Alloy 625 and other nickel alloys at very high speed. Plasma cutting is an efficient method for rough cutting of plates, sheets and angles compared to other cutting methods.

6.3.3.5 Laser Beam Machining

Laser beam machining (LBM) uses heat directed from a laser beam to remove material from metallic or non-metallic surfaces. When a high frequency of monochromatic light falls on a surface, photons transfer the energy to heat, melt and vaporize the material. Laser beam machining is best suited for brittle materials with low conductivity but can be used on most materials [32]. The cutting depth of a laser is directly proportional to its power and inversely proportional to the cutting speed and the diameter of the laser beam. The depth of the cut is influenced by the reflectivity, density, specific heat, and melting point of the workpiece. Laser beam machining can drill holes through all types of materials and superalloys in a very short time. For example, a 0.5 mm diameter hole can be drilled through a 2.5 mm thick superalloy sheet within 3 seconds.

6.4 Welding of Alloy 625

This section describes the joining of Alloy 625 by fusion welding. In principle, metals can be joined by various types of non-mechanical techniques, like fusion welding, solid-state welding, and brazing. Of these, fusion welding is the principal technique for producing high strength joints for all types of superalloys. The section focuses on the welding metallurgy, weldability and post welding heat treatment of the fusion welds in Alloy 625.

6.4.1 Common Welding Practices for Alloy 625

Welding is the joining of two or more components of similar or dissimilar metals, using a metallurgical bond to form a single piece. A metallurgical bond involves the diffusion of the material across the interface. It relies on melting and solidification of either the base alloy or the base alloys and the filler material (i.e., welding rod). During welding, the workpieces that are to be joined and the filler material are heated to a sufficiently high temperature to melt the metal. An electric arc or a gas may do the heating. The molten metal solidifies to form a fusion joint between the work-pieces. The filler materials are characterized by: (i) the same nominal composition of the base alloys for similar metal components; or (ii) a composition compatible with the chemistry of the components being joined to produce a joint with acceptable environmental and mechanical properties. Alternatively, the joint may have properties similar to the base metal but may not necessarily have the composition of either of the component. Welding, however, introduces a cast structure of variable size and properties, which may vary based on the metals being welded and the welding technique employed.

Alloy 625 is readily joined by conventional Gas Tungsten Arc Welding (GTAW), Gas Metal Arc Welding (GMAW) and Shielded Metal Arc Welding (SMAW) welding techniques. Besides, other welding techniques like plasma arc welding, resistance spot welding, laser beam welding, and electron-beam welding can also be used. Alloy 625 exhibits a sluggish welding and shallow penetration than steels and austenitic stainless steels. Therefore, extra care is required in the joint design and weld bead placement to ensure sound welds with the proper tie-in of the weld beads.

Several common filler metals for gas tungsten arc and gas metal arc can be used for welding Alloy 625 with other metals. A list of these filler metals, as per the American Welding Society (AWS) classification, is given in Table 6.7 [33]. Recommended use of these filler metals for the welding of Alloy 625 with itself or with other metals is shown in Table 6.8.

Many advanced welding techniques can be used as alternate welding techniques. A few frequently used advanced techniques are laser welding, electron-beam welding and solid-state welding. In laser beam welding, a highly focused and intense laser beam melts the base metal, and a fusion joint is formed upon solidification, often

Table 6.7 Nominal compositions of filler metals used for welding of Alloy 625

AWS class	UNS No	Chemical composition ^a						
		C	Cr	Fe	Mn	Ni	Mo	Si
ERNiCrMo-3	N06625	0.1	20-23	5.0	0.50	58.0 min	8-10	0.5
ENiCrMo-3	W86112	0.10	20-23	7.0	1.0	55.0 min	8-10	0.75
ERNiCrWMo-1	N06231	0.05-0.15	20-24	3.0	0.3-1.0	Bal	1-3	0.25-0.75
ERNiMo-3	-	0.12	4.0-6.0	4.0-7.0	1.0	Bal	23.0-26.0	1.0
ER 3556	R30556	0.15	21.0-23.0	Bal	0.5-2.0	19.0-22.5	2.5-4.0	0.8

^a Single number refers to the maximum value

Table 6.8 Filler metals for fusion welding of Alloy 625 with other metals

Alloy type	Typical alloys	Filler metal alloy
Self	Alloy 625	ERNiCrMo-3, ENiCrMo-3
Fe-base, Fe–Ni-based, ferritic alloys	Carbon steels, HSLA steels, Ferritic- and austenitic-stainless steels, Alloy 330, 800, 800H, etc	ERNiCrMo-3, ER3556, ENiCrMo-3
Ni-based, low alloy	Alloy 825, 600, 601, 75, and 80–20 alloys	ERNiCrMo-3, ENiCrMo-3, ER NiMo-3
Ni-based, high Mo/W	Hastelloy B,N,S,W and X, Alloy 230, 242, 617	ERNiCrMo-3, ERNiMo-3, ERNiCrWMo-1
Ni-based, high Al, Ti and Nb	Haynes R-41, 214, 262, Alloy 718, X-750, Waspaloy alloys	ERNiCrMo-3, ERNiMo-3
Cobalt-based & high cobalt	Haynes 25, 31, 150 and 188 alloys	ERNiCrMo-3, ER3556

without filler metal. Since the energy input to the workpiece is low, the fusion zone size is small and very precise, and the heat-affected zone size is minimal. Laser beam welding produces porosity-free welds having a strength equal to or better than the base metal. It is an automated and noncontact process that eliminates mechanical distortion of the workpiece.

Electron-beam welding (EBW) is similar to laser welding, in which a beam of high-velocity electrons is utilized to make the fusion joint. When electrons with high kinetic energy strike the workpiece, they transfer their kinetic energy into heat, which melts the metal. The electron-beam welding offers all the advantages of laser welding, but it needs to be performed under vacuum to prevent the dissipation of the electron energy. This technique is quite effective in welding similar and dissimilar joints of different types of solid-solution strengthened superalloys including Alloy 625.

In solid-state welding, two pieces of metals are bonded under pressure providing intimate contact between them and at a temperature below the melting point of the base material. It creates the same result as fusion welding without melting the contacting surfaces. The bond forms when the interface atoms from one metal diffuse into the other due to the high pressure and temperature. The solid-state bonding does not require consumables like filler metal, fluxes or shielding gas but often need a thin interlayer of third metal when bonding two dissimilar metals with negligible solid solubility. The third metal should have sufficient solid solubility in the two work-pieces of different metals to be joined. The weld is excellent and free from defects like pores, non-metallic inclusions, segregation of alloying elements, etc. as no melting and solidification is involved. The mechanical properties of the weld are similar to those of the parent metals. Solid-state welding allows the joining of precipitation-hardened superalloys without the need for post-weld aging.

Table 6.9 Solid-solubility, partitioning coefficients and terminal eutectic temperatures of sulfur, phosphorous, boron and silicon in their binary alloys with nickel. Their maximum limit in superalloys to avoid impurities related liquation-type hot cracking is also given [13]

Element	Maximum solubility (wt%)	Partitioning coefficient, k	Terminal eutectic temperature (°C)	Recommended solubility (wt%)
Sulfur	~ 0	~ 0	637	0.015
Phosphorus	0.02	0.02	870	0.015
Boron	0.7	0.04	1093	0.7
Silicon	8.2	0.70	1143	0.02

6.4.2 Pre-welding Treatment of Alloy 625

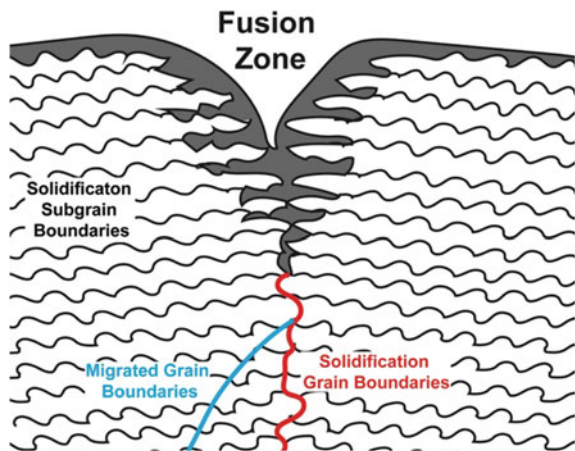
The solid-solution strengthening of Alloy 625 makes its welding straightforward and can be welded without special preheat or post-heat treatment. However, the cleanliness of the Alloy 625 is essential because contaminations by machining greases and oils, corrosion products, and low melting point elements like lead, sulfur, etc. may hinder achieving welds free of defects. Introducing oils and greases to the fusion zone causes fissuring and porosity, leading to severe cracking problems. The presence of low melting elements and alloys in the heat-affected zone (HAZ) may cause fissuring by liquation cracking, as discussed later in Sect. 6.4.5.2. Sulfur, phosphorus, lead, and boron in alloy chemistries are potential sources of liquation cracking. In addition, oxygen and nitrogen have also been reported to have a deleterious effect on the welds. Table 6.9 gives the maximum limit of these impurities to restrict liquation cracking in superalloys [13]. A pre-weld heat treatment is necessary for cold-work or work-hardened alloy, which must be done in a limited temperature range to avoid annealing of the metal. The inter-pass temperature should be kept low during welding. If needed, auxiliary cooling methods may be used between weld passes, provided they do not introduce contaminants.

6.4.3 Welding Metallurgy of Alloy 625

6.4.3.1 Microstructural Evolution in The Fusion Zone

Microstructural evolution in fusion weld zones of Alloy 625 is very sensitive to the concentration of niobium and carbon [34–40]. The basic principles of the partitioning behavior of solutes during solidification of Alloy 625 have been mentioned in Sect. 3.3. The same principles govern the distribution of solutes during the solidification of the fusion zone. The last liquid that solidifies is enriched with niobium, carbon and silicon. The solute rich liquid tends to form the Laves and NbC phases due to eutectic-like reactions in the interdendritic and intergranular regions. These phases form as the concentration of niobium, carbon and silicon in the dendrites exceeds the

Fig. 6.9 The schematic illustrates the formation of typical boundaries in the fusion zone of a single phase austenitic weld



solid solubility of the γ matrix. Likewise, impurity elements like phosphorous, sulfur and boron tend to segregate aggressively to the liquid and form low melting eutectic phases during solidification. The formation of low melting eutectic phases in the interdendritic and grain boundary regions significantly increases cracking susceptibility of the weld [41]. The elements boron and sulfur are more harmful because they lower the solid/liquid surface energy and promote extensive wetting of boundaries by the eutectic liquid films. Silicon also forms a low melting point nickel silicide, but it is less harmful than other impurities unless present in relatively large amounts.

The fusion zone of a single phase austenitic weld is typically characterized by the formation of three types of boundaries (Fig. 6.9) [42]. These boundaries are: (i) solidification sub-grain boundaries, that separate cells and dendrites and are characterized by low-angle boundaries; (ii) solidification grain boundaries, that separate packets of sub-grain boundaries forming as a result of competitive growth at the end of solidification and are characterized by high-angle boundaries with high concentrations of solute and impurity elements; the grain boundaries have both compositional and crystallographic components; and, (iii) migration grain boundaries, that form when the crystallographic components of the solidification grain boundaries migrate away from the composition component.

6.4.3.2 Heat Affected Zone

A region of the base metals, adjacent to the fusion zone experiences microstructural and properties alterations. This region is termed the “heat-affected zone”. The heat-affected zone stretches from base metal to the edge of the fusion zone. As all superalloys solidify over a range of temperatures, a part of the heat-affected zone adjacent to the fusion zone is characterized by solidified intergranular liquid. This zone is called “partially melted” or “mushy zone”. The heat-affected zone of all superalloys’ welds contains a mushy zone, including all or a part of the partly melted/solidified zone.

The mushy zone liquid generally does not affect the weldability of the alloy because, during the normal course of solidification, it is always open to the fusion zone.

Several metallurgical reactions in the heat-affected zone influence properties and weldability of an alloy. These reactions may include one or more of the reactions like recrystallization, grain growth, grain boundary segregation, precipitation of second-phase particles and grain boundary liquation. But the HAZ of Alloy 625 welds does not usually exhibit these reactions because of the alloy's solid-solution nature, except for some grain growth. However, welding the alloy in cold-worked or hot-worked conditions containing some "residual strain" may cause the recrystallization of grains. The degree of grain growth depends upon the initial microstructure of the base metal and the weld heat input.

The alloy may also undergo grain boundary liquation in the region of the HAZ adjacent to the fusion boundary due to eutectic reactions. Such liquation may result from impurity, solute segregation, or both along the grain boundary or due to a phenomenon known as "constitutional liquation. For this reason, high heat input welding processes are usually not recommended for solution annealed materials. The segregation of sulfur, phosphorous and boron has the most profound effect on grain boundary liquation if their concentration is not restricted to very low levels. Their segregation to grain boundaries causes a local depression of the melting temperature and promotes continuous liquid film formation [43–45]. Likewise, the presence of TiC, NbC and TCP phases in the base metal may lead to constitutional liquation at their interface with the austenitic matrix. [46, 47]. Rapid heating associated with the weld thermal cycle does not dissolve these phases. But an interfacial liquid film of eutectic composition forms at particle/matrix interfaces at temperatures above the eutectic temperature. This liquid can subsequently penetrate the grain boundaries. This type of liquation has been observed at carbides and intermetallic phases in several nickel-base alloys [48–52]. Both of these liquation mechanisms promote cracking in the HAZ.

6.4.4 Mechanical Properties of Weldments

In general, the solid-solution strengthened alloys retain near base metal properties in the as-welded condition because the loss in the solid-solution strengthening due to segregation in the fusion zone is compensated by the second-phase strengthening due to particles that form inter-dendritically. Similarly, the mechanical properties of the HAZ do not deviate significantly from those of the base metal because of limited grain growth. However, the HAZ in the cold worked welded structures may lose strength due to recrystallization and grain growth. Therefore, little degradation in the strength and ductility of solid-solution alloys is expected due to welding. The weld metals for Alloy 625 (the ERNiCrMo-3 types) exhibit a tensile strength of about 90% of the base metal [41]. However, a loss in the weld metal ductility may occur when the welding is conducted with shielding gases containing > 1% hydrogen [53], as in the gas tungsten arc welding using argon–hydrogen gas mixtures for improving

the wetting and flow characteristics of the weld metal. This loss in ductility is due to hydrogen pickup in the weld metal, which causes hydrogen embrittlement. Young et al. [53] have shown that an increase in the hydrogen levels from 3 to 12 ppm reduces the UTS of filler metal 82 multi-pass deposits from about 760 to 620 MPa, and the ductility from 50 to 20%. Changing shielding gas to 100% helium or argon-helium mixtures restored the mechanical properties of the filler metal deposits. A similar effect on the mechanical properties of the welds is when the flux absorbs moisture while welding with a flux-based welding process.

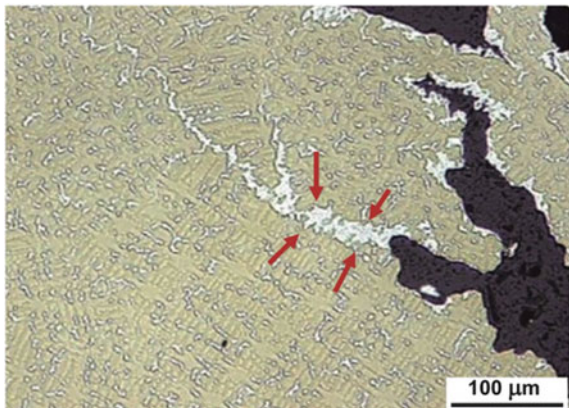
6.4.5 Weldability of Alloy 625

The weldability of an alloy is related to its hot cracking susceptibility. Hot cracking occurs to varying degrees, depending on the amount of weldment restraint, welding condition, alloy composition, etc. The cracking susceptibility is primarily controlled by the solidification temperature range and the amount and distribution of the terminal liquid at interdendritic regions [34, 35, 36, 54, 55–58]. The terminal liquids in Alloy 625 form Laves and carbide phases by eutectic reactions at temperatures lower than the alloy's solidus temperature. The formation of these eutectics lowers the melting temperature at interdendritic and intergranular regions, making the alloy susceptible to cracking at high temperatures. Similarly, the liquation of low melting eutectics formed by the segregation of sulfur, phosphorous and boron at grain boundaries influences the susceptibility of intergranular hot cracking. These two hot-cracking mechanisms also influence hot cracking susceptibility in the heat-affected zones during reheating or post-weld heat treatment of the weld. A detailed description of these mechanisms is given below.

6.4.5.1 Fusion Zone Solidification Cracking

Alloy's susceptibility to fusion zone cracking is a function of metallurgical factors and the local strain accumulated at the end of solidification. As noted above, solute distribution during solidification affects the solidification temperature range and the interfacial terminal liquid, which forms carbide and Laves phases. Either way, the segregation of solutes promotes hot cracking. Besides, the segregation of impurity elements like phosphorous, sulfur and boron also promote hot cracking. The distribution of terminal eutectic liquid at interdendritic and intergranular regions causes appreciable shrinkage strain across boundaries. If the terminal liquid is distributed as a continuous film along the boundaries, the boundaries may not accommodate the strain and may separate to form a crack. Therefore, better control of terminal stages of solidification improves the weldability of the alloy. Figure 6.10 shows solidification cracks along solidified grain boundaries in the fusion zone of Alloy 625, where the

Fig. 6.10 Solidification cracks along solidified grain boundaries and interdendritic regions in the fusion zone of Alloy 625. The figure also shows the healing of the cracks, indicated by arrow marks, by backfilling the low melting eutectic liquid. Reprinted by permission from Springer [41]. Copyright (2008)



solidification cracks reside along solidification grain boundaries and interdendritic regions that solidify last.

The solidification cracking susceptibility of Alloy 625 as a function of niobium, silicon and carbon concentration and their harmful influence on its weldability has been investigated by Ceislak [34]. He has shown that, although Nb is added to Alloy 625 as a solid-solution strengthener, it mostly ends up forming NbC and Laves phases in the weld metal (~ 85 to 90 wt% niobium in NbC and ~ 22 to 36 wt% niobium in the Laves phase) because of its segregation tendency [34, 35, 36, 59]. The tendency to form the NbC and Laves phases, and consequently cracking susceptibility of the alloy weld, increases with the niobium content. Besides, NbC and Laves phase formation during terminal solidification lowers the solidification temperature. The Laves phase, in particular, reduces the solidification temperature of Alloy 625 most, up to about 1150 °C [34, 41, 42]. Similar results are reported for other niobium-bearing alloys also [35, 56].

As noted earlier, phosphorous, sulfur and boron also form low melting point liquid films at interdendritic regions and grain boundaries. The low melting film formation significantly increases the alloy's hot cracking susceptibility. The boron and sulfur are particularly more harmful because their segregation lowers the solid/liquid surface energy and promote extensive wetting of the boundaries by the low temperature melting films. The cracking susceptibility increases as the amount of sulfur and phosphorous increases. Therefore, the alloy's sulfur and phosphorous levels are kept low, typically below 0.003 wt% and 0.01 wt %, respectively, to minimize solidification cracking. As pointed out in Sect. 3.1.13, the presence of a small amount of manganese is often beneficial because it reduces the tendency of sulfur to wet the grain boundaries. Manganese combines with sulfur to form manganese-sulfide (MnS) particles with globular morphology.

The cracking susceptibility of Alloy 625 ranges from intermediate to high [41]. Lippold et al. [41] have studied the solidification cracking susceptibility of filler metals of 617, 625, X and W alloys using the Varestraint test. Alloys 625 was the most susceptible among the alloys studied (Fig. 6.11). Varestraint testing is a commonly

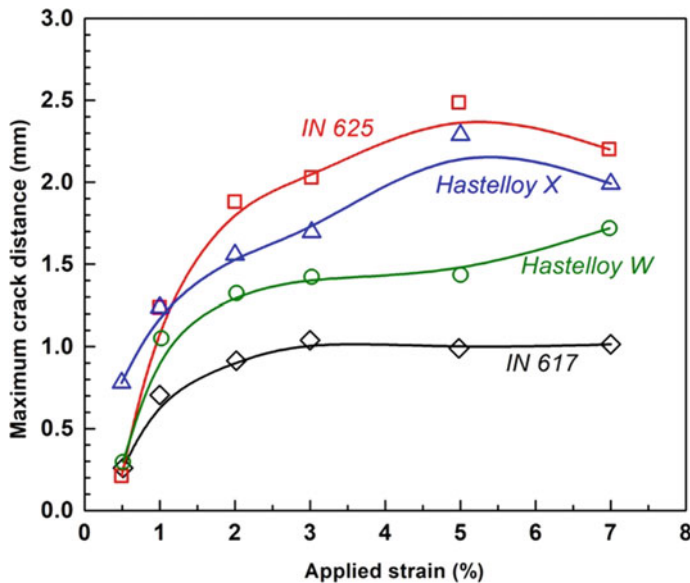


Fig. 6.11 A comparison of maximum crack distance versus strain for different solid-solution strengthened filler metals [41]

used technique of determining the susceptibility of the materials to solidification and liquation cracking.

Despite its wide solidification range, sound and crack-free welds can be made in Alloy 625 using Nb-bearing Ni–Cr–Fe–Mo consumables by carefully controlling weld beads. The alloy exhibits good weldability concerning weld solidification cracking, particularly at low to medium restraints. The apparent disagreement between the Varestraint results in Fig. 6.11 and actual practice is attributed to the crack backfilling phenomenon in Alloy 625. The reported Varestraint data is from samples tested at high applied strains. However, the behavior of the liquid films along solidified grain boundaries is different at lower strains. The Alloy 625 forms a considerable amount of low melting eutectic liquid at the end of solidification (the light contrast region marked by arrows in Fig. 6.10). Under low strain conditions, the eutectic liquid heals the cracks by a backfilling mechanism. However, at higher strains, the eutectic backfilling is not effective to overcome the strain resulting in the formation of cracks.

6.4.5.2 HAZ Liquation Cracking

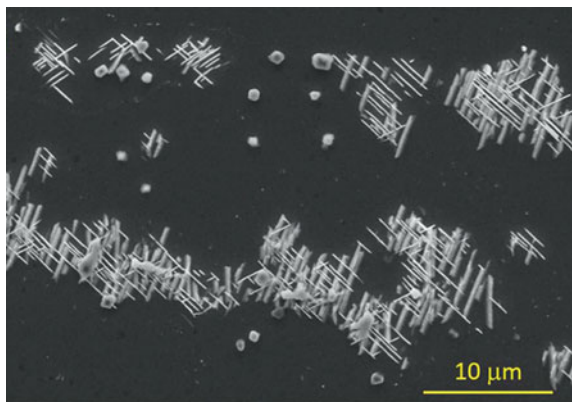
As noted above, Alloy 625 exhibits broad melting and solidification temperature ranges due to its high alloying contents. The base metal adjacent to the fusion zone

may also experience a temperature between liquidus and the local solidus temperatures during welding. This melting may cause liquation cracking in the mushy zone when the melt cannot sustain the applied strain. Alloys welded with high heat input welding processes, like gas metal arc welding (GMAW) in the spray transfer mode, tend to form such liquation cracks in the HAZ. The liquation cracking mechanisms involve the liquation of eutectic phases formed by impurities and the carbide and Laves phases, as mentioned in Sect. 6.4.5.1 above. The only difference here is that the liquation of phases in the HAZ is controlled by the impurities levels and the concentrations of niobium and titanium in the base metal.

Impurities like phosphorous, sulfur and boron aggravate the liquation cracking by making a low-temperature film at the grain boundaries. Phosphorous generally harms the least and boron the most, while sulfur in between the two [60]. A rule of thumb is to maintain impurities as low as possible to avoid HAZ cracking. The total content of sulfur plus phosphorous less than 100 ppm (0.01 wt%) causes no liquation cracking.

Constitutional liquation of NbC and TiC phases in the austenitic Alloy 625 matrix may also cause HAZ liquation cracking [43, 50, 52]. A particular case of HAZ liquation cracking is the cracking in multi-pass welds where the initial weld passes to become the HAZ for the subsequent passes. In this case, liquation occurs due to local melting along grain boundaries in the underlying weld metal. The reheating of the initial weld makes it susceptible to cracking at segregated solutes and impurities along solidification grain boundaries and migrated grain boundaries. Besides, solidified NbC particles in regions away from grain boundaries may liquefy to form a localized solid solution highly concentrated in niobium. The niobium enriched localized areas may precipitate out the embrittling δ phase particles during subsequent thermal exposure in the temperature range of the δ phase precipitation. Figure 6.12 shows an example of a precipitation of δ phase particles in the interdendritic regions during subsequent heating of a welded Alloy 625 structure [61].

Fig. 6.12 SEM image of δ precipitates at interdendritic locations of liquated NbC particles in Alloy 625.
Reprinted by permission from Springer [61].
Copyright (2018)



6.4.6 Post Weld Heat Treatment

In general, a post-weld heat treatment (PWHT) is regularly performed to relieve residual stresses, reduce hydrogen content, homogenize the microstructure, dissolve undesirable secondary phases that may have formed in the fusion zone or HAZ. A PWHT is also given to improve the corrosion properties of the weld. However, cracking is sometimes observed, particularly in nickel-base superalloys containing aluminum and titanium, like Alloy X-750, when the welded structures are heated to temperatures within their aging temperature range or when the alloy is slowly cooled from the solution temperature through this temperature range. Figure 6.13 schematically depicts this type of cracking. The frequency of cracking increases when the alloys are reheated through the hardening temperature range in the presence of residual or applied stress in constrained conditions. PWHT cracking in Alloy X-750 occurs when aluminum and titanium induce rapid precipitation of the γ' phase particles that harden the alloy. Figure 6.14 illustrates the alloy's behavior that leads to PWHT cracking of such alloys. Figure 6.14a shows a typical variation in residual stresses away from the weld centreline. After welding, the HAZ retains high residual stresses. When the welded part experience elevated temperature during a heat treatment or service exposure, the residual stresses first relax as the temperature rises. But the stresses start building up again when the precipitation of the hardening phase begins at temperatures above the precipitation temperature (Fig. 6.14b). A reduction in ductility accompanies strengthening. As the precipitation continues, the welded part experiences an instantaneous catastrophic failure when the built-up stresses reach a critical stress level σ_C . The higher the volume fraction of the γ' precipitates, the greater the tendency to crack.

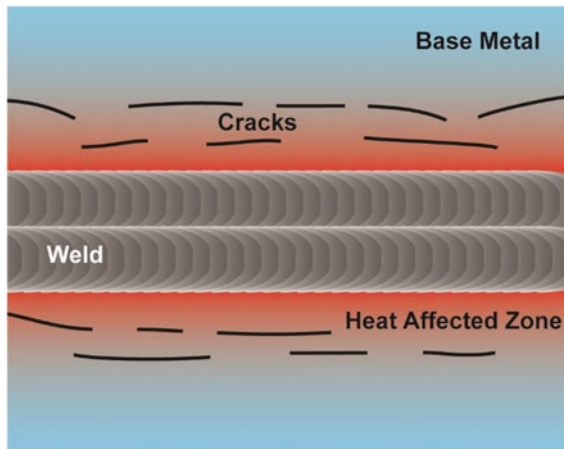


Fig. 6.13 Schematic illustrating strain-age cracking in the heat-affected zone after a post-welding ageing treatment of the alloy. Such cracking is common in many γ' phase precipitating nickel superalloys

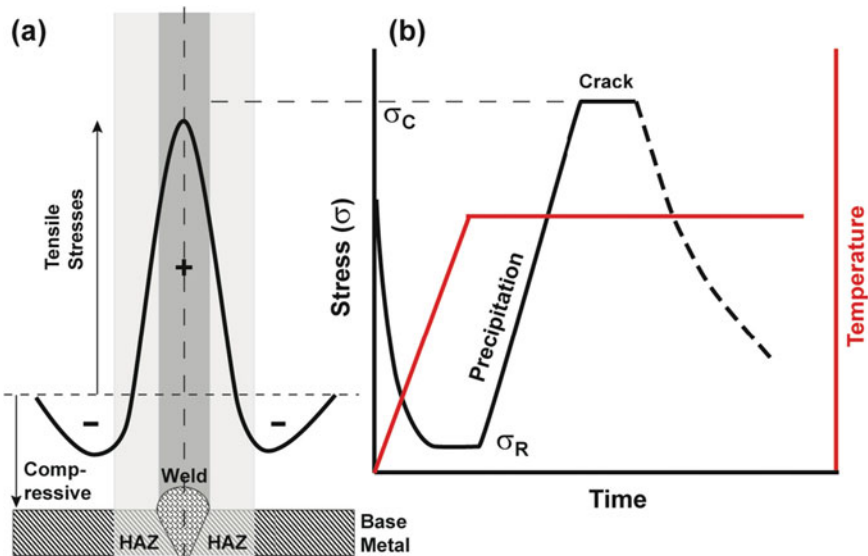


Fig. 6.14 **a** Typical residual-stress distribution across a welded joint; **b** Schematic illustrating the variation in the residual stress and γ' phase particles induced cracking in the HAZ when a γ' -bearing nickel-based superalloy is heated to its ageing temperature range during post-weld heat treatment

The amount of aluminum and titanium in Alloy 625 is too low to cause the precipitation of the γ' phase. However, post-weld heat treatment of the alloy may cause the precipitation of other hardening phases noted in Chap. 4. Cortial et al. [62] have investigated the influence of post-weld heat treatment, over a temperature range from 600 to 1000 °C, on the mechanical properties of Alloy 625 welds [62] and reported a loss in the strength and ductility of the alloy (Fig. 6.15), consistent with the aging behavior of the alloy presented in Chap. 4. A sharp drop in the toughness is observed after an annealing treatment in the 750–950 °C range. This toughness drop is associated with the formation of the δ phase (Fig. 6.16). The formation of

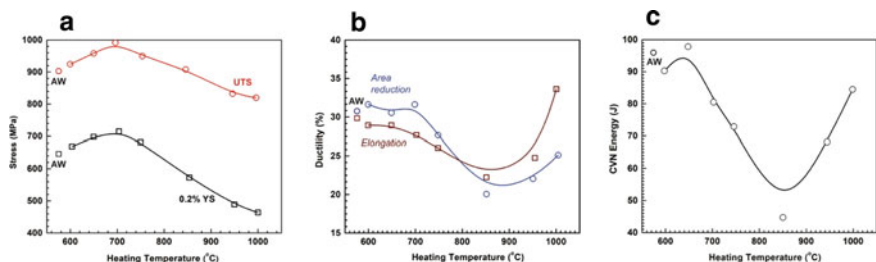


Fig. 6.15 Variation in room temperature mechanical properties of Alloy 625 welds as a function of heat treatment for 8 h: **a** strength; **b** ductility; and **c** impact energy. The “AW” data points indicate the property in the as-welded condition [62]

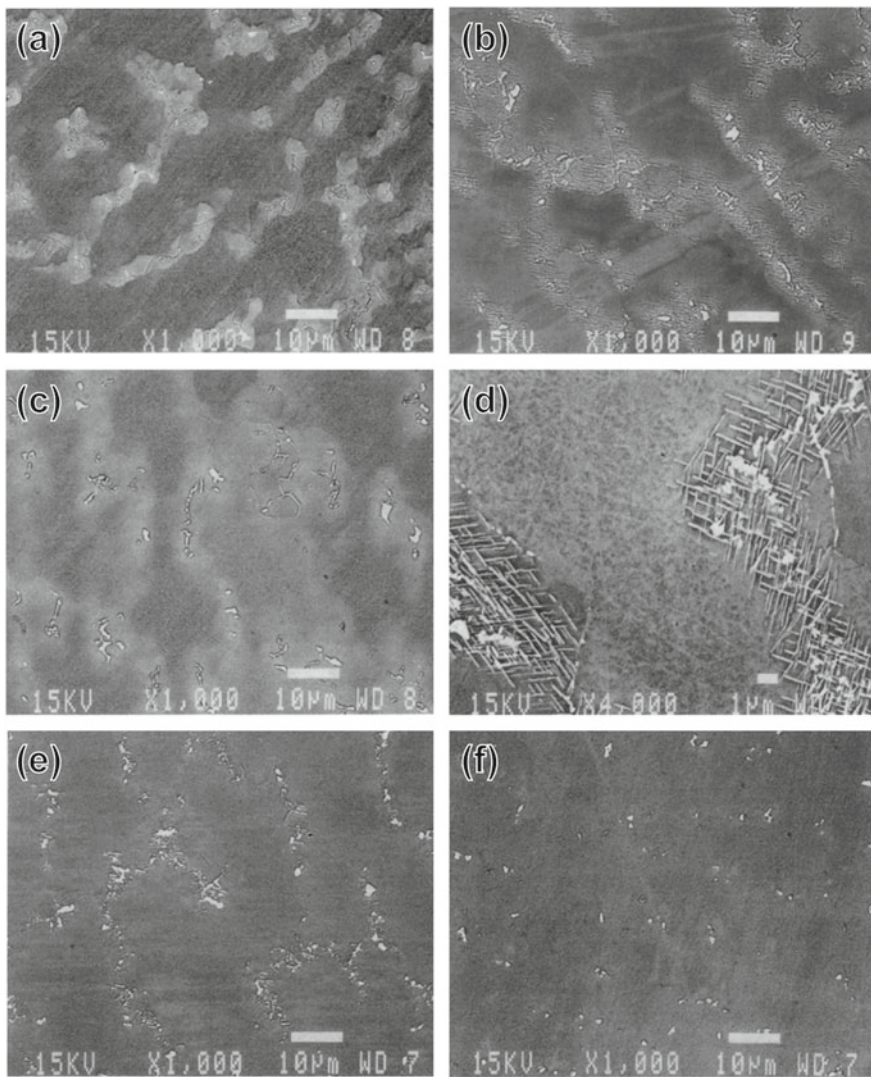


Fig. 6.16 Microstructures of Alloy 625 welds after post weld heat treatment for 8 h: **a** 600 °C; **b** 750 °C; **c** 800 °C; **d** 850 °C; **e** 950 °C; **f** 1000 °C. Reprinted by permission from Springer [62]. Copyright (1995)

$M_{23}C_6$ carbides and the δ phase particles in the segregated regions of the weld may embrittle it further. At 1000 °C, the ductility is restored due to the dissolution of δ phase. However, grain growth occurs as the δ phase particles no longer pin the grain boundaries. This behavior is similar to that noted in Chap. 4, where aging of the alloy over a temperature range from 600 to 900 °C is reported to adversely affect its mechanical properties due to the formation of γ'' , δ and carbide phase particles. The

formation of the $\text{Ni}_2(\text{Cr},\text{Mo})$ phase particles also affect mechanical properties but their formation during a PWHT is ruled out because of its large incubation period. Thus, there is little benefit of heat treating Alloy 625 welds from a mechanical properties standpoint because as-welded properties are generally close to the base metal properties (Chap. 4). However, a PWHT on Alloy 625 weld is often performed to reduce residual stresses and improve corrosion resistance, including the resistance against intergranular attack. Therefore, the post-weld heat treatment of Alloy 625 should be controlled carefully to prevent the loss in its ductility and toughness. A heat treatment within a narrow temperature range of 950–1000 °C, with careful control of the exposure time commensurate to the section thickness, is recommended to remove residual stresses and improve resistance to stress corrosion cracking in the welded Alloy 625. This heat treatment helps prevent the intergranular attack (IGA) by forming stable grain boundary carbide particles as in many other solid-solution alloys like 600, 690 and 825.

6.4.7 Welding Behavior of Alloy 625 PLUS

The solidification behavior of the age-hardened Alloy 625 PLUS is very similar to that of Alloy 625. It is mainly related to the segregation behavior of niobium, which is critical during the solidification of the fusion zone. The γ/Laves eutectic in Alloy 625 PLUS forms at about 1126 °C. The extra titanium in Alloy 625 PLUS does not appear to influence the amount of eutectic constituent compared to Alloy 625. Alloy 625 PLUS therefore exhibits hot cracking susceptibility similar to that of Alloy 625, but much superior to Alloy 718 [63].

The Alloy 625 PLUS exhibits the precipitation of the γ'' adjacent to the Laves phase during cooling of the weld metal to room temperature. This precipitation behavior is similar to that observed in Alloy 718 [64]. However, the slow age-hardening response of Alloy 625 PLUS compared to γ' strengthened alloys like Waspaloy, Alloy 693, etc. dramatically reduces its susceptibility to strain-age cracking during welding. The mechanical properties of the as-welded Alloy 625 PLUS are similar to those observed in Alloys 625 and 718. The effect of heat treatment on room-temperature tensile properties of Alloy 625 PLUS welded samples is shown in Table 6.10 [63]. Welded joints subjected to standard solution annealing and double-aging treatments (Sect. 5.2) show yield strength and ductility similar to the base metal. The double-aging heat treatment to Alloy 625 PLUS weld results in a yield strength above 827 MPa with good ductility. Solution annealing the weld before an aging treatment may improve its strength and ductility.

Table 6.10 Effect of heat treatment on room temperature tensile properties of GTA Welds of 625 PLUS Alloy^a [63]

Condition ^b	0.2% yield strength (MPa)	Ultimate tensile strength (MPa)	Elongation (%)	Reduction in area (%)
As welded	510	827	41	48
Direct aged	848	1124	22	34
Solution anneal + aged (weld)	876	1220	26	51
Solution anneal + aged (base metal)	896	1276	31	55

^a 11.68 mm thick plate with 60° V-groove GTA welded in 13 passes using matching filler metal; 6.40 mm gauge diameter all-weld-metal tensile specimens

^b Solution annealed = 1038 °C/1 h/AC; Age = 732 °C/8 h/FC to 621 °C/8 h/AC

6.5 Additive Manufacturing

6.5.1 Additive Manufacturing of Metals

Additive manufacturing (AM), also known as 3D printing, is an innovative way of fabricating three-dimensional structures by progressively depositing layers of material. It allows the creation of complex three-dimensional shapes with complex geometries, such as internal cavities and lattice structures, where traditional manufacturing like casting, forging, or machining are time-consuming or incapable of achieving desired geometries. Over the last few decades, many additive techniques have evolved based on how the layers are deposited to create the component and the materials used. These techniques can be categorized into seven based on the printing technologies [65].

- (I) Powder bed fusion
- (II) Directed energy deposition
- (III) Material Jetting
- (IV) Binder jetting
- (V) Material extrusion
- (VI) Vat photopolymerization
- (VII) Sheet lamination

Each technique has advantages and limitations associated with printing/manufacturing processes such as speed, type of the feedstock material, geometrical limitations, tolerances, properties, costs, etc. But all the additive manufacturing techniques have shown the potential to lower the overall cost. They can manufacture parts on-demand, reducing maintenance time and the need for inventory management [66]. Additive manufacturing is being used to print tissues [67, 68], implants and prostheses [69], mechanical components [70], electronics

[71], etc. using a wide range of materials, including polymeric [72] materials, stainless steels [73, 74], nickel-based superalloys [75] and titanium alloys [76, 77].

Metal AM techniques primarily use powder bed fusion, directed energy deposition, binder jetting and sheet lamination. The powder bed fusion technique uses a high-density power source to scan and fuse layers by selective fusion of the powder bed in multiple layers. As a layer is built, another layer of the powder is added, and the power source moves up to fuse it. The process is repeated until the part is built-up. The scan speed plays a decisive role in densification and good metallurgical bonding during selective laser melting (SLM). The printer lays down successive layers of the metallic powder based on three dimensional computer-aided design (CAD) models. The layers are melted together by a computer-controlled power source of a laser or electron beam. The main factors that influence the properties of an additively manufactured component are: (i) the orientation of the CAD geometry across which the part is sliced into layers to build the part, (ii) processing parameters like scan velocity, power density, etc. Parameters like powder properties and processing environmental influence the melt pool size in the powder bed. After a layer is deposited, a new powder layer with a predefined thickness is placed on the powder bed. For successful deposition, the melt pool must be large enough to fuse and connect adjacent tracks in each layer and deep enough to fuse and bond with the previous layers. Incomplete fusion may occur if the energy density is insufficient, while excessive energy may lead to defects in the fabricated part. An increase in the energy density increases track overlap and improves fusion.

Among different powder bed techniques, selective laser melting (SLM) and electron-beam melting (EBM) are mainly used for the rapid production of net-shaped or near-net-shaped components by a high-power density laser or electron-beam. The powder bed fusion method directly produces highly dense metal parts from metal powder with characteristics close to the bulk material. Choi et al. [78] have reported SLM made Alloy 718 with 99.8% density.

Selective laser melting, also known as direct metal laser melting or laser powder bed fusion, uses a high power-density laser to melt and fuse metallic powders. The high-energy laser melts the powder to create a fully dense metal layer with mechanical properties similar to conventionally manufactured metals. The scan patterns are rotated from layer to layer to obtain a more uniform layer-to-layer and stripe-to-stripe fusion. Two types of layering strategies, based on the rotation of the scan patterns with respect to the previous layer, either by 90° (i.e., scan patterns alternated in orthogonal directions) or by about 67° from layer to layer, are adopted (Fig. 6.17). Ozel et al. [79] have shown that the rotation of the scan orientation by 67° results in wider fused tracks with larger overlaps for a given energy density. Dinda et al. [80] have shown a significant effect of the scanning pattern on the solidification morphology during the deposition of a multiple layer Alloy 718 component. Unidirectional laser scanning results in the formation of primary dendrites at an angle of 60° with the substrate in all layers. In contrast, the primary dendrites in a bidirectional scanning change by 90° in each layer with respect to their growth direction in the previous layer [80]. This effect of laser scanning on the solidification pattern may result in printing components of precisely the same geometry with strikingly different solidification

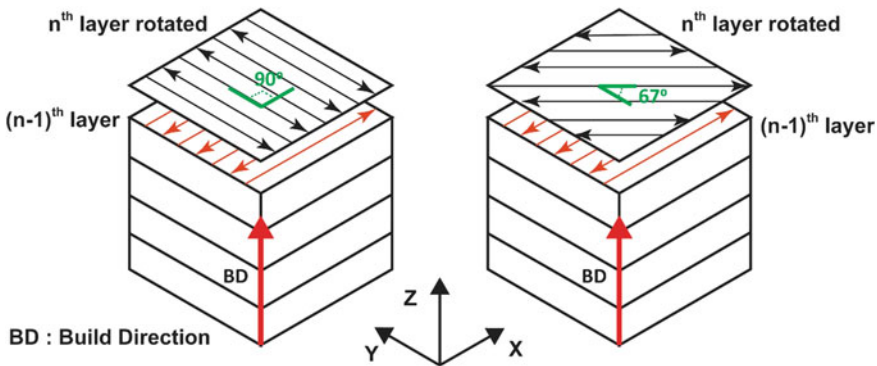


Fig. 6.17 Schematic depicting 90° and 67° rotation of the stripe patterns, with respect to the previous layer, during 3-D printing of an alloy by selective laser melting

patterns [80, 81]. Trosch et al. [82] have shown the SLM process can produce Alloy 718 components with mechanical properties better than forged and cast material at room temperature and similar to forged products at elevated temperatures.

The microstructure of additively manufactured superalloys may be quite different from their wrought or cast counterparts. A textured microstructure characterizes the microstructure of an additively manufactured alloy built by an SLM process due to the growth of columnar grains across multiple layers parallel to the building (Z-axis) direction. The columnar grains are separated by high-angle boundaries and are characterized by substructures of packets of parallelly arranged dendrite cells with low-angle boundaries. As a result, the AM alloy exhibit a variation in mechanical properties of the alloy in the scan and built directions. A heat treatment at high temperatures may not entirely change the elongated shape and crystallographic orientations of the grains. Still, it may eliminate the dendritic substructure and bring the properties close to the wrought alloys.

Although AM results in a near-net shape geometry of the component, post-manufacturing treatments and finish machining are often required to relieve high residual stresses and undesired porosity to achieve the final desired geometry, dimensional tolerances, and surface quality [83]. The technique has been used to additively manufacture parts of materials like stainless steel [84], Alloy 625 [85, 86] and Alloy 718 [65, 87], Ti6Al4V alloy [88, 89], etc.

Electron-beam additive manufacturing of metals produces similar columnar architecture parallel to the build direction. EBM utilizes an electron beam to selectively melt the powder bed layer by layer in a high vacuum. Unlike metal sintering techniques that operate below the melting point, EBM parts are void-free [86, 90]. The process occurs under a vacuum, making it suitable to manufacture parts of reactive materials, like titanium, with a high oxygen affinity. The process is carried out at high temperatures (up to 1000 °C) to allow partial sintering of the powder bed and minimize residual stresses during the build, leading to differences in phase

formation through solidification and solid-state phase transformation. The high-temperature processing of the powder results in microstructural differences between the component made by an EBM technique compared to that produced by SLM.

In a powder-fed directed energy deposition, a high-power laser melts the metal powder before it is supplied to the focus of the laser beam. A hermetically sealed chamber filled with inert gas or a local inert shroud gas is often used to shield the melt pool from atmospheric oxygen to better control material properties. The technique offers a high degree of control and freedom because multiple powders can be fed simultaneously through the nozzle [65]. With this technique, desired chemical composition and microstructural features can be obtained by adjusting the feed rate [91]. The technique is best suitable for manufacturing near-net shape components and repairing high-value parts with little wastage [92–94]. The process supports various metallic materials, including titanium, stainless steel, aluminum, speciality materials, composites, and functionally graded material. However, a post-manufacturing operation like machining is often required to obtain tight tolerances because of poor resolution and rough surface finish [95].

Additive manufacturing has the potential to reduce scrap generation, saves the cost of machining, has high material utilization, reduce the manufacturing time and can fabricate complex shapes that are otherwise impossible via conventional routes [65]. Due to these advantages, AM has a significant impact on the manufacturing of advanced components of Jet engines, turbine blades, rocket engines and many other applications. However, controlling the fabricated components' mechanical texture and chemical properties is crucial for obtaining target properties in AM parts that cannot be made by any other means.

6.5.2 Additive Manufacturing of Alloy 625

Alloy 625 is an attractive material for 3D printing by selective layer melting and electron-beam melting techniques. The two techniques give good metallurgical bonding of the powder with minimal defects and fine dendritic microstructure. Both methods produce similar columnar microstructures of the alloy. However, a significant difference is reported in the size and shape of the γ'' phase particles and the spacing, width, and texture of the columnar grains [86] due to the difference in the cooling rates of the melt pools in the two processes. The scheme of rastering does not appear to have any significant effect on tensile properties of the alloy [96]. Table 6.11 shows mechanical properties of the 3D printed alloy produced by selective laser melting and electron-beam melting.

Figure 6.18 shows typical optical microstructure of Alloy 625 3D printed by an SLM technique adopting a 67° layer rotation scheme. The microstructure revealed laser fused stripes in the surface layer (XY plane) and overlapped fusion zones in the XZ plane. Inverse pole figure (IPF) maps of three orthogonal XY, XZ and YZ planes in as-built revealed a columnar architecture of the grains in the build direction, wherein individual columnar grains of solid solution γ phase

Table 6.11 Tensile properties of some 3-D printed Alloy 625 additively manufactured by selective laser melting and electron-beam melting

AM sample	Rastering	YS (MPa)	UTS (MPa)	Ductility (%)	Charpy energy (J)	Reference
SLM1	0°	572	920	48	104	[96]
SLM2	90°	568	925	46	102	[96]
SLM3	Mixed	571	915	49	103	[96]
SLM4	–	540	690	36	–	[85]
SLM5	–	477–518	744–797	31–48	–	[97]
SLM + anneal	–	395	824	51	110	[96]
SLM + HIP1	–	360	880	58	–	[86]
EBM	–	410	750	44	–	[86]
EBM + HIP2	–	330	770	69	–	[86]

YS Yield strength; UTS Ultimate tensile strength; Ductility Elongation; HIP Hot isostatic pressed

were separated by high-angle boundaries (Fig. 6.19). This microstructure is consistent with most as-built SLM microstructure (see, e.g., see [96]). The deflection of the columnar grains away from the build direction is attributed to the moving laser source. The YZ plane is characterized by columns of grains, separated mainly by low-angle boundaries, oriented in a slightly zigzag fashion with respect to the build direction.

The melt pool morphology on the top (XY plane) of the deposited layers and the XZ plane shows a typical Gaussian morphology, oriented in the direction of scanning/building, with a structure containing fine columnar grains of small dendritic arm spacing (Fig. 6.20). This melt pool morphology is due to the multi-pass melting with significant overlapping in horizontal and vertical planes. A schematic of the overlapping of the melt pools in the two planes is shown in Fig. 6.21. The horizontal interactions are usually governed by the laser beam overlapping in the XY plane. In

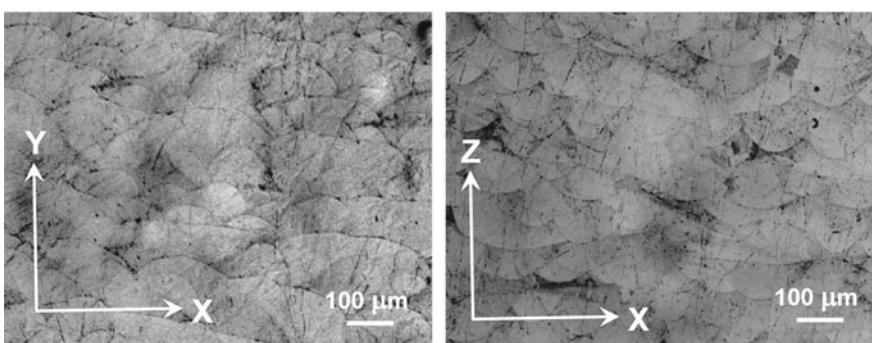


Fig. 6.18 Typical optical microstructure of the as-printed alloy showing the laser fused stripes on the surface layer (horizontal plane) and the overlapped fusion zones in an orthogonal vertical plane

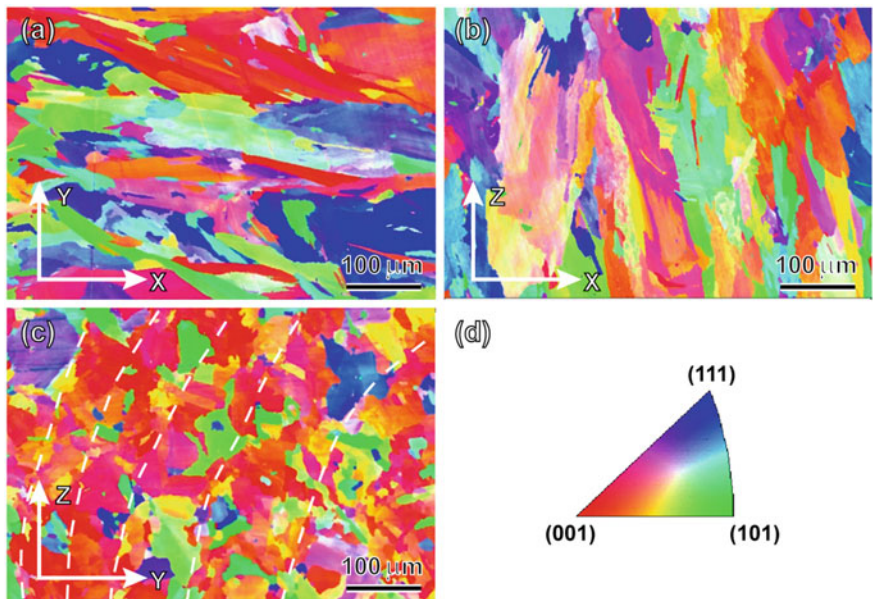


Fig. 6.19 Inverse pole figure (IPF) maps of the three orthogonal surfaces generated by electron-backscattered diffraction revealing columnar architecture of the grains in the building direction: **a** XY plane; **b** XZ plane; **c** YZ plane; **d** IPF triangle for the orientation labels of grains in **(a–c)**

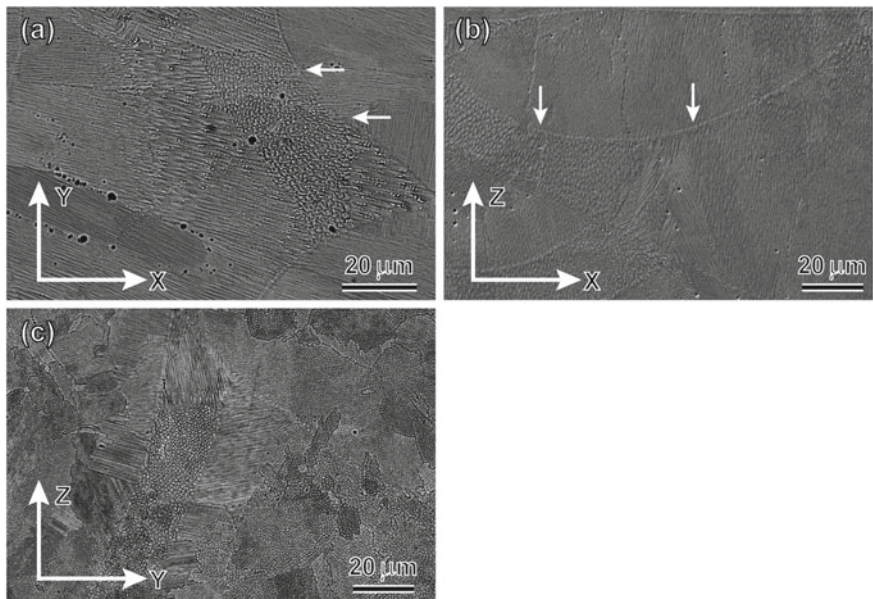


Fig. 6.20 Scanning electron micrographs delineating the melt pool morphology, marked by arrows, in the three orthogonal planes: **a** XY plane; **b** XZ plane; **c** YZ plane

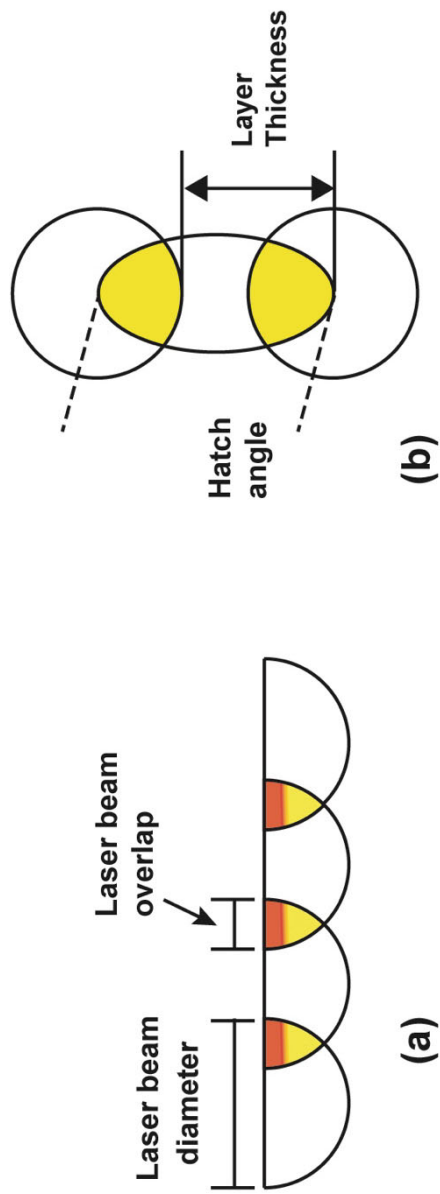


Fig. 6.21 Schematic drawings showing overlapping of the melt pools during selective laser melting: **a** horizontal overlapping; **b** vertical overlapping

contrast, the vertical overlapping is governed by the layer thickness and the hatch angle.

The 3D printed microstructure is characterized by chemical inhomogeneities between dendritic cells and overlapping regions of adjacent racks and layers. These inhomogeneities are due to the segregation of niobium and molybdenum (Fig. 6.22). This microstructure is different from the typical solidification microstructures because the rapid melt solidification during SLM prevents macro-segregation.

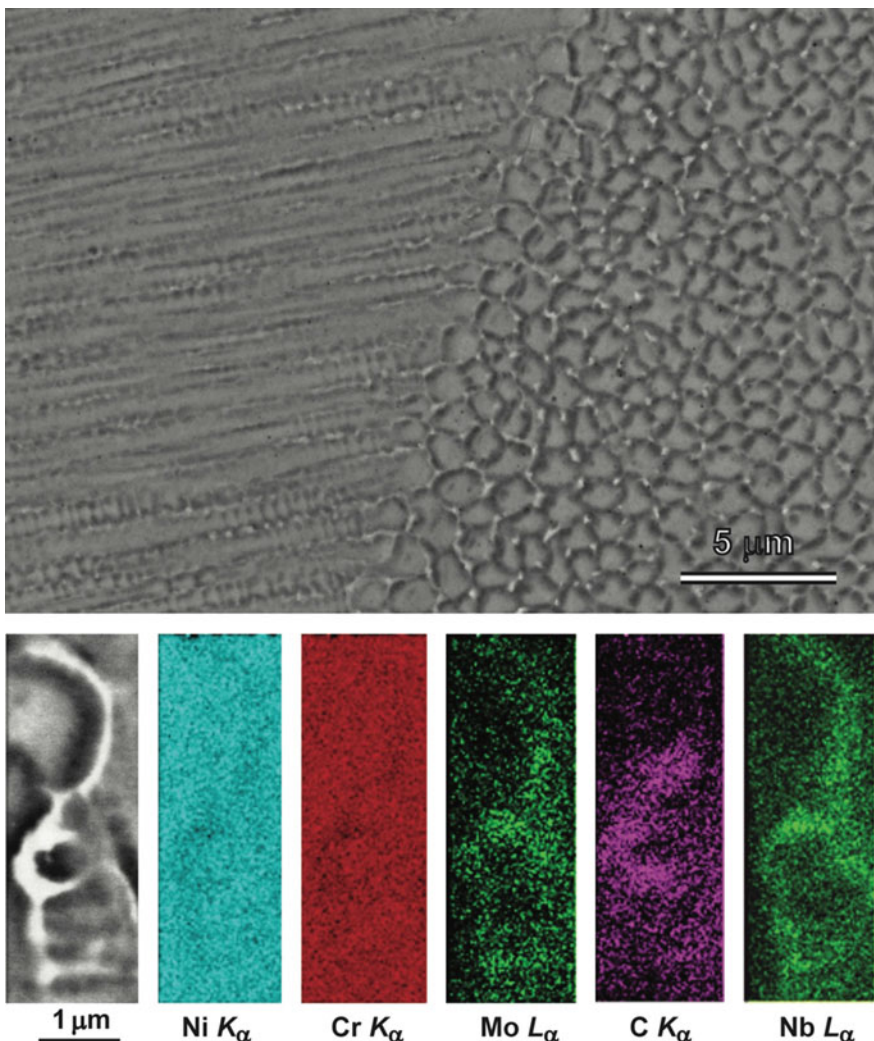


Fig. 6.22 Segregation of niobium, molybdenum and carbon at interdendritic regions of the solidified melt in a selective laser melted Alloy 625 sample. The lower panel shows maps of different elements of a segregated region

However, the microsegregation of niobium and molybdenum in SLM is also susceptible to forming the non-equilibrium Laves phases at interdendritic regions, grain boundaries and layer interfaces due to the eutectic formation noted earlier. Chlebus et al. [98] have shown the occurrence of tiny particles of the eutectic mixture (γ + Lave phase) or its divorced form and fine MC type carbides in the interdendritic regions of SLM printed Alloy 718. Dinda et al. [99] have shown that the columnar dendritic structure is stable up to 1000 °C and have demonstrated the formation of a fully recrystallized equiaxed structure at around 1200 °C.

Ganesh et al. [85] have studied the mechanical and fatigue behavior of a laser-printed Alloy 625. They have reported yield strength and tensile strengths of the laser-printed Alloy 625 to be about 540 and 690 MPa with ductility of about 36%. These properties were consistent with those reported by Xue et al. [97]. The yield strength of the laser-printed alloy is higher compared to a wrought alloy, but the ultimate tensile strength and ductility are lower (Sect. 4.5.1). The laser printed alloy exhibited stable crack growth during the J-integral test and fracture toughness values ($J_{0.2}$) in the range of about 200–255 kJ/m². The crack propagated along the growth direction of the specimens, which was predominantly along the {111} plane. Under fatigue conditions, the laser-printed alloy showed a consistently steady-state fatigue crack growth rate within the Paris' Law regime (Sect. 4.6) when examined in the stress intensity (ΔK) range of 14–38 MPa \sqrt{m} . The fatigue crack growth rate within this ΔK range is lower than that for a wrought Alloy 625. However, the difference in fatigue crack growth rate of the laser printed and wrought Alloy 625 diminishes with an increase in ΔK . Table 6.12 compares empirical constants of the Paris' equation (Eq. 4.18) for the laser-printed Alloy 625 with those for the wrought Alloy 625 [100]. Authors have attributed the improved fatigue crack growth resistance of the laser-printed Alloy 625 in the low-stress intensity range to its higher yield strength and residual stresses.

Additive manufacturing technologies have opened up new vistas of industrial production processes to create components of complex materials with complex shapes at promisingly low costs. However, to obtain good quality final components, high-quality control of the additive printing processes and the raw material, starting from the production of the powder itself, is necessary.

Table 6.12 A comparison of fatigue crack growth rate constants in the laser-printed and wrought Alloy 625 samples within the Paris' law regime

Alloy sample	ΔK (MPa \sqrt{m})	Stress ratio	C	m	Reference
SLM1	14–25	0.3	3.23×10^{-12}	5.21	[85]
SLM1	21–31.1	0.1	1.48×10^{-12}	5.42	[85]
SLM1	27.6–36.1	0.1	1.95×10^{-12}	5.33	[85]
Wrought1	21.1–54.4	0.05	8.55×10^{-10}	3.73	[100]
Wrought2	23–41	0.05	4.48×10^{-10}	3.8	[100]

6.6 Summary

Ease of fabrication is an integral part of an alloy's importance. The success of Alloy 625 is its ease of fabrication, apart from its excellent combination of strength and corrosion behavior. The excellent deformability and welding of the alloy allow to fabricate various shapes and structures for different applications, ranging from pressure vessels to vacuum bellows for exploiting different alloy's properties. Conventional welding processes and procedures can readily join it with itself and to other materials. The alloy usually requires no post-weld heat treatments to maintain its high strength and ductility. However, machining of the alloy may be somewhat tricky. The alloy is also finding excellent acceptance for 3D printing of components by additive manufacturing techniques.

References

1. Sellars CM, McTegart WJ (1966) On the mechanism of hot deformation. *Acta Metall* 14:1136–1138
2. Sakai T, Belyakov A, Kaibyshev R, Miura H, Jonas JJ (2014) Dynamic and post-dynamic recrystallization under hot, cold and severe plastic deformation conditions. *Prog Mater Sci* 60:130–207. <https://doi.org/10.1016/j.pmatsci.2013.09.002>
3. Livesey DW, Sellars CM (1985) Hot-deformation characteristics of Waspaloy. *Mater Sci Technol* 1:136–144. <https://doi.org/10.1179/mst.1985.1.2.136>
4. Lopez B, Urcola JJ (1996) Hot deformation characteristics of Inconel 625. *Mater Sci Technol* 12:673–678
5. Guo Q, Li D, Guo S, Peng H, Hu J (2011) The effect of deformation temperature on the microstructure evolution of Inconel 625 superalloy. *J Nucl Mater* 414:440–450. <https://doi.org/10.1016/j.jnucmat.2011.05.029>
6. Zhou HT, Liu RR, Liu ZC, Zhou X, Peng QZ, Zhong FH, Peng Y (2013) Hot deformation characteristics of GH625 and development of a processing map. *J Mater Eng Perform* 22:2515–2521
7. Sun D, Jiang X, Shi J, Huang J, Jiang Y (2017) Hot forging behavior of Inconel 625 superalloy based on processing map. In: China materials conference, pp 643–652
8. Jia Z, Gao Z-X, Ji J-J, Liu D-X, Guo T-B, Ding Y-T (2021) High-temperature deformation behavior and processing map of the as-cast Inconel 625 alloy. *Rare Met* 40:2083–2091
9. Ferrer L, Pieraggi B, Uginet JF (1993) International conference on recrystallization and related phenomena. In: Sevillano JGF, Sevillano M (ed) Recrystallization and related annealing phenomena. Trans Tech Publications Ltd, pp 417–422
10. Zhou LX, Baker TN (1994) Effects of strain rate and temperature on deformation behaviour of IN 718 during high temperature deformation. *Mater Sci Eng A* 177:1–9
11. Singh JB, Verma A, Thota MK, Kapoor R (2020) Dynamic recrystallization during hot-deformation of a newly developed Alloy 693. *Mater Charact* 167:110529. <https://doi.org/10.1016/j.matchar.2020.110529>
12. McQueen HJ, Sankar J, Fulop S (1979) In: 3rd international conference of mechanical. Cambridge, UK, p 675
13. Donachie MJ, Donachie SJ (2002) Superalloys: a technical guide. ASM international, Materials Park, OH
14. Special Metal corporation, Fabricating the special metals corporation alloys. <http://selector.specialmetalswelding.com/publica/fab.pdf>

15. Yang F, Dong L, Hu X, Zhou X, Xie Z, Fang F (2020) Effect of solution treatment temperature upon the microstructure and mechanical properties of hot rolled Inconel 625 alloy. *J Mater Sci* 55:5613–5626. <https://doi.org/10.1007/s10853-020-04375-2>
16. Singh JB, Verma A, Thota MK, Chakravarthy JK (2014) Brittle failure of Alloy 693 at elevated temperatures. *Mater Sci Eng A* 616:88–92. <https://doi.org/10.1016/j.msea.2014.08.015>
17. Breitzig RW (2003) Machining of nickel and nickel alloys, ASM Metals Handbook
18. Rodrigues MA, Hassui A, Lopes da Silva RH, Loureiro D (2016) Tool life and wear mechanisms during Alloy 625 face milling. *Int J Adv Manuf Technol* 85:1439–1448. <https://doi.org/10.1007/s00170-015-8056-4>
19. Parida AK, Maity K (2018) Comparison the machinability of Inconel 718, Inconel 625 and Monel 400 in hot turning operation. *Eng Sci Technol Int J* 21:364–370. <https://doi.org/10.1016/j.jestch.2018.03.018>
20. Ezugwu EO (2005) Key improvements in the machining of difficult-to-cut aerospace superalloys. *Int J Mach Tools Manuf* 45:1353–1367. <https://doi.org/10.1016/j.ijmachtools.2005.02.003>
21. Zlámal T, Hajný J, Petruš J, Mrkvica I (2018) Effect of the cutting tool geometry on the tool wear resistance when machining inconel 625. *Adv Sci Technol Res J* 12
22. Yıldırım ÇV, Kivak T, Sarıkaya M, Erzincanlı F (2017) Determination of MQL parameters contributing to sustainable machining in the milling of nickel-base superalloy waspaloy. *Arab J Sci Eng* 42:4667–4681. <https://doi.org/10.1007/s13369-017-2594-z>
23. Yıldırım ÇV, Kivak T, Sarıkaya M, Şirin Ş (2020) Evaluation of tool wear, surface roughness/topography and chip morphology when machining of Ni-based alloy 625 under MQL, cryogenic cooling and CryoMQL. *J Mater Res Technol* 9:2079–2092. <https://doi.org/10.1016/j.jmrt.2019.12.069>
24. Nurul Amin AKM, Ginta TL (2014) 11.13—heat-assisted machining. In: Hashmi S, Batalha GF, Van Tyne GF, Yilbas BBT-CMP (eds) Elsevier, Oxford, pp 297–331. <https://doi.org/10.1016/B978-0-08-096532-1.01118-3>
25. Kansal HK, Singh S, Kumar P (2007) Effect of silicon powder mixed EDM on machining rate of AISI D2 die steel. *J Manuf Process* 9:13–22. [https://doi.org/10.1016/S1526-6125\(07\)70104-4](https://doi.org/10.1016/S1526-6125(07)70104-4)
26. Garg MP, Kumar A, Sahu CK (2017) Mathematical modeling and analysis of WEDM machining parameters of nickel-based super alloy using response surface methodology. *Sādhanā* 42:981–1005. <https://doi.org/10.1007/s12046-017-0647-3>
27. Kumar A, Upadhyay C, Kukkala V (2020) Study of surface characterization and parametric optimization during wire electric discharge machining for Inconel 625. *Mater Sci Forum* 978:97–105. <https://doi.org/10.4028/www.scientific.net/MSF.978.97>
28. Singh VK, Singh S Multi-objective optimization using Taguchi based Grey relational analysis for wire EDM of Inconel 625. *J Mater Sci Mech Eng* 2:38–42
29. Valenti M (2001) Making the cut. *Mech Eng* 123:64–67. <https://doi.org/10.1115/1.2001-NOV-4>
30. Todd RH, Allen DK, Alting L (1994) Manufacturing processes reference guide. Industrial Press Inc.
31. Degarmo EP, Black JT, Kohser RA (2003) Materials and processes in manufacturing, 9th edn. 32. https://books.google.co.uk/books/about/Materials_and_processes_in_manufacturing.html?id=depTAAAAMAAJ&pgis=1
32. Dubey AK, Yadava V (2008) Laser beam machining—a review. *Int J Mach Tools Manuf* 48:609–628. <https://doi.org/10.1016/j.ijmachtools.2007.10.017s>
33. Alloys H, Working H, Working C, Treating H (2002) Fabrication of Haynes ® and Hastelloy ® solid-solution-strengthened high-temperature alloys general guidelines for. <https://www.inkosas.cz/download/niklove-slitiny/htafab.pdf>
34. Cieslak MJ (1991) The welding and solidification metallurgy of alloy 625
35. Knorovsky GA, Cieslak MJ, Headley TJ, Romig AD, Hammetter WF (1989) INCONEL 718: A solidification diagram. *Metall Trans A* 20:2149–2158. <https://doi.org/10.1007/BF02650300>

36. J.N. Dupont, A.R. Marder, C. V Robino, Solidification and weldability of Nb-bearing superalloys, 77 (1998). <https://www.osti.gov/biblio/655470>
37. Cieslak MJ, Headley TJ, Romig AD, Kollie T (1988) A melting and solidification study of alloy 625. Metall Trans A 19:2319–2331. <https://doi.org/10.1007/BF02645056>
38. DuPont JN, Marder AR, Notis MR, Robino CV (1998) Solidification of Nb-bearing superalloys: Part II. Pseudoternary solidification surfaces. Metall Mater Trans A 29:2797–2806. <https://doi.org/10.1007/s11661-998-0320-x>
39. DuPont JN, Notis MR, Marder AR, Robino CV, Michael JR (1998) Solidification of Nb-bearing superalloys: Part I. Reaction sequences. Metall Mater Trans A 29:2785–2796. <https://doi.org/10.1007/s11661-998-0319-3>
40. DuPont JN, Robino CV, Marder CV (1998) Modeling solute redistribution and microstructural development in fusion welds of Nb-bearing superalloys. Acta Mater 46:4781–4790. [https://doi.org/10.1016/S1359-6454\(98\)00123-2](https://doi.org/10.1016/S1359-6454(98)00123-2)
41. Lippold JC, Sowards JW, Murray GM, Alexandrov BT, Ramirez AJ (2008) Weld solidification cracking in solid-solution strengthened Ni-base filler metals BT—hot cracking phenomena in welds II. In: Böllinghaus T, Herold H, Cross CE, Lippold JC (eds) Springer Berlin Heidelberg, Berlin, Heidelberg, pp 147–170. https://doi.org/10.1007/978-3-540-78628-3_9
42. DuPont JN, Lippold JC, Kiser SD (2009) Solid-solution strengthened Ni-base alloys. In: Welding metallurgy and weldability of nickel-base alloys. Wiley, p 47 (Chap. 3)
43. Lippold JC (1983) Investigation of heat-affected zone hot cracking in Alloy 800. Weld J 62
44. Hondors E, Seah MP (1984) Physical metallurgy, 3rd edn. New Holland, Amsterdam
45. Lippold JC, Baeslack W, Varol I (1988) Heat-affected zone liquation cracking in austenitic and duplex stainless steels. Weld J 71:1
46. Pepe JJ (1970) The weld heat-affected zone of the 18Ni maraging steels. Weld J 49:545-s
47. Pepe JJ (1967) Effects of constitutional liquation in 18-Ni maraging steel weldments. Weld J 46:411s–422s
48. Duvall DS (1967) Further heat-affected-zone studies in heat-resistant nickel alloys. Weld J 46:423s–432s
49. Lin W, Nelson TW, Lippold JC, Baeslack W (1992) A study of the HAZ crack susceptible region in Alloy 625. Int Trends Weld Sci Technol 695–702
50. Owczarski WA, Duvall DS, Sullivan CP (1966) A model for heat affected zone cracking in nickel-base superalloys. Weld J 45:145
51. Savage WF, Krantz BM (1966) An investigation of hot cracking in Hastelloy X. WELD J 45:13
52. Thompson RG, Genculu S (1983) Microstructural evolution in the Haz of Inconel 718 and correlation with the hot ductility test. Weld J (Miami, Fla) 62:337–345
53. Young GA, Battige CK, Liwus N, Penik MA, Kikel J, Silvia AJ, McDonald CK (2001) Factors affecting the hydrogen embrittlement resistance of Ni–Cr–Mn–Nb welds. United States. <https://doi.org/10.2172/821694>
54. Cieslak MJ, Headley TJ, Romig AD (1986) The welding metallurgy of HASTELLOY alloys C-4, C-22, and C-276. Metall Trans A 17:2035–2047. <https://doi.org/10.1007/BF02645001>
55. DuPont JN, Michael JR, Newbury BD (1999) Welding metallurgy of alloy HR-160. <https://www.osti.gov/biblio/7067>
56. Heubner U, Kohler M, Prinz B (1988) Determination of solidification behaviour of some selected superalloys. Superalloys 1988:437–446
57. Mizia RE, Michael JR, Williams DB, Dupont DB, Robino CV (2004) Physical and welding metallurgy of Gd-enriched austenitic alloys for spent nuclear fuel applications. Part II, nickel base alloys. <https://www.osti.gov/biblio/952808>
58. Webb GL, Burke MG (1995) Stress corrosion cracking behavior of Alloy 600 in high temperature water
59. Perricone MJ (2003) Microstructural development of superaustenitic stainless steel and Ni-base alloys in casting and conventional arc welds, PhD Thesis, Lehigh University, Bethlehem, PA.

60. Richards NL, Chaturvedi MC (2000) Effect of minor elements on weldability of nickel base superalloys. *Int Mater Rev* 45:109–129. <https://doi.org/10.1179/09506600010152831>
61. Silva CC, de Albuquerque VHC, Miná EM, Moura EP, Tavares JMRS (2018) Mechanical properties and microstructural characterization of aged nickel-based Alloy 625 weld metal. *Metall Mater Trans A* 49:1653–1673. <https://doi.org/10.1007/s11661-018-4526-2>
62. Cortial F, Corrieu JM, Vernot-Loier C (1995) Influence of heat treatments on microstructure, mechanical properties, and corrosion resistance of weld alloy 625. *Metall Mater Trans A* 26:1273–1286. <https://doi.org/10.1007/BF02670621>
63. Frank RB (1991) Customage 625 plus alloy-a higher strength alternative to Alloy 625. In: Oria EA (ed) Superalloys 718, 625 various derivatives
64. Onyewuenyi OA (2012) Alloy 718: alloy optimization for applications in oil and gas production 345–362. https://doi.org/10.7449/1989/superalloys_1989_345_362
65. Yong SH, Gibbons GJ, Wong CC, West G (2020) A critical review of the material characteristics of additive manufactured IN718 for high-temperature application. *Metals* 10. <https://doi.org/10.3390/met10121576>.
66. Khajavi SH, Partanen J, Holmström J (2014) Additive manufacturing in the spare parts supply chain. *Comput Ind* 65:50–63. <https://doi.org/10.1016/j.compind.2013.07.008>
67. Murphy SV, Atala A (2014) 3D bioprinting of tissues and organs. *Nat Biotechnol* 32:773–785. <https://doi.org/10.1038/nbt.2958>
68. Miller JS, Stevens KR, Yang MT, Baker BM, Nguyen D-HT, Cohen DM, Toro E, Chen AA, Galie PA, Yu X, Chaturvedi R, Bhatia SN, Chen CS (2012) Rapid casting of patterned vascular networks for perfusable engineered three-dimensional tissues. *Nat Mater* 11:768–774. <https://doi.org/10.1038/nmat3357>
69. He Y, Xue G, Fu J (2014) Fabrication of low cost soft tissue prostheses with the desktop 3D printer. *Sci Rep* 4:6973. <https://doi.org/10.1038/srep06973>
70. Hofmann DC, Kolodziejska J, Roberts S, Otis R, Dillon RP, Suh J-O, Liu Z-K, Borgonia J-P (2014) Compositionally graded metals: a new frontier of additive manufacturing. *J Mater Res* 29:1899–1910. <https://doi.org/10.1557/jmr.2014.208>
71. Zheng Y, He Z, Gao Y, Liu J (2013) Direct desktop printed-circuits-on-paper flexible electronics. *Sci Rep* 3:1786. <https://doi.org/10.1038/srep01786>
72. Melchels FPW, Domingos MAN, Klein TJ, Malda J, Bartolo PJ, Hutmacher DW (2012) Additive manufacturing of tissues and organs. *Prog Polym Sci* 37:1079–1104. <https://doi.org/10.1016/j.progpolymsci.2011.11.007>
73. Yan C, Hao L, Hussein A, Young P, Raymont D (2014) Advanced lightweight 316L stainless steel cellular lattice structures fabricated via selective laser melting. *Mater Des* 55:533–541. <https://doi.org/10.1016/j.matedes.2013.10.027>
74. Manvatkar V, De A, DebRoy T (2015) Spatial variation of melt pool geometry, peak temperature and solidification parameters during laser assisted additive manufacturing process. *Mater Sci Technol* 31:924–930. <https://doi.org/10.1179/1743284714Y.0000000701>
75. Liu Z, Qi H (2014) Numerical simulation of transport phenomena for a double-layer laser powder deposition of single-crystal superalloy. *Metall Mater Trans A* 45:1903–1915. <https://doi.org/10.1007/s11661-013-2178-9>
76. Xu W, Brandt M, Sun S, Elambasseri J, Liu Q, Latham K, Xia K, Qian M (2015) Additive manufacturing of strong and ductile Ti–6Al–4V by selective laser melting via in situ martensite decomposition. *Acta Mater* 85:74–84. <https://doi.org/10.1016/j.actamat.2014.11.028>
77. Carroll BE, Palmer TA, Beese AM (2015) Anisotropic tensile behavior of Ti–6Al–4V components fabricated with directed energy deposition additive manufacturing. *Acta Mater* 87:309–320. <https://doi.org/10.1016/j.actamat.2014.12.054>
78. Choi J-P, Shin G-H, Yang S, Yang D-Y, Lee J-S, Brochu M, Yu J-H (2017) Densification and microstructural investigation of Inconel 718 parts fabricated by selective laser melting. *Powder Technol* 310:60–66. <https://doi.org/10.1016/j.powtec.2017.01.030>
79. Öznel T, Altay A, Donmez A, Leach R (2018) Surface topography investigations on nickel alloy 625 fabricated via laser powder bed fusion. *Int J Adv Manuf Technol* 94:4451–4458. <https://doi.org/10.1007/s00170-017-1187-z>

80. Dinda GP, Dasgupta AK, Mazumder J (2012) Texture control during laser deposition of nickel-based superalloy. *Scr Mater* 67:503–506. <https://doi.org/10.1016/j.scriptamat.2012.06.014>
81. David SA, Debroy T (1992) Current issues and problems in welding science. *Science* (80-) 257:497–502. <https://doi.org/10.1126/science.257.5069.497>
82. Trosch T, Strößner J, Völkl R, Glatzel U (2016) Microstructure and mechanical properties of selective laser melted Inconel 718 compared to forging and casting. *Mater Lett* 164:428–431. <https://doi.org/10.1016/j.matlet.2015.10.136>
83. Wiederkehr P, Bergmann JA (2018) An integrated macroscopic model for simulating SLM and milling processes. *Prod Eng* 12:465–472. <https://doi.org/10.1007/s11740-018-0822-3>
84. Kalentics N, de Seijas MOV, Griffiths S, Leinenbach C, Logé RE (2020) 3D laser shock peening—a new method for improving fatigue properties of selective laser melted parts. *Adm Manuf* 33:101112. <https://doi.org/10.1016/j.admna.2020.101112>
85. Ganesh P, Kaul R, Paul CP, Tiwari P, Rai SK, Prasad RC, Kukreja LM (2010) Fracture behavior of laser-clad joint of Stellite 21 on AISI 316L stainless steel. *Mater Sci Eng A* 527:7490–7497. <https://doi.org/10.1016/j.msea.2010.08.034>
86. Amato KN, Hernandez J, Murr LE, Martinez E, Gaytan SM, Shindo PW (2012) *J Mater Sci Res* 1(2)
87. Amato KN, Gaytan SM, Murr LE, Martinez E, Shindo PW, Hernandez J, Collins S, Medina F (2012) Microstructures and mechanical behavior of Inconel 718 fabricated by selective laser melting. *Acta Mater* 60:2229–2239. <https://doi.org/10.1016/j.actamat.2011.12.032>
88. Levy D, Shirizly A, Rittel D (2018) Static and dynamic comprehensive response of additively manufactured discrete patterns of Ti6Al4V. *Int J Impact Eng* 122:182–196. <https://doi.org/10.1016/j.ijimpeng.2018.07.014>
89. Mazur M, Leary M, McMillan M, Sun S, Shidid D, Brandt M (2017) 5—mechanical properties of Ti6Al4V and AlSi12Mg lattice structures manufactured by selective laser melting (SLM). In: Brandt MBT-LAM (ed) Woodhead publishing series in electronic and optical materials. Woodhead Publishing, pp 119–161. <https://doi.org/10.1016/B978-0-08-100433-3.00005-1>
90. Murr LE, Martinez E, Gaytan SM, Ramirez DA, Machado BI, Shindo PW, Martinez JL, Medina F, Wooten J, Cisel D, Ackelid U, Wicker RB (2011) Microstructural architecture, microstructures, and mechanical properties for a nickel-base superalloy fabricated by electron beam melting. *Metall Mater Trans A* 42:3491–3508. <https://doi.org/10.1007/s11661-011-0748-2>
91. Graf B, Gumenyuk A, Rethmeier M (2012) Laser metal deposition as repair technology for stainless steel and titanium alloys. *Phys Procedia* 39:376–381. <https://doi.org/10.1016/j.phpro.2012.10.051>
92. Zhong C, Kittel J, Gasser A, Schleifenbaum JH (2019) Study of nickel-based super-alloys Inconel 718 and Inconel 625 in high-deposition-rate laser metal deposition. *Opt. Laser Technol* 109:352–360. <https://doi.org/10.1016/j.optlastec.2018.08.003>
93. Sun GF, Shen XT, Wang ZD, Zhan MJ, Yao S, Zhou R, Ni ZH (2019) Laser metal deposition as repair technology for 316L stainless steel: influence of feeding powder compositions on microstructure and mechanical properties. *Opt Laser Technol* 109:71–83. <https://doi.org/10.1016/j.optlastec.2018.07.051>
94. Kumar LJ, Nair CGK (2017) Laser metal deposition repair applications for Inconel 718 alloy. *Mater Today Proc* 4:11068–11077. <https://doi.org/10.1016/j.matpr.2017.08.068>
95. Saboori A, Gallo D, Biamino S, Fino P, Lombardi M (2017) An overview of additive manufacturing of titanium components by directed energy deposition: microstructure and mechanical properties. *Appl Sci* 7. <https://doi.org/10.3390/app7090883>
96. Paul CP, Ganesh P, Mishra SK, Bhargava P, Negi J, Nath AK (2007) Investigating laser rapid manufacturing for Inconel-625 components. *Opt Laser Technol* 39:800–805. <https://doi.org/10.1016/j.optlastec.2006.01.008>
97. Xue L, Islam MU (2000) Free-form laser consolidation for producing metallurgically sound and functional components. *J Laser Appl* 12:160–165. <https://doi.org/10.2351/1.521927>
98. Chlebus E, Gruber K, Kuźnicka B, Kurzak J, Kurzynowski T (2015) Effect of heat treatment on the microstructure and mechanical properties of Inconel 718 processed by selective laser melting. *Mater Sci Eng A* 639:647–655. <https://doi.org/10.1016/j.msea.2015.05.035>

99. Dinda GP, Dasgupta AK, Mazumder J (2009) Laser aided direct metal deposition of Inconel 625 superalloy: Microstructural evolution and thermal stability. Mater Sci Eng A 509:98–104. <https://doi.org/10.1016/j.msea.2009.01.009>
100. Cited as Ref 28 in [85]. http://www.ascgenoa.com/main/newsletter/9/%5B2%5D6-07_AIAA_2007_2381-metal-Fatigue.pdf

Chapter 7

Corrosion Behavior of Alloy 625



Alloy 625 belongs to the Ni–Cr–Mo series of nickel alloys known for their excellent resistance against uniform corrosion, localized corrosion and stress-corrosion cracking in both oxidizing and reducing media. Ni–Cr–Mo alloys also provide exceptional resistance to chloride-induced localized corrosion and stress-corrosion cracking. The chromium content in these alloys may vary from about 15 to 25 wt% and molybdenum from about 8 to 17 wt%. The high concentration of molybdenum imparts excellent corrosion resistance in non-oxidizing (or reducing) media like hydrochloric and sulfuric acids, and chromium imparts corrosion resistance in oxidizing aqueous environments like nitric acid. Alloys with such a combination of alloying additions find their application in chemical and metal processing industries. Alloy 625 contains 20 to 23 wt% chromium and 8 to 10 wt% molybdenum along with about 3 to 4 wt% niobium. These elements give Alloy 625 excellent corrosion properties over a broad spectrum of corrosive chemical and gaseous environments. For instance, the alloy can be used for fabricating storage tanks for chemical wastes, including hydrochloric and nitric acids. The two acids represent reducing and oxidizing types of corrosion behavior, respectively, and material with good corrosion resistance against one usually corrodes severely against the other. This chapter describes, in brief, the corrosion behavior of Alloy 625 in different types of environments and compares it with other alloys. In the last section, a brief account of the corrosion behavior of Alloy 625 PLUS, a precipitation-hardened variant of Alloy 625 (Chap. 5), has also been included to give an idea that the precipitation of γ'' does not affect its corrosion behavior. However, the precipitation of the $\text{Ni}_2(\text{Cr}, \text{Mo})$ phase may affect the corrosion behavior, though no reports supporting such a claim are available.

Throughout the chapter, the compositions of various environments are mentioned in weight per cent (wt%) for liquids and volume per cent (vol%) for gases, unless specified otherwise.

7.1 The Basic Concepts of Corrosion

7.1.1 The Electrochemical Principle

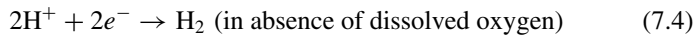
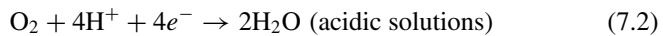
The chemical and electrochemical destruction of metals and alloys in the presence of reactive environments is termed corrosion. Corrosion of metals transforms them into “rust”, a term commonly used for iron corrosion products that predominantly contain oxides, hydroxides, and aqueous salts. During corrosion, an electrolytic cell sets up comprising [1]:

- (i) an anode that ionizes the metal to metal ions (cations) as per the oxidation reaction



which pass the ions into the solution, leaving their electrons within the original metal surface.

- (ii) a cathode that consumes the free electrons within the metal by reducing O₂ and H₂O as per following reduction reactions



- (iii) a conductive liquid that acts as an electrolyte through which positively charged cations are transferred to the cathode and negatively charged anions (OH⁻) to anode simultaneously,
- (iv) a metallic path, which completes the electrical circuit between the two electrodes to migrate electrons from anode to cathode.

Figure 7.1 shows a schematic diagram of a typical electrochemical cell depicting the corrosion of a metal M immersed in water. The anodic and cathodic reactions proceed in balance to maintain the overall electrical neutrality of the system. For instance, in an iron alloy, two hydrogen ions are reduced for oxidation (corrosion) of every iron atom ($Fe \rightarrow Fe^{+2} + 2e^-$, $2H^+ + 2e^- \rightarrow H_2$). In the presence of dissolved oxygen in water, the cathodic reaction reduces oxygen to produce hydroxide ions as per Eq. 7.3. This reaction corrodes more rapidly as it only involves oxygen diffusion to cathodic areas. Therefore, an increase in dissolved oxygen increases the corrosion rate.

Metallic materials have varying tendencies to oxidize depending upon their oxidizing potential. An electrochemical series rank the relative corroding tendencies

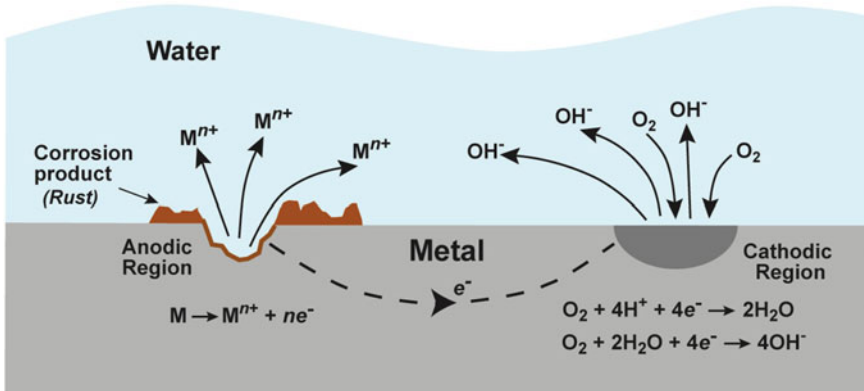


Fig. 7.1 A schematic diagram of a typical electrochemical cell formed during the corrosion of a metal M immersed in water

of metals and alloys based on their oxidation potentials [1]. Metals/alloys with more positive potential placed higher on the noble side, gold being the noblest. The driving force for the corrosion reaction is the difference between the oxidation potentials of anode and cathode, and the cathodic reaction controls the rate of corrosion. Anode and cathode are set up based on relative oxidation potential of regions—a region with more positive oxidation potential becomes the cathode. In a bi-metallic joint, the inherent difference between the two metals decides the anode and cathode. In contrast, within a single piece of metal, local variation in the oxidation potential due to inherent factors like inclusions, chemistry, microscopic surface imperfections, or even exposure of different crystallographic planes create a potential difference within adjacent regions.

The corrosive medium is the most crucial factor that influences the rate of corrosion attack. The aggressiveness of a corrosive media is governed by factors like acidity, temperature, concentration, motion relative to the metal surface, degree of oxidizing power and aeration, and the presence of inhibitors or accelerators.

The corrosion media can be categorized as oxidizing or reducing in nature. The aqueous environments are usually oxidizing due to dissolved oxygen unless specifically treated for its removal. The cathodic reactions mainly reduce water to form hydroxyl ions (Eq. 7.3). On the other hand, acidic environments containing most dilute acids are reducing in nature and liberate hydrogen gas at the cathode as per Eq. 7.4 [1]. Likewise, chemical environments can be broadly categorized as oxidizing and reducing. A solution containing compounds like chromic acid, nitric acid, concentrated sulfuric acid and oxidizing salts such as ferric or cupric salts, nitrites, chromates, etc. form the oxidizing media. The cathodic reactions in oxidizing media reduce anions or high valence cations (e.g., ferric to ferrous). On the other hand, lowering chemicals like dilute halogen or other mineral acids and alkalis form the reducing media. In reducing environments, the cathodic reaction usually reduces hydrogen ions to generate the atomic hydrogen or gas.

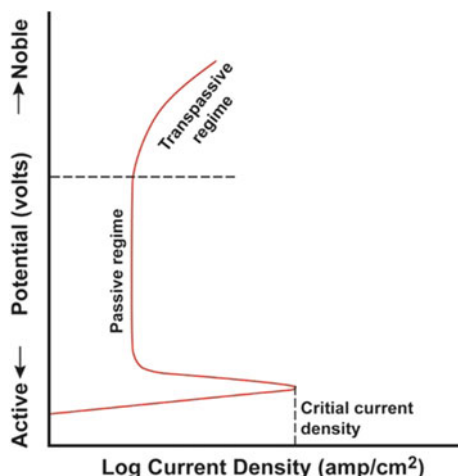
When the corrosion occurs uniformly over a metal surface, it is termed general or uniform corrosion. On the other hand, corrosion attacks can be very local or on specific features like the grain boundaries of the structure.

7.1.2 *Polarization and Passivity*

Nobel metals like gold and platinum have little susceptibility to oxidation due to their sizable positive oxidation potential. That is why they are found in nature in their pure metallic state. On the other hand, metals like zinc and iron are very active due to their negative oxidation potential and oxidize readily [1]. An increase in dissolved oxygen in a corrosive solution further increases the corrosion rate of an active metal (Eq. 7.3). However, at very high concentrations of dissolved oxygen, the corrosion rate may drop to a very low value because of the chemisorption of oxygen at the metal surface, which prevents it from further coming in contact with the electrolyte. This stabilizes the corrosion and reduces its rate to a very low value. Such a loss in chemical reactivity of metals and alloys under a particular environment is referred to as “Passivity”. Polarization refers to a shift in the potential away from the free corroding potential (termed as open circuit potential). A potential change in the “positive” direction is called “anodic polarization”. On the other hand, a potential change in the “negative” direction is termed “cathodic polarization”.

An S-shaped curve depicts the polarization behavior of a metal exhibiting a typical active–passive behavior (Fig. 7.2). The behavior of an alloy can be divided into three regions: active, passive and transpassive. As the oxidation potential of the anode (or the oxidizing power of the solution) increases toward noble, the current per unit area (or the corrosion rate) increases as the metal behaves identically to that of a normal metal until a critical current density is reached at which the maximum corrosion rate

Fig. 7.2 A schematic depicting the typical polarization behaviour of an active–passive metal



is observed. This region is termed as “active”. An increase in the potential further (i.e., oxidizing power of the solution) causes a corresponding fall in the corrosion rate by orders of magnitude as the protective passive film forms. This corresponds to the “passive” region, and the phenomenon is called passivation. Further increase in the oxidizing potential (power) produces little change in the corrosion rate of the material. But at very high values of the potential (concentrations of the oxidizers), the corrosion rate may again start increasing with an increase in the potential. This region is termed the “transpassive” region. Nickel, chromium, titanium, and zirconium spontaneously passivate in air. Alloying iron with chromium above 11 wt% Cr produces famously known passive stainless steel [1]. In nickel–chromium alloys, passivity arises due to the formation of a thin invisible protective film of a metal oxide or an insoluble salt.

7.1.3 *Corrosion Rate Expression*

The corrosion rate can be expressed in several ways. The most common is based on the rate of penetration inside the surface or the thinning of the structure, which is used to predict the life of corroding components assuming uniform corrosion. The most common expression is “mils per year (mpy)”, which can be measured as mass loss per unit area and time, as [1].

$$\text{mpy} = \frac{534W}{DAT} \quad (7.5)$$

where W is the weight loss (in mg), D is the density of the metal/alloy (in g/cm³), A is the area of the surface exposed to the environment (in square inch), and T is the time of exposure (in hours). Another similar expression is millimeters per annum (mm/a). Forty mpy equals about one mm/a. Throughout this chapter, the corrosion rate is expressed in mpy unless specified.

7.2 Role of Alloying Elements

Nickel-based alloys are designed to deal with the aggressive nature of the chemical industry. Nickel has a much higher tolerance for alloying additions in solid solution than iron or other Iron-based alloys with excellent metallurgical stability of its face-centered structure. These properties allow large amounts of alloying addition to tailor properties of alloys for a wide range of corrosive environments with little compromise in microstructure or mechanical properties required. Inherently, pure nickel is more stable and noble than iron in the electrochemical series [1]. It resists the corrosive nature of reducing acids, hydrofluoric acid and stress-corrosion cracking, particularly in chlorides and caustic environments. It forms a stable oxide in weak alkaline

solutions even at high anodic potentials but fails in acidic solutions. Other elements are added to form protective, stable oxides under acidic and oxidizing environments. From the corrosion perspective, the major alloying additions are chromium, copper, molybdenum, tungsten, niobium, and iron. Each element imparts resistance against a specific form of corrosion or media, in addition to their role in improving mechanical properties. The following gives a brief description of the role of alloying addition that contributes to the corrosion resistance of Alloy 625.

Chromium—Chromium provides resistance to the alloy in oxidizing environments and high-temperature oxidation and sulfidation by forming a layer of passive Cr_2O_3 film. However, this film cannot protect the alloy from pitting and crevice corrosion under harsh conditions and protects only in the presence of molybdenum. In oxidizing environments, a higher chromium content imparts a higher corrosion resistance, particularly at concentrations above 20 wt%. At high temperatures, the protective nature of the oxide film decreases due to an increase in its crystallinity.

Molybdenum—Chemically, molybdenum behaves similar to chromium but is less resistant against oxidizing solutions. It dissolves quickly by converting to its hexavalent species. However, its addition improves the resistance of the alloy in reducing media like hydrochloric acid and pitting and crevice corrosion in aqueous chloride-containing environments. In combination with chromium, it provides resistance in extremely versatile environments of both oxidizing and reducing chemicals. It improves the stability of the Cr_2O_3 film by protecting it by forming a Mo-rich outer layer of molybdate ions. Molybdate ions protect the film by inhibiting the initiation and propagation of localized corrosion and promoting re-passivation.

Iron—Iron does not play any significant role in the corrosion resistance of Alloy 625, except for its small contribution to the resistance to certain concentrated sulfuric and nitric acids and high-temperature carburizing environments.

Niobium—Niobium forms a stable pentavalent oxide, but its maximum concentration in Alloy 625 is too low to form a complete oxide layer. However, its addition helps in reducing the susceptibility of the alloy to intergranular corrosion as carbon prefers to combine with niobium to form more stable carbide particles. Likewise, it also improves the resistance to pitting and crevice corrosion.

Aluminum—Aluminum addition improves the resistance to oxidation at elevated temperatures.

Titanium—Titanium plays a role similar to niobium in enhancing corrosion resistance by combining with carbon to reduce the alloy's susceptibility to intergranular corrosion due to the precipitation of chromium carbide particles during heat treatments.

Nitrogen—Nitrogen improves pitting and crevice corrosion resistance, but it is usually restricted to a very low level of about less than 50 ppm due to its other attended effects.

Rare Earth elements—Sometimes, rare earth elements like yttrium, lanthanum and cerium are also added in very small quantities to improve high temperature and hot corrosion resistance.

7.3 General Corrosion

Several solution-dependent and material-dependent factors determine general or uniform corrosion in aqueous media. Solution-dependent factors like density, temperature, pH value, and electrochemical potential of the solution govern the aggressiveness of the corrosive media as they influence the solubility and dissociation of attacking anions and corrosion products. High values of both parameters favor ionic reactions and thus, accelerate the corrosion process. Material-dependent factors include parameters like alloy composition, surface condition, material purity, heat treatment, etc. which primarily influence corrosion initiation.

7.3.1 Hydrochloric Acid

Hydrochloric acid is a reducing acid across its entire concentration range. Its strongly acidic character and the harmful effect of chloride ions make it a severe corrosive medium. The presence of oxidizing contaminants (e.g., ferric or cupric ions) can drastically change the corrosive characteristics of hydrochloric acid. Alloy 625 has good resistance to dilute hydrochloric acid due to its 9 wt% molybdenum content. The general corrosion resistance of the alloy in hydrochloric acid is summarized in the iso-corrosion chart (Fig. 7.3) as a function of acid concentration at different temperatures [2]. Figure 7.4 compares 20 mpy iso-corrosion lines of Alloy 625 with other Ni–Cr–Mo alloys in the hydrochloric acid [2]. Alloys C-276 and 686

Fig. 7.3 Iso-corrosion lines depict the corrosion behaviour of Alloy 625 in hydrochloric acid as a function of temperature and acid concentration [2]

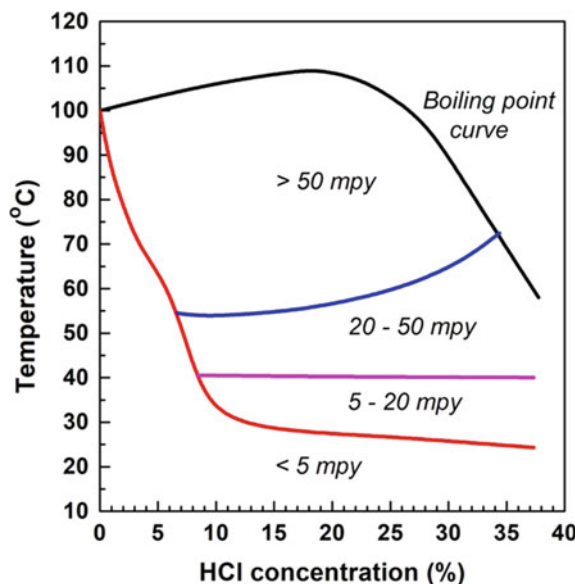


Fig. 7.4 A comparison of the corrosion behaviour of nickel–chromium alloys in hydrochloric acid as a function of temperature and acid concentration. The figure shows iso-corrosion lines corresponding to a corrosion rate of 20 mpy [2]

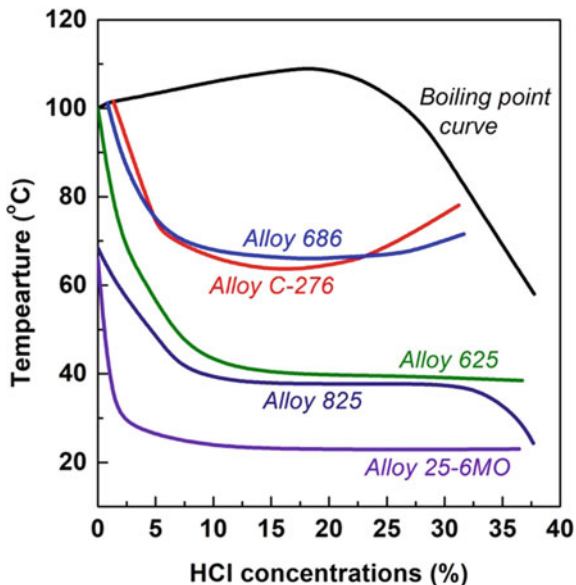


exhibit nearly similar resistance in hydrochloric acid due to similar molybdenum and tungsten contents. The two alloys exhibit corrosion resistance better than Alloy 625 due to higher molybdenum content and extra addition of tungsten, which also behaves in the same manner as molybdenum in improving corrosion resistance in reducing chemical solutions. Alloys like 825 and 25-6MO, on the other hand, exhibit low corrosion resistance. Adding the oxidizing species like Fe^{3+} ions may decrease the corrosion rate of the Alloy 625 [3].

7.3.2 Sulfuric Acid

Sulfuric acid has a dual nature. It behaves as reducing acid in dilute and intermediate concentrations, up to about 25 wt% [2]. At higher concentrations, it starts acting as oxidizing in nature. At concentrations above 87 wt%, a concentration most commonly encountered in a commercial product is strongly oxidizing in nature at room temperature [2]. The nature of the sulfuric acid may further vary depending upon aeration, temperature and nature of impurities present. With an increase in temperature, it becomes more oxidizing. Therefore, materials resistant to reducing media are preferred for sulfuric acid in dilute and intermediate concentrations, while materials resistant to oxidizing conditions are preferred for higher concentrations of sulfuric acid. Ni–Cr–Mo alloys like C-22, 625 and 686 show excellent resistance to sulfuric acid, particularly in a hot environment, due to their high molybdenum and chromium contents. Alloy 625 offers even better resistance due to the presence of

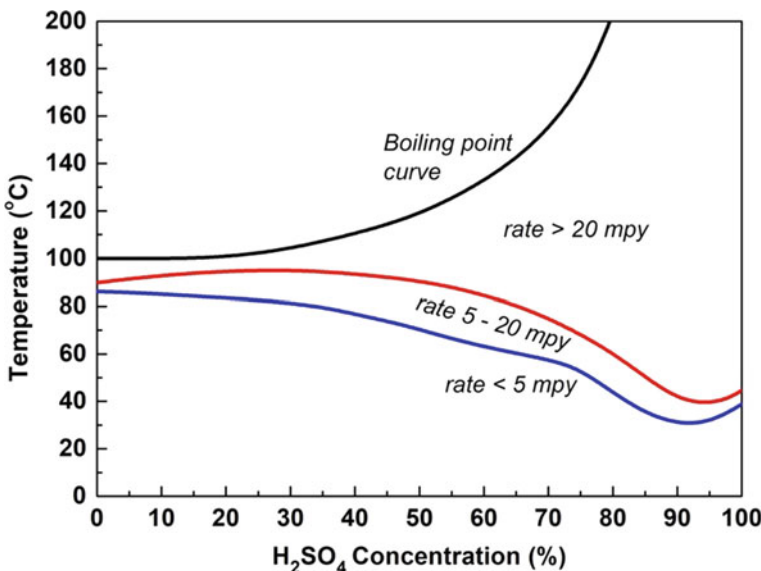


Fig. 7.5 Iso-corrosion lines depict the corrosion behaviour of Alloy 625 in sulphuric acid as a function of temperature and concentration [3]

niobium. Figure 7.5 shows the general corrosion behavior of Alloy 625 as a function of acid concentration and temperature [3]. Its corrosion resistance deteriorates at higher concentrations of the acid.

Figure 7.6 compares the 20 mpy iso-corrosion plots of C-276, 625, G-3, 825 and SS 316 alloys in sulfuric acid [2–4]. At lower concentrations, Alloy 625 shows resistance similar to that of Alloy C-276.

7.3.3 Nitric Acid

Nitric acid is strongly oxidizing in nature. Since the resistance to nitric acid is essentially due to the formation of a passive film on the surface, alloys with high chromium offer the best resistance in a nitric acid environment as they quickly form the passive Cr_2O_3 film. Among nickel-based superalloys, Alloy 690 exhibits the least corrosion rate of about 0.03 mpy (Fig. 7.7) [2] as it contains the highest chromium content (~30 wt%). The performance of Ni–Cr–Mo alloys in nitric acid is strongly related to their chromium content only. Therefore, Alloy 625 offers much better corrosion resistance than Alloy C-276 by virtue of the higher chromium concentration in Alloy 625. Therefore, alloys with higher chromium concentrations provide better resistance than those with lesser content. Iron addition in nickel alloys improves their resistance in the nitric acid, as demonstrated by the reduced corrosion rate of Alloy 825, which

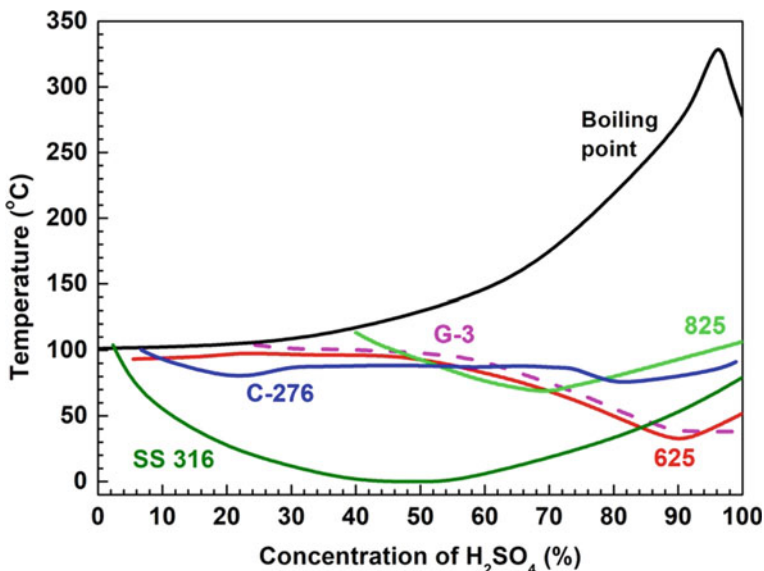
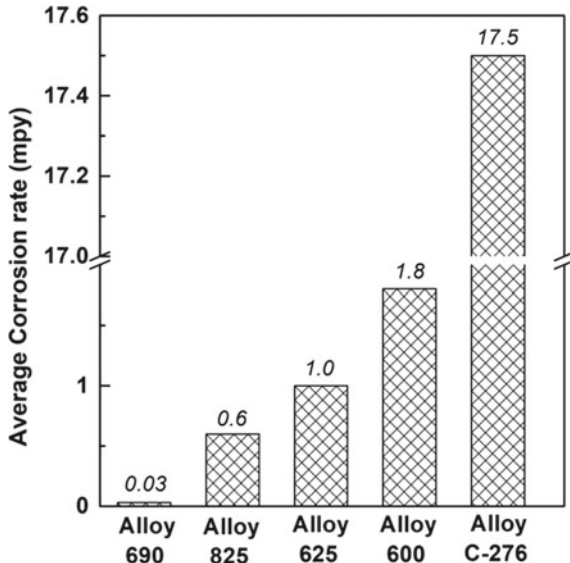


Fig. 7.6 Comparative corrosion behaviours of Alloy 625, C-276, 825, G-3 and 316 stainless steel corresponding to 20 mpy corrosion rate in sulphuric acid solutions as a function of concentration and temperature [3]

Fig. 7.7 Average corrosion rates of some nickel alloys in boiling 10% nitric acid solution [2]



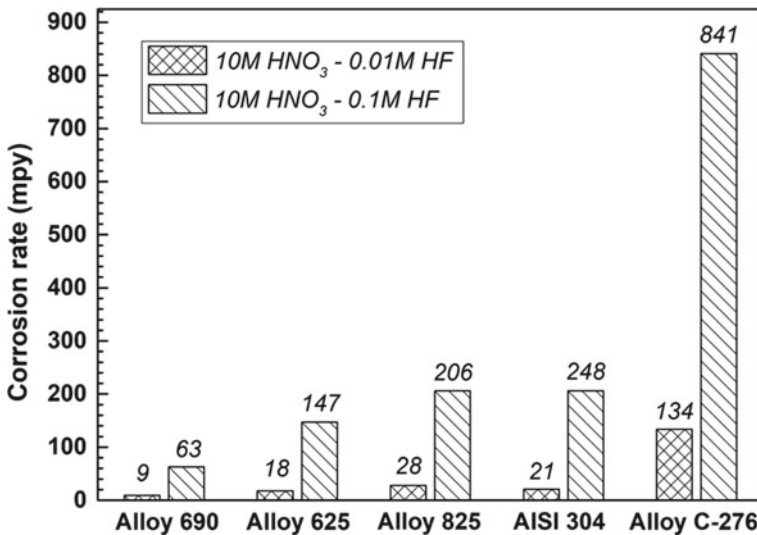


Fig. 7.8 A comparison of the corrosion rates of different high-performance alloys in $10\text{ M HNO}_3 - 0.01\text{ M HF}$ and $10\text{ M HNO}_3 - 0.1\text{ M HF}$ solutions [2]

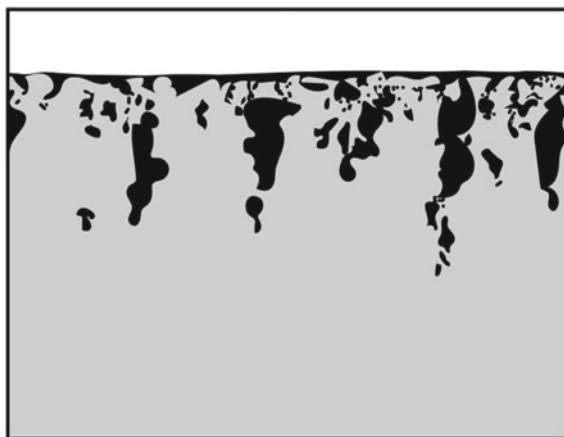
contained nearly identical chromium content as that in Alloy 625 (Fig. 7.7). In boiling 65% nitric acid, Alloy 625 exhibits a corrosion rate of about 30 mpy [2].

In general, stainless steels perform better than most nickel-base alloys in nitric acid. Nickel alloys are more effective in resisting corrosion in mixed acid media. The nickel alloys are typically used in nitric acid solutions that contain small amounts of chlorides or fluorides from other sources like hydrofluoric acid, chlorinated water, etc. For example, in a boiling 15% nitric acid solution containing 3% hydrofluoric acid solution, AISI 316 stainless steel corrodes at a rate of about 236 mpy, Alloy 625 corrodes at a rate of about 34 mpy [2]. Figure 7.8 shows a comparison of the corrosion behavior of Alloy 625 with other alloys in $10\text{ M HNO}_3 - 0.01\text{ M HF}$ and $10\text{ M HNO}_3 - 0.1\text{ M HF}$ solutions [2]. Alloy 625 exhibits much better corrosion resistance than iron-chromium and other Ni–Cr–Mo alloys.

7.3.4 Hydrofluoric Acid

Hydrofluoric acid is considered a reducing acid and chemically weaker than sulfuric or hydrochloric acid [5]. However, it is extremely corrosive and toxic in nature and hazardous to health than most acids. Further, unlike other acids, the hydrofluoric acid usually attacks in a non-uniform manner and mainly penetrates the metal surface in the form of thin cracks, pits, voids, trenches and sometimes on grain boundaries [5] as it readily dissolves the passive oxide films that protect against corrosion. Figure 7.9 schematically illustrates this behavior of the hydrofluoric acid. Standard

Fig. 7.9 The schematic illustrates the non-uniform attack and penetration of the hydrofluoric acid into the metal surface



acid-resistant materials, like titanium, zirconium, reactive metals, etc. or glass, are not suitable for resistance against hydrofluoric acid solutions. Non-metallic materials like polythene are the best. Among metals, only gold and platinum are entirely resistant to attack in aqueous hydrofluoric acid solutions.

Nickel alloys offer moderate corrosion resistance to hydrofluoric acid over many wet acid concentrations and temperatures. Chromium and copper additions in nickel alloys are beneficial for vapor phase applications, while the iron is detrimental. Monel 400 is among the few alloys that offer good corrosion resistance to aqueous hydrofluoric acid [2]. A comparison of the corrosion resistance of Alloy 625 with Monel 400 and some other nickel alloys in non-deaerated hydrofluoric acid is shown in Fig. 7.10 [6].

7.3.5 Phosphoric Acid

Pure phosphoric acid has no adequate oxidizing power and is not very aggressive. Industrial phosphoric acid, also known as wet-process acid, is made by reacting the phosphate rock with sulfuric acid and is quite oxidizing in nature and corrosive due to the presence of impurities like various metallic ions, unreacted sulfuric acid, fluorides and chlorides. The corrosivity of the wet process acid is not directly related to the concentration of the P_2O_5 compound because an increase in the concentration of the P_2O_5 compound decreases the concentration of impurities. The corrosivity of the wet process acid is maximum at a concentration between about 42 and 54 wt% of P_2O_5 [5]. The most commonly used nickel alloys for aggressive and hot phosphoric acid environments are G-30, 625, C-22, C-276 and 686 alloys. Figure 7.11 shows the corrosion rate of Alloy 625 as a function of temperature in 42 wt% wet-process phosphoric acids compared to some other nickel alloys [5]. These alloys owe their excellent corrosion resistance in the phosphoric acid to their high chromium and

Fig. 7.10 A comparison of the 20 mpy iso-corrosion curves for different nickel-based superalloys and 316L stainless steel in hydrofluoric acid solution [6]

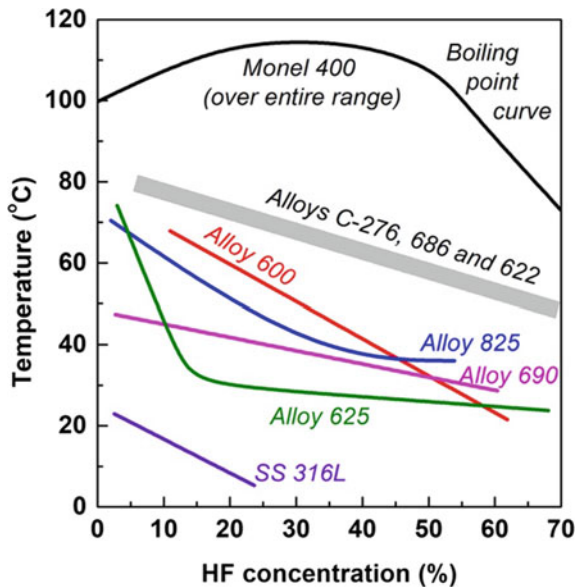
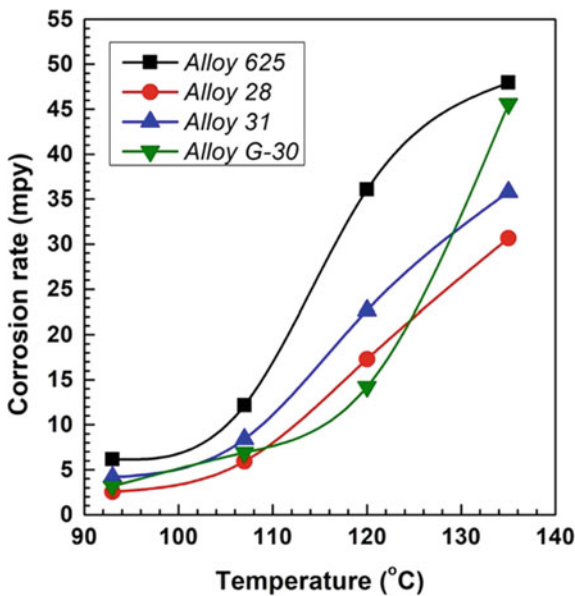


Fig. 7.11 Variation in the corrosion rate with temperature in 42% wet-process phosphoric acid [5]



molybdenum contents and the small amounts of niobium or tungsten additions. In a solution of 25 wt% phosphoric and 2 wt% hydrofluoric acids, at boiling temperature, Alloy 625 corroded at a rate of about 2 mpy in a 48 h test [2]. More extended tests in different concentrations of evaporating wet-process phosphoric acid, containing various acid impurities, showed very low rates and no localized attack [2]. Alloy 625 is generally used for 70 wt% wet phosphoric acids [5].

7.3.6 Organic Acids

Organic acids are less corrosive than inorganic acids because they do not ionize easily [7] though aeration and temperature may increase their corrosivity. Acetic, formic, propionic, butyric, and sulphonic acids are among the important organic acids. With a few exceptions, organic acids are weak and non-oxidizing. Alloy 625 has excellent resistance to organic acids. In boiling acid solutions, Alloy 625 exhibits corrosion rates of < 1 mpy in glacial acetic, ~ 4 mpy in 1:1 acetic-acetic anhydride solution, ~ 1 mpy in 10% acetic + 2% formic solution, 3 mpy in 5% formic acid solution [2]. The relative corrosion behavior of Alloy 625 in 40% and 88% formic acid solutions, compared to some other similar alloy, is shown in Fig. 7.12 [5]. It exhibits the highest corrosion rate of about 9.1 mpy in 40% boiling methane sulphonic acid. However, the corrosion rate of Alloy 625 is much lower than the corrosion rates of other similar alloys (Table 7.1) [4].

Fig. 7.12 Corrosion behaviour of alloys 625, C-276 and 825 in 40 and 88 wt% boiling formic acid [5]

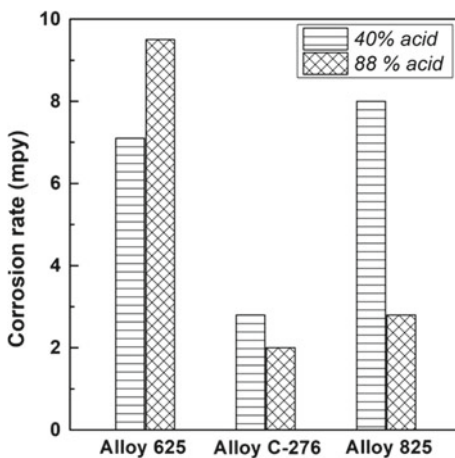


Table 7.1 Corrosion rates of different Ni–Cr–Mo alloys in methane sulphonic acid environments (all concentrations are in wt%) [4]

Acid condition	Corrosion rate of alloys (mpy)			
	Alloy 625	Alloy C-22	Alloy C-2000	Alloy G-30
20% boiling	5.5	36	23	30
40% at 93 °C	4.0	< 0.4	< 0.4	< 0.4
40% boiling	9.1	80.4	32	33
70% at 79 °C	0.4	< 0.4	< 0.4	< 0.4

7.3.7 Salts

Corrosion in salt solutions is more pronounced than in pure water because the salt's dissolution in water increases its conductivity. Salts can be broadly categorized into two categories, namely, halides and non-halides, each of which is further classified into different categories based on the nature of their solutions (Table 7.2). Halide salts are very damaging because of their insidious and unpredictable nature, leading to premature failure of components. Chlorides are most common among the halide salts and promote stress-corrosion cracking, pitting and crevice attack. Fluoride salts are less common but more harmful to reactive metals like titanium, zirconium, niobium, etc. Figure 7.13 shows the effect of different sodium halides at 50 °C on the re-passivation potential of Alloy 625 and other Ni–Cr–Mo alloys [5]. The re-passivation potential directly measures the localized corrosion resistance, and a higher value of the re-passivation potential means more resistance. The strong effect of sodium chloride on the resistance of Ni–Cr–Mo alloys to localized corrosion is reflected in a significant change in their re-passivation potential with a change in the alloy composition. In contrast, minimal change in the re-passivation potential occurs in sodium iodide or fluoride solutions (Fig. 7.13). Higher values of the re-passivation potential for alloys containing higher chromium and molybdenum signify their benefits against localized corrosion in sodium chloride solutions.

High contents of molybdenum and chromium in Alloy 625 makes it very resistant to pitting and crevice corrosion in all classes of salts. The addition of niobium along with chromium and molybdenum in the alloy gives it an excellent resistance to stress-corrosion cracking and intergranular corrosion in aqueous salt solutions at high temperatures. For example, a U-bent Alloy 625 specimen, subjected to 45% magnesium chloride solution for various exposure periods, does not show evidence of cracking [2]. Alloy 625 exhibits corrosion rates less than 4 mpy across multiple salt environments at temperatures up to 235 °C for durations up to 200 h [2].

Table 7.2 Classification of salts based on the corrosive nature of their solutions [2]

Nature	Halide	Non-halide
Neutral	Sodium-chloride Potassium-chloride	Sodium-sulfate Potassium-sulfate
Neutral and Alkaline-oxidizing	Sodium-hypochlorite Calcium-hypochlorite	Sodium-nitrate Sodium-nitrite Potassium-permanganate
Acid	Magnesium-chloride	Potassium-bisulphate Ammonium-sulphate Aluminum-sulfate
Acid-oxidizing	Cupric-, ferric-, mercuric-, stannic-chloride	Cupric-, ferric-, mercuric-nitrate or sulfate
Alkaline	Potassium fluoride	Sodium- and potassium-phosphates and carbonates
Nature	Halide	Non-halide
Neutral	Sodium-chloride Potassium-chloride	Sodium-sulfate Potassium-sulfate
Neutral and Alkaline-oxidizing	Sodium-hypochlorite Calcium-hypochlorite	Sodium-nitrate Sodium-nitrite Potassium-permanganate
Acid	Magnesium-chloride	Potassium-bisulphate Ammonium-sulphate Aluminum-sulfate
Acid-oxidizing	Cupric-, ferric-, mercuric-, stannic-chloride	Cupric-, ferric-, mercuric-nitrate or sulfate
Alkaline	Potassium fluoride	Sodium- and potassium-phosphates and carbonates

7.3.8 Seawater

Seawater contains a vast amount of chlorine which makes passive metals prone to general and localized corrosion. Alloy 625 is one of the best alloys for applications in seawater or marine environments owing again to its high chromium and molybdenum contents. It is placed very close to noble metals compared to most other alloys in the seawater galvanic series (Fig. 7.14) [2, 8, 9]. It behaves mainly as a cathode when in contact with other materials in seawater. Under stagnant and flowing conditions, it shows extremely low (negligible) weight loss in seawater [2]. Its high chromium and molybdenum content also give it excellent resistance against pitting corrosion, crevice corrosion and stress corrosion cracking. Figure 7.15 compares the corrosion fatigue strength of Alloy 625 with other alloys in seawater. Alloy 625 and its low cycle fatigue (LCF) variant (Alloy 625LCF) both exhibit excellent corrosion fatigue strength in seawater (Fig. 7.15) [10]. The two variants have the same chemical composition and mechanical properties. Still, the LCF variant has better cyclic and thermal fatigue properties due to a tighter control of the trace elements like carbon, silicon,

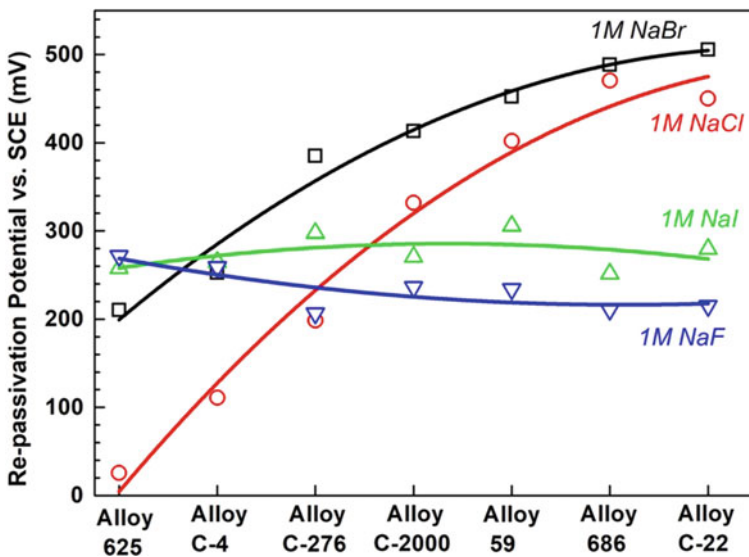


Fig. 7.13 Re-passivation potentials for different Ni–Cr–Mo alloys in 1 M solution each of NaF, NaI, NaCl and NaBr (Cyclic potential at 50 °C and 0.5 mV/s) [4]

and nitrogen during manufacturing of the alloy. The corrosion fatigue strength is an essential parameter for metals subjected to cyclic stress in corrosive environments as the joint action of corrosion and fatigue greatly intensifies the damage.

7.3.9 Alkaline Solutions

Alkaline environments refer to environments with a pH > 7.0. These environments are basic in nature due to the presence of alkali components and are less corrosive than acidic environments. However, alkaline environments can be very corrosive in the presence of dissolved oxygen. A higher amount of chromium in alloys for alkaline solutions is always beneficial. In alkaline environments, corrosion may often cause pitting and other localized attacks when the attack is concentrated at susceptible anodic areas. Increasing the nickel amount generally improves the resistance to attack in alkaline solutions. The most commonly used nickel alloys for alkaline solutions are Nickel 200, Alloy 400, Alloy 600 and Alloy 625. All these alloys show corrosion rates of < 1 mpy in boiling 50% caustic (NaOH) solution when tested at 720 h [2]. However, oxidizing species may cause preferential de-alloying of molybdenum in Ni–Cr–Mo alloys [11, 12]. Figure 7.16 shows the general corrosion rates of some nickel-alloys in electrolyte solutions of pure sodium hydroxide (NaOH) and 50% caustic soda contaminated with 500 ppm ferric ions (Fe^{3+}), 1% sodium hypochlorite (NaOCl) and 1% sodium chlorate (NaClO₃) [13] oxidizing species. Nickel 200 exhibited

Fig. 7.14 Galvanic series of high-performance alloys in seawater [2]

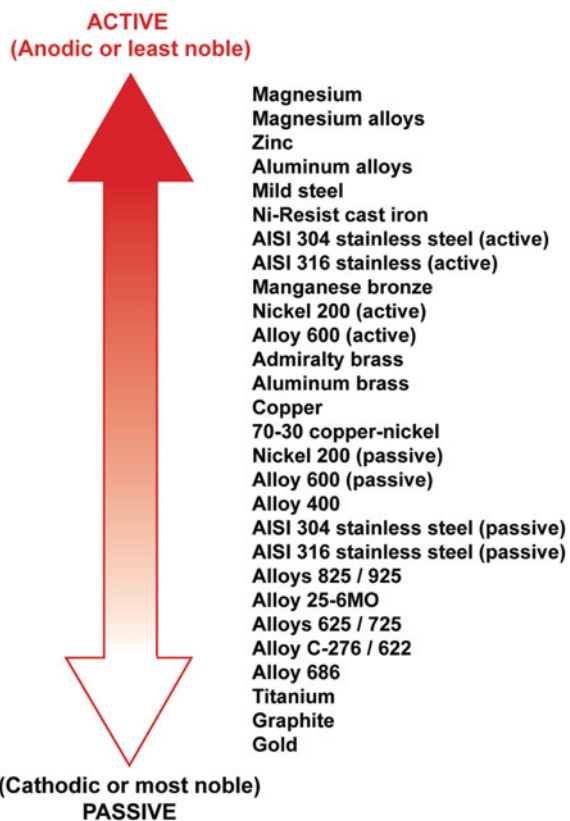
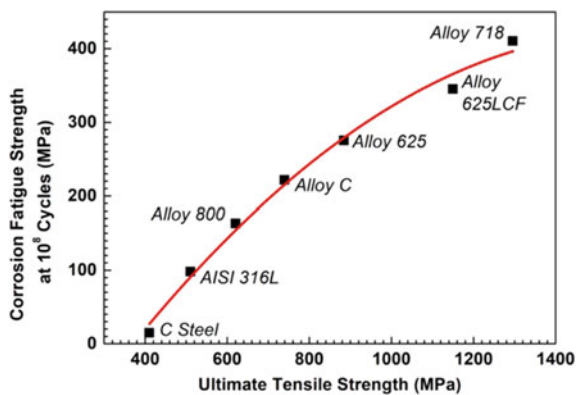


Fig. 7.15 Variation in the corrosion fatigue strength with ultimate tensile strengths of alloys in seawater [2]



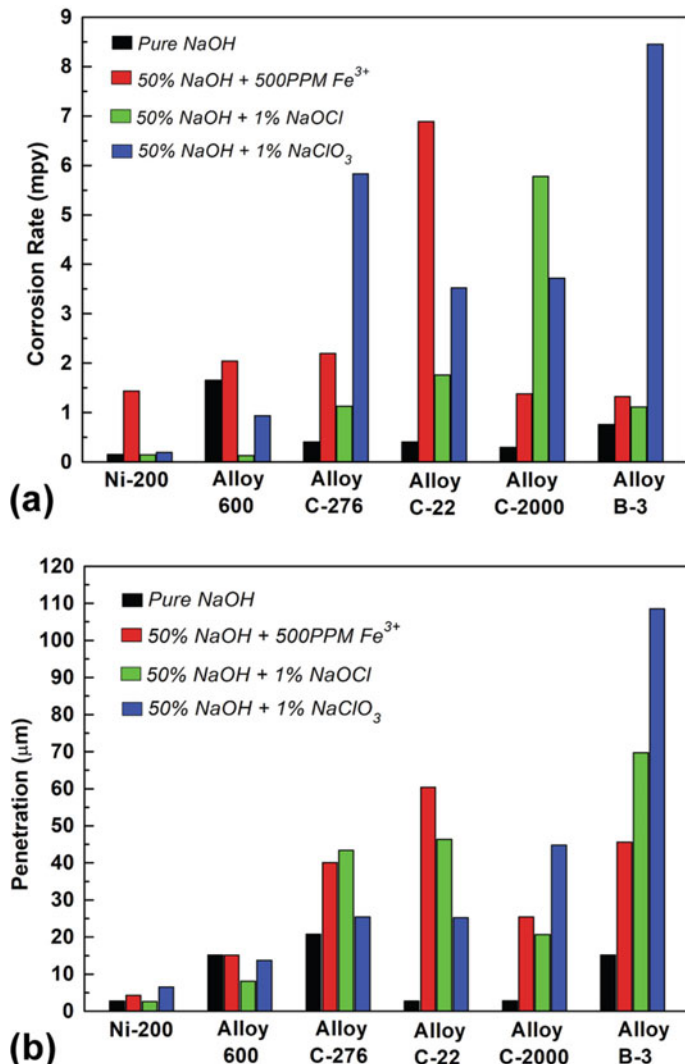


Fig. 7.16 **a** General corrosion and **b** internal damage as crack or dealloying in some Ni-alloys in electrolyte solutions of pure NaOH and 50% caustic soda contaminated with oxidizing species such as 500 ppm ferric ions (Fe^{3+}), 1% sodium hypochlorite (NaOCl) and 1% sodium chlorate (NaClO₃) [13]. The alloys containing high Mo exhibited the highest corrosion rate in contaminated electrolytes

the lowest corrosion rate among the tested alloys, and the B-3 alloy exhibited the highest. In general, alloys containing a high amount of molybdenum suffered high corrosion rates due to its de-alloying [12, 14]. The corrosion damage was due to internal penetration of the media. For the Nickel 200 alloy, the internal penetration was restricted mainly to surface roughening, while in molybdenum-containing alloys (C-276, 22, B-3), it caused de-alloying and some intergranular attacks [13]. In Alloy 600, the internal penetration resulted in surface roughening, cracks, fissures and intergranular attack. The depth of internal attack increased with the temperature [13]. The sub-surface microstructure of molybdenum de-alloyed alloys typically shows a spongy nickel layer of the leftover de-alloyed alloy matrix, covered by an outer layer of pure nickel formed as a result of the re-precipitation of the previously dissolved nickel [13]. Potassium hydroxide is reportedly less aggressive than sodium hydroxide concerning de-alloying [11].

7.4 Localized Corrosion

Localized corrosion is an accelerated attack at discrete sites when the anodic areas on a metal surface remain stationary, rather than mobile, under certain conditions. The metal at the localized sites corrodes much faster than the rest of the metal surface. Once initiated, the attack is stabilized by the development of localized aggressive conditions resulting from metal cation hydrolysis and chloride migration. The localized attack is insidious as it may fail the component prematurely without any warning. Typical forms of localized corrosion include pitting on an exposed non-corroding surface and corrosion in a creviced region shielded from the bulk environment. An exciting form of localized corrosion is microbially induced corrosion (MIC), of both pitting and crevice type. MIC is caused by bacteria of various types that live and multiply in standing water at places like pits, grain boundaries, weld undercuts, inside walls of pipes and tubing and other metallic structures. Ni–Cr–Mo alloys are generally immune to the microbially induced corrosion attack.

Alloys containing chromium and molybdenum are usually more resistant to localized corrosion. The relative resistance of an alloy against localized corrosion can be measured based on parameters like pitting resistance equivalency number (PREN), critical pitting temperature (CPT) and critical crevice temperature (CCT). PRENs for nickel- and iron-based superalloys are empirically calculated based on their molybdenum, chromium, tungsten, niobium and nitrogen concentrations (in wt%) as [2]:

$$\text{PREN} = \% \text{Cr} + 1.5 (\% \text{Mo} + \% \text{W} + \% \text{Nb}) + 30 (\% \text{N}) \quad (7.6)$$

A higher value of PREN is indicative of superior resistance of the alloy to localized corrosion, though alloys having similar values may differ considerably in actual service. Table 7.3 compares the PREN of Alloy 625 with some similar corrosion-

Table 7.3 Pitting resistance equivalency number (PREN), critical pitting temperature (CPT) and critical crevice temperature (CCT) of Alloy 625 and some other corrosion-resistant alloys

Alloy	Composition (wt%)						PREN	CPT (°C)	CCT (°C)
	Ni	Cr	Mo	W	Nb	N			
316 stainless steel	12	17	2.2	—	—	—	20.4	20	< 0
Alloy 825	42	21.5	3	—	—	—	26.0	30	5
Alloy 25-6MO	25	20	6.5	—	—	0.20	35.8	70	30
Alloy 625	62	22	9	—	3.5	—	40.8	> 85	35
Alloy C-276	58	16	16	3.5	—	—	45.2	> 85	45
Alloy C-22	60	20.5	14	3.5	—	—	46.8	> 85	> 85
Alloy 686	58	20.5	16.3	3.5	—	—	50.8	> 85	> 85

PRENs are estimated using Eq. 7.6. CPT and CCT were determined by ASTM G-48 standard tests, methods C and D, respectively [2]

resistant superalloys. All nickel alloys with a PREN greater than 40 are resistant to crevice corrosion in seawater. Alloy 625 has a PREN value of about 40.8.

The critical pitting/crevice temperature refers to the temperature above which pitting/crevice for an alloy occurs in a specific environment. The higher the CPT or CCT, the more resistant the alloy is to pitting or crevice corrosion.

7.4.1 Pitting Corrosion

Pitting corrosion occurs when the passive film breaks down locally in corrosive environments, making the localized sites anodic. The locally exposed metal corrodes much faster than the rest of the surface. When this occurs, corrosion takes the form of pits rather than uniform thinning. Although pitting can occur for various reasons, like a local variation in concentration or defects, certain chemicals such as chloride salts are known to promote pitting. The passive metals are particularly susceptible to pitting in chloride environments. The accumulation of chloride ions dissolves the passive film locally, resulting in pit formation. The pit initiation events are relatively scarce and stochastic in nature. The exact time and location of the passive film breakdown cannot be predicted. Once pits are initiated, they grow very fast because of the continuous change in the local chemistry that moves the interface rapidly.

The pitting corrosion occurs at temperatures above a critical pitting temperature, which depends on material factors like alloy composition, impurities concentrations, surface condition, and solution chemistry, such as chloride ion concentration, pH value, and electrochemical potential. The oxidizing chlorides (e.g., FeCl_3 , CuCl_3 , etc.) are the most aggressive pitting agents. The non-oxidizing chlorides (e.g., NaCl) reduces oxygen at the cathode.

Pitting is an autocatalytic process in which the corrosion products promote further corrosion reactions [1]. Figure 7.17 illustrates the autocatalytic nature of a pit in an

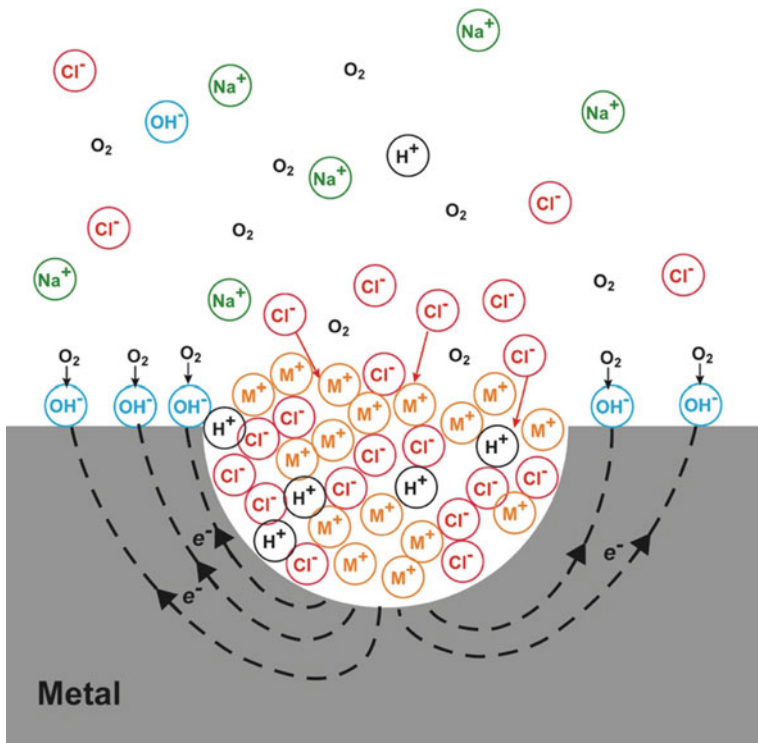


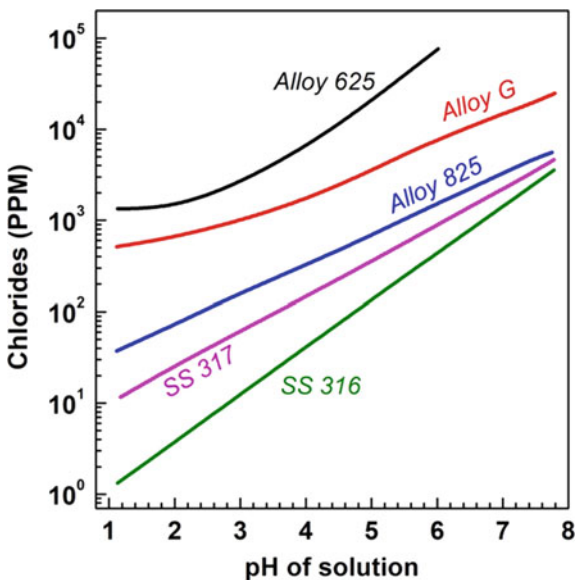
Fig. 7.17 The autocatalytic mechanism of pitting corrosion

oxygenated NaCl electrolyte. The pit is the anode, and the metal surface is the cathode. The production of positive metal ions in the pit gives a local excess of positive charge, which attracts the negative chloride ions from the electrolyte to maintain neutrality and produce neutral MCl molecules resulting in increased MCl concentration. “M” refers to metal in MCl. MCl hydrolyzes in water and forms insoluble MOH and free acid (H^+ and Cl^-). Both H^+ and Cl^- ions accelerate metal dissolution. Increased dissolution increases Cl^- ion migration making the process self-stimulating and self-propagating (Fig. 7.17).

Alloy 625 possesses excellent resistance against localized corrosion in sulfur dioxide scrubbing environments containing ppm levels of chloride ions. Figure 7.18 shows the resistance of Alloy 625 to localized corrosion as a function of the pH level of the sulfur dioxide containing part-per-million (ppm) levels of chloride ions [15]. The areas below the line for each alloy represent the combination of pH and chloride ion content below which severe pitting is not observed. Alloy 625 possesses the pitting corrosion resistance much superior to many other alloys.

The critical pitting temperature (CPT) of an alloy depends upon the service environment and conditions. It can be determined experimentally using ASTM Standard Test Method G-48, Method C. In this method, the alloy is immersed in a standard

Fig. 7.18 The resistance of Alloy 625 to localized corrosion as a function of the pH level of the sulphur dioxide containing ppm levels of chloride ions [15]



acidic 6 wt% ferric chloride solution at a set temperature for test durations from 24 to 72 h. The test temperature is raised incrementally until the onset of pitting. New and unexposed samples are exposed in new test solutions at each test temperature. Table 7.3 compares the CPT of Alloy 625 with some other alloys. A significantly improved CPT of nickel alloys compared to iron-base alloys, stainless steels, and nickel alloys containing higher molybdenum can be noticed. Thus, Alloy 625 is more resistant to pitting than Alloy 825 or AISI 316 stainless steel.

7.4.2 Crevice Corrosion

Crevice corrosion is another form of localized attack and, as the name implies, occurs within crevices formed in between overlapping sections of metallic or non-metallic structures. Like pitting corrosion, it is also hard to detect by exterior examination. It occurs due to the formation of differential ion concentration or oxygen cells. Halide salts promote both mechanisms. Initially, corrosion reaction occurs uniformly over the entire surface, including the interior of a crevice. Every electron generated during the formation of metal ions is consumed by the oxygen reduction reaction (Eq. 7.3) and produces one hydroxyl ion in the solution to maintain charge neutrality. However, the oxygen in the crevice is depleted after some time because of restricted convection, which becomes more pronounced with time. No further oxygen is available after finishing oxygen, although the metal dissolution continues as Eq. 7.1 [1]. The continued dissolution produces an excess of positive charge, balanced by the migration of chloride ions into the crevice. This results in an increased concentration

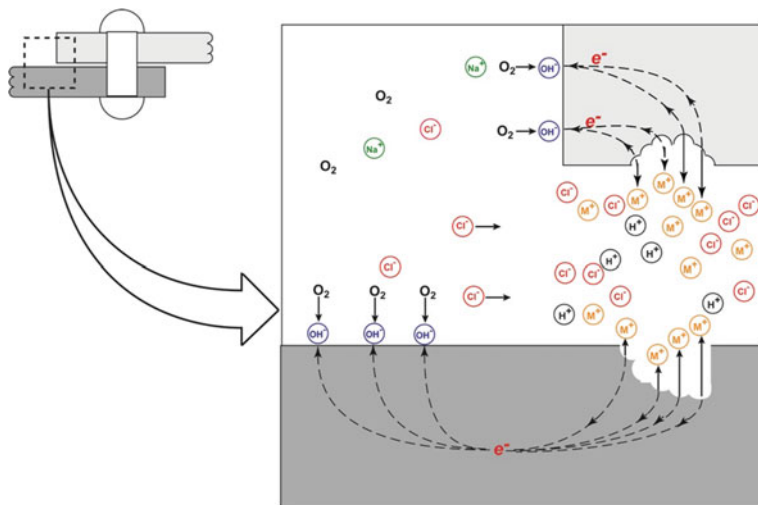
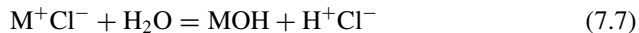


Fig. 7.19 A schematic drawing illustrating the autocatalytic nature of crevice corrosion [1]

of chloride ions within the crevice. Hydroxyl ions also migrate, but they are less mobile than chloride ions and migrate slowly. Metal salts hydrolyze in water to form insoluble hydroxide and free acid, according to the reaction



Both chloride and hydrogen ions increase the metal dissolution rate within the crevice. This makes the crevice corrosion an autocatalytic reaction. A schematic representation of the crevice corrosion is shown in Fig. 7.19.

Molybdenum plays a vital role in resistance against crevice corrosion. Even highly corrosion-resistant alloys without molybdenum may incur crevice corrosion. For example, Alloy 690 containing about 29% chromium has an excellent resistance against chloride stress-corrosion cracking owing to its high chromium contents. Still, it exhibits crevice corrosion in coastal zones over prolonged periods [16]. Alloy 625 containing molybdenum provides a better resistance against crevice despite its chromium concentration being less than Alloy 690. Nonetheless, Alloy 625 is not entirely immune to the crevice attack. For example, Alloy 625 tubes suffered crevice corrosion under vinyl hoses secured with serrated nylon hose clamps as part of a flow loop containing chlorinated seawater [17]. This behavior has been attributed to adding extra chlorine to the seawater, which raised the alloy's potential to the point that crevice corrosion initiated.

Like, CPT for pitting corrosion, critical crevice temperature (CCT) for an alloy is determined by conducting a test as per ASTM Standard Test Method G-48, Method D. This test is similar to the Method G-48, Method C test for the CPT. It uses a

multiple crevice device (TFE-fluorocarbon washer) attached to the surface of the specimen. Table 7.3 also gives the CCT of Alloy 625 with other alloys.

7.4.3 Intergranular Corrosion

Intergranular corrosion (IGC) is a localized attack along the grain boundaries of a metal or alloy. Corrosion can proceed to the point where whole metal grains fall away, and the metal loses its strength and metallic characteristics. A schematic representing the IGC attack is shown in Fig. 7.20. Intergranular corrosion is usually caused by improper heat treatment or in the heat-affected welding zones when chromium carbide particles precipitate along grain boundaries. The precipitation of grain boundary carbides creates chromium depleted zones in the vicinity of boundaries (Fig. 7.20a). This phenomenon is commonly known as sensitization. For instance, heating of an 18–8 stainless steel (AISI 304 grade) at temperatures between about 425 and 750 °C causes the precipitation of chromium carbide at the grain boundaries, which depletes chromium from the matrix in the vicinity of grain boundaries [1]. This makes the chromium depleted area anodic with respect to the rest of the grain. Sensitization of an alloy makes it susceptible to intergranular attack and may cause failure along grain boundaries (Fig. 7.20b).

Alloy 625 is stabilized against intergranular attack by tying up the carbon with niobium as niobium carbide, making it less available to precipitate as chromium carbides at grain boundaries. However, the alloy may become susceptible to intergranular attack due to improper annealing treatments that inhibit the formation of niobium carbides, leaving carbon available for precipitation as chromium carbides

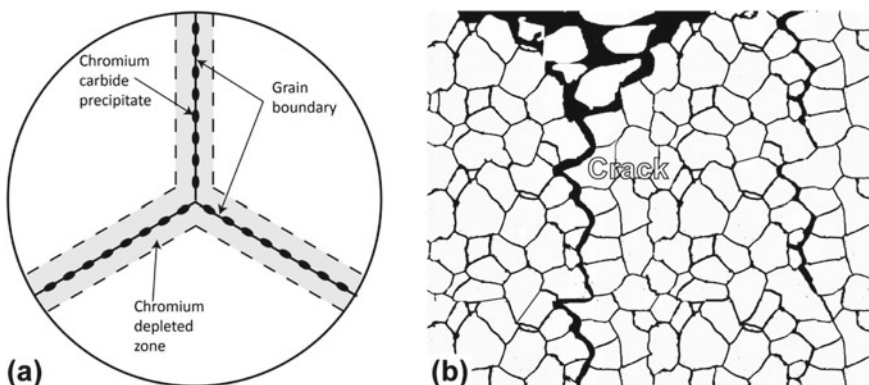
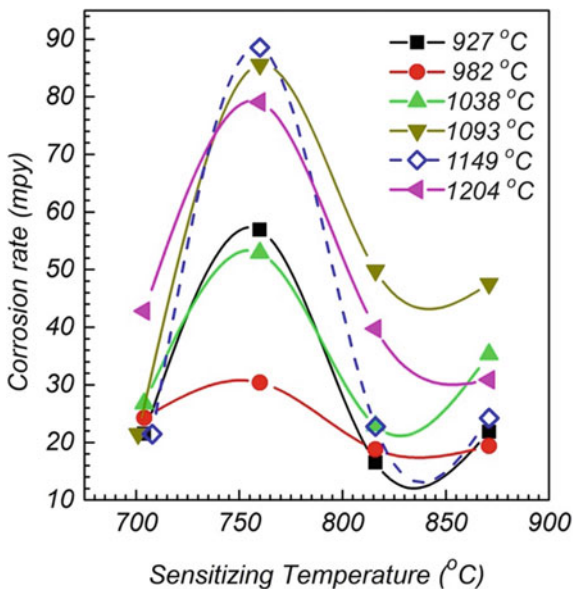


Fig. 7.20 Schematic drawings depict inter-granular corrosion of a metal. **a** Sensitization of the metal due to the formation of chromium depleted zone along grain boundaries. **b** Intergranular failure of the metal along weakened grain boundaries

Fig. 7.21 The corrosion behaviour of sensitized Alloy 625 in boiling 65% nitric acid after 1 h. Alloy samples were first subjected to annealing treatments at a temperature between 925 and 1050 °C, followed by sensitization treatments at temperatures between 700 and 875 °C [18]



by a subsequent heat treatment in the temperature range over 650–816 °C. Solution annealing increases the alloy's susceptibility to sensitization in this temperature range. Figure 7.21 shows the intergranular corrosion behavior of Alloy 625 due to sensitized grain boundaries [18]. Alloy samples were annealed at temperatures between 925 and 1205 °C for 1 h and water quenched. Samples were then subjected to sensitizing heat treatments at temperatures 704, 760, 816 and 871 °C for 1 h to precipitate out chromium carbides precipitates along grain boundaries, followed by air cooling. Annealed and sensitized samples were subjected to boiling 65% nitric acid as per the standard ASTM A262 test. The alloy exhibited the maximum sensitization at 760 °C for all the samples annealed in the range 1093–1204 °C as they displayed the highest corrosion rate. Samples annealed at 982 °C showed the lowest corrosion rate, followed by sample annealed at 927 °C. Low corrosion rates at temperatures less than 1050 °C were due to the precipitation of MC and M₆C carbides that contain niobium and molybdenum predominantly. During annealing at 927 and 982 °C temperatures, the MC and M₆C carbides bound the free carbon with niobium and molybdenum, leaving little carbon for chromium to interact during the subsequent sensitizing heat treatment at temperatures in the range 704–871 °C. As a result, little or no precipitation of chromium carbides occurred at grain boundaries during the sensitization treatment. A comparatively higher corrosion rate of the alloy annealed at 927 °C compared to that annealed at 982 °C could be attributed to the precipitation of higher volume fractions of the MC and M₆C carbides in the latter owing to the faster precipitation kinetics at this temperature (see, Fig. 3.20 in Chap. 3). When the alloy is annealed at temperatures above the solution annealing temperature, carbides particles dispersed throughout the matrix dissolve leaving free carbon in the matrix. When such

solutions are exposed to sensitization temperatures, chromium-containing carbide precipitates preferentially along grain boundaries. Formation of the grain carbides results in continuous chromium depleted zones along grain boundaries which are susceptible to attack by oxidizing media.

7.5 Corrosion in High Temperature Pressurized Waters

The high-temperature water is described as (i) steam, when $T < T_c$ (sometimes may be above T_c also) and $p < p_{\text{Saturation}}$; (ii) subcritical water, when $T < T_c$ and $p > p_{\text{Saturation}}$ (sometimes may be above p_c also) (iii) supercritical water, when $T > T_c$; $p > p_c$, where T_c ($= 374^\circ\text{C}$) and p_c ($= 22.05 \text{ MPa}$) are critical temperature and pressure of the water above which it becomes supercritical [19–21]. Supercritical water is also described as a dense gas. Its density is between the liquid and gaseous states of the water and is characterized by high diffusivity and good heat-transporting properties.

The physical properties of pressurized high-temperature water vary significantly with temperature and pressure [22]. The density and ionic product of the high-temperature water drop drastically in the vicinity of T_c (Fig. 7.22). With increased pressure, this drop shifts toward a higher temperature with a reduced magnitude.

The solvent character of the high-temperature water may vary from highly polar at high densities to nearly non-polar at low densities. The low-density water suppresses

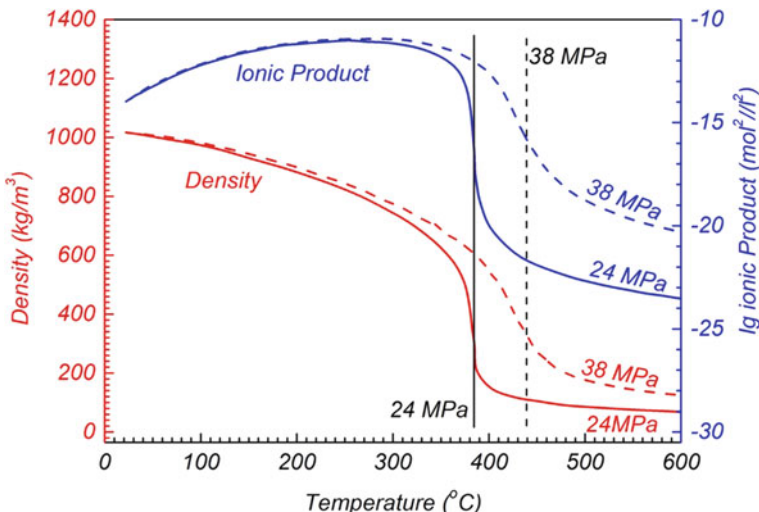


Fig. 7.22 Variation in density and ionic product of water as a function of temperature at different pressures. The two properties drop drastically in the vicinity of the critical temperature, T_c . The drop shifts towards higher temperatures at higher pressures [22]

ionic reactions and favors radical reactions. Steam and low-density supercritical water thus behave like non-polar solvents with low solvency for ionic compounds. On the other hand, high densities favor the solubility and the dissociation of ionic species like salts, acids, and bases. The supercritical high-density water thus possesses complete solvency for most gases and organic compounds [23]. As a result, organic and inorganic materials containing corrosive agents like chlorine, sulfur, phosphorous, etc. react and dissolve immediately to form one single phase.

Aqueous corrosion in ambient conditions is due to ionic reactions. In acidic solutions at ambient conditions, the corrosion resistance of nickel–chromium alloys is generally due to the formation of thermodynamically stable protective Cr_2O_3 film (Cr^{3+} compound). At a temperature $> \sim 100^\circ\text{C}$, the solubility of oxygen in water, and consequently the oxidizing power of the solution, increases with temperature (Fig. 7.23) [22]. At the same time, the resistance of Cr^{3+} oxide against oxidation decreases by the formation of soluble Cr^{4+} compounds [24], which makes the film unstable above a specific temperature and result in its transpassive dissolution. This instability is different from the local attack on Cr_2O_3 film by halide ions at low temperatures. Alloy 625 exhibits a similar tendency to change from pitting corrosion to uniform corrosion in subcritical water [22].

Figure 7.24 illustrates the electrochemical and chemical dissolution behavior of nickel–chromium alloys in high-temperature solutions. Chromium is more stable against the acidic solution, while nickel tolerates better oxidizing conditions. When the solution density is high, the concentration of H^+ ions is high (low pH values) as

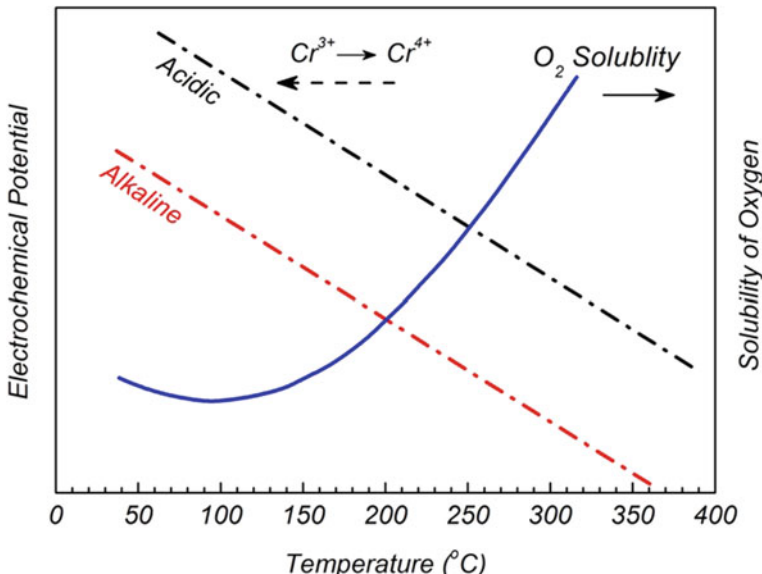


Fig. 7.23 A schematic representation of the variation in the electrochemical potential as a function of temperature for the formation of soluble chromate in acidic and alkaline solutions [22]

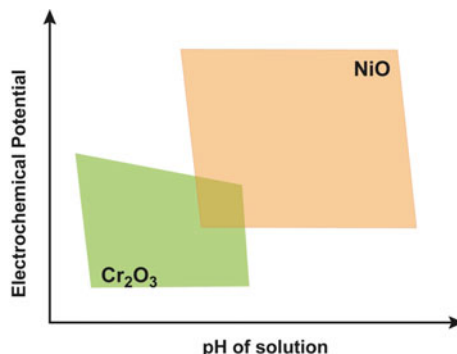


Fig. 7.24 Schematic electrochemical potential and pH value map of the stability of chromium and nickel oxide films on nickel–chromium alloys in high-temperature water solutions. Increasing the electrochemical potential at low pH values dissolves chromium electrochemically as chromate. At the same time, it makes nickel chemically unstable, which dissolves as soluble Ni^{2+} aqueous complexes. On the other hand, a subsequent increase of the pH value at high potentials NiO becomes stable above a specific pH value. Therefore, at high electrochemical potentials and high pH values, NiO provides the protective film [22]

essentially acids dissociate in the high-temperature dense water. An increase in the electrochemical potentials results in the electrochemical dissolution of chromium as chromates while nickel dissolves as soluble Ni^{2+} aqueous complexes [22]. On the other hand, high pH values at high potentials stabilize the NiO phase, forming a protective layer. A situation with a high pH value may arise when OH^- ions are added to the solution from an external source or the dissociation of acid reduces. When the water passes from subcritical to supercritical water conditions, a drop in the solution density reduces the dissociation of acid. No oxide is stable when the pH is low, and the potential is high, and, in such situations, the alloy will undergo general corrosion.

The high temperature also affects the pitting corrosion behavior of the alloy. With increasing temperature, the pitting potential decreases due to decreasing protective character of the oxide film [25, 26]. Still, it reaches a level at which it stays constant above a specific temperature, and the alloy is no more susceptible to pitting. This temperature is called the inversion temperature [27]. The inversion temperature may vary significantly with the chloride media. For instance, the inversion of the Alloy 625 in a sodium chloride solution containing 0.1 mol/kg of NaCl is 150 °C [26], while in a hydrochloric acid solution containing 0.05 to 0.2 mol/kg of the acid is above 250 °C [28]. The morphology of corrosion pits at low temperatures is typically hemispherical [22]. At the inversion temperature, corrosion morphologies change from isolated hemispherical pits at low temperatures to shallow interconnected pits covering the entire surface at higher temperatures [22], similar to the general corrosion. Some authors attributed this transition to a change in the characteristics of the oxide film, while others attributed it to its transpassive dissolution [22].

7.5.1 Acidic High-Temperature Waters

Kritzer et al. [22] have done an exhaustive review of Alloy 625 corrosion behavior in strongly oxidizing and pressurized high-temperature solutions of many acids. These solutions comprised solutions of hydrofluoric acid (HF), hydrochloric acid (HCl), hydrobromic acid (HBr), sulfuric acid (H_2SO_4), nitric acid (HNO_3) and phosphoric acid (H_3PO_4) in the concentration range over 0.05 mol/kg to 1.0 mol/kg, and oxygen concentrations from 0.5 mol/kg to 3.6 mol/kg.

At temperatures up to about 100 °C, no severe corrosion is observed in any acid solution. In the temperature range of about 100–150 °C, the only slight intergranular attack may be observed due to impurities like phosphorus, sulfur, and silicon present in concentrations higher than 10–100 ppm [22]. Prior precipitation of chromium carbides along grain boundaries may also cause some dissolution of the chromium depleted regions adjacent to carbides [29–31].

At temperatures above about 150 °C, severe pitting may occur in HCl and HBr solutions [32–34] (see, e.g., Fig. 7.25a [23]) as the critical pitting temperatures for the two acid solutions is about 150 °C, though the lowest temperature for the bromide solution is higher than that of the chloride solution. Typical pit penetration rates of about 600 to 1000 μm in 100 h have been reported for Alloy 625 [28]. Other acid solutions show only minor corrosion in this temperature range. Observation of pits in HCl and HBr solutions is consistent with the aggressive natures of the two halide ions. Mitton et al. [35] have reported stress-corrosion cracking at temperatures less than 200 °C after several hundreds of hours.

At temperatures above 250 °C, the alloy may exhibit severe general corrosion in HCl, HBr, H_2SO_4 , and HNO_3 solutions, independent of pressures above 22 MPa [28, 32, 33, 36–38]. This behavior is attributed to the increased solubility of the oxygen in the water, which makes it highly oxidizing [22]. At the same time, the oxidation resistance of passive film decreases due to decreasing stability of the Cr^{3+} oxide film [24]. The morphology of the general attack has the shape of interconnected shallow pits (Fig. 7.25b [23]). The HF and H_3PO_4 solutions cause low levels of corrosion at

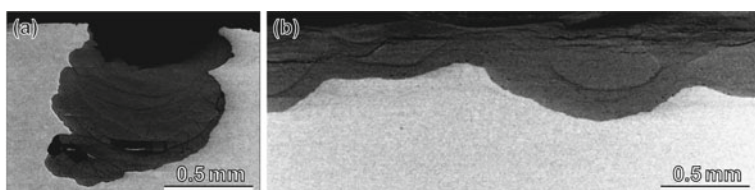


Fig. 7.25 Change in the corrosion behaviour of Alloy 625 in hydrochloric acid solutions containing 0.05 mol/kg hydrochloric acid and 0.48 mol/kg of oxygen at 24 MPa pressure. The alloy exhibited pitting during corrosion at lower temperatures, which tend to change to a general form of corrosion at high temperatures due to reduced stability of the Cr^{3+} oxide film. **a** A scanning electron micrograph of a pit formed at 160 °C; **b** Typical wave-like appearance of corrosion product due to the formation of interconnected shallow pits at 350 °C. Reprinted from [23], Copyright (2004), with permission from Elsevier

these temperatures [28, 32], which can be attributed to (i) extremely low degree of dissociation of the two acids even at these high temperatures; (ii) the formation of insoluble phosphates or fluorides that provide secondary protection.

The typical corrosion parameters of Alloys 625 in pressurized oxidizing solutions of different acids at subcritical temperatures are summarized in Table 7.4 [22]. Based on corrosion rates, the corrosivity of acids in these environments can be arranged in the following order: $\text{HNO}_3 > \text{HBr} > \text{HCl} > \text{H}_2\text{SO}_4 > \text{H}_3\text{PO}_4 \approx \text{HF}$.

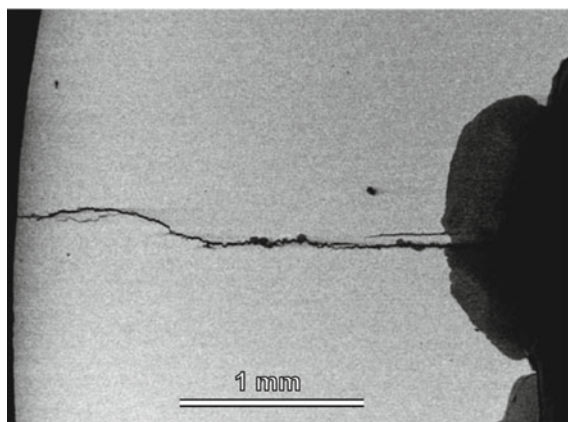
Stress-corrosion cracking (SCC) is a common phenomenon in oxidizing high-temperature solutions [22, 23]. Figure 7.26 shows the failure of an Alloy 625 tube by SCC in a solution containing 0.10 mol/kg HCl and 0.48 mol/kg oxygen at 220 °C and 38 MPa pressure. This condition corresponds to a temperature transition region between passive and transpassive states. The SCC started at the bottom of a shallow pit, and the tube failed in about 25 h [23]. This cracking is due to the breaking of the protective layer under high-temperature water's highly chemically aggressive environment, rather than high mechanical stresses generally responsible for local destruction of the protective film in SCC. Kritzer et al. [22] have contested for chemical destruction of the film under such an aggressive environment because

Table 7.4 Typical minimum corrosion temperatures and corrosion rates of intergranular corrosion, pitting and transpassive dissolution of Alloy 625 in oxidizing aqueous solutions of different acids containing 0.05–0.2 mol/kg acid and 0.5 mol/kg of oxygen at 24 MPa pressure [22]

	HF	HBr	HCl	HCl ^a	H_2SO_4	H_3PO_4	HNO_3
Intergranular corrosion (°C)	170	150	110	110	145	50	10
Pitting (°C)	–	170	140	215	–	–	–
Pitting rate ($\mu\text{m}/100 \text{ h}$)	–	1000	1000	1000	–	–	–
Transpassive dissolution (°C)	–	320	300	290	300	–	270
Corrosion rate ($\mu\text{m}/100 \text{ h}$)	< 30	800	400	400	300	< 10	1800

^a Polished inner surface

Fig. 7.26 Failure of an Alloy 625 tube by SCC in a solution containing 0.10 mol/kg HCl and 0.48 mol/kg oxygen at 220 °C and 38 MPa pressure. Reprinted from [23], Copyright (2004), with permission from Elsevier



the applied load is too low to break the oxide film. On the other hand, the observation of the stress-corrosion cracking by Mitton et al. [35] at temperatures less than 200 °C, mentioned above, is attributed to the high penetration rates of pitting leading to a severe thinning of the wall that increased mechanical stresses. Hydrogen appears to play no role in stress-corrosion cracking of the alloy in these conditions. Its evolution is significant only at high anodic potentials in strongly oxidizing high-temperature waters [22].

Surprisingly, increasing the temperature to supercritical values reduces the corrosion rates by at least two orders of magnitude. Kritzer et al. [22] have attributed the behavior to the low density of the supercritical water, which makes it a non-polar solvent with very low solvency for inorganic compounds, leading to low corrosion rates. Nonetheless, an increase in the density of the supercritical solution still increases the corrosion rate. For example, the alloy exhibits an increase in the corrosion rate by a factor of 50 in oxidizing supercritical HCl or H₂SO₄ solutions when the density of the solution is increased from about 150 kg/m³ (at 24 MPa pressure and 400 °C temperature) to about 510 kg/m³ (38 MPa pressure) [22, 28, 38]. In general, the severe corrosion of the alloy ceases when the density of the solution decreases to values less than 200 kg/m³ due to the protective nature of the nickel oxide layer at low densities (Fig. 7.22).

The melting of corrosion products in high-temperature pressurized water solutions unexpectedly increases corrosion rates due to the formation of corrosive two-phase environments. For example, Alloy 625 in an oxidizing solution containing 0.1 mol/kg phosphoric acid (at $T = 430\text{--}470\text{ }^{\circ}\text{C}$; $p = 24\text{ MPa}$) exhibits negligible corrosion. However, the corrosion rate increased tremendously to about 850 $\mu\text{m}/\text{h}$ when the acid concentration is increased to 0.2 mol/kg [37]. This unexpected increase in the corrosion rate is attributed to the formation of a two-phase environment when nickel (III) phosphate corrosion product, which has a melting point lower than the process temperature, melted in the pressurized high-temperature water [38].

7.5.2 Neutral High-Temperature Waters

Neutral high-temperature water containing only oxygen is not very corrosive. It does not corrode even after relatively prolonged exposure. For example, the alloy exhibits a corrosion rate $< 10\text{ }\mu\text{m}$ in 100 h, though some pitting was observed in supercritical low-density solutions after 800 h [22]. The low corrosion rate is attributed to the protection by the NiO film. NiO is the most stable oxide film in neutral supercritical water. On the other hand, chromium and molybdenum oxides dissolve by forming their hexavalent acids H₂CrO₄ and H₂MoO₄, respectively. Likewise, the alloy may exhibit a low corrosion rate in oxidizing salt solutions of chlorides and sulfates due to the low solubility of the NiO film. However, the alloy may exhibit severe pitting in oxidizing sodium chloride solutions at temperatures higher than 200 °C because it is higher than the critical pitting temperature in HCl solutions [22].

7.5.3 Alkaline High-Temperature Waters

In oxygenated dilute sodium hydroxide (NaOH) solutions, the alloy is protected by the formation of NiO layer at subcritical temperatures (Fig. 7.24) since the nickel oxide has the lowest solubility in the weak alkaline pH range compared to chromium and molybdenum oxides [39]. At high pH values, the alkaline solutions also inhibit chloride-induced pitting corrosion as the alkaline solutions quickly neutralize the H^+ ions formed during pit initiation suppressing the pit's possible growth [22]. Alloy 625, therefore, exhibit very low corrosion in oxygenated alkaline solutions at subcritical temperatures. The alloy is non-corrosive in oxygenated sodium hydroxide water solutions at subcritical temperatures [39].

However, at supercritical temperatures and low densities, the alloy exhibit severe corrosion in oxidizing solutions of NaOH [40]. The severe corrosion is due to the melting point of NaOH (320°C) lower than the temperature of the supercritical water and its poor miscibility in low-density supercritical water. As a result, a condition of two phases exists in low-density supercritical temperatures containing high NaOH concentrations. This two-phase contains an oxidizing NaOH melt as an additional phase with enhanced solvency for salts, which can dissolve even the nickel oxide [40, 41]. In oxygen-free NaOH solutions, no severe corrosion is observed even at supercritical temperatures because of the absence of metal oxide-producing reduction reaction.

Chromium does not protect nickel–chromium alloys in subcritical and supercritical water solutions. At subcritical temperatures, chromium dissolves by forming hydrogen chromate $[\text{HCrO}_4^-]$ or chromate $[\text{CrO}_4^{2-}]$ in the aqueous phase [22]. In contrast, at supercritical temperatures, it dissolves by forming chromic acid $[\text{H}_2\text{CrO}_4]$ or salts in the melt phase.

7.6 High-Temperature Corrosion

High-temperature corrosion is the degradation of materials due to chemical attacks from solids, liquids (molten metals or salts) or gases at elevated temperatures, typically above $0.4T_m$. The modes of high-temperature corrosion include oxidation, carburization, sulfidation, metal dusting, corrosion by halogens, etc.

7.6.1 Oxidation

Nickel-based alloys are superior to Iron-based or cobalt-based alloys for high-temperature applications because of their excellent oxidation resistance. These alloys gain their high-temperature resistance primarily due to the formation of the protective Cr_2O_3 oxide film, and the extent of resistance is directly related to the chromium

concentration. However, the Cr_2O_3 film becomes volatile at temperatures above 980 °C [5], which reduces the protection of the alloy. At higher temperatures, alloys containing a small amount of aluminum (e.g., Alloy 214) exhibit better resistance to oxidation due to the formation of a more protective Al_2O_3 film. Sometimes rare earth elements like lanthanum and yttrium are also added to enhance the resistance of the oxide scales to spallation [42].

The damage of metal during oxidation is due to its conversion into an external oxide scale. In addition, oxidation may cause an internal attack and the formation of isolated internal voids. The degree of oxidation generally increases with an increase in temperature. During exposure in the air, the internal attack may also result in the formation of internal nitrides along with internal oxides when significant spallation of Cr_2O_3 film occurs in alloys with insufficient aluminum. Thermal cycling has a marked effect on oxidation attacks due to the spallation of the oxide scales, with a higher frequency of causing more significant damage.

Alloy 625 has good resistance to oxidation and scaling at high temperatures. The primary protective oxide layer is Cr_2O_3 . The oxide layer becomes enriched with Cr_2O_3 as the temperature increases from 600 °C [43]. Between 800 and 1050 °C, the oxide scale is almost exclusively of Cr_2O_3 . At temperatures above about 1050 °C, the oxide layer gets enriched with niobium and titanium [43]. The oxidation resistance of the alloy is comparable to that of alloys 600 and 800 and better than Alloy C-276 [8]. Figure 7.27a compares the oxidation behavior of Alloy 625 with some other alloy based on the mass change in air containing 5% water vapor at 1000 °C for up to 1000 h. Alloy 625 is among the best materials for oxidation resistance in air containing about 5% water vapor. Figure 7.27b shows the results of cyclic oxidation tests of Alloy 625 and other nickel-base alloys at 982 °C, subjected to 2880 cycles (over 40 days) of 15 min heating cycles up to 982 °C, followed by cooling in the air

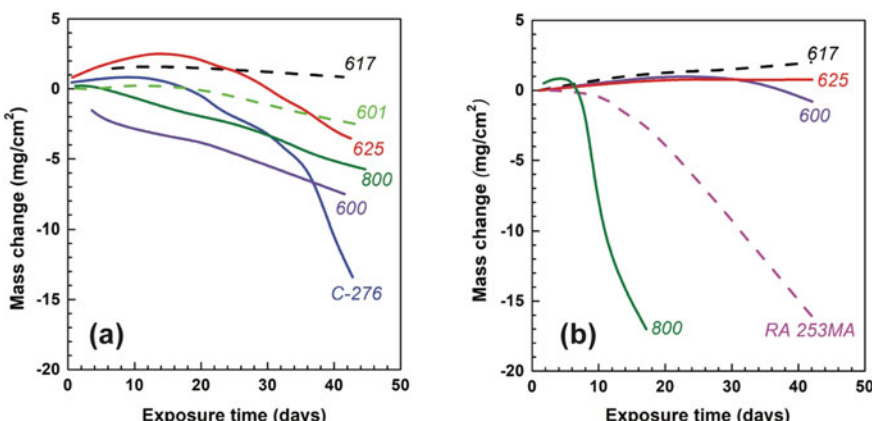


Fig. 7.27 **a** Oxidation behaviour of Alloy 625 and some other nickel alloys exposed to air containing 5% water vapour at 1000 °C. **b** Scale adherence of oxide films during cycling oxidation of Alloy 625 and other alloys at 982 °C [8]

for 5 min [8]. Alloy 625 shows excellent adherence to its oxide scale. It exhibited an outstanding ability to retain the protective oxide coating under this cyclic condition.

7.6.2 Carburization

Carburization occurs in environments that contain carbonaceous gases like CO, CO₂, CH₄ and other hydrocarbons when the carbon diffuses into the metal surface and combines with alloying elements to form various carbides. The formation of internal carbides may lead to metal degradation and embrittlement, which result in a reduction in tensile and Charpy impact properties [44]. The corrosion damage is directly related to the magnitude of carburization. Carburization can be quantified in terms of the mass of the carbon gained (mg/cm²) and the depth of carburization. Often, the gaseous carburization environments are also oxidizing in nature. In such environments, the dominant character of the damage is governed by the partial pressure of carbon and its activity at a given temperature [45]. In general, carburization occurs at temperatures above 800 °C and carbon activity < 1 [44].

The low solubility of carbon in nickel alloys and the formation of a protective, stable oxide scale make them inherently resistant to carburization. However, these alloys contain many carbide-forming elements that may form their carbides. Figure 7.28 compares the mass of carbon gained in Alloy 625 and other alloys after carburization for about 1000 h in a mixture of H₂-1% CH₄ at 1000 °C [8]. The Alloy 625 exhibited a carburization resistance better than that of Alloy 800. Its mass change in a slightly oxidizing carburizing environment of H₂-5.5% CH₄-4.5% CO₂ gaseous mixture (oxygen partial pressure ~ 10⁻²⁰ atm) at 1000 °C for about 1000 h was comparable to Alloys 600 and better than Alloy 800 and 601 [8].

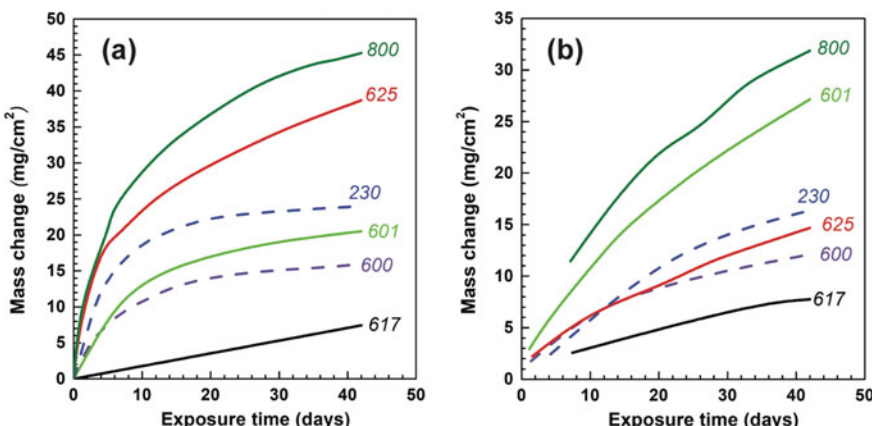


Fig. 7.28 Carburization behaviour of Alloy 625 at 1000 °C compared to other alloys in **a** H₂-1% CH₄ and **b** H₂-5.5% CH₄-4.5%CO₂ environments [8]

Table 7.5 Carburization behavior of alloys in 5% H₂ + 5% CO + 5% CH₄ argon gas [46]

Alloy	Carbon mass gain per unit area (mg/cm ²)		
	871 °C for 215 h	927 °C for 215 h	982 °C for 55 h
Alloy 214	0.14	0.3	0.6
Alloy 617	0.26	2.4	5.0
Alloy 625	0.31	1.1	5.3
Alloy S	0.32	1.6	2.1
Alloy 600	0.40	1.3	2.8
Alloy 230	0.40	2.0	2.5

Table 7.5 compares carburization behavior of Alloy 625 in an atmosphere containing 5% H₂ + 5% CO + 5% CH₄ (by volume) in argon gas at 871, 927 and 982 °C temperatures [46]. The partial pressure of oxygen at different test temperatures corresponded to 8.13×10^{-23} , 2.47×10^{-22} and 6.78×10^{-22} atm, respectively. The magnitude of the carbon pick-up increased significantly at 982 °C despite a shorter duration of exposure.

7.6.3 Sulfidation

Sulfidation corrosion occurs when a metal is exposed to sulfur compounds in high-temperature environments. Unlike oxide scales, sulfide scales are not protected as they contain many defects, which allows a faster diffusion of metal ions through the scale. Nickel alloys form a low-temperature Ni₃S₂ eutectic compound at 635 °C when exposed to an environment comprising only H₂ and H₂S [5]. As a result, the liquid Ni₃S₂ sulfide accelerates corrosion significantly. The formation of the low-melting eutectic restricts the use of nickel alloys in such environments at temperatures up to about 600 °C only.

Nickel alloys owe their resistance to sulfidation to the protective Cr₂O₃ film as the Cr₂O₃ film is impervious to sulfur diffusion. A small addition of aluminum or silicon further enhances the sulfidation resistance by forming an Al₂O₃- or SiO₂-rich sub-layer. The destructive sulfidation attack occurs mainly at sites where the protective oxide breaks down. Once sulfide phases include, they oxidize preferentially and form new sulfides deeper inside the alloy, often at grain boundaries or at the sites of other chromium- or aluminum-rich phases. Most sulfur-bearing high-temperature environments also contain gases like SO₂, CO, CO₂ and H₂O. In such sulfidizing-oxidizing environments, relative partial pressures of oxygen and sulfur govern the formation of oxide or sulfide scales. Table 7.6 compares the sulfidation of Alloy 625 with some other heat-resistant alloys in an argon gas environment comprising 5% H₂, 5% CO, 1% CO₂, 0.15% H₂S at 871 °C for 215 h. The alloy exhibits a maximum metal loss of more than 24 mils. This corrosion rate had consumed more than half the

Table 7.6 Metal loss of Alloy 625 and some other heat-resistant alloys at 871 °C after 215 h in argon gas containing 5% H₂, 5% CO, 1% CO₂, 0.15% H₂S [5]

Alloy	Metal loss (mils)	Maximum metal affected ^b (mils)
Alloy 230	Consumed ^a	> 19.5
Alloy 625	Consumed ^a	> 24.0
Alloy 800 H	7.6	> 30.0
Alloy 617	3.8	21.3
Alloy HR 160	0.8	6.2

^a Consumed refers to the state of the sample when the maximum metal affected is greater than one-half of the sample thickness

^b Maximum metal affected = metal loss + maximum internal attack

thickness of the coupon kept for testing [5]. Cuevas-Arteaga et al. [47] have shown that cobalt addition significantly reduces the sulfidation rate.

7.6.4 Halide Corrosion

High-temperature halide corrosion is common in fossil fuel boilers, coal gasification equipment, gas turbines, and municipal and chemical waste incinerators. Halide corrosion refers to corrosion by gaseous Cl₂/HCl. It can be more harmful than oxidation. It proceeds by the formation and volatilization of chloride scales due to lower melting points of metal chlorides (e.g., 696 °C for FeCl₂) and higher vapor pressures of corresponding oxides. For environments dominated by gaseous chlorine, chromium bearing nickel alloys are preferred due to relatively high melting points of NiCl₂ (1030 °C) and CrCl₃ (1150 °C) [5]. In the presence of oxygen, corrosion involves the formation of oxides and volatile oxychlorides (e.g., chromium oxychlorides and molybdenum oxychlorides) depending upon relative partial pressures of oxygen and chlorine. In such environments, high nickel contents in the alloys are beneficial because nickel forms one of the least volatile chlorides [5].

The use of a nickel alloy for environments containing chlorine may depend upon the relative concentration of the chlorine. For instance, Alloy 625 exhibits an intermediate resistance level in air containing 2% chlorine. Table 7.7 compares the corrosion behavior of Alloy 625 with some other nickel superalloys in air containing 2% chlorine after exposure for 50 h at 900 °C [48]. In this environment, Alloy 214 exhibits the best resistance to halide corrosion due to the presence of aluminum in the alloy, which forms the impervious protective Al₂O₃ scale. However, Alloy 600, which contains chromium lesser than Alloy 625, exhibits better resistance. The low resistance of Alloy 625 than that of Alloy 600 could be due to molybdenum (9 wt%) in the former. Molybdenum and tungsten are known to be detrimental against the halide atmosphere [5]. This does not mean that Alloy 625 always performs poorly in all halide environments. In gaseous environments containing a mixture of HCl,

Table 7.7 Metal loss of Alloy 625 and some other heat-resistant alloys after 50 h of exposure at 900 °C in air containing 2% chlorine [48]

Alloy	Metal loss (mils)	Total depth (mils)
Alloy 214	0.6	1.6
Alloy 800 H	1.0	4.3
Alloy 600	2.0	5.0
Alloy 601	0.2	5.2
Alloy 625	4.0	7.0
Alloy C-276	6.1	8.1
Alloy 230	1.3	8.2
Alloy 617	3.8	11.8

Table 7.8 Mass change in alloys exposed to a nitrogen gas environment containing 10% CO₂, 9% O₂, 4% HCl, 130 ppm HBr and 100 ppm SO₂ after 300 h [8]

Alloy	Mass change (mg/cm ²)			
	593 °C	704 °C	816 °C	927 °C
SS 309	-2.62	-117.89	-	-77.70
SS 316	-5.48	-152.08	-32.75	-45.74
SS 347	-1.61	-327.80	-221.65	-68.36
Alloy 600	-0.32	-0.98	-6.93	-10.18
Alloy 601	-0.50	-2.19	-7.24	-29.53
Alloy 617	-0.51	-8.38	-10.81	-44.64
Alloy 625	-0.52	-2.06	-5.86	-5.91
Alloy 690	-0.13	-1.12	-14.27	-24.21
Alloy 800	-0.53	-245.22	-6.63	-18.98
Alloy 825	-1.53	-127.34	-8.52	-25.89

HBr and SO₂, Alloy 625 is one of the best materials, especially at high temperatures. Table 7.8 compares the metal loss of Alloy 625 with other alloys tested in a gaseous mixture of N₂-10% CO₂-9% O₂-4% HCl-130 ppm HBr-100 ppm SO₂ environment at 593, 704, 816, and 927 °C for 300 h. All the alloys exhibited metal loss (expressed as negative mass change) suggesting of their spalling or vaporisation loss or both. The rate of metal loss in most alloys increased with increasing temperature. The high-iron alloys show higher mass losses at 704 °C than at 927 °C [8] due to extensive internal oxidation triggered by the molten FeCl₂ (melting point = 696 °C). The morphology of the corrosion scale at high temperatures (e.g., 927 °C) is distinctly different from that at low temperatures. At higher temperatures, voids are frequently seen that are more pronounced in iron-rich alloys. Figure 7.29 shows these effects in 316-grade stainless steel and Alloy 625 after exposures at 704 and 927 °C. Evidently, for the test temperature regime of 593–927 °C, the nickel-base alloys are better for avoiding 704 °C liquid phase corrosion.

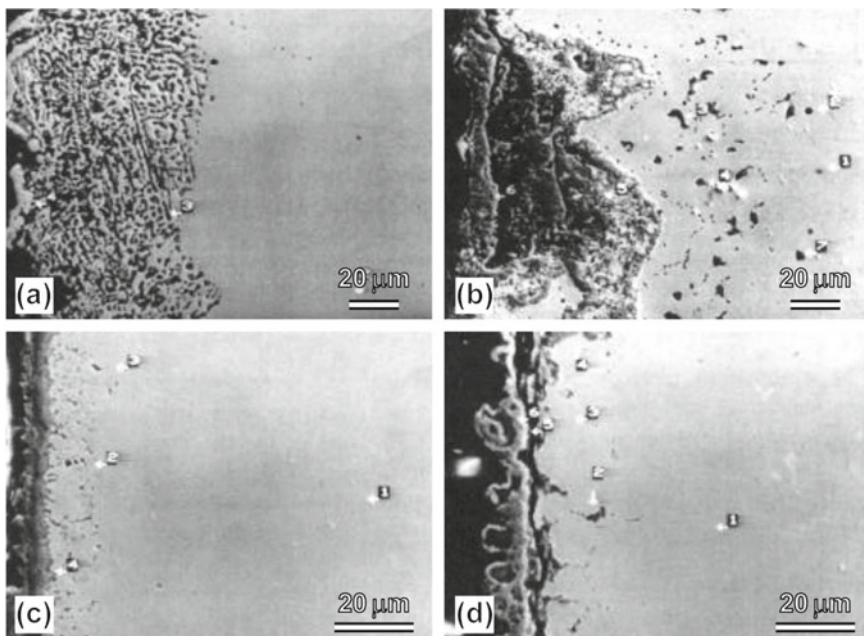


Fig. 7.29 Typical scanning electron subsurface micrographs of 316 stainless steel and Alloy 625 alloys exposed to a gaseous mixture of N₂-10% CO₂-9% O₂-4% HCl-130 ppm HBr-100 ppm SO₂ environment at 704 and 927 °C. **a** 316 stainless steel exposed at 704 °C; **b** 316 stainless steel exposed at 927 °C; **c** Alloy 625 exposed at 704 °C; **d** Alloy 625 exposed at 927 °C. Reprinted from [8]. Copyright 1991 by The Minerals, Metals & Materials Society. Used with permission

7.6.5 Molten Salt Corrosion

Molten salt corrosion at high temperatures is often encountered in heat-transfer and energy-storage media used in solar energy and nuclear systems, fuel cells, high-temperature batteries, metallurgical extraction processes and heat-treating industry. Molten salts dissolve the protective oxide scales from the metal surface, exposing the surface for a further oxidation cycle, followed by the dissolution of the oxide film in the molten salt. Oxygen and water vapor in the molten salts accelerate the kinetics of molten salt corrosion. Metals react with molten sodium hydroxide to form metal oxides, sodium oxide, and hydrogen. The attack mechanism is predominantly intergranular corrosion by the salt components, especially chlorine [49]. Table 7.9 compare the corrosion damage of Alloy 625 with other nickel alloys after their exposure in a sodium chloride bath at 840 °C after 100 h [49]. A fresh salt bath was used for each run, and the air was used as the cover gas. Alloy 625 exhibited an intermediate level of corrosion resistance in the molten NaCl salt bath.

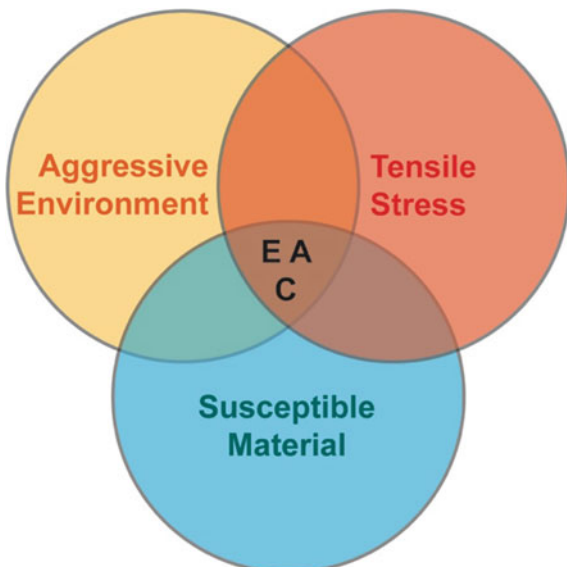
Table 7.9 Depth of the salt penetration in Alloy 625 and some other alloys when tested in a sodium chloride bath at 840 °C for 100 h [49]

Alloy	Total depth	
	mm	mils
Alloy 601	0.066	2.6
Alloy 214	0.079	3.1
Alloy 800 H	0.109	4.3
Alloy 625	0.112	4.4
Alloy 617	0.122	4.8
Alloy 230	0.140	5.5
Alloy 600	0.196	7.7

7.7 Environmentally Assisted Cracking

Environmentally assisted cracking refers to the phenomenon by which an ordinarily ductile material loses its toughness and ductility when subjected to mechanical loading in the presence of specific corrosion environments. Three factors, namely, (i) a specific aggressive environment, (ii) mechanical tensile stress, and (iii) a susceptible microstructure, are simultaneously needed for an alloy to exhibit environmentally assisted cracking (Fig. 7.30). Alteration or elimination of any one of the three mitigates the occurrence of environmentally assisted cracking. Of these, alteration of the environment or the change of the alloy is the best solution as the complete elimination of stresses is somewhat tricky due to geometrical considerations of components. When neither the alloy nor the environment can be changed, environmentally assisted

Fig. 7.30 A schematic diagram depicting factors essential for the occurrence of environmental assisted cracking



cracking can be mitigated by eliminating tensile stresses on the exposed surface by introducing compressive stresses using techniques like shot peening.

Environmentally assisted cracking generally includes phenomena like stress-corrosion cracking, hydrogen embrittlement and sulfide stress cracking.

7.7.1 Stress-Corrosion Cracking

Nickel-base alloys are, in general, not prone to stress-corrosion cracking in chloride environments compared to stainless steels. They are also preferred in caustic, polythionic acid, and some deep sour gas well environments. Figure 7.31 shows the effect of nickel on the susceptibility to chloride ion stress-corrosion cracking in boiling 42% magnesium chloride test solution [15]. Figure 7.31 shows that all alloys containing more than 45% nickel are immune to chloride stress cracking. Alloy 625 has a minimum of 58% nickel and will not crack in a chloride environment. However, it suffers stress-corrosion cracking in conditions associated with supercritical water oxidation, as discussed in Sect. 7.5.1. It undergoes intergranular cracking when exposed to supercritical water and chlorides at high temperatures. Kim et al. [50] have shown that subcritical and supercritical pressurized hydrochloric acid water solutions of pH two cause stress-corrosion cracking of Alloy 625 along grain boundaries. In subcritical solution conditions, the stress-corrosion cracking occurs under the combined influence of stresses and the defective de-alloyed oxide layer formed due to de-alloying of nickel and iron and the oxidation of chromium and molybdenum. In such conditions, the stress-corrosion cracking may occur at stresses as low as 30% of the yield strength. In supercritical conditions, no de-alloying occurs, and the stress-corrosion cracking is a direct consequence of the chemical attack of hydrochloride molecules at grain boundaries under the influence of stress. Table 7.10

Fig. 7.31 The classic indicator of the susceptibility to chloride-ion stress-corrosion cracking of nickel-containing alloys in the boiling 42% magnesium chloride test. The threshold represents the minimum time beyond which cracking starts for a given amount of nickel present in the alloy. Alloys containing more than 45% nickel are immune to chloride stress cracking [15]

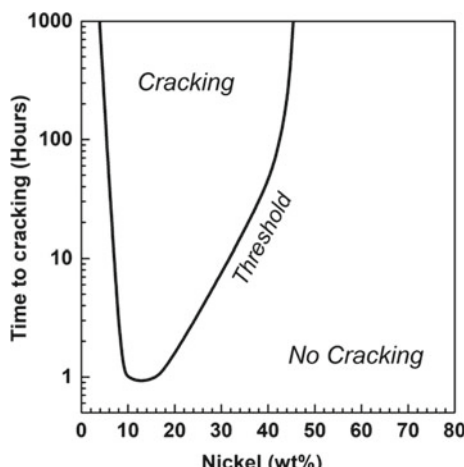


Table 7.10 Environments in which Alloy 625 exhibited stress-corrosion cracking [51]

Thermal history	Environment for SCC
Annealed	High-temperature water, degassed
Annealed	Polythionic acid
Annealed	Oxygenated water plus lead
Annealed	Water containing 21 ppm O ₂ at 316 °C
Annealed	Steam, cycled between 318 and 385 °C, 10 ppm Cl ⁻ , 8 ppm O ₂
Cold worked	Water containing 100 ppm O ₂ at 288 °C
Cold worked and aged at 204 °C	Water saturated with H ₂ S + 5% NaCl + 0.5% acetic acid (NACE solution) at room temperature
Cold worked and aged at 500 °C	Water with 5% NaCl and 0.5% acetic acid at room temperature
As produced tube	Hydrochloric acid solutions of pH 2, 300 to 426 °C, 24.1 MPa

lists environments in which stress-corrosion cracking has been observed in Alloy 625 [51].

7.7.2 Hydrogen Embrittlement

Hydrogen embrittlement refers to the loss of ductility caused by hydrogen ingress into the metal. It may cause intergranular, transgranular, or quasi-cleavage cracking. The degree of susceptibility to hydrogen embrittlement can be measured as a function of the ductility loss. Like ferrous alloys, nickel alloys are also susceptible to hydrogen damage in both aqueous and gaseous hydrogen environments, but to a lesser extent owing to greater ease of slip and reduced solute diffusivities in their face-centered cubic lattice.

Variables that affect hydrogen embrittlement the most are [52]: (i) the surface hydrogen fugacity for gaseous hydrogen and cathodic charging current density for the electrolytically charged hydrogen; (ii) impurities like sulfur, phosphorus, arsenic, antimony and tin; (iii) temperature. Under the gaseous atmosphere, hydrogen pressure has a steep dependence on the embrittlement at low pressures, followed by a region of cracking that is independent of pressure [52]. For electrolytically charged hydrogen, the time to failure decreases monotonically with charging current density [52]. Presence of alloying impurities such as sulfur, phosphorus, antimony and tin aid the entry of adsorbed hydrogen into the metal by inhibiting the recombination of hydrogen adatoms (adsorbed atoms) from forming hydrogen gas which can then escape. Besides, these impurities increase the embrittlement of alloys by forming low-melting eutectic compounds at grain boundaries that cause decohesion of grains. Hydrogen embrittlement decreases with an increase in temperature

[52]. The maximum embrittlement temperature depends on the composition and microstructure of the alloy. This hydrogen embrittlement behavior contrasts to stress-corrosion cracking in chloride environments, in which it increases with an increase in temperature [52, 53].

Nickel-base superalloys show a reduction in tensile ductility when charged with hydrogen, depending on the thermo-mechanical history of the alloy. They are generally more resistant to hydrogen stress cracking in as-cold-worked conditions compared to cold-worked and aged states [54]. Age-hardenable alloys age-hardened to peak or near-peak strength show the least hydrogen embrittlement resistance. Stabilization treatments, followed by aging, reduce the resistance of these alloys compared to direct aging. Hydrogen stress cracking of nickel alloys may also occur without losing tensile ductility when alloys possess high yield strengths or are under high hydrogen fugacity [54].

Alloy 625 possesses an intermediate level of resistance against hydrogen embrittlement induced by both gaseous hydrogen and internal hydrogen. Hydrogen embrittlement has little effect on the yield strength of the alloy. In contrast, it reduces alloy's notch tensile strength, ductility and threshold stress intensity for subcritical crack growth. The severity of internal hydrogen embrittlement increases with the dissolved hydrogen, up to 50 part-per-million (ppm) hydrogen by weight. Increasing dissolved hydrogen contents causes a change in the fracture mode from ductile to brittle, which manifests itself in fractographic changes from dimpled features at low dissolved hydrogen contents to {111} planar facets at higher dissolved hydrogen contents (up to 50 wt. ppm hydrogen) [55]. The alloy is resistant to hydrogen-stress cracking when cold worked to a yield strength above 1240 MPa [54]. However, when the cold-worked alloys are aged at low temperatures, their resistance to hydrogen cracking reduces considerably. This behavior is attributed to the segregation of phosphorus and sulfur to grain boundaries, which provide low-energy fracture paths or an ordering reaction of the form $\text{Ni}_2(\text{Cr}, \text{Mo})$. Figure 7.32 relates the ductility loss (reduction in area) with hydrogen charged to the precipitation of the ordered $\text{Ni}_2(\text{Cr}, \text{Mo})$ phase in the alloy [56].

7.7.3 Sulfide Stress Cracking

Sulfide stress cracking is another form of hydrogen embrittlement prevalent commonly in the oil and gas industry or environments containing water and hydrogen sulfide. Sulfide stress cracking usually results in a brittle failure of the alloy under tensile loading above a threshold stress. Atomic hydrogen diffuses into the metal at cathodic sites in hydrogen sulfide environments and causes embrittlement in the localized hard zones or weldment of sensitive materials. Table 7.11 gives the minimum stress (threshold stress) required for Alloy 625 and some other alloys to initiate cracking in a sulfide environment at room temperature under constant load [57]. The atmosphere contained a mixture of oxygen-free water containing 3000 ppm dissolved H_2S , 5% NaCl and 0.5% acetic acid (NACE solution). Alloy 625 exhibited threshold

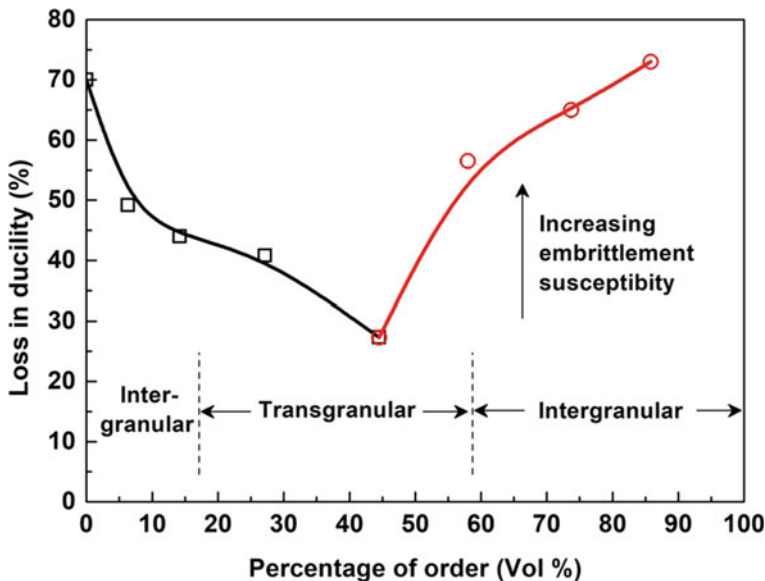


Fig. 7.32 Effect of the degree of order on the hydrogen embrittlement susceptibility due to the precipitation of Ni₂(Cr, Mo) [56]

Table 7.11 The threshold stress required for Alloy 625 and other alloys to initiate cracking at room temperature under constant load in a mixture of oxygen-free water containing 3000 ppm dissolved H₂S, 5% NaCl and 0.5% acetic acid (NACE solution) [57]

Alloy	Thermal history	Yield strength (MPa)	Ultimate tensile strength (MPa)	Threshold stress (MPa)
MP35N	Cold rolled and annealed	2005	2046	1965
C-276	Cold rolled	1503	1631	1473
G	Cold rolled	1496	1617	1470
K-500	Cold rolled and annealed	1124	1317	1101
625	Annealed	558	979	546
625	Cold rolled	1327	1355	1301
718	Solution annealed and aged	986	1172	960
X-750	Solution annealed and aged	1304	1318	1013
Nitronic 50	Cold rolled	880	1076	862

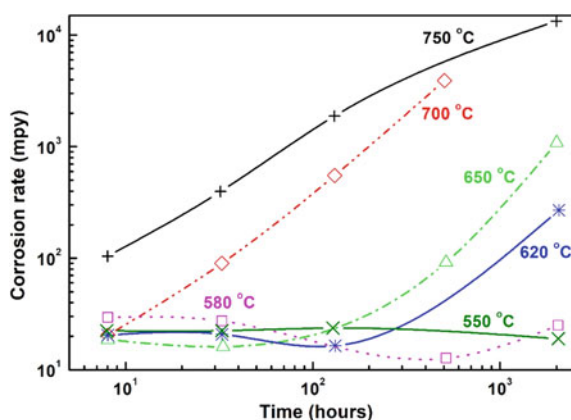
stress close to its yield strength in both annealed and cold rolled conditions (Table 7.11). Alloys with a higher yield strength cracked at a higher threshold stress value.

7.8 Corrosion Behavior of Alloy 625 PLUS

As noted in Chap. 5, Alloy 625 PLUS is a precipitation-hardened variant of Alloy 625 in which a higher amount of titanium (~1.4%) is added to accelerate the precipitation of the γ'' phase particles. Since titanium plays only a limited role in enhancing the resistance against intergranular corrosion in Alloy 625, the corrosion behavior of the age-hardened Alloy 625 PLUS against all other forms of corrosion is similar to that of Alloy 625. Cozar et al. [58] have studied the effect of titanium on the intergranular corrosion resistance of age-hardened Alloy 625. These studies were carried out using the standard ASTM G 28 A procedure in a boiling aqueous solution of 50% sulfuric acid and ferric sulfate. They have shown that age-hardening of an Alloy 625 containing 1.2% titanium decreases its corrosion resistance slightly. The corrosion rate increases with time and temperature of aging at temperatures above 600 °C (Fig. 7.33). The aging of the alloy at 550 and 580 °C does not sensitize this alloy. On the other hand, its resistance to pitting corrosion is less affected by aging [58].

The corrosion resistance of the age-hardened Alloy 625 PLUS is compared with age-hardened Alloy 718 that has identical strength but inadequate corrosion resistance. On the other hand, Alloy 625 has similar corrosion resistance but requires warm or cold working to increase its strength, which is not always feasible, particularly for larger cross-section components. The following compares the corrosion behavior of age-hardened Alloy 625 PLUS (1040 °C/2 h/AC + 732 °C/8 h/FC to 621 °C/8 h/AC) with those of age-hardened Alloy 718 and cold-worked Alloy 625.

Fig. 7.33 The effect of ageing time and temperature on the corrosion rate of Alloy 625 containing 1.2% titanium, tested as per the ASTM G 28 A standard. Before the ageing treatments, the alloy was annealed at 1050 °C for one hour, followed by water quenching [58]



In general, age-hardened Alloy 625 PLUS exhibits corrosion resistance superior to that of aged Alloy 718 and similar or superior to cold worked Alloy 625 [59-62]. Besides, Alloy 625 PLUS is resistant to stress-corrosion cracking in chloride and sulfide environments. The aged alloy also exhibits excellent stress-corrosion resistance in slow strain rate conditions. Slow strain rate tests conducted on double-aged Alloy 625 PLUS in a severe oil field environment at 177 °C containing sour brine (16.5% NaCl + 1 MPa H₂S and 1 MPa CO₂, added at room temperature) with 10 g/l elemental sulfur exhibited excellent resistance to cracking with a ratio of time-to-failure in the corrosive environment versus the inert atmosphere exceeding 0.9 with no secondary cracking [60]. The mechanical and fatigue properties of the age-hardened Alloy 625 PLUS are better than that of 718 and K-500 alloys [61]. The aged alloy can resist sulfide stress-corrosion cracking for over 1000 h during tests conducted in the NACE TM0177 environment at room temperature [59]. The NACE TM0177 environment comprises a room temperature solution of 5% sodium chloride and 0.5% acetic acid, continuously purged with hydrogen sulfide. The alloy exhibits excellent resistance to sulfide stress-cracking/hydrogen embrittlement at ambient temperature. Samples of age-hardened Alloy 625 PLUS tested at 100% yield strength resisted cracking at 204 °C for 28 days showed no crack growth in any of the fatigue pre-cracked samples with stress intensities of 58 to 75 MPa m^{1/2}, while one of the nine Alloy 625 samples, in cold-worked condition, cracked and three of the four aged Alloy 718 samples cracked [59]. The yield strength of different aged Alloy 625 PLUS samples varied from 827 to 958 MPa.

Age-hardened Alloy 625 PLUS has excellent resistance against pitting and crevice corruptions by chlorides. Its pitting resistance, evaluated in a ferric chloride/hydrochloric acid solution and a “modified green death” solution, is similar to that of cold-worked Alloy 625 and superior to that of age-hardened Alloy 718 (Table 7.12) [59]. Resistance at higher temperatures indicates excellent resistance of the alloy. The crevice corrosion resistance of Alloy 625 PLUS, evaluated using

Table 7.12 Pitting temperature test results for 625 PLUS, 625 and 718 alloys pitting temperature (°C) [59]

Alloy	Condition	Pitting temperature (°C)	
		6 wt% FeCl ₃ + 1wt% HCl (24 h exposure)	Modified green death ^a (96 h exposure)
Alloy 625 PLUS	1040 °C/2 h/AC + 732 °C/8 h/FC to 621 °C/8 h/AC	> 98, > 98	75, 80
Alloy 625	25% cold rolled	> 98, > 98	80, 90
Alloy 718	1025 °C/2 h/WQ + 788 °C/8 h/AC	56, 62	45, 45

^a Modified green death = 7 vol% H₂SO₄ + 3 vol% HCl + 5 wt% CuCl₂·2 H₂O + 5 wt% FeCl₃·6 H₂O

Table 7.13 Crevice corrosion test results for 625 PLUS, 625, and 718 alloys (°C) [59]

Alloy	Condition	Crevice corrosion weight loss (mg/cm ²)		Crevice temperature (°C) Yellow death ^a (96 h exposure)	
		6 wt% FeCl ₃ + 1wt% HCl (40 °C/72 h) (55 °C/72 h)			
		(40 °C/72 h)	(55 °C/72 h)		
Alloy 625 PLUS	1040 °C/2 h/AC + 732 °C/8 h/FC to 621 °C/8 h/AC	1.2	6.0	40, 40	
Alloy 625	25% Cold Rolled	3.7	13.7	35, 40	
Alloy 718	1025 °C/2 h/WQ + 788 °C/8 h/AC	35.0	47.2	< 25, < 25	

^a Yellow death = 4 wt% NaCl + 0.1 wt% Fe₂(SO₄)₃ + 0.01 M HCl

constant-temperature weight-loss tests in the ferric chloride (FeCl₃)/hydrochloric acid (HCl) solution and "yellow death" solution, was also similar to that of Alloy 625 and superior to that of Alloy 718. Table 7.13 compares the crevice corrosion behavior of alloys 625 PLUS and 718 in aged conditions and Alloy 625 in cold-worked condition [59]. The temperature at which the crevice corrosion initiated on Alloy 625 PLUS is significantly higher than the Alloy 718 in "yellow death" solution. Similar trends were observed in the weight loss tests in 6 wt% FeCl₃ + 1 wt% HCl at higher temperatures of 40 °C and 55 °C. The higher level of corrosion resistance of the Alloy 625 PLUS is attributed to its higher chromium and molybdenum contents compared to Alloy 718.

7.9 Summary

Alloy 625, in general, offers good resistance to uniform and localized corrosion in various kinds of environments, e.g., inorganic and organic acids, molten salts, pressurized waters, gaseous environments etc. due to its high Chromium and Molybdenum contents. Chromium provides resistance to oxidizing chemicals, while the molybdenum and high nickel improve the alloy's resistance to non-oxidizing environments. The presence of niobium prevents it from sensitization and thus, stabilizes against intergranular attack. Under the pressurized water conditions, Alloy 625 undergoes severe pitting corrosion in acidic water at subcritical temperatures, which leads to stress-corrosion cracking on prolonged exposure. While at supercritical temperatures, the corrosion rate reduces. On the other hand, the alloy exhibits a low corrosion rate in neutral water at supercritical temperatures and in alkaline water at subcritical temperatures, owing to the protection provided by the NiO film. At high temperatures, Alloy 625 exhibits good resistance to oxidation, carburization and sulfidation

while exhibiting an intermediate level of resistance to gaseous halides and molten salt environments. This combination of corrosion resistance properties against a broad range of environment makes Alloy 625 one of the most acceptable materials in the chemical and petrochemical industries.

References

1. Fontana MG (1987) Corrosion engineering, 3rd edn. McGraw-Hill, Singapore
2. Special metals corporation (2000), High-performance alloys for resistance to aqueous corrosion, Publication SMC-026 (2000)
3. Crum JR, Adkins ME (1985) Correlation of Alloy 625 electrochemical behaviour with the sulfuric acid isocorrosion chart. In: Symposium on corrosion in sulfuric acid, National Association of Corrosion Engineers. Unit Committee T-5A on Corrosion in Chemical Processes, p 25
4. Metals Handbook, Corrosion, vol 13, 9th edn. ASM International, Metals Park, Ohio (1987)
5. Crook P (2005) Metals handbook, vol 13B. In: Corrosion: materials. ASM International, Materials Park, Ohio
6. Crum JR, Smith GD, McNallan MJ, Hirnyj S (1999) Characterization of corrosion resistant materials in low and high temperature HF environments. Corrosion 99. NACE-99382
7. Sedricks AJ (1996) Corrosion of stainless steels. Wiley-Interscience, p 378
8. Ganesan P, Renteria CM, Crum JR (1991) Versatile corrosion resistance of INCONEL Alloy 625 in various aqueous and chemical processing environments. In: Superalloys 718,625 and various derivatives. In: Loria EA (ed) TMS, 1991, pp 663–680. 10.7449/1991/superalloys_1991_663_680
9. Lennox CW, Peterson MH, Billow (1982) Corrosion resistance and response to cathodic protection of advanced alloys in sea water. In: Corrosion/82, NACE, Houston, Texas
10. Sedricks AJ (1982) Corrosion resistance of austenitic Fe-Cr-Ni-Mo alloys in marine environments. Int Met Rev 27:321–353. <https://doi.org/10.1179/imr.1982.27.1.321>
11. Chambers GB (2003) Stain. Steel World 57–60
12. Crook P, Meck NS, Houlle P (2005) The caustic dealloying of molybdenum-bearing nickel alloys. In: EUROCORR 2005, Lisbon, Portugal
13. Rebak RB (2006) Industrial experience on the caustic cracking of stainless steels and nickel alloys—a review. Corrosion 2006. NACE-06501
14. Rebak RB, Chambers GB (2001) Corrosion behavior of nickel alloys in caustic solutions. Indianapolis
15. Powell CA (1982) Industrial mechanical engineering, C73/82, 1982, pp 35–43
16. Kain RM (1986) Effect of alloy content on the localized corrosion resistance of several nickel base alloys in seawater. In: Corrosion/86, National Association of Corrosion Engineers, Houston, TX
17. Klein PA, Ferrara RJ, Kain RM (1989) In: Corrosion/89. Proceedings of the 44th NACE Annual Conference. National Association of Corrosion Engineers, 1989
18. Harris JA, Scarberry RC (1971) Effect of metallurgical reactions in INCONEL nickel-chromium-molybdenum Alloy 625 on corrosion resistance in nitric acid. JOM 23:45–49. <https://doi.org/10.1007/BF03355727>
19. Franck EU (1984) Physicochemical properties of supercritical solvents (invited lecture). Berichte Der Bunsengesellschaft Für Phys Chemie 88:820–825. <https://doi.org/10.1002/bpdc.19840880910>

20. Ulrich Franck E (1987) Fluids at high pressures and temperatures. *J Chem Thermodyn* 19:225–242. [https://doi.org/10.1016/0021-9614\(87\)90130-3](https://doi.org/10.1016/0021-9614(87)90130-3)
21. Shaw RW, Brill TB, Clifford AA, Eckert CA, Franck E (1991) Supercritical water a medium for chemistry. *Chem Eng News* 69:26–39. <https://doi.org/10.1021/cen-v069n051.p026>
22. Kritzer P, Boukis N, Dinjus E (2000) Review of the corrosion of nickel-based alloys and stainless steels in strongly oxidizing pressurized high-temperature solutions at subcritical and supercritical temperatures. *Corrosion* 56:1093–1104. <https://doi.org/10.5006/1.3294394>
23. Kritzer P (2004) Corrosion in high-temperature and supercritical water and aqueous solutions: a review. *J Supercrit Fluids* 29:1–29. [https://doi.org/10.1016/S0896-8446\(03\)00031-7](https://doi.org/10.1016/S0896-8446(03)00031-7)
24. Chen CM, Arai K, Theus GJ (1983) Computer-calculated potential pH diagrams to 300 °C. In: EPRI Report NP-3137, vol 2. EPRI, Palo Alto, CA. <https://doi.org/10.2172/5871912>
25. Karaminezhaad-Ranjbar M, Mankowski J, Macdonald DD (1985) Pitting corrosion of Inconel 600 in high temperature chloride solution under controlled hydrodynamic conditions. *Corrosion* 41:197–204. <https://doi.org/10.5006/1.3581991>
26. Postlethwaite J, Scoliar RJ, Dobbin MH (1988) Localized corrosion of molybdenum-bearing nickel alloys in chloride solutions. *Corrosion* 44:199–203. <https://doi.org/10.5006/1.3583925>
27. Stellwag B, Beyer W, Wieling N (1986) In: Electrochemical corrosion testing with special consideration of practical applications. Electrode potentialmonitoring in hot water systems-a method to identify critical corrosion conditions. Germany: VCH Verlagsges, Ref. No.:19009141, INIS Vol 19(3)
28. Kritzer P, Boukis N, Dinjus E (1998) Corrosion of alloy 625 in aqueous solutions containing chloride and oxygen. *Corrosion* 54
29. Bruemmer SM (1989) Grain boundary chemistry and intergranular failure of austenitic stainless steels. In: Materials science forum, pp 309–334
30. Kain V, Prasad RC, De PK (1997) Detection of sensitization and intergranular corrosion of Fe–Cr–Ni alloys. *High Temp Mater Process* 16:183–200
31. Cowan RL, Tedmon CD (1973) Intergranular corrosion of iron-nickel-chromium alloys. In: Advances in corrosion science and technology. Springer, Berlin, pp 293–400
32. Kritzer P, Schacht M, Dinjus E (1999) The corrosion behaviour of nickel-base alloy 625 (NiCr₂₂Mo₉Nb; 2.4856) and ceria stabilized tetragonal zirconia polycrystal (Ce-TZP) against oxidizing aqueous solutions of hydrofluoric acid (HF), hydrobromic acid (HBr), and hydriodic acid (HI) at sub- and supercritical temperatures. *Mater Corros* 50:505–516. [https://doi.org/10.1002/\(SICI\)1521-4176\(199909\)50:9<505::AID-MACO505>3.0.CO;2-X](https://doi.org/10.1002/(SICI)1521-4176(199909)50:9<505::AID-MACO505>3.0.CO;2-X)
33. Kritzer P, Boukis N, Dinjus E (1997) Über die transpassive Auflösung von Nickel-Basis-Legierungen und Edelstählen in sauerstoff-und chloridhaltigem Hochtemperatur-Wasser. *Mater Corros* 48:799–805
34. Kritzer P, Boukis N, Dinjus E (2000) Transpassive dissolution of Alloy 625, chromium, nickel, and molybdenum in high-temperature solutions containing hydrochloric acid and oxygen. *Corrosion* 56:265–272
35. Mitton DB, Zhang SH, Hautanen KE, Cline JA, Han EH, Latanision RM (1997) Evaluating stress corrosion and corrosion aspects in supercritical water oxidation systems for the destruction of hazardous waste. In: NACE international, Houston, TX, USA. <https://www.osti.gov/biblio/509461>
36. Kritzer P, Boukis N, Dinjus E (1998) Corrosion of Alloy 625 in high-temperature, high-pressure sulfate solutions. *Corrosion* 54:689–699
37. Kritzer P, Boukis N, Dinjus E (1998) The corrosion of Alloy 625 (NiCr₂₂Mo₉Nb; 2.4856) in high-temperature, high-pressure aqueous solutions of phosphoric acid and oxygen. *Corrosion* at sub- and supercritical temperatures. *Mater Corros* 49:831–839
38. Kritzer P, Boukis N, Dinjus E (1999) The corrosion of nickel-base Alloy 625 in sub- and supercritical aqueous solutions of HNO₃ in the presence of oxygen. *J Mater Sci Lett* 18:771–773. <https://doi.org/10.1023/A:1006628831166>

39. Tremaine PR, Leblanc JC (1980) The solubility of nickel oxide and hydrolysis of Ni²⁺ in water to 573 K. *J Chem Thermodyn* 12:521–538
40. Kritzer P, Boukis N, Dinjus E (1999) Investigations of the corrosion of reactor materials during the process of supercritical water oxidation (SCWO). In: 6th meeting on supercritical fluids, chemistry and materials, pp 433–442 (English)
41. Borovaya, F.E. , and M.I. Ravich (1968) Solubility of sodiumcarbonate and orthophosphate in aqueous solutions of sodium hydroxide at elevated temperatures, Russian J of Inorganic Chemistry 13(12): 1720–1722.
42. Donachie MJ, Donachie SJ (2002) Superalloys: a technical guide. In: ASM international, Materials Park (Chap. 3)
43. Kumar L, Venkataramani R, Sundararaman M, Mukhopadhyay P, Garg SP (1996) Studies on the oxidation behavior of Inconel 625 between 873 and 1523 K. *Oxid Met* 45:221–244. <https://doi.org/10.1007/BF01046827>
44. Rothman MF (1984) In: Ninth international congress on metallic corrosion, Toronto, Canada
45. Grabke HJ (1998) Carburization: A high temperature corrosion phenomenon, MTI Publication No.: 52, Material Technology Institute of the Chemical Process Industries, St. Louis, Missouri, 1998
46. Lai GY (1984) Internal Report 11620, Haynes International, Inc., 1984
47. Cuevas-Arteaga C, Verhelst D, Alfantazi A (2010) Performance of Alloy 625 under combustion gas environments: A Review. *ECS Trans* 28(24): 61–76<https://doi.org/10.1149/1.3496422>
48. Elliott EA, Ansari AA, Prescott R, RothmanMF (1986) In: Corrosion 85, p13, NACE International, 1985
49. Lai GY, Rothman MF, Fluck DE (1985) In: Corrosion 85, p14, NACEInternational, 1985
50. Kim H, Mitton DB, Latanision RM (2010) Stress corrosion cracking of Alloys 625 in pH 2 aqueous solution at high temperature and pressure. In: Corrosion 2010
51. Copson HR (1962) Effect of nickel content on he resistance to stress-corrosion cracking of iron-nickel-chromium alloys in chloride environments. In: First international congress on metallic corrosion Butterworth, London
52. Sridhar N, Wilde BE, Manfredi C, Kesavan S, Miller C (1991) Hydrogen absorption and embrittlement of candidate containermaterials, Prepared for Nuclear Regulatory Commission Contract NRC-02-88-005, Center for Nuclear Waste Regulatory Analyses – CNWRA 91-008, 1991.
53. Vaughn GA, Greer JB (1980) High strength nickel-alloy tubulars for deep, sour gas well application. In: SPE annual technical conference and exhibition. SPE-9240-MS. <https://doi.org/10.2118/9240-MS>
54. Craig B (2003) Hydrogen damage, corrosion: fundamentals, testing and protection, ASM handbook. *ASM Int* 13:367–380
55. Hicks PD, Altstetter CJ (2012) Comparison of internal hydrogen embrittlement of superalloys 718 and 625. 635–651. 10.7449/1991/superalloys_1991_635_651
56. Berkowitz BJ, Kurkela M, Latanision RM (1981) Effect of ordering on the hydrogen permeation and embrittlement of Ni₂Cr. *Met Soc AIME* 411
57. Watkins M, Greer JB (1976) Corrosion testing of highly alloyed materials for deep, sour gas well environments. *J Pet Technol* 28:698–704. <https://doi.org/10.2118/5622-PA>
58. Cozar R, Rouby M, Mayonobe B, Morizot C (1991) Mechanical properties, corrosion resistance and microstructure of both regular and titanium hardened 625 alloys. *Superalloys* 423–436
59. Frank EA (1991) Custom age 625 PLUS—a higher strength alternative to Alloy 625. In: *Superalloys 718, 625 and various derivatives*, The Metals, Minerals and Materials Society Warrendale, PA, Warrendale, pp 879–893
60. Frank RB, Grimes R (1994) Properties of ultra-high-strength custom age 625 plus alloy. *Superalloys* 718:625–706

61. Czyryca EJ (1997) Fatigue and corrosion fatigue properties of Alloys 625 plus, 718,725 AND K-500. In: Loria EA (ed) Superalloys 718,625,706 and various derivatives, the minerals, metals, and materials society, p 639
62. Data Sheet Custom Age 625 PLUS Alloy <https://f.hubspotusercontent20.net/hubfs/7407324/Material%20Safety%20Data%20Sheets/625%20Plus.pdf>

Chapter 8

Life Management of Alloy 625 Components



Alloy 625 is being used for various applications in the chemical, marine, nuclear, power generation, and aerospace industries [1–9]. These applications range from process tubing, feedstock superheaters, bubble caps, distillation columns for the petrochemical industry [9, 10], heat exchangers and reactor core in pressurized water reactors in the nuclear industry [7], and for marine application [5], owing to its outstanding and versatile corrosion resistance over a wide range of temperatures and pressures. Alloy 625 is also used as turbine shrouds, spray bars, hydraulic tubing, thrust reverser systems, etc. in the aerospace industry. Most of these applications remain at temperatures in the intermediate range of about 0.45–0.63 T_m (where T_m is the melting temperature in Kelvin). The alloy undergoes significant service degradation during service exposure due to microstructure modifications and, consequently, mechanical properties changes [11–13]. Many critical components of Alloy 625 in various plants are likely to have operated for long durations and even may have outlived their design life. Such components need to be replaced beyond their stipulated life. Since the economy of an industrial plant or machinery is directly linked to the service life of its components, efforts are always made to maximize the life of components with their safe operations. A logical and economical decision is to extend the life of a component before its retirement. Life extension of service-spent components is common in thermal power plants based on their operating history, inspections, material testing, and remaining life assessment.

As Alloy 625 is used for applications at temperatures in the intermediate range, slight corrosion or no loss of thickness is envisaged during its thermal exposure in most industrial applications. The alloy, however, undergoes significant microstructural modifications during long-term thermal exposure at intermediate temperatures. It develops complex microstructures by precipitating out several competing phases, namely, γ'' , δ , $Ni_2(Cr, Mo)$ and various carbide phases in the disordered matrix. It has been noted in Chaps. 3 and 4 that the precipitation of γ'' and $Ni_2(Cr, Mo)$ phase particles hardens the austenitic matrix while that of the δ and carbide phases impairs tensile ductility and impact strength of Alloy 625. Available experience with the service exposure of Alloy 625 has demonstrated that it is possible to reverse the

degraded microstructure and rejuvenate the lost properties, at least for the components that have experienced negligible creep deformation [11, 12]. Since the alloy is costly, there are strong economic reasons to delay the retirement of Alloy 625 components merely based on the design life and utilize the alloys to the maximum by extending its life by rejuvenating the lost properties. This chapter aims to assess the performance of Alloy 625 and evaluate its damage and failure mechanisms during industrial application. These mechanisms can be used to devise strategies for the life extension of Alloy 625 components. A few case studies illustrate the successful life extension of Alloy 625 tubes and specific circumstances that led to their failure during service.

8.1 Definitions of Damage, Failure, and Life

Any progressive and cumulative change in the alloy due to service exposure that causes deviations in its properties away from the initial properties and has the potential to affect its current and future performance adversely can be termed as “damage”. The performance in the present context refers to the structural performance of load-bearing components of a plant. Any damage, unless reversed, may lead to the failure of a component.

Failure of a component may be defined as its inability to perform its intended function in a safe, reliable, and economical manner. This inability may be caused by cracking, breaking away, or degradation in the component’s properties below the codal requirement, forcing its premature retirement to avoid unforeseen and catastrophic failure.

The life of a component may be defined as the “period during which the component can perform its intended function safely, reliably, and economically” [14] and is a function of operating conditions. The life of a component is considered expended when one or more of the following criteria is satisfied [14].

- The component has spent more time in the service than the life, based on the design life.
- There is a high probability of its failure based on previous failure statistics.
- The frequency of the repair renders its continued operation uneconomical.
- Observing cracks during a non-destructive examination, which can propagate catastrophically under operating conditions.
- Excessive surface degradation by corrosion or erosion, including the degradation of coatings.
- Excessive grain boundary attack and pitting by oxidation or hot corrosion.
- Severe structural damage by a foreign object.
- Life exhaustion as indicated by destructive sampling and testing.
- Excessive deformation due to creep resulting distortions and unfavorable changes.
- Sudden and complete fracture.

8.2 Basic Philosophy of Life Management

Life assessment and life extension of critical components are essential for the economy and the safety of plants. The basic philosophy of the life management of structural components stems from their damage-tolerance philosophy used for maintaining the structural integrity of commercial transport vehicles, military aircraft, structures, and pressure vessels. The damage tolerance philosophy has evolved on fracture mechanics principles, which envisages the presence of a crack of length, a , in a material and its resistance against the growth of crack under stress (Fig. 8.1a). Under tensile conditions, all structures fail by catastrophic propagation of the crack in the material when its size reaches a critical size (length) a_c , even though the gross stress may be much below the yield or failure stress. The critical crack size depends on factors like fracture toughness, ligament size, loading conditions, etc. The material degradation during service exposure embrittles the alloy and reduces its fracture toughness and resistance against catastrophic growth of the crack, as illustrated in Fig. 8.1b. In a virgin (unexposed) material, the nucleation and growth of a crack follows a two-step sequence as depicted by Curve A. The first step, Region I, correspond to an embryonic, microscopic damage event that may lead to the nucleation of a microscopic crack. The microcrack may even be inherently present in the virgin material or may have nucleated due to events like dislocation rearrangements, coarsening of precipitates, formation of cavities, and microcracks during deformations like creep, fatigue, etc. The second step, Region II, depicts the growth and propagation of the nucleated microcrack with time (Curve A), till it reaches the critical size a_c in a period of t_1 , beyond which the material may fail by the rapid growth of the crack. Reduction in the fracture toughness due to service degradation significantly reduces the critical size, depicted by curve B. In the service degraded alloy, the structure fails

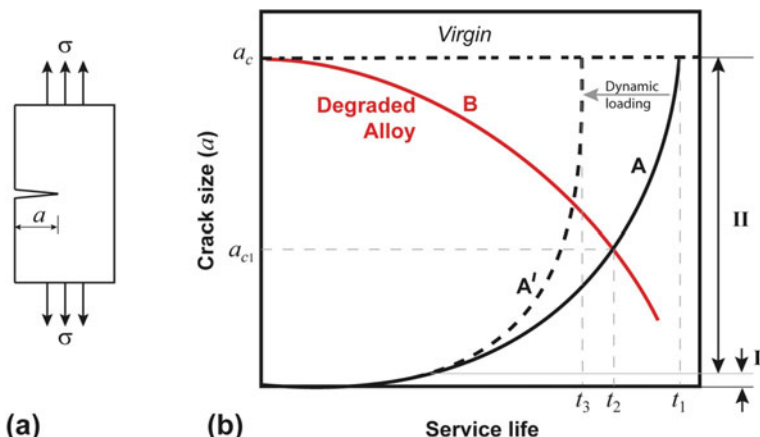


Fig. 8.1 a Schematic depicting a crack of size a under a tensile stress σ . b Variation in the crack size during service exposure in virgin and service degraded material

at a critical size, a_{c1} , which reduces its time to failure to t_2 ($t_2 < t_1$). Dynamic loading conditions, like fatigue, vibrations, etc. accelerate the stage II growth behavior of cracks, resulting in the shift of the failure point toward the left (depicted by the A' curve) to a shorter failure period t_3 .

Conventional non-destructive examination (NDE) techniques like dye-penetrant inspection, ultrasonic measurements, radiography, eddy-current testing, etc. may be used to monitor the stage II size and growth of cracks during periodic inspection of components. However, these techniques are based on the premise that cracks of size larger than their detectable limits exist and will grow slow enough to permit their periodic examination during the regular in-service inspection (ISI). Regular inspections help retire a component before its catastrophic failure. However, there are many instances when these techniques failed to detect cracks before the failure. In such cases, the material degradation during the service has either reduced the crack's critical size below the detectable limit or accelerated its growth too fast to be detected by the NDE technique employed. In such instances, the initiation of the crack alone may lead to the component's failure.

8.3 Damage Mechanisms in Alloy 625 During Service Exposure

Damage mechanisms in Alloy 625 components may change depending upon their operating history. For instance, at “low temperatures”, failure may occur by microstructural modifications, resulting in the degradation of properties below the codal requirement. At “high temperatures”, failure may be dominated by cracking and fracture, which may or may not be promoted by microstructural modifications. The two temperature regimes can be defined based on the rupture ductility of Alloy 625, which depends upon its relative strength compared to the loading stress at operating conditions. As noted in Chap. 4, service age-hardening of the alloy by intermetallic phase precipitates dominate the strength of the alloy up to about 750 °C. Above 750 °C, most intermetallic precipitates coarsen or dissolve, and phenomenon like creep starts dominating. However, the precipitation of intermetallic phases hardens the alloy and reduces its rupture ductility significantly (Sect. 4.5). Service age-hardening may force the retirement of the component or may cause its failure in a brittle manner. On the other hand, above 800 °C, the failure modes may differ due to creep rupture, thermal or mechanical fatigue, tensile properties modified by environmental interactions, or a combination of such processes. Accordingly, the service damage in Alloy 625 can be broadly classified into two categories. First, the microstructural damage, which involves a significant change in the microstructure due to the precipitation of intermetallic and carbide phases that may embrittle the alloy. Second, the structural or mechanical damage, which involves the formation of microcracks and cavities due to deformation of the alloy because of fatigue,

creep, etc. Microscopic studies and mechanical properties evaluation of the service-exposed components can estimate both the damages. Besides, several surface crack detection NDE techniques, like liquid-penetrant tests, ultrasonic inspection, eddy-current inspection, and internal crack detection techniques such as ultrasonic and radiography, can also identify the two damages.

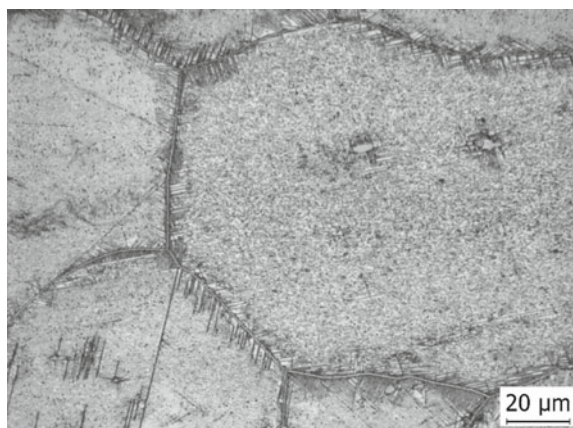
8.3.1 Microstructural Damage

The microstructure of an alloy may change significantly depending upon the operating temperature, exposure time, and loading conditions. In addition, corrosion and oxidation of exposed surfaces may also occur at intermediate to high temperatures depending on ambient conditions. This section primarily summarizes the types of microstructural changes the Alloy 625 undergoes as a function of temperature and time. Detailed descriptions of these changes have been given in Chap. 3. Under deforming conditions, the applied stress may accelerate these changes. At temperatures up to about 450 °C, practically, there may not be any change in the microstructure. However, microstructural defects, like dislocations present due to cold working steps in the fabrication process, may be relieved during exposure at around 400 °C or above.

When the alloy is exposed to temperatures in between about 540–750 °C, fine precipitates of the Ni₂(Cr, Mo) and γ'' phases forms, though the Ni₂(Cr, Mo) phase may not remain stable at temperatures above about 628 °C (Fig. 3.20). During prolonged thermal exposure at temperatures above 650 °C, the δ phase may nucleate at grain boundaries, and the γ'' phase may also transform to its stable δ phase structure (Fig. 8.2).

In the temperature range of about 750 to 950 °C, microstructural changes occur readily due to faster diffusion kinetics. This temperature range is characterized by the

Fig. 8.2 Optical microstructure of a service exposed Alloy 625 tube sample showing the predominant formation of δ phase particles in the vicinity of grain boundaries during prolonged exposure of the alloy at temperatures above 650 °C



precipitation of $M_{23}C_6$ secondary carbides and the δ phase particles at temperatures up to about 900 °C (Fig. 3.20). The two processes extend the precipitation sequences at temperatures < 750 °C but their mechanisms may change due to enhanced kinetics. At temperatures > 950 °C, the molybdenum-rich M_6C carbides may form. Precipitation of secondary carbides (both $M_{23}C_6$ and M_6C) is a consequence of the degeneration of the primary carbides (Sect. 3.2.5). Alloy 625 shows less tendency to form topologically close-packed phases, compared to other Ni–Cr–Mo-based alloys like Hastelloy X, in this temperature range.

At temperatures > 1100 °C, the alloy may experience a high oxidation rate and even incipient melting at about 1288 °C (Fig. 8.3) (Sect. 1.1). The alloy may reach such high temperatures due to overheating or temperature excursions. Although the highest operating temperature of an alloy for structural applications is determined based on its strength and oxidation resistance under operating conditions, the risk of incipient melting during overheating restricts its usage to temperatures up to about 150 °C less than its liquidus temperature. Overheating may cause the failure of components due to local melting (Fig. 8.4) or dissolution of the hardening phases that causes a sudden drop in the strength. Overheating may also deplete alloying elements that provide oxidation resistance and may, therefore, accelerate the oxidation process of the alloy even when it returns to the normal operating temperature. Further, even if the prolonged exposure to over temperature does not result in the mechanical failure, it may cause excessive surface corrosion damage, particularly under hot corrosion conditions, which can reduce the strength of the alloy.

Microstructural modifications may embrittle Alloy 625. Embrittlement of the alloy may nucleate microcracks when the movement of dislocations is impeded by the interfaces between second phase particles, like carbides or δ -phase particles, and the matrix or grain boundaries. Accumulation of dislocations at these interfaces builds up stress at the intersection of slip bands and particles that nucleates crack when the stress concentration is large enough.

Fig. 8.3 An optical micrograph showing incipient melting of grain boundaries in Alloy 625

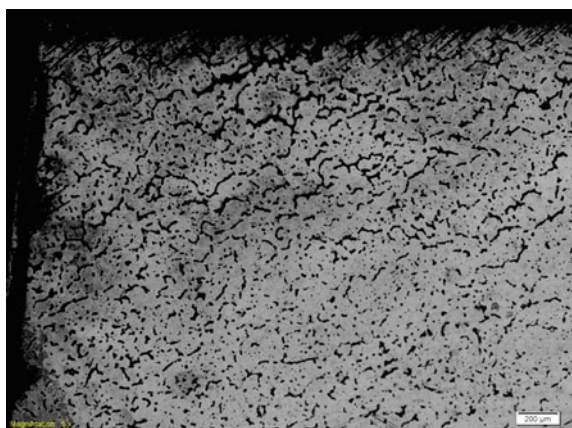


Fig. 8.4 Failure of an Alloy 625 tube due to local melting of the alloy



8.3.2 Structural Damage

Structural damage is due to the accumulation of strain over a long period. The principal types of damages at elevated temperatures may be creep, low- or high-cycle fatigue, thermal fatigue, and even degradation in the coatings of coated surface components like gas turbines. Most of the damages caused by these mechanisms may be localized. However, high-temperature creep may also cause bulk damage in the form of dimensional changes or distortions, which can be easily detected and measured with an accuracy of 0.1% of the strain. This strain can give an idea of the extent of damage compared to the expected failure strain. The localized damage may be in the form of cavitation, which can be evaluated by metallographic or other techniques like radiography and ultrasonic measurements. Standard relationships developed for steels can be used to correlate the degree of creep cavitation with the life expended [15].

8.4 Damage Assessment in Alloy 625

The principal objective of the damage assessment is to extend the life of critical components. This assessment is based on regular monitoring of their health at appropriate intervals for parameters like dimensional change, distortions, microstructure, cavitation, hardness, etc. using non-destructive examination techniques, and repairing and maintaining their health at regular intervals. The challenge is to identify the time of intervals for inspection and life assessment such that it ascertains the uninterrupted performance of components without failures in between such intervals. These intervals are chosen based on conservative estimates of the degradations in the microstructure and the design limiting properties in previous components under typical plant conditions during the period of interval. Under normal circumstances, the remaining life is estimated based on NDE results during such

inspection considering the available data. However, when the access of NDE equipment is limited, a similar analysis of post-service samples extracted from components may be used to estimate the expended life. Any life-limiting defect or flaw observed during inspections makes the basis of its removal.

Alloy 625, in general, offers excellent resistance to uniform and localized corrosion in various kinds of oxidizing and reducing environments (Chap. 7), in most industrial environmental conditions. At high temperatures, the alloy exhibits good resistance to oxidation, carburization, and intermediate resistance levels in molten salt and gaseous environments containing sulfur and halides. However, the alloy is susceptible to hydrogen embrittlement to a certain extent. It reduces the alloy's notch tensile strength, ductility, and threshold stress intensity for subcritical crack growth with little effect on the yield strength. Hydrogen embrittlement may cause the brittle failure of the alloy under tensile loading above a threshold stress. Under pressurized water conditions, the alloy may undergo severe pitting corrosion in acidic waters at subcritical temperatures, which leads to stress corrosion cracking on prolonged exposure. Therefore, in most of its forms, corrosion does not fail Alloy 625 but may adversely affect in exceptional cases like hydrogen embrittlement. Therefore, unfavorable environments of halides, sulfides, and acidic waters at subcritical temperatures may reduce the life expectancy of components. However, estimating the remaining life of components damaged by localized corrosion is somewhat tricky. Nonetheless, localized corrosion mechanisms need to be monitored carefully. Identifying the presence of such life-limiting corrosion mechanisms would provide guidelines to avoid such corosions, which, in turn, would be effective in the component's life management.

The assessment of the damage in Alloy 625 at intermediate temperatures is mainly reported as a loss in mechanical properties due to microstructural modifications. Traditionally, microstructure-based and hardness-based techniques have been used to assess the condition of blades and tubular components of power plants. Similar approaches can be utilized for the assessment of Alloy 625 components, based on the precipitation behavior of $\text{Ni}_2(\text{Cr}, \text{Mo})$, γ'' , δ , M_{23}C_6 and M_6C phases in conjunction with creep rupture data of the alloy at elevated temperatures. If the damage is by creep, standard models [15] correlating microstructural features like cavities can be used to predict life. The expenditure of creep and fatigue life can sometimes be estimated by removing samples from the component and conducting accelerated tests in the laboratory. However, temperatures of the accelerated tests on Alloy 625 are limited up to about 750 °C because tests above it modify the microstructure significantly (Chap. 3). Impact or fracture-toughness tests can determine service degradation in the toughness. However, continuous monitoring of the toughness degradation is rather difficult due to difficulties involved with the extraction of samples on a regular basis.

The remaining life-assessment methodologies depend upon the nature of the dominant damage. Over the years, several techniques have evolved for assessing the service damage, particularly for the life management of power plants [15], based on service degraded properties of the material (microstructural and mechanical properties). The analyzed damage is then utilized to assess the remaining life using standard analytical models based on the operating history, component geometry, and

the nature of the damage. The life assessment of Alloy 625 components can adapt some standard life-assessment procedures of power plants. The following gives a brief description of such life-assessment procedures. These procedures are based on extrapolating past failures and the measurements of hardness, microstructural and ultrasonic data during in-service inspections. In addition, the life-assessment methods based on fracture mechanics analysis of the localized damage can be adopted. All the life-assessment procedures contain inherent deficiencies and uncertainties, leading to inaccuracies in the assessment results. However, a good combination of multiple procedures may evaluate the remaining life with better accuracy.

8.4.1 Assessment Based on Extrapolation of Statistics of Past Failures

History of past failures can provide valuable details about a potential future failure. Historical data provides a limit for the uninterrupted operation of a component with no significant failure. This information can be utilized to determine the time for necessary corrective actions for the good health of a component. This method, however, has limitations as the necessary details about microstructural, thermal, and operating histories of failed components and their failure mechanisms are often difficult to obtain. Further, Alloy 625 with similar life history may have different microstructures or equal strength and hardness with varying life histories because the microstructure of the alloy is susceptible to change at temperatures in the range of 600 – 725 °C (Chap. 3). Variations in the microstructures and histories may bring a significant error in assessing the predicted life.

8.4.2 Assessment Based on Hardness

Strength of the alloy changes during service exposure depending on the time and temperature of the exposure. Change in the strength parameters, like hardness and tensile strength, may be used to estimate an average temperature the alloy has experienced during its service exposure, based on the previous history database. Figure 8.5 shows variation in the hardness with time when Alloy 625 tubes were exposed to service at temperatures about 650 °C. The variation in the hardness can be fitted to a parabolic relation $H = H_0 + At + Bt^2$, where t is the exposure time in hours, H_0 is the initial hardness (of virgin alloy), and A and B are hardness constants. A and B could be fitted to 2.9×10^{-2} and -1.4×10^{-8} , respectively. When the hardness changes as a function of the service temperature (T) as well as the exposure time (t), the hardness change can be correlated to a Larson-Miller parameter (LMP) relationship given by $LMP = T(20.7 + \log t)$ (Sect. 4.7), where, T is temperature (in Kelvin) and t is the exposure time in hours. However, the hardness-based analysis requires good

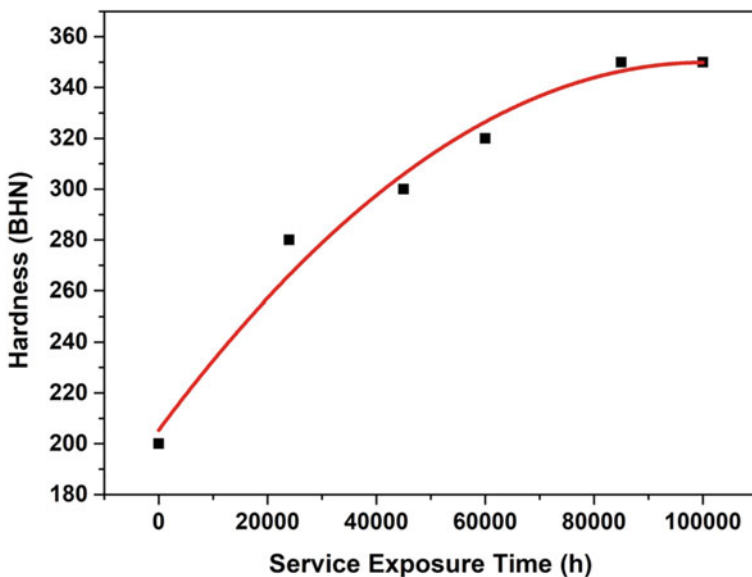


Fig. 8.5 Variation in the hardness of Alloy 625 as a function of time during prolonged thermal exposure at temperatures around 650 °C

statistics of independent measurements because of the poor reproducibility and large scatter in the data due to sensitivity of the hardness to local microstructure. A similar correlation may be established using the tensile strength data, but obtaining a large number of tensile data with varying service histories is rather tricky.

8.4.3 Assessment Based on Microstructure Cataloging

Microstructural modifications can also assess the damage at elevated temperatures. Microstructure-based and hardness-based damage assessments are commonly used to monitor the conditions of blades and tubular components of power plants. Viswanathan [15] has used semi-quantitative and qualitative approaches involving microstructural “cataloging” as a function of temperature to assess the remaining life. He has shown a reasonably good correlation of microstructure with a “weighted average” service temperature for ferritic steels [16]. Similar cataloging of microstructures as a function of an LMP-type parameter, incorporating time and temperature, can be created for Alloy 625. This catalogue can be used as a guide to predict the temperature and the life spent based on the microstructure of the service-exposed samples. However, care would be required in using such catalogues as the microstructural damage up to about 725 °C is primarily due to the precipitation of Ni₂(Cr,Mo) and γ'' phase particles and the two phases impart similar nature of hardening effects. Above this temperature, dissolution and coarsening of particles, or the both, of the

two phases, precipitation of the δ phase and carbide particles start dominating during prolonged exposure. This decreases the alloy's creep strength, which is reflected in the change in the slope of the LMP plot (Fig. 4.38). Nonetheless, the precipitation of the $\text{Ni}_2(\text{Cr}, \text{Mo})$, γ'' , δ , M_{23}C_6 and M_6C phase in Alloy 625 can be utilized to identify the typical temperature range within which the alloy has been exposed during most of the service life [11]. However, this procedure may suffer from the limited microstructure catalog data of Alloy 625. The qualitative microstructural analysis can be coupled with hardness, impact energy, and fracture-toughness data to make semi-quantitative life assessments.

8.4.4 Assessment of Damage by Ultrasonic Measurements

Ultrasonic measurements can be used as an excellent in-situ non-destructive technique to assess the progress of in-service degradation in Alloy 625 based on the ultrasonic measurement parameters in conjunction with hardness. Ultrasonic measurements exploit the reflection of sound waves of high frequency, transmitted through metals, from discontinuities like cracks, cavities, pores, grain boundaries, etc. Kumar et al. [17] have extensively studied the effect of the thermal history of Alloy 625 on ultrasonic parameters. They have correlated variations in the ultrasonic measurements to hardness change with the progress of microstructural degradations [18]. The hardness variation can be due to the precipitation of γ'' , δ and $\text{Ni}_2(\text{Cr}, \text{Mo})$ phases. Kumar et al. [17] have examined many ammonia cracker tubes service exposed at 650 to 680 °C for different periods and compared them with virgin tubes to understand the effect of the progress of microstructural degradation on the ultrasonic parameters. These tubes were divided into six categories, namely: (1) virgin tubes; (2) virgin tubes after a short period of exposure of 747 h in service; (3) virgin tubes after an intermediate period of exposure of 57,194 h in service; (4) virgin tubes after a long period of exposure of 120,000 h in service; (5) re-solution annealed (RSA) tubes; (6) RSA tubes after their second service exposure of 23,000 h. The resolution annealed (RSA) tubes refer to those tubes which had already been exposed for a service of 120,000 h in the ammonia cracker plant, removed from the plant, and subjected to a solution annealing treatment of 1150 °C/0.5 h [19] to restore their mechanical properties to the codal requirements.

Figure 8.6 shows the variation in Poisson's ratio and the attenuation measured in many ammonia cracker tubes in the categories mentioned above. The scatter in the data observed in different types of tubes is listed in Table 8.1. The Poisson's ratio decreases with the progress of microstructural degradation, as reflected in its decrease with an increase in the hardness (Fig. 8.6a). During the initial stages of precipitation, the hardness does not change appreciably and remains within the virgin alloy's scatter band (Table 8.1). However, a noticeable change in Poisson's ratio can be observed. The values of hardness and Poisson's ratio of the virgin tubes lie in the ranges of 140–174 VHN and 0.314–0.318, respectively. In contrast, the Poisson's ratio decreases to between 0.309–0.313 during age-hardening within 747 h,

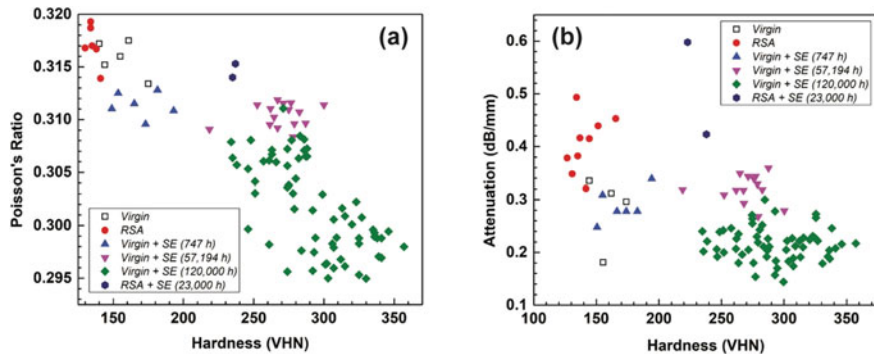


Fig. 8.6 Variation in **a** Poisson's ratio of Alloy 625 and **b** attenuation of longitudinal ultrasonic waves with an increase in the alloy's hardness with the progress of service degradation (after [17])

though the hardness does not change much (140–200 VHN) compared to the virgin tubes, except for a slight increase in the upper bound. This behavior is attributed to the depletion of alloying elements from the matrix, which increases the alloy's modulus and decreases the Poisson's ratio. The hardness/yield strength does not change much because the particles at the initial stages of precipitation are very small to impede dislocations effectively. However, the maximum change in the Poisson's ratio is observed after short exposure times during service, while the shift remains insignificant during the prolonged exposures.

On the other hand, appreciable variation in both hardness and Poisson's ratio is observed during service degradation at intermediate and later stages, though the hardness increase is more prominent. The hardness at intermediate and later stages are in the range of 250–300 and 230–360 VHN, respectively, while the Poisson's ratio at the two stages is in the range 0.309–0.312 and 0.295–0.308, respectively. This data shows that the Poisson's ratio does not change appreciably during prolonged aging. However, a significant increase in the hardness is due to enhanced nucleation and growth of hardening precipitates. A substantial scattering in the hardness and Poisson's ratio values is due to varying extents of damage/degradation upon service exposure for the same duration.

Interestingly, the RSA tubes exhibit lower hardness (126–135 VHN) and slightly higher Poisson's ratio (0.317–0.319) than the virgin tube. The RSA treatment involved solution annealing of the service-exposed tubes, while the virgin tubes are usually supplied in as-annealed condition. The annealing temperature is below the solution annealing temperature, and the alloy's microstructure in the two conditions may vary differently (Sect. 6.3). The annealed alloy may contain some fine precipitates of a second phase. This sensitivity of the Poisson's ratio on microstructure indicates that the Poisson's ratio is a better parameter for monitoring the degradation during the initial period, while hardness is a better parameter for the intermediate and later stages. This is consistent with the response of the ultrasonic velocity on precipitation-hardened aluminum alloys [20, 21] and nickel-base superalloy PE16

Table 8.1 Variations in the Poisson's ratio and the attenuation of ultrasonic longitudinal waves with the hardness of ammonia cracker tubes of Alloy 625 service exposed at temperatures in the range 650–680 °C [17]

Thermal history of tubes	Hardness (HVN)			Poisson's ratio			Attenuation (dB/mm)		
	Range	Mean	Range	Mean	Range	Mean	Range	Mean	Range
Virgin tubes	140–174	155.0 ± 14.0	0.314–0.318	0.3159 ± 0.0017	0.18–0.34	0.281 ± 0.067			
RSA tubes ^a	126–135	135.3 ± 3.9	0.317–0.319	0.3171 ± 0.0019	0.35–0.50	0.405 ± 0.054			
Virgin + SE (747 h) ^b	140–200	169.2 ± 16.8	0.309–0.313	0.3114 ± 0.0012	0.25–0.34	0.288 ± 0.031			
Virgin + SE (57,194 h)	250–300	269.5 ± 18.3	0.309–0.312	0.3104 ± 0.0011	0.27–0.36	0.320 ± 0.026			
Virgin + SE (120,000 h)	230–360	293.4 ± 30.8	0.295–0.308	0.3017 ± 0.0044	0.15–0.28	0.216 ± 0.032			
RSA + SE (23,000 h)	220–240	236 ± 1.4	0.314–0.315	0.3146 ± 0.0009	0.43–0.60	0.510 ± 0.124			

^aRSA: Re-solution annealed. RSA tubes refer to rejuvenated service degraded tubes after a solution annealing treatment of 1150 °C/0.5 h. The tubes were service exposed for 120,000 h [17, 19]

^bSE: Service Exposed. Numbers in the parenthesis refer to the period of exposure. RSA + SE tubes refer to the RSA tubes that were put in the service for the second time

[22]. The ultrasonic velocity and Poisson's ratio in these alloys decrease with their hardness increase. A decrease in the Poisson's ratio with an increase in the precipitation is due to a larger influence of the precipitates on the ultrasonic shear wave velocity than the longitudinal wave velocity. The larger influence of the microstructural change on the shear wave velocity is attributed to its association to two perpendicular planes (propagation and vibration) than the one plane in the case of longitudinal waves [23]. Kumar et al. [17] have also noticed that the nature of precipitates in Alloy 625 affect the ultrasonic velocity and the yield strength/hardness differently. The dissolution of the $\text{Ni}_2(\text{Cr}, \text{Mo})$ phase and the precipitation of the δ phase influence the ultrasonic velocity more than the yield strength. In contrast, dissolution and precipitation of the γ'' phase influence the yield strength more than the ultrasonic velocity.

The attenuation of ultrasonic waves may help identify the abnormal microstructure during in-service inspections. Figure 8.6b shows the variation in attenuation of ultrasonic longitudinal waves with microstructural conditions. All the virgin tubes and the service-exposed virgin tubes exhibited lower attenuation (<0.36 dB/mm). In contrast, the RSA tubes and the service-exposed RSA tubes showed a higher attenuation (>0.36 dB/mm). Even though the starting microstructure and hardness of the RSA and virgin tubes were similar, high attenuation for the RSA tubes has been attributed to the microcracks/voids that formed during service exposure and to the grain growth during their resolution annealing treatment [10]. The effect of microcracks/voids on increasing the attenuation value is consistent with an independent study on a failed tube, which exhibited very high attenuation (0.51 dB/mm) despite low hardness (233 VHN) and high value of Poisson's ratio (0.315) [17]. In addition to Poisson's ratio and hardness, the periodic attenuation measurements may help identify an abnormal change in the microstructure, such as an increase in the grain size or the formation of creep cracks due to abnormal service conditions or an accidental increase in the temperature or load. The limitations of ultrasonic measurements are that it needs extensive technical expertise and knowledge for meaningful results. They cannot be done on parts/sections that are rough, irregular in shape, or very small or thin. Reference standards are needed to calibrate the equipment and characterize flaws.

8.4.5 Assessment Based on Bulk Creep Damage

The bulk creep-damage of components can be assessed by two approaches based on: (1) plant operation data on the time–temperature history of the component in conjunction with standard material-property and plant in-plant inspection (ISI) data [15]; (2) post-service evaluation of the actual component. The damage rules are based on the time spent or the strain accrued at a given time t_i , which can be related to corresponding rupture time or strain [15].

The remaining fraction of the life during service can be calculated as a ratio of the time to rupture of the service-exposed specimen to the expected time to rupture for

the virgin alloy tested under the same conditions. The expended life fraction can be calculated using the life-fraction rule (LFR) by subtracting the remaining life fraction from unity. According to LFR, a failure occurs when $\sum t_i/t_r = 1$, where t_i is the time spent at given stress and temperature, and t_r is the rupture life of the material for the same test conditions. For many materials like steel, the LFR may utilize different temperatures for a given stress value when the material's microstructure remains unchanged. Therefore, this rule must be applied to Alloy 625 keeping in mind the microstructural changes that occur at about 725 °C.

A similar rule can be followed for the accumulated strain, which can be measured with an accuracy of 0.1%. This strain can be compared with the expected failure strain for the material under service conditions to estimate the remaining lives. A sudden increase in the creep rate may indicate its entry into the tertiary creep stage and hence provide a forewarning to failure. The limitation of this damage rule is that it gives a gross estimate of the creep damage due to errors associated with creep test data. Besides, the assumed history based on the material properties may itself bring in significant error due to similar effects of the hardening phases.

The post-service evaluation of actual components involve conventional NDE techniques, dimensional measurements, and creep-life evaluation by accelerated creep-rupture testing. Each of them may also have its source of errors. For instance, dimensional measurements may fail to detect the local creep damage caused by localized strains in the heat-affected zones and regions of stress concentrations in the base metal, which may even cause accelerated failure. Estimating the remaining creep life based on accelerated creep-rupture tests at temperatures well above the service temperature requires the stress value as close to the service stress value as possible because of the compliance of only iso-stress creep conditions with the life-fraction rule employed. Despite these limitations, the post-service evaluation techniques make better estimations based on actual properties developed during ISI intervals. However, this technique is relatively expensive and time-consuming as it involves destructive tests requiring the removal of samples from operating components. Removal of samples limits their number and locations and requires plant shutdown for extended periods.

The best strategy can be to combine the two approaches. The plant operation data can be utilized to identify critical locations and the extent of detailed evaluations required, followed by a reasonable selection of samples and test conditions of post-service assessment.

8.4.6 Assessment Based on Fracture Mechanics Analysis

The remaining life of thick-wall components can be estimated by combining damage initiation criteria with crack-growth data using fracture-mechanics analysis under different loading conditions. The driving force for the crack growth is a function of the stress and the strain rate far from the crack tip, depth of the crack, and the microstructural state of the alloy. Correlations between the crack growth rate in the material

as a function of the service life and the microstructure can be established based on prior data or testing of the samples harvested from service-exposed components. As noted earlier, the precipitation of various intermetallic phases during service exposure of Alloy 625 manifests itself in reducing its fracture toughness, while grain boundary carbides and embrittling phases like δ -phase enhance the crack growth rate along their interfaces. The effect of such microstructural modifications on the component's life can be estimated using finite-element analysis or standard analytical models to calculate the crack growth rate as a function of the loading stress, crack size (a), material constants, and geometry of the component.

Fracture mechanics analysis-based assessment is illustrated considering an example of the growth of a longitudinal crack on the outer surface of an Alloy 625 tube of an outer diameter of 89 mm and thickness 9 mm under fatigue loading at about 650 °C. The internal pressure of the tube would tend to open up the crack along axial direction under the influence of the hoop stress, which may lead to its failure when the crack reaches a critical size, a_c , beyond which it may rupture the tube by catastrophic propagation of the crack. The value of the a_c would be governed by factors like K_{IC} , J_{IC} , wall thickness, and remaining ligament thickness. For the virgin alloy ($K_{IC} = 140 \text{ MPa m}^{1/2}$ [24]), the critical crack size a_c can be calculated using widely accepted analytical or numerical approaches. The critical size can be calculated using the following relationship [25]

$$a_c = \frac{K_c \pi}{8\sigma_f \ln \left\{ \sec \left(\frac{\pi M \sigma_h}{2\sigma_f} \right) \right\}} \quad (8.1)$$

where K_c is the fracture toughness, σ_f is the flow stress, σ_h is the hoop stress given by $\frac{pd}{2t}$, p is the internal pressure, d and t are inner diameter and thickness of the tube, and M is the “Folias factor” expressed as $\sqrt{1 + \frac{a^2}{(r_i * t)}}$, where r_i is the inner radius of the tube. The flow strength σ_f was taken as $(\sigma_y + \sigma_u)/2$, where σ_y and σ_u are yield strength and ultimate tensile strength of the virgin alloy, taken from the Special Metals data sheet [26]. Equation 8.1 gives a critical crack length of 65 mm for the catastrophic propagation of the crack in the virgin tube.

Assuming the crack growth in the Paris Law regime under fatigue loading conditions, the fatigue crack growth rate per cycle, da/dN , can be given by the following.

$$\frac{da}{dN} = C(\Delta K)^m \quad (8.2)$$

where C and m are material constants. The life of the tube is estimated as a function of initial crack size (i.e., 4, 6, 8, 10 mm) and a width (depth) up to half-thickness (i.e., 4.5 mm) using the three-dimensional Finite Element Method (FEM) analysis. A cyclic load of the amplitude of 14 MPa with zero stress ratio ($\sigma_{min}/\sigma_{max}$) was applied on the inner surface of the tube till its failure. The tube was assumed to have failed when the axial size of the crack reached a critical value beyond which it may rupture

by catastrophic propagation of the crack or its size along the radial direction reaches through-thickness where it would develop a leak before catastrophic rupture. The fatigue life estimation analysis was carried out for the virgin and service-exposed materials.

Virgin Alloy For the virgin alloy, fracture toughness and fatigue parameters are $K_{IC} = 140 \text{ MPa m}^{1/2}$ and m and C as 2.798 and $5.7 \times 10^{-12} \text{ Nm}^{3/2}$, respectively [24]. Figure 8.7 shows variation in the crack length in axial and radial tube directions. The number of cycles to failure decreased with increasing the initial size of the crack. This analysis shows that the virgin tube would fail by the through-thickness leak of the tube for all the cases of initial crack length considered. The crack reached through-thickness in the radial direction much before it reached the critical size of 63 mm in the axial direction. The tube would develop a leak after about 1.95×10^5 cycles of fatigue if the initial crack length were 4 mm and would fail after about 7.2×10^4 cycles if the initial crack length were 10 mm. The axial length of the crack in both cases would be about 22 mm at the time of the leak, which was much below the catastrophic failure of the tube under hoop stress conditions.

Service-Exposed Alloy Two types of service degradations, namely: (1) simply a reduction in the toughness of the alloy by about 50%, as caused by the precipitation of the hardening Ni₂(Cr, Mo) and γ'' phase particles; and (2) 50% reduction in the toughness and 30% increase in crack propagation rate due to the precipitation of embrittling phases, like the δ phase and grain boundary carbide films, were considered. The critical crack length along the axial direction for catastrophic failure in such service-exposed alloys (50% toughness loss) would be reduced to about 38.5mm (by about 40%), indicating that the tube would develop a leak much before its catastrophic failure. The toughness and fatigue parameters for the two service degraded conditions were assumed as (1) $K_{IC} = 70 \text{ MPa m}^{1/2}$ (50% decrease with respect to that of the virgin alloy), and $m = 2.798$ and $C = 5.7 \times 10^{-12} \text{ N/m}^{3/2}$, and (2) $K_{IC} =$

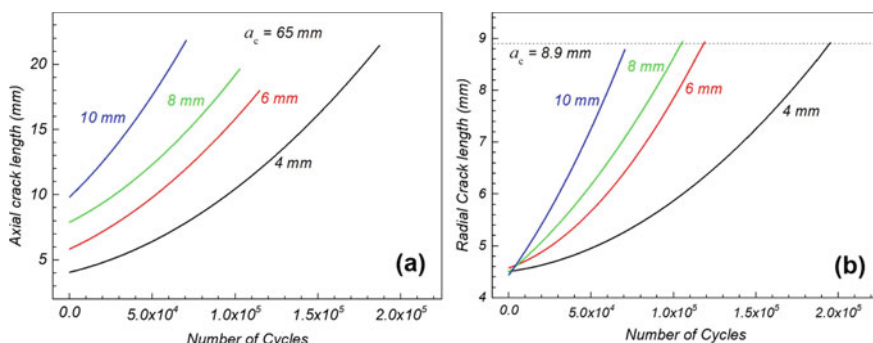


Fig. 8.7 Variation in **a** axial and **b** radial length of cracks as a function of 14 MPa of fatigue cycles in a virgin 8.9 mm thick Alloy 625 tube. The horizontal broken line signifies the size at which the tube would fail by developing a through-thickness leak

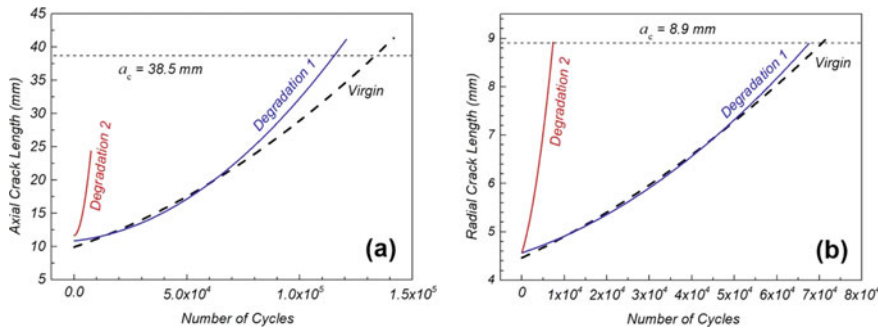


Fig. 8.8 Plots represent the effect of different types of service degradations on the fatigue life of the tube. Service ‘degradation 1’ assumes a reduction in the alloy’s toughness by about 50%, while ‘degradation 2’ assumes a 50% toughness reduction along with a 30% increase in crack propagation rate. Plots show variation in the **a** axial length and **b** radial length of a 10 mm long crack as a function of 14 MPa of fatigue cycles in virgin and service exposed Alloy 625 tubes. The horizontal broken line signifies the size at which the tube would fail by catastrophic failure or developing a through-thickness leak

70 MPa m^{1/2} (about 50% decrease), and $m = 3.637$ (30% increase in crack propagation rate with respect to that in virgin alloy) and $C = 5.7 \times 10^{-12}$ N/m^{3/2}. The fracture analysis of such alloys indicates that the precipitation of grain boundary carbides and embrittling δ phase significantly reduces the life of the tube. 30% increase in the crack growth rate reduced the life by about 90% as the tube would develop leak after about 7.4×10^3 fatigue cycles compared to about 7.2×10^4 cycles when the crack growth rate was increased by 30% (Fig. 8.8). Simply reducing the fracture toughness by 50% would reduce the fatigue cycles to about 6.7×10^4 for a crack with an initial length of 10 mm size. The number of cycles can be translated into the period for the remaining life based on the frequency of the load cycle.

A similar analysis can be performed for the damage caused by creep conditions. The essential parameters required for life assessment of a component under creep loading are creep rate constant (A), creep rate exponent (n), crack-growth rate coefficients (b), and crack-growth rate exponents (m), crack size, a , and geometry of the component. These parameters can be either assumed from the previous data or generated by non-destructive examination during ISI and creep testing of samples. A detailed description of this approach is given by Viswanathan [15].

This analysis demonstrates that the remaining life for failure can be predicted as a function of defects and service degradation for a given loading condition and can be utilized for life assessment of structures in which microcracks are observed during routine in-service inspections. The crack growth period, t_g , can be assumed as the remaining life. The approach can be combined with the incubation time for crack initiation in the service degraded material when no crack is observed. The incubation time, t_i , of the crack can be estimated using the reference stress and samples representing the component’s microstructural state and service life. If the incubation time t_i is less than the desired service life, a crack-growth analysis can be

performed to calculate the crack growth life, t_g . The safe operation of the component for the remaining period can be decided if the total crack life, $t_i + t_g$, is less than the desired service life. Inaccuracies in this technique may arise due to errors in selecting proper values for the constants because of the large scatter in the crack-growth data. However, better accuracy can be achieved by performing tests on actual samples.

8.4.7 Assessment Based on Microstructural Examination of Cavitation Damage

Cavitation may be the principal damage mechanism at heat-affected zones, high-stressed regions, and embrittled regions like grain boundary carbide films and δ phase particles. The damage by creep cavitation can be assessed by microstructural examination of the surface. The microstructural studies can be carried out by replicating or in-situ examination of the surface and ex-situ investigation of the extracted service-exposed samples during preventive maintenance. Neubauer and Wedel [27] have classified the stage-wise creep damage in steels' microstructures and classified the damage into four classes. These classes are (1) Class A damage when the cavities are isolated; (2) Class B damage when cavities are oriented; (3) Class C damage when cavities are linked, and microcracks appear; and (4) Class D damage when macrocracks form. Figure 8.9 depicts different stages of creep and concomitant microstructural damage. The four damage classes have been correlated to 0.46, 65, 0.81, and 1.0 fractions of the expended life [27]. This type of microstructural-based damage analysis is often utilized to estimate the remaining life of thermal power plants. Alloy 625 may also exhibit similar microstructural damage in creep dominant service conditions (Fig. 8.10). The plant history data can establish similar correlations between creep damage microstructures and operation history parameters like tensile stress, temperature, and time through the Larson and Millar Parameter (LMP). These correlations can be used to semi-quantify the creep damage in Alloy 625 components and estimate their remaining life.

8.5 Life-Limiting Damage Criteria for Alloy 625 Components

Life-limiting damage refers to the extent of the damage beyond which it is unsafe to operate critical components due to catastrophic consequences. Such damages call for immediate replacement of components. Several such damages have been identified, which can be used to define the life-limiting damage criteria in Alloy 625. These criteria may make the basis for the acceptance of the service exposure damage for the continued operation of Alloy 625 components. They may be employed

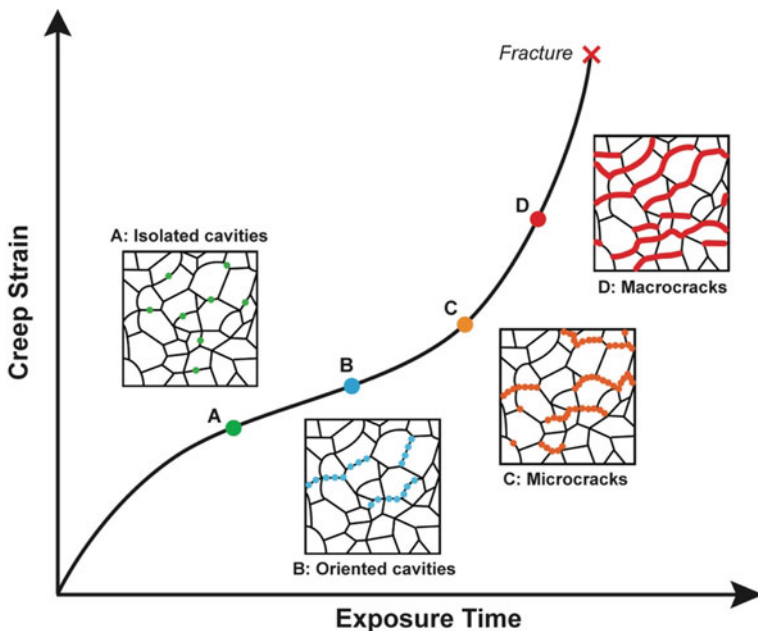
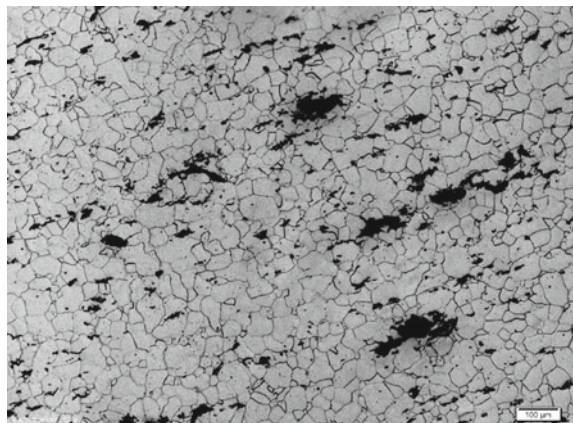


Fig. 8.9 Schematic illustration of different stages of creep cavitation and concomitant microstructural damage [27]

Fig. 8.10 An optical micrograph exhibiting Class D creep damage in an Alloy 625 tube



with pre-defined tolerances depending upon the criticality of the component and its function.

8.5.1 Maximum Hardness of 350 BHN

The hardness of Alloy 625 increases with service exposure at intermediate temperatures (600 - 725 °C). Figure 8.5 shows the hardness variation of the alloy with time when exposed at about 650 °C. The alloy tends to reach a plateau in hardness at a value of about 350 BHN. The alloy with a hardness in this range is very brittle with little ductility at room temperature. It exhibits very low impact energy (~10 J) and limited flaw tolerance capability with $K_{IC} \approx 40 \text{ MPa m}^{1/2}$ [11]. The alloy's microstructure contains a high-volume fraction of embrittling intermetallic and carbide phase particles. The alloy may be susceptible to catastrophic failure for impact loading conditions. A criterion limiting the maximum hardness of the service-exposed alloy to 350 BHN can be easily employed based on hardness measurements during routine maintenance. However, the hardness measurements are associated with significant errors, particularly during ISI, as they are usually carried out using a portable rebound type hardness tester, which is highly dependent on surface preparation and skills of the person carrying out the test.

8.5.2 Minimum 10% Elongation at the Operating Temperature

This criterion is developed considering the most conservative approach of nuclear reactor pressure vessel design, which is one of the most critical engineering components with respect to its operation and consequential damage. Neutron irradiation of components in a nuclear reactor severely affects material's yield strength, ductility, and creep properties. In general, the yield strength increases, and ductility reduces with neutron irradiation. Studies have shown that a minimum 10% elongation at operating temperatures is a safe limit with a minimum of 95% confidence (Fig. 8.11) [28] for the safe operation of the reactor pressure vessel. The service exposure of Alloy 625 at intermediate temperatures exhibits embrittling behavior similar to that of neutron irradiation, i.e., a reduction in ductility and an increase in the yield strength. A similar acceptance criterion of a minimum of 10% elongation at operating conditions may be adopted for the safe operation of Alloy 625 critical components. Multiple testing of samples from a given location may be considered to take care of the scattering associated with sample location, specimen preparation, and testing errors.

8.5.3 Maximum Microstructural Damage

In-situ metallography is commonly used to assess damage in carbon and low alloy steels due to carbide coarsening and cracking by creep, fatigue, high-temperature corrosion, hydrogen embrittlement, intergranular corrosion, etc.

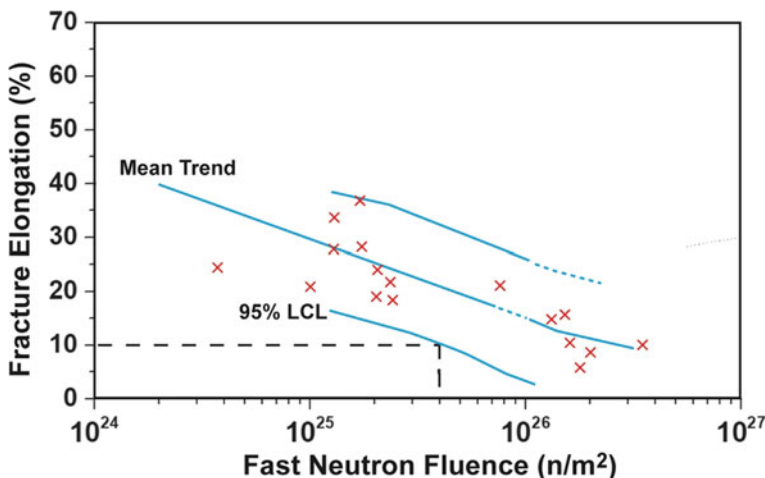


Fig. 8.11 The figure depicts a minimum 10% elongation at operating temperature as a safe limit with a minimum of 95% confidence for the safe operation of a nuclear pressure vessel. The data shows variation in fracture elongation as a function of accumulated fast neutron radiation damage (fluence) in SS304 steel irradiated at 550 °C [28]

Maximum microstructural damage is identified to limit the life of the component. Establishing a similar microstructure-based criterion for Alloy 625 is rather challenging to define because of the limitation of the standard ISI techniques to resolve its life-limiting microstructural features. As noted earlier, age-hardening of the alloy is due to the precipitation of intermetallic phase particles of various types. These particles can only be imaged by electron microscopy (Chap. 3). Even a criterion based on the precipitation of grain boundary carbides, similar to that used for steel structures in power plants, is rather difficult to adopt for Alloy 625 because grain boundary carbides in nickel-base superalloys grow at very slow rates and remain very fine. The thickness of grain boundary carbide films is often close to the resolution limit of the optical microscope. Further, grain boundaries thickness measurement may be associated with significant errors due to improper (deeper) surface etching or the replication process. These limitations may result in a substantial error in quantifying grain boundary carbides in any nickel-base superalloys. Such quantification requires advanced metallography techniques, such as scanning and transmission electron microscopy, capable of analyzing microstructures with higher resolution, which are usually beyond the scope of regular ISI. However, precipitation of the δ phase in Alloy 625 coincides with the precipitation of grain boundary carbides, and profuse formation of the δ phase particles (as needle shape particles) can be observed by optical microscopy unambiguously (see, Fig. 8.2). A criterion based on the precipitation of the δ phase particles may be developed for defining the maximum microstructural damage.

8.5.4 Life Expenditure and Minimum Thickness Criteria for the Creep Dominant Damage

When creep deformation is predominant, the fraction of the expended creep life can be estimated based on creep-rupture tests of service-exposed samples. The fraction of the life spent during service can be calculated using the ratio of the time to rupture of the service-exposed specimen to the expected time to rupture for the virgin alloy under the same conditions. A fixed percentage of the expended life can be defined as the life-limiting damage criterion for self-loaded components depending upon their criticality. However, for pressure-containing components, the criterion should be based on the minimum thickness of the pressure-retaining boundary to keep the hoop stress at the maximum operating pressure below the allowable design stress, including the safety factor.

8.5.5 Class D Damage for Creep Cavitation

The Neubauer and Wedel [27] classification of creep cavitation damage mentioned in Sect. 8.4.7 calls for different actions for the continuing service of the component. While the Class A damage does not require immediate remedial action, the Class B damage calls for their continuous monitoring and reinspection within a period of 1½ to 3 years. The Class C damage calls for limited service until repair, while the Class D damage calls for an immediate repair or replacement [15]. These recommendations are quite conservative, and a similar criterion of Class D damage for limiting the life of creep damage in Alloy 625 components can be adopted.

8.6 Case Studies on the Performance of Alloy 625 Ammonia Cracker Tubes

Alloy 625 is being used for various applications ranging from tubing in the process industry to thrust-reverser systems in the aerospace and exhaust manifolds of Formula 1 automobiles. Many researchers have reported service degradation of ammonia cracker Alloy 625 tubes during prolonged exposure at about 650 °C [10–12, 29–31]. Most of these studies have reported service degradation due to microstructural modifications and little creep deformation. These tubes are designed for service in annealed conditions with a maximum permissible creep of 1% in 10^5 h at 717 °C and 15.7 MPa pressure [12]. A battery of ammonia cracker tubes are stacked in a vertical rectangular furnace, which heats them from outside to maintain the process temperature of the endothermic cracking reaction (Fig. 8.12). Each tube measures approximately 90 mm in outer diameter, 8.9 mm in wall thickness, and 13 m in length with an effective height of about 12 m inside the furnace. This section gives

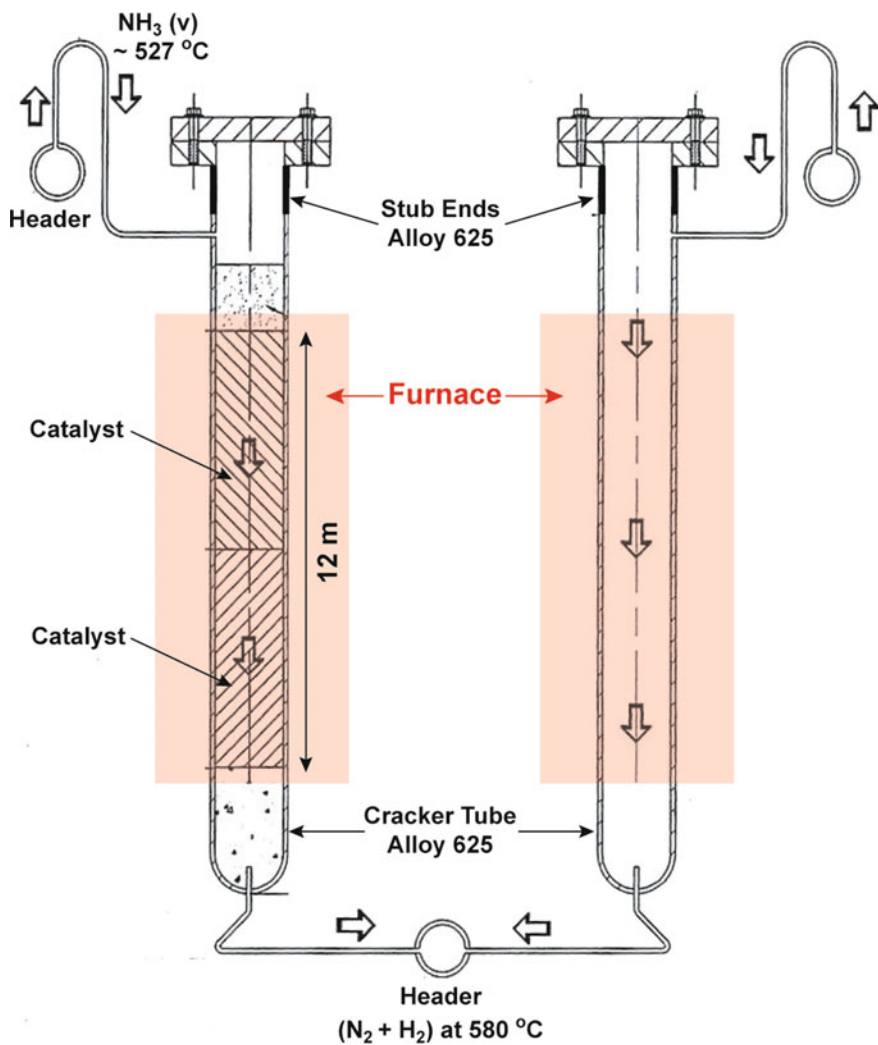


Fig. 8.12 A schematic depicting the arrangement of Alloy 625 tubes in an ammonia cracker unit

a brief description of a few cases that illustrate the performance of Alloy 625 tubes, including their failure in unusual conditions in ammonia cracker plants.

8.6.1 Service Degradation of Tubes and Rejuvenation of Lost Properties

Chakravarty et al. [11] have carried out extensive studies on microstructural modifications and concomitant mechanical properties' degradation of an Alloy 625 tube during service exposure of 100,000 h. They have shown that mechanical properties degradation is a consequence of microstructure modifications, which are sensitive to temperature. They have used the precipitation behavior of various phases as markers to delineate the actual temperatures the tube had experienced at different tube locations during service (Fig. 3.20). They studied the microstructural degradation at three areas designated as "top", "middle", and "bottom", respectively at 1, 6, and 11 m distance from the top of the 12 m length inside the furnace. Chakravarty et al. [11] have demonstrated that the examined ammonia cracker tube had experienced increasing temperature from top to bottom in the range of about 600 - 800 °C. The service-exposed alloy exhibited a mixture of fine Ni₂(Cr, Mo) and γ'' precipitates in the top section, predominantly coarse γ'' phase particles in the middle section, and the co-precipitation of very coarse γ'' and δ phase particles in the bottom section of the tube (Fig. 8.13). In addition, the tube exhibited the precipitation of M₂₃C₆ carbides at grain boundaries in the entire length of the tube. The thickness of the carbide layer increased monotonically from top to bottom (Fig. 8.14).

The precipitation of the Ni₂(Cr, Mo) phase in Alloy 625 is known to occur during prolonged aging at temperatures lower than 628 °C and that of the γ'' particles over a temperature range of 600 to 750 °C, with its nose corresponding to the fastest kinetics at around 650 °C (Fig. 3.15). The precipitation of the Ni₂(Cr, Mo) and γ'' phases indicated that the temperature of the tube did not exceed beyond about 650 °C in the top section and about 750 °C in its middle section, at least for a significant period toward the end of its service life. Co-precipitation of carbide and the δ phases occurs only at temperatures around 800 °C. The observation of M₂₃C₆ carbide in the entire tube length is consistent with its precipitation at temperatures in the range of 550–1000 °C. The size of the γ'' phase particles increased monotonically from top to bottom. The precipitation of the δ phase occurred at the expense of γ'' phase, as evidenced by the γ''-precipitate free zones around δ particles (Fig. 6 of Ref. [11]). An increase in the size of particles and the thickness of the grain boundary carbide film from top to bottom also attested to the increasing tube temperature from top to bottom as the exposure period was the same for the entire tube length.

Table 8.2 compares the mechanical properties data of the service-exposed tube with that of the virgin tube material. From this table, it was clear that a significant loss of properties had occurred throughout the cracker tube during service with a progressive increase in microstructural degradation from top to bottom. After service exposure, the room temperature yield strength along the tube length had almost doubled. This increase in strength was accompanied by a massive reduction in the ductility and impact properties, making the alloy vulnerable to catastrophic failure. While the exposed tube was uniformly hardened due to the precipitation of γ'' particles, the top section of the tube was hardened most due to the precipitation of additional

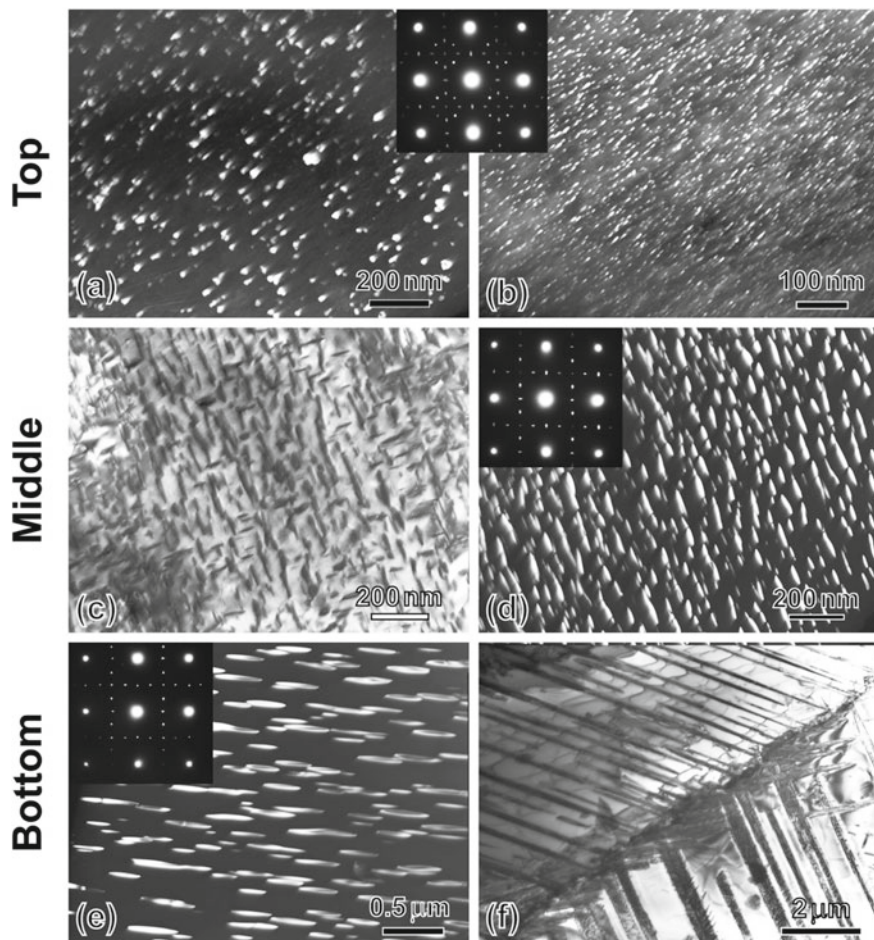


Fig. 8.13 Microstructural conditions of the alloy at the top, middle and bottom sections of an Alloy 625 ammonia cracker tube, as revealed by transmission electron microscopy. The ammonia cracker tube was exposed for 100,000 h at about 650 ± 50 °C. Insets show electron diffraction patterns from corresponding regions confirming the presence of different phases

Ni₂(Cr, Mo) particles, whose volume fraction was as high as that of γ'' particles. However, these properties improved at elevated temperatures. Yield strengths of all the sections showed a decreasing trend with increasing test temperatures, except in the temperature range 300–550 °C where the yield strength showed either a plateau or a slight increase within the temperature range [11]. The ultimate tensile strength of both bottom and middle sections showed a slight increase with test temperature up to 600 °C, whereas the ultimate tensile strength of the top area showed a slight decrease up to about 450 °C. The UTS of all the sections dropped drastically with

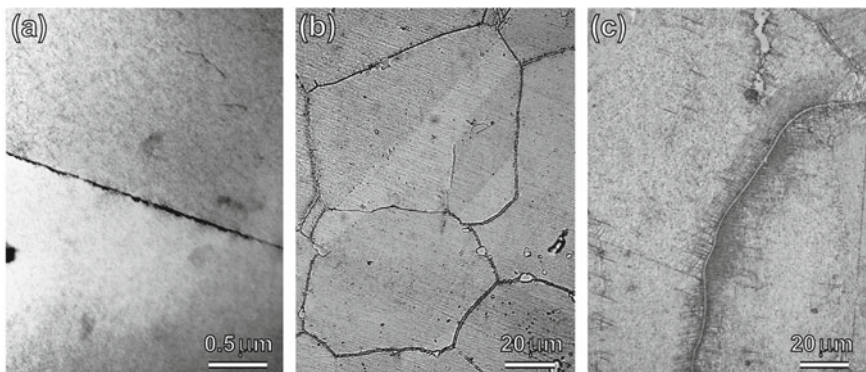


Fig. 8.14 Precipitation of carbide films along grain boundaries at the **a** top, **b** middle and **c** bottom sections of Alloy 625 ammonia cracker tube after a service exposure of 100,000 h at about $650 \pm 50^\circ\text{C}$. (**a**) is a transmission electron microscopy image, while (**b**) and (**c**) are optical images

Table 8.2 A comparison of room temperature tensile strength and ductility of virgin and service-exposed wrought Alloy 625 ammonia cracker tubes [11]

Property	Virgin	Service-exposed alloy		
		Top	Middle	Bottom
Yield strength (MPa)	345	785	710	613
UTS (MPa)	758	1051	867	810
Elongation (%)	50	18	10	9

The virgin tube properties are averages of corresponding ranges given in the source

a further increase in the test temperature. However, the ductility improved initially, followed by a rapid rise, with temperature for all the sections.

The presence of continuous and thick carbide precipitation at grain boundaries reduced the toughness of the tube, as observed in middle and bottom specimens. The specimens from the bottom section exhibited the maximum microstructural damage. It showed a continuous carbide film at grain boundaries and the conspicuous acicular δ precipitates in its vicinity and within the matrix. Similar degradation in mechanical properties, particularly fracture properties, have been reported in other nickel-base superalloys [32, 33]. The poor room-temperature ductility and low impact toughness (10–40 J) of the bottom section even at 300°C made the exposed tube vulnerable to catastrophic failure. Fracture mechanics evaluation indicated that the exposed material had the minimal flaw tolerance capability at a $K_{\text{IC}} \approx 40 \text{ MPa}\sqrt{\text{m}}$ [11], consistent with another report by Thomas and Tait [9]. The severe loss of ductility in the bottom section can be attributed to the profuse precipitation of δ particles, which act as internal notches at grain boundaries, and the continuous carbide films that block the transfer of the slip across grain boundaries. These factors promote

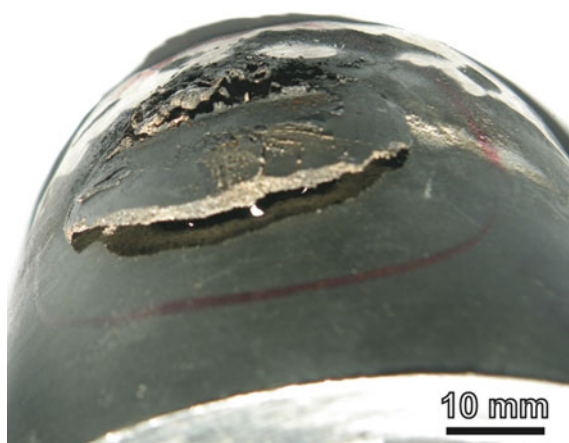
cracking locally, thereby limiting the attainment of the ultimate strength and lowering of ductility and fracture toughness.

A solution annealing treatment at 1160 °C for 2 h reversed the damage due to service exposure. The solution annealing treatment dissolved all the hardening phase particles and carbides formed during service exposure and recovered all mechanical properties to the codal requirements [11].

8.6.2 Failure of Tubes at a Temperature Less Than 550 °C

The top ends of cracker tubes are butt welded by stub ends (Fig. 8.12) that facilitate lip-sealed and flange joints for leak tightness and strength. The stub ends remain outside the furnace. The ammonia vapors from the inlet header enter the tubes at 527 °C below the stub ends outside the furnace. Stub ends, therefore, experience a temperature not more than about 525 °C. However, in an incident, multiple stub ends failed in a brittle manner (Fig. 8.15), at a location sufficiently away from the weld joints, only after a service exposure of about 47,000 h [30]. Transmission electron microscopy evidence confirmed that the failed stub end alloy always experienced a temperature much below 600 °C as its hardness and microstructure remained similar to that of the virgin, devoid of any precipitate like $\text{Ni}_2(\text{Cr}, \text{Mo})$, γ'' or δ phase particles which form at about 600°C and above. However, the microstructure exhibited the formation of continuous layer of M_{23}C_6 carbide film along grain boundaries, which had caused its failure in a brittle manner (Fig. 8.15). The formation of grain boundary carbides after 47,000 h of operation at a temperature less than about 550 °C was somewhat surprising because the cracker tubes are known to easily survive a full-service life of 100,000 h at a much higher average temperature of about 670 °C [11]. The subsurface in the vicinity of the ruptured stub end revealed a homogeneous network of secondary and tertiary cracks around primary cracks, indicating

Fig. 8.15 A photograph of a stub-end failed at a temperature less than 550 °C. Reprinted from Ref. [30], Copyright (2013), with permission from Elsevier



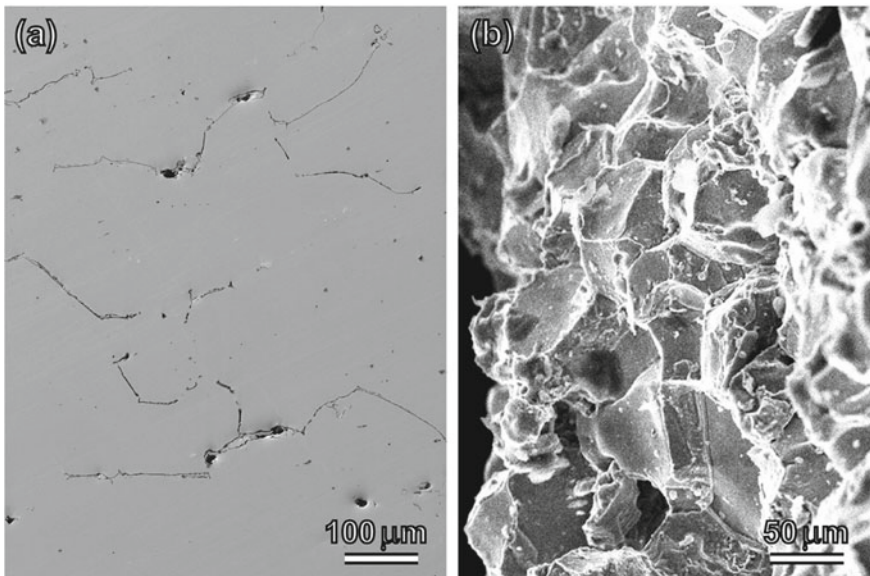


Fig. 8.16 **a** Optical micrograph of an un-etched failed stub-end sample revealing thick carbide layers along grain boundaries. **b** Secondary electron micrograph of the fractured surface of a failed stub-end showing intergranular brittle nature of the fracture. Reprinted from Ref. [30], Copyright (2013), with permission from Elsevier

a weakening of grain boundaries due to the formation of a thick $M_{23}C_6$ film along with them (Fig. 8.16a). The weak nature of grain boundaries was evident from the brittle intergranular fracture mode (Fig. 8.16b). This unusual precipitation of the $M_{23}C_6$ carbide film at grain boundaries, at low temperatures, and in a shorter life span was found to be due to the alloy's chemistry, which contained much higher nitrogen content than usually present nickel-base superalloys.

The stub end alloy contained about 250 ppm of nitrogen, which was about an order higher than that Alloy 625 (Chap. 3), along with about 330 ppm of carbon. The formation of the $M_{23}C_6$ carbide film occurred in less than half the designed life and at a temperature much below its formation temperature. Nitrogen levels in superalloys are usually kept at less than 50 ppm. The carbon content is also kept low to about 300 ppm. This carbon is further reduced to negligible levels in the austenite matrix by scavenging out by strong carbide formers like titanium, niobium, and hafnium that form MC carbides during solidification. The secondary $M_{23}C_6$ carbide precipitates due to the degeneration of the primary MC carbides during service exposure at temperatures between 550 and 1000 °C, which is a prolonged process. Hence, the service exposure of even 100,000 h in Sect. 8.6.1 was insufficient to form enough grain boundary carbide film to cause the rupture. However, when a high amount of nitrogen was present, primary carbide forming elements (titanium, niobium, and hafnium) preferred to form nitrides, instead of carbides, due to their stronger affinity to nitrogen [30]. The formation of the nitrides appeared to

consume titanium/niobium required to form primary MC carbides and, consequently, left free carbon in the matrix for the formation of $M_{23}C_6$ carbides, which otherwise form after slow degeneration of the primary MC carbides at higher temperatures. This free carbon easily formed carbide layers at grain boundary during service at a lower temperature and comparatively in a shorter time period. The higher nitrogen content in the alloy may have resulted from a poor quality of the raw material used or a poor control of the melting conditions.

8.6.3 Fish Mouth Opening of a Tube by Temperature Excursion

In an unusual incident, a cracker tube failed by creep rupture after an operation period of about 5600 h. The ruptured tube showed a typical “Fish-Mouth Opening” of about 400 mm length and 150 mm width (Fig. 8.17). The tube’s “fish-mouth” opening in the longitudinal direction is a classical failure mode when the hoop stress exceeds the yield stress at high temperatures. The thickness of a middle portion of the “fish mouth” had reduced by about 50% to 4.6 mm, from an initial thickness of 8.9 mm. This heavy deformation indicated that the tube was subjected to creep deformation for a considerable time. This type of rupture was rather unusual for ammonia cracker tubes as it was the first such incident in about 75 years of the cumulative history of ammonia cracker plants. However, such types of failures are quite common in tubular boiler structures due to temperature excursion beyond their design temperature due to (1) short-term overheating and (2) long-term overheating [15].

The short-term overheating failure occurs when the temperature excursion exceeds 870 °C, above which the harder ferrite phase in steels is completely converted into the softer austenite phase. This transformation results in a drastic drop in the strength causing failure of the tube. The short-term overheating failures are characterized by considerable metal deformation, visible as elongation or thinning of the fractured surface. Wall thinning and local bulging precede the fracture because of the material's loss of strength at high temperatures. The wide “fish-mouth” opening, often much wider than the tube's diameter, has thin-edge fractured surfaces due to considerable swelling. Single or multiple short-term temperature excursions beyond 870 °C raise tube's temperature to an extent that it deforms under internal pressure. When the thickness of the tube reaches a limit, it yields to the hoop stress to cause the failure.

On the other hand, long-term overheating occurs at temperatures below 870 °C but above the normal operating temperature until the creep life is expended. During long-term overheating, steel's strength reduces gradually as it remains within the ferritic-bainitic microstructure regime. The failed tube is characterized by minimal swelling thickness reduction and a longitudinal split that is much narrow, compared to that in a short-term overheating failure, often less than the diameter of the tube itself.

Fig. 8.17 A photograph of an Alloy 625 tube failed by a characteristic fish-mouth opening of the tube under the influence of hoop stress



In the present case of fish-mouth failure of Alloy 625 tube, bulging and deformation of the metal before the fish-mouth opening and its width more than the diameter of the tube points to be a characteristic “short-term overheating” type of failure.

Conservative estimates give hoop stress of about 63 MPa to 8.9 mm thick cracker tubes of internal diameter about 71 mm and pressurized at 14 MPa. This hoop stress would rupture the tube at a thickness of about 4.6 mm at uniaxial stress above 106 MPa [34]. This stress exceeds the yield stress of Alloy 625 at temperatures above 1000 °C [26], indicating that the tube failed at a temperature above 1000 °C. Microstructural analysis of the region around the fish mouth revealed the presence of recrystallized grains. Recrystallization in this alloy occurs at temperatures over 1000 °C (Sect. 6.1). The microstructural analysis established temperature excursion of the tube over 1000 °C, which was attributed to burners or some other external heating source malfunctioning. At temperatures above 1000 °C and an internal pressure of 14 MPa, the tube would fail by creep rupture in about 2.8 h.

8.7 Summary

High-temperature creep and corrosion are the two most common life-limiting damage mechanisms at elevated temperatures. Alloy 625 is inherently stable against these two damages, at least in the intermediate range of its applications, because of its chemistry. While the alloy embrittles significantly during service degradation due to extensive microstructural modifications, it may not contribute towards the failure of components. Still, the alloy may be vulnerable to catastrophic failure under unfavorable conditions. This service damage can be reversed by appropriate solution annealing treatments. Several standard life management techniques can be effectively adapted to monitor service degradation and predict the remaining service life of Alloy 625 components.

References

1. Cortial F, Corrieu JM, Vernot-Loier C (1995) Influence of heat treatments on microstructure, mechanical properties, and corrosion resistance of weld alloy 625. *Metall Mater Trans A* 26:1273–1286. <https://doi.org/10.1007/BF02670621>
2. Floreen S, Fuchs GE, Yang WJ (1994) The metallurgy of alloy 625. In: Loria EA (ed), *Superalloys 718, 625, 706 various derivatives*. The Minerals, Metals & Materials Society, Pittsburgh, PA, USA, pp 13–38.
3. Eiselstein HL, Tillack DJ (1991) Superalloys 718, 625, 706 and various derivatives, In: Loria EA (ed) *Superalloys 718, 625, 706 various derivatives*. The Minerals, Metals, and Materials Society, Pittsburgh, PA, pp 1–14
4. Shoemaker LE (2005) In: Loria EA (ed) *Superalloys 718, 625, 706 derivatives*. The Minerals, Metals, and Materials Society, Pittsburgh, PA, pp 409–418
5. Vernot-Loier C, Cortial F (1991) Loria EA (ed) *Superalloys 718, 625 various derivatives*. The Minerals, Metals, and Materials Society, Pittsburgh, PA, pp 409–422
6. Rakowski JM, Stinner CP, Lipschutz M, Montague JP. In: Loria EA (ed) *Superalloys 718, 625, 706 derivatives*. The Minerals, Metals, and Materials Society, Pittsburgh, PA, pp 271–286
7. Shankar V, Bhanu Sankara Rao K, Mannan SL (2001) Microstructure and mechanical properties of Inconel 625 superalloy. *J Nucl Mater* 288:222–232. [https://doi.org/10.1016/S0022-3115\(00\)00723-6](https://doi.org/10.1016/S0022-3115(00)00723-6)
8. Sundararaman M, Kumar L, Prasad GE, Mukhopadhyay P, Banerjee S (1999) Precipitation of an intermetallic phase with Pt2Mo-type structure in alloy 625. *Metall Mater Trans A* 30:41–52. <https://doi.org/10.1007/s11661-999-0194-6>
9. Thomas C, Tait P (1994) The performance of Alloy 625 in long-term intermediate temperature applications. *Int J Press Vessel Pip* 59:41–49. [https://doi.org/10.1016/0308-0161\(94\)90140-6](https://doi.org/10.1016/0308-0161(94)90140-6)
10. Shankar V, Valsan M, Bhanu Sankara Rao K, Mannan SL (2001) Room temperature tensile behavior of service exposed and thermally aged service exposed alloy 625. *Scr Mater* 44:2703–2711. [https://doi.org/10.1016/S1359-6462\(01\)00965-4](https://doi.org/10.1016/S1359-6462(01)00965-4)
11. Chakravarthy JK, Singh JB, Sundararaman M (2012) Microstructural and mechanical properties of service exposed Alloy 625 ammonia cracker tube removed after 100,000 h. *Mater Sci Technol* 28:702–710. <https://doi.org/10.1179/1743284711Y.0000000118>
12. Singh JB, Verma A, Jaiswal DM, Kumar N, Patel RD, Chakravarthy JK (2015) Rejuvenation of service exposed ammonia cracker tubes of cast Alloy 625 and their re-use. *Mater Sci Eng A* 644:254–267. <https://doi.org/10.1016/j.msea.2015.06.098>
13. Suave LM, Cormier J, Villechaise P, Soula A, Hervier Z, Bertheau D, Laigo J (2014) Microstructural evolutions during thermal aging of alloy 625: Impact of temperature and forming process. *Metall Mater Trans A Phys Metall Mater Sci* 45:2963–2982. <https://doi.org/10.1007/s11661-014-2256-7>
14. Viswanathan R, Dooley RB (1986) Creep life assessment techniques for fossil power plant boiler pressure parts. In: Life prediction for high temperature gas turbine materials, pp 2.1–2.28
15. Viswanathan R (1989) Damage mechanisms and life assessment of high temperature components. ASM international
16. Coade R (1985) Temperature determination based on microstructural changes occurring in 1% Cr-0.5% Mo steel, Report No. SO/85/87. State Electricity Commission of Victoria, Australia
17. Kumar A, Rajkumar KV, Jayakumar T, Raj B, Mishra B (2006) Ultrasonic measurements for in-service assessment of wrought Inconel 625 cracker tubes of heavy water plants. *J Nucl Mater* 350:284–292. <https://doi.org/10.1016/j.jnucmat.2006.01.011>
18. Kumar A, Shankar V, Jayakumar T, Rao KBS, Raj B (2002) Correlation of microstructure and mechanical properties with ultrasonic velocity in the Ni-based superalloy Inconel 625. *Philos Mag A* 82:2529–2545. <https://doi.org/10.1080/01418610208240051>
19. Shankar V, Valsan M, Rao KBS, Mannan SL (2004) Effects of temperature and strain rate on tensile properties and activation energy for dynamic strain aging in alloy 625. *Metall Mater Trans A* 35:3129–3139. <https://doi.org/10.1007/s11661-004-0057-0>

20. Rosen M, Horowitz E, Fick S, Reno RC, Mehrabian R (1982) An investigation of the precipitation-hardening process in aluminum alloy 2219 by means of sound wave velocity and ultrasonic attenuation. *Mater Sci Eng* 53:163–177. [https://doi.org/10.1016/0025-5416\(82\)90049-0](https://doi.org/10.1016/0025-5416(82)90049-0)
21. Rosen M, Ives L, Ridder S, Biancaniello F, Mehrabian R (1985) Correlation between ultrasonic and hardness measurements in aged aluminum alloy 2024. *Mater Sci Eng* 74:1–10. [https://doi.org/10.1016/0025-5416\(85\)90104-1](https://doi.org/10.1016/0025-5416(85)90104-1)
22. Jayakumar T (1997) Microstructural characterisation in metallic materials using ultrasonic and magnetic methods. Saarbruecken, Germany
23. Kumar A, Jayakumar T, Raj B, Ray KK (2003) Correlation between ultrasonic shear wave velocity and Poisson's ratio for isotropic solid materials. *Acta Mater* 51:2417–2426. [https://doi.org/10.1016/S1359-6454\(03\)00054-5](https://doi.org/10.1016/S1359-6454(03)00054-5)
24. James LA (n.d.) Effect of temperature upon the fatigue-crack propagation behavior of Inconel 625. <https://doi.org/10.2172/7257141>
25. Anderson TL (2017) Fracture mechanics: fundamentals and applications. CRC Press, p 64
26. Data sheet Inconel alloy 625 (2013). <https://www.specialmetals.com/documents/technical-bulletins/inconel/inconel-alloy-625.pdf>
27. Neubauer B, Wedel U (1983) Rest life estimation of creeping components by means of replicas. In: Woodford DA, Whitehead JR (eds) Advances in life prediction methods. American Society of Mechanical Engineers, New York, pp 307–314
28. Aoto K, Wada Y (1995) Concept of design criteria of low dose irradiation for FBR structural materials. International Atomic Energy Agency (IAEA), IAEA-TECDOC-817, pp 79–87. http://inis.iaea.org/search/search.aspx?orig_q=RN:26077454
29. Raman VV, Prasad GE, Das Gupta P (1987) Deformation behaviour of Inconel 625 at various temperatures. *Trans Ind Inst Met* 40:113–120
30. Singh JB, Verma A, Paul B, Chakravarty JK (2013) Failure of Alloy 625 tube stub ends—Effect of primary nitrides. *Eng Fail Anal* 32:236–247. <https://doi.org/10.1016/j.engfailanal.2013.03.018>
31. Mathew MD, Bhanu Sankara Rao K, Mannan SL, Creep properties of service-exposed Alloy 625 after re-solution annealing treatment, *Mater Sci Eng A* 372:327–333. <https://doi.org/10.1016/j.msea.2004.01.042>
32. Mills WJ (1987) Fracture toughness of thermally aged alloy 718 weld metal. *Weld J* 66:113
33. Liu P, Nilsson J-O (1990) Effect of long term aging on mechanical properties and microstructure of nickel base weld. *Mater Sci Technol* 6:764–771. <https://doi.org/10.1179/mst.1990.6.8.764>
34. Singh JB, Verma A, Murty TN, Khan S, Karri M, Fish-mouth opening of an Alloy 625 ammonia cracker tube. *Eng Fail Anal* (Under Review)

Appendix A

Superalloy Compositions

This appendix gives nominal compositions of commonly used iron-based, nickel-based and cobalt-based superalloys. Some alloys, like Inconel 718, Incoloy 903, etc., contain nickel and iron in comparable amounts. Such alloys are also classified as iron-nickel alloys. However, this classification is ignored to restrict alloys to the three major categories based on the highest elemental concentration in their nominal compositions. These compositions are compiled based on the literature and the alloy's datasheets (Tables A.1, A.2, A.3, A.4).

Table A.1 Nominal compositions of selected wrought iron base superalloys

Alloy	Ni	Fe	Co	Cr	Mo	W	Nb	Al	Ti	C	Others
<i>Solid Solution hardened iron base superalloys</i>											
Alloy N-155 (Multimet)	20.0	32.2	20.0	21.0	3.0	2.5	1.0	—	—	0.15	0.15 N, 0.2 La, 0.02 Zr
Haynes 556	21.0	29.0	20.0	22.0	3.0	2.5	0.1	0.3	—	0.10	0.50 Ta, 0.02 La, 0.002 Zr
I9-9 DL	9.0	66.8	—	19.0	1.25	1.25	0.4	—	0.3	0.30	1.10 Mn, 0.60 Si
Incloy 800	32.5	45.7	—	21.0	—	—	—	0.38	0.38	0.05	—
Incloy 800 H	33.0	45.8	—	21.0	—	—	—	—	—	0.08	—
Incloy 800 HT	32.5	46.0	—	21.0	—	—	—	0.4	0.4	0.08	0.8 Mn, 0.5 Si, 0.4 Cu
Incloy 801	32.0	46.3	—	20.5	—	—	—	—	1.13	0.05	—
Incloy 802	32.5	44.8	—	21.0	—	—	—	0.58	0.75	0.35	—
Alloy 25-6Mo	25.0	Bal	—	20.0	6.5	—	—	—	—	—	2* Mn
RA 235MA	11.0	Bal	—	21.0	—	—	—	—	—	0.1*	0.8* Mn, 2.0* Si, 0.2* N, 0.055 Ce
<i>Precipitation hardened iron base superalloys</i>											
A-286	26.0	55.2	—	15.0	1.25	—	—	0.2	2.0	0.04	0.005 B, 0.3 V
Discaloy	26.0	55.0	—	14.0	3.0	—	—	0.25	1.7	0.06	—
Incloy 903	38.0	41.0	15.0	0.1*	0.1	—	3.0	0.7	1.4	0.04	—
Incloy 909	38.0	42.0	13.0	—	0.0	0.0	4.7	0.0	1.5	0.01	0.4 Si, 0.001 B
Pyromet CTX-1	37.7	39.0	16.0	0.1*	0.1	—	3.0	1.0	1.7	0.03	—
Incloy 907	38.4	42.0	13.0	—	—	—	4.7	0.03	1.5	0.01	0.15 Si
Incloy 909	38.0	42.0	13.0	—	—	—	4.7	0.03	1.5	0.01	0.4 Si

Table A.2 Nominal compositions of selected wrought cobalt base superalloys

Alloy	Ni	Fe	Co	Cr	Mo	W	Nb	Al	Ti	C	Others
<i>Solid solution hardened cobalt base superalloys</i>											
Haynes 25 (L605)	10.0	3.0	50.0	20.0	—	15.0	—	—	—	0.1	1.5 Mn
Haynes 188	22.0	3.0*	37.0	22.0	—	14.5	—	—	—	0.1	0.90 La
Alloy S-816	20.0	4.0	42.0	20.0	4.0	4.0	—	—	—	0.38	—
MP35-N	35.0	—	35.0	20.0	10.0	—	—	—	—	—	—
MP159	25.0	9.0	36.0	19.0	7.0	—	0.6	0.2	3.0	—	—
Stellite B	1.0	1.0	61.5	30.0	—	4.5	—	—	—	1.0	—
UMCo-50	—	1.0	49.0	28.0	—	—	—	—	—	0.12	—

Table A.3 Nominal compositions of selected wrought nickel base superalloys.

Alloy	Ni	Fe	Co	Cr	Mo	W	Nb	Al	Ti	C	Others
<i>Solid solution hardened nickel base superalloys</i>											
Alloy 28	31	37.0	—	27	3.5	—	—	—	—	0.02*	1.0 Cu, 2.0* Mn, 0.7* Si
Alloy 59	60	1.5*	0.3*	23	15.8	—	0.25	—	0.01*	0.1* Si	—
Haynes 214	76.5	3.0	—	16.0	—	—	4.5	—	0.03	—	—
Haynes 230	55.0	3.0*	5.0*	22.0	2.0	14.0	—	0.35	—	0.10	0.015* B, 0.02 La
Monel 400	65.0	2.5*	—	—	—	—	—	—	—	0.3*	31.0 Cu, 2.0* Mn, 0.5* Si,
Inconel 600	76.0	8.0	—	15.5	—	—	—	—	0.08	0.25 Cu	—
Inconel 601	60.5	14.1	—	23.0	—	—	—	1.35	—	0.05	0.5 Cu
Inconel 602	63.5	9.5	—	25.0	—	—	—	2.1	—	0.05	0.5 Zr, 0.5* Si
Inconel 617	55.0	—	12.5	22.0	9.0	—	—	1.0	—	0.07	—
Alloy 622	Bal	4.0	2.5*	21.5	13.5	3.0	—	—	—	0.015*	0.35* V, 0.5* Mn, 0.08* Si
Inconel 625	61.0	2.5	—	21.5	9.0	—	3.6	0.2	0.2	0.05	—
Inconel 686	Bal	5.0*	—	21.0	16.0	3.7	—	—	0.14	0.01*	0.75* Mn
Inconel 690	58.0	9.0	—	29.0	—	—	—	—	—	0.05*	0.5* Si, 0.5* Mn, 0.015* S, 0.5* Cu
RA333	45.0	18.0	3.0	25.0	3.0	3.0	—	—	—	0.05	—
Hastelloy B	63.0	5.0	2.5*	1.0*	28.0	—	—	—	—	0.05*	0.03 V
Hastelloy B3	65	1.5	3.0*	1.5	28.5	3.0*	0.2*	0.5*	0.2*	0.01*	3.0* Mn, 0.1* Si, 0.2* V, 0.2* Cu, 0.2* Ta, 0.01* Zr
Hastelloy C-4	65	3.0*	2.0*	16.0	16.0	—	—	—	0.7*	0.01*	1.0 Mn, 0.08 Si, 0.5 Cu
Hastelloy C-22	51.6	5.05	2.5	21.5	13.5	4.0	—	—	—	0.01*	1.0 Mn, 0.1 Si, 0.3 V
Hastelloy C-276	59.0	5.0	—	15.5	16.0	3.7	—	—	—	0.02*	1.0 Mn, 0.1 Si, 0.3 V
Hastelloy C-2000	59.0	3.0*	2.0*	23.0	16.0	—	0.5*	—	0.01*	1.6 Cu, 0.5 Mn, 0.08 Si	—

(continued)

Table A.3 (continued)

Alloy	Ni	Fe	Co	Cr	Mo	W	Nb	Al	Ti	C	Others
Hastelloy G	45.0	19.5	2.5*	22.3	6.0	1.0*	2.2	—	—	0.05*	1.5 Cu, 1.0* Si
Hastelloy G3	45.0	19.5	5.0*	22.3	6.0	1.5*	0.5*	—	—	0.05*	2.0 Cu, 1.0* Si
Hastelloy G-30	43.0	15.0	5.0*	30.0	5.5	2.5	0.8	—	—	0.03*	1.5* Mn, 0.8* Si, 2.0 Cu
Hastelloy N	72.0	5.0*	—	7.0	16.0	—	—	0.5*	0.06	—	
Hastelloy S	67.0	1.0	—	15.5	15.5	—	0.2	—	0.02*	0.02 La	
Hastelloy W	61.0	5.5	2.5*	5.0	24.5	—	—	—	0.12*	0.6 V	
Hastelloy X	49.0	15.8	1.5*	22.0	9.0	0.6	—	2.0	—	0.15	—
Haynes HR-120	37.0	33.0	3.0	25.0	2.5	2.5	0.7	0.1	—	0.05	0.7 Mn, 0.6 Si, 0.2 N, 0.004 B
Haynes HR-160	37.0	2.0	29.0	28.0	—	—	—	—	—	0.05	2.75 Si, 0.5 Mn
Nimonic 75	75.0	2.5	—	19.5	—	—	0.15	0.4	0.12	0.25* Cu	
Nimonic 86	65.0	—	—	25.0	10.0	—	—	—	—	0.05	0.03 Ce, 0.015 Mg
<i>Precipitation hardened Nickel base superalloys</i>											
Astroloy	56.5	< 0.3	15.0	15.0	5.25	—	—	4.4	3.5	0.06	0.03 B, 0.06 Zr
Custom Age 625 PLUS	61.0	5.0	—	21.0	8.0	—	3.4	0.2	1.3	0.01	—
Haynes 242	62.5	2.0*	2.5*	8.0	25.0	—	—	0.5*	—	0.10*	0.006* B
Haynes 244	61.0	1.0*	2.0*	8.0	22.5	6.0	—	0.5*	—	0.03*	—
Haynes 263	52.0	0.7	11.0	20.0	6.0	—	—	0.6	2.4	0.06	0.6 Mn, 0.4 Si, 0.2 Cu
Haynes R-41	52.0	5.0	15.0	19.0	10.0	—	—	1.5	3.1	0.09	0.5 Si, 0.1 Mn, 0.006 B
Inconel 100	60.0	< 0.6	15.0	10.0	3.0	—	—	5.5	4.7	0.15	1.0 V, 0.06 Zr, 0.015 B
Inconel 102	67.0	7.0	—	15.0	2.9	3.0	2.9	0.5	0.5	0.06	0.005 B, 0.02 Mg, 0.03 Zr
Alloy 901	42.5	36.2	—	12.5	6.0	—	—	2.7	0.10*	—	

(continued)

Table A.3 (continued)

Alloy	Ni	Fe	Co	Cr	Mo	W	Nb	Al	Ti	C	Others
Inconel 702	79.5	1.0	—	15.5	—	—	3.2	0.6	0.05	0.5 Mn, 0.2 Cu, 0.4 Si	
Inconel 706	41.5	37.5	—	16.0	—	—	0.2	1.75	0.03	2.9 (Nb + Ta), 0.15* Cu	
Incoloy 825	42.0	30.0	—	21.5	3.0	—	—	0.9	0.01	1.8 Cu, 1* Mn	
Incoloy 925	44.0	29.0	—	20.5	2.8	—	0.2	2.1	0.01	1.8 Cu	
Inconel 718	52.5	18.5	—	19.0	3.0	—	5.1	0.5	0.9	0.08*	
Inconel 721	71.0	6.5	—	16.0	—	—	—	—	3.0	0.4	2.2 Mn, 0.1 Cu
Inconel 722	75.0	7.0	—	15.5	—	—	0.7	2.4	0.04	0.5 Mn, 0.2 Cu, 0.4 Si	
Inconel 725	57.0	9.0	—	21.0	8.0	—	3.5	0.35*	1.5	0.03*	—
Inconel 751	72.5	7.0	—	15.5	—	—	1.0	1.2	2.3	0.05	0.25* Cu
Inconel 693	Bal	4.25	—	29.0	—	—	1.5	3.25	1.0*	0.15*	0.5* Si, 1.0* Mn, 0.01* S, 0.5* Cu
Inconel X-750	73.0	7.0	—	15.5	—	—	1.0	0.7	2.5	0.04	0.25* Cu
M-252	56.5	<0.75	10.0	19.0	10.0	—	—	1.0	2.6	0.15	0.005 B
MERL-76	54.4	—	18.6	12.4	3.3	—	1.4	5.1	4.3	0.02	0.35 Hf, 0.06 Zr
Nimonic 80A	73.0	1.5	1.0	19.5	—	—	—	1.4	2.25	0.05	0.10* Cu
Nimonic 90	55.5	1.5	18.0	19.5	—	—	—	1.4	2.4	0.06	—
Nimonic 95	53.5	5.0*	18.0	19.5	—	—	—	2.0	2.9	0.15*	+ B, + Zr
Nimonic 100	56.0	2.0*	20.0	11.0	5.0	—	—	5.0	1.5	0.30*	+ B, + Zr
Nimonic 105	54.0	—	20.0	15.0	5.0	—	—	4.7	1.2	0.08	0.005 B
Nimonic 115	55.0	1.0	15.0	15.0	4.0	—	—	5.0	4.0	0.20	0.04 Zr
C-263	51.0	0.7*	20.0	20.0	5.9	—	—	0.45	2.1	0.06	—
Pyromet 860	44.0	28.9	4.0	13.0	6.0	—	—	1.0	3.0	0.05	0.01 B

(continued)

Table A.3 (continued)

Alloy	Ni	Fe	Co	Cr	Mo	W	Nb	Al	Ti	C	Others
Pyromet 31	55.5	14.5	—	22.7	2.0	—	1.1	1.5	2.5	0.04	0.005 B
Refractaloy 26	38.0	16.0	20.0	18.0	3.2	—	0.2	2.6	0.03	0.015 B	
Rene 41	55.0	< 0.3	11.0	19.0	10.0	—	—	1.5	3.1	0.09	0.01 B
Rene 88	56.4	—	13.0	16.0	4.0	4.0	0.7	2.1	3.7	0.03	0.03 Zr
Rene 95	61.0	< 0.3	8.0	14.0	3.5	3.5	3.5	—	2.5	0.16	0.01 B, 0.05 Zr
Rene 100	61.0	1.0*	15.0	9.5	3.0	—	—	5.5	4.2	0.16	0.015 B, 0.06 Zr, 1.0 V
Udimet 500	48.0	4.0*	19.0	19.0	4.0	—	—	3.0	3.0	0.08	0.005 B
Udimet 520	57.0	—	12.0	19.0	6.0	1.0	—	2.0	3.0	0.08	0.005 B
Udimet 630	50.0	18.0	—	17.0	3.0	3.0	6.5	0.7	1.0	0.04	0.004 B
Udimet 700	53.0	< 1.0	18.5	15.0	5.0	—	—	4.3	3.4	0.07	0.03 B
Udimet 710	55.0	—	14.8	18.0	3.0	1.5	—	2.5	5.0	0.07	0.01 B
Udimet 720	55.0	—	14.8	18.0	3.0	1.25	—	2.5	5.0	0.035	0.03 Zr
Udimet 720LI	57.0	—	15.0	16.0	3.0	1.25	—	2.5	5.0	0.025	0.03 Zr
Unitemp AF2-1DA	59.0	< 0.5	10.0	12.0	3.0	6.0	—	4.6	3.0	0.35	1.5 Ta, 0.015 B, 0.1 Zr
Waspaloy	57.0	2.0*	13.5	19.5	4.3	—	—	1.4	3.0	0.07	0.006 B, 0.09 Zr

Table A.4 Nominal compositions of selected cast superalloys

Alloys	Ni	Fe	Co	Cr	Mo	W	Ta	Al	Ti	C	Other
<i>Nickel base superalloys</i>											
B-1900	64.0	—	10.0	8.0	6.0	—	4.0	6.0	1.0	0.1	0.015 B, 0.1 Zr
CMSX-2	66.2	—	4.6	8.0	0.6	8.0	6.0	5.6	1.0	—	6.0 Zr
CMSX-4	Bal	·	9.0	6.5	0.6	6.0	6.5	5.6	1.0	—	—
CMSX-6	Bal	—	5.0	10.0	3.0	—	2.0	4.8	4.7	—	—
CMSX-10 SC	Bal	—	1.5–9.0	1.8–4.0	0.25–2.0	3.5–7.5	7.0–10.0	5.0–7.0	0.1–1.2	—	6.0* Re
CoTaC 744	Bal	—	2.0	10.0	—	10.0	—	4.0	—	0.6	4.9 Nb
Hastelloy X	50.0	18	1.0	21.0	9.0	1.0	—	—	—	0.1	—
Inconel 100	60.5	—	15.0	10.0	3.0	—	—	5.5	5.0	0.18	0.01 B, 0.06 Zr, 1.0 V
Inconel 713C	74.0	—	—	12.5	4.2	—	1.75	6.0	0.8	0.12	0.012 B, 0.1 Zr, 0.9 Nb
Inconel 713LC	75.0	—	—	12.0	4.5	—	4.0	6.0	0.6	0.05	0.01 B, 0.1 Zr
Inconel 738	61.5	—	8.5	16.0	1.75	2.6	—	3.4	3.4	0.17	0.01 B, 0.1 Zr, 2.0 Nb
Inconel 792	60.0	—	9.0	13.0	2.0	4.0	—	3.2	4.2	0.2	0.02 B, 0.1 Zr, 2.0 Nb
Inconel 718	53.0	18.0	—	19.0	3.0	—	—	0.5	0.9	0.04	0.1 Cu, 5.0 Nb
X-750	73.0	7.0	—	15.0	—	—	—	0.7	2.5	0.04	0.25 Cu, 0.9 Nb
M-252	56.0	—	10.0	20.0	10.0	—	—	1.0	2.6	0.15	0.005 B
MAR-M 200	59.0	1.0	10.0	9.0	—	12.5	—	5.0	2.0	0.15	0.015 B, 0.05 Zr, 1.0 Nb
MAR-M 246	60.0	—	10.0	9.0	2.5	10.0	1.5	5.5	1.5	0.15	0.015 B, 0.05 Zr
MAR-M 247	59.0	0.5	10.0	8.25	0.7	10.0	3.0.	5.5	1.0	0.15	0.015 B, 0.05 Zr, 1.5 Hf
PWA 1480	Bal	—	5.0	10.0	—	4.0	12.0	5.0	1.5	—	—
PWA 1484	Bal	—	10.0	5.0	2.0	6.0	9.0	5.6	—	—	—

(continued)

Table A.4 (continued)

Alloys	Ni	Fe	Co	Cr	Mo	W	Ta	Al	Ti	C	Other
Rene 41	55.0	—	11.0	19.0	10.0	—	—	1.5	3.1	0.09	0.01 B
Rene 77	58.0	—	15.0	15.0	4.2	—	—	4.3	3.3	0.07	0.015 B, 0.04 Zr
Rene80	60.0	—	9.5	14.0	4.0	—	—	3.0	5.0	0.17	0.015 B, 0.03 Zr
Rene 80 Hf	60.0	—	9.5	14.0	4.0	—	—	3.0	4.8	0.08	0.015 B, 0.02 Zr, 0.75 Hf
Rene 100	61.0	—	15.0	9.5	3.0	—	—	5.5	4.2	0.18	0.015 B, 0.06 Zr, 1.0 V
Rene N4	62.0	—	7.5	9.8	1.5	6.0	4.8	4.2	3.5	0.06	0.004 B; 0.5 Nb, 0.15 Hf
RR 2000	Bal	—	15.0	10.0	3.0	—	—	5.5	4.0	—	—
SRR 99	Bal	—	5.0	8.0	—	10.0	3.0	5.5	2.2	—	—
Rene N5	Bal	—	8.0	7.0	2.0	5.0	7.0	6.2	—	—	—
Rene N6	Bal	—	10.0–15.0	4.25–6	0.5–2.0	5.0–6.5	7.0–9.25	5.0–6.25	—	—	—
Udimet 500	53.0	2.0	17.0	18.0	4	—	—	3.0	3.0	0.1	—
Udimet 700	53.5	—	18.5	15.0	5.25	—	—	4.25	3.5	0.1	0.03 B
Udimet 710	55.0	—	15.0	18.0	3.0	1.5	—	2.5	5.0	0.13	0.08 Zr
Waspaloy	57.5	1.0	13.5	19.5	4.2	—	—	1.2	3.0	0.07	0.005 B, 0.09 Zr
WAX-20(DS)	72.0	—	—	—	20	—	20	6.5	—	0.20	1.5 Zr
<i>Cobalt base superalloys</i>											
Haynes 21	3.0	1.0	64.0	27.0	5.0	—	—	—	—	0.25	—
Haynes 25; L-605	10.0	1.0	54.0	20.0	—	15.0	—	—	—	0.1	1.5 Mn, 0.4 Si
J-1650	27.0	—	36.0	19.0	—	12.0	2.0	—	3.8	0.20	0.02 B
MAR-M 302	—	0.5	58.0	21.5	—	10.0	9.0	—	—	0.85	0.005 B, 0.2 Zr
MAR-M 322	—	0.5	60.5	21.5	—	9.0	4.5	—	0.75	1.0	2 Zr

(continued)

Table A.4 (continued)

Alloys	Ni	Fe	Co	Cr	Mo	W	Ta	Al	Ti	C	Other
MAR-M 509	10.0	—	54.5	23.5	—	7.0	3.5	—	0.2	0.6	0.5 Zr
MAR-M 918	20.0	—	52.0	20.0	—	—	7.5	—	—	0.05	0.1 Zr
NASA Co-W-Re	—	—	67.5	3.0	—	25.0	—	—	1.0	0.40	1.0 Zr, 2.0 Re
S-816	20.0	4.0	42.0	20.0	4.0	4.0	—	—	—	0.4	4.0 Nb, 1.2 Mn, 0.4 Si
V-36	20.0	3.0	42.0	25.0	4.0	2.0	—	—	—	0.27	2.0 Nb, 1.0 Mn, 0.4 Si
W-152	—	2.0	63.5	21.0	—	11.0	—	—	—	0.45	2.0 (Nb + Ta)
X-40 (Stellite 31)	10.0	1.5	57.5	22	—	7.5	—	—	—	0.50	0.5 Mn, 0.5 Si

* Maximum; SC Single crystal

Appendix B

Mechanical Properties

See Tables B.1 and B.2.

References

1. Donachie MJ (2002) Superalloys: a technical guide, 2nd edn. Chapter 2, ASM International. ISBN 0-87170-749-7
2. Data Sheet Inconel 690 alloy, 2021. <https://www.specialmetals.com/documents/technical-bulletins/inconel/inconel-alloy-690.pdf>
3. Data Sheet Inconel 693 alloy, 2021. <https://www.specialmetals.com/documents/technical-bulletins/inconel/inconel-alloy-693.pdf>
4. Data sheet Custom Age 625 PLUS Alloy, 2021. <https://www.carpentertechnology.com/hubfs/7407324/Material%20Saftey%20Data%20Sheets/725.pdf>
5. Data sheet HAYNES 242 alloy, 2021. http://haynesintl.com/docs/default-source/pdfs/new-alloy-brochures/high-temperature-alloys/brochures/242-brochure.pdf?sfvrsn=a17229d4_28
6. Data sheet HAYNES 244 alloy, 2021. <http://haynesintl.com/docs/default-source/pdfs/new-alloy-brochures/high-temperature-alloys/brochures/244-brochure.pdf>
7. Khan T, Stohr JF, Bibring H (1980) Cotac 744: An optimized D.S. Composite for turbine blades. Superalloys 531–540. 10.7449/1980/Superalloys_1980_531_540

Table B.1 Room temperature tensile properties of selected wrought superalloys [1–6]

Alloy	Product form	Yield strength (MPa)	Ultimate tensile strength (MPa)	Elongation (%)	Thermal history
<i>Nickel base alloys</i>					
Astroloy	Bar	1050	1415	16	1093 °C/4 h/OQ + 871 °C/8 h/AC + 982 °C/4 h/AC + 649 °C/24 h/AC + 760 °C/8 h/AC
Cabot 214	–	560	915	38	1121 °C
Custom Age 625 Plus	Bar	1007	1287	31	1038 °C/2 h/AC + 760 °C/8 h/FC + 650 °C/8 h/AC
Custom Age 625 Plus Direct Age	Bar	1324	1448	21	732 °C/8 h/FC + 620 °C/8 h/FC
Custom Age 625 Plus CW & Age	Bar	1007	1287	31	38% CW + 650 °C/8 h/FC + 580 °C/8 h/AC
C-2000	Bar	359	758	67	1150 °C/WQ
D-979	Bar	1005	1410	15	1038 °C/1 h/OQ + 815 °C/6 h/AC + 704 °C/16 h/AC
Hastelloy C-22	Sheet	405	800	57	1121 °C/RQ
Hastelloy G-30	Sheet	315	690	64	1177 °C/RAC-WQ
Hastelloy S	Bar	455	845	49	1066 °C/AC
Hastelloy X	Sheet	360	785	43	1177 °C/1 h/RAC
Haynes 242	Bar	845	1290	45.7	925–1120 °C/AC + 650 °C/48 h
Haynes 244	Sheet	894	1387	35	1120 °C/WQ + 760 °C /16 h/ FC + 650 °C/32 h/AC
Haynes 230	Sheet	390	870	48	1232 °C/AC
Inconel 600	Bar	285	660	45	1121 °C/2 h/AC
Inconel 601	Sheet	455	740	40	1149 °C/1 h
Inconel 617	Bar	295	740	70	1177 °C/AC
Inconel 617	Sheet	345	770	55	1177 °C/0.2 h/AC
Inconel 625	Bar	490	965	50	1149 °C/1 h/WQ
Inconel 706	Bar	1005	1310	20	982 °C/1 h/AC + 815 °C/3 h/AC + 718 °C/8 h/FC + 621 °C/8 h/AC

(continued)

Table B.1 (continued)

Alloy	Product form	Yield strength (MPa)	Ultimate tensile strength (MPa)	Elongation (%)	Thermal history
Inconel 718	Bar	1185	1435	21	980 °C/1 h/AC + 718 °C/8 h/FC + 621 °C/18 h/AC
Inconel 718 Direct Age	Bar	1365	1530	16	718 °C/8 h/SC + 621 °C/8 h/AC
Inconel 718 Super	Bar	1105	1350	16	927 °C/1 h/AC + 718 °C/8 h/SC + 621 °C/8 h/AC
Inconel 690	Rod	334	690	50	1040 °C
Inconel 693	Rod	827	1210	47	1010 °C/0.5 h/AC + 650 °C/1000 h/AC
Inconel X750	Bar	815	1200	27	1150 °C/2 h/AC + 843 °C /24 h/AC + 705 °C/20 h/AC
M-252	Bar	840	1240	16	1038 °C/4 h/AC + 760 °C/16 h/AC
Nimonic 75	Bar	285	745	40	1052 °C/1 h/AC
Nimonic 80A	Bar	620	1000	39	1079 °C/8 h/AC + 704 °C/16 h/AC
Nimonic 90	Bar	810	1235	33	1079 °C/8 h/AC + 704 °C/16 h/AC
Nimonic 105	Bar	830	1180	16	1149 °C/4 h/AC + 1060 °C/16 h/AC + 849 °C/16 h/AC
Nimonic 115	Bar	865	1240	27	1191 °C/1.5 h/AC + 1099 °C/6 h/AC
Nimonic 263	Sheet	580	970	39	1149 °C/0.2 h/WQ + 799 °C/8 h/AC
Nimonic PE 11	Bar	720	1080	30	-
Nimonic PE 16	Bar	530	885	37	1038 °C/4 h /AC + 799 °C/2 h/AC + 699 °C/16 h /AC
Nimonic PK 33	Sheet	780	1180	30	1099–1156 °C/0.25 h/AC + 849 °C/4 h/AC
Pyromet 860	Bar	835	1295	22	-
Rene 41	Bar	1060	1420	14	1066 °C/4 h/AC + 760 °C/16 h/AC

(continued)

Table B.1 (continued)

Alloy	Product form	Yield strength (MPa)	Ultimate tensile strength (MPa)	Elongation (%)	Thermal history
Rene 95	Bar	1310	1620	15	899 °C/24 h + 1121 °C/1 h/OQ + 732 °C/64 h/AC
Udimet 500	Bar	840	1310	32	1079 °C/4 h/AC + 815 °C/24 h/AC + 760 °C/16 h/AC
Udimet 520	Bar	860	1310	21	1107 °C/4 h/AC + 815 °C/24 h/AC + 760 °C/16 h/AC
Udimet 700	Bar	965	1410	17	1177 °C/4 h/AC + 1079 °C/4 h/AC + 815 °C/24 h/AC + 760 °C/16 h/AC
Udimet 710	Bar	910	1185	7	1177 °C/4 h/AC + 1079 °C/4 h/AC + 815 °C/24 h/AC + 760 °C/16 h/AC
Udimet 720	Bar	1195	1570	13	1113 °C/2 h/AC + 1079 °C/4 h/OQ + 649 °C/24 h/AC + 760 °C/8 h/AC
Unitemp AF2-1DA6	Bar	1015	1560	20	1149 °C/4 h/AC + 760 °C/16 h/AC
Waspaloy	Bar	795	1275	25	1079 °C/4 h/AC + 815 °C/24 h/AC + 760 °C/16 h/AC
<i>Iron-base alloys</i>					
A-286	Bar	725	1005	25	982 °C/1 h/OQ + 718 °C/16 h/AC
Alloy 901	Bar	895	1205	14	1093 °C/2 h/WQ + 788 °C/2 h/AC + 718 °C/24 h/AC
Discaloy	Bar	730	1000	19	1010 °C/2 h/OQ + 732 °C/20 h/AC + 649 °C/20 h/AC
Haynes 556	Sheet	410	815	48	1177 °C/AC
Incoloy 800	Bar	250	595	44	980 °C/0.25 h
Incoloy 825	Bar	310	690	45	940 °C/1 h

(continued)

Table B.1 (continued)

Alloy	Product form	Yield strength (MPa)	Ultimate tensile strength (MPa)	Elongation (%)	Thermal history
Incoloy 903	Bar	1105	1310	14	815 °C/1 h/WQ + 718 °C/8 h/FC + 621 °C/8 h/AC
Incoloy 907	...	1110	1365	12	980 °C/1 h/AC + 720 °C/8 h/FC + 620 °C/8 h/AC
Incoloy 909	Bar	1020	1310	16	982 °C/1 h/WQ + 718 °C/8 h/FC + 621 °C/8 h/AC
N-155	Bar	400	815	40	1177 °C/1 h/WQ + 816 °C/4 h/AC
V-57	Bar	830	1170	26	982 °C/2–4 h/OQ + 732 °C/16 h/AC
<i>Cobalt base Alloys</i>					
Haynes 188	Sheet	485	960	56	1177 °C/1 h/RAC
L-605	Sheet	460	1005	64	1232 °C/1 h/RAC
MAR-M918	Sheet	895	895	48	1191 °C/4 h/AC
MP35N	Bar	1620	2025	10	53% CW + 566 °C/4 h/AC
MP159	Bar	1825	1895	8	48% CW + 679 °C/4 h/AC
Stellite 6B	Sheet	635	1010	11	1232 °C/AC

OQ Oil quench; AC Air cooled; RQ Rapid quench; RAC Rapid air cooled; WQ Water Quenched; FC Furnace cooled; CW Cold worked; SC Slow cooled

Table B.2 Room temperature tensile properties of selected cast superalloys [1, 7]

Alloy	0.2% Yield strength (MPa)	Ultimate tensile strength (MPa)	Tensile elongation (%)
<i>Nickel base</i>			
B-1900	825	970	8
CMSX-2(<i>a</i>)	1135	1185	10
CoTaC 744 DS(<i>b</i>)	–	1505	13
GMR-235	640	710	3
IN-100	850	1018	9
IN-162	815	1005	7
IN-625	350	710	48
IN-713 C	740	850	8
IN-713 Hf(<i>c</i>)	760	1000	11
IN-713 LC	750	895	15
IN-718	915	1090	11
IN-731	725	835	6.5
IN-738	950	1095	-
IN-792	1060	1170	4
IN-939	800	1050	5
M-22	685	730	5.5
MM 002(<i>d</i>)	825	1035	7
MAR-M 200 Hf(<i>e</i>)	825	1035	5
MAR-M200	840	930	7
MAR-M246	860	965	5
MAR-M 246 Hf(<i>f</i>)	860	1105	6
MAR-M247	815	965	7
MAR-M421	930	1085	4.5
MAR-M432	1070	1240	6
MC-102	605	675	5
Nimocast 75	179	500	39
Nimocast 80	520	730	15
Nimocast 90	520	700	14
Nimocast 242	300	460	8
Nimocast 263	510	730	18
PWA-1480(<i>a</i>)	895	-	4
Rene 125 Hf(<i>g</i>)	825	1070	5

(continued)

Table B.2 (continued)

Alloy	0.2% Yield strength (MPa)	Ultimate tensile strength (MPa)	Tensile elongation (%)
Udimet 500	815	930	13
Udimet 710	895	1075	8
<i>Cobalt-base</i>			
Haynes 1002	470	770	6
MAR-M 302	690	930	2
MAR-M 322	630	830	4
MAR-M 509	570	785	4
W-152	585	750	5
X-40	525	745	9

(a) Single crystal [001]; (b) Directionally solidified; (c) MM 004;
 (d) RR-7080; (e) MM 009; (f) MM 006; (g) M 005

Appendix C

Physical Properties of Alloy 625

This appendix gives important physical, thermal and electrical constants and hydrogen permeability of Alloy 625 as a function of temperature. [1,2,3]

1. Thermal Conductivity, Electrical Resistivity and Coefficient of Thermal Expansion

Figure C.1 shows variation in thermal conductivity (K), electrical resistivity (ρ) and coefficient of thermal expansion (α) as a function of temperature, which can be expressed in the form of polynomial relationships.

$$1.1. \text{Thermal Conductivity (in W/m}\cdot\text{C):} K = 9.3 + 0.016 T$$

$$1.2. \text{Electrical Resistivity (in }\mu\Omega\text{-cm):} \rho = 129.08 + 0.03 T - 2.02 \times 10^{-5} T^2$$

$$1.3. \text{Coefficient of Thermal Expansion (in }\mu\text{m}/\mu\Omega\cdot\text{C):} \alpha = 12.65 + 0.01 T - 3.47 \times 10^{-6} T^2 - 5.91 \times 10^{-10} T^3$$

2. Modulus of Elasticity

Modulus of elasticity in tension and shear are commonly known as Young's modulus (E) and shear modulus (G). Fig.C.2 shows variations in the two moduli of Alloy 625 as a function of temperature. These moduli of the alloy, in solution treated and annealed conditions, can be expressed as:

$$E_{\text{Solution Treated}} = 205.58 - 0.052 T - 1.52 \times 10^{-5} T^2$$

$$E_{\text{Annealed}} = 207.45 - 0.035 T - 3.75 \times 10^{-5} T^2$$

$$G_{\text{Annealed}} = 82.02 - 0.019 T - 1.27 \times 10^{-5} T^2$$

$$G_{\text{Solution Treated}} = 78.47 - 0.02 T - 5.08 \times 10^{-5} T^2$$

Where moduli are expressed in GPa and temperature in degree Celsius.

3. Hydrogen Gas Permeability

The hydrogen permeation of Alloy 625 is controlled by bulk diffusion of hydrogen. The permeation rate (ϕ) of hydrogen as a function of temperature across a sheet

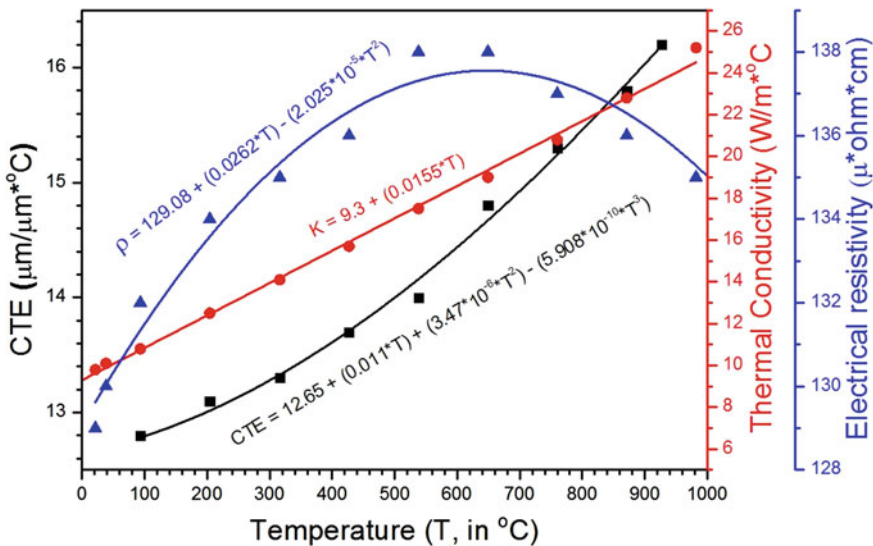


Fig. C.1 Coefficient of thermal expansion (CTE), thermal conductivity and electrical resistivity of Alloy 625 as a function of temperature

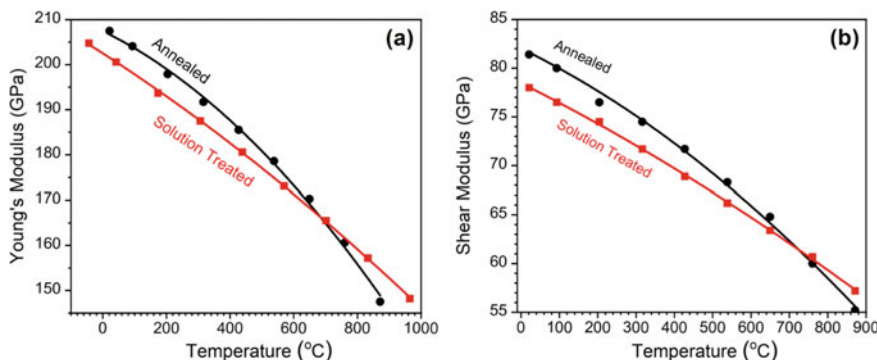


Fig. C.2 Variation in the (a) Young's and (b) shear moduli of Alloy 625, in solution treated and annealed conditions, as a function of temperature.

of Alloy 625 of surface area (A) and thickness (x) obeys a half-power pressure (P) dependence given by the equation [3]

$$\phi = \phi_o \left(\frac{A}{x} \right) P^{1/2} \exp \left(\frac{60, 128}{RT} \right)$$

where ϕ is in units of μmol (of H_2)/s, $\phi_0=8.113 \mu\text{mol}$ (of H_2)/ $\text{m}\cdot\text{s}\cdot\text{kPa}^{1/2}$, P is in kPa, T is temperature in Kelvin (K), x and A are in m and m^2 , respectively, $R = 8.3147 \text{ J/mol}\cdot\text{K}$.

References

1. Inconel alloy 625 Data Sheet, 2021,<https://www.specialmetals.com/documents/technical-bulletins/inconel/inconel-alloy-690.pdf>
2. Haynes 625 alloy Data sheet, 2021, https://www.haynesintl.com/docs/default-source/pdfs/new-alloy-brochures/high-temperature-alloys/brochures/625-brochure.pdf?sfvrsn=967229d4_26
3. E.H. Van Deventer and V.A. Maroni, Journal of Nuclear Materials, vol. 92, (1980) pp.103-111.

Appendix D

Metallography of Alloy 625

Alloy 625 sample preparations for metallographic examination is relatively straightforward. Still, special precautions are required during sample preparations to reveal the actual microstructure comprising of the various hardening phases. Further, the alloy's high corrosion resistance makes its etching somewhat tricky. This appendix gives some guidelines to prepare metallography samples of Alloy 625. Though most procedures are standard for all superalloys, specific ones for Alloy 625 are highlighted.

Grinding and Polishing

Sectioning of samples is recommended by quality carborundum/diamond cut-off wheels to minimise damage to the sample. Grinding of the alloy must be performed using a series of water-lubricated SiC papers of 120, 240, 320, 400 and 600 grit sizes. The sample must be ground for about 1 – 2 min with each grit paper on a rotating wheel at a speed of about 240–300 rpm or on a belt with equivalent speed. The specimen must be rotated by 45° to 90° between papers to remove the effects of grinding direction. Table D.1 gives metallography steps and parameters

Table D.1 Steps and parameters recommended for the preparation of metallography samples of Alloy 625

Preparation steps	Abrasive type	Speed (rpm)	Time (minutes)
Grinding	SiC water-cooled paper (Size 120 – 600 grit)	250–300	Until plane surface
Polishing	Diamond suspension/paste (9 µm)	100–150	5
	Diamond suspension/paste (3 µm)	100–150	4
	Diamond suspension/paste (1 µm)	100–150	3
Finishing	Alumina slurry (0.05 µm)	80–150	2

for preparing Alloy 625 samples. The samples must be washed thoroughly using a soap solution or a suitable solvent while going to the higher grit size paper. If the samples are likely to contain pores and cracks, ultrasonic cleaning is recommended during their washing. The ground samples should be polished following a four-step polishing commencing with a 9 or 6 μm diamond abrasive paste or slurry with an appropriate liquid extender/lubricant on a cloth pad. Wheel speeds are lower for polishing, generally 100–150 rpm. The polishing steps are listed in Table D.1. Careful cleaning of the sample between polishing steps, as in grinding, is required during polishing. The finishing polish must be with abrasive alumina of 0.3 μm alpha-alumina or 0.05 μm gamma-alumina suspension. The use of colloidal silica for the final polish may be problematic as it may darken the surface while etching, as noted later. After the final polish, clean the surface carefully to remove abrasives by scrubbing with a cotton soaked in a liquid detergent solution. Dry the surface with hot air.

Etching

The use of etchant depends upon the specific feature to be revealed. Alloy 625 microstructure may contain various second-phase particles in an austenitic matrix. The alloy may contain particles of the γ'' , δ , nitrides or carbides of MC, M_2C_6 and M_6C types and topologically-close packed phases. The precipitation-hardenable variant of the alloy, Alloy 625 PLUS, may also contain γ' phase particles. Particles of the γ' or γ'' phase are too fine to resolve by optical microscopy. However, overaged γ'' phase particles can be seen in a scanning electron microscope equipped with a field emission gun. Optical microscopy can reveal the dendritic structure of a cast alloy, and grain boundaries and coarse particles of the δ and carbide phases of a wrought alloy. Figure D.1 shows an optical microstructure of cast Alloy 625.

Etchants commonly used to reveal the general structure of superalloys are listed in Table D.2. Due to the excellent corrosion resistance of superalloys, most etchants work best by swabbing the specimen with cotton soaked in the etchant. Immersion etching without stirring may result in irregular etching. Most etchants must be mixed fresh and used within a short period. Glyceregia is the mildest of all. Etchants 2 and 3 are listed in increasing strength. The quality of etching of Alloy 625 is sensitive to the surface finish, especially for wrought alloys. The surface must be scratch-free to reveal the structure properly. Figure D.2 compares the quality of the microstructures of a sample after different levels of the surface finish.

Etching of a polished surface with scratches, particularly with chloride ion containing etchants like Glyceregia. Glyceregia takes about a minute of swabbing to reveal the microstructure. However, reagents like Glyceregia with chloride ions may cause ‘flashing’ of the surface upon etching, particularly when colloidal silica is used for the final surface polish. Flashing refers to the darkening of the surface immediately upon etching. Examination of the surface shows deep scratches while

Table D.2 A list of etchants that can be used to etch Alloy 625 samples. It is recommended to prepare fresh etchants every time and use them for a short period

S. No	Etchant		Comment
	Acid solution	Common name	
1	15 ml HCl, 10 ml glycerol, 5 ml HNO ₃	Glyceregia	General-purpose etching. Swab for about 30 s to a minute
2	15 ml HCl, 10 ml Acetic acid, 5 ml HNO ₃ , 2 drops glycerol	Acetic glyceregia	General-purpose etching. Swab for about 30 s to a minute
3	15 ml HCl, 10 ml Acetic acid, 10 ml HNO ₃	15–10–10 reagent	General-purpose etching. Swab for a few seconds
4	5 g CuCl ₂ , 100 ml HCl, 100 ml ethanol	Waterless Kalling's reagent	Good grain boundary etching. Swab for a few seconds
5	150 ml HCl, 50 ml lactic acid, 3 g oxalic acid	Lucas reagent	General-purpose etchant. Etch the surface electrolytically at 1–2 V dc for 10 – 20 s

the microstructure is poorly revealed. Flashing occurs due to the passivation of the surface. The surface needs to be re-polished to remove these scratches.

Colour etching of nickel-based superalloys is rather tricky. Very high-quality surface polish is required to develop the tint. After the final polish, the sample should be electropolished in a supersaturated oxalic acid solution at ~ 2 V at about –40 °C. After electropolishing, the sample surface must be cleaned carefully with cotton soaked in a soap solution to remove any residue interfering with film formation in tint etching. For tint etching, an etchant comprising 50 ml demineralised water, 50 ml HCl, 0.8 g Potassium Metabisulfite (K₂S₂O₅) and 15 g Ammonium bifluoride (NH₄HF₂) may be used. The etchant should be prepared in a polypropylene beaker by first adding 50 ml HCl to 50 ml DM water and stirring. 0.8 g K₂S₂O₅ and 15 g NH₄HF₂ are added by continuous stirring until they dissolve completely. Etching must be done by immersing the electropolished sample in the solution for about 15 min until a blue surface colouration is developed. A continuous gentle swirling is required to avoid settling any reaction by-products on the sample surface. After etching, wash the sample with water and dry. Examine the etched surface under an optical microscope with bright field illumination using the colour filter. The δ phase appears as light blue and carbides as golden yellow in a light brown background of the γ phase matrix (Fig. D.3).

Fig. D.1 Optical microstructure of cast Alloy 625 etched with 15-10-10 etchant

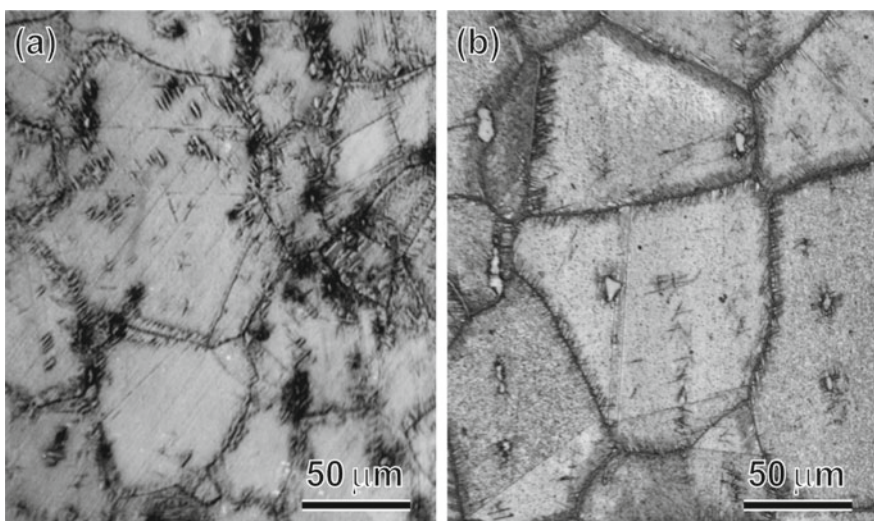
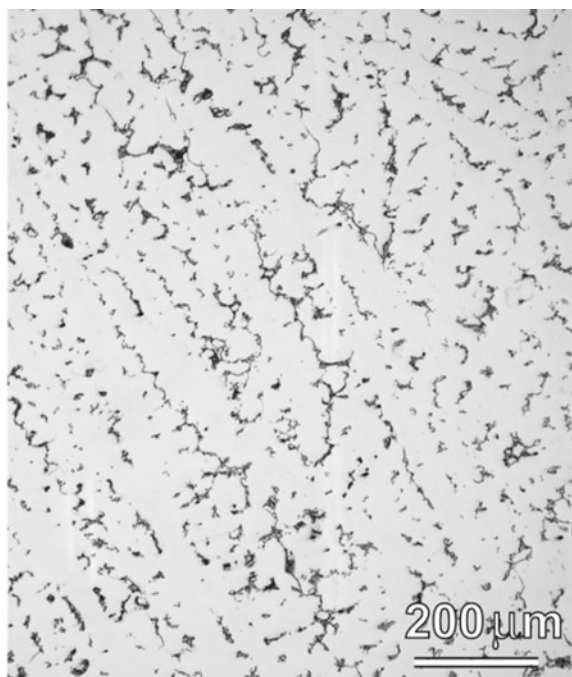


Fig. D.2 Optical microstructure of a service exposed wrought Alloy 625 etched with 15-10-10 etchant. The quality of the surface after the final polish in (a) was relatively poor compared to that in (b)

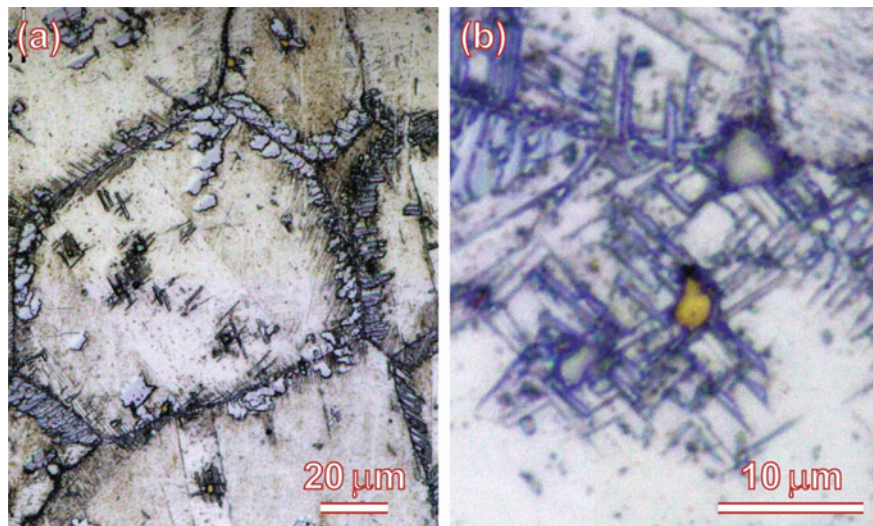


Fig. D.3 Tint microstructure of the wrought Alloy 625 shown in fig.D.2 showing **a** the δ phase particles in light blue and **b** a primary carbide particle in golden yellow in a light brown background of the γ phase matrix.

Appendix E

Hardness Conversion Table

The hardness of a material can be measured using various techniques. All these techniques have their own scales. The use of a technique and the scale depends on the material's strength and work-hardening behaviour. The scales and their ranges are limited by the type of indenter (penetrator), and the capacity of the load applied. The most commonly used hardness techniques are Rockwell hardness, Vickers hardness and Brinell hardness. The Brinell hardness tester uses a 10-mm-diameter steel ball at a load of 3000 kg, while the Vickers tester uses a square-base diamond pyramid indenter with an angle of 136° between the opposite faces. Vickers and Brinell hardness numbers are designated by VHN and BHN, respectively. The Rockwell technique uses many indenters with different loads. The Rockwell technique measures hardness over a wide range and rates it on multiple scales depending upon the indenter and the load used. Different Rockwell hardness scales are identified by letters indicating A, B, C, D, etc. For example, HRA refers to Rockwell hardness scale A, HRB refers to Rockwell hardness scale B, etc. Rockwell A, B and C scales are the most commonly used. Rockwell A and C use a 120° diamond cone indenter with a slightly rounded point, called a *Braze indenter*, at 60 kg and 150 kg loads, respectively. The Rockwell C scale is used for harder materials with a range of about 20 to 70 HRC. On the other hand, the Rockwell A scale provides the most extended Rockwell hardness scale for various materials over a wide range of hardness values. The softer materials are usually tested on the Rockwell B scale with a 1.6 mm diameter steel ball and a 100 kg load. The range of the Rockwell B scale is from 0 to 100 HRB.

A direct correlation between different hardness scales is difficult to establish because of inaccuracies associated with its measurements by different indenters and the local variations in the material's strength. Nonetheless, some empirical hardness conversion tables have been established based on the vast data for various steel grades. Besides, the hardness of steels has also been correlated with their ultimate tensile strengths. This appendix gives these tables, which can help convert the hardness of one scale to another in the overlapping hardness range (Table E.1).

Table E.1 Table correlates the room temperature hardness on different hardness scales and tensile strength of steels

Rockwell C (HRC)	Rockwell B (HRB)	Rockwell A (HRA)	Brinell (HBN)	Vickers (HVN)	Tensile strength (MPa)
	56.2		95	100	320
	62.3		105	110	350
	66.7		114	120	385
	71.2		124	130	415
	75.0		133	140	450
	78.7		143	150	480
	81.7		152	160	510
	85.0		162	170	545
	87.1		171	180	575
	89.5		181	190	610
	91.5		190	200	640
	93.5		199	210	675
	95.0		209	220	705
	96.7		219	230	740
20	97.6	60.5	226	238	760
21	98.1	61	231	243	770
22	99.0	61.5	237	248	790
23		62	243	254	810
24		62.4	247	260	820
25		62.8	253	266	850
26		63.3	258	272	860
27		63.8	264	279	880
28		64.3	271	286	900
29		64.6	279	294	930
30		65.3	286	302	950
31		65.8	294	310	970
32		66.3	301	318	1010
33		66.8	311	327	1030
34		67.4	319	336	1050
35		67.9	327	345	1080
36		68.4	336	354	1110
37		68.9	344	363	1140
38		69.4	353	372	1180
39		69.9	362	382	1220

(continued)

Table E.1 (continued)

Rockwell C (HRC)	Rockwell B (HRB)	Rockwell A (HRA)	Brinell (HBN)	Vickers (HVN)	Tensile strength (MPa)
40		70.4	371	392	1250
41		70.9	381	402	1300
42		71.5	390	412	1340
43		72	400	423	1390
44		72.5	409	434	1430
45		73.1	421	446	1480
46		73.6	432	458	1520
47		74.1	442	471	1580
48		74.7	455	484	1640
49		75.2	468	498	1700
50		75.9	482	513	1760
51		76.3	496	528	1820
52		76.8	512	544	1880
53		77.4	525	560	1950
54		78	543	577	2010
55		78.5	560	595	2070
56		79	577	613	2160
57		79.6	595	633	2240
58		80.1	615	653	2330
59		80.7	634	674	2420
60		81.2	654	697	—
61		81.8	670	720	—
62		82.3	688	746	—
63		82.8	706	772	—
64		83.4	722	800	—
65		83.9	739	832	—
66		84.5	—	865	—
67		85	—	900	—
68		85.6	—	940	—